A STUDY OF BREAKWATER GAP WAVE DIFFRACTION USING CLOSE RANGE PHOTOGRAMMETRY AND FINITE AND INFINITE ELEMENTS

by

J.D. POS

A thesis submitted for the degree of Doctor of Philosophy in the Faculty of Engineering, University of Cape Town

February 1984

Department of Civil Engineering
University of Cape Town

INSTRUCTIONS FOR THE USE OF THE POCKET STEREO VIEWER

1) Lay the book down flat on a table.

2) Hold the stereo viewer approximately 110 mm above the stereo-pair so that the left eye-piece is directly above the left photo and the right eye piece is directly above the right photo.

3) Adjust the eye base of the viewer to be compatible with that of the observer.

4) Rotate the viewer slightly about the vertical axis until the stereomodel is established.

to

my parents

DECLARATION

I, John Daniel Pos, hereby declare that this thesis is my own work and that it has not been submitted for a degree at any other University.

Signed by candidate

February, 1984

ABSTRACT

In this thesis the diffraction of water waves passing through a gap in a breakwater is investigated experimentally, using close range photogrammetry, and numerically, using finite and infinite elements. The author was particularly interested in validating specific breakwater gap diffraction diagrams given in popular coastal engineering design manuals. Breakwater gap configurations with the following gap width to wave length ratios (B/L ratios) were analysed, both experimentally and numerically, namely: B/L = 1,64; 1,41; 1,2; 1; 0,75; 0,5. These configurations are symmetrical, i.e. both breakwater arms lie on the same straight line. An asymmetrical B/L = 1,64 breakwater gap configuration was also analysed.

Previous experimental breakwater gap diffraction investigations are reviewed leading to the conclusion that the reported results are inconclusive due to (1) the relatively poor accuracy with which the wave heights were measured and (2) secondary basin effects which were superimposed upon and thus distorted the pure diffraction phenomena.

In the experimental breakwater gap configurations investigated by the author, splitter plates were used to eliminate the reflection problems on the seaward side of the breakwaters, whilst a novel photogrammetric wave height measurement technique was used to measure accurately the wave heights in the entire basin, before they could be distorted by reflecting waves, basin resonance effects, etc. This "infinite basin technique" was used to simulate experimentally and measure the diffraction of a continuous wave train entering an infinite basin via a gap in an approximate totally absorbing breakwater.

A number of different photogrammetric wave height measurement techniques based on analogue procedures, the theory of projective transformations, and the theory of the deformed reference plane, are investigated and developed. It was found that the technique based on the projective transformation theory, and in which the plates are analysed using a stereocomparator linked to a microcomputer, is the most accurate. Using this technique it was found that, with the cameras situated approximately 5 m above the water surface, the wave heights in the basin can be measured with an accuracy of better than 2 mm. The above method, in conjunction with the infinite basin technique, was used to analyse the experimental breakwater gap configurations.

The basic linear wave theory is described leading to the derivation of the Helmholtz diffraction equation. The classical diffraction theories for the semi-infinite breakwater and breakwater gap configurations are reviewed and compared. The Berkhoff refraction - diffraction equation is then briefly derived.

A review of previous numerical refraction - diffraction investigations, and also of modern numerical methods for water wave diffraction and refraction - diffraction, is given. This review led to the adoption of the finite and infinite element program "WAVE", developed at the University College of Swansea, to model numerically the experimental breakwater gap configurations. The use of the "WAVE" program to model breakwater gap wave diffraction is novel and certain conceptual problems had to be overcome.

Finally, the experimental and numerical diffraction diagrams obtained were compared to analytical diagrams where these were available. The correlation between the finite element and analytical results is excellent. When comparing the experimental and finite element results the general conclusions are : 1) in regions outside the shadow zones the linear diffraction theory is conservative except close to small gaps ($B/L \leq 1$); and 2) within the shadow zones the linear theory is <u>not</u> conservative and one will have to allow for non-linear effects such as radiating second-order waves generated at the breakwater tips, and increased wave orthogonal spreading near the gap centre line and subsequent orthogonal bunching in the shadow zones caused by wave steepness differences along the crests.

Other conclusions drawn are : 1) the photogrammetric techniques described are the best available for the experimental simulation and analysis of infinite domain diffraction and refraction - diffraction problems; and 2) the finite and infinite element program "WAVE" is a very useful tool for the prediction of wave heights in large harbour basins.

ACKNOWLEDGEMENTS

I would like to thank my thesis supervisors Professor F.A. Kilner of the Department of Civil Engineering, and Professor L.P. Adams of the Department of Surveying, University of Cape Town, for their encouragement and assistance during the four plus years of this project. Their patience and guidance was much appreciated. I would also like to thank Professor G.B. Brundrit; Head of the Department of Physical Oceanography, for his help with the theoretical aspects of this thesis.

A particular word of thanks must go to Dr. Peter Bettess of the University College of Swansea, Wales, for his help and support to date. Dr. Bettess, through his prompt and helpful correspondence, has in no small part ensured the success of the finite element aspects of this thesis.

I extend thanks to past and present staff and graduate students of the Department of Civil Engineering and the Nonlinear Structural Mechanics Research Group, and particularly to Professor J.B. Martin. I would also like to thank, in alphabetical order, Gino Duffett, Dave Hawla, Graham Howell, Dr. Andy Loyd, Colin Mercer, Dr. Daya Reddy and Luis Resende for their assistance with the numerical aspects of this thesis.

I would also like to thank Dr. Heinz Rüther and Linsey Welham (ex post-grad student) of the Department of Surveying for their help with the photogrammetric aspects of this thesis. I would like to thank Mrs Alice Ackhurst for the accurate stereoplotter work that she did during the initial experimental phase.

As regards the technical and experimental aspects, I would like to thank Messrs R.F. Beverton, G. Bertuzzi, D.J. Botha and R. Edge for their help with the construction of the experimental photogrammetric wave basin configuration. I would like to thank Robin Edge for also making the pocket stereo viewers. I would like to thank Mr H.F. Weehuizen (ex Dept. Electrical Engineering) for the design and construction of the electronic parallax bar (and interface) and the stereocomparator/micro-computer interfaces. I would also like to thank Richard Smith, Jonathan Rosenblitt and Alton Hulme for their assistance with certain aspects of the experimental work.

I would also like to extend thanks to my current associates at the National Research Institute for Oceanology (NRIO). In particular,

I would like to thank Dr. John Gonsalves for his help with the finite element aspects. I would also like to thank Mr F.P. Anderson and Mr K.S. Russell for allowing me to take leave to complete my thesis.

A final word of thanks must go to Ms A Edwards and Mrs A Burbach who skilfully typed this thesis.

CONTENTS

NOMENCLATURE

a_0 -- a_5 or a_6	transformation parameters for the deformed reference plane equations
a_{ij}	transformation parameter
$\bar{a}$	the vector of nodal unknowns (finite elements)
$\bar{a}_i$	the nodal unknowns
arg	argument
A	matrix of the coefficients of the unknowns (photogram.)
A^T	transpose of the A matrix
AE	average absolute error
b_{ij}	(new) projective transformation parameter = a_{ij}/a_{34} when unbarred denotes parameter for left plate and when barred i.e. $\bar{b}_{ij}$ denotes parameter for right plate
B	matrix of coefficients of the corrections to the measurements (photogram.) also : width of breakwater gap
B^T	transpose of the B matrix
B_d	dimensionless gap width = B/L
B	base length (photogram.)
c	wave celerity
$\bar{c}$	$= (\pi B/L)^2$
c_g	group velocity = $\bar{n}c$
C_i	constants
d	water depth
d´	dimensionless water depth = $d/\bar{D}$
dh_i	$= h_i - h_{CR_i}$ = height difference due to deformation of the reference plane

D	distance from the wave paddle to the back wall beach
$\bar{D}$	mean water depth
De_n	Mathieu coefficients
e	base of natural logarithms
exp	exponential
f	principal distance (photogram.)
f_x, f_y	calculated principal distances eq.(Ch.4-23) average of both = f
$\bar{f}$	global load vector (finite elements)
$\bar{f}_i$	terms of the global load vector
$\bar{f}^e$	element load vector
$\bar{f}^e_i$	terms of the element load vector
$f(\bar{\sigma})$	see equation (Ch. 2-38)
f_1	see equation (Ch. 2-46)
F_1	$= - f_1 \pm g_1$
F_R	weighting factor for the second term of equation (Ch. 2-36) for various degrees of reflection
g	acceleration due to gravity
g_1	see equation (Ch. 2-47)
G	matrix of the transformation parameters for the deformed reference plane
h_i	height of point i above datum (photogram.)
h_{CR_i}	crude height of point i
H	wave height at any point
H_i	incident wave height
H_r	reflected wave height
$\bar{H}$	Hankel function of the first kind

H_f	flying height (photogram.)
i	imaginary unit = $\sqrt{-1}$
I	Intensity Factor
I_1, I_2, I_3	shape functions in the $\bar{s}$ direction for the infinite element
J	Bessel function of the first kind
Je_m	radial Mathieu function
k	wave number = $\pm k_0 \pm \sum_{j=1}^{\infty} k_j$
k_0	real part of k = $2\pi/L$
k_j	imaginary parts of k
K	global stiffness matrix (finite elements)
K_{ij}	terms of the global stiffness matrix
K^e	element stiffness matrix
K^e_{ij}	terms of the element stiffness matrix
K'	diffraction coefficient = H/H_i
ℓ	see Fig. 2-18
L	wave length at a particular depth also : matrix of image point (or plate) coordinates (photogram.)
L_0	deep water wave length
L_1, L_2, L_3	triangular element co-ordinate system
L_c	characteristic length (Berkhoff equation)
L_d	decay length (infinite element)
m	an index number
mod	modulus
M	cylindrical surface : equation (Ch. 2-52)
M_1, M_2, M_3	shape functions in the $\bar{\eta}$ direction for the infinite element
n	number of points observed (photogram.)
n'	normal to the surface
$\bar{n}$	the shoaling factor

N_i	shape function for node i
N_m	normalization factor equation (Ch. 2-51)
o	theoretical non-dimensional complex reflection coefficient = $o_1 + i\ o_2$
o_1	real part of o
o_2	imaginary part of o
p	pressure
$p'(\bar{s})$	polynomial in the $\bar{s}$ direction
P_A	absolute parallax of point A (photogram.)
$\bar{P}$	quasi weight matrix (calculation of b_{ij} terms)
$\dot{P}$	quasi weight matrix (calculation of object space co-ordinates)
q	arbitrary point on segment OA (see Fig. 2-19)
$\bar{q}$	fluctuating pressure distribution on the free surface
r	radial distance from the origin
R	radius of the measuring circle for $\bar{T}$
$R(\ell)$	see Fig. 2-18
Re	real part
RXYZ	root mean square residual of the calculated space co-ordinates of a control point
s	scale = f/H_f
$\bar{s}$	new co-ordinate in the ξ direction for the infinite element
S	standard deviation of object space co-ordinates
S_s	standard deviation of the standard deviations of object space co-ordinates
$\bar{S}$	phase or phase difference (waves)
Se_m	see equation (Ch. 2-51)
S_1	inner solid boundary

t	time
T	wave period
$\bar{T}$	Total Transmission Factor
T_E	time required for the wave energy front to traverse the basin
T_p	the paddle start-up time
u	velocity in the x direction
$\dot{u}$	number of unknowns in equation (Ch. 4-42)
U_R	Ursell number
v	velocity in the y direction
$\underline{v}$	three-dimensional velocity vector (components u, v, w)
v_x	least squares adjustment corrections to the measurements in the x direction
v_y	as above but for the y direction
V	matrix of the corrections to the measurements namely v_x and v_y
w	velocity in the z direction
w_x	x component of the discrepancy vector
w_y	y component of the discrepancy vector
W	the discrepancy vector
W_i	Gaussian quadrature weighting factor for the i^{th} integration point
x, y, z	general orthogonal co-ordinate system(waves)
x', y', z'	dimensionless co-ordinates equal to x/L, y/L, z/L
$\bar{x}, \bar{y}$	dimensionless co-ordinates equal to x/L_c, y/L_c
x_i, y_i	image (or plate) co-ordinates of a point i (photogram.)
x_p, y_p	principal point co-ordinates
$\dot{z}$	the "z" term given by equation (Ch. 4-50)

X	matrix of the unknowns
X_1	matrix of the projective transformation parameters : first approximation
Y	Bessel function of the second kind
X_i, Y_i, Z_i	space co-ordinates of a point i(photogram.)
X_0, Y_0, Z_0	space co-ordinates of the perspective centre
$Z(z)$	separation of variables term for the z direction
α	constant for equation (Ch. 3-12)
$\bar{\alpha}$	= H/d
$\dot{\alpha}$	angle of incidence equivalent to angle θ_3 in Fig. 2-19
α_1	angle of incidence see Fig. 2-16
β	phase shift
$\bar{\beta}$	constant for equation (Ch. 3-12)
γ	wave steepness = H/L
γ_m	see equation (Ch. 2-51)
δ	$=\omega^2 L/g$
ϵ_i	= ground co-ordinate - calculated co-ordinate - bias for a particular co-ordinate (X_i, Y_i or Z_i) of a point i
$\bar{\epsilon}$	elliptic cylinder co-ordinate
ϵ'	see equation (Ch. 2-55)
ζ	elliptic cylinder co-ordinate
$\bar{\zeta}$	$= z'/\Pi$
η	free surface elevation (waves)
$\bar{\eta}$	normalized local finite element co-ordinate in the y direction
$\bar{\eta}_o$	$= \bar{\eta}\ \bar{\eta}_i$
θ	angle as defined in Fig. 2-8

θ_1	angle formed by two breakwater arms
θ_2	angle as defined in Fig. 2-18
θ_3	angle as defined in Fig. 2-19
κ	rotation about the Z axis (photogram.)
λ	non zero scalar (photogram.)
μ	$= m\ \pi/\theta_1$
$\bar{\mu}$	$= \bar{D}/L$
ν	angle as defined in Fig. 2-8
ν_1	angle as defined in Fig. 2-18
$\bar{\nu}$	$= \bar{D}\ /\ \sqrt{LL_c}$
ξ	normalized local finite element co-ordinate in the x direction
ξ_o	$= \xi\ \xi_i$
π	$= 3.14159$
ρ	mass density of fluid
$\bar{\rho}$	$= kr$ (see equation (Ch. 2-42))
σ	standard deviation of a single observation (photogram.)
$\bar{\sigma}$	$= \sqrt{4(r-y)/L}$
$\bar{\sigma}'$	$= \sqrt{4(r+y)/L}$
Σ	summation also : cylindrical surface : equation(Ch. 2-52)
τ	a real dimensionless damping coefficient
$\phi(x,y)$	two dimensional complex velocity potential function consisting of a real part ϕ_0 and imaginary parts ϕ_j also : rotation about the Y axis (photogram.)
ϕ^I	the incident wave potential
ϕ^R	the scattered wave potential

$\Phi(x,y,z,t)$	the velocity potential function
Φ_1	= Φ, first order solution
Φ_2	second order correction to be added to Φ_1
$\emptyset\ (x,y,z)$	the three dimensional complex velocity potential function = $\emptyset_1 + i\ \emptyset_2$
$\emptyset_1$	real part of $\emptyset$
$\emptyset_2$	imaginary part of $\emptyset$
χ	reflection coefficient for normal incidence = H_r/H_i
$\bar{\chi}$	practical reflection coefficient = $\chi e^{i\beta}$
$\psi_1,\ \psi_2$	see equation (Ch. 2-52)
ω	angular frequency = $2\pi/T$
	also : rotation about the X axis (photogram.)
ω_1	angle as defined in Fig. 2-19

1. INTRODUCTION

Theoretical diffraction diagrams for the semi-infinite and breakwater gap situations have been made available to coastal engineers over the last thirty years. These diagrams have enabled harbour designers to predict the wave heights behind breakwaters and inside harbour basins. This thesis describes research carried out by the author towards experimentally validating existing diffraction diagrams for the breakwater gap situation, as found in popular coastal engineering design manuals such as the CERC (1977) Manual. It is the author's opinion that previous experimental diffraction results are inconclusive due to (1) the relatively poor accuracy with which the wave heights were measured and (2) secondary basin effects which were superimposed upon and thus distorted the pure diffraction phenomena.

To model experimentally the breakwater gap configurations given in the CERC (1977) manual we require (1) the waves striking the seaward side of the breakwaters to be totally reflected to infinity and (2) the waves passing through the gap to radiate to infinity. To try and model this situation in a basin of finite dimensions has its difficulties . On the seaward side of the breakwaters the waves reflect backwards and forwards between the breakwaters and the wave paddle, and in turn excite resonant cross waves between the basin walls, resulting in a very distorted situation in front of the gap. In the lee of the breakwaters the waves cannot radiate to infinity, but instead are partially reflected by the circumferential beaches and thus distort the pure diffraction pattern.

The distorted experimental situation seaward of the breakwaters can be largely eliminated by placing splitter plates from the breakwater tips extending to the wave paddle, and placing absorbing beaches on the seaward side of the breakwaters. One is now effectively modelling an approximate totally absorbing breakwater situation. Splitter plates have been used by a number of experimenters, for example, Blue and Johnson (1949), Putnam and Arthur (1948), and Harms (1979b). However, these experimenters assumed that the circumferential beaches were effectively totally absorbing. Therefore, all previous experimental results were distorted by secondary phenomena such as reflected waves, cross waves and basin resonance effects. The author thus substantiates the statement made by Silvester and Lim (1968) that for the breakwater gap situation : "The results as presented cannot be

accepted as verification of the theoretical curves, so that further practical work appears necessary". In the experimental breakwater gap configurations investigated by the author, splitter plates were used to eliminate the reflection problems on the seaward side of the breakwaters, whilst a novel photogrammetric wave height measurement technique was used to measure accurately the wave heights in the entire basin, before they could be distorted by reflecting waves, basin resonance effects, etc. The technique enables one to simulate experimentally an infinite basin situation.

Breakwater gap configurations with the following gap width to wave length ratios (B/L ratios) were analysed, both experimentally and numerically, namely; B/L = 1,64; 1,41; 1,2; 1; 0,75; 0,5. These configurations were symmetrical i.e. both breakwater arms lie on the same straight line. An asymmetrical B/L = 1,64 breakwater gap configuration was also analysed. The experimental breakwater gap diffraction configurations tested were modelled numerically using the finite and infinite element program "WAVE" developed at the Department of Civil Engineering, University College of Swansea. The "WAVE" program, which was written for an ICL computer, had to be extensively modified before it would run on the UNIVAC 1100 at U.C.T.

The general philosophy adopted by the author when writing this thesis was to describe novel or poorly documented concepts in detail, while only broadly outlining those concepts which are well documented in the literature. The author adopted the nomenclature most commonly used for each sub-discipline encompassed by the thesis. In a few cases this has led to duplication of terms and these cases are clearly noted. The topics covered by each chapter will now be very briefly summarised.

Chapter Two deals with the basic linear wave theory leading to a very brief derivation of the Helmholtz two-dimensional wave diffraction equation. The boundary conditions for two-dimensional water wave diffraction are then discussed. The classical/fundamental wave diffraction theories for the semi-infinite breakwater and breakwater gap configurations are reviewed and compared, with particular emphasis on those aspects relating to the present research work. A very brief derivation of the Berkhoff (1972) refraction - diffraction equation is then given. Finally, a brief review of Biesel's (1963, 1966) work regarding "radiating second-order

phenomena in gravity waves" is given since such phenomena were observed experimentally.

Chapter Three starts with a brief review of previous analytical and numerical combined refraction-diffraction investigations. A review of modern numerical methods for water wave diffraction and refraction-diffraction is then given. This is followed by a review of finite element formulations of the Berkhoff equation for infinite domain problems. The finite and infinite element program "WAVE" is then described. Finally, the use of the "WAVE" program to model the experimental breakwater gap configurations, as well as a fully reflecting breakwater configuration, is described.

Chapter Four describes, in detail, the novel photogrammetric wave height and pattern measurement equipment and techniques developed by the author. After a brief review of previous photogrammetric wave height studies the laboratory equipment developed and used by the author is described. A description of the author's investigation and development of techniques based on analog procedures, the theory of projective transformations, and the theory of the deformed reference plane, is given. A detailed description of the projective transformation theory is included. Basic photogrammetric concepts such as the principle of the floating mark are described for the benefit of the coastal engineer. Also, stereopairs (which can be viewed using the simple viewer enclosed), have been included in the text to highlight the various topics discussed.

Chapter Five starts with an overview of previous wave diffraction experimental work with particular emphasis on breakwater gap diffraction configurations and results. The initial diffraction experiments undertaken by the author are then discussed. A description of the subsequent investigation into the generation of long-crested waves in a laboratory basin, and the development of the infinite basin technique, is given. The infinite basin technique is a photogrammetric method which was used to simulate experimentally and measure the diffraction of a continuous wave train entering an infinite basin via a gap in an approximate totally absorbing breakwater. The use of this technique to model various breakwater gap configurations is then described and stereopairs of the configurations are included. Finally, an investigation of the radiating secondary waves (and also the vortices) generated at the breakwater tips is described.

In Chapter Six, the experimental and numerical breakwater gap diffraction diagrams are given and compared to analytical diagrams where available. A summary of the breakwater gap diffraction results and the trends observed is then given. The non-linear experimental phenomena observed are then discussed. This is followed by a discussion on and a summary of the photogrammetric wave height measurement techniques developed by the author, with particular emphasis on the infinite basin technique. Finally, the modelling of breakwater gap diffraction configurations using the finite and infinite element program "WAVE" is discussed.

In Chapter Seven, general conclusions regarding breakwater gap wave diffraction, laboratory photogrammetric wave height measurement, and the use of finite and infinite elements, are given.

2. THEORY

2.1 Introduction.

In this chapter a brief review of the linear water wave theory is given, leading up to a description of the familiar diffraction equations and boundary conditions. The classical diffraction theories for the semi-infinite breakwater and breakwater gap configurations are then reviewed and compared. The combined refraction-diffraction equations of Berkhoff (1976) are then summarised, and finally a brief review of the theoretical and experimental work carried out by Biesel to describe radiating second-order phenomena in gravity waves, is given. A broader account of the theoretical/numerical investigations of water wave diffraction and diffraction-refraction problems is given in Chapter 3.

2.2 Linear Water Wave Theory.

2.2.1 Potential Formulation.

Classical wave theories are normally expressed in terms of a potential formulation (Berkhoff, 1976; Le Méhauté, 1976). For a potential formulation it is necessary to assume that the motion of the fluid is irrotational or alternatively that the curl of the velocity field is zero i.e.

$$\nabla \times \underline{v} = 0 \tag{1}$$

where ∇ is the gradient operator and $\underline{v}$ is the three-dimensional velocity vector with components u, v and w in the x, y and z directions respectively.

Now a velocity potential function $\Phi(x,y,z,t)$ can be defined from which the velocity field can be obtained by taking the gradient

$$\underline{v} = \nabla\Phi \tag{2}$$

where the components of $\underline{v}$ are given by

$$u = \frac{\partial\Phi}{\partial x} \quad , \qquad v = \frac{\partial\Phi}{\partial y} \quad , \qquad w = \frac{\partial\Phi}{\partial z}$$

The field equation for the potential function can be derived by subsituting (2) into the continuity equation (derived from the principle of conservation of mass of an incompressible fluid) namely:

$$\nabla \cdot \underline{v} = 0 \tag{3}$$

to yield the well known equation of Laplace

$$\nabla^2\Phi = 0 \tag{4}$$

From Berkhoff (1976) the equation of Bernouilli in terms of Φ is given as

$$\frac{\partial\Phi}{\partial t} + \tfrac{1}{2}(\nabla\Phi \cdot \nabla\Phi) + \frac{p}{\rho} + gz = 0 \tag{5}$$

from which the pressure p can be computed.

2.2.2 Surface and Bottom Boundary Conditions.

To solve equations (4) and (5) for the unknown three-dimensional potential function Φ and pressure p, a set of conditions at the boundary of the solution domain must be given.

If it is assumed that the free surface elevation is given by the relation $z = \eta\ (x,y,t)$ (see Fig. 2-1), the following kinematic condition must hold for a particle belonging to the free surface;

$$w = \frac{\partial\eta}{\partial t} + u\,\frac{\partial\eta}{\partial x} + v\,\frac{\partial\eta}{\partial y}$$

and in terms of the potential function Φ:

$$\frac{\partial\eta}{\partial t} + \frac{\partial\Phi}{\partial x}\frac{\partial\eta}{\partial x} + \frac{\partial\Phi}{\partial y}\frac{\partial\eta}{\partial y} - \frac{\partial\Phi}{\partial z} = 0 \text{ at } z = \eta\ (x,y,t) \tag{6}$$

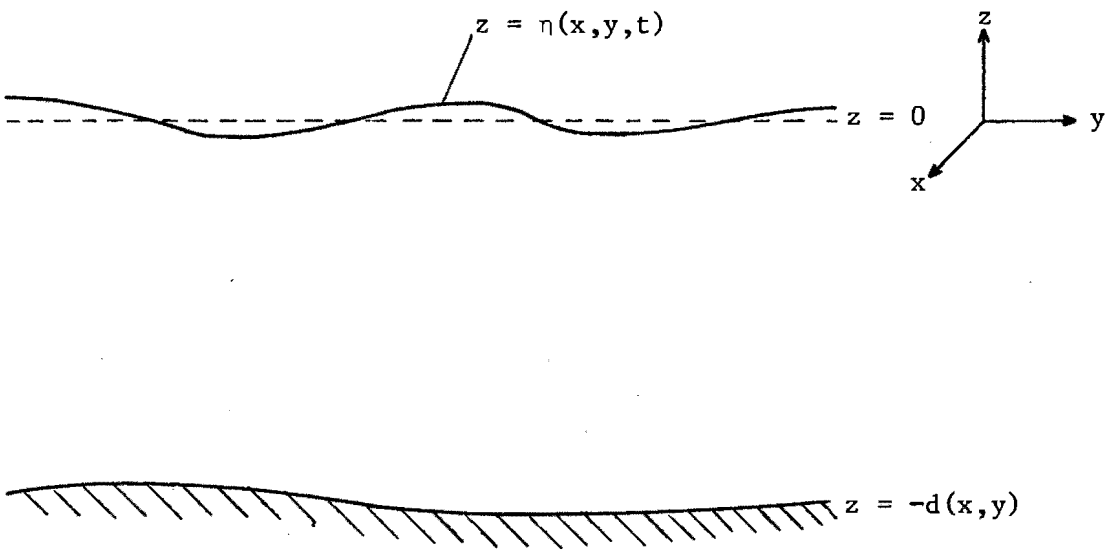

Fig. 2-1 Definition sketch of free surface and bottom.

A second condition at the unknown free surface $z = \eta\ (x,y,t)$ is that of atmospheric pressure, which can be taken as zero i.e. the dynamic condition at the free surface is

$$p = 0$$

or with the aid of Bernoulli's equation (5)

$$\frac{\partial \Phi}{\partial t} + \tfrac{1}{2}\ (\nabla\Phi \cdot \nabla\Phi) + g\eta = 0 \text{ at } z = \eta\ (x,y,t) \qquad (7)$$

In the case of an impermeable bottom, given by the relation $z = -d(x,y)$ (d = depth below mean level), the normal velocity must be zero, leading to the equation

$$u \frac{\partial d}{\partial x} + v \frac{\partial d}{\partial y} + w = 0$$

or with the potential function

$$\frac{\partial \Phi}{\partial x}\frac{\partial d}{\partial x} + \frac{\partial \Phi}{\partial y}\frac{\partial d}{\partial y} + \frac{\partial \phi}{\partial z} = 0 \text{ at } z = -d\ (x,y) \qquad (8)$$

At solid boundaries other than the bottom, the normal velocity must also be prescribed, and in the case of an unbounded solution domain in the horizontal plane, some additional conditions at infinity must be imposed.

2.2.3 Linear Equations.

The non-linear boundary conditions (6) and (7), and the fact that these conditions are imposed upon the unknown free surface $z = \eta\ (x,y,t)$ make it very difficult to find an applicable way of solving this three-dimensional problem.

These boundary conditions can be linearised with respect to certain small parameters. There are three characteristic lengths in the problem.

L : the characteristic wave length
d : the water depth
H : the wave height

In the case of deep water (small L/d) the parameter γ for the linearisation of the equation is

$$\gamma = H/L \quad \text{(wave steepness)}$$

but in the case of shallow water (large L/d) the parameter

$$\bar{\alpha} = H/d$$

must also be small.

A derivation of the infinitesimal-wave approximation can be found in Lamb (1932), Stoker (1957) and Wehausen and Laitone (1960).

The resulting equations are:

The field equation (4)

$$\nabla^2 \Phi = 0$$

The linearised kinematic free surface boundary condition

$$\frac{\partial \eta}{\partial t} - \frac{\partial \Phi}{\partial z} = 0 \quad \text{at } z = 0 \tag{9}$$

The linearised dynamic free surface boundary condition

$$\eta + \frac{1}{g}\frac{\partial \Phi}{\partial t} = 0 \quad \text{at } z = 0 \tag{10}$$

The bottom boundary condition equation (8)

$$\frac{\partial \Phi}{\partial x}\frac{\partial d}{\partial x} + \frac{\partial \Phi}{\partial y}\frac{\partial d}{\partial y} + \frac{\partial \Phi}{\partial z} = 0 \quad \text{at } z = -d\ (x,y)$$

Equations (9) and (10) can be combined (by eliminating η) to yield

$$\frac{\partial \Phi}{\partial z} + \frac{1}{g}\frac{\partial^2 \Phi}{\partial t^2} = 0 \quad \text{at } z = 0 \tag{11}$$

2.2.4 Harmonic Solutions.

Now that the equations have been linearised it is possible to seek a solution of equations (4), (8) and (11) which is simple harmonic in time.

$$\Phi\ (x,y,z,t) = \phi_1(x,y,z) \cos \omega t + \phi_2(x,y,z) \sin \omega t - \tag{12}$$

In which ω is the angular frequency and ϕ is the complex potential function defined as

$$\phi = \phi_1 + i\,\phi_2$$

and ϕ_1 = the real part of ϕ

ϕ_2 = the imaginary part of ϕ

$i = \sqrt{-1}$

The simple harmonic solution (12) can also be written with the aid of the complex potential function as

$$\Phi = \mathrm{Re}\ (\phi e^{-i\omega t})$$

with Re indicating the real part of the expression between brackets.

The complex potential function ϕ must satisfy equations (4), (8) and also (11) which becomes

$$\frac{\partial \phi}{\partial z} - \frac{\omega^2}{g}\phi = 0 \quad \text{at } z = 0 \tag{13}$$

Once the solution of ϕ has been found all other functions of interest can be computed.

The free surface function η can be found with the aid of equation (10) giving:

$$\eta\ (x,y,t) = \mathrm{Re}\ (\frac{i\omega}{g}\phi\ e^{-i\omega t})\ z = 0 \tag{14}$$

The wave height which is twice the amplitude of the free surface elevation, is thus

$$H = \frac{2\omega}{g}\sqrt{(\phi_1^2 + \phi_2^2)}\quad z = 0 \tag{15}$$

The phase $\bar{S}$ of the free surface elevation is given by

$$\bar{S} = -\arctan\ (\phi_1/\phi_2)\ z = 0 \tag{16}$$

The linearised pressure is given by

$$p\ (x,y,z,t) = -\rho g z + \omega\rho(\phi_1 \sin \omega t - \phi_2 \cos \omega t) \tag{17}$$

The restrictions of the mathematical formulation developed to this point are:

(1) An ideal fluid, which means no viscosity;
(2) an incompressible and homogeneous fluid;
(3) a gravity force field;
(4) an irrotational motion which leads to a potential formulation;
(5) infinitesimally small amplitude waves;
(6) a motion which is only simple harmonic in time.

2.3 Wave Diffraction Equations and Boundary Conditions.

2.3.1 Wave Diffraction Equations.

In the pure wave diffraction case the water depth is constant and the bottom condition (equation 8) becomes

$$\frac{\partial \phi}{\partial z} = 0 \quad \text{at } z = -d \tag{18}$$

A solution of the Laplace Equation (4) which satisfies the vertical boundary condition equations (13) and (18) can now be found by the method of separation of variables. By writing

$$\phi\,(x,y,z) = Z\,(z)\;\phi\,(x,y) \tag{19}$$

and substituting the above into the Laplace equation, derive

$$\frac{1}{Z}\frac{d^2Z}{dz^2} = \frac{1}{\phi}\left(\frac{\partial^2\phi}{\partial x^2} + \frac{\partial^2\phi}{\partial y^2}\right) \tag{20}$$

giving the two equations

$$\frac{1}{Z}\frac{d^2Z}{dz} = k^2 \tag{21}$$

and

$$\frac{1}{\phi}\left(\frac{\partial^2\phi}{\partial x^2} + \frac{\partial^2\phi}{\partial y^2}\right) = -k^2 \tag{22}$$

where k is a complex constant and the eigenvalue(s) of the problem.

The boundary conditions in the vertical direction are now

$$\frac{dZ}{dz} = 0 \quad \text{at } z = -d \tag{23}$$

and

$$\frac{dZ}{dz} - \frac{\omega^2}{g}Z = 0 \quad \text{at } z = 0 \tag{24}$$

A solution of (21) satisfying equations (23) and (24) is

$$Z\,(z;k) = C\,(k)\,\cosh\,\{k(z + d)\} \tag{25}$$

provided that the eigenvalue k is a root of the dispersion relation

$$\omega^2 = g\,k\,\tanh\,(kd) \tag{26}$$

where k can now be recognised as the familiar wave number. The dispersion relation can be derived by subsituting equation (25) into the boundary condition given by equation (13).

Equation (26) has the real roots $k = \pm k_0$ and an infinite number of pure imaginary roots $k = \pm ik_j$ where $j = 1, 2, 3 \ldots\ldots\infty$.

The general solution is then

$$\phi(x,y,z) = C_0 \cosh\{k_0(z + d)\}\phi_0(x,y) + \sum_{j=1}^{\infty} C_j \cosh\{k_j(z + d)\}\, \phi_j(x,y) \tag{27}$$

In which ϕ_0 is a solution of the familiar Helmholtz equation

$$\frac{\partial^2\phi_0}{\partial x^2} + \frac{\partial^2\phi_0}{\partial y^2} + k_0^2\, \phi_0 = 0 \tag{28}$$

and the functions ϕ_j of

$$\frac{\partial^2\phi_j}{\partial x^2} + \frac{\partial^2\phi_j}{\partial y^2} + k_j^2\, \phi_j = 0 \tag{29}$$

Usually in diffraction problems the form of the incoming wave is prescribed and a scattered wave will be sought. In the case of the two dimensional function ϕ we can consider this function to consist of ϕ^I the incident wave potential and ϕ^R the scattered wave potential. In the two dimensional diffraction model, in addition to the constant depth requirement, all obstacles are considered to have vertical sides extending from the bottom to the free surface. Generally the two-dimensional diffraction problem can be reduced to finding a solution to the Helmholtz equation (28) (in ϕ^R) that satisfies the radiation condition and the prescribed normal velocity boundary conditions at the walls; since it can be shown that the functions $\phi_j(x,y)$ for $j = 1, 2 \ldots\ldots\infty$ must be identically zero.

The radiation condition and the boundary conditions at the walls are described in the next section.

2.3.2 Boundary Conditions.

The boundary conditions which the diffraction equation (28) must satisfy must be specified.

On solid (vertical) boundaries the normal velocity must be zero and hence

$$\frac{\partial\phi}{\partial n} = 0 \tag{30}$$

where n is the outward normal to the surface. This implies total reflection of the wave, such as may occur at an impermeable vertical wall.

In practical problems the walls of obstacles are not always vertical and also not fully reflecting. To deal with these boundaries the walls must be schematized as vertical, but it is possible to introduce partial reflection into the model by using the mixed boundary condition

$$\frac{\partial \phi}{\partial n'} + k_0 \, o \, \phi = 0 \qquad (31)$$

at the partial reflecting boundaries, in which $o(= o_1 + io_2)$ is a theoretical non-dimensional complex reflection coefficient. Total reflection is given by $o = 0$ (o_1 & $o_2 = 0$) and total absorbtion by $o_2 = 1$. The mixed boundary condition is only applicable for the case in which the theoretical reflection coefficient a is not dependant on the solution ϕ.

In practical hydraulic work the reflection coefficient is introduced in a more physical way and is defined as the ratio between a reflected wave and an incident wave. This ratio is only useful in the case of the reflection of long-crested plane waves by an infinitely long straight breakwater, assuming partial reflection has no influence upon the plane wave form of the reflected wave. In this case it is possible to obtain a relation between the theoretical reflection coefficient $o(= o_1 + io_2)$ and the practical reflection coefficient $\overline{\chi}$ where

$$\overline{\chi} = \chi e^{i\beta} \qquad (32)$$

in which

χ is the familiar reflection coefficient for normal incidence (equation (3) of Section 5.3.3.3)

β is the phase shift.

In Fig. 2-2 the values of o_1 and o_2 are given as functions of χ for different values of β.

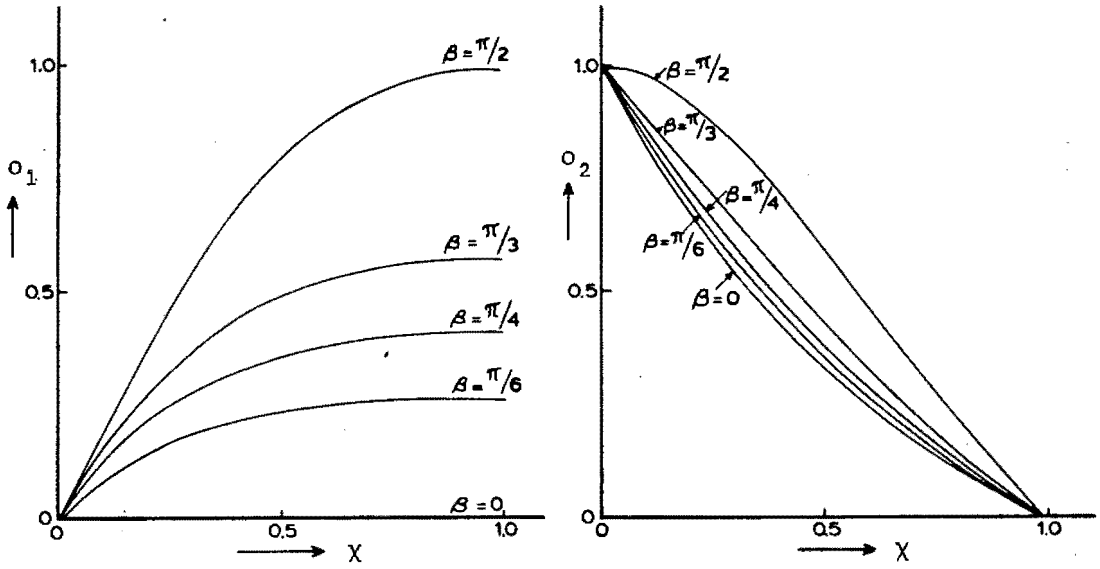

Fig. 2-2 Relation between theoretical and practical reflection coefficients. (Berkhoff, 1976)

At the infinite boundary two conditions are required, namely:

(1) ϕ corresponding to outgoing waves (ϕ^R) tends to zero as the distance tends to infinity

(2) no return of reflected waves from infinity.

These conditions are satisfied by the Sommerfeld radiation condition (Sommerfeld 1896, 1949), namely:

$$\lim_{r\to\infty} \sqrt{r}\,\left(\frac{\partial\phi}{\partial r} + i\,k_0\,\phi\right) = 0 \qquad (33)$$

2.4 Classical Wave Diffraction Theories for the Semi-Infinite Breakwater and Breakwater Gap Configurations.

2.4.1 Semi-Infinite Breakwater.

Penney and Price (1952) developed the classical wave diffraction theory for the diffraction of waves round a semi-infinite breakwater. Their theories were originally published in 1944 (Penney and Price, 1944), however, their later (1952) reference is more readily available and is therefore quoted throughout. They showed that the general distribution of surface waves on a sheet of water (uniform depth) could be expressed in terms of the two dimensional complex potential function $\phi(x,y)$ which they termed the wave function. They discovered that the differential equations and boundary conditions satisfied by $\phi(x,y)$ are, in certain cases, identical with those satisfied by a corresponding function in the theory of the diffraction of light. By making use of Sommerfeld's (1896) solution for the diffraction of light waves at the edge of a semi-infinite screen, Penney and Price were able to determine $\phi(x,y)$ for the diffraction of sea waves round the end of a semi-infinite straight breakwater, with the incident wave directions both normal and oblique to the breakwater.

Penney and Price (1952) derive the solution of the Laplace equation (4) which satisfied the linearised free surface boundary condition (13) and the bottom boundary condition (18) (all in Φ). Using the method of separation of variables (19), they show that the two dimensional diffraction problem reduces to a solution of the Helmholtz equation (28) which satisfies the relevant boundary conditions at the vertical walled breakwater and at infinity.

Penney and Price consider two types of ideal breakwaters, namely, (I) rigid breakwaters and (II) flexible or "cushion" breakwaters. Of these (I) is of the most practical importance, however, examples of (II) have been designed, constructed and tested (eg. Hales 1981). Penney and Price deal firstly with the case of incident wave approach which is normal to the breakwaters and then with the more general oblique approach ease. Only the first case will be dealt with here.

The breakwater is assumed to be "thin" and to extend along the positive x axis from origin to infinity. The incident waves are

assumed to travel in the positive y direction. In terms of $\phi(x,y)$ progressive waves travelling in the positive y direction are given by

$$\phi(x,y) = e^{-iky} \tag{34}$$

The boundary conditions at the breakwater, in terms of $\phi(x,y)$, are as follows. If the breakwater is "rigid", the normal component of the fluid velocity must be zero at the breakwater face, so that

$$\frac{\partial \phi}{\partial y} = 0 \quad \text{at } y = 0, \quad x \geq 0 \tag{35a}$$

If the breakwater is of the "cushion" type, the pressure remains constant and equal to the hydrostatic pressure at all depths, so that

$$\phi = 0 \quad \text{at } y = 0, \quad x \geq 0 \tag{35b}$$

The Helmholtz equation (28) and equations (34), (35a) and (35b) are identical to the equation of Sommerfeld's (1896) problem of the diffraction of light by a semi-infinite perfectly reflecting screen, the conditions (35a) and (35b) corresponding respectively to the cases where the light is (a) polarized in a plane parallel to the edge of the screen and (b) polarized in a plane perpendicular to the edge. Sommerfeld's solution of these equations may be reduced to

$$\phi(x,y) = \frac{1+i}{2}\left\{e^{-iky}\int_{-\infty}^{\bar{\sigma}} e^{-\frac{1}{2}\pi u^2}\,du \pm e^{iky}\int_{-\infty}^{\bar{\sigma}'} e^{-\frac{1}{2}\pi i u^2}\,du\right\} \tag{36}$$

The + or - sign corresponds to conditions (35a) or (35b) respectively and

$$\bar{\sigma}^2 = \frac{4}{L}(r - y) \; ; \quad \bar{\sigma}'^2 = \frac{4}{L}(r + y) \; ; \quad L = \frac{2\pi}{k}$$

and $r = \sqrt{x^2 + y^2}$ or the distance of point (x,y) from the origin.

Penney and Price suggested that equation (36) could be evaluated using tables of Fresnel's integrals or by graphical methods using Cornu's spiral (Jahnke and Emde, 1945). More sophisticated numerical techniques are now available for example Fan et al (1967) developed a numerical formulation of the Penney and Price (1952) solution. Fan et al solved the Fresnel integrals using asymptotic

series for $r \geq 8$ and MacLaurin series for $r < 8$.

The solution of (36) for various limiting positions of the point (x,y) is shown in Fig. 2-3 below.

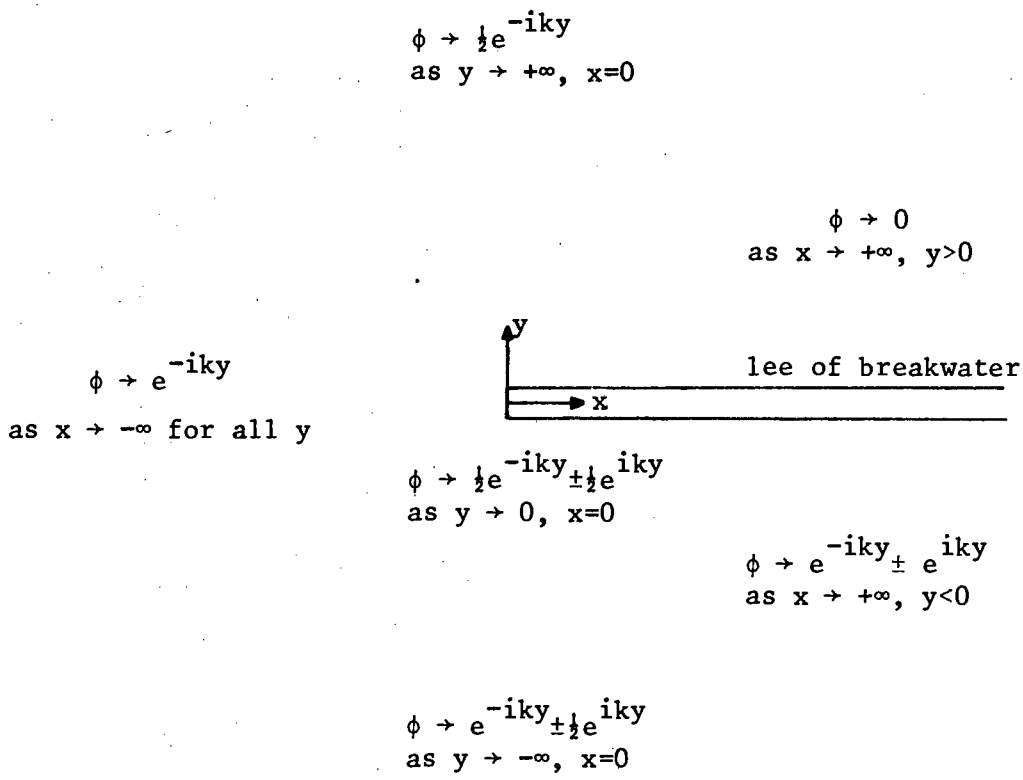

Fig. 2-3 Limiting cases of the diffraction solution.

On the leeward side of the breakwater ϕ tends to zero for large positive x, agreeing with the obvious fact that the screening becomes more effective as we move further away from the open end. At points directly behind the open end ($x = 0$), ϕ tends to $\frac{1}{2}e^{-iky}$ for large y, indicating that the amplitude of the waves is there reduced to half that of the waves in the open sea.

On the windward side of the breakwater, ϕ contains the term e^{iky}, corresponding to reflected waves moving in the negative y direction. These combine with the incident waves to form standing waves. At points well removed from the open end of the breakwater (x large and positive) the amplitude of the standing waves is twice that of the incident waves. For a rigid breakwater, $\phi \to e^{-iky} + e^{iky}$ as $x \to \infty$ for negative y, indicating that the breakwater ($y = o$) is at an anti-node of the oscillating water surface. On the other hand, for a cushion-type breakwater, $\phi \to e^{-iky} - e^{iky}$ as $x \to \infty$, showing that the breakwater is at a node, so that the water level remains constant.

Penney and Price found that for values of $y \geq 2L$ the second integral in (36) is small. For this case $\phi(x,y)$ approximates to

$$\phi(x,y) = f(\bar{\sigma})e^{-i2\pi y/L} \tag{37}$$

where

$$f(\bar{\sigma}) = \tfrac{1}{2}(1 + i) \int_{-\infty}^{\bar{\sigma}} e^{\frac{1}{2}i\pi u^2}\, du \tag{38}$$

and

$$\bar{\sigma} = \pm \sqrt{4(r - y)/L} \tag{39}$$

with σ negative when x is positive and visa versa (r is the distance from the origin to the point (x,y)).

The diffraction coefficient K', which is the ratio of maximum height of waves at a point (x,y) to the incident wave height, is given by (incident wave has unit amplitude)

$$K' = \text{mod } \phi(x,y) \tag{40}$$

The phase difference of the waves is given by

$$\bar{S} = \arg \phi(x,y) \tag{41}$$

Equations (40) and (41) correspond to equations (15) and (16) discussed earlier.

A convenient way of exhibiting the wave height distribution behind the breakwater is by means of a contour plot. Fig. 2-4 shows a plot of equal diffraction coeffecients behind a perfectly reflecting breakwater, the waves being incident normally. The corresponding diffraction diagram from Fan et al (1967) is shown in Fig. 2-6. From Fig. 2-4 it is apparent that there are narrow bands extending behind the breakwater in the region beyond the open end ($x < 0$) in which the wave height is slightly greater than in the open sea, but in the lee of the breakwater the wave height is always less than one half that in the open sea. For $y > 2L$ $\phi(x,y)$ can be approximated by equation (37), but in regions closer to the breakwater the full equation (36) should be used. Diffraction diagrams for the semi-infinite breakwater have been drawn up by CERC (1977) (based on the work of Wiegel, 1962) and Fan et al (1967).

Fig. 2-5 shows the graphs of modulus and argument of the function $f(\bar{\sigma})$, given by equation (38), for the positive y region (behind

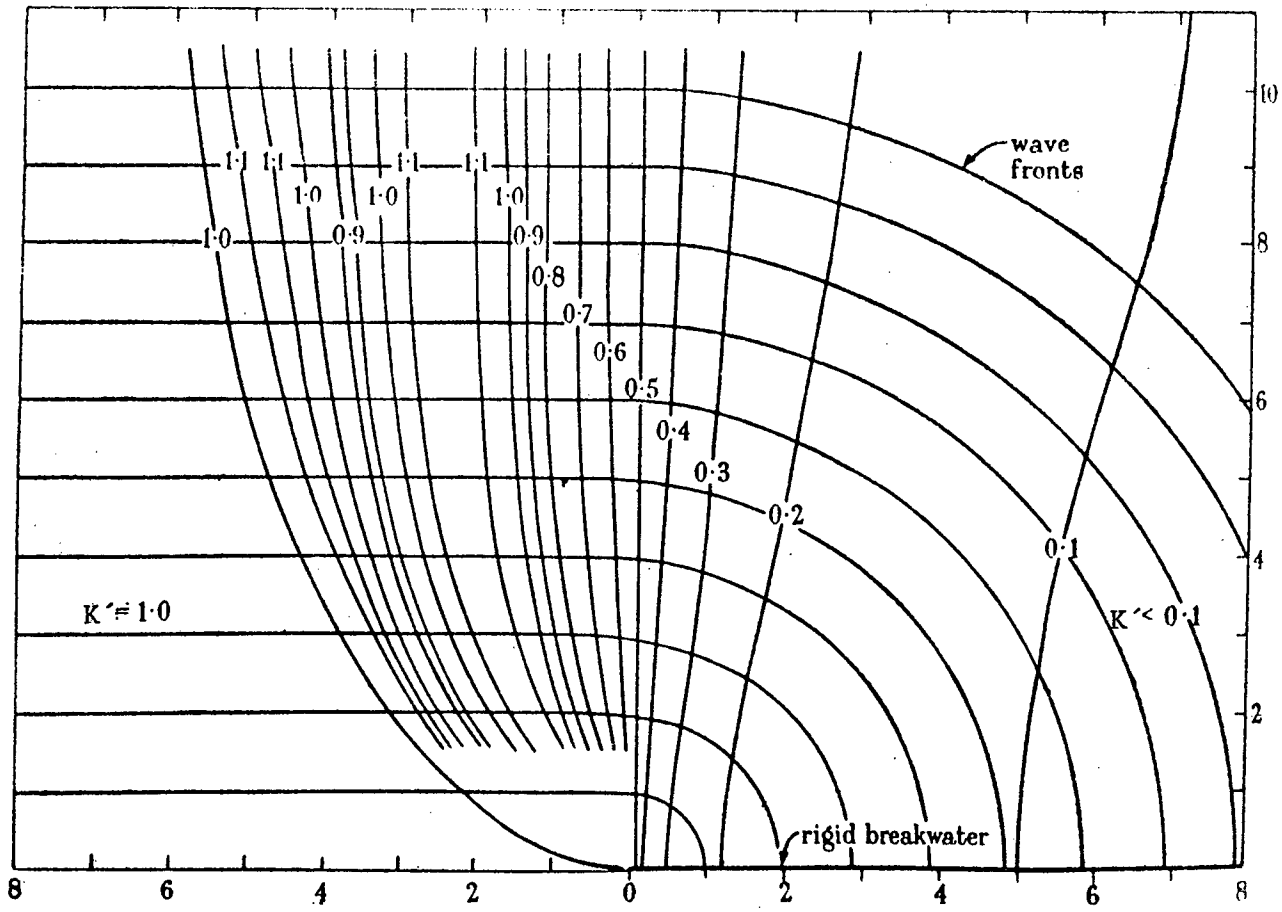

Fig. 2-4 Wave fronts and K′ contour lines in the lee of a rigid breakwater, the waves being incident normally (from Penney and Price, 1952).

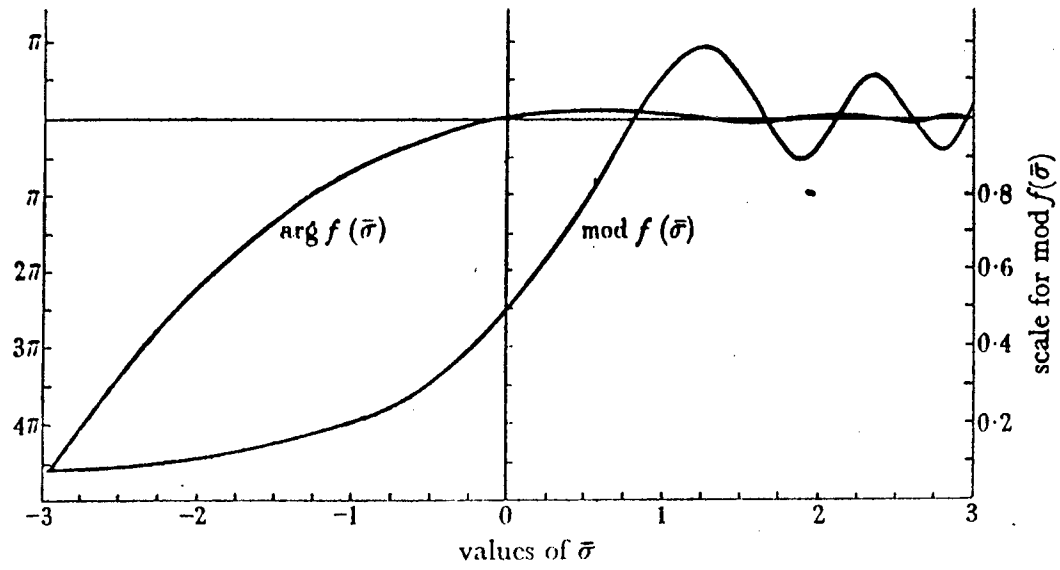

Fig. 2-5 Graphs of the modulus and argument of the function $f(\bar{\sigma})$ given by (38) (from Penney and Price, 1952).

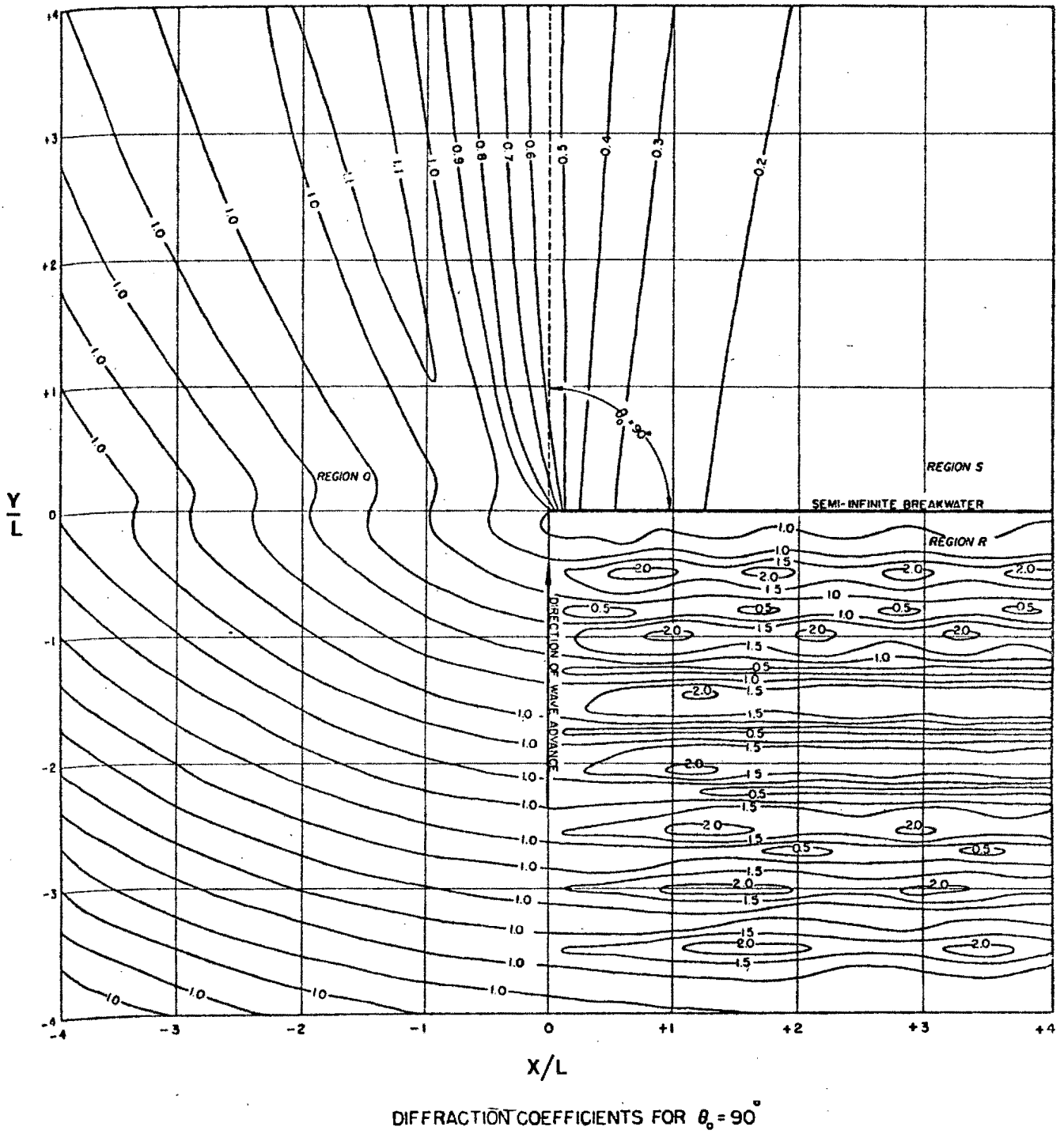

Fig. 2-6 Diffraction diagram for the semi-infinite breakwater; the normal incidence case (from Fan et al, 1967).

the line of the breakwater). To obtain the wave pattern we require the lines of constant phase. These are given by equation (41) where $\phi(x,y)$ is given by equation (37) for $y > 2L$. Beyond the open end of the breakwater (x negative) $\bar{\sigma}$ is positive and it can be seen from Fig. 2-5 that arg $f(\bar{\sigma})$ is then only slightly different from zero. Hence the wave fronts are only slightly deformed from the straight line fronts in the open sea. In the lee of the breakwater $\bar{\sigma}$ is negative and consequently arg $f(\bar{\sigma})$ is negative, which indicates a phase lag. This phase lag increases with increasing x so that the wave fronts bend round towards the lee side of the breakwater. From Fig. 2-5 it can be seen that in the lee of the breakwater, the wave fronts are very nearly arcs of circles centred at the open end.

Putnam and Arthur (1948) derived a simplified form of the Penney and Price (1952) solution (for the semi-infinite breakwater) which, however, is not discussed here. Putnam and Arthur also carried out an extensive experimental investigation of the diffraction of waves at the end of a long breakwater. Their experimental investigation is briefly described in Section 5.1.1.

Silvester and Lim (1968) and also Larras (1966) have suggested that each diffraction coefficient K′ in the lee of a semi-infinite breakwater, should be seen as the sum of an incident and a reflected term. The first term would be for the diffraction of the incident waves into the shadow zone and the second term would be for the diffraction of the reflected waves (reflected from the windward side of the breakwater) into the shadow zone. Silvester and Lim suggest that the first term of equation (36) represents the diffraction of the incident wave from the shadow line into the shadow zone and the second term represents the diffraction of the reflected wave into the shadow zone. Fig. 2-7 shows their solution for K′ in the lee of a semi-infinite breakwater and the limits of its applicability. The no reflection case (approximated experimentally by the use of wave splitters) was calculated by neglecting the second term of equation (36).

A solution for the diffraction round a breakwater with a wave splitter at its tip is available from the exact solution for the diffraction of waves by semi-infinite vertical wedges. Mitsui

and Murakami (1967) have derived solutions for different wedge angles and all wave directions (see Fig. 2-8). For example, the solution for a rectangular wedge is given by

$$\phi(\bar{\rho},\theta)_{\nu=\frac{3}{2}\pi} = \frac{4}{3} J_0(\bar{\rho}) + \frac{8}{3}\sum_{n=1}^{\infty} e^{in\pi/3} \cdot J_{2n/3}(\bar{\rho}) \cdot \cos\frac{2}{3}n\alpha \cdot \cos\frac{2}{3}n\theta \qquad (42)$$

with

$J_0(\bar{\rho})$, $J_{2n/3}$ = BESSEL functions, first kind

$$\bar{\rho} = k \cdot r = \frac{2\pi}{L} \cdot r$$

Daemrich and Kohlhase (1978) compared (Fig. 2-9) both the full Sommerfeld solution (equation (36) for normal incidence) and the simplified (no reflection) solution of Silvester and Lim (1968) and Larras (1966), described above, with the solution of Mitsui and Murakami (1967). Daemrich and Kohlhase suggest that, based on the results shown in Fig. 2-9, the Mitsui solution may be approximated by a modified Sommerfeld solution. The difference between the full solution and the simplified solution corresponds to the influence of the second term of the Sommerfeld solution (equation (36) for normal incidence) and therefore they suggested that the weighting of this second term may be a good approximation.

Daemrich and Kohlhase (1978) state "comparative calculations have shown that the difficult solutions according to Mitsui can be approximated well in the region of diffraction by an adequate modified Sommerfeld solution, which needs only a half percent of the computer time. This modified solution consists in a weighting of the second term of the Sommerfeld solution depending on the wave direction θ_0" (see Fig. 2-10). θ_0 is the angle formed by the breakwater and the line of incidence through the breakwater tip. As can be seen from Fig. 2-10, the modified solution has the advantage that partial reflections can now be considered.

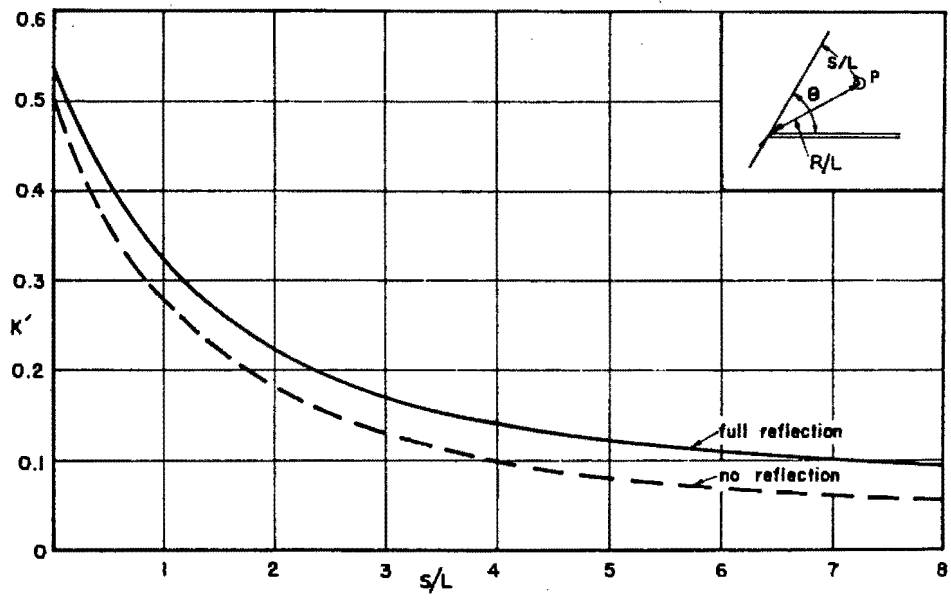

Fig. 2-7 K′ along crest for $60° \leqq \theta \leqq 150°$ and $3 \leqq R/L \leqq 10$ (from Silvester and Lim, 1968).

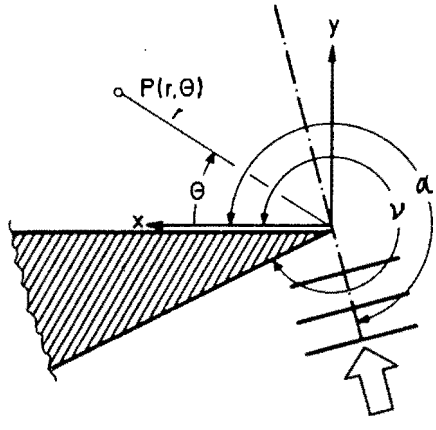

Fig. 2-8
Definition sketch for the MITSUI solution.

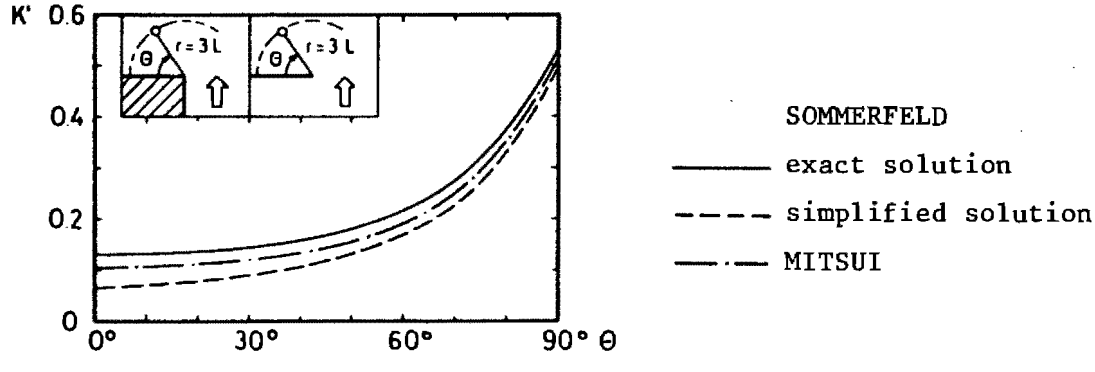

Fig. 2-9 Comparison of the diffraction coefficient K′ for different theories (from Daemrich and Kohlhase, 1978).

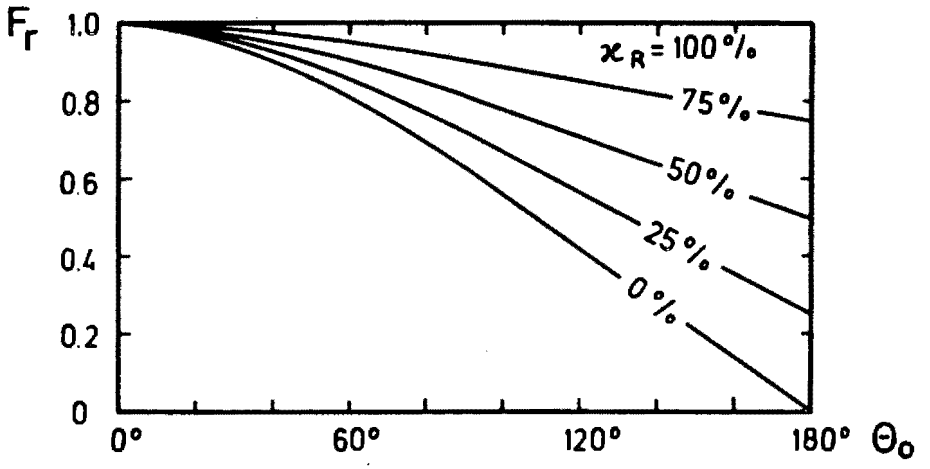

Fig. 2-10 Weighting factor F_r for the second term of the Sommerfeld solution for various degrees of reflection (from Daemrich and Kohlhase, 1978).

2.4.2 Breakwater Gap.

2.4.2.1 Introduction.

Four fundamental theoretical solutions for the diffraction of water waves passing through a breakwater gap will be discussed. The first is the solution of Penney and Price (1952) based on the solution of Sommerfeld (1896) for the diffraction of light by a semi-infinite perfectly reflecting screen. The second is the solution of Carr and Stelzriede (1952) based on the solution of Morse and Rubenstein (1938) for the diffraction of sound and electromagnetic waves by a slit in an infinite plane. The third is the solution of Lacombe (1952). The 4th is that of Memos (1976).

2.4.2.2 The Sommerfeld / Penney and Price Solution.

Penney and Price (1952) deal with the diffraction of waves through a gap of breadth B, in a very long breakwater on which the waves are incident normally. They suggest that if the gap is small, i.e. B small compared with the wave length L of the incident waves, the gap will act as a point source, semi-circular waves diverging from it and having the same height practically all round any semi-circle. If, however, the gap is larger than a wave length, the energy of the waves penetrating the gap will propagate mainly in the original direction of the incident waves. The wave pattern at considerable distances from the gap will still be approximately semi-circles, but the wave heights will vary along the semi-circles, being greatest in the direction of propagation of the incident waves. Penney and Price suggest that when B is greater than L a good approximation can be obtained by superposition from the solution of the semi-infinite breakwater. This method is stated to give an exact solution for all values of B when one of the barriers is of the rigid type and the other of the cushion type; a case which, since it has no practical applications for the author, will not be treated here.

The origin is taken to be at the centre of the gap, the x axis along the breakwater and the y axis in the direction of propogation of the incident waves. The problem reduces to finding $\phi(x,y)$ which satisfies equation (28) and the boundary condition (35a) or (35b) corresponding to the rigid and cushion type breakwaters respectively and which also contains a term e^{-iky} for y negative corresponding to the incident waves.

Now suppose that the part of the breakwater to the left of the gap is removed, we now have the case of a semi-infinite barrier for which the solution is given by (36). This solution may be analysed in two parts, one of which corresponds to the shadow and reflection as given by geometrical optics, and the other corresponds to diffraction waves diverging from the end of the barrier. Equation (36) can therefore be written in the forms

$$\phi(x,y) = e^{-iky} - f_1 \pm g_1 \qquad \text{for } x < \tfrac{1}{2}B \text{ and for all } y \qquad (43)$$

$$= + f_1 \pm g_1 \qquad \text{for } x > \tfrac{1}{2}B \text{ and } y > 0 \qquad (44)$$

$$= e^{-iky} \pm e^{+iky} - f_1 \pm g_1 \qquad \text{for } x > \tfrac{1}{2}B \text{ and } y < 0 \qquad (45)$$

where $f_1 = \psi(r_1,y) = e^{-iky}\, f(-\sqrt{4(r_1 - y)/L}$ (46)

$$g_1 = \psi(r_1,-y) \qquad (47)$$

and r_1 is the distance of the point (x,y) from the end of the barrier $(\frac{1}{2}B,0)$.

The diffraction waves in the region $x < \frac{1}{2}B$, due to the barrier along the line segment $y = 0$, $x > \frac{1}{2}B$, are represented by the terms $-f_1 \pm g_1$ ($=F_1$ say) in equation (43). From (46) and (47) we find that these diffraction waves satisfy the following conditions along the unoccupied part of the x axis, namely

$$F_1 = 0, \quad \frac{\partial F_1}{\partial y} = -2\,\frac{\partial \psi(r_1,y)}{\partial y} \quad \text{at } y = 0,\ x < \tfrac{1}{2}B \qquad (48)$$

for a rigid breakwater, and

$$F_1 = 2\psi(r_1,0), \quad \frac{\partial F_1}{\partial y} = 0 \quad \text{at } y = 0,\ x < \tfrac{1}{2}B \qquad (49)$$

for a flexible breakwater.

Now if a second barrier is introduced along the line segment $y = 0$, $x < -\frac{1}{2}B$, the diffraction waves arising at the first barrier would satisfy the boundary conditions at the second barrier, which are appropriate to a barrier of the opposite type from the first. When both barriers are of the same type, the boundary conditions at each barrier are not automatically satisfied by the diffraction waves arising from the incident waves on the other barrier, so that a second system of diffraction waves would need to be introduced to obtain an exact solution. Penney and Price suggest,

however, that these secondary waves are relatively unimportant if B is not less than one wave length. Fig.2-11 shows the scheme of values for $\phi(x,y)$ when both barriers are rigid breakwaters.

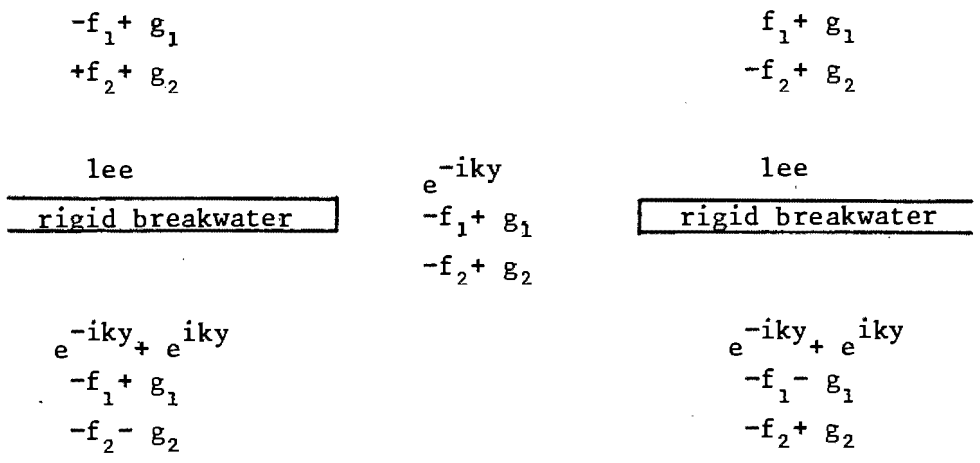

Fig. 2-11 Scheme of $\phi(x,y)$ values for the breakwater gap configuration.

As for the semi-infinite breakwater case, the wave pattern will be given by the lines arg $\phi(x,y)$ = constant, and the diffraction coefficient by mod $\phi(x,y)$. A contour plot is thought to be the most useful way of showing the wave height distribution behind a breakwater and Fig. 2-9 shows such a plot of equal diffraction coefficients behind a gap of width 2 L in a perfectly reflecting breakwater, the waves being incident normally.

Blue and Johnson (1949) propose a simplified form of the Penney and Price (1944; 1952) solution to account for the effect of wave splitters, which are convenient to use in model studies. Physically, the wave splitters eliminate the diffraction influence of the front faces of the breakwater wings; since they prevent the reflected waves from being diffracted into the path of the waves entering the breakwater gap. Blue and Johnson suggest that mathematically, this effect appears to be given by the g_1 and g_2 terms shown in Fig.2-11 since these are the only terms affected by the type of breakwater face. They propose a simplified solution which is obtained by omitting the g

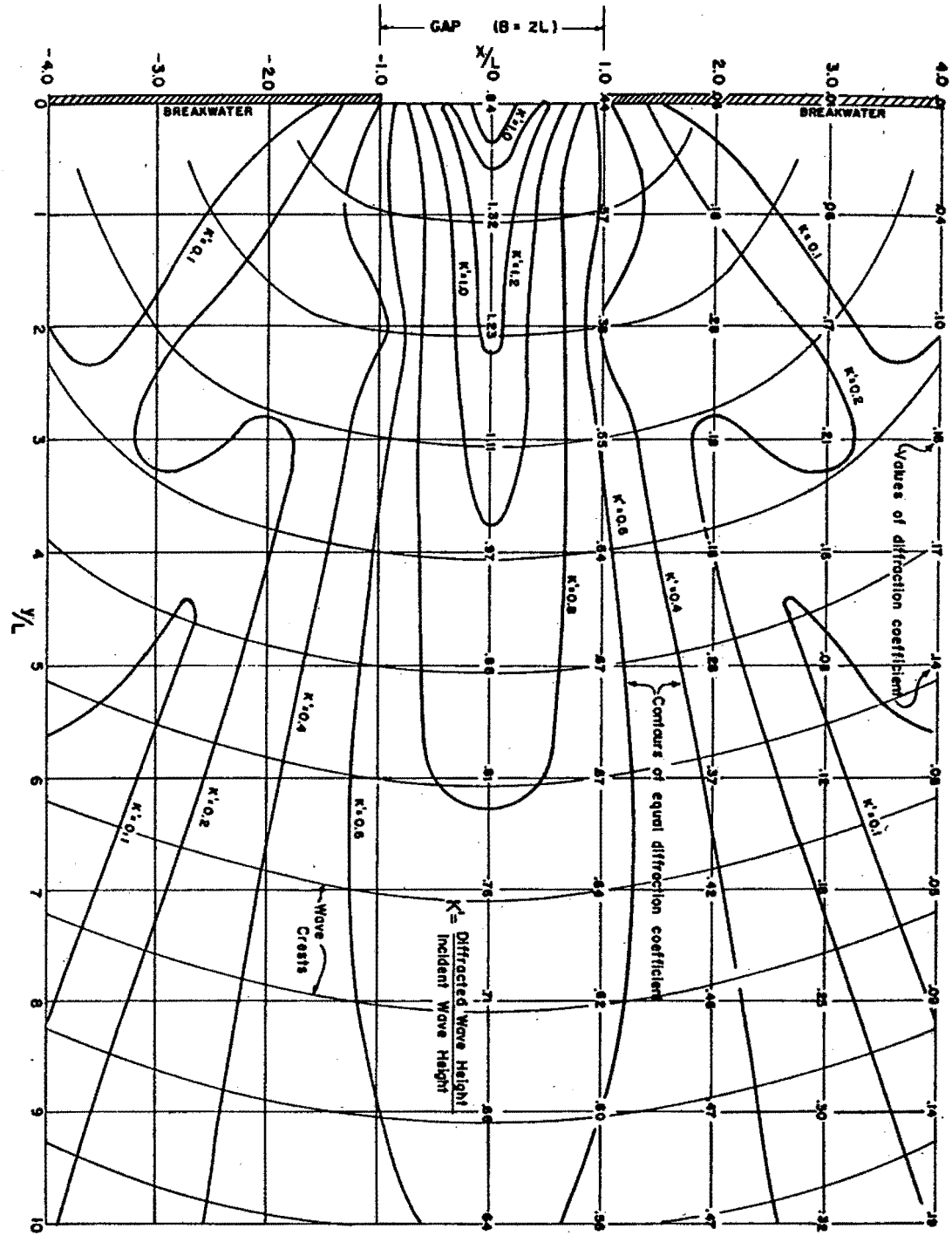

Fig. 2-12 Diffraction diagram for the B = 2 L breakwater gap configuration (from CERC, 1977) constructed using the method described by Johnson (1953).

terms shown in Fig. 2-11. Fig. 2-13 shows the scheme of values for $\phi(x,y)$ when Blue and Johnson's simplified solution is used.

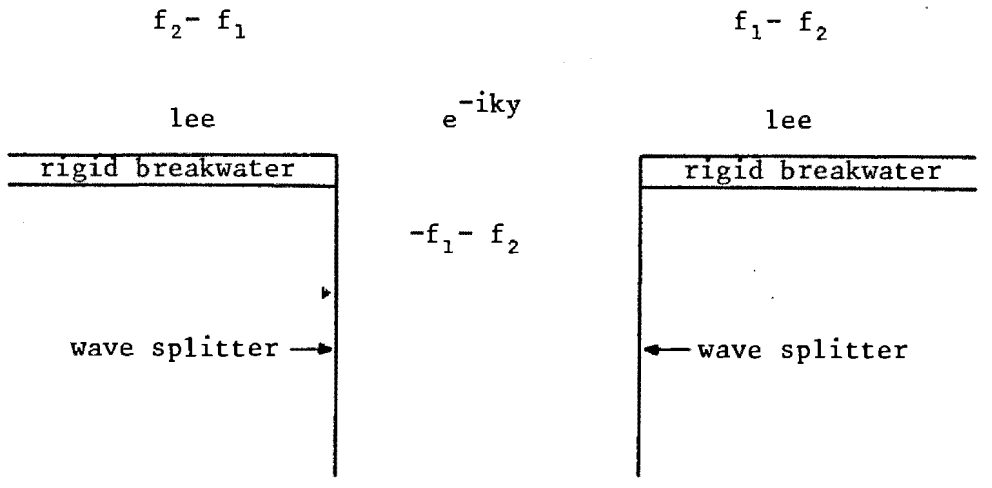

Fig. 2-13 Scheme of $\phi(x,y)$ values for the breakwater gap configuration when using Blue and Johnson's simplified solution.

Blue and Johnson's simplified solution was of particular interest to the author since splitter plates were used for all the diffraction experiments described in this thesis. Fig. 2-14 shows a comparison between diffraction coefficients calculated using both the complete and simplified solutions for two breakwater gap configurations experimentally investigated by the author; namely the B/L = 1,41 and B/L = 1,64 configurations. From the diagrams it is apparent that the two solutions give almost identical results for distances greater than 2 L from the breakwater gap, however, in the region close to the breakwater gap the two solutions give markedly different results.

Johnson (1953) describes in detail a method for constructing diffraction diagrams for breakwater gap configurations based on the Penney and Price (1952) solution. According to Camfield (1983) the above method was used to construct the breakwater gap diffraction diagrams, for the configurations having gap widths of B = 1,41 and greater, shown in CERC (1977). The majority of the breakwater gap diffraction diagrams shown in the above manual were taken from Johnson (1952).

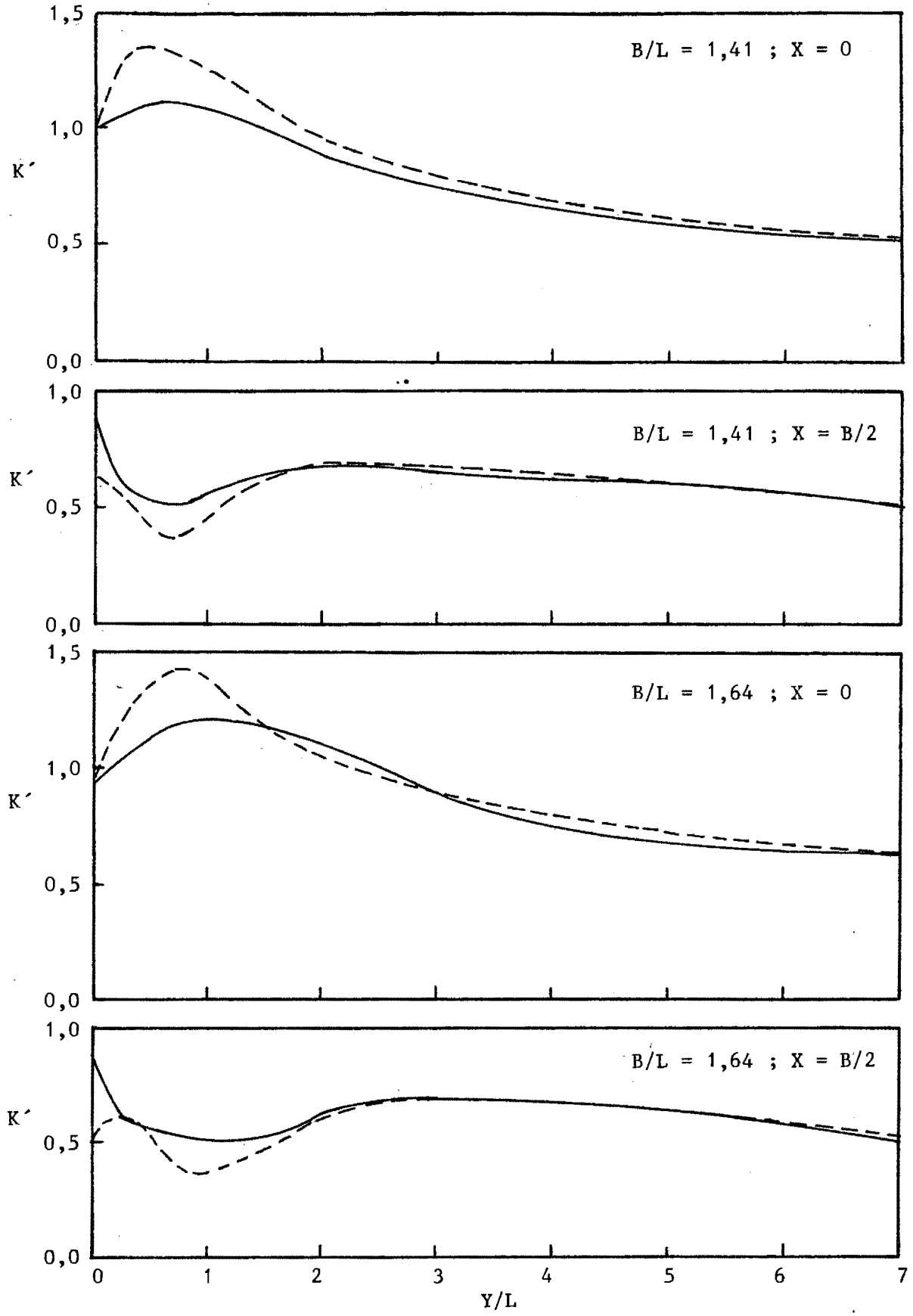

Fig. 2-14 Comparison of the Penney and Price (1952) (solid lines) and the Blue and Johnson (1949) (dashed lines) solutions for the B/L = 1,64 and 1,41 breakwater gap configurations.

Daemrich and Kohlhase (1978) applied the simplified Sommerfeld solution (of Silvester and Lim) and the Mitsui solution (see Section 2.4.1) to the diffraction of waves passing through a breakwater gap which has long splitter plates extending from the breakwater tips to the wave generator. Fig. 2-15 shows the two solutions compared to experimental results obtained by Daemrich (1978) for the B/L = 2 breakwater gap configuration.

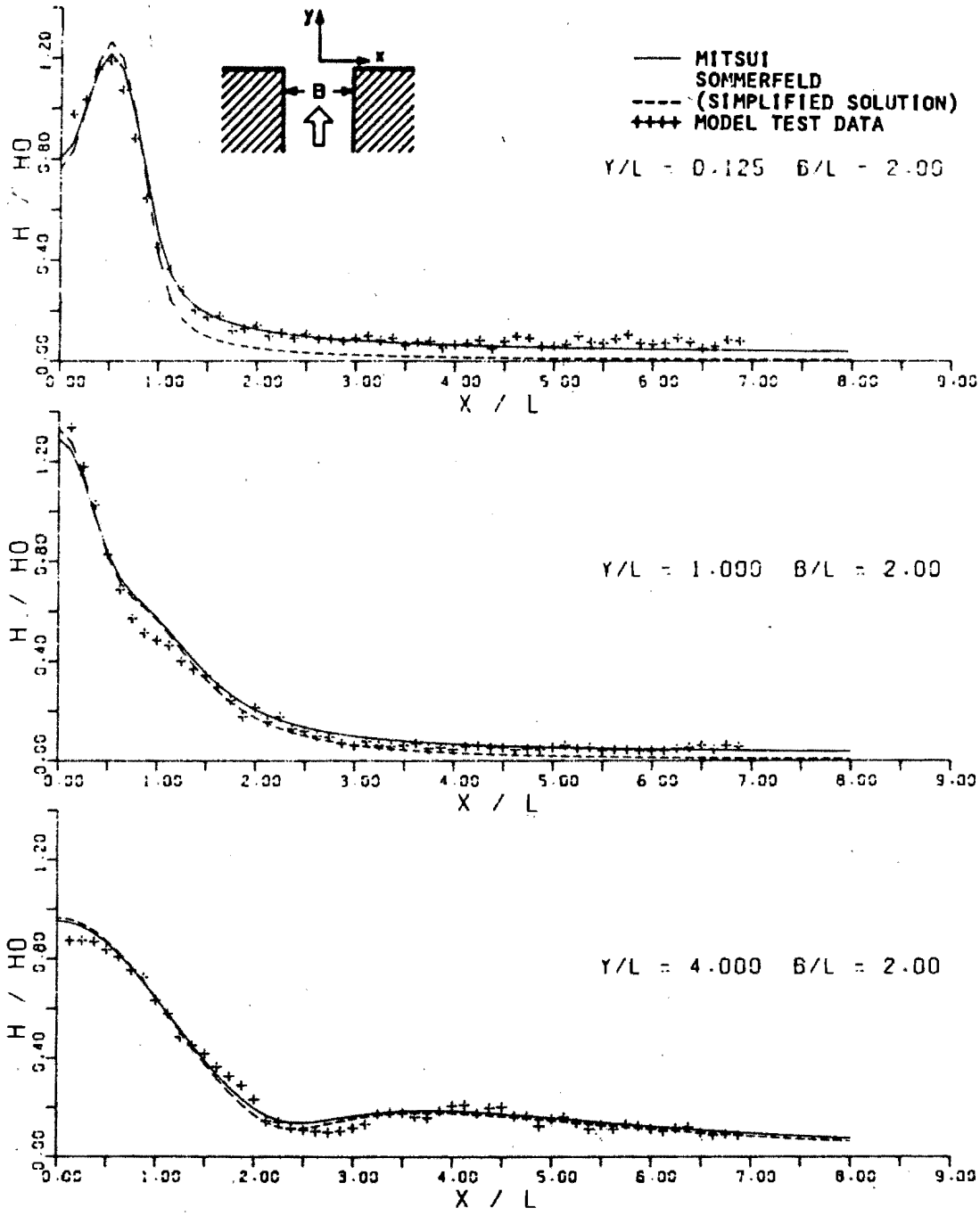

Fig. 2-15 Experimental and theoretical results for the B/L = 2 breakwater gap (with splitter plates) configuration (from Daemrich and Kohlhase, 1978).

The breakwater gap configurations described above are for the case of normal incidence of the incoming waves. Johnson (1952) proposes an approximate method for constructing a breakwater gap diffraction diagram for the case of oblique incidence. A line is drawn through the gap centre, normal to the incident wave direction, and then the diffraction coefficients are calculated as though the breakwater were along this line, the ends of the imaginary gap being at the projections on this line of the true gap ends. Johnson (1952) has shown that this approximation gives very good results when compared to the exact solution calculated using the method of Carr and Stelzriede (1952).

To this point, only the case of the diffraction of waves passing through a gap in a long straight breakwater, the waves being incident both normally and obliquely, has been discussed. Memos (1980b) proposes an approximate solution for the diffraction of waves passing between two breakwater arms forming an angle θ_1 (see Fig. 2-16).

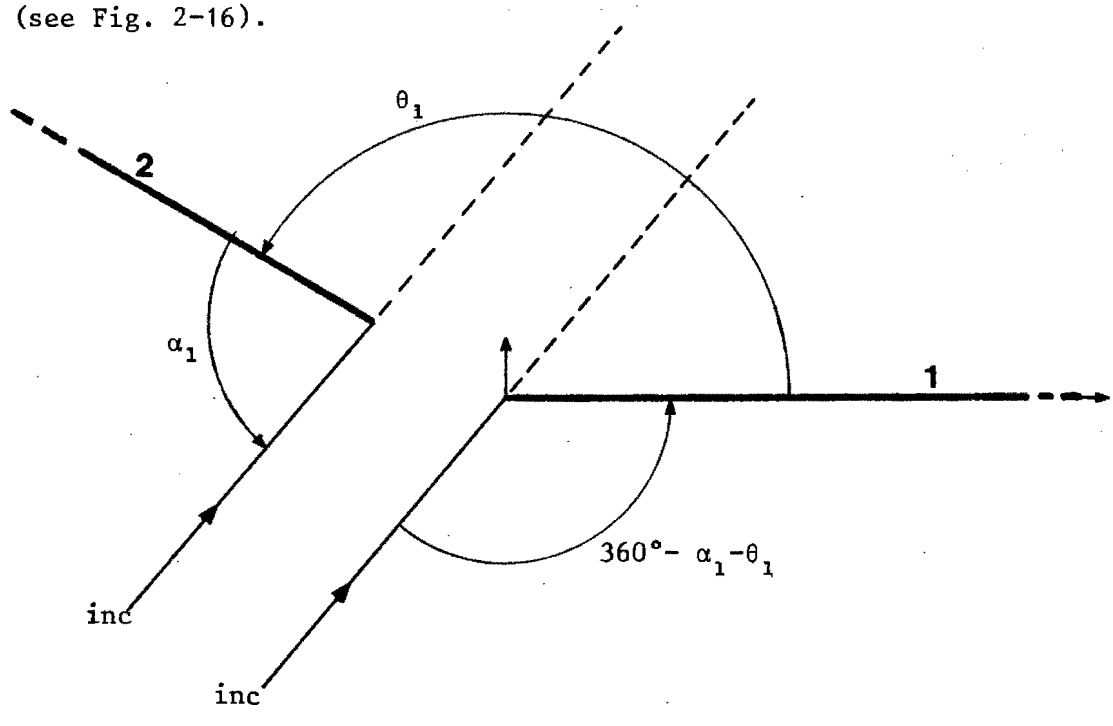

Fig. 2-16 Gap between two breakwater arms forming an angle θ_1.

If we assume that the angle of incidence for the left hand breakwater is α_1 then the corresponding angle of incidence for the right hand breakwater is $360° - \alpha_1 - \theta_1$ Memos proposes that each breakwater arm should be analysed as an isolated semi-infinite breakwater with the incoming waves incident as shown in Fig. 2-16.

The diffraction coefficients behind each breakwater arm can then be solved using the Penney and Price (1952) solution for waves obliquely incident upon a semi-infinite breakwater. Memos (1980b) proposes that an approximate solution for the breakwater gap configuration can be obtained by the superposition of the two semi-infinite breakwater solutions. He points out however, that there are only certain ranges of θ_1 and B for which the approximate solution gives accurate results.

2.4.2.3 The Morse and Rubenstein / Carr and Stelzriede Solution.

Carr and Stelzriede (1952) propose an exact solution for the diffraction of waves passing through a gap of width B less than 3 L, in a straight breakwater, for the case of both normal and oblique incidence of the incoming waves. Their solution is based on the approach outlined by Morse and Rubenstein (1938) for the diffraction of sound and electromagnetic waves by a slit in an infinite plane. The two dimensional velocity potential function ϕ is expressed as a product of functions of one variable by the use of elliptic-cylinder co-ordinates $(\zeta, \bar{\varepsilon})$ where

$$x = \frac{B}{2} \cosh \zeta \cos \bar{\varepsilon}$$

$$y = \frac{B}{2} \sinh \zeta \sin \bar{\varepsilon} \qquad (50)$$

$$z = z$$

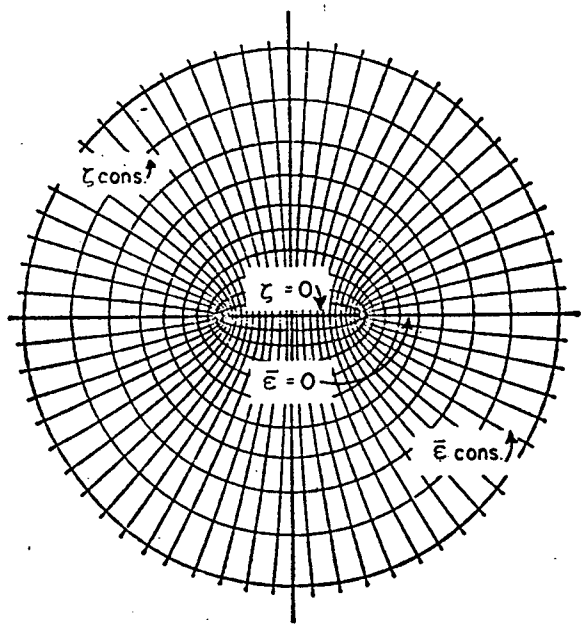

Fig. 2-17 Elliptic cylinder co-ordinates.

For constant z, lines of constant ζ and $\bar{\varepsilon}$ become, respectively, confocal ellipses and hyperbolas of focal length B (Fig. 2-17). The suitability of these co-ordinates for the expression of the desired boundary conditions lies in the fact that, for $\bar{\varepsilon} = 0$, the hyperbolas degenerate into a straight line with a gap of width B. On the other hand, diffraction around both ends of a barrier of finite length (the reciprocal case to the breakwater with a gap) could be investigated by using the degenerate ellipse, corresponding to $\zeta = 0$.

The diffracted wave behind the rigid breakwater with a gap is expressed by the equation

$$\phi(\zeta,\bar{\varepsilon}) = (8\pi)^{\frac{1}{2}} \sum_{m=0}^{\infty} \left\{ \frac{i^{m-1}}{N_m} \sin \gamma_m \exp(i\gamma_m)\, Se_m(\bar{c},\dot{\alpha} - \pi) \right.$$

$$\left. Se_m(\bar{c},\bar{\varepsilon}) - \left| Je_m(\bar{c},\zeta) + iYe_m(\bar{c},\zeta) \right| \right\} \qquad (51)$$

where:

m is an index number 0, 1, 2 ... ∞

N_m is a normalization factor

γ_m = arccotan $(Ye_m(\bar{c},0) \;/\; Je_m(\bar{c},0))$

$\bar{c} = (\pi B \;/\; L)^2$

$Je_m(\bar{c},\zeta)$, $Ye_m(\bar{c},\zeta)$ the radial Mathieu functions

$Se_m(\bar{c},\bar{\varepsilon}) = \sum_{n=0}^{\infty} De_n \cos n\bar{\varepsilon}$ where De_n denotes the Mathieu coefficients.

The modulus of equation (51) represents the amplitude of the diffracted wave. The definitions of the Intensity and Total Transmission factors, discussed by Carr and Stelzriede, as well as a description of their experimental work is given in Section 5.1.2.2.

The above method was used by Johnson (1952) to construct the diffraction diagrams for the B/L = 0,5 and 1 breakwater gap configurations given in his paper. These diagrams are included in the CERC Manual (CERC, 1977).

2.4.2.4 The Lacombe Solution.

Lacombe (1952) derives an approximate solution for the diffraction of waves passing through a breakwater gap for all angles of incidence. His solution is based on a generalization of Huyghen's principle under certain assumptions. The wave function ϕ satisfies the Holmholtz equation (28) at every point of the water surface under consideration.

Applying Green's theorem to the volume V contained between two cylindrical surfaces Σ and M which are limited at the bottom ($z = -d$) and at the surface ($z = 0$), the following relation is obtained:-

$$\iiint_V (\psi_1 \Delta\psi_2 - \psi_2 \Delta\psi_1) dv = \iint_{\Sigma \& M} (\psi_1 \frac{\partial \psi_2}{\partial n'} - \psi_2 \frac{\partial \psi_1}{\partial n'}) ds \qquad (52)$$

where ψ_1 and ψ_2 both satisfy Laplace's equation (4).

From the above, Lacombe obtains the following fundamental equation:-

$$\int_l (\phi \frac{\partial \bar{H}_0}{\partial n'} - \bar{H}_0 \frac{\partial \phi}{\partial n'}) dl = 4i\phi \qquad (53)$$

in which H_0 is the Hankel function of the first kind and zeroth order.

The above relationship can be applied to the problem of finding the agitation in the lee of the breakwater with a gap under the classical Kirchhoff's assumptions:

1) The function ϕ is zero along the inner faces of the breakwaters.

2) Along the gap, ϕ has the same value as if there were no obstacles.

3) Green's theorem can be applied despite the discontinuities in ϕ and $\frac{\partial \phi}{\partial n'}$ along the contour.

Using the asymptotic expression for the Hankel function for large arguments, the following expression for ϕ (two dimension velocity potential) is derived (Fig. 2-18).

$$\phi(x,y) = \frac{L^{-\frac{1}{2}}}{2} \int_{OA} (\cos\nu_1 - \sin\theta_2) R(1)^{-\frac{1}{2}} \cdot$$

$$\exp\{-ik|1\cos\theta_2 - R(1)| - \frac{1}{4} i\pi\} \, dl \qquad (54)$$

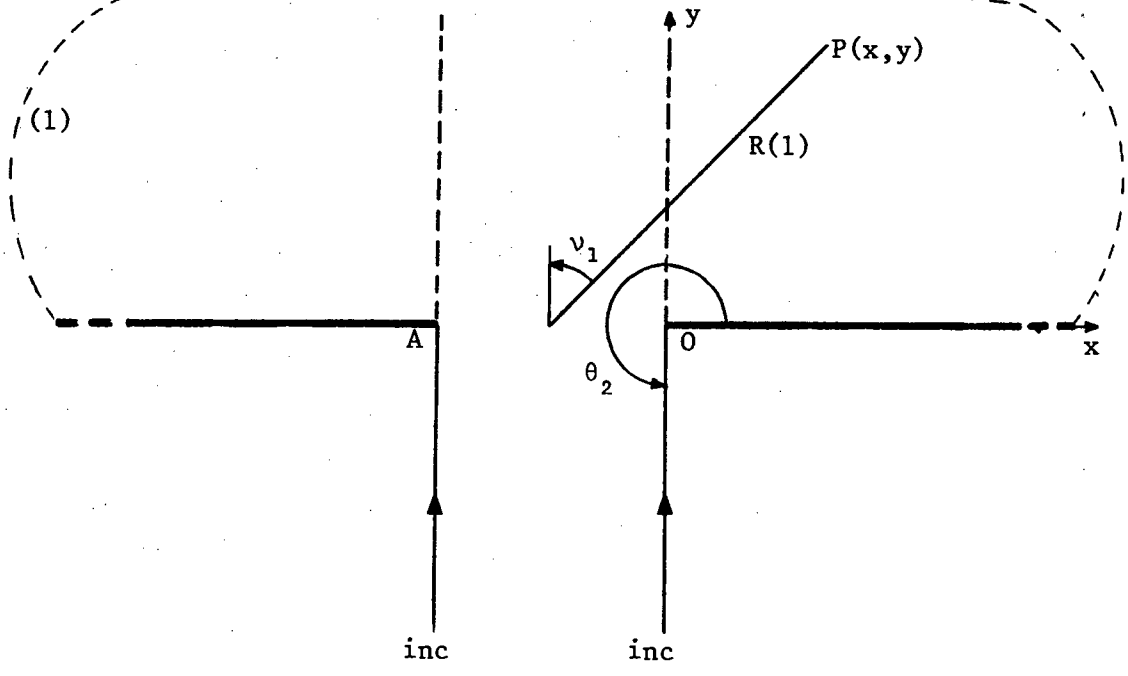

Fig. 2-18 Nomenclature for Lacombe's solution.

2.4.2.5 The Memos Solution.

Memos (1976, 1980c) derives a solution for the diffraction of waves passing between two breakwater arms forming an angle θ_1 (Fig. 2-19). His solution is based on the principle that under certain assumptions, the velocity potential of a scattered wave can be determined by knowing the gradient of this potential along the surface of the obstacle and the expression of an appropriate Green's function. For this case the suitable Green's function is the solution for the diffraction by a wedge of waves emanating from a line source. In Fig. 2-19 the faces of a perfectly reflecting wedge would occupy the semi-infinite planes $\omega_1 = 0$ and $\omega_1 = \theta_1$, the region $0<\omega_1<\theta_1$ being free space.

The diffracted wave in the lee of the breakwaters can be expressed by the equation:

$$\phi(r,\omega_1) = \frac{-\pi^2}{L\theta_1}\sin(\theta_1-\theta_3)\int_0^{B_d}\exp\{-ikq\cos(\theta_1-\theta_3')\}$$

$$\cdot\sum_{m=0}^{\infty}(-1)^m\varepsilon_m'J_\mu(kr_<)\bar{H}_\mu(kr_>)\cos\mu\omega_1 dq \qquad (55)$$

where:

J is the Bessel function of the first kind

$\bar{H}$ is the Hankel function of the first kind

B_d is the dimensionless gap width = B/L

q is an arbitrary point in the segment of OA

$\mu = m\pi/\theta_1$

$\varepsilon' = 1$ for $m = 0$, $\varepsilon' = 2$ for $m \geq 1$

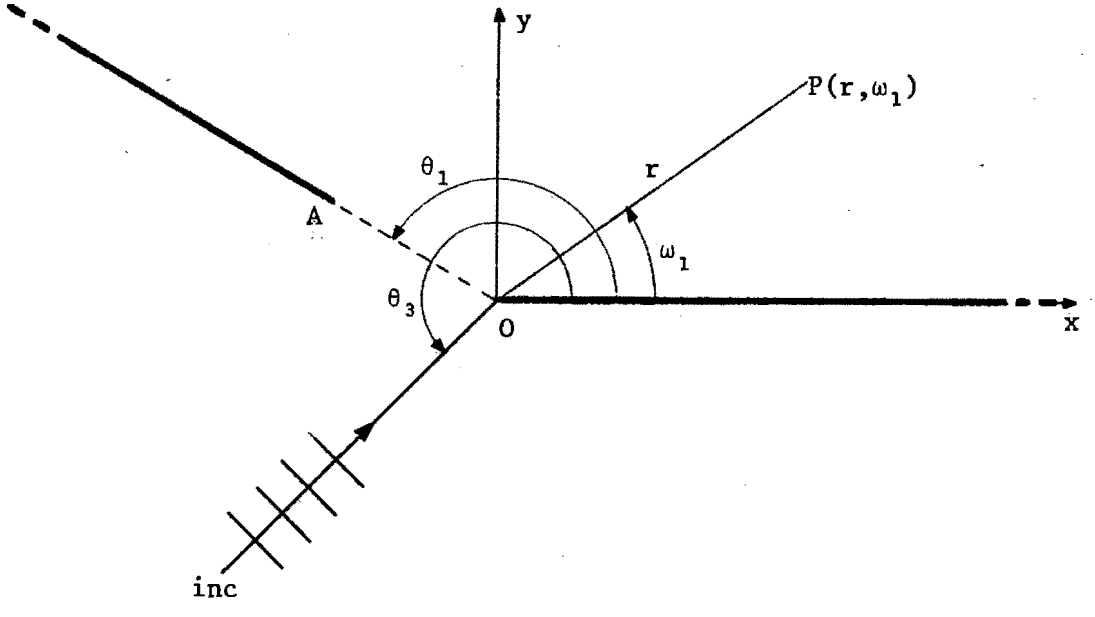

Fig. 2-19 Nomenclature for the Memos solution.

The diffraction coefficient K′ is given by the modulus of equation (55) since the incident wave is of unit amplitude.

Memos compared his theoretical solution with experimental measurements. Fig. 2-20 shows the theoretical diffraction diagram for a configuration with a gap of B_d = 1,85 and a subtended angle of 120°. The experimental results are given at the points (small crosses), where measurements were taken. A description of the experimental configuration and technique used by Memos is given in Section 5.1.2.3.

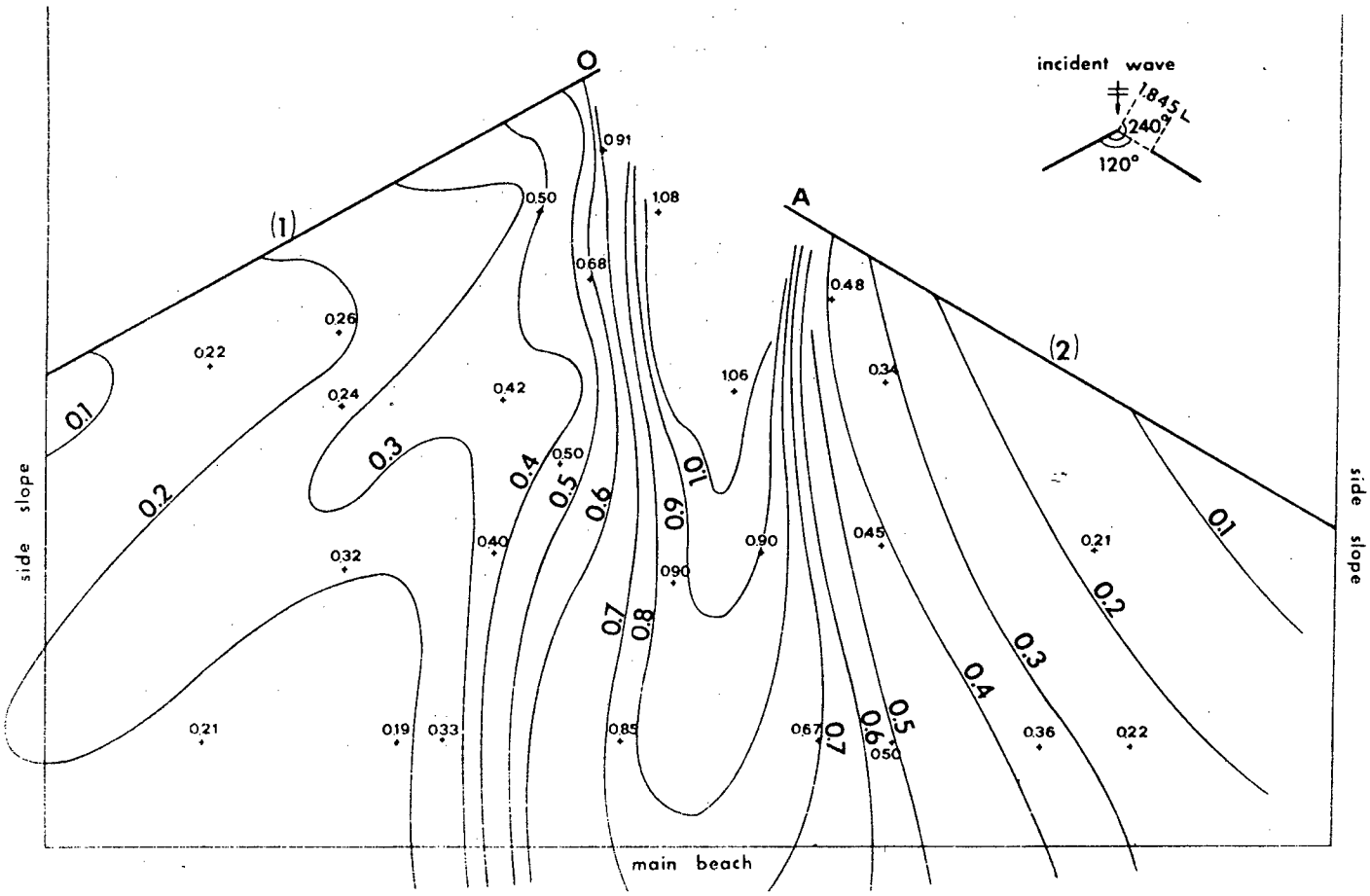

Fig. 2-20 Contours of equal K′, calculated using the Memos solution, compared to experimental results (from Memos 1980c).

2.4.2.6 A Comparison of Breakwater Gap Diffraction Theories.

Before a comparison of the breakwater gap theories previously discussed is given, it should be noted that the fundamental breakwater gap theory of Lamb (1932) should also be included in this comparison. Lamb derived a theory for breakwater gap wave diffraction for the case when the gap width B is small compared to the wave length L. For this case the streamlines of the motion of the water waves through the gap are like those of a flow of liquid through the same aperture. The breakwater gap is assumed to act as a point source, the waves radiating radially outwards with uniform wave heights along individual crests. Since Lamb's solution is strictly only valid for B/L ratios < 0,5 (outside the range of the experimental configurations tested), it has not been discussed in detail. A recent application of Lamb's theory is described by Hotta (1978) who has adapted the theory to predict the diffraction of waves passing through a small gap in a permeable breakwater. Hotta supplies diffraction diagrams for both the B/L = 0,1 and 0,2 configurations for a range of transmission coefficients.

Silvester and Lim (1968) compared the theories of Sommerfeld / Penney and Price, Morse and Rubenstein / Carr and Stelzriede and Lacomb (Sections 2.4.2.2-4). Two breakwater gap configurations, namely the B/L = 1 and 2 configurations, were analysed using the above mentioned theories for angles of incidence 90° (normal incidence) plus 60° and 30°. The Penney-Price theory was only applied to the normal incidence case. The results of their investigation are given in Figs. 2-21. As can be seen from Figs. 2-21, the solution of Sommerfeld / Penney and Price is extremely close to the solution of Morse and Rubenstein / Carr and Stelzriede for the incident angle of 90° and the limit of α to which the latter is carried. For this same normal incidence, the Lacombe approximation is sensibly the same. It is not until θ = 30° that major deviations occur between the Lacombe and the Morse-Rubenstein solutions, the latter solution being more accurate for oblique incidence.

Memos (1980c) analysed a B/L = 2 breakwater gap configuration, for the case of normal incidence, using both his solution (Section 2.4.2.5) and the Sommerfeld / Penney-Price solution. The results

of this comparison are shown in Table 2-1. The values given refer to positions along the axis of symmetry and along the protected faces of the barriers. Distances are measured from the theoretical opening. $K\sqrt{\frac{R}{L}}$ can be seen there is good agreement between the theoretical solutions of diffraction coefficient for breakwater gap ($\frac{B}{L} = 1$) and the solution for the case of oblique incidence ($\theta_0 = 45°$ incident orthogonals form an angle of 45° with the breakwater) by Lacombe (1952). In this solution the Morse-Rubenstein / Carr-Stelzriede solution and the approximate theory of Johnson (1952) (see Section 2.4.3). The results for this comparison are shown in Fig. 2-21.

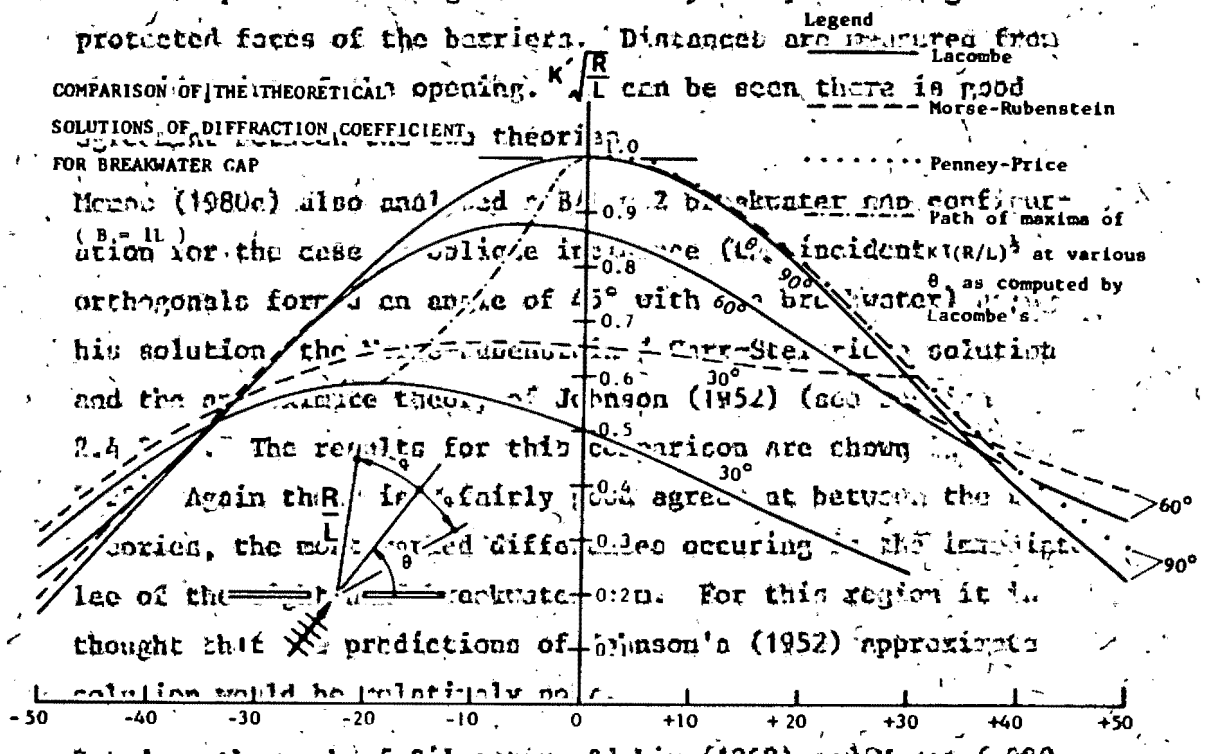

Again the $K\sqrt{\frac{R}{L}}$ is fairly good agreement between the theories, the most marked differences occuring in the immediate lee of the breakwater. For this region it is thought that the predictions of Johnson's (1952) approximate solution would be relatively poor.

Based on the work of Silvester and Lim (1968) and Memos (1980 b & c), the regions of validity for the various theories discussed (for the fully reflecting breakwater case) are:

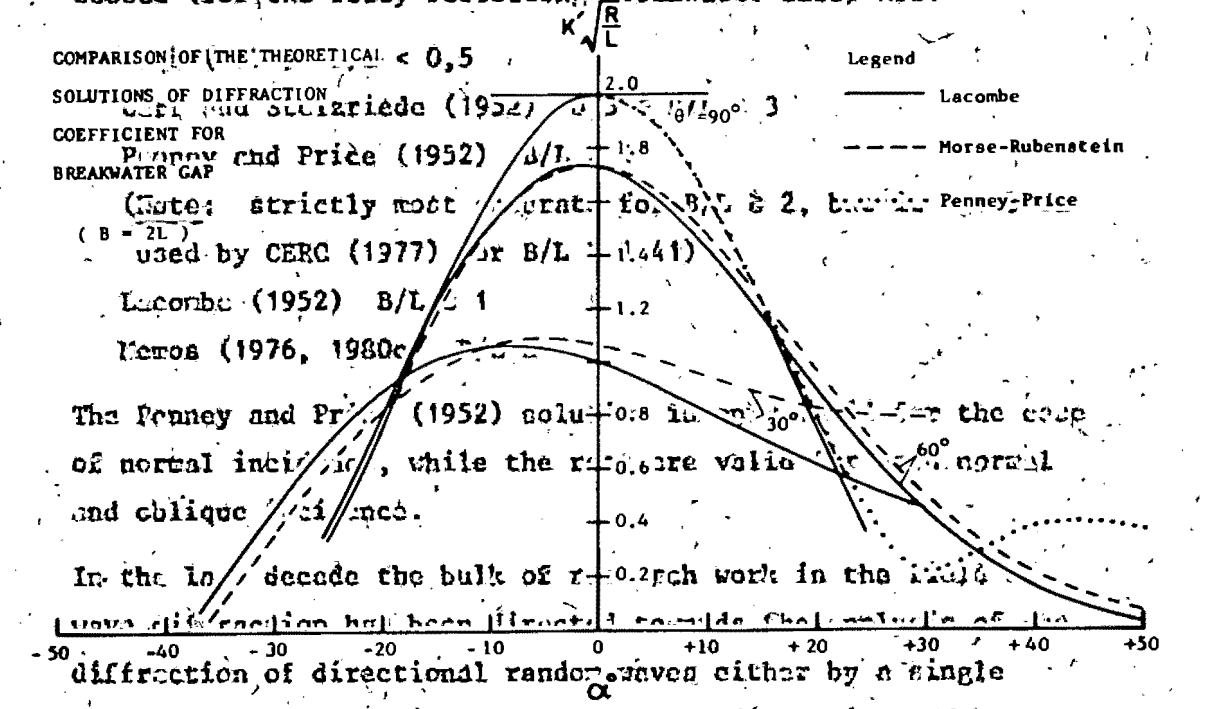

COMPARISON OF THE THEORETICAL SOLUTIONS OF DIFFRACTION COEFFICIENT FOR BREAKWATER GAP

< 0,5

Carr and Stelzriede (1952) B/L = 1 (θ_0 = 90° ?)

Penney and Price (1952) B/L = 1

(Note: strictly most accurate for B/L = 2, but see also Penney-Price ($B = 2L$) used by CERC (1977) for B/L = 1.441)

Lacombe (1952) B/L = 1

Memos (1976, 1980c)

The Penney and Price (1952) solution is only for the case of normal incidence, while the remainder are valid for normal and oblique incidence.

In the last decade the bulk of research work in the field of wave diffraction has been directed towards the evaluation of the diffraction of directional random waves either by a single breakwater, or by some breakwater gap configuration. Mobarek

Fig. 2-21. Comparison of theoretical diffraction solutions for diffraction the B/L = 1 and 2 breakwater gap configurations

in order to (from Silvester and Lim, 1968) action theory could be applied with sufficient accuracy to irregular waves with a

K′ along axis of symmetry									
Y/L	1	2	3	4	5	6	7	8	9
Penney & Price's theory	1.32	1.23	1.11	0.97	0.88	0.81	0.76	0.71	0.66
Present theory	1.36	1.26	1.09	0.97	0.88	0.81	0.75	0.70	0.66
K′ along leeside of barriers									
X/L	1	2	3	4					
Penney & Price's theory	0.44	0.06	0.01	0.01					
Present theory	0.42	0.07	0.03	0.02					

Table 2-1 Comparison of the Penney-Price and Memos solutions for a B/L = 2 breakwater gap configuration (normal incidence) (from Memos 1980c).

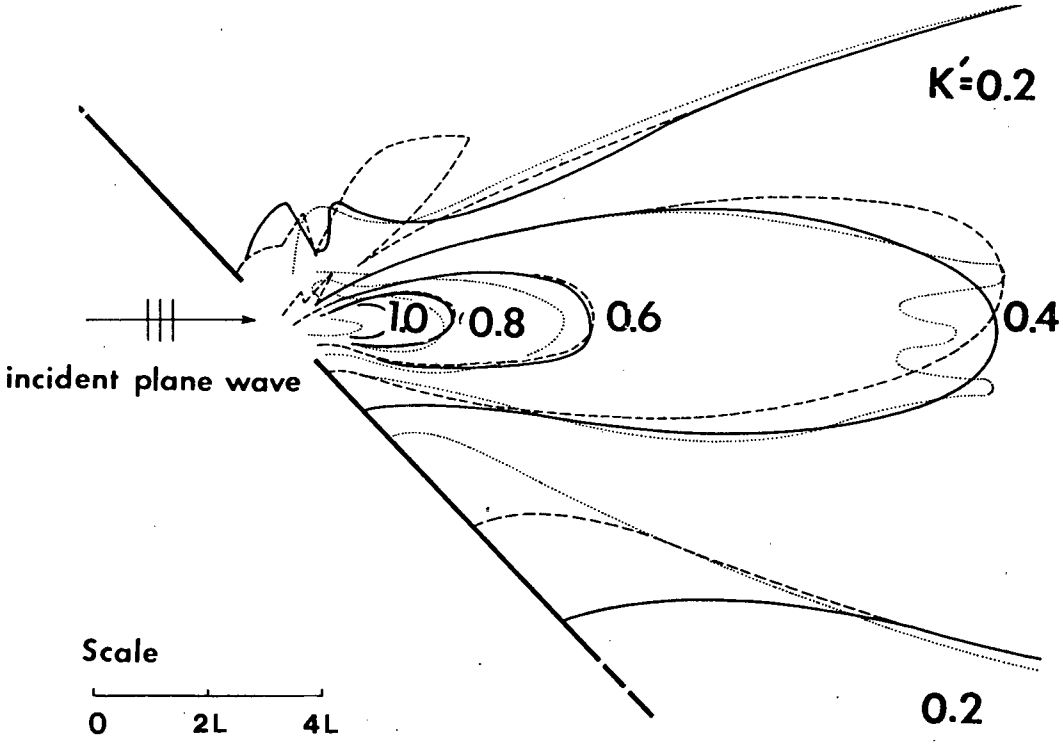

Fig. 2-22 Comparison of the Memos (solid lines), Carr-Stelzriede (dashed lines) and Johnson (dotted lines) solutions, B/L = 2 and oblique (45°) incidence (from Memos 1980c).

directional spectrum. Their investigation showed that a knowledge of directional spectra can be used together with diffraction theory to predict energy spectra of waves in the lee of breakwaters with an accuracy acceptable for many engineering problems. Fan and Borgman (1970) describe a numerical technique to model the diffraction of wind waves by a semi-infinite breakwater, while Takayama and Kamiyama (1977) describe a numerical technique to model the diffraction of both regular and unidirectional irregular waves by a range of breakwater gap configurations.

Raissi and Wiegel (1978) extended the earlier work of Mobarek and Wiegel (1966) to the diffraction of wind generated waves by a breakwater gap. The directional spectra of the incident waves were used together with the theory of Penney and Price (1952) for a breakwater gap to predict, fairly successfully, the energy spectra of the diffracted waves. Goda et al (1978) have constructed a set of breakwater gap diffraction diagrams for random waves with the directional spectrum proposed by Mitsuyasa et al (1975).

2.5 Combined Refraction-Diffraction.

2.5.1 Introduction.

The wave refraction theory fails when caustics, a shore line or other boundary conditions in the horizontal plane are present. In these cases diffraction and reflection of the waves play a part. To solve these problems one could return to the three-dimensional model, but this would be a very rigorous step in practical problems. It would be more convenient to maintain a two dimensional model in which the diffraction effects can be taken into account.

In the past many attempts have been made to derive a two-dimensional equation which describes the combined refraction-diffraction effects in an appropriate way. Pierson (1951), Eckart (1952), Battjes (1968), Biesel (1972) and Ito and Tanimoto (1972) have made some suggestions, but none of these equations is applicable in the whole field from deep to shallow water. Berkhoff (1972) and independently of him, Schönfeld (1972) have succeeded in deriving such an equation. This equation is commonly known as the Berkhoff or mild slope equation. Different derivations of the same result have been given by Smith and Spinks (1975) and Lozano and Meyer (1976). The basic assumption used in the equation is that there is only a gradual variation in water depth within the domain of interest.

For the case of a shore-connected breakwater on a linear plane beach, Liu and Mei (1976) and Lozano and Liu (1980) showed that an approximate closed form solution can be obtained via a parabolic approximation. The parabolic approximation extends the geometric ray theory (Keller, 1958) to allow for the effect of diffraction in the shadow zone behind the breakwater. The parabolic approximation was also used successfully to describe the wave field near a caustic (Radder, 1979; Lozano and Liu, 1980). For the breakwater case the parabolic approximation becomes invalid near the breakwater tip. To remove this weakness, Liu et al (1979) constructed a uniform asymptotic solution for the same problem. The beach topography for the asymptotic solution is required to be uniform in the along-shore direction, but can be arbitrary in the onshore-offshore direction.

Tsay and Liu (1982) developed a numerical formulation of the parabolic approximation to overcome the limitations of the analytical

solution, which was restricted to the case of a uniform plane beach with a breakwater perpendicular to the shoreline. Their numerical (finite difference) formulation allowed the breakwater to be inclined at an angle to the shore line. Tsay and Liu (1982) compared the parabolic approximation, and Liu (1982) the uniform asymptotic theory, to the experimental results of Pantazaras (1979) and Hales (1980). Both theories were shown to supply accurate predictions.

2.5.2 The Berkhoff Refraction-Diffraction Equation.

The Berkhoff equation is the basis of the variational formulation of the finite and infinite element program "WAVE" (Bettess and Zienkiewicz, 1977) used by the author to numerically model the experimental configurations tested (see Chapter Three). A brief derivation of the equation will now be given.

The derivation starts with the basic equations (4) and (8) (in terms of the complex potential function $\emptyset$) and equation (13). However, the co-ordinates are now made dimensionless with the aid of the mean wave length L and the mean water depth in the area of interest, $\bar{D}$ (see Fig. 2-23). For the slope of the bottom the horizontal length L_c will be used as a characteristic length.

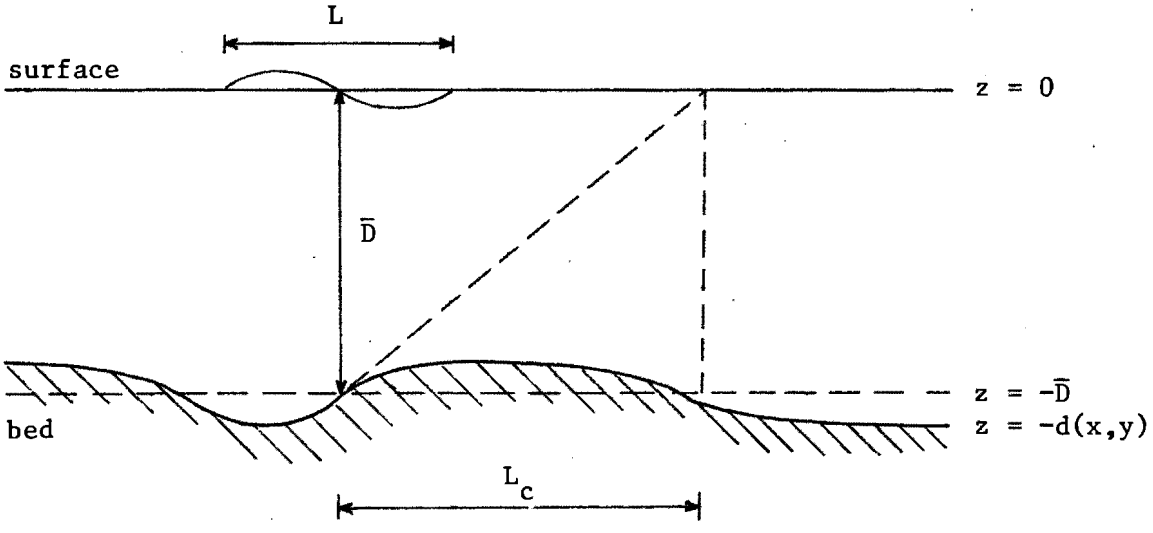

Fig. 2-23 Definition sketch for the derivation of the Berkhoff equation.

The dimensionless parameters used are:

$$x' = x/L \; ; \quad y' = y/L \; ; \quad z' = z/L \quad \text{and} \quad d' = d/\bar{D}$$

$$\bar{x} = x/L_c \quad \text{and} \quad \bar{y} = y/L_c$$

The equations written in these dimensionless quantities are:

$$\frac{\partial^2 \phi}{\partial x'^2} + \frac{\partial^2 \phi}{\partial y'^2} + \frac{\partial^2 \phi}{\partial z'^2} = 0 \tag{56}$$

$$\frac{\partial \phi}{\partial z'} - \delta \phi = 0 \text{ at } z' = 0 \tag{57}$$

$$\frac{\partial \phi}{\partial z'} + \frac{\bar{\nu}^2}{\bar{\mu}} \left(\frac{\partial \phi}{\partial x'} \frac{\partial d'}{\partial \bar{x}} + \frac{\partial \phi}{\partial y'} \frac{\partial d'}{\partial \bar{y}} \right) = 0 \text{ at } z = -\bar{\mu} d' \tag{58}$$

with

$$\delta = \frac{\omega^2 L}{g} \; ; \quad \bar{\mu} = \frac{\bar{D}}{L} \text{ and } \bar{\nu} = \frac{\bar{D}}{\sqrt{L L_c}}$$

Assuming the complex potential function ϕ can be written in the form

$$\phi(x',y',z') = Z(d',z';\bar{\mu}) \phi(x',y',\bar{\nu}\bar{\zeta}) \tag{59}$$

in which $\bar{\zeta} = z'/\bar{\mu}$ and developing the function ϕ into a Taylor-series with respect to $\bar{\nu}\bar{\zeta}$

$$\phi(x',y';\bar{\nu}\bar{\zeta}) = \phi_0(x',y') + \bar{\nu}\bar{\zeta}\phi_1(x',y') + \bar{\nu}^2\bar{\zeta}^2\phi_2(x',y') \tag{60}$$

the following results with dimensional quantities can be obtained after integration of equation (4) (in ϕ) over the water depth (Berkhoff, 1973)

$$Z(d;z) = \frac{\cosh \{k_0(d + z)\}}{\cosh (k_0 d)} \tag{61}$$

and the function $\phi_0(x,y)$ satisfying the equation:

$$\frac{\partial}{\partial x} \left(\frac{\bar{n}}{k_0^2} \frac{\partial \phi_0}{\partial x} \right) + \frac{\partial}{\partial y} \left(\frac{\bar{n}}{k_0^2} \frac{\partial \phi_0}{\partial y} \right) + \bar{n} \phi_0 = 0 \tag{62}$$

in which k_0 $(=2\pi/L)$ is the wave number and $\bar{n}$ the shoaling factor

$$\bar{n} = \tfrac{1}{2}(1 + 2k_0 d/\sinh 2k_0 d)$$

With $c = \omega/k_0$ (the phase velocity) and $c_g = \bar{n}c$ (the group velocity) the equation can be written in the form commonly recognisable as the Berkhoff or mild slope equation :

$$\frac{\partial}{\partial x}\left(cc_g \frac{\partial \phi_0}{\partial x}\right) + \frac{\partial}{\partial y}\left(cc_g \frac{\partial \phi_0}{\partial y}\right) + \omega^2 \frac{c_g}{c} \phi_0 = 0 \qquad (63a)$$

or in vector notation

$$\nabla \cdot (cc_g \nabla \phi_0) + \omega^2 \frac{c_g}{c} \phi_0 = 0 \qquad (63b)$$

for $kd \gg 1$ (deep water conditions) and for kd corresponding to intermediate but constant depth conditions equations (63) reduce to the diffraction (Helmholtz)equation (28). For $kd \ll 1$, which corresponds to the shallow water wave situation, equations (63) reduce to the familiar shallow water wave equation

$$\nabla \cdot (d \nabla \phi_0) + \frac{\omega^2}{g} \phi_0 = 0 \qquad (64)$$

The boundary conditions which the Berkhoff equation must satisfy are the same as for the diffraction or Helmholtz equation (28). These boundary conditions are described in Section 2.3.2.

2.6 Radiating Second-Order Phenomena in Gravity Waves.

For all the breakwater gap configurations tested by the author secondary waves were seen to be generated at and radiate from each breakwater tip every time a crest or a trough passed the tip. This phenomenon is one of a class of phenomena described by Biesel (1963, 1966) as "radiating second-order phenomena in gravity waves".

Biesel carried out a detailed theoretical and experimental investigation of these phenomena which can occur when waves refract, diffract, break and are generated. Of particular interest to the author was Biesel's experimental and numerical investigation of the radiating secondary waves generated at each breakwater tip when water waves pass through a breakwater gap. Biesel stated that in the lee of the breakwater arms two systems of circular waves,

radiating from each breakwater tip, are superimposed upon the primary diffracted waves. That this is in fact the case was clearly shown in the experimental investigation of this phenomenon carried out by the author (see Section 5.6).

A detailed mathematical treatment of the above second order phenomenon is given in Biesel (1966). Biesel has shown that this second-order solution can be constructed in the following way :

1 A first-order solution Φ_1 (= Φ given by equation (12)) is found.

2 A second-order correction Φ_2 is added to Φ_1 and must satisfy the following conditions : Φ_2 must be a solution of the same linearised equations that are satisfied by Φ_1, but with different "second members" which are quadratic functions of Φ_1 and its derivatives.

Thus the first-order solution creates what amounts to generating boundary conditions for the second-order solution. The most important of these generating conditions are those created at the free surface where they will have the same generating effect as a pressure fluctuation. The second-order phenomenon can therefore be considered as a "wave" system obeying the usual (linearised) wave equation but generated by a fluctuating pressure distribution on the free surface. This pressure $\bar{q}$ is given by

$$\bar{q}\ (x,y,t) = -\frac{\rho}{g} \int^{t} \frac{\partial \Phi_1}{\partial t} \frac{\partial}{\partial z} \left(\frac{\partial \Phi_1}{\partial t^2} + g \frac{\partial \Phi_1}{\partial z} \right) dt + \rho (\nabla \Phi_1)^2 \qquad (65)$$

all values being at z = 0 (the free surface).

Biesel states that any local surface pressure fluctuation of a given frequency will give rise to a circular wave of the same frequency and radiating energy in all directions. He also shows that the frequency of the pressure fluctuations is twice that of the first-order waves. Second-order waves can be considered as resulting from waves emitted by practically all points of the free surface at which some first-order motion occurs.

Thus the second-order waves are generated by the first-order phenomena and then radiate independently, as free waves with velocities corresponding to their own wavelength and frequency.

Classical second-order solutions, apart from predicting the local profile distortion of individual waves (e.g. crests sharper than troughs) show no apparent generation of such second-order waves. The explanation of this apparent contradiction is that the second-order solutions in fact only concern simple cases, in which all the second-order "radiation" is cancelled out by interference. For example, in two-dimensional monochromatic waves, the second-order emission is distributed along the entire course of the first-order waves, the phase distribution being uniform through all possible angles. Therefore, for second-order radiation to occur "something" must happen to the waves to disrupt their orderly array and upset the finely balanced mutual cancelling out of their second-order emissions. In nature, of course, real waves do not conform to the rigid patterns of available second-order theories; they diffract, refract, break, etc. and thus provide the mechanisms which allow second-order radiation to occur. Ample proof of the above phenomenon for the case of breakwater gap wave diffraction is given in Section 5.6.

Biesel concedes that in most cases these second-order phenomena may well be insignificant when compared to the primary first-order phenomena. However, there are cases, for example in the lee of a breakwater where the second-order phenomenon becomes very significant. The author found that in the lee of a breakwater gap this phenomenon had a very significant influence on the diffracted wave height distribution in an approximate semi-circular region centered at the gap mid-point and with a radius of 2 to 3 L (where L is the primary wave length).

3. NUMERICAL ANALYSIS

3.1 Introduction

The author needed a mathematical model which could exactly simulate the experimental breakwater gap configurations tested using the infinite basin technique (see Section 5.5). In other words, a mathematical model was required that could model intermediate water waves entering an infinite basin of uniform depth via a rectangular channel for both symmetrical and asymmetrical cases. Clearly the Mitsui or modified Penney and Price solutions (see Sections 2.4.1 and 2.4.2.2) could be used to model the symmetrical configurations, but not, however, the asymmetrical configuration. Furthermore the author was also engaged in experimentally investigating certain refraction - diffraction configurations so therefore, ideally, a mathematical/numerical model was needed which could incorporate refraction effects. Therefore, rather than be restricted to an analytical diffraction model of limited application the author decided to obtain a powerful general purpose numerical model which could model the combined refraction - diffraction of water waves by arbitrarily shaped obstacles in water of varying depths. A lot of work has been done in the field of combined refraction- diffraction and this will now, very briefly, be reviewed.

The bulk of the refraction - diffraction research work has been directed towards the problem of the combined refraction - diffraction of water waves by an island. Homma (1950) derived an analytical solution of the tsunami response for a circular island with a parabolic bottom profile. The island was modelled as a circular cylinder sitting on top of a circular shoal of parabolic bottom profile. Vastano and Reid (1967) derived a finite difference formulation for the same problem and found that their numerical results agreed closely with the analytical solution of Homma (1950). Vastano and Reid (1970) also used their finite difference model to investigate the tsunami response at Wake Island in the Pacific Ocean. They compared their numerical results with the experimental findings of Van Dorn (1970) who constructed and tested a laboratory model of the above-mentioned island.

Lautenbacher (1970) investigated refraction of tsunamis by conical islands. He converted the differential equation for long wave propagation into an integral equation to which a grid based numerical method is applied. Vastano and Bernard (1973) used the finite difference model developed by Vastono and Reid (1967) to investigate the tsunami response of a multiple island system namely the Hawaiian three-island system of Kauai, Niihau and Oahu.

Christiansen (1974) developed a theoretical formulation for long wave refraction - diffraction around circular islands with concave, conical and convex bottom profiles, in accordance with J.B. Keller's Geometrical Theory of Diffraction (Keller, 1962). Smith and Sprinks (1975) derive the mild slope equation (Berkhoff, 1972), and then use both a truncated modal expansion and a finite difference formulation of the above equation to model the same conical island problems investigated by Lautenbacher (1970). The mild slope equation was also derived by Lozano and Meyer (1976) who investigated the trapping of water waves by round islands.

Jonsson et al (1976) compare a classical refraction solution based on geometrical optics, with a diffraction solution, based on the Berkhoff (mild-slope) equation, for the refraction - diffraction problem investigated by Homma (1950) and Vastano and Reid (1967). Berkhoff (1972, 1976) investigated the same problem using a coupled finite element/source distribution formulation of his mild-slope equation. The above problem was also investigated by Bettess and Zienkiewicz (1977) using a finite and infinite element formulation of the Berkhoff equation, while Zienkiewicz et al (1978) compared solutions of this problem in which the exterior region was modelled using infinite elements, an exterior series solution and a "direct" boundary integral method. They found that all three methods gave almost exactly identical results for this problem.

Houston (1976, private communication with Mei, 1978) extended the coupled finite element and hybrid element formulation of Chen and Mei (1974) to deal with variable depth problems. He used this formulation to model the response of the Hawaiian islands to the 1960 Chilean and the 1964 Alaskan earthquakes. Yue et al (1978) extended the two-dimensional hybrid element formulation of Chen and Mei (1974)

to three-dimensions and then used this formulation to model the refraction - diffraction of water waves by a steep sided elliptical island with a circular base.

Both Houston (1981) and Tsay and Liu (1983) developed finite element models based on the Berkhoff equation and the hybrid element method of Chen and Mei (1974). These models are used to model the island on a parabolic shoal problem of Homma (1950) and Vastano and Reid (1967) and also the elliptical island problem of Yue et al (1978). For the parabolical island problem Houston (1981) used a 2640 and a 10560 element mesh for the symmetrical half model while Tsay and Liu (1983) use only 672 elements for the full model. For the elliptical island problem, Tsay and Liu used a 480 element mesh for the whole domain while Houston used 1200 elements for the full domain. It should be noted that Houston (1981) was able to use the very finely discretised finite element meshes described above since he had the very powerful CRAY-1 computer at his disposal.

Another field which has generated interest is the refraction - diffraction problem of wave height prediction in regions where caustics are predicted using conventional (geometrical optics) refraction ray theory. Apart from the area in the lee of an island, as discussed above, such caustics occur when waves are refracted by an isolated shoal. The particular case of the propagation of short waves (short with respect to the size of the disturbance of the bottom) over a circular shoal with a parabolic bottom profile has been investigated by a number of researchers. This problem was investigated by Ito and Tanimoto (1972), both experimentally and using a finite difference formulation, while Berkhoff (1972, 1974, 1975, 1976) analysed this problem using a coupled finite element and source distribution formulation. Bettess and Zienkiewicz (1977) analysed the same problem using finite and infinite elements and compared their results to those of Berkhoff; while Radder(1979) analysed this problem using a finite difference formulation of the parabolic approximation and found that his results closely matched those of Ito and Tanimoto (1972) and of Flokstra and Berkhoff (1977). The similar problem, namely the propagation of long waves over a parabolic shoal was investigated by Berkhoff (1972) and Bettess and Zienkiewicz (1977).

Lozano and Liu (1980) investigated the problem of wave convergence over a semi-circular step shoal. They used a finite difference formulation of the parabolic approximation to model, with good results, the experimental configuration of Whalin (1971). Tsay and Liu (1982) used a similar formulation to model the more complex problem of waves propagating over a parabolic shoal superimposed upon a plane beach. More recently, Bettess et al (1983) have investigated the combined refraction - diffraction of long waves by a semi-infinite breakwater superimposed upon a parabolic shoal, using finite and infinite elements. This research work is described in more detail in Section 3.4.6.

Another interesting refraction - diffraction problem is that of a shore connected breakwater on a linear plane beach. As mentioned in Section 2.5.1 this problem was modelled by Lozano and Liu (1980) (analytical formulation) and Tsay and Liu (1982) (finite difference formulation) using the parabolic approximation. Liu et al (1979) and Liu (1982) also investigated this configuration using a uniform asymptotic solution and as mentioned previously, when compared to the experimental results of Pantazaras (1979) and Hales (1980), both theories were found to give accurate predictions. Houston (1981) also investigated this problem, both experimentally and using a hybrid finite element method. He compared his finite element and experimental results to predictions determined using the uniform asymptotic theory of Liu et al (1979). He found that the uniform asymptotic theory predictions were in excellent agreement with the experimental results. The finite element predictions, on the other hand, agreed quite well with the experimental results in the shadow zone. However, the agreement was not as good outside the shadow zone.

So far all the theoretical/numerical models mentioned are based on linear (small amplitude) water wave theories. To model finite amplitude water waves the linear theory is not strictly valid. Abbott et al (1978) developed a finite difference formulation based on the theory of Boussinesq (1872) to model finite amplitude shallow water waves. More recent work, using the above formulation, has been carried out by Abbott et al (1980) and McCowan (1982). Hauguel (1980) and Hauguel and Pechon (1982) have used a finite difference formulation based on the theory of Serre (1953) to model extremely non-linear

transient events such as a solitary wave entering a harbour basin and the simulation of the effects of a submarine land slide. These transient non-linear problems, as regards computation time and core requirements, can be extremely costly to model. For many coastal engineering problems much cheaper and quite adequate results can be obtained using the linear models described in this section.

3.2 Modern Numerical Methods for Water Wave Diffraction and Refraction - Diffraction

Three general water wave diffraction and refraction - diffraction numerical methods will be considered, namely : integral equation methods, finite element and exterior element methods and finally, coupled finite element and exterior solution methods. The method of finite differences will not be discussed since it is not considered to be as flexible or as general as the three methods listed above. However, the finite difference method has been widely used in the past and is still used today (e.g. Tsay and Liu 1982 and Hauguel and Pechon, 1982).

3.2.1 Integral Equation Methods

The method of integral equations has been used extensively in elliptic boundary value problems (Garabedian, 1964). The typical procedure for this method begins with a singular solution such as a Green function that satisfies the governing equations and nearly all the boundary conditions except that on the body surface. Applying the boundary condition on the body, an integral equation is then obtained for the strength of the singularities. Only in a few exceptional cases can the integral equation be solved exactly. With the use of a computer one can discretize the surface of an arbitrarily shaped body so as to replace the integral equation by a finite but large system of algebraic equations for the average strengths over the surface elements. Once the strength is known the potential everywhere can be found by quadrature. A comprehensive survey of integral equations methods is given by Mei (1978). It should be mentioned that integral equation methods are also referred to as "boundary element procedures" (e.g. Shaw, 1979). The name "boundary elements" being coined by the research group at Southampton University (Brebbia, 1978). Integral equation formulations may yield non-unique solutions at certain discrete frequencies which are given by the eigenvalues associated with the interior Dirichlet problem, within the boundary on which the integral equation is applied (Zietsman, 1982). John (1950) refers to these phenomena as "irregular" frequencies.

Generally for integral equation solutions the ocean bottom is assumed flat and all walls vertical. The problem of acoustic diffraction by an arbitrary body has been investigated by Banaugh (1962) and this work was extended by Harms (1976, 1979a) to deal with the diffraction of water waves by cylindrical structures of arbitrary shape. Hwang and Tuck (1970) used the source integral equations directly for a harbour behind a straight coastline. In principle, they had to discretize the infinite solid boundary, the harbour rim and the coast. To avoid the infinite coastline, Lee(1971) considered as unknown the normal velocity U(S) across the harbour entrance. The field on the ocean side was expressed as an integral of U(S) by means of the Green function for a half plane. Vanishing of the normal velocity on the harbour boundary and matching of the pressure across the harbour mouth lead to coupled integral equations for ϕ along the harbour boundary and U(S) along the harbour entrance.

Mattioli (1981) used an integral equation approach which is a simplified form of the procedure described by Mattioli and Tinti (1980) to model a straight breakwater protruding normally from the coast, a straight breakwater parallel to the coast, an "elbow-shaped" breakwater with one end connected to the coast, a pair of straight breakwaters protruding normally from the coast (similar to the problem investigated by Liu, 1975) and a series of three equal straight breakwaters parallel to the coast. Mattioli (1978) also developed an integral equation formulation of the Helmholtz equation which he used to model the problem of wave-induced oscillations in harbours of variable depth.

For the calculation of forces on structures (floating, submerged, fixed, etc.) a number of integral equation formulations have been developed. For example, the general 3D implementation of Garrison and Rao (1971) is a formulation which has been widely adopted. The formulation of Garrison and Rao (1971) is based on the source distribution formulation of the integral equation. Zienkiewicz et al (1979) call this formulation the "indirect" boundary integral method. Further applications of the source distribution formulation are described by Garrison (1974, 1978) and Boreel (1974).

A second form of the integral equation follows directly from Green's second identity. This form is termed Green's integral equation by Mei (1978) and is called the "direct" boundary integral equation by Zienkiewicz et al (1979). In this formulation, independent interpolation functions may be assumed for the velocity potential and its normal derivatives on the boundary. This formulation has been applied to the calculation of forces on ocean structures by Bai and Yeung (1974), Black (1975), Fenton (1978) and Eatock Taylor and Dolla (1980).

3.2.2 Finite Element and Exterior Element Methods

In this method, the fluid domain which we need to model is subdivided into a number of finite elements and the velocity potential within each element is approximated by a set of polynomial shape functions. Outside the finite element domain the radiation condition (equation (Ch. 2 - 33)) can be modelled using one of two exterior elements namely :

(1) Boundary damper elements. These are elements which are placed around the boundary of the domain modelled using finite elements. They apply the radiation condition at this boundary. If the boundary on which the condition is applied is made sufficiently distant, the results can be quite accurate. This method is described in detail by Zienkiewicz et al (1977a, 1978) who have applied it to the problem of the diffraction of water waves by a cylinder. Similar boundary damper elements were also used by Bai (1972).

(2) Infinite elements. These elements are linked to the finite elements at the inner domain boundary. The infinite elements are defined in a manner very similar to finite elements, the only difference being that their domain extends to infinity, and so exponential shape functions are used. Such shape functions, based on exponential decay were introduced by Bettess (1977) for steady state problems. Zienkiewicz and Bettess (1975) used infinite elements in the study of fluid-structure interaction problems. To test the finite and infinite element method they modelled the proposed Atlantic Generation Station and found that their results agreed closely

with those of Chen and Mei (1974). Bettess and Zienkiewicz (1977) used finite and infinite elements (and a variational formulation based on the Berkhoff equation) to model a variety of diffraction and refraction - diffraction configurations. As described previously, they modelled refraction - diffraction problems such as both short and long waves propagating over a parabolic shoal and long waves propagating around an idealised island. The diffraction configurations tested,plus the more recent work of Bettess et al (1983) are discussed in detail in Section 3.4.6. A detailed description of the finite and infinite program used is given in Section 3.4.

3.2.3 Coupled Finite Element and Exterior Solution Methods

In these methods, the immediate neighbourhood of the body is discretized into the usual finite elements so that their power to fit any geometry is fully utilized, while away from the body where the boundaries are simple or infinite an analytical representation is used. These methods can be divided into two groups, namely :

(1) Coupled Finite Element and Exterior Series Solution Methods

Chen and Mei (1974) (also Mei and Chen, 1975) for the case of water wave diffraction, developed a suitable variational statement leading to the coupling of finite elements with an exterior series solution in Hankel functions. They called their formulation "the hybrid element method" and a comprehensive survey of this method is given by Mei (1978). Eatock Taylor and Zietsman (1981a) name this method "the boundary series element method". The exterior series solution method represents the far field behaviour by an eigenfunction series of wave potentials, the coefficients of which are constrained by a variational principle to provide continuity with the nodal potentials on the localized finite element boundary. A similar formulation was also derived by Bai and Yeung (1974).

As mentioned in Section 3.1, both Houston (1981) and Tsay and Liu (1983) developed finite element models based on the Berkhoff equation and the hybrid element method of Chen and Mei (1974) and used these to model the refraction - diffraction of water waves by idealised islands. Tsay and Liu (1983) also used this method to model wave forces on floating docks. Three-dimensional formulations using the above method have been

developed by Yue et al (1978), Aranha et al (1979) and Eatock Taylor and Zietsman (1981b). Yue et al (1978) use their formulation to determine the wave forces on a square barge and the wave run up on an elliptic island. A more general formulation of this method is given by Zienkiewicz et al (1977b, 1978) who compare it to alternative techniques.

(2) Coupled Finite Element and Boundary Integral Solution Methods

Zienkiewicz et al (1977b) have shown that "boundary integrals" (or integral equations) of the two types, source distributions and Green's identity, can be used as exterior solutions and coupled to finite elements. Hara et al (1979) and Zienkiewicz et al (1979) call the two corresponding formulations respectively the "indirect boundary integral method" and the "direct boundary integral method". As mentioned in Section 3.1 Berkhoff (1972, 1974, 1975, 1976) used a coupled finite element and source distribution formulation to model various refraction-diffraction configurations. Unfortunately, however, his formulation destroys the symmetry of the equations which leads to greater requirements for computer time and storage.

The "direct" method which Eatock Taylor and Zietsman (1981a) name the "boundary integral element method" seems to be the most promising. 2 D formulations of this method are used by Zienkiewicz et al (1977b), Hauguel (1978) and Eatock Taylor and Zietsman (1981a). Hauguel (1978) used the method to model the tides in the North Sea, the response of Marseilles harbour to long waves, diffraction round a vertical cylinder and the combined refraction - diffraction of waves by an idealised island. 3 D formulations are described by Zienkiewicz et al (1978, 1979), Eatock Taylor and Zietsman (1981b) and Zietsman (1982). In the formulations of Eatock Taylor and Zietsman (1981) and Zietsman (1982) the local finite element boundary was chosen as a rectangle in two dimensions, and a rectangular box in three dimensions, which was raised from the sea bed. This feature makes their formulation very flexible when compared to "hybrid element" methods and also the boundary integral methods of Zienkiewicz et al (1977b, 1978, 1979) in which the finite element domain must extend from the free surface to the bottom.

3.3 Finite Element Formulations of the Berkhoff Equation for Infinite Domain Problems.

As can be seen from the previous sections, the finite element formulation of the Berkhoff equation offers a very powerful method of solving general water wave diffraction and combined refraction - diffraction problems, particularly when linked to some method of modelling the exterior regions in infinite domain problems. The general approach in infinite domain problems is to split the problem domain into an inner region, discretized using finite elements, which can accommodate depth variations and an outer infinite region of constant depth modelled using various methods.

The advantages of a finite element formulation of the equations in the inner domain are :

(1) Inhomogeneities such as variations in depth (or even salinity or temperature) are easily dealt with.

(2) Complex shapes can be modelled. This is particularly so, if polynomial isoparametric elements are employed.

(3) Extensions to non-linear formulations are straight forward.

(4) Where a full dynamic analysis of both fluid and structure is needed, it is natural to model the structure and the foundation using finite elements. When the fluid is also modelled at least partially using finite elements, it is relatively simple to formulate the coupling equations.

(5) Conventional integral equation formulations are economical for simple geometries, but in general they are expensive. The equations associated with them are full, non-symmetric and complex. Since a constant distribution of the governing variable is assumed over each panel, a large number of panels is required to model complex shapes. Furthermore, unpredictable non-unique solutions can occur for arbitrary bodies at certain frequencies. Finite element methods, on the other hand, can easily model complex shapes and if based on variational principles their coefficient matrices are banded and symmetric. Furthermore, finite element methods do not suffer from "irregular" frequencies.

We will now consider methods which have been used, in conjunction with finite element formulations of the Berkhoff equation, to model the outer domain. In the outer domain four methods have been used in

conjunction with finite elements to satisfy the infinity conditions. These are :

(1) Boundary "dampers" based on the radiation boundary conditions applied at finite distance. Details and examples are given by Zienkiewicz et al (1977a, 1978).

(2) Exterior analytical or series solutions. The general formulation is described by Zienkiewicz et al (1977b, 1978) while Houston (1981) and Tsay and Liu (1983) use formulations which are based on the hybrid element method of Chen and Mei (1974).

(3) Exterior boundary integral formulations, using source distribution or Green's identity. Zienkiewicz et al (1977b, 1978, 1979) have described and used an energy based method for coupling finite elements and boundary integrals. Berkhoff (1972, 1974, 1975, 1976) also used a source distribution method to model the outer domain.

(4) Infinite elements. These are simply elements which extend to infinity. They have shape functions which include a periodic term and an exponential decay towards infinity. They were introduced by Bettess (1977) and used by Bettess and Zienkiewicz (1977) and Bettess et al (1983) to model water wave diffraction and refraction problems.

A powerful finite element program based on the Berkhoff equation has been developed at University College of Swansea, Wales, over the period from 1975 to date. The latest version of the program, called "WAVE" (Bettess and Bettess, 1976), includes 2D and 3D finite elements and incorporates all four of the outer domain solutions described above. This program has been used to solve a variety of water wave diffraction and refraction - diffraction problems,and examples of its utility are given by Zienkiewicz and Bettess (1975), Bettess and Zienkiewicz (1977), Zienkiewicz et al (1977, 1978, 1979), Hara et al (1979) and Bettess et al (1983).

The author managed to obtain two versions of the "WAVE" program, namely a 1978 version, a card listing of which had been sent to NRIO (National Research Institute for Oceanology), and a much expanded late 1981 version (plus documentation) which was obtained directly from Dr. Bettess. The earlier version included only 2D finite and

infinite elements and was thus considerably smaller than the late 1981 version which included 2D and 3D elements as well as incorporating all four of the outer domain solutions listed above.

The smaller program seemed ideally suited to modelling the experimental breakwater gap configurations described in Section 5.5.3 since only 2D elements were needed and infinite elements seemed to be the best method to model the outer domain. The outer domain methods (1) to (3) did not appear to be suitable for modelling the outer domain of these breakwater gap configurations. The boundary damper elements needed to be a fair distance from reflecting surfaces to be effective and were thus not ideal. The exterior series solution method and the exterior boundary integral method both had to be applied along a boundary encircling the problem domain and since both the channel entrance and the breakwaters were to be modelled as semi-infinite, it was difficult to see how these exterior methods could be applied. Finally, infinite elements were also selected by Bettess et al (1983) to model the outer domain of the semi-infinite breakwater configurations investigated.

All the finite element work described in this thesis was carried out using the smaller 1978 version of the "WAVE" program and all references to the above program apply to the smaller version. The expanded late 1981 version is in the process of being installed and will be used to model various combined refraction - diffraction configurations. A fair amount of work was required to install the "WAVE" program (which was written for an ICL computer) on the UNIVAC 1100 at U.C.T. The sophisticated data structure (developed by J.A. Bettess(1977)) had to be extensively modified and other problems such as common blocks being redefined, etc. had to be solved before the program ran correctly on the UNIVAC.

3.4 The Finite and Infinite Element Program "WAVE".

3.4.1 Basic Principles.

A detailed description of the finite element method is beyond the scope of this thesis. Fortunately, however, there are a number of excellent finite element text books available, for example by Zienkiewicz (1977), Hinton and Owen (1979), Becker, Carey and Oden (1981), Chung (1978) and many others. The reader is referred to these text books for a detailed description of the terms used.

The general procedure for the finite element method when applied to a linear boundary value problem such as the linearised wave equation is as follows :

(1) Express the boundary-value problem as a variational principle where a certain functional is stationary.

(2) Discretize the region into finite elements (usually triangles, quadrilaterals, etc.).

(3) Select interpolating functions (shape functions) that approximate the solution inside the finite elements (linear, quadratic, etc.). For the diffraction problems discussed in this thesis the solution is the complex two dimensional velocity potential function $\phi(x,y)$. The interpolating functions involve unknown coefficients $\bar{a}_i$ which are the values of ϕ at the nodes.

(4) For each element, perform the differentiations and the integrations in order to express the functional as a bilinear form for the unknown coefficients.

(5) Assemble the element bilinear forms (element stiffness matrices and load vectors) so that the total functional is expressed as a global bilinear form.

(6) Minimize the functional with respect to each unknown coefficient and obtain a set of linear algebraic equations for the coefficients.

(7) Solve the equations for the coefficients on a computer to obtain the velocity potentials at the nodes.

(8) Compute quantities of physical interest, for example, water surface elevations, wave heights, etc.

The global system of equations is represented by

$$K\bar{a} + \bar{f} = 0 \tag{1a}$$

such that

$$K_{ij} = \sum_{e=1}^{m} K^{e}_{ij} \quad \text{and} \quad \bar{f}_i = \sum_{e=1}^{m} \bar{f}^{e} \tag{1b}$$

where

K	is the global stiffness matrix
K_{ij}	are terms of the global stiffness matrix
K^{e}_{ij}	are terms of the element stiffness matrices
$\bar{a}$	is the vector of $\bar{a}_i$ the nodal unknowns
$\bar{f}$	is the global load vector
$\bar{f}_i$	are terms of the global load vector
$\bar{f}^{e}_i$	are terms of the element load vectors.

3.4.2 Finite Elements.

For the "WAVE" program the problem is discretized in the standard finite element manner and the unknown function ϕ or ϕ^R is described in terms of the nodal unknowns $\bar{a}_i$, and prescribed shape functions

i.e. $$\phi = N_i \bar{a}_i \tag{2}$$

Two finite elements are used in the inner region, these are the isoparametric forms of the 6-noded triangle and 8-noded quadrilateral elements. The parent and deformed shapes of both the 6-noded triangle and the 8-noded quadrilateral are shown in Figures 3-1 and 3-2. Detailed formulations are given by Zienkiewicz (1977).

The shape functions for the 6-noded quadratic triangular element will now be defined. A convenient set of coordinates L_1, L_2, L_3 for a triangle 1, 2, 3 (see Fig. 3-1a) is defined by the following linear relation between these and the cartesian system.

$$\begin{aligned} x &= L_1 x_1 + L_2 x_2 + L_3 x_3 \\ y &= L_1 y_1 + L_2 y_2 + L_3 y_3 \\ 1 &= L_1 + L_2 + L_3 \end{aligned} \tag{3}$$

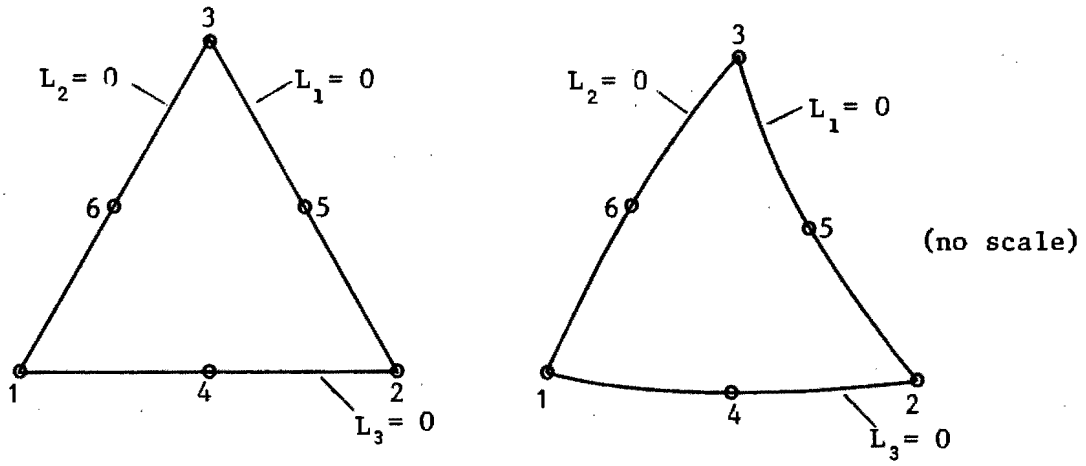

(a) parent shape (b) deformed shape

Fig. 3-1 6 noded quadratic triangle.

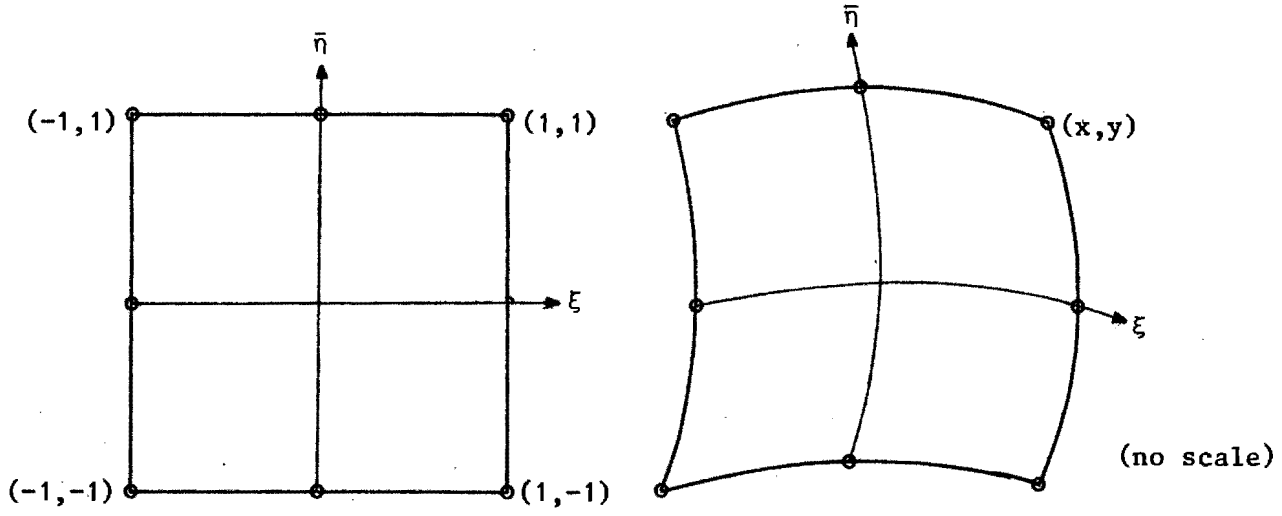

(a) parent shape (b) deformed shape

Fig. 3-2 8 noded quadratic serendipity quadrilateral.

The shape functions for the quadratic triangle are

for corner nodes

$$N_1 = (2\ L_1 - 1)\ L_1, \text{ etc.} \tag{4a}$$

for mid-side nodes

$$N_4 = 4\ L_1\ L_2\ , \text{ etc.} \tag{4b}$$

Note For the "WAVE" program the nodes of the triangular element were numbered consecutively, in an anti-clockwise direction starting with the bottom left-hand node, and not as shown in Fig. 3-1. The convention shown in Fig. 3-1 is used for the purpose of defining the shape functions.

The shape function for the quadratic quadrilateral are now defined in terms of the local $(\xi,\bar{\eta})$ coordinate system and two new variables

$$\xi_o = \xi\ \xi_i \quad , \quad \bar{\eta}_o = \bar{\eta}\ \bar{\eta}_i \tag{5}$$

The shape functions for the corner nodes (see Fig. 3-2a) are defined by :

$$N_i = \frac{1}{4}\ (1 + \xi_o)\ (1 + \bar{\eta}_o)\ (\xi_o + \bar{\eta}_o - 1) \tag{6a}$$

and for the mid-side nodes

$$\begin{aligned} &\text{for} \quad \xi_i = 0 \quad N_i = \frac{1}{2}\ (1 + \xi^2)\ (1 + \bar{\eta}_o) \\ &\qquad\ \ \bar{\eta}_i = 0 \quad N_i = \frac{1}{2}\ (1 + \xi_o)\ (1 + \bar{\eta}^2) \end{aligned} \tag{6b}$$

Integration over the parent elements was carried out using standard Gauss-Legendre numerical integration procedures. For example, the one dimensional Gaussian quadrature formula is written as

$$I = \int_{-1}^{+1} f(\xi)\ d\xi \ = \ \sum_{1}^{n} W_i f(\xi_i) \tag{7}$$

where

W_i = weighting factor for the i^{th} integration point

ξ_i = coordinate of the i^{th} integration point

n = total number of integration points.

A table of abscissae and weight coefficients for the Gaussian quadrature formula is given on page 198 of Zienkiewicz (1977).

3.4.3 Infinite Elements

The detailed description given by Bettess and Zienkiewicz (1977) is summarised here. In the outer domain which extends to infinity a different approach is adopted. Here special infinite elements are used which approximate to the true solution. The parent shape of the infinite element is the strip shown in Fig. 3-3(a). The element has 3 reference points in each of the ξ and $\bar{\eta}$ directions, giving a total of nine points for which global x,y coordinates are specified. The single node variable is the complex value of the velocity potential ϕ. To model the element geometry a parametric representation is used. For this the third reference point in the ξ direction is assumed to be at a large but not infinite distance. In ξ coordinates the nodes are taken to be at 0, 2 and 30. This choice is arbitrary. In the $\bar{\eta}$ direction, as usual, the coordinates are -1, 0, 1. In both directions conventional Lagrange interpolation is used. For each integration coordinate the Jacobian matrix is calculated at ξ = 0, 2 and 30. Now a new coordinate $\bar{s}$ is defined in the ξ direction. It is scaled so that lengths along it

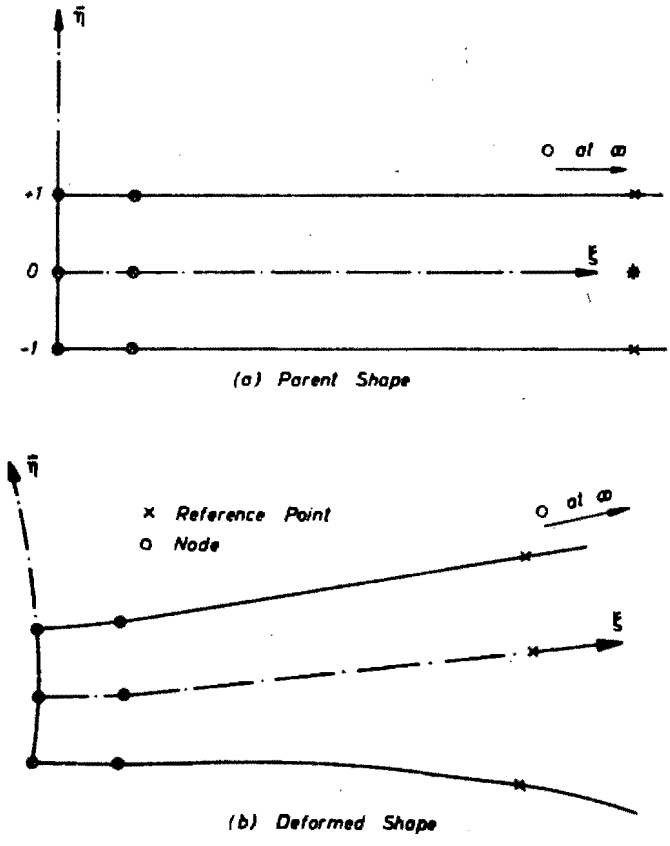

Fig. 3-3 Infinite element (from Bettess and Zienkiewicz, 1977).

are as they are in the x,y coordinates of the problem. Hence

$$\frac{d\bar{s}}{d\xi} = \sqrt{\left[\left(\frac{dx}{d\xi}\right)^2 + \left(\frac{dy}{d\xi}\right)^2\right]} \tag{8}$$

The quantity $d\bar{s}/d\xi$ is calculated at 3 points and the mean value is taken. It is clear then that although the chosen representation allows variations in plan, the element must not be telescoped or stretched in the ξ direction, and this restriction must be observed when choosing the coordinates of the reference points.

The shape functions used to represent the field variable ϕ are now discussed. The shape function chosen is a conventional Lagrange polynomial in the $\bar{\eta}$ direction and hence standard Gauss-Legendre numerical integration is used in that direction. A special shape function is used, however, in the $\bar{s}$ direction. This is of the general form

$$p'(\bar{s})e^{-\bar{s}/L_d}e^{ik\bar{s}} \tag{9}$$

where $p'(\bar{s})$ is a polynomial in $\bar{s}$, L_d is a decay length and k is the wave number. The reasoning behind this choice is that the last term can represent the basic wave shape and the second term the decay of the wave with increasing $\bar{s}$. The shape function chosen satisfies the Sommerfeld radiation condition, i.e. it represents a wave travelling outwards, in the direction of increasing $\bar{s}$, which tends towards zero. This shape function, and its nodal values are now complex, and are such that they have absolute values of 1 or 0 at each node. L_d was chosen by ensuring that in the region close to the area of diffraction or refraction, the decay of e^{-s/L_d} matched roughly the decay of the first term of the general series solution, $\bar{H}_o(k\bar{s})$, where $\bar{H}_o$ is the zeroth Hankel function of the first kind.

The shape functions for the 9-noded infinite element are as follows:

In the $\bar{s}$ direction

$$I_1 = \left(\frac{2 - \bar{s}}{2}\right) e^{-\bar{s}/L_d}e^{ik\bar{s}} \tag{10a}$$

$$I_2 = \left(\frac{\bar{s}}{2}\right) e^{(2-\bar{s})/L_d}e^{ik\bar{s}} \tag{10b}$$

$$I_3 = 1 - I_1 - I_2 \tag{10c}$$

In the $\bar{\eta}$ direction

$$M_1 = (\bar{\eta}^2 - \bar{\eta})/2 \tag{11a}$$

$$M_2 = 1 - \bar{\eta}^2 \tag{11b}$$

$$M_3 = (\bar{\eta}^2 + \bar{\eta})/2 \tag{11c}$$

In the $\bar{s}$ direction Gauss Legendre numerical integration is not appropriate and a specially designed integration formula is used. The formula is essentially similar to the Newton-Coates formulae and was devised to account for the harmonic terms in the shape function. The formula evaluates integrals of the form

$$\int_0^\infty p'(\bar{s}) e^{-\alpha \bar{s}} \, e^{i\bar{\beta}\bar{s}} \, d\bar{s} \tag{12}$$

where $p'(\bar{s})$ is a polynomial and α and $\bar{\beta}$ are constants. The sampling points were chosen arbitrarily to be at $(2n + 1)/4$ multiples of the wavelength, to avoid the zeros of real and imaginary parts of $e^{i\bar{\beta}\bar{s}}$. A series of formulae for polynomials up to quintic was developed and checked. As an example the three point formula is derived by Bettess and Zienkiewicz (1977). In practice a 6-point formula has been used most often.

Finally, in comparison with the other main infinite domain methods, those of boundary integrals and series solutions coupled to finite elements, infinite elements have the following disadvantages and advantages. The infinite elements use more parameters, so more equations must be solved and secondly, the choice of a decay length is somewhat arbitrary. On the other hand, the infinite elements are simpler theoretically; no special variational formulations or boundary integral procedures are needed, they simply appear as a slightly different element type. The infinite elements do not destroy either the symmetry of the equations, or their banded structure, and require no special solution techniques.

3.4.4 Variational Formulation and Solution of Equations

The variational formulation derived by Bettess and Zienkiewicz (1977) for the "WAVE" program is based on the Berkhoff equation (Ch.2-63) described in Section 2.5.2 and the boundary conditions described in Section 2.3.2. Slightly different formulations of the boundary conditions described in Section 2.3.2 have been used. For the

variational formulation used in "WAVE" the mixed boundary condition (Ch. 2-31) at vertical walled boundaries is given as

$$\frac{\partial \phi}{\partial n'} = i\tau k\phi \qquad (13)$$

where τ is a real dimensionless damping coefficient. Total reflection is given by $\tau = 0$ and total absorption is given by $\tau = 1$. For the version of "WAVE" used by the author total reflection was assumed at all solid boundaries.

At infinite boundaries Zienkiewicz and Newton(1969) derived an infinite boundary condition, for periodic motion, namely :

$$\frac{\partial \phi}{\partial r} = - i\, k\, \phi \qquad (14)$$

which is a special case of the Sommerfeld radiation condition (Ch. 2-33).

The variational formulation of the Berkhoff equation (Ch. 2-63), summarised from Bettess and Zienkiewicz (1977), is now described It is convenient to split the domain of the problem into inner and outer parts. The velocity potential in the outer domain is written as

$$\phi = \phi^I + \phi^R \qquad (15)$$

where ϕ^I is the known incident wave and ϕ^R is the outgoing wave, unknown at present. The variational functional corresponding to equation (Ch.2 - 63) is given as

$$\Pi = \iint \tfrac{1}{2}[cc_g(\nabla\phi)^2 - \frac{\omega^2 c_g}{c}\phi^2]dxdy - \int_{S_1} \tfrac{1}{2} i\omega\pi c_g\phi^2 ds \qquad (16)$$

The natural boundary condition now corresponds to equation (13) on the inner solid boundary S_1. In the outer domain the same functional is used, but now equation (15) is substituted i.e.

$$\Pi = \iint \tfrac{1}{2}[cc_g(\nabla(\phi^I+\phi^R))^2 - \frac{\omega^2 c_g}{c}(\phi^I+\phi^R)^2]dxdy \qquad (17)$$

The outer domain functional can be simplified. The quadratic terms in ϕ^I are not subject to variation and can thus be discarded. As ϕ^I is already a solution of equation (Ch. 2-4), the linear terms in ϕ^I can be transformed to a line integral on the inner domain boundary. For constant depths, implying constant c and cg, the functional for waves in the outer region can be written as

$$\Pi = \iint \tfrac{1}{2}\left[cc_g(\nabla\phi^R)^2 - \frac{\omega^2 c_g}{c}(\phi^R)^2\right] dxdy + \oint cc_g \left| \frac{\partial\phi^I}{\partial x}\phi^R dy - \frac{\partial\phi^I}{\partial y}\phi^R dx \right| \tag{18}$$

The second term of equation (18) vanishes at the infinitely distant boundary as ϕ^R and $\partial\phi^R/\partial n$ both become zero there in addition to the requirement of equation (Ch. 2-33). On the inner boundary the integral produces a 'forcing' term. The only restriction on the incoming wave, in this formulation, is that it is a solution of the wave equation. The program "WAVE" allows only two kinds of incident waves. These are a plane monochromatic wave, and the same wave plus its total reflection at an infinite straight wall. The second option was not used.

The procedure used in "WAVE" to assemble and solve the equations is the frontal solution algorithm due to Irons (1970), adapted to the solution of equations with complex coefficients. Further details of this solution program are given by Irons and Ahmad (1980). The call chart for the program "WAVE" plus a description of the subroutines used is given in Appendix 3A.

3.4.5 The "IFS" Boundary Condition

When using the "WAVE" program the boundary between the inner and outer region is specified by means of the "IFS" boundary condition. This boundary condition is generally applied at the finite/infinite element interface. The "WAVE" program was originally formulated to deal with the problem of a uniform progressive wave field over an infinite area which is slightly altered by the presence of an obstacle, say a vertical cylinder or an island, i.e. the program assumes that the incident wave is defined everywhere (Bettess, 1983). For this case in the outer region (beyond IFS) it is assumed that the solution will tend to the incident wave potential ϕ^I. That is ϕ^R tends to zero in the manner defined by Sommerfeld (equation(Ch.2-33)) leaving just ϕ^I. Thus the IFS boundary can be thought of as an edge load in the form of the line integral given as the second term of equation (18).

For the basic configuration studied by the author, i.e. an incident wave train entering an infinite basin via a rectangular channel, the assumption that the incident wave train is defined everywhere is invalid. For this configuration the incident wave exists only in

the channel while in the basin the solution should tend to zero and not the incident wave (because logically we do not expect the incident wave to appear inside the basin). The above configuration, which approximates the situation of waves passing through a gap between two totally absorbing breakwaters, was successfully modelled by applying the "IFS" boundary condition only at the finite/infinite element interface within the channel.

3.4.6 Previous Diffraction Work

Zienkiewicz and Bettess (1975) modelled three 2D diffraction problems using the "WAVE" program. The first problem was that of waves diffracted by a cylinder. They found that the wave elevations on the surface of the cylinder, calculated using finite and infinite elements, were in good agreement with the analytical solution of MacCamy and Fuchs (1952). The second problem they investigated was that of a rectangular harbour set in an infinite straight coastline and subject to waves incident normal to the coast. Again the finite and infinite element configuration gave good results when compared to the previous numerical and experimental work reported by Chen and Mei (1974). The third problem was that of the response of the Atlantic Generating Station's harbour to incident long waves. Zienkiewicz and Bettess (1975) again found that the finite and infinite element model gave good results when compared to the original work carried out by Chen and Mei (1974) using a "hybrid" element model. These three diffraction examples are again given by Bettess and Zienkiewicz (1977),who in addition modelled the problem of a circular segment of breakwater adjacent to an infinite coastline. Agreement between the finite and infinite elements results and the analytic results of Chen and Mei (1974) is good.

The recent work of Bettess et al (1983) is of particular interest to the author. Bettess et al (1983) used the 2D finite and infinite elements of the "WAVE" program to model the problem of waves diffracted by a semi-infinite breakwater, the waves being incident 45°, 90°, and 135° to the breakwater. They also modelled the refraction - diffraction problem of waves incident 90° to a semi-infinite breakwater superimposed upon a parabolic shoal. Two different shoals were considered. Both a radial and a rectangular

mesh were used to model the diffraction configurations and it was shown that the shape of the mesh had no appreciable effect on the results. The singularity in the velocity at the breakwater tip was modelled as described in Section 3.6. The finite and infinite element results were compared to analytical results calculated at the nodal positions using the numerical formulation of Fan et al (1967) based on the Sommerfeld (1896)/Penney and Price (1952) solution.

The results for the normal incidence case of the semi-infinite breakwater problem, given by Bettess et al (1983) are given here since these results are thought pertinent to the present study. These results can be compared to the diffraction diagrams given in Figs. 2-4 and 2-6. The radial mesh which was used by Bettess et al (1983) to model the semi-infinite breakwater configuration is shown in Fig. 3-4. The radial distance from the centre to the finite/infinite element interface is 162 m. The incident waves had the following characteristics : amplitude 1 m, period = 20 seconds and wave length = 242.6 m. The water depth was a constant 15 m. It can be seen that

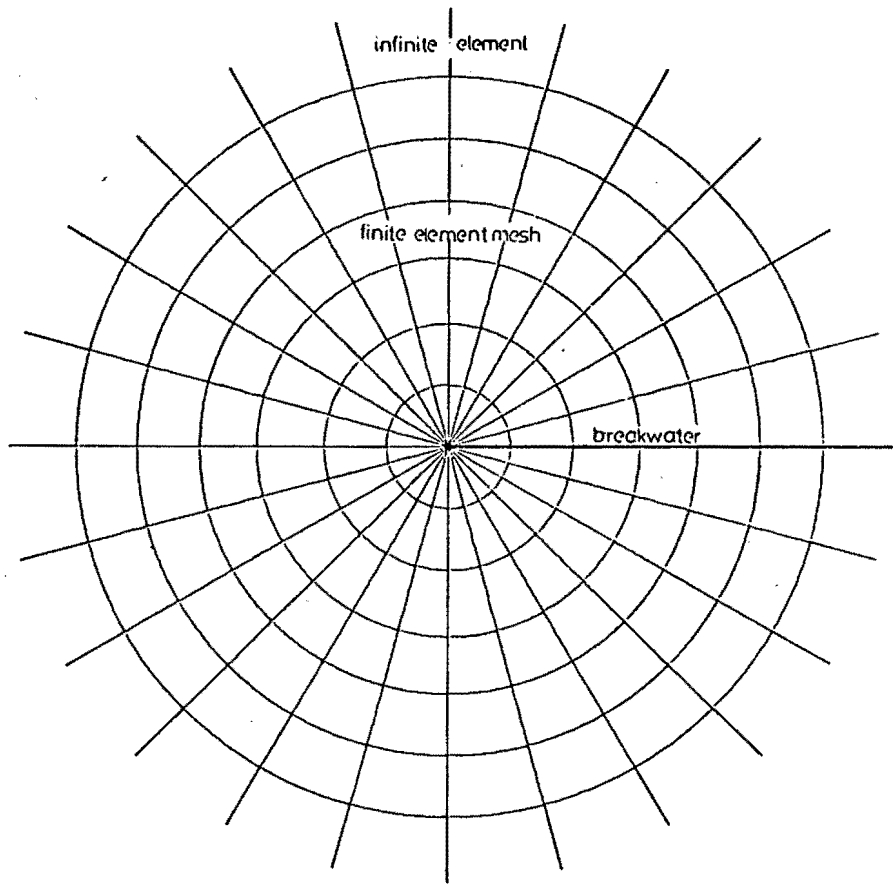

Fig. 3-4 Radial mesh used by Bettess et al (1983) to model the semi-infinite breakwater problem.

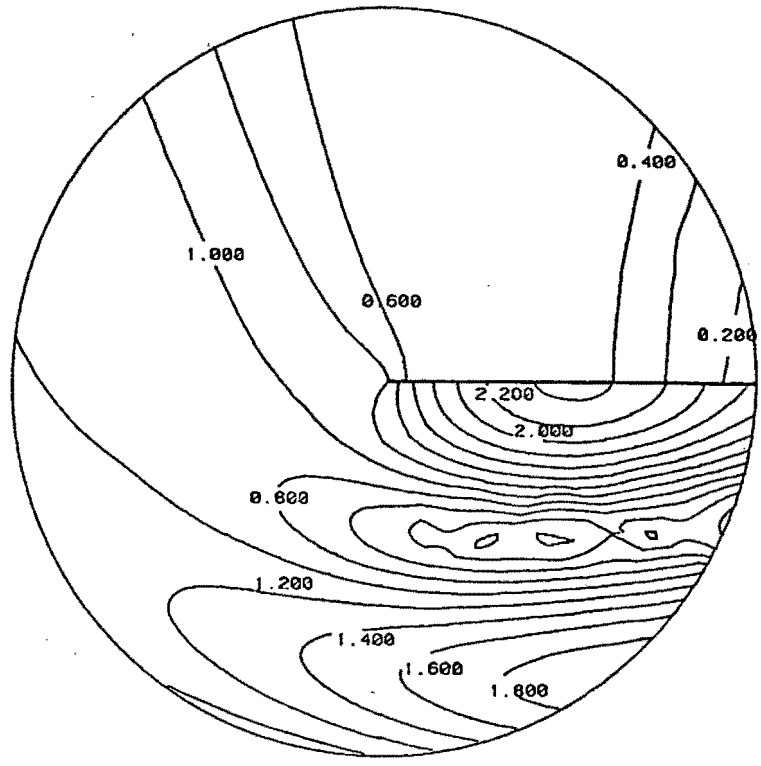

Fig. 3-5 Finite and infinite element results for semi-infinite breakwater, normal incidence case, from Bettess et al (1983)

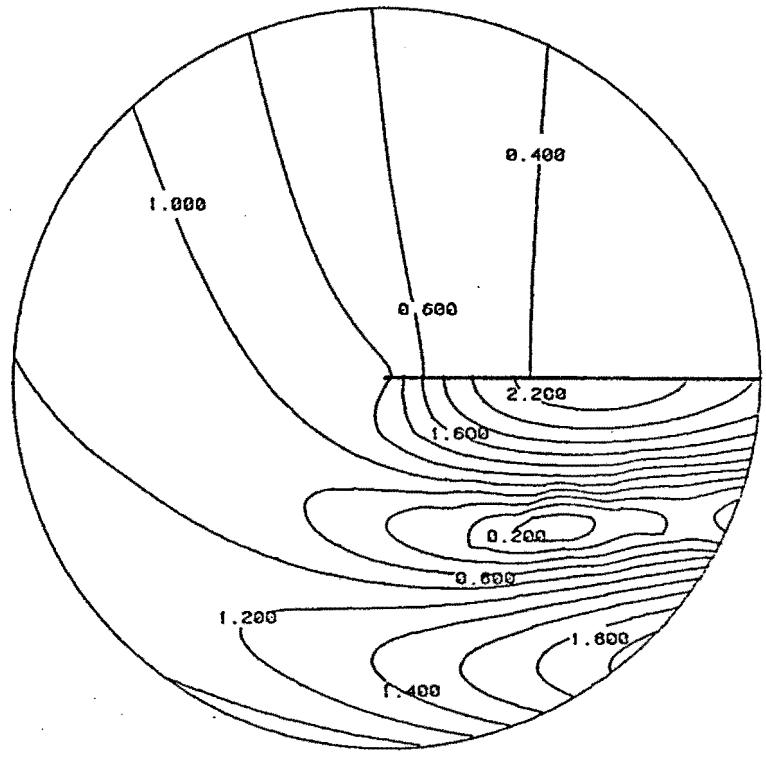

Fig. 3-6 Analytical results for semi-infinite breakwater, normal incidence case, from Bettess et al (1983)

only a very small area, with a radius of 0,67 L from the breakwater tip, has been modelled. The finite and infinite element diffraction diagram is shown in Fig. 3-5 and the corresponding analytical diffraction diagram is shown in Fig. 3-6. From these diagrams it can be seen that there is excellent agreement between the finite element and analytical results in the region seaward of the breakwater but that the results differ significantly in the lee. As expected, there is a good correlation between Figures 2-6 and 3-6 since both these diagrams were calculated using the numerical formulation of Fan et al (1967). It should be noted that in Fig.2-6 the 1.5 and 2.0 contours adjacent to the seaward face of the breakwater have been omitted.

3.5 Finite and Infinite Element Modelling of the Experimental Breakwater Gap Diffraction Configurations

The program "WAVE" was used to model the experimental breakwater gap diffraction configurations described in Section 5.5.3. The finite and infinite element meshes used to model the experimental configurations are shown in Appendix 3B. Six of the seven experimental configurations investigated are symmetrical about the breakwater gap centre line and for these only the left-hand side of the basin was modelled. To test this assumption, the full basin and channel of the B/L = 1 configuration were also modelled and the results obtained were almost exactly identical to those obtained using the half model. For the experimental asymmetrical configuration, however, it is obvious that the full basin and channel had to be modelled. For all 7 of the channel entrance configurations modelled using the "WAVE" program, the "IFS" boundary condition was applied only at the finite/infinite element interface within the channel.

The infinite basin was modelled using a radial mesh centred at the breakwater gap mid-point. This mesh was generated using a radial mesh generator written by Ms J A Bettess of the University College of Swansea. The entrance channel mesh was generated by hand and linked to the radial mesh. The radial mesh generator was extensively modified by the author to make it more flexible and to facilitate the linking of the channel mesh to the basin mesh.

Bettess et al (1983) recommend that at least 4 elements per wave length are needed to obtain satisfactory resolution of the wave detail. Based on the work undertaken for this thesis, the author believes that a more flexible approach to the discretization is possible if the number of elements per wave length is made a function of the wave height gradient in the basin. In regions of large wave height gradients a fine mesh would be used, while a coarser mesh could be used in regions where the wave height varied more slowly. This is analogous to the structural analysis problem where a fine mesh would be used to model regions of stress concentration, while a coarser mesh would be used to model adjacent areas.

Based on the above argument, it is apparent that a radial mesh, centred at the breakwater gap mid-point, would be best suited to model the diffraction of the waves entering the infinite basin since the finest discretization would be concentrated in the region of greatest wave

height variation. The author found, after experimenting with a large number of different mesh configurations, that the best compromise (between the need for adequate accuracy and the need to limit the number of elements used) was to have in the radial direction, on average, a minimum of 6 elements per wave length in the breakwater gap region and, on average, a minimum of 2,5 elements per wave length outside this region. The circumferential partitioning of the mesh into 10° sectors was found to be adequate for the diffraction problems modelled.

For each experimental breakwater gap configuration the experimental water depth, wave period and wave height were modelled exactly. The diffraction coefficient K' was calculated over each element by dividing the integral of the absolute amplitudes over the element by the product of the incident wave amplitude and the element area. The resultant contour plots of equal diffraction coefficients are shown in Section 6.1 where they are compared to the corresponding experimental and analytical diffraction diagrams. The finite element results were plotted using the Saclant Graphics Package (described in Section 4.8.5.4). The average run time on the UNIVAC 1100 for the 6 symmetrical half models was 90 seconds while the run time for the asymmetrical model was 254 seconds (for a mesh consisting of 405 finite elements and 25 infinite elements).

3.6 Finite and Infinite Element Modelling of the Diffraction of Waves Passing Through a Gap in a Perfectly Reflecting Breakwater

The theoretical diffraction diagrams commonly given in coastal engineering design manuals such as CERC (1977) (e.g. Figs. 6-3, 6, 11, 16) are for the case of waves passing through a gap in a perfectly reflecting breakwater. As described in Section 5.2.2.1 the author attempted to model experimentally the fully reflecting breakwater situation and found that in the small wave basin at his disposal, it was difficult to prevent wave energy reflecting off the wave paddle and entering the basin. The author found that by placing splitter plates at the breakwater tips extending to the paddle (absorbing beaches were also placed on the paddle side of the breakwaters) and using the infinite basin technique described in Sections 5.4 and 5.5, an undistorted diffracted wave field could be obtained in the model basin. This configuration which approximated the fully absorbing breakwater situation, was successfully modelled using finite and infinite elements.

Even though the author recognised that the differences between the theoretical diffraction diagrams for the fully absorbing and fully reflecting breakwater cases would be quite small (compare the Mitsui solution results for a guided entrance with those obtained using the Sommerfeld solution in Fig. 2-9) it was decided that the fully reflecting breakwater case should be modelled using finite and infinite elements. As pointed out by Bettess et al (1983) one of the difficulties associated with numerically modelling the diffraction of water waves passing through a gap between two infinitesimally thin fully reflecting breakwaters is that there is a singularity in the velocity at each breakwater tip. This singularity is of the form

$$\nabla\phi \simeq r^{-\frac{1}{2}} \quad (r = \text{radius from tip}) \tag{19}$$

This singularity can be modelled quite effectively using the technique described by Hensell and Shaw (1975) and Barsoum (1976, 1977) to model the corresponding singularity at the tip of a crack in an elastic or perfectly plastic material. These researchers have shown that if the mid-side node of an 8-noded isoparametric rectangular element is moved to the quarter point, a singularity is induced in the element at the closest corner. The same phenomenon occurs when using a 6-noded isoparametric triangular element. This singularity is

precisely the kind which is needed at the tip of each breakwater.

It should be noted that although this device enables the numerical technique to simulate the singularity found in the analytical solutions, this singularity does not occur in real water waves. In real water waves the high velocity gradients at the breakwater tips produce viscous forces which retard the flow leading to separation and the formation of vortices. Experimentally, as described in Sections 5.5 and 5.6, both vortices and radiating secondary waves were generated at the breakwater tips by the primary wave train as it entered the model harbour basin.

To test the technique described above, a fully reflecting B/L = 1 breakwater gap configuration was modelled. The finite and infinite element mesh used to model this configuration is shown in Fig. 3-7. This mesh is identical to the mesh used to model the corresponding channel entrance configuration, shown in Appendix 3B, except that now the area between the channel wall and the breakwater has been filled. The singularity at the breakwater tip was modelled, as described above, by placing all the mid-side nodes adjacent to the tip at the quarter points. The IFS boundary condition was applied only along the finite/infinite element surface on the seaward (waveward) side of the gap. The wave input data was the same as that used for the channel entrance case. The diffraction diagram calculated for the fully reflecting B/L = 1 breakwater gap configuration (for the model basin area only) is shown in Fig. 3-8. This is the best result obtained for this configuration and initial results using a coarser mesh (Pos, 1983) are poorer.

If one compares Fig. 3-8 with Fig. 6-10 (the F.E. diffraction diagram for the channel entrance case) it is apparent that the wave height attenuation in the incident wave direction occurs more rapidly for the fully reflecting case. This is contrary to the findings of Daemrich and Kohlhase (1978) (Fig. 2-9).

If Fig. 3-8 is compared to the corresponding analytical diffraction diagram Fig. 6-11 (from Johnson, 1952) it is apparent that the correlation between the finite element and analytical results is particularly poor in the incident wave direction. However, in the immediate lee of the breakwaters the agreement between the two diagrams is good.

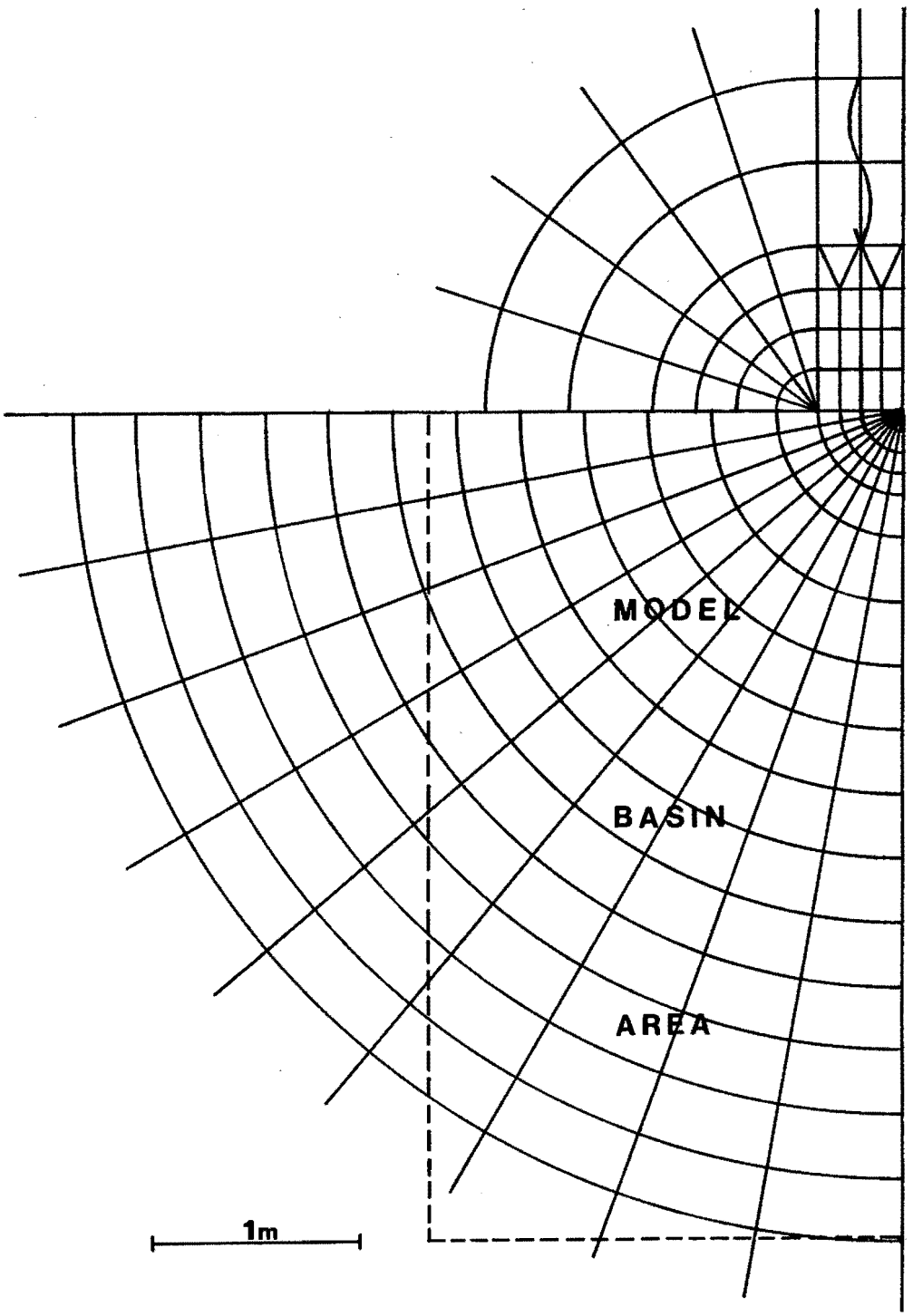

Fig. 3-7 Element mesh for the B/L = 1 breakwater gap configuration; fully reflecting breakwater case.

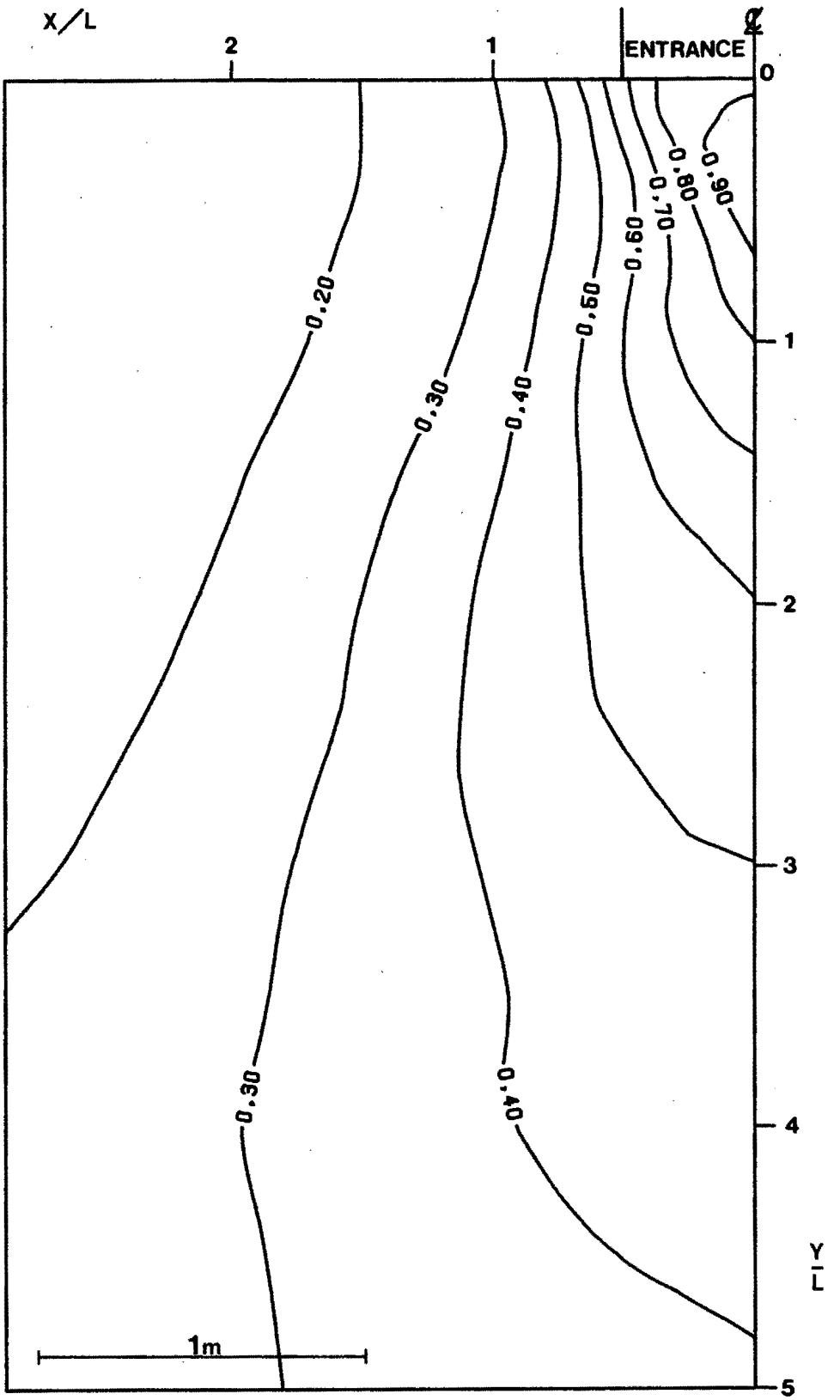

Fig. 3-8 Finite element diffraction diagram for the B/L = 1 breakwater gap configuration; fully reflecting breakwater case.

To try and understand, and possibly solve, the above anomaly the author entered into correspondence with Dr Peter Bettess of Swansea (Bettess, 1983). Certain illogicalities became apparent, such as the way the "WAVE" program treats the reflected wave on the seaward side of the breakwater where it tends to infinity, and it was agreed that the results obtained were the best that could be achieved with this formulation and this program. The author thus decided that the "WAVE" program would be used exclusively to model the experimental fully absorbing (approximated by a channel entrance) configurations tested and that both the experimental and finite element results would be compared to the corresponding analytical results (for fully reflecting breakwaters) where these were available.

4. PHOTOGRAMMETRIC WAVE HEIGHT MEASUREMENT

4.1 Close Range Photogrammetry

4.1.1 Introduction

Photogrammetry may be defined as the art, science and technology of obtaining reliable information about physical objects and the environment through processes of recording, measuring and interpreting photographic images and patterns of recorded radiant electromagnetic energy (Wolf 1974). Included within the definition of photogrammetry are two distinct areas (1) metric photogrammetry, which involves precise measurements and computations to determine sizes and shapes of objects, and (2) interpretive photogrammetry encompassing the branches of photographic interpretation and remote sensing, which deals with the recognition and identification of objects. The first area, metric photogrammetry, is applied primarily in the preparation of planimetric and topographic maps from photographs. The photographs are most often aerial (taken from an airborne vehicle), but terrestial photos, (taken from earth based cameras) are also used.

Close range photogrammetry (or short range photogrammetry) lies within the definition of metric photogrammetry but covers measurement situations where the object to camera distance is limited. A maximum limit of 300m (Atkinson 1980) has been advocated while the minimum distance can be as little as a fraction of a millimetre in the case of microscope photographs.

In comparison with other measuring techniques close range photogrammetry has many advantages: (Atkinson 1980)

(i) the object is not touched during measurement;

(ii) data capture (acquisition) is rapid;

(iii) the photographs store both semantic and metric data with very high density;

(iv) the photographs are documents related to the time when they were taken and they can be used as legal evidence;

(v) not only rigid and fixed objects but also deformation and movement can be measured;

(vi) time dependent parameters such as velocity, acceleration and frequency can be determined;

(vii) evaluation of the metric photographs can be done at any time in the office and repetition and amendment are always possible;

(viii) photography and evaluation are flexible and can easily be optimised to the project requirements as, for example, in accuracy;

(ix) the invisible part of the spectrum can be used for creating images;

(x) complicated shapes and movements are easily measured;

(xi) stereoscopy is the basis for continuous contouring of irregular objects;

(xii) analytical methods provide a means of integration with succeeding calculations and data handling.

There are however certain drawbacks which have to be overcome:

(i) the result of the measurement is not immediately at hand, because time is needed for photographic processing and for evaluation;

(ii) except for the simplest problems, the need for specialised and expensive equipment makes the method expensive;

(iii) errors during photography and development of the film can ruin the whole measuring project;

(iv) it must be possible to photograph the object;

(v) specialised instrumentation and personnel are not always available.

The photography may be static (stationary objects) or dynamic (moving objects). For static photography, slow fine grained, high resolution films may be used, with time exposures of a number of seconds. Stereo pairs can be made by using a single camera and making successive exposures at both ends of a base line. In taking dynamic photographs, fast films and rapid shutter speeds are necessary. If stereo pairs of dynamic occurrences are required, two cameras located at the ends of a base line must take simultaneous exposures. It was the authors intent to develop a system whereby dynamic close range photogrammetry could be used to measure precisely all the wave parameters of wave patterns in model harbours.

4.1.2 General Applications of Close Range Photogrammetry

A detailed description of all the applications of close range photogrammetry is beyond the scope of this document. Architectural, archeological, medical, engineering and industrial applications of close range photogrammetry are described in detail in publications

by Atkinson (1969, 1976, 1980), Karara (1976, 1979), Torlegard (1976), Oshima (1976) and Schwidefsky (1970). Previous applications in the field of waveheight and pattern measurement is described in Section 4.2.

4.1.3 Basic Theory of Stereophotogrammetric Measurement.

First consider the simple situation of a camera mounted with its axis truly vertical above a horizontal terrain (i.e. with no tilt whatsoever, fig. 4-1). The image in the photograph will be a projection of the photographed terrain, and the distance between points on the ground at equal elevation can be determined fairly simply if the scale of the photography is known. This scale can be expressed in terms of f and H_f in the form below:-

$$s = f/H_f \qquad (1)$$

where s is the scale, defined as the ration of corresponding linear lengths in the terrain and in the photograph, f is the principal distance of the lens, and H_f is the altitude above the terrain level ABC. If the values of f and H_f are known, the positions of A, B, and C can be determined relative to the camera from the images a, b, and c. But if the terrain had any non-horizontal profile, two photographs would be needed to determine the complete geometry of that terrain.

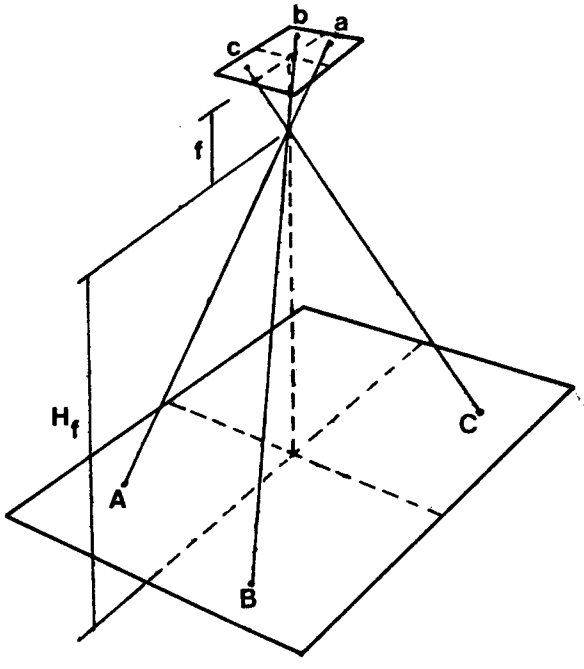

Fig. 4-1 Vertical photography of plane ABC

To describe the latter situation two photographs are illustrated in Fig. 4-2 below. Consider them to be taken truly vertically by two identical cameras from the same altitude. The image of a point A at a height h_A above the ground datum appears at a_1 and a_2 on the equivalent positives taken at two successive air stations S_1 and S_2. The distance S_1S_2 is the "air base" $\dot{B}$. From the diagram if one draws $S_1\bar{a}_2$ parallel to S_2a_2 then by similar triangles

$$\frac{a_1\bar{a}_2}{S_1PP_1} = \frac{\dot{B}}{H_f - h_A}$$

Now $S_1PP_1 = f$ and $a_1\bar{a}_2$ is known as the "absolute parallax" of A. Therefore in general the absolute parallax P_A of a point is given by

$$P_A = \frac{f \times \dot{B}}{H_f - h_A} \qquad (2)$$

and hence

$$h_A = H_f - \frac{\dot{B} \times f}{P_A} \qquad (3)$$

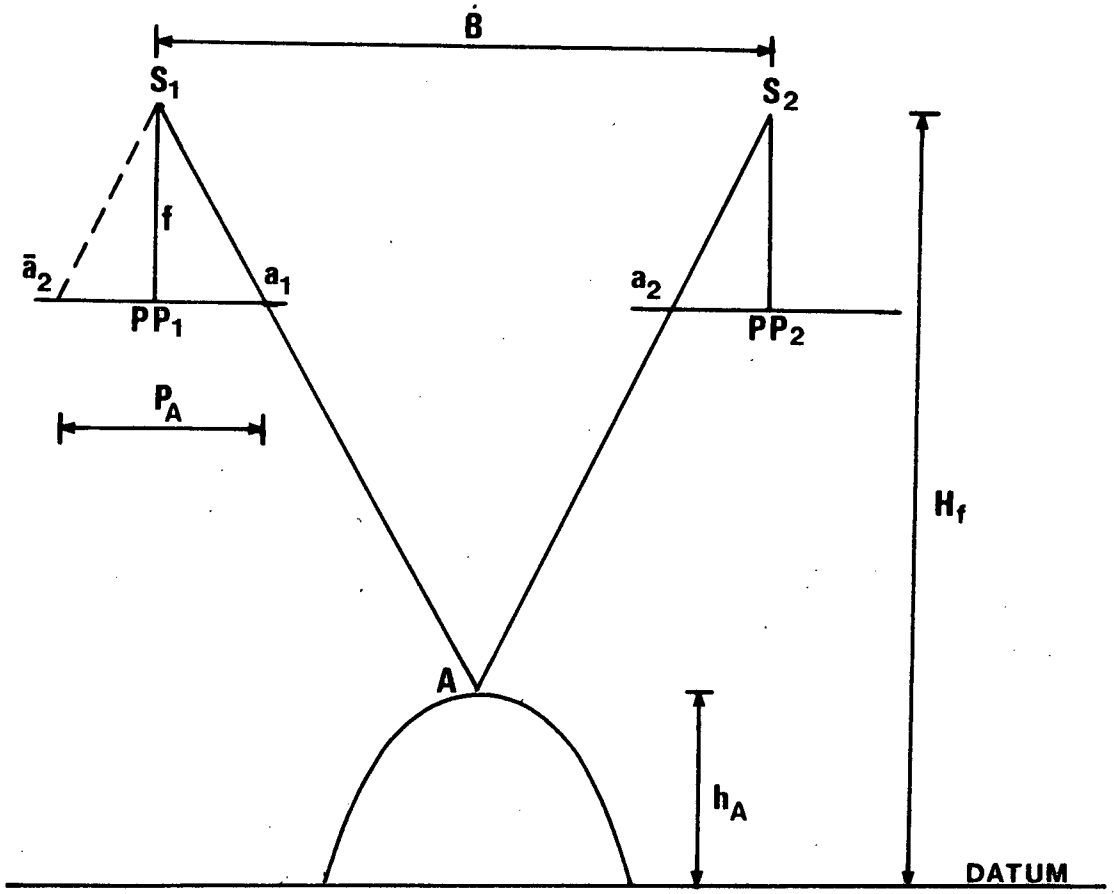

Fig. 4-2 Two photographs are needed to determine the complete geometry of the terrain.

In practice it is difficult to measure the absolute parallax of a point, but using a parallax bar, stereocomparator or digitiser tablet, it is simple to measure the difference in parallax between points. If the height h_A of a point A above the datum is known, the height of any point in the stereoscopic overlap area, say point D can be found by the following procedure:

First substitute the value of h_A into equation (2), and since f, B and H_f are known, P_A can be calculated. Secondly, measure the difference of parallax between A and D, namely $P_A - P_D$. Since P_A is known P_D can be found. The height h_D of the point D above the datum is then calculated by substituting P_A into equation (3). h_D is called the crude height of point D and refered to as h_{CRD}.

All the above parallax equations are based on the assumptions that the camera's axes are truly vertical (no camera tilts) and that the camera stations are at the same height. This situation is the exception rather than the rule. The general case is dealt with in Section 4.9.2.1.

4.2 Previous Waveheight and Pattern Measurement Using Photogrammetry

4.2.1 An Overview of Photogrammetic Wave Height and Pattern Measurement

The earliest photogrammetric wave height and pattern measurements were made in Germany just after the turn of the century. These early attempts have been described by Schumacher (1952). The first useful photogrammetric wave height measurements were taken during the Atlantic cruise of the German research vessel "Meteor" in 1925 (Schumacher 1939). The two main measurement cameras were rigidly mounted on the ship with their axes parallel. In order to ensure that the reciprocal position of the cameras could be reconstructed for each stereopair, an auxillary camera was rigidly fixed to each of the main cameras and facing the opposite pair of cameras. The photographic procedure must have been fairly time consuming since for each stereo-pair four plate holders had to be prepared and four plates had to be simultaneously and correctly exposed. Also the horizon would have to be imaged in each plate since it was the only line of reference. This equipment was also successfully used on the liners "Deutschland" and "San Francisco" during the period up to 1934. A more sophisticated system was then developed using two Zeiss aerial photography cameras capable of taking up to 30 stereopairs a second. There were no proper auxillary cameras, but by the aid of a lens and a prism the picture of the other camera and especially that of a mark lamp was projected onto that portion of the wave film where the sky appeared. This equipment was installed aboard the line "Europa" and the first films were taken early in 1939. It must be noted that the "Meteor" and "Europa" photography was horizontal (normal case) (i.e. the camera axes were approximately parallel with each other and to the sea surface) as opposed to the more conventional aerial photography approach where the cameras axes are approximately perpendicular to the sea surface. Furthermore relatively little useful wave height and pattern information emerged from these investigations since with ship mounted cameras it is often difficult to fulfill the two fundamental demands which must be met in stereophotogrammetry, viz, a base line of suitable length at a sufficient height above the sea surface. Also the bulk of the "Europa" films were never analysed. A more recent application of horizontal photography from ships is described by Monahan (1969) who undertook a study of fresh water whitecapping on the large North American Lakes. Wave crest elevations have also been measured using horizontal stereophotography techniques, with cameras mounted along

the sea shore. This technique has been used by researchers such as Dickerson (1950), Maresca and Seibel (1976) and Adams (1978a).

During World War II, aerial photos of waves were combined with wave shoaling analyses to obtain estimates of bottom topography in areas where little information about bottom topography was available. This led to further research into the measurement of water depths from aerial or space photographs, and multispectral signatures of sea bed reflection. The basic techniques used are described by Polcyn and Sattinger (1969). MacPhee (1981) also describes recent laser bathymetry techniques.

Marks and Ronne (1955) addressed the problem of the measurement of the two dimensional wave energy spectrum at sea. Previous researchers such as Pierson and Marks (1952) had calculated spectra using the wave records from a single gauge. However the problem with the wave records from a single gauge is that many different wave conditions can lead to similar wave records. For example, a complex wave record may have resulted from a complex waveform arriving from a discrete direction, or from a combination of simple waves arriving from many directions. Thus the wave gauge record from a single gauge provides little information about the geometry of the wave field and the missing information is estimated invoking a hypothesis about the two-dimensional characteristics of the wave field with little attempt at verification.

Marks and Ronne (1955) reasoned that high altitude stereophotography could provide a wealth of information about the two dimensional wave energy spectrum at sea without appeal to any theoretical concepts. In order to capture enough of the sea surface for the purpose of analysis two aeroplanes were used. The two aeroplanes flew in tandem 2 000 ft (609.6 m) apart (one behind the other) and at an elevation of 3 000 ft (914.4 m). Each plane was equipped with a CA-8 mapping camera and the cameras were triggered simultaneously from the forward (master) plane by an FM radio link. The planes flew directly into the wind. The distance between the two planes was maintained nearly constant (at about 2 000 ft) by means of a range finder located in the slave plane and utilizing the wing span of the masterplane as a base line. To help establish some sort of ground control in the area of operation a target raft was towed 500 ft (152.2 m) behind the research vessel "Atlantis". The analysis

procedure was as follows. From the stereopairs, elevations were read at discrete points, where the spacing of the points depended upon the properties of the sea surface and the resolution of the spectrum desired. The information was then fed into a computer which produced a two-dimensional energy spectrum of the waves.

McClenan and Harris (1975) supplied proof in the form of aerial photographs, that commonly applied concepts about wave characteristics in the coastal zone are incorrect. They examined more than 40 000 photographs for information about wave conditions in coastal waters and made the following observations about the aerial photography of a "random sea". In a photograph taken at an elevation of less that 2 000 feet, the sea often appears to be a random sequence of humps and and hollows with little or no organized structure; at elevations of 5 000 feet and greater, the general impression is one of highly organized but complex patterns. Generally, it is possible to distinguish from two to five distinct wave trains. When the water is deep enough, relative to the wavelength for refraction to be unimportant, most waves appear to be long-crested (crest lengths 10 to 20 times the wavelengths), the disappearance of a wave crest in a photograph may depend as much on shortcomings in the photography as physical reality. These long-crested wave trains appear to move through each other. When two wave trains have nearly the same wavelength but different directions of propagation, they reinforce or cancel each other in regular patterns. When only a small part of the resulting pattern is seen, the dominant impression is one of short-crested waves or randomness. When many repetitions of the pattern are seen at once, usually the result of viewing the scene from a greater altitude, the eye readily filters out the breaks in wave trains resulting from the cancellation, and the dominant impression is one of intersecting but well organized long-crested waves.

It should be noted that McClenan and Harris were interested in the interpretation of individual aerial photographs and not stereopairs. They also describe a technique whereby the two dimensional wave energy spectrum for a particular area can be determined from individual aerial photographs taken in conjunction with wave height measurements using a single wave gauge. The technique will not be as accurate as the determination of the spectrum from aerial stereopairs of the area.

Polderman (1976) employed a pair of Hasselblad cameras, initially

fixed on outriders built on a helicopter, but then progressed to the use of cameras in two separate helicopters flying in formation, with auxillary photographic recordings of the position of each helicopter in relation to the other at the moment of the (simultaneous) exposure of each of the downward facing cameras. The water surface was recorded by the use of flash photography. Polderman's research work was essentially very similar to that of Holthuijsen (1979) which is described in detail in the next section.

The author found the papers by Holthuijsen (1979) and Szczechowski and Mucha (1980) a most useful source of information during the development of the waveheight measurement techniques at the University of Cape Town (U.C.T.). A detailed summary and discussion of these papers is given in the next section.

4.2.2 An Appraisal of Two Pertinent Papers.

4.2.2.1 An Appraisal of the Paper "Stereophotography of Ocean Waves" by L.H. Holthuijsen.

The primary aim of this investigation was to estimate the two dimensional spectrum of ocean waves and thus determine the distribution of wave energy over wavelengths and directions. Holthuijsen (1979) aimed at working within the following limitations of camera position and orientation:-

(1)	altitude difference.	<10%
(2)	overlap of pictures in y direction.	>80%
(3)	overlap of pictures in x direction.	50-70%
(4)	tilt.	<3°
(5)	difference in orientation.	<15°

The x direction is taken to be along a line joining the principal points and in this case is perpendicular to the flight direction. The acceptable limit for the time difference between the firing of the two cameras was set at 5 ms. The exposure time for the film varied from 5 to 10 ms.

The standard deviation of camera delay for standard aerial photo cameras was found to be too large. Cameras found more suitable were the Hasselblad 500 EL and Zeiss Jena UMK/1318 with standard deviations of camera delay 0,3 ms and 1,5 ms respectively. The Hasselblad was finally adopted due to its higher resistance to vibration.

Three Hasselblads were mounted in two helicopters. One camera in each helicopter pointed vertically downwards and was used to take the stereo pairs. The third camera was mounted in one of the helicopters with the other helicopter in its field of view through an open window. This camera was used to compute the distance between the helicopters. Photographs were taken at flight speeds of approx 10 m/s at altitudes from 200 to 500 m with the two helicopters flying side by side.

The results were analysed using a stereo plotter. A cartesian system of x, y and z co-ordinates was defined in the three-dimensional space created in the stereoscopic viewing device. The x and y axes defined the horizontal plane and the z axis was pointing upwards. The mode of operation was a profiling method: the sea surface was scanned along the grid lines parallel to the y-axis (which pointed in the flight direction). While the x and y position was controlled automatically, the operator controlled the vertical position of the floating point which followed the sea surface as closely as possible. Everytime the horizontal position of the floating point crossed a grid point the three co-ordinates of that point were recorded on tape. The analysis of each picture set resulted in a set of observations of the elevation of the sea surface relative to an arbitrary frame.

The surface information was then adapted in order to meet the specifications required for the use of the fast Fourier transform method of spectral analysis.

Comments.

Holthuijsen set out to achieve a maximum time difference between the firing of both cameras of 5 ms. This was based on observations of other researchers, namely Cote et al (1960), and Cruset (1952) and on the fact that the significant wave phase speed was 10 m/s. The value of 5 ms seems to be unnecessarily small when compared to the exposure time of the film which is 5 to 10 ms. But the effect of the finite exposure time is to "blur" the image, which in turn "blurs" the parallax". The difference in timing, however, produces false parallax which can cause larger errors. However, for the configurations at the University of Cape Town (U.C.T.), the maximum phase velocity was of the order of 1 m/s and not 10 m/s, indicating that a time difference of greater than 5 ms could possibly be allowed.

Holthuijsen used a novel approach to the synchronization of the firing of the two cameras. Each camera was provided with an electronic unit to generate an additional delay for each camera, such that the total average delays for both cameras were equal within acceptable narrow limits. This approach, however, is complicated, and therefore for the pusposes of the configuration at U.C.T. the use of an electronic flash to synchronise the cameras was thought to be preferable. However, at U.C.T. a control unit was first used to electronically fire the cameras simultaneously. The difference in time between the firing of the two cameras using this control unit was found to be 8 ms.

Holthuijsen found the UMK camera to be superior optically to the Hasselblad, but inferior in its resistance to vibration. This was not a problem for the configuration at U.C.T. where the UMK camera was used.

The method of analysing the results mentioned is obviously designed to interface with the use of the fast Fourier transform analysis. This method is, however, not practicable for the analysis of diffraction patterns - where a far less rigid approach would give better results.

4.2.2.2 An Appraisal of the Paper "The Photogrammetric Measurements of Water Ripples on Hydrotechnic Models" by Bogden Szczechowski and Andrzej Mucha.

The above paper was delivered at the XIVth Congress of the International Society for Photogrammetry held in Hamburg in 1980.

Szczechowski and Mucha set out to map the wave patterns around various model hydraulic structures in a wave basin. An area of the basin 10 m x 10 m was utilised for these experiments. Pairs of stereo photographs were taken using two Zeiss UMK FF 10/1318 photogrammetric cameras situated 10-12 m above the water surface. Illumination was by means of flashes which could be triggered by the wave generator. The water surface was identified by using aluminium powder. High Speed Aviphot pan 33 photographic plates were used.

The resultant water surface patterns were plotted using two methods:-

(1) The direct plotting of the water surface image using a stereo plotter.

(2) Creating a numerical model of the water surface.

The numerical model technique involved using a stereo comparator and observing up to 1 000 points on each plate, i.e. approx 10 points per 1 m^2 of model surface. These results were then processed on a digital computer to produce three dimensional field co-ordinates of the observed points. A map of the water surface was then plotted. The accuracy of the stereo plotter results were found to be $\pm$ 2 mm in the x and y directions and $\pm$ 4 mm vertically. Wave heights measured were as high as 120 mm.

Comments

Szczechowski and Mucha maintained that the camera shutters must be synchronised within 0,001 sec or 1 ms of each other. This seems extreme when compared to other investigators. Cote et al (1960) recommended less than 10 ms, Cruset (1952) less than 5 ms, and Holthuijsen used 5 ms. However, their method of overcoming this problem was very novel. By using a flash they not only solved the synchronisation problem, they also effectively froze the water surface (in the <1 ms duration of the flash, the water surface waves would move less than a millimetre or two).

Szczechowski and Mucha maintained that the flashes could be controlled by the wave generator. However, how exactly they used this facility is vague. They certainly do not indicate that they have taken measurements with the waves in the 1st stereo pair 180° out of phase relative to the waves in the 2nd stereo pair as was done at U.C.T. Also it appears they were only interested in obtaining specific data for hydraulic models of various proposed hydraulic structures, and not in basic concepts such as diffraction and refraction.

Aluminium powder was used to identify the water surface. This has been found inconvenient and ineffective compared with the soluble oil and overhead projector approach developed at U.C.T.

The numerical model approach to mapping the water surface does not appear as effective as direct stereo plotting or the projective transformation technique developed at U.C.T. Unless a very fine grid of points is chosen it is possible for important data to be overlooked.

The stereo plotting accuracy was good when one considers the water surface wave heights. It is of the order of accuracy obtained at U.C.T.

4.3 The Origins of Photogrammetric Wave Height and Pattern Measurement at U.C.T.

The formation of the Coastal Photogrammetric Research Unit, by Professor L.P. Adams and Dr H. Rüther of the Department of Land Surveying (in 1976), heralded the beginning of wave height and pattern measurement at U.C.T. This unit uses a World War II F24 aircamera mounted in a small single engined aircraft to carry out aerial surveys for national bodies such as the Fisheries Development Corporation of South Africa. This unit has also undertaken terrestrial and close range photogrammetric studies for the National Research Institute for Oceanology(NRIO). The basic scope of the work undertaken by the unit has been described in detail by Adams (1978a). The terrestrial and close range work undertaken by the unit will be described briefly since it led directly to the present research work.

Two Zeiss Jena UMK 10/1318 survey cameras were used in a horizontal (normal case) mode to measure the wave heights and directions of breaking waves at the proposed site of the Koeberg nuclear power station near Cape Town. For this study the two cameras were placed 60 m apart along the shoreline and by using the cameras' precision horizontal circle and theodolite facility, aligned to produce parallel lines of sight (perpendicular to the base direction). From a knowledge of the inner orientation elements of the individual cameras, and comparator measurements of image pairs on the photographic plates, it is possible to compute three dimensional co-ordinates of discrete points imaged in the stereoscopic overlap without recourse to ground control.

The stereoscopic pair of photographs (Fig 4-3) were analysed to yield the local wave direction and wave crest elevations at discrete points as shown in Fig 4-4. Although the stereoscopic pair can be viewed stereoscopically, large variation of picture separation distances is necessary during the scanning process to ensure three dimensional viewing of different features due to the very large Z (depth) variation. For this reason direct plotting using conventional stereophotogrammetric plotters is normally not possible because of instrumental Z range restrictions. Analytical stereophotogrammetry is therefore indicated for studies of this nature, but because of the possibility of controlling the position and levelling of the cameras the mathematics involved in handling the analytical solution is elementary which is not the case when dealing with the analytical problem of near vertical aerial photographs.

Fig 4-3 Stereoscopic pair of wave photographs.

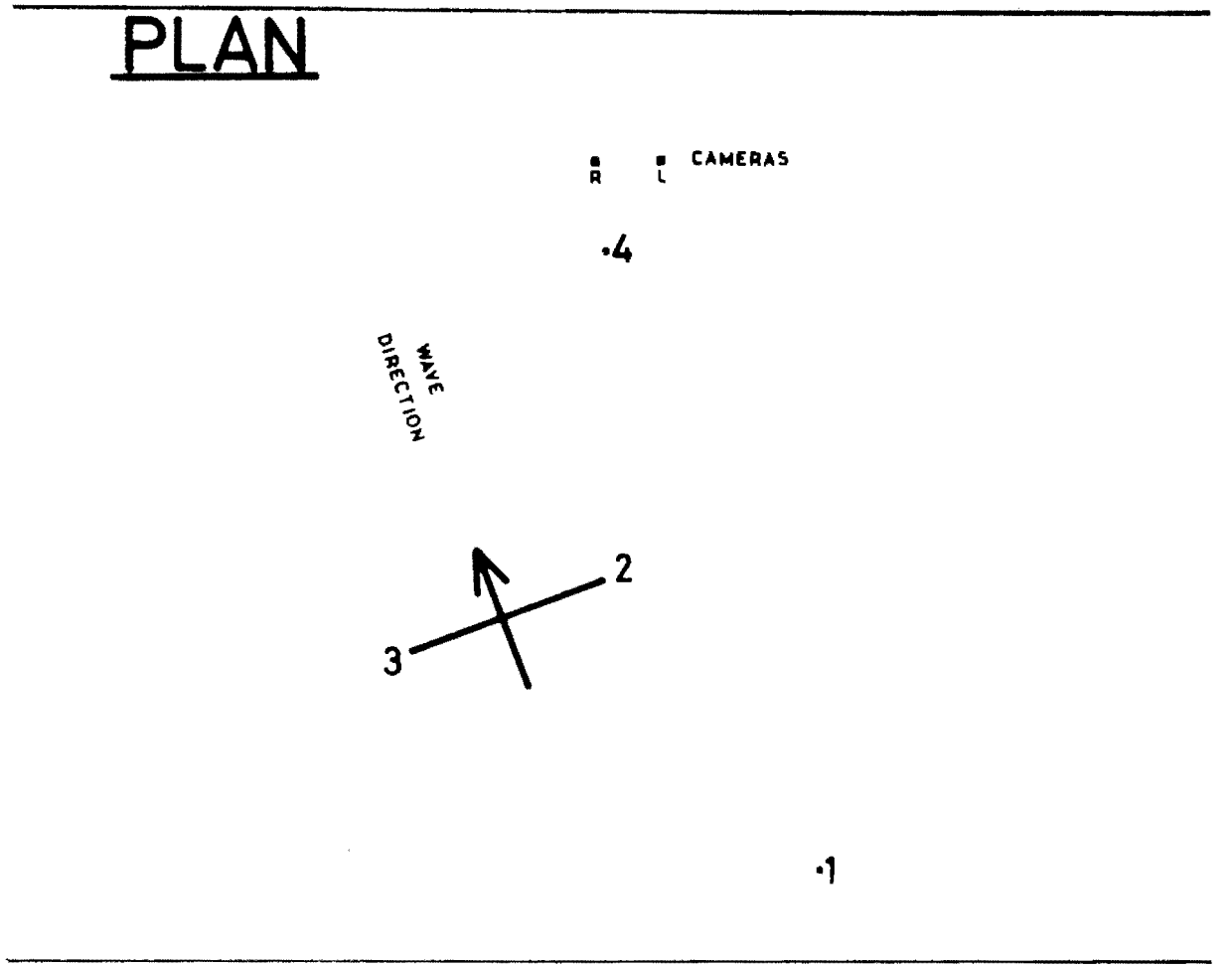

Fig 4-4 Wave information plotted from analytical data derived from stereoscopic pair of photographs (Fig. 4-3) from Adams (1978a).

The two Zeiss UMK cameras were used in an air camera mode to measure wave heights and patterns in the Gansbaai harbour model configuration in the laboratories of the National Research Institute for Oceanology (NRIO). The cameras were suspended above the model harbour basin and a series of synchronised stereopairs of the waves in the basin were obtained. The resulting stereopairs were controlled by pre-marked and prefixed ground control points in the form of iron pins protruding through the water. To achieve the simultaneous exposures required for the stereopairs, both cameras' shutters were opened (using the time exposure settings) and then the water surface in the basin was illuminated using a battery of synchronised electronic flash lamps. The cameras' shutters were then closed subsequent to the completion of the flash. A stereopair of the model harbour configuration plus a discussion on the water penetration problems encountered is given in section 4.6.1.

In 1979 an undergraduate thesis project was undertaken in the Department of Civil Engineering with the co-operation of the Department of Surveying to try and develope a technique to measure wave diffraction patterns in model harbours using close range photogrammetry.

The experimental configuration utilised for the undergraduate work consisted of two F24 air cameras mounted 1,5 m apart and 5 m above the water surface in the wave basin. Illumination was provided by two 250 w overhead projectors which projected a pattern of concentric circles on the water surface. The water was rendered opaque white (with only a few millimetres of light penetration) by the addition of soluble cutting oil. Results obtained were inconclusive - the only fact being established was that one could use close range stereophotogrammetry to map the water surface profile within the model harbour.

Furthermore, there were basic equipment inadequacies evident in the above research. For example the cameras' shutters were of the "focal plane" type. This shutter consists of a blind with a slot cut in it. The exposure is made by causing this slot to travel across the face of the film. Thus the water surface has a chance to move before the entire film format has been exposed.

Another factor influencing the quality of the results in this work was the fact that the images were slightly out of focus. This arose

from the problem of focusing the F24 air camera, the focus of which was fixed at infinity. A spacer was placed between the lens and picture plane, of a thickness calculated using the lens formula. However, the thickness of the composite camera lens was not taken into account, with the result that the spacer thickness was incorrect and the camera slightly out of focus.

Due to the above factors the photographs produced were found to be of a poor quality. This resulted in the experienced stereoplotting machine operator having difficulty in clearly discerning the position of the imaged water surface, i.e. the water surface appeared fuzzy.

A set of photographs were also taken with a pair of Zeiss Jena UMK 10/1318 cameras, and the resultant photographs proved vastly superior to those achieved with the F24 cameras. As a result of this observation the Zeiss Jena cameras have been used for all subsequent wave height and pattern measurements.

The challenge of overcoming the large number of problems exposed by the undergraduate project led the author to undertake the research described in this thesis document.

4.4 Equipment

4.4.1 Zeiss Jena UMK 10/1318 Universal Measuring Cameras.

A pair of Zeiss Jena UMK 10/1318 metric cameras was used for the investigations described in this study. The camera (Fig. 4-6) is mounted on a single second theodolite alidade and equipped with a near distortion free Lamegon 8/100 lens system. This system was used for all the test field photography while for the wave height measurement photography the cameras were mounted in specially designed holders above the wave basin (see Section 4.6.3).

The principal distance of the camera can be changed to allow focusing for distances from 3,6 m to infinity.

Some of the camera's specifications are:

Focal distance for infinity setting:	99 mm (approximately)
Distortion (focusing to infinity):	max. 5 µm
Average resolution:	55 lines/mm
Shutter speed:	1 sec. to 1/400 sec.
Stop setting:	8 to 32
Focus setting for distances:	∞; 25 m; 12 m; 8 m; 6 m; 5 m; 4,2 m; and 3,6 m.
Image size:	120 mm x 166 mm.

The fields of view of the camera are shown in Fig. 4-5. The horizontal (long format) and vertical (short format) fields of view are 78° and 58° respectively.

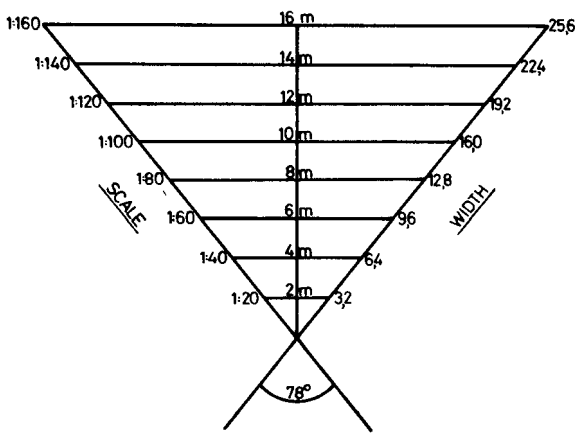

Horizontal field of view of Zeiss UMK 10/1318 Camera

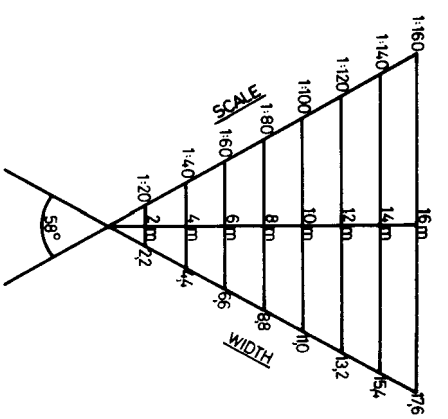

Vertical field of view of Zeiss UMK 10/1318 Camera

Fig. 4-5 The horizontal and vertical fields of view of the Zeiss UMK 10/1318 camera.

The calibration values for the principal distance of the two cameras are given by the manufacturer as:

Distance setting	P.D. (Camera 74)	P.D. (Camera 49)
∞	98,84 mm	99,09 mm
25,0 m	99,26 mm	99,52 mm
12,0 m	99,68 mm	99,95 mm
8,0 m	100,10 mm	100,37 mm
6,0 m	100,52 mm	100,80 mm
5,0 m	100,94 mm	101,23 mm
4,2 m	101,36 mm	101,66 mm
3,6 m	101,78 mm	102,08 mm

Table 4-1 Calibration values for the principal distance of the UMK 10/1318 cameras 74 and 49.

Both cameras were re-calibrated by Dr H. Rüther of the Department of Surveying for distances of 12 m, 5 m and 3,6 m and their inner orientation elements were found to agree (within 0,05 mm) with the calibration values listed in Table 4-1. The cameras were independently re-calibrated by the author for the 5 m distance (using projective transformations) with very similar results. The principal distances as given by the manufacturers were therefore accepted for all analysis done using the stereoplotter.

Both the cameras' shutter speeds and their synchronised exposure device was tested electronically as described in Section 4.6.5. The recorded shutter speeds of the cameras are given in Table 4-2. To ensure correct exposures the deviations from the normal shutter speed had to be taken into consideration when setting aperature and shutter speed.

The cameras are designed to be used with glass plates and Kodak Tri-X Panochromatic Type B plates (black and white ± 320 ASA) were used throughout the investigation. The flatness of glass plate was measured by means of a Tallysurf instrument and found to be better than 5 μm. The glass plates where found to provide better stability than other systems tested such as cut sheet and roll film glued (with a UHU glue stick) to used glass plates.

Fig. 4-6 Views of a UMK 10/1318 camera showing the camera with its theodolite mounting, the fiducial marks and the axis studs.

Nominal shutter speed		Recorded shutter speed			
		Camera 74		Camera 49	
Sec	milli sec	milli sec	deviation	milli sec	deviation
1/15	67	54-67	-	52-60	-
1/30	33	28-37	-	23-28,5	-
1/60	16,7	15,5	7%	23	38%
1/125	8	9	13%	10,5	31%
1/250	4	4,5	13%	6,5	63%
1/400	2,5	3,5	40%	4	60%

Table 4-2 Recorded camera shutter speeds.

4.4.2 Carl Zeiss Jena Topocart B Stereoplotter.

The stereoplotter which was used to analyse the initial wave stereo-pairs is a Carl Zeiss Jena Topocart B photogrammetric stereoplotter (Fig. 4-7) which can accept transparency and paper print stereo-photography produced by cameras comprising a wide range of principal distances. A description of the optical/mechanical principles upon which the stereoplotter operates can be found in any modern textbook on photogrammetry.

Fig. 4-7 Zeiss Jena Topocart B stereoplotter.

4.4.3 Carl Zeiss Jena Steko 1818 Stereocomparator.

The bulk of the plate analysis was done using a Carl Zeiss Jena Steko 1818 stereocomparator both in monoscopic and stereoscopic mode. The Steko 1818 (Fig. 4-8) has a reading accuracy of better than 10 μm in x and y co-ordinates and 2 μm for px and py readings. A Motronic electronic analoque to digital conversion display unit connected to the comparator not only serves to display the results but also interfaces the comparator with a typewriter for permanent recording of the image co-ordinates. To speed up the analysis procedure the Motronic unit was interfaced to a Tektronix micro-computer as described in Section 4.4.5.

Fig. 4-8 The stereocomparator and peripherals (Digital readout and typewriter)

4.4.4 Tektronix Microcomputer System

All the projective transformation analysis was carried out using the Tektronix microcomputer system (Fig. 4-9) located in the Photogrammetric Laboratory of the Department of Surveying. The system consists of:

(i) Central Processing Unit Tektronix 4051 Graphic System
With a 32k bytes memory and a memory allocation of 8 bytes for each array variable. The C.P.U. is equipped with a high resolution graphics screen plus tape drive and understands the 4051 Graphic System BASIC language. The numeric accuracy of the unit is 14 digits.

(ii) Tally Line-Printer

(iii) Tektronix 4662 Interactive Digital Plotter
The active plotting area of the plotter is 25,4 cm by 38,1 cm with a claimed resolution of 0,06 mm.

(iv) Tektronix 4907 Filemanager
This flexible disk storage system is designed for flexible disks with a storage capacity of 600k bytes.

(v) Summagraphics Digitiser with I.D. Data Tablet
See Section 4.4.7

Fig. 4-9 Tektronix microcomputer system consisting of (from left to right) digitiser tablet and digitiser control unit, central processing unit with VDU, line printer, file manager and plotter.

4.4.5 Stereocomparator/Tektronix 4051 Interface

Initially the plates were observed using the stereocomparator system described in Section 4.4.3 and then the x, y, px, py data was manually entered into the Tektronix 4051. This proved to be a very tedious process. To speed up the data transferal it was decided to link the Motronic analogue to digital conversion unit directly to a 2nd Tektronix 4051 microcomputer (not part of the system described in Section 4.4.4).

The first piece of equipment needed was a Tektronix 4051 Option 1 Data Communication Interface which behaves as a data port between the 4051 microcomputer and a RS-232 compatible device. The second piece of equipment needed was a device that could convert the digital output of the Motronic unit to a RS-232 format. The Data Communication Interface was imported from America while the Motronic/RS-232 converter was constructed by H.F. Weehuizen of the Department of Electrical Engineering at U.C.T.

Using this system the x, y and px, py data could be fed directly into the 4051 and stored on magnetic tape. The Tektronix 4051 was also linked directly to the UNIVAC 1100 at U.C.T. via the communications interface and a remote terminal cable. This facilitated the rapid transfer of XYH and XYH/H_i data to the UNIVAC for analysis.

4.4.6 UNIVAC 1100 System

The finite element analysis described in chapter three and the contour plotting of the theoretical and experimental results was carried out using the UNIVAC 1100/81 of the University of Cape Town. This computer has one C.P.U. with 1×10^6 words of in-core storage. The external storage consists of:-

(1) fixed discs - 270×10^6 words
(2) removable discs - 90×10^6 words
(3) drum - 2×10^6 words

This computer has all the standard peripherals including a Calcomp plotter, which was used to plot the theoretical and experimental diffraction diagrams.

4.4.7 Digitiser Tablet, Modified Mirror Stereoscope and Electronic Parallax Bar System

This configuration was used as an alternative analysis system to the stereocomparator/microcomputer configuration described in

Sections 4.4.3 and 4.4.5. The system consists of:

(i) Summagraphics Digitiser Tablet

The digitiser tablet used for the analysis is a Summagraphics ID-2-11/48 digitiser tablet of external dimensions 1,1 m by 1,4 m. It is interfaced to the Tektronix 4051 described in Section 4.4.4 via its control unit.

(ii) Modified Mirror Stereoscope

To allow for stereoscopic inspection of the pair of photographs, an old fashioned mirror stereoscope mounted on a XY rail system was modified to fit over the digitiser tablet. See Fig. 4-10.

Fig. 4-10 Modified mirror stereoscope over digitiser tablet

(iii) Electronic Parallax Bar

The normal cursor used with the digitiser is unsuitable for digitising a space body stereoscopically as misidentification of the common left and right image points is likely. The problem of common image identification was overcome by designing a double electronic cursor mounted on a bar which, when activated, introduced a slight delay in the "reading" of the left and right hand digitiser x,y co-ordinates. A small electric motor allows for the movement of the right hand cursor down the bar to cater for the change of x parallax of common images. The normal etched cross was replaced by small red dots. The apparatus is, in fact, an electronic parallax bar but with the added advantage of being able to record y parallax in addition to x parallax. See Fig. 4-11.

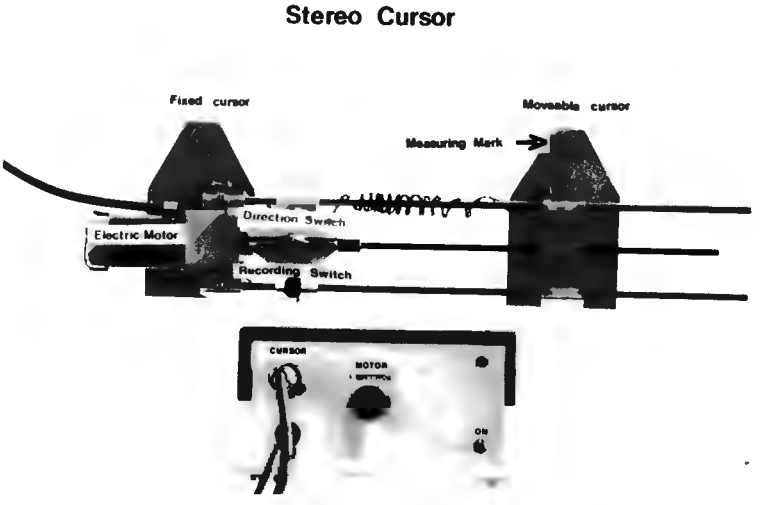

Fig. 4-11 The electronic parallax bar

4.4.8 Conventional Mirror Stereoscope and Parallax Bar

A wild (Heerbrugg) mirrorstereoscope and parallax bar (Fig. 4-12) was used for part of the analysis described in Section 4.9.

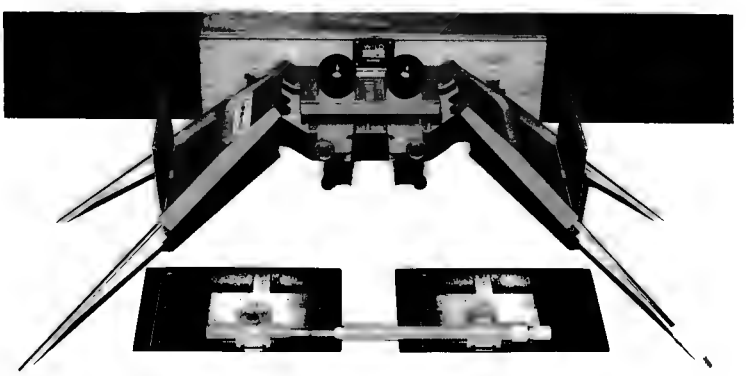

Fig. 4-12 Wild mirror stereoscope and parallax bar.

4.5 Close Range Precision Test Field

A test field comprising of a number of well defined and symmetrically distributed points can be useful for the testing of mathematical models for close-range photogrammetry as well as for the calibration of metric and non-metric cameras.

An 80 target test field has been established in a laboratory of the Department of Surveying at the University of Cape Town. The point configuration of the test field was designed to resemble a typical object space as found in close-range photogrammetry. The test field is shown in Fig. 4-13 and the test field dimensions in Fig. 4-14.

Fig. 4-13 Test field

The targets consist of brass discs with a diameter of 25 mm (Fig. 4-15). With the exception of 16 wall markers in the far vertical plane all targets are attached to steel rods with a diameter of 12 mm. The rods are suspended from the ceiling and are constrained to hang truly vertically without rotation about the vertical axis. Four target discs are attached to each rod. The maximum separation of two markers on a rod is 2,2 m; over this distance a temperature change of 1° Celsius results in a relative position change of 0,025 mm. Temperature expansion of the field can be catered for if required for high precision tests.

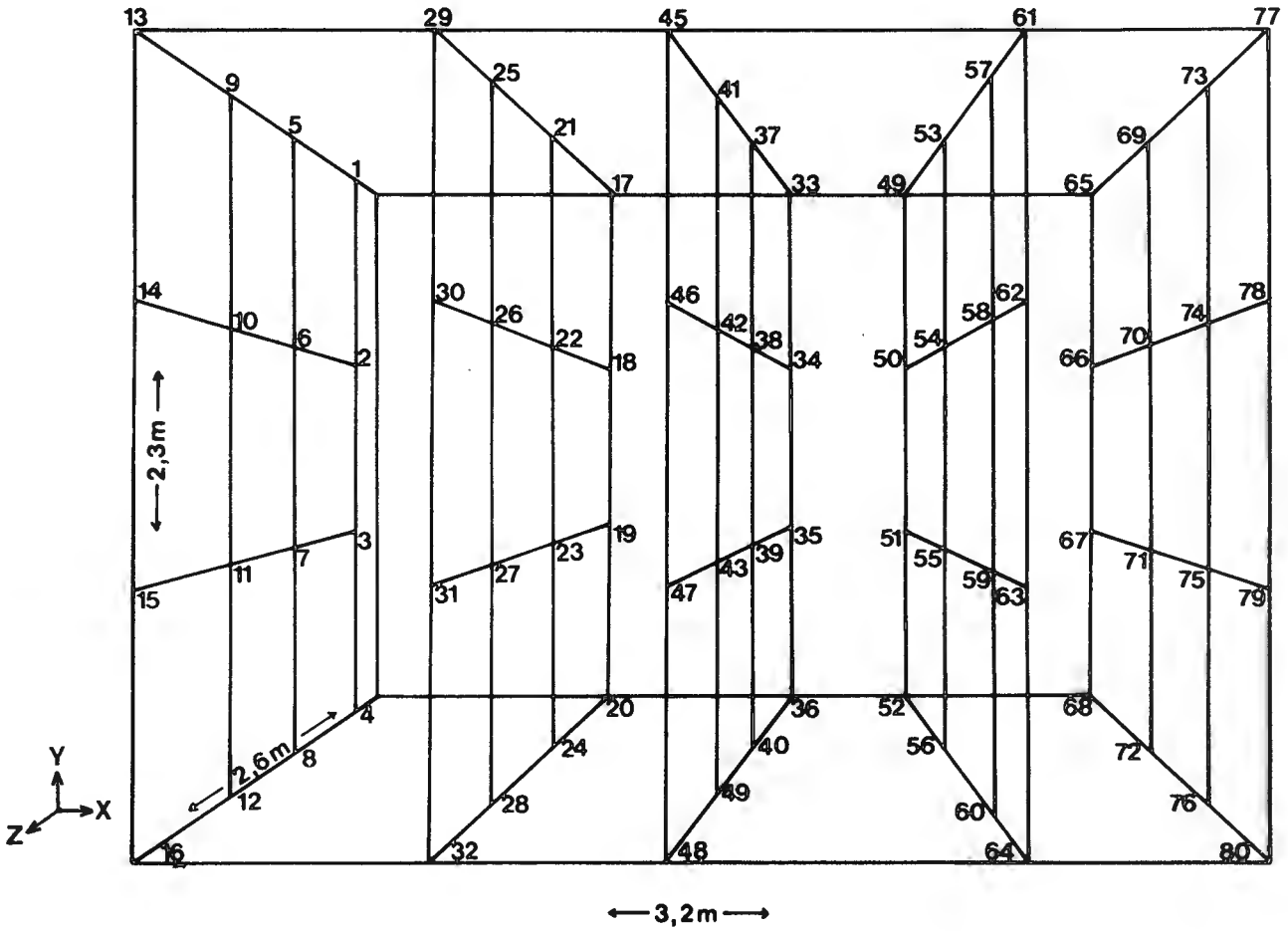

Fig. 4-14 Perspective view of the test field

Fig. 4-15 Test field target

The test field targets were co-ordinated in three dimensions using horizontal and vertical circle readings obtained from theodolite observations in which the theodolite was mounted on three separate and precisely co-ordinated metal tripods attached to the floor of the room. The space co-ordinates of the targets were then derived as an exercise in three dimensional intersection with an estimated m.s.e. of ±0,4 mms. The test field targets' space co-ordinates are given in Table 4-3.

TEST FIELD CO-ORDINATES

	X	Y	Z
1	10.2934	11.3908	4.1075
2	10.2904	10.6396	4.1030
3	10.2820	9.9069	4.1019
4	10.2837	9.1437	4.1004
5	10.2934	11.3981	4.5783
6	10.2875	10.6483	4.5783
7	10.2833	9.8976	4.5783
8	10.2784	9.1479	4.5768
9	10.2912	11.3958	5.4823
10	10.2884	10.6483	5.4835
11	10.2848	9.8967	5.4844
12	10.2796	9.1461	5.4867
13	10.2839	11.3915	6.3760
14	10.2882	10.6466	6.3770
15	10.2896	9.8935	6.3794
16	10.2869	9.1436	6.3839
17	11.0986	11.3849	3.8356
18	11.1143	10.6391	3.8276
19	11.1130	9.8904	3.8280
20	11.0982	9.1462	3.8341
21	11.1061	11.3973	4.5753
22	11.1026	10.6492	4.5764
23	11.0975	9.8990	4.5774
24	11.0927	9.1485	4.5799
25	11.1144	11.3982	5.4776
26	11.1090	10.6483	5.4775
27	11.1068	9.8963	5.4790
28	11.1017	9.1465	5.4807
29	11.1074	11.3911	6.3837
30	11.1048	10.6410	6.3836
31	11.1003	9.8899	6.3829
32	11.0922	9.1393	6.3820
33	11.9088	11.3791	3.8335
34	11.9196	10.6417	3.8260
35	11.9308	9.8909	3.8276
36	11.9194	9.1485	3.8322
37	11.9309	11.3942	4.5795
38	11.9253	10.6459	4.5805
39	11.9217	9.8950	4.5801
40	11.9213	9.1445	4.5776

	X	Y	Z
41	11.9320	11.3956	5.4796
42	11.9281	10.6447	5.4793
43	11.9227	9.8962	5.4798
44	11.9153	9.1450	5.4816
45	11.9272	11.3848	6.3822
46	11.9222	10.6346	6.3825
47	11.9217	9.8842	6.3821
48	11.9239	9.1324	6.3805
49	12.7671	11.3788	3.8318
50	12.7491	10.6442	3.8229
51	12.7486	9.8961	3.8231
52	12.7327	9.1584	3.8312
53	12.7564	11.4016	4.5763
54	12.7516	10.6507	4.5769
55	12.7464	9.8986	4.5755
56	12.7362	9.1501	4.5719
57	12.7536	11.4001	5.4716
58	12.7511	10.6479	5.4702
59	12.7421	9.8978	5.4704
60	12.7326	9.1479	5.4805
61	12.7520	11.3878	6.3810
62	12.7479	10.6390	6.3801
63	12.7444	9.8872	6.3814
64	12.7384	9.1383	6.3848
65	13.5831	11.3797	3.8305
66	13.5607	10.6514	3.8217
67	13.5652	9.8994	3.8216
68	13.5513	9.1631	3.8292
69	13.5708	11.4072	4.5792
70	13.5656	10.6580	4.5808
71	13.5595	9.9057	4.5823
72	13.5542	9.1581	4.5828
73	13.5751	11.4012	5.4793
74	13.5705	10.6523	5.4796
75	13.5648	9.9013	5.4780
76	13.5576	9.1503	5.4777
77	13.5651	11.3986	6.3738
78	13.5607	10.6488	6.3740
79	13.5582	9.8976	6.3751
80	13.5524	9.1470	6.3771

Table 4-3

4.6 Laboratory Photogrammetric Wave Height and Pattern Measurement: Development of the Apparatus and Technique

4.6.1 Water Penetration

One of the main problems encountered when taking photographs of a water surface is that of water penetration. A stereoscopic study of stereogram Fig. 4-16 illustrates this problem. The stereogram shows waves approaching a breakwater in a model harbour (Gansbaai model harbour NRIO). Large numbers of circular white floats were thrown onto the water surface before photography commenced, and simultaneous exposures of both cameras was effected by opening both camera shutters and then illuminating the water surface by means of high powered electronic flashes. The monocular viewing of the stereogram illustrates the dangers of photographic interpretation. Using single photographs the dark lines would probably be interpreted as wave crests, while in fact when studied stereoscopically it is evident that they are shadows of the wave crests cast on the basin floor.

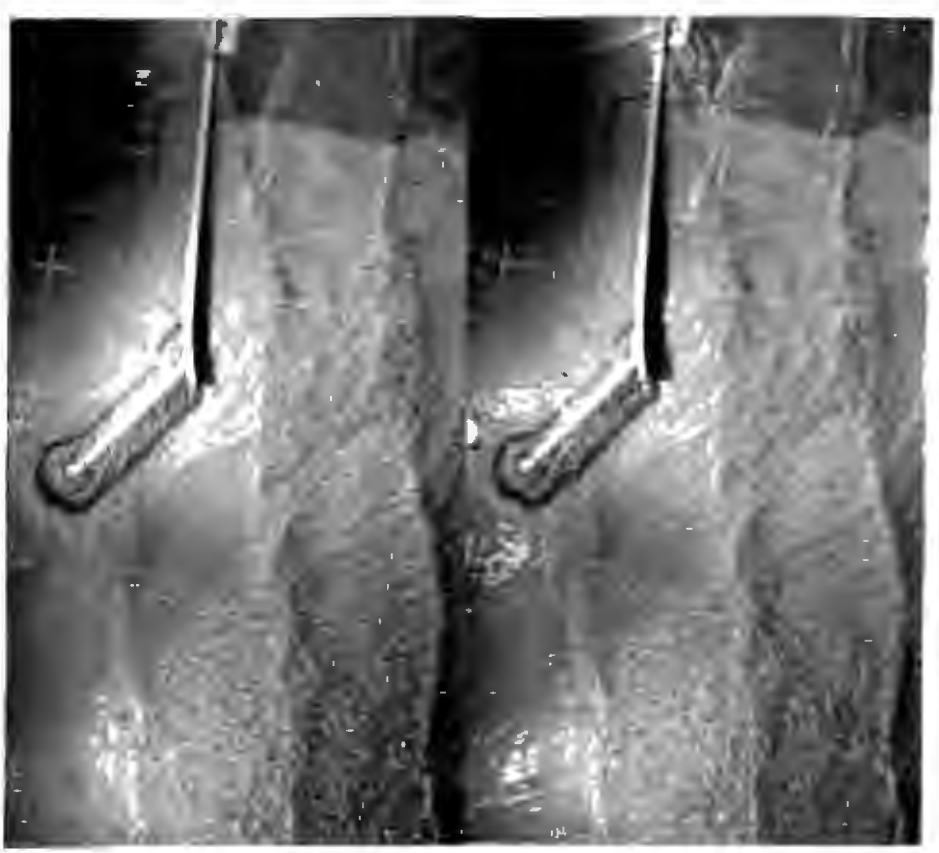

Fig. 4-16 Stereogram of Gansbaai model harbour showing water penetration problem.

Although stereoscopically interesting, Fig. 4-16 can only provide three dimensional information for discrete points on the water surface represented by the floats, and the water surface as a whole cannot be measured or plotted.

Two basic approaches have been adopted in the past to signal or define the water surface for photographic purposes, namely:-

(1) Discolouring the water in some way, so that the light penetration of its surface is minimal. A white solution is favoured.

(2) Creating a thin flexible opaque film of some substance on the water surface.

The first approach was used by Döhler (1956) and later by Jaggi (1975) for the photogrammetric analysis of laboratory hydraulic models of river retainment structures. They found that the addition of small quantities of flourescein (1 part per 100 000) to the water in conjunction with ultraviolet illumination was effective in signalling the water surface.

The second approach has been used with success by Szczechowski and Mucha (1980). They sprayed fine aluminium powder on the water surface directly before photography. The second approach was also adopted by Moffitt (1968) for the mapping of the wake of a ship model in a test basin. He sprinkled confetti over the water surface before each run of the ship model. Both these methods were tested at U.C.T. and were found to be inconvenient and ineffective when compared to the method which was finally adopted.

The first approach was adopted at U.C.T. and initially three solvents were tried, namely:-

Starch,
P.V.A. Brilliant White,
Water soluble cutting oil.

The first two solvents tended to settle out within a few hours after mixing, while the cutting oil solution remained stable for days. Initially a concentration of 3 ml cutting oil per litre of water, was adopted after a very brief water penetration test had been carried out. It was subsequently discovered, when analysing stereopairs taken of the deformed water surface, that the 3 ml/litre concentration allowed unacceptably high light penetration of the

water surface particularly when the solution was a few weeks old. It became obvious that a higher oil/water concentration was needed and that the oil/water solution should be replaced at least once a month during testing. A thorough oil/water concentration versus light penetration test was carried out to determine an optimum solution. It was decided that light penetration of approximately 1 mm into the water surface would be acceptable.

The light penetration test configuration is shown in Fig. 4-17. A perspex ramp with a slope of 1 in 8 was constructed. Parallel black lines 4 mm apart, were etched into the face of the ramp and then the ramp was placed in a small flume. The water depth in the flume was kept a constant 30 mm. The oil/water concentration was increased from 1 ml/l to 8 ml/l in 0,5 ml/l increments. For each oil/water concentration the ramp/water interface was carefully marked using black arrows as shown in Fig. 4-18. This interface was always constrained to be coincident with one of the parallel black lines. A vertical photograph was then taken of the ramp (using a flash since the room was darkened before taking the photo). A photo of the 7 ml/litre situation is shown in Fig. 4-18. From the photo it can be seen that for this concentration the light penetration is approximately 1 mm. Consequently all subsequent wave analysis was carried out with the oil/water concentration in the range 7-8 ml/litre.

The cutting oil used throughout the experimentation was Shell Drombus B soluble cutting oil which has a density of 0,922 Kg/litre. The viscosity of the 0,7 ml/litre solution was compared to clear water using a Brookfield Synchro-Electric Viscometer and no significant difference in viscosity between the two liquids could be detected.

4.6.2 Illumination

There were two basic illumination requirements, namely:-

(1) Sufficient illumination of the water surface in order to allow adequate exposure of the photographic emulsion at high shutter speeds,

(2) The projection of a finely focused pattern, consisting initially of concentric circles, onto the water surface to provide photographic contrast (see Section 4.6.7)

Fig. 4-17 Light penetration test configuration.

Fig. 4-18 Photo of ramp with a 7 ml/litre oil/water concentration.

It was decided to use "Vista Varia" overhead projectors which had 250 w incandescent bulbs. Using these projectors the illumination configuration constraints were:-

(1) The area of basin to be illuminated was 6 m x 6 m.

(2) Four overhead projectors would have to be used, each illuminating a 3 m x 3 m area.

(3) To illuminate a 3 m x 3 m area, the projector would have to be at least 4 m above the water surface (measured from the mirror perpendicular to the water surface).

(4) Each projector mirror would have to be directly above the centre of its 3 m x 3 m area to produce an undistorted image of whatever pattern was being projected onto the water surface.

(5) The projectors would have to be positioned so that they did not obscure the illuminated area from the cameras.

Four suspended projector platforms were then built (see Fig. 4-19). The two southern platforms were suspended from the beams supporting the grid floor built above the wave basin. The two northern projector platforms were suspended from two 150 mm x 50 mm beams bolted to steel angles which were in turn raw bolted into the concrete roof.

Fig. 4-19 Projector platforms above wave basin.

The overhead projectors were bolted to the platforms once their optimum position on the platform had been determined. The optimum position for each projector was determined by trial and error adjustment to both their horizontal positions on the platforms and the focus arm settings, relative to the focus of the pattern on the wave basin floor. The fine focusing was achieved by focusing the projected image onto the upper surface of 125 mm high wooden blocks. These blocks represented the eventual water surface.

4.6.3 Camera Configuration

The Zeiss Jena UMK cameras used had a focal length of approximatly 100 mm and a negative format of 120 mm x 166 mm. For the purposes of the "field of view" calculations, an effective format size of 120 mm x 160 mm was used. Based on the camera being a minimum of 5 m above the water surface, this gave an effective field of view of 6 m x 8 m.

A camera spacing of 1,9 m was adopted, based on the experiments carried out in the Surveying Department (see Section 4.8.4). This gave an overlap area of 6,1 m when both cameras were aligned with the long axis of their negative format parallel to the wave paddle. The cameras were aligned relative to the basin and the overhead projector as shown in Fig. 4-45.

Since the cameras were very expensive and would be damaged by long periods of exposure to the moist air above the wave basin, a camera mounting had to be developed which allowed quick placement and removal. Furthermore, the mounting would need a levelling facility so that the cameras could be levelled each time they were placed in position. A wooden camera mounting was designed and made. Fig. 4-20 shows the camera in position in its mounting.

Four polypropelene rings were made which fitted over the four camera axis studs. The camera was then lowered so that the studs fitted into four slots which were carefully machined to a width slightly greater than the external diameter of the polypropelene rings. Electronic connections to the camera were achieved by two copper rings which fitted over the electronic contact rings on opposite camera studs(see Fig. 4-20). These rings were linked to the camera firing box.

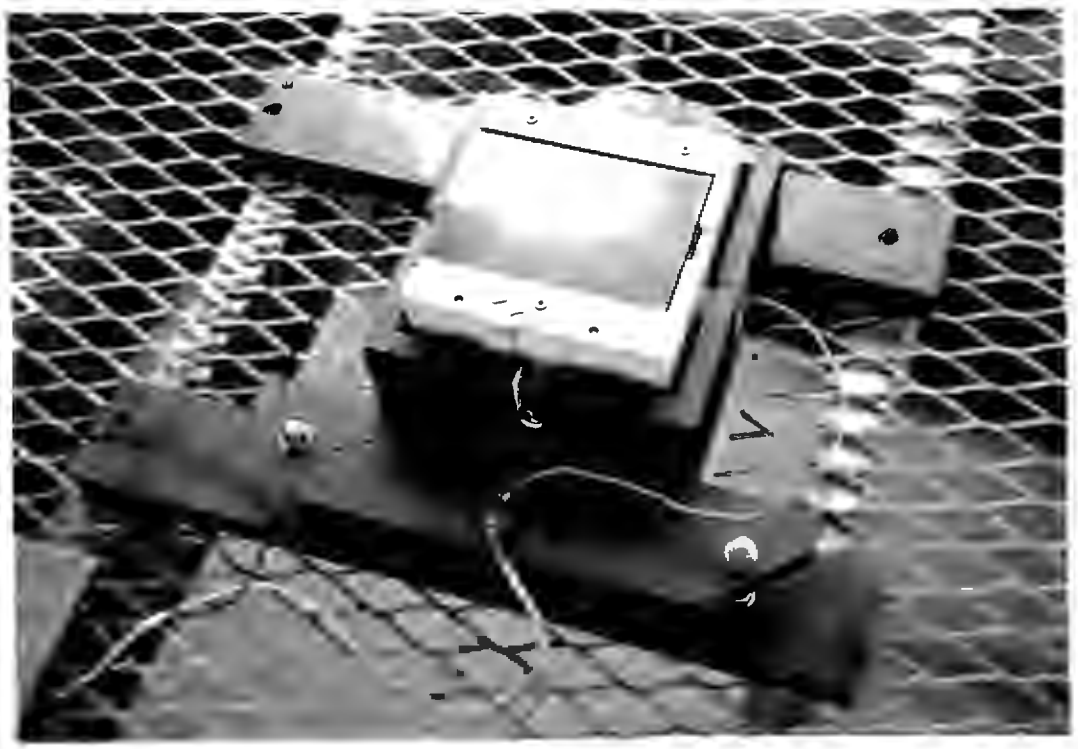

Fig. 4-20 Zeiss camera in wave basin mounting.

Levelling of the cameras, once in their mountings, was achieved by removing the back steel dust cover from each camera and placing an exposed glass plate on the focal plane of the camera. A sensitive tubular level was then placed on the glass plate and the camera levelled by means of the three camera mounting levelling screws.

4.6.4 Camera Firing System.

4.6.4.1 Introduction

It was realised that a permanent record of all the required wave height and pattern data inside a model harbour could be obtained by taking two stereopairs with the waves imaged in the 1st stereopair 180° out of phase relative to the waves imaged in the 2nd stereopair. This is valid provided the incident wave is of constant period (T) and constant height, and provided all factors such as minor wave reflections are kept constant.

Furthermore, since the water is in motion during stereophotography, it is necessary to use a pair of cameras which must be synchronized for simultaneous exposure. It also follows that, in order to overcome the effect of image movement of the dynamic surface, a short exposure time must be employed. This immediately

poses the problem of providing sufficient illumination to activate the photographic emulsion commensurate with the speed of the available film.

The cameras in the experimental configuration at U.C.T. were fired apparently simultaneously by the camera firing box when one of two micro-switches attached to the wave paddle mechanism was activated. It was subsequently found (see Section 4.6.5) that the two cameras were approximately 8 milliseconds out of synchronization.

4.6.4.2 Wave Paddle Camera Triggers

The problem was to fire the cameras so that two sets of photographs could be taken, in which the waves in one set were 180° out of phase with the waves in the other set. This was solved by placing two micro-switches 180° apart as shown in Fig. 4-21.

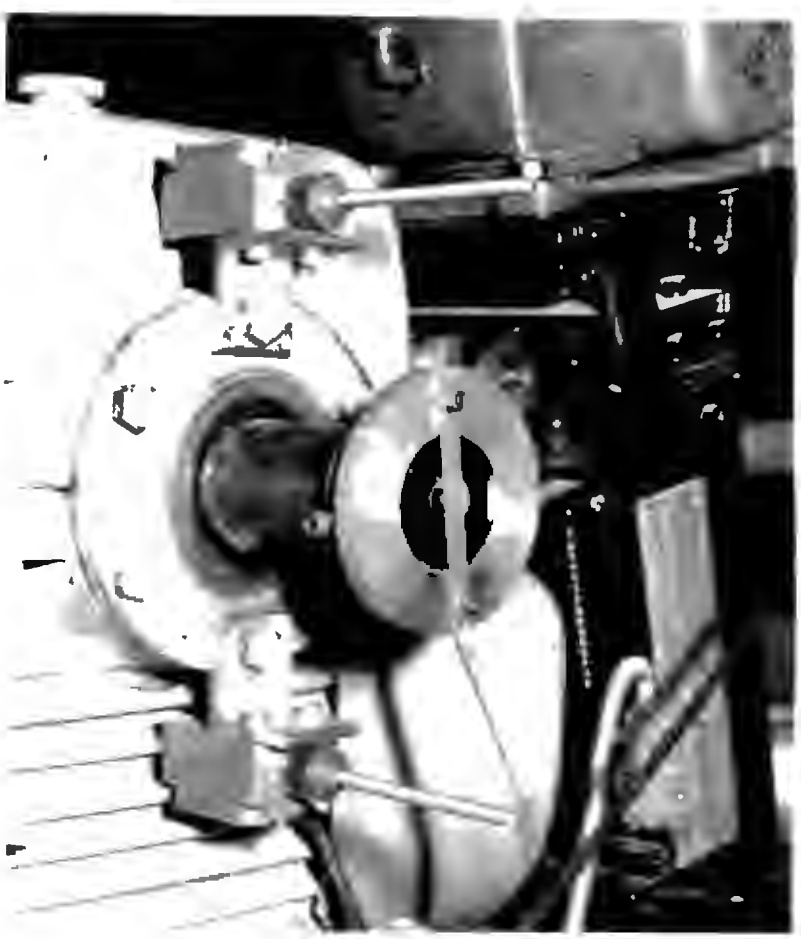

Fig. 4-21 Camera firing micro-switches, located 180° apart.

The gearbox through which the drive from the electric motor was transmitted to the wave paddle had two drive shafts, one on either side. The drive shaft on the one side was used to drive the wave paddle, while the second drive shaft was normally not used. This second drive shaft was used to fire the cameras. Two Omron micro-switches were placed on a vertical axis drawn through the centre of the shaft, one above and one below. A trigger arm was connected to a steel ring which was keyed into the drive shaft. When the shaft rotated the trigger arm triggered first one microswitch and then the other. Thus both micro-switches were constantly being triggered whenever the shaft was turning.

To fire the cameras either one of the micro-switches was activated by switching it into the camera firing circuit. Once the micro-switch was activated it would cause the cameras to be fired when triggered by the trigger arm. Either the top or the bottom micro-switch could be activated at any one time by switches mounted in the camera firing box.

4.6.4.3 Camera Firing Box

In order to use a pair of UMK cameras in stereometric mode, a synchronization box is provided which allows both cameras to be electronically fired simultaneously when a manual switch is operated. For this exercise it was necessary to replace the manual switch with a relay and a timer. The timer was required since the synchronization box switch has to be in the operational position for 2,5 seconds to allow a capacitor to discharge and fire the cameras. Fig. 4-22 shows the camera firing box with the synchronization box in the top half and the variable timer (0,3 to 6 seconds) in the bottom left hand corner. The switches shown bring either the top or bottom micro-switches into the circuits.

The sequence of operation was as follows:- (see Fig. 4-23 below). First the required micro-switch was selected. Then the reset button was pressed to fire the cameras operating the relay R. Contact R_1 closed and kept the relay operational (i.e. holding in the circuit through T_1). Contact R_2 closed, which prepared an operating path for the timer T which had two change over contacts T_1 and T_2. When the selected micro-switch was operated by the wave generator, the timer T was operated. Contact T_1 changed over to form a holding path for the timer circuit, and

Fig. 4-22 Camera firing box.

the relay dropped out. At the same time contacts T_2 switched the camera synchronization box to its operating situation. The cameras then fired and the timer dropped out after the preset time, switching the synchronization box back to its standby situation. The circuit was then inactive until reset.

4.6.4.4 Camera Synchronization Box

The sequence of operation was as follows:- (see Fig. 4-24). When the power was switched on the synchronizer went into a standby situation. In this situation there was a potential across the capacitor C. The current input into this capacitor was controlled by the fixed 180 ohm resistor (wire wound) and the variable resistance potentiometer (this determined the amount of charge stored in the capacitor and the discharge time).

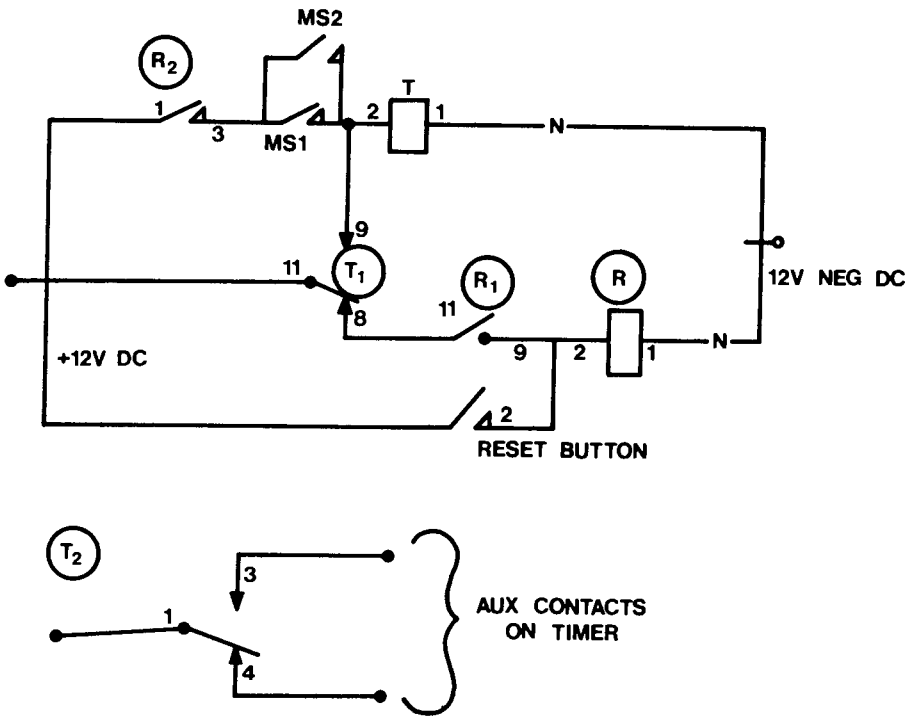

Fig. 4-23 Camera firing circuit

There was a constant 12 v potential across pins 4(-ve) and 51(+ve) which were the power imputs to both cameras. In the standby situation the lamp in the synchronizer box was on.

The original toggle switch was replaced by an auxiliary set of contacts on the variable timer (0,3 to 6 seconds). When the wave paddle operated the micro-switch, the timer switched to its auxiliary contacts and switched the synchronizer to its operating situation for the preset time (in this case 3,5 seconds). This caused the relay R1 of the synchronizer to operate, which changed contacts DE to EF, preparing a discharge path for the capacitor C. At the same time contacts A - B were disconnected and the lamp went out signalling that the synchronizer was in its operating situation. The capacitor then discharged through the timer auxiliary contacts, through EF, through the second set of positive pins, No's 56 (on the camera plug) through each camera shutter solenoid to earth. When the discharge reached the shutter

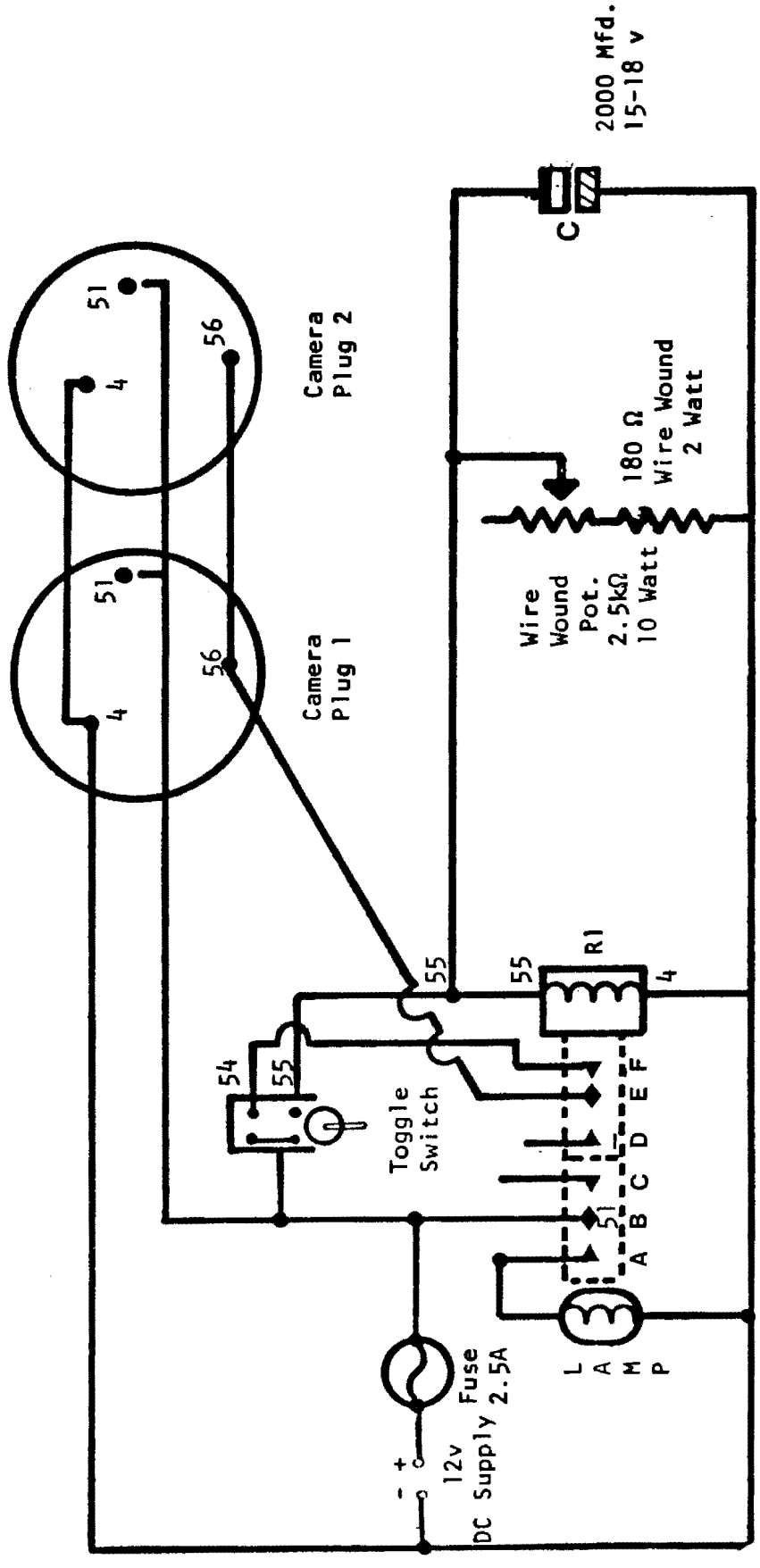

Fig. 4-24 Camera synchronizer circuit.

operating solenoid, the solenoid charged up (producing a finite electromechanical camera delay) and then operated the shutter. At the same time the solenoid operated a slugged relay which switched power to the fiducial light circuit of the camera. This relay was a mechanical relay which held the circuit closed for a fixed preset time (approx 2,5 seconds) sufficient to expose the film emulsion.

4.6.5 Problems Initially Encountered in the Plotting of the 3 Dimensional Water Surface using a Stereoplotter.

In order to perceive a 3 dimensional image of a particular water surface situation in the stereoplotter, the operator follows a certain procedure. The two glass plates which comprise the stereo-pair are placed in their perspective holders on the stereoplotter. The plates are then illuminated and their images are projected via lens and mirrors to the eyes of the operator. The image of the left plate is received by the operator's left eye, the image of the right plate by the right eye. The operator then perceives a three dimensional stereo model of the water surface.

If the photography is good, the surface of the model is well defined. However, if for any reason there is a deficiency in the quality of the photography, the surface of the model will be ill-defined and appear hazy. This means that the machine operator will experience difficulty in placing the floating dot accurately on the model's surface, thus leading to a decrease in the accuracy of any water surface elevation plots.

This problem of a hazy or ill-defined stereo model surface (and subsequent decreased accuracy of elevation readings) was encountered during the initial stages of the present research work. It is suggested that there are six main problems contributing towards this effect, namely:-

(1) Insufficient illumination
(2) Image movement
(3) Lack of camera synchronization
(4) Shutter speed anomalies
(5) Photographic contrast problems
(6) Water surface penetration

Problems (1) and (2) are self-explanatory when we consider the photography of a dynamic water surface, and problems (5) and (6) are discussed in sections 4.6.7 and 4.6.1 respectively. Problems (3) and (4) were investigated extensively. When the first stereo-pairs of the model harbour configurations were taken using the illumination from the standard overhead projectors, it became evident that there was a difference in shutter speeds between the cameras. This led to a detailed measurement of the shutter speeds of each camera, and also of the synchronized firing of the cameras.

The experimental configuration used to test the cameras is shown in Fig. 4-25. Incandescent lamps were set up behind the cameras with the camera plate covers removed. They were placed in such a way that when the camera shutters were open the lamp light would be focused on the silicon photo voltaic cell in front of each camera. Each photo cell was connected to a type 741 operational amplifier which in turn was connected to a twin trace storage oscilloscope.

The shutter speeds measured for both cameras are shown in Table 4-2. Furthermore, it was found that the shutter of camera 49 opened consistently 8 ms after the shutter of camera 74 had opened. When the flash system, described in the next section, was adopted this consistent 8 ms synchronization error dictated that the cameras were set at a shutter speed setting of 1/60 second or slower to ensure that both shutters were open during the firing of the flash.

Fig. 4-25 Configuration used to test the cameras.

4.6.6 Development of the Flash System

4.6.6.1 Introduction

The first four problems listed in the previous section could be solved by having both shutters open at the same time and illuminating the water surface with a powerful flash. Since an electronic flash has an illumination duration of less than 1 ms, the resulting photographs would show almost no image movement, i.e. in the photographs, the water surface would appear as though it had been instantaneously frozen. Furthermore, since both camera shutters would be open when the flash was fired, there would be no shutter speed or synchronization problems.

A conventional flash system, however, would be useless, since in using such a system there would be no way of focussing any contrast pattern on the water surface. However, if a flash pulse were directed through the lens and focusing system of an overhead projector, any desired pattern could be flashed on the water surface. If the required pattern was focused on the water surface using a conventional overhead projector, and then the incandescent bulb was replaced with a flash bulb of similar dimensions, the resulting flashed pattern should also be in focus. This was the principle used here.

4.6.6.2 An Overview of the Flash System

The basic flash system and its sequence of operation is shown schematically in Fig. 4-26. As shown, the flash system was fired by the external flash contact of the slower camera, in this case the left camera, to ensure that the shutters of both cameras were open when the flash was fired. The flash duration of half a millisecond was calculated by taking a photograph of a disc (Fig. 4-27) rotating with a constant, known, angular velocity.

A shutter speed of 1/60 second and later 1/30 second was used for the following reasons:-

(a) At these settings the independently illuminated control points came out well exposed in the photographs.

(b) At these settings the shutters of both cameras would be open when the flash was fired by the slower camera.

The arrangement of the cameras, and the camera/flash firing apparatus on the platform above the wave basin is shown in Fig. 4-28.

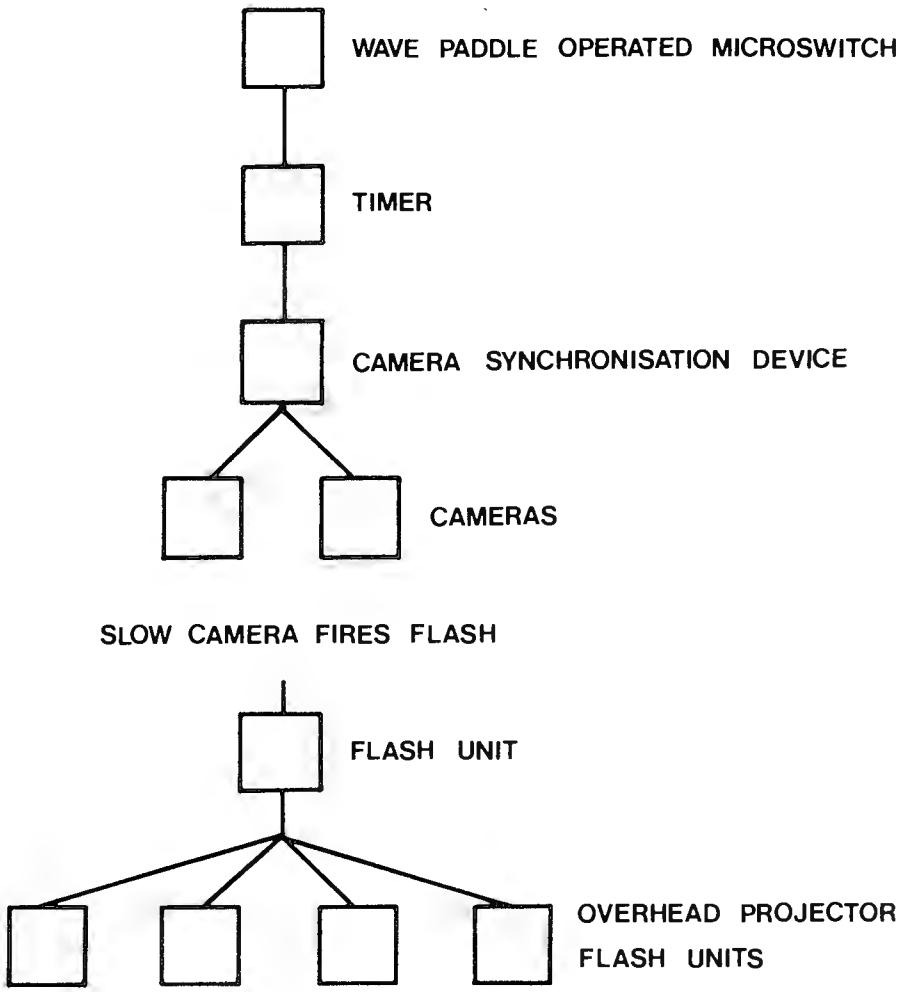

Fig. 4-26 Basic sequence of operation.

Fig. 4-27 Apparatus used to determine flash duration.

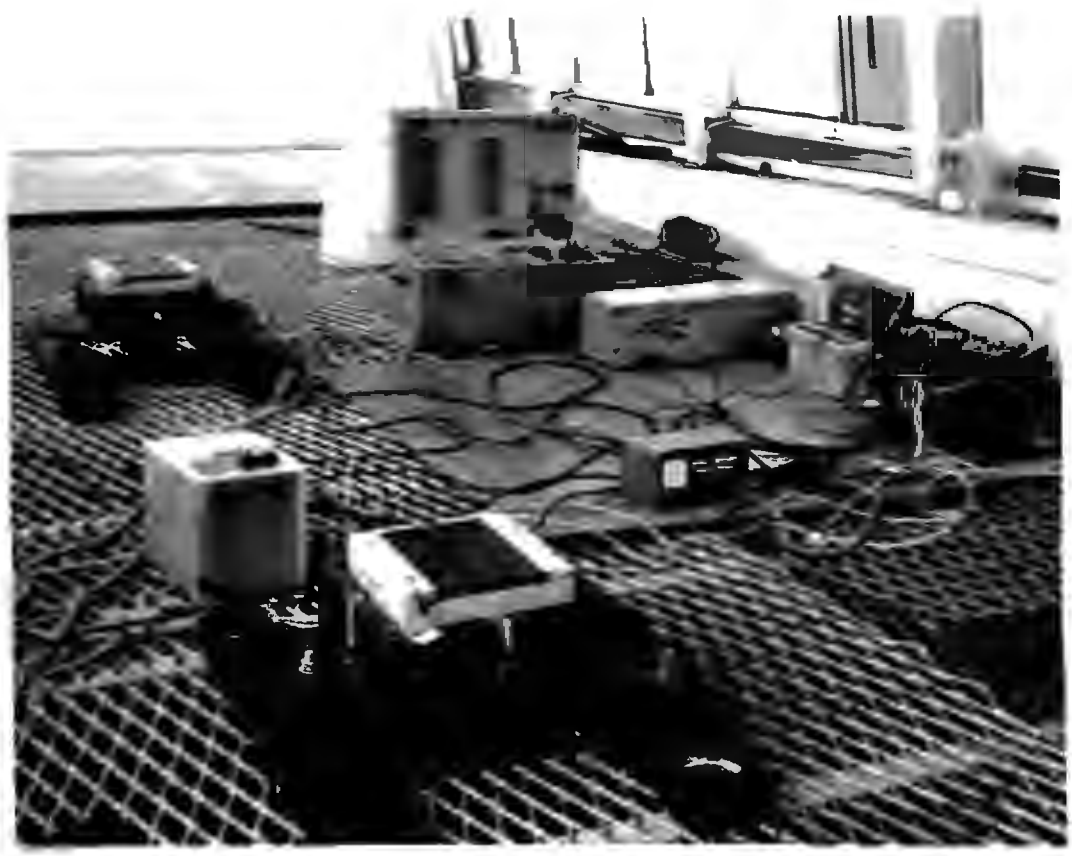

Fig. 4-28 Arrangement of apparatus on platform.

4.6.6.3 The Overhead Projector Flash Units and Flash Circuitry.

To modify the overhead projectors they each had to be dismantled. The incandescent bulb and its mountings were removed and all related electrical attachments disconnected. A flash tube rated at 50 joules was then mounted in exactly the position normally occupied by the incandescent bulb. Each projector was then reassembled and remounted on its platform and the previously noted focusing settings re-established.

The flash circuit (Fig. 4-29), used to fire the four overhead projector flash units, was connected to the flash contact of the camera with the greatest electromagnetic delay, and was triggered when the camera shutter opened.

The flash circuit, shown in Fig. 4-29, can be divided into two parts.

(a) The circuit to the left of A-A consists of a 500 V stablised voltage supply which is stepped down with a 560 Ω resistor to charge the bank of capacitors. The bank

of capacitors consists of eight 450 V by 500 μF capacitors arranged as shown in Fig. 4-29. This delivered 1 000 μF at 900 V to the four flash tubes.

(b) The circuit to the right of A-A is repeated four times and all four sub-circuits are fired simultaneously by a common lead from the slower camera.

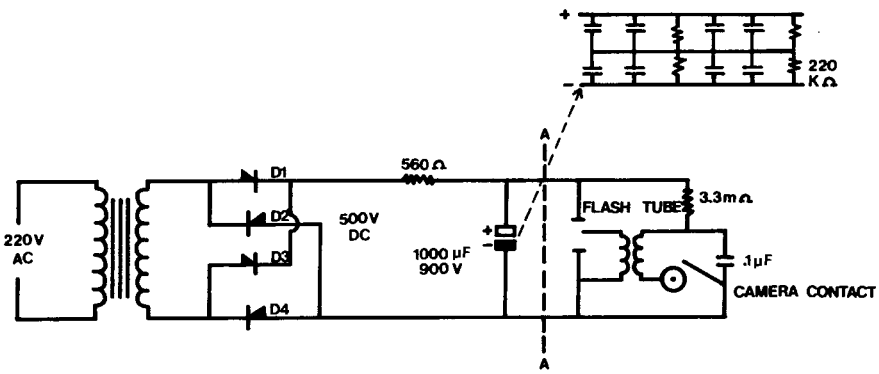

Fig. 4-29 Flash circuit.

4.6.7 Photographic Contrast

4.6.7.1 Introduction

Although soluble cutting oil solves the problem of water penetration (see Section 4.6.1), it introduces serious photographic contrast problems, since the water surface takes on the appearance of a large white projection screen.

Adams (1980) overcame the problem of lack of photographic contrast in the stereogrammetric study of white skeletal remains by projection a grid onto the surface of the object. This method was used, with the aid of overhead projectors, to solve the water surface contrast problem. However, the use of a regular grid pattern in water surface studies, although successful from a photographic contrast point of view, introduced serious problems in the stereoscopic study of resulting stereograms, as depth perception is continually frustrated by the incorrect fusion of repeated similar grid intersections. This problem was overcome by using projector transparencies of concentric circles.

4.6.7.2 Contrast Patterns Tested

The use of overhead transparencies of concentric circles overcame

the problem of false stereoscopic fusion, but the unnatural regular pattern, when viewed as a stereogram, introduced stereo-plotting problems from the stereo-operator's point of view. The concentric circles have an almost mesmeric effect on the operator, appreciably increasing the mental effort required in plotting the wave crests. It was due to this optically disturbing effect caused by a regular pattern that a series of irregular random patterns were tested for their photographic contrast qualities.

Random pattern transparencies using three different pattern making methods were tested. The three random pattern making methods used were:-

(1) Letraset patterns of random stars and arrows applied to a transparent plastic sheet.

(2) Patterns consisting of random koki scribbles on a transparent plastic sheet.

(3) Different Letratone patterns applied to a transparent plastic sheet.

All the patterns were tested using the following technique:- Four overhead projector transparencies of the pattern were made using one of the three methods described above. The transparencies were then attached to the projector flash units and a stereopair was taken of the deformed water surface. The stereopair was then set up in a stereoplotter and a subjective assessment made of the photographic contrast afforded by the pattern.

It was evident that the Letraset patterns and the random scribbles worked well. However, all the Letratone patterns were under exposed due to the translucent nature of the Letratone material, which prevented a large percentage of the flash light from reaching the water surface. After comparing the contrast afforded by the Letraset and the random scribbles in the stereoplotter, it was evident that the letraset pattern was superior. Thus, the random Letraset pattern, as shown in Fig. 4-30, was adopted and used successfully for all subsequent photography.

It soon became evident that the pattern projected by one of the overhead projectors was slightly out of focus. This problem was solved by interfacing an ordinary 35 mm camera with the flash system by means of the camera's external flash contact. A series

of photographs of the water surface were then taken, one for each setting of the projector focusing system. The setting for each photograph was carefully noted, and the photograph itself was identified by a number placed in the camera's field of view. The correct focus setting was then determined by examining the negatives with an eyepiece and finding the one showing the pattern in focus.

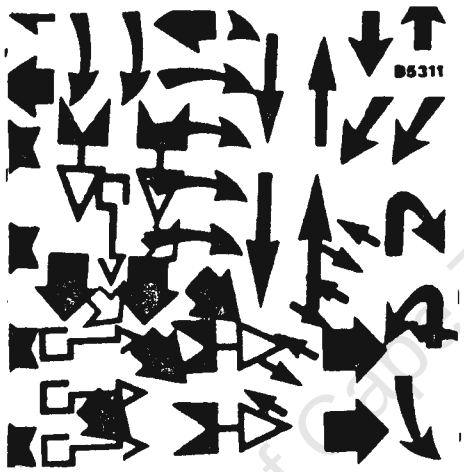

Fig. 4-30 Letraset pattern adopted to provide photographic contrast.

4.6.8 Summary of the Basic Wave Height and Pattern Measurement Technique.

At this point the development of the basic wave height and pattern measurement technique has been described in detail up to the stage when the stereopairs of the deformed water surface are taken. The control point configurations needed in the basin will be described in the following sections since they depend upon the particular procedure used to analyse the plates. Two control point configurations were set up in the wave basin namely:-

(1) the control point configuration for the stereoplotter analysis procedure (Section 4.7.2).

(2) the control point configuration for the analysis procedures based upon the theory of projective transformations (Section 4.8.5.3).

To summarise: to measure the wave heights and patterns within a model harbour, using the procedures described we need:

(1) Two metric cameras or alternatively two precision non-metric cameras.

(2) One or more overhead projector flash unit/s to project a focused random pattern onto the water surface.

(3) Electronic circuitry to simultaneously fire all the flash units at the time when both cameras' shutters will be open.

(4) Triggering devices which enable two stereopairs to be taken such that the waves imaged in the 1st stereopair are 180° out of phase relative to those imaged in the 2nd stereopair. Note, monochromatic waves are assumed to be used throughout.

(5) The water surface to be rendered virtually opaque. A cutting oil/water solution of 7 ml/litre is suggested which should be renewed once a month during testing.

(6) A control point configuration tailored to suit the analysis procedure.

4.7 Wave Height and Pattern Measurement Using a Stereoplotter.

4.7.1 Stereophotographic Requirements for Stereoplotter Analysis.

Holthuijsen (1979) recommended five limitations on camera position and orientation when taking stereopairs of a dynamic water surface, which are subsequently to be analysed using a stereoplotter. The five limitations are repeated here for ease of reference.

(1)	altitude difference between cameras	<10%
(2)	overlap of pictures in the y direction	>80%
(3)	overlap of pictures in the x (flight) direction	50-70%
(4)	difference in orientation (κ error)	<15°
(5)	tilt (ω and ϕ errors)	<3°

The first four requirements were very easily achieved using the camera configuration described in Section 4.6.3. Care, however, had to be taken to achieve the fifth requirement. To minimise the tilt errors as much as possible, the cameras were carefully levelled before each stereopair sequence, using the procedure described in Section 4.6.3.

The stereoplotter used to analyse the stereopairs was a Zeiss Jena Topocart B (see Section 4.4.2). To operate a stereoplotter the following procedure is followed:- The two glass plates which comprise the stereopair are placed in their respective holders on the stereoplotter. The plates are then illuminated and their images are projected via lenses and mirrors to the eyes of the operator. The image of the left plate to the operator's left eye, and the image of the right plate to the right eye. The operator then perceives a three dimensional stereo model of the water surface. The operator can plot the 3 dimensional position of any point on the water surface by bringing the floating dot to rest on the surface of this point on the stereo model (the theory of the floating dot is explained in Section 4.9.2.3). The 3 dimensional co-ordinates can then be read off the X, Y, and Z scales on the stero-plotter. At the same time the X , Y positions can be plotted on the plotting table and a contour map of the Z values drawn up.

4.7.2 Control

4.7.2.1 Inner, Relative and Absolute Orientation

When analysing wave forms using a stereoplotter, it is very important to recover the stereo model correctly. This means

that the relative positions of the two photographs (i.e., the stereopair) in the stereoplotter are identical to the relative positions of the two cameras at the instant of photography.

To satisfy the above condition in the plotter the following procedures are carried out, namely:-

(1) Inner Orientation. This involves correct centering of the negatives (or diapositives) and setting the correct principal distances of the cameras on the machine.

(2) Relative Orientation. This is to provide the correct orientation between the two photographs. When the photographs were exposed, any tilts which may have occured must be correctly set in the plotting machine. Any tilts present can be duplicated by three rotations about three axes i.e., omega (ω), phi (ϕ), and kappa (κ) (Fig. 4-31), and three shifts i.e., b_x, b_y, and b_z caused by variations in the height of the cameras.

For this procedure to be carried out, a minimum of 5 suitably sited orientation points, clearly imaged on the overlap of two negatives, are used. A sixth point is usually added as a check.

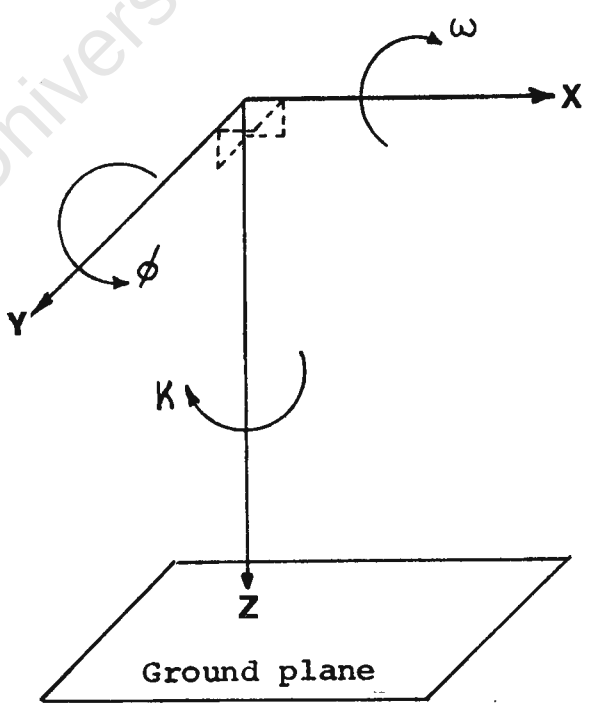

Fig. 4-31 Co-ordinates of a rigid body showing the rotations about the three co-ordinate axes.

(3) Absolute Orientation. After relative orientation has been carried out, the stereo model is not yet correct, since it may occur at the incorrect spatial position. In order to correct this, the whole model has to be rotated about three axes - first about the X-axis giving the common omega (ω) rotation and then about the Y-axis giving the common phi (ϕ) rotation. The above two rotations are carried out on the machine, while the third rotation about the Z-axis giving the common kappa (κ) is carried out on the plotting table, by rotating the drawing paper.

A minimum of three control points are usually used for absolute orientation, two of which may be used to "scale" the three dimensional model. These control points must also appear within the overlap area of the two photographs.

4.7.2.2 Convergency Error

In very short range photogrammetry, large discrepancies can result from what is generally referred to as convergence (Thompson 1975) and this has been born out by Adams (1978b) who states:

"In topographic mapping using air photographs, the variation of ground height of the land surface is normally small in comparison with the flying height and the base:height ratio is such that, after relative and absolute orientation, the deformation of the three dimensional body resulting from residual errors in the elements of relative orientation is so small that the effects of the errors are ignored or conveniently forgotten.

Neglect of the effects of convergence in very short range photogrammetry of an object which contains large variations in heights and with a less than ideal base:height ratio can lead to unacceptable inaccuracies, particularly in height if the stereomodel is to be mapped using a stereoplotter. A study of the deformations produced in a stereomodel resulting from errors in the elements of relative orientation shows that most of these errors can be eliminated or much reduced in the absolute orientation process provided that control is situated in the four corners of the neat model. However, the deformation of the model caused by convergence and due to equal and unlike effect of the ϕ errors (a raising or lowering and a slight cylindrical

warping of the body) is not eliminated and must be adjusted by applying equal and unlike tilts by means of two instrumental ϕ dials. This is achieved by checking the height values at the base and at the top of an elevated height control point. The height control pole can be positioned anywhere within the model overlap, which is convenient since a position can be chosen which will not interfere with the object being photographed."

For the stereoplotter wave height measurement analysis undertaken at U.C.T., no convergency error corrections were made due to the relatively small variations in Z encountered and the efforts made to elliminate the camera tilts.

The U.C.T. configuration consisted of two cameras 1,9 m apart (see Section 4.8.4) and approximately 5,2 m above the mean water level. The control point configuration for the stereoplotter was approximately 170 mm above the mean water level, while the maximum wave heights were in the order of 80-90 mm. It was calculated that for the wave height measurement accuracy required, the convergency error corrections for this configuration would not be needed. If, however, the "flying height" of the cameras for the above configuration was considerably reduced, it would be necessary to introduce convergency error corrections. In order to apply these corrections, it would be necessary to have at least one height control pole positioned within the model overlap.

4.7.2.3 Control Point Configuration Adopted for Stereoplotter Analysis.

For the relative orientation procedure to be carried out in the stereoplotter (see Section 4.7.2.1), a minimum of 5 suitably sited points, clearly imaged on the overlap of the two negatives, are required. Six relative orientation points (R1 to R6), were set up in the wave basin, as shown in Fig. 4-32, one point being a check point.

For the absolute orientation procedure to be carried out in the stereoplotter (see Section 4.7.2.1), a minimum of 3 control points, clearly imaged on the overlap of the two negatives, are required (two of these points are used to scale the 3D model). Four absolute orientation points (C1, C2, C3, C4) were set up in the wave basin, as shown in Fig. 4-32, one being used as a check.

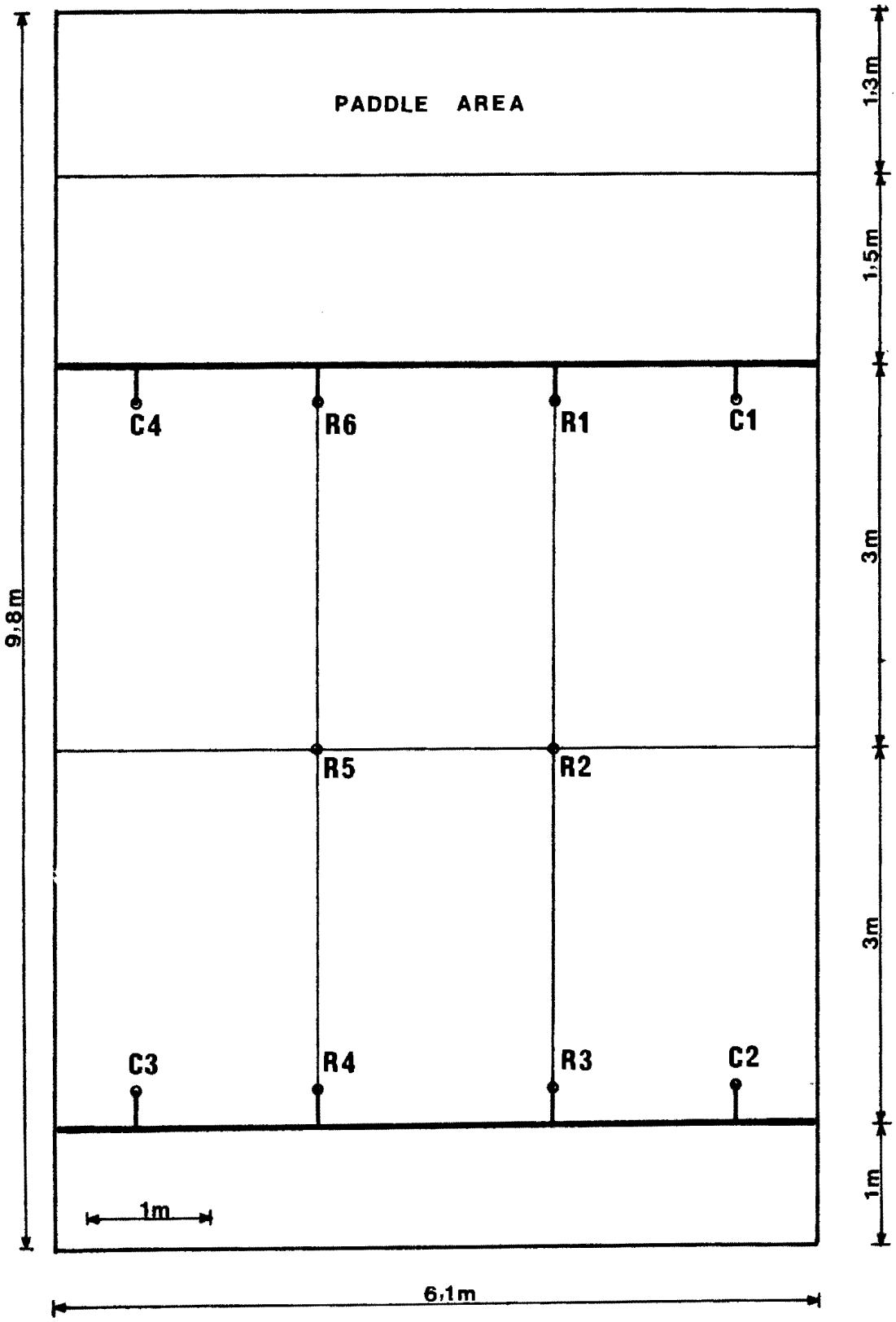

Fig. 4-32 Plan view of wave basin control point configuration adopted for stereoplotter analysis.

All the points, except for R2 and R5, consisted of individually illuminated small round targets fixed to brackets as shown in Fig. 4-33. The points R2 and R5 were positioned approximately at the principal points of the left and right cameras respectively. Their positions were fixed by piano wire stretched across the wave basin as shown in Fig. 4-32.

Fig. 4-33 Control point used for stereoplotter control point configuration.

The levels of the absolute and relative orientation points were determined using an automatic level and a steel metre rule, whilst the X,Y co-ordinates of the absolute orientation points were determined using a steel tape and the least square trilateration adjustment procedure described in Section 4.8.5.3.B.

The control points should be positioned in the basin such that they are not imaged too close to the edge of the image format for two reasons, namely:

(1) If the relative orientation points are imaged too close to the edge of the image format, it is possible (as was the case, initially, for the U.C.T. configuration) that

some of these points will be obscured by the cameras fiducial marks.

(2) Lens distortions tend to be most extreme towards the edge of the image format, and thus for optimum accuracy the control point images should be kept away from these regions.

4.7.3 Potential Wave Height Measurement Accuracy using the Stereoplotter.

To test the plotting accuracy of the Zeiss Jena Topocart B stereoplotter, it was decided that the wave basin configuration should be simulated in the Photogrammetry Laboratory of the Department of Surveying. The two Zeiss cameras were mounted at a spacing of 1,9 m apart and approximately 5 m from the 3rd plane (from the back wall) of the test field described in Section 4.5. The 3rd plane of the test field was assumed to simulate the water surface to be measured. The configuration of the cameras relative to the test field is shown in Fig. 4-36 of Section 4.8.4.

A stereopair of photographs was taken using Kodak Tri-X panachromatic plates. The camera settings were f stop 32 and a 3 second time exposure under normal lab illumination. The cameras were aligned perfectly parallel to each other and perpendicular to the base using the horizontal circle facilities of the cameras mountings.

The plates were developed and set up in the stereoplotter. The stereoplotter was then orientated on the 3rd plane of the test field and the elevations of all 20 targets measured. The stereoplotter measurements were then compared to the known test field co-ordinates to determine the measurement accuracy achieved (the test field co-ordinates were assumed error free). The average absolute error in heighting was ±1,7 mm and the standard deviation for a single observation was ±2,2 mm (see Section 4.8.4 for definitions of the above statistical terms). It is therefore suggested that the potential wave height measurement accuracy of the stereoplotter is approximately 2,4 to 3,1 mm ($\sqrt{2}(AE_Z)$ and $\sqrt{2}(\sigma_Z)$).

4.7.4 Wave Height and Pattern Measurement Procedure when using a Stereoplotter.

At this stage only the wave height measurement procedure will be described; a detailed description of the model harbour configurations analysed using the stereoplotter and the interpretation of

the resultant wave height plots will be given in Chapter Five.

Very briefly, the procedure was as follows. A model harbour configuration was set up in the wave basin. The basin was filled with water to the correct depth and the paddle started. The 1st stereopair was then taken with the cameras triggered by the top micro-switch (see Section 4.6.4.2). The 2nd stereopair was taken with the cameras triggered by the bottom micro-switch (the waves in the 2nd stereopair were 180° out of phase relative to the waves in the 1st stereopair). The plates were then developed and left to dry for 24 hours before being set up in the stereoplotter.

To produce a wave height and crest pattern plot from the two stereopairs, using the stereoplotter the following procedure was adopted:

(1) The 1st stereopair was set up and oriented in the stereoplotter using the control points imaged on the plates. The crest lines imaged in the stereopair were then plotted to a particular scale. Spot elevation points were selected along the wave crests and plotted on the crest lines. These spot elevation points were numbered consecutively and a list made of the measured spot elevations.

(2) The 2nd stereopair was then set up and oriented in the stereoplotter using the control points imaged on the plates. The crest lines imaged in the 2nd stereopair were then plotted to the same scale as the crest lines of the 1st stereopair and on the same piece of paper. Spot elevation points were selected, plotted and numbered along the crest lines of the 2nd stereopair, and a note made of their elevations. The plotting pen of the stereoplotter was then manually positioned over each spot elevation point for the crest lines plotted from the 1st stereopair and a note was made of the water surface elevation of the corresponding point imaged in the 2nd stereopair. This was repeated for all the 1st stereopair crest line spot elevation positions, which now, of course, corresponded with the trough positions in the 2nd stereopair.

(3) The 1st stereopair was again set up and oriented in the stereoplotter. The plotting pen of the stereoplotter was

then manually positioned over each spot elevation point for the crest lines plotted from the 2nd stereopair and a note was made of the water surface elevation of the corresponding trough position imaged in the 1st stereopair. The stereopair analysis was now complete.

(4) The wave heights were then calculated for each crest line spot elevation position by subtracting the trough elevation measured at this point from the corresponding crest elevation. A contour plot of wave height distribution can then be interpolated from the wave height spot heights. The final product was a plot showing the crest lines plotted from each stereopair and the wave height distribution within the model harbour. The contour interpolation from the wave height spot values can either be carried out by hand or with the use of a computer. Both contour plotting techniques were used during the course of this research project. All numerical contour interpolation was done using the Saclant Graphics Package installed on the UNIVAC 1100 at U.C.T. This package is described in Section 4.8.5.4. When a wave diffraction diagram was drawn, each wave height spot value was divided by the incident wave height to yield the diffraction co-efficient at the point. A contour plot, showing contours of equal diffraction co-efficient, was then plotted. Further details are given in Section 5.2.

4.7.5 Sample Plots

The stereoplotter was used to measure and plot the following.

(1) Surface elevations of a deformed water surface

Fig. 4-34 shows a contour plot of a deformed water surface plotted from a single stereopair. The situation depicted is that of waves entering a model harbour basin through a 1 m wide gap between two breakwaters. The basin configuration is described in Section 5.2.2.1. The incident wave train had the following characteristics; period = 0,99 seconds, wave height approximately 80 mm and calculated wave length (Airy wave theory) = 1 m. The water depth was 125 mm. A contour plot of the water surface is shown with a contour interval of 10 mm. The crest and trough lines are shown and spot elevation points are plotted at regular

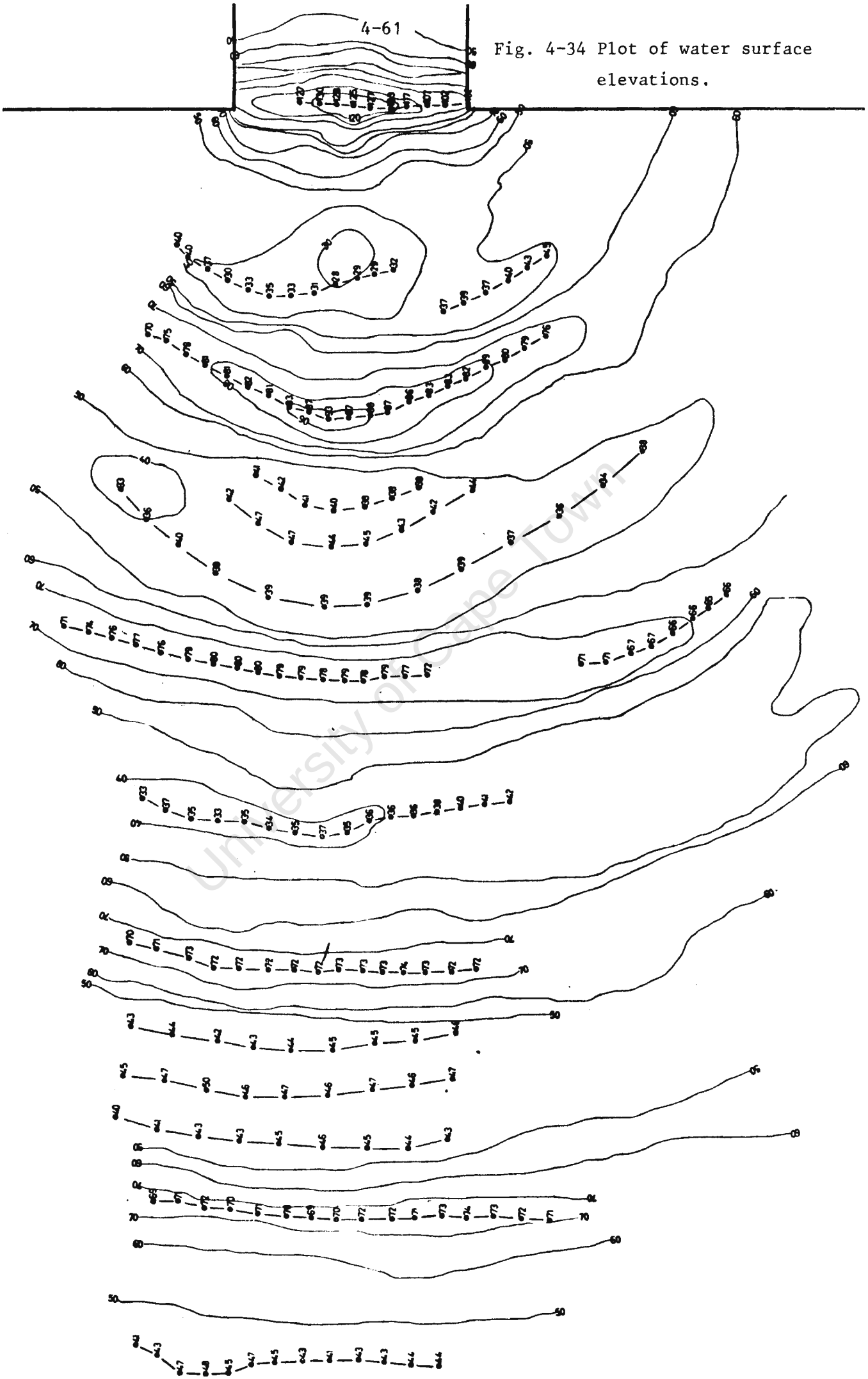

Fig. 4-34 Plot of water surface elevations.

intervals. Secondary crests are evident in the middle of the primary troughs and are caused by the wave paddle. These secondary generated waves were investigated and minimised as described in Section 5.3.3.2.

(2) Wave Height and Diffraction Diagrams

Sample experimental diffraction diagrams plotted using a stereoplotter are given in Section 5.2.3.

4.7.6 Problems Encountered in the Use of a Stereoplotter for Wave Height and Pattern Measurement.

During the course of the investigation it became apparent that there are a number of disadvantages in using a stereoplotter for wave height and pattern measurement. It was these disadvantages which led the author to investigate alternative techniques to analyse the stereopairs as described in Sections 4.8 and 4.9. It is the author's opinion that the major disadvantages in the use of a stereoplotter for the analysis of stereopairs to determine the wave heights and the crest and trough positions are:

(1) A modern stereoplotter is a very sophisticated piece of equipment, and too expensive for any small or medium sized engineering consulting or research organisation, interested in wave height measurement.

(2) A modern stereoplotter is a very complex device and would probably need a specially trained, full time operator, to undertake the complicated relative and absolute orientation and convergency error correction procedures, as well as the actual plotting work. This would mean that the coastal engineer would probably not be able to analyse the stereopairs himself. This would be very inefficient, since the coastal engineer would know exactly what information he was looking for from the stereopairs, whilst the specialised stereoplotter operator would only plot what to him was a meaningless surface. This problem was very evident during the present research project since the stereoplotter operator often failed to recognise and therefore plot wave features which were of particular interest to the author.

(3) In order to carry out the inner orientation procedure in the stereoplotter, the principal distance and principal

point of each plate or photograph has to be known. This means that the stereopairs would have to be taken with very expensive metric cameras or specially "metricised" high precision non-metric cameras. If however, conventional non-metric cameras were used to take the stereopairs, the principal point and principal distance for each photograph would have to be determined using techniques such as described in Section 4.8.

(4) There are marked limitations to the relative tilts of the cameras, when the stereopairs are taken, and also to the cameras principal distances, when the stereopairs are analysed using a stereoplotter. Furthermore large variations in Z (as is often encountered in close range stereophotography), cannot be accomodated in a conventional stereoplotter.

4.8 Wave Height and Pattern Measurement using Projective Transformations.

4.8.1 Motivation for the Development of the Projective Transformation Wave Height and Pattern Measurement Technique.

Due to the limitations (listed in Section 4.7.6) in using the stereoplotter for analysing the stereopairs, it was decided to adopt an alternative and potentially more accurate analysis technique. It was decided that the wave heights and patterns should be measured using the theory of Projective Transformations. All the disadvantages which were encountered in the analysis of the stereopairs, using a stereoplotter, could be overcome if the plates were analysed using a technique incorporating the above mentioned theory. The projective transformation technique would eliminate the need for a stereoplotter, a specially trained stereoplotter operator and the use of expensive metric cameras (however, the accuracy of the technique is directly dependant on the precision of the cameras used).

4.8.2 The Theory of Projective Transformations.

4.8.2.1 Calculation of the Transformation Parameters and the Inner Orientation Elements for a Single Photograph.

A linear transformation

$$\begin{bmatrix} x' \\ y' \\ z' \\ w' \end{bmatrix} = A \begin{bmatrix} x \\ y \\ z \\ w \end{bmatrix} \qquad (4)$$

of homogeneous co-ordinates in space is known as a projective transformation when the matrix A is non-singular (Thompson, 1971a)

In terms of non-homogeneous co-ordinates it takes the more familiar form (from Klein, 1908)

$$X' = \frac{a_{11}X + a_{12}Y + a_{13}Z + a_{14}}{a_{41}X + a_{42}Y + a_{43}Z + a_{44}}$$

$$Y' = \frac{a_{21}X + a_{22}Y + a_{23}Z + a_{24}}{a_{41}X + a_{42}Y + a_{43}Z + a_{44}} \qquad (5)$$

$$Z' = \frac{a_{31}X + a_{32}Y + a_{33}Z + a_{34}}{a_{41}X + a_{42}Y + a_{43}Z + a_{44}}$$

where a_{ij} is a typical element of A in (4).

That is to every point X, Y, Z there corresponds a definite finite point X', Y', Z' provided only that the common denominator is not zero. Note:

$$X' = \frac{x'}{w'}, \quad Y' = \frac{y'}{w'}, \quad Z' = \frac{z'}{w'}$$

When the accented and unaccented co-ordinates are referred to the same system equations, (4) and (5) represent a linear mapping of space on itself which is known as "collineation", and is non-singular since A is non-singular. The most important difference is that photography induces a singular transformation which cannot be uniquely inverted, for to each picture point correspond an infinity of space points. Let us suppose the picture plane to be the plane Z' = k (Fig. 4-35), then we must have Z' = k for all X, Y, Z. In the photographic case Z' = k can be interpreted as the principal distance and the origin O as the interior perspective centre of the lens.

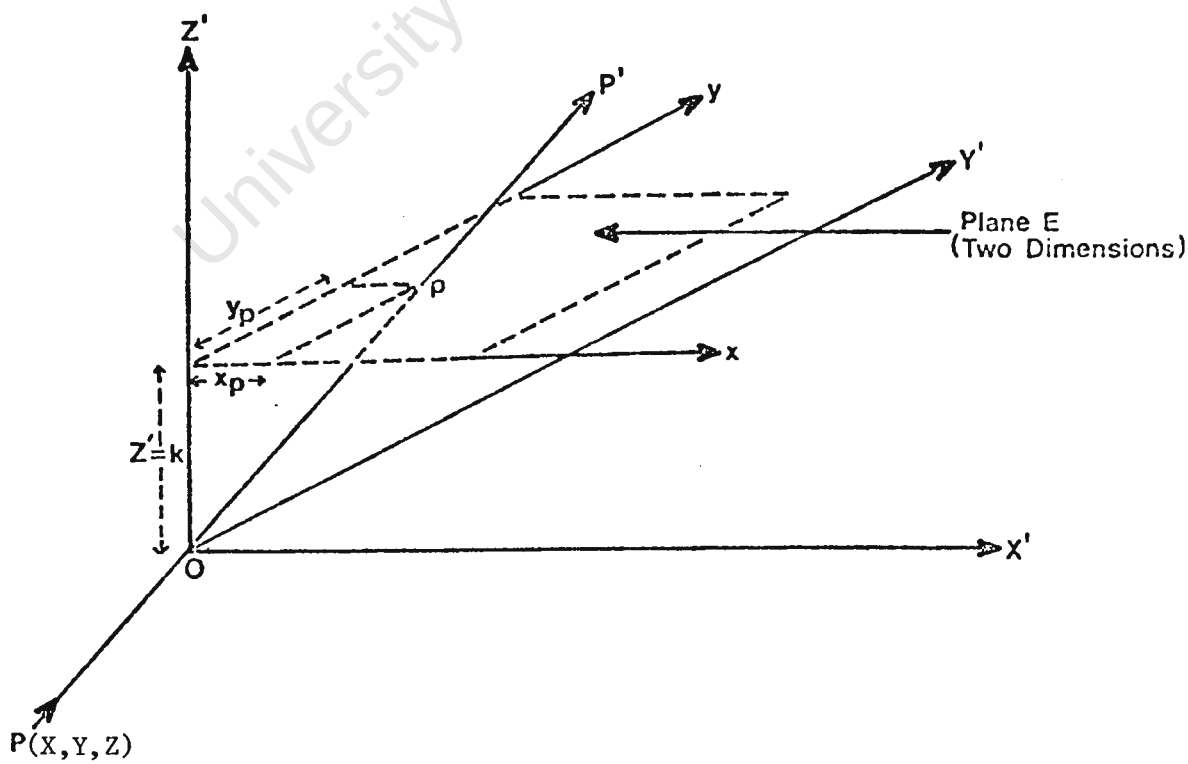

Fig. 4-35

The collinearity equations (5) are for an arbitrarily oriented X', Y', Z', orthogonal system but for two dimensional co-ordinates x, y say and treating co-ordinates X', Y', Z', as homogeneous co-ordinates Adams and Hurly (1983) have shown that, where the x, y, plane is parallel to the X', Y', plane and Z' is arbitrary and constant, then

$$x = \frac{X'}{Z'} \qquad \text{and} \qquad y = \frac{Y'}{Z'}$$

and subsituting in equations (5) therefore

$$x = \frac{a_{11}X + a_{12}Y + a_{13}Z + a_{14}}{a_{31}X + a_{32}Y + a_{33}Z + a_{34}}$$

$$y = \frac{a_{21}X + a_{22}Y + a_{23}Z + a_{24}}{a_{31}X + a_{32}Y + a_{33}Z + a_{34}} \qquad (6)$$

In the photographic case this is a convenient way of expressing x and y (the plate co-ordinates of an image) in terms of X, Y, Z (the space or ground co-ordinates of the point).

We can eliminate one of the transformation parameters (a_{34}) by dividing all terms on the right hand side of the equation by a_{34} and introducing new transformation parameters b_{ij} where

$$b_{ij} = \frac{a_{ij}}{a_{34}}$$

Equations (6) becomes now, for the general case:

$$x_i = \frac{b_{11}X_i + b_{12}Y_i + b_{13}Z_i + b_{14}}{b_{31}X_i + b_{32}Y_i + b_{33}Z_i + 1}$$

$$y_i = \frac{b_{21}X_i + b_{22}Y_i + b_{23}Z_i + b_{24}}{b_{31}X_i + b_{32}Y_i + b_{33}Z_i + 1} \qquad (7)$$

where:-

$X_iY_iZ_i$	are space co-ordinates of point P_i
x_iy_i	are digitised image co-ordinates of point P_i, refered to an arbitrary origin
b_{ij}	are transformation parameters

Since we have to find 11 ratios, six space points giving 12 image co-ordinates will provide a solution with one redundancy. Of the six points no more than four may be coplanar and no more than three points may be colinear. In practice more than the minimum 6 points needed to provide a unique solution to the 11 transformation parameters, are used. A discussion on the question of measurement accuracy versus number of control points is given in Section 4.8.5.3. A way of finding a solution when redundant information is used is called: "The method of least squares". A detailed account of the use of least square techniques in close range photogrammetry is given by Rüther (1982). A description of the application of the least square method to the solution of the transformation parameters is given by Welham (1982).

The equations (7) fit a least squares mathematical or "functional" model called a quasi-parametric adjustment. The measurements (x_i, y_i) relate to the unknown quantities (b_{ij}) in a system of condition equations. The least squares model requires condition equations that contain the unknowns in a linear form. However, the equations (7) are non-linear. Linearization is achieved by means of a Taylor series expansion about provisional values for the unknowns, retaining only the linear terms.

Before the equations can be linearized it is necessary to decide which terms are to be treated as known and unknown respectively. The word known is used here to mean that the term is not subject to adjustment and is therefore assumed to be free of error for all intent and purposes. It is a generally accepted practice to assume that the space co-ordinates (X,Y,Z) of control points are known and without errors (Abdel-Aziz and Karara 1974, Bopp and Krauss 1978, Adams 1979). It is also general practice to assume that the image co-ordinates are subject to errors of observation. However Adams (1979) writes:

> "that this is a somewhat debatable point since for very short range photogrammetry the comparator measurements of clear image points are probably observed to a higher accuracy than the object control co-ordinates were determined, since we are dealing with control assumed fixed to mm accuracy which is difficult to achieve in practice."

Adams (1979) assumes that both the image and the object co-ordinates are error free and this is though to be valid for the stereo-comparator analysis technique (Section 4.8.5), due to the high precision with which the image points can be measured using a stereocomparator. For the digitiser tablet/mirrorstereoscope/ electronic parallax bar technique (Section 4.8.6), Welham (1982) assumes the image co-ordinates to be subject to error and the control point co-ordinates to be error free. All image measurements are assumed to have the same precision. The least square solution of the transformation parameters is now described.

Equations (7) can be rewritten as shown below:

$$0 = b_{11}X_i + b_{12}Y_i + b_{13}Z_i + b_{14} - b_{31}x_iX_i - b_{32}x_iY_i - b_{33}x_iZ_i - x_i \quad (8)$$

$$0 = b_{21}X_i + b_{22}Y_i + b_{23}Z_i + b_{24} - b_{31}y_iX_i - b_{32}y_iY_i - b_{33}y_iZ_i - y_i \quad (9)$$

From equations (8) and (9) we obtain the two condition equations to be used in the least squares adjustment. But first we must linearise. Expand equation (8) in a Taylor series ignoring second and higher order terms:- (the i subscript is left out for ease of notation).

$$\begin{aligned} 0 = {} & b_{11_0}X + b_{12_0}Y + b_{13_0}Z + b_{14_0} - b_{31_0}xX - b_{32_0}xY - b_{33_0}xZ - x \\ & + Xdb_{11} + Ydb_{12} + Zdb_{13} + db_{14} - xXdb_{31} - xYdb_{32} - xZdb_{33} \\ & - (Xb_{31} + Yb_{32} + Zb_{33} + 1)dx \end{aligned} \quad (10)$$

where the b_{ij_0} terms are the initial approximations.

Traditionally in least square adjustments corrections to observations are refered to as v and we therefore replace the last term of equation (10) by bv_x. By re-arranging (10) and substituting, we obtain the condition equation for an x co-ordinate measurement:-

$$\begin{aligned} 0 = {} & -bv_x + Xdb_{11} + Ydb_{12} + Zdb_{13} + db_{14} - xXdb_{31} - xYdb_{32} \\ & - xZdb_{33} + w_x \end{aligned} \quad (11a)$$

where:

$$w_x = -x + b_{11_0} X + b_{12_0} Y + b_{13_0} Z + b_{14_0} - b_{31_0} xX - b_{32_0} xY - b_{33_0} xZ \quad (11b)$$

Similarly the condition equation for a y co-ordinate measurement can be derived:-

$$0 = -bv_y + Xdb_{21} + Ydb_{22} + Zdb_{23} + db_{24} - yXdb_{31} - yYdb_{32}$$

$$-yZ_{33} + w_y \quad (12a)$$

where:-

$$w_y = -y + b_{21_0} X + b_{22_0} Y + b_{23_0} Z + b_{24_0} - b_{31_0} yX - b_{32_0} yY - b_{33_0} yZ \quad (12b)$$

Equations (11a) and (12a) are condition equations of the combined adjustment case, which expressed in matrix notation is:-

$$BV + AX + W = 0 \quad (13)$$

where:-

B = matrix of the coefficients of the corrections to the measurements.

V = matrix of the corrections to the measurements namely v_x and v_y.

A = matrix of the coefficients of the unknowns

X = matrix of the unknowns, namely the corrections to the approximations of the unknown parameters - db_{ij}.

W = the discrepancy vector.

The general solution of the combined adjustment case is:-

$$X = -(A^T(BB^T)^{-1}A)^{-1}A^T(BB^T)^{-1}W \quad (14)$$

Now examining the B matrix we find that it is a diagonal matrix of order (2n, 2n), where n is the number of points in the adjustment. The terms of the Principal Diagonal are:-

$$b_x = (X_i b_{31} + Y_i b_{32} + Z_i b_{33} + 1)$$

$$b_y = (X_i b_{31} + Y_i b_{32} + Z_i b_{33} + 1)$$

$$b_i = b_x = b_y$$

$$B = \begin{bmatrix} b_1 & 0 & 0 & 0 & 0 & 0 & 0 & 0 \\ 0 & b_1 & 0 & 0 & 0 & 0 & 0 & 0 \\ - & - & - & - & - & - & - & - \\ 0 & 0 & 0 & b_i & 0 & 0 & 0 & 0 \\ 0 & 0 & 0 & 0 & b_i & 0 & 0 & 0 \\ - & - & - & - & - & - & - & - \\ 0 & 0 & 0 & 0 & 0 & 0 & b_n & 0 \\ 0 & 0 & 0 & 0 & 0 & 0 & 0 & b_n \end{bmatrix}$$

The $(BB^T)^{-1}$ is also a diagonal matrix:-

$$(BB^T)^{-1} = \begin{bmatrix} b_1^{-2} & 0 & 0 & 0 & 0 & 0 & 0 & 0 \\ 0 & b_1^{-2} & 0 & 0 & 0 & 0 & 0 & 0 \\ - & - & - & - & - & - & - & - \\ 0 & 0 & 0 & b_i^{-2} & 0 & 0 & 0 & 0 \\ 0 & 0 & 0 & 0 & b_i^{-2} & 0 & 0 & 0 \\ - & - & - & - & - & - & - & - \\ 0 & 0 & 0 & 0 & 0 & 0 & b_n^{-2} & 0 \\ 0 & 0 & 0 & 0 & 0 & 0 & 0 & b_n^{-2} \end{bmatrix}$$

The $(BB^T)^{-1}$ in the above form is a principal diagonal matrix and thus similar in form to the standard weight matrix of observations of the least squares adjustment. The algorithm is simplified if $(BB^T)^{-1}$ is treated as a quasi weight matrix by setting:-

$$\bar{P} = (BB^T)^{-1} \tag{15}$$

Equation (14) then becomes

$$X = -(A^T\bar{P}A)^{-1}A^T\bar{P}W \tag{16}$$

With L = -W we can rewrite requation (16)

$$X = (A^T\bar{P}A)^{-1}A^T\bar{P}L \tag{17}$$

Equation (17) can be interpreted as the parametric case of the least squares adjustment.

$\bar{P}$ as defined in equation (15) is not a true weight matrix and therefore this type of adjustment is refered to as a quasi parametric adjustment. By converting the combined adjustment case into the quasi parametric adjustment, the matrix manipulation is reduced considerably and the system can be solved using a microcomputer, which would probably not be possible for the full combined case.

In order to determine the unknown transformation parameters (db_{ij} terms), provisional values (b_{ij_0} terms) have to be assumed and substituted into the adjustment formula. The provisional values are updated by the addition of the unknowns db_{ij}, and the adjustment process re-iterated until the value for the equation $V^T \bar{P} V$ converges.

As a first approximation to the transformation parameters the provisional values are set to zero. The effect on the adjustment is:-

(i) the quasi-weight matrix $\bar{P}$ reduced to the unit matrix:-

$$\bar{P} = \begin{pmatrix} 1 & 0 & 0 & 0 & 0 & 0 & 0 & 0 \\ 0 & 1 & 0 & 0 & 0 & 0 & 0 & 0 \\ - & - & - & - & - & - & - & - \\ 0 & 0 & 0 & 1 & 0 & 0 & 0 & 0 \\ 0 & 0 & 0 & 0 & 1 & 0 & 0 & 0 \\ - & - & - & - & - & - & - & - \\ 0 & 0 & 0 & 0 & 0 & 0 & 1 & 0 \\ 0 & 0 & 0 & 0 & 0 & 0 & 0 & 1 \end{pmatrix}$$

(ii) the matrix L becomes:-

$$L = \begin{pmatrix} x_1 \\ y_1 \\ - \\ x_i \\ y_i \\ - \\ x_n \\ y_n \end{pmatrix}$$

(iii) the unknown matrix X becomes:-

$$X_1 = \begin{pmatrix} b_{11_1} \\ - \\ - \\ b_{ij_1} \\ - \\ - \\ b_{33_1} \end{pmatrix}$$

(iv) $X_1 = (A^T IA)^{-1} A^T IL = (A^T A)^{-1} A^T L$

The first approximation to the transformation parameters is therefore:-

$$X_1 = (A^T A)^{-1} A^T L \qquad (18)$$

Iteration is normally assumed necessary, but research has shown (Adams 1979) that for the particular case of projective transformations the first approximation yields very accurate results. Adams writes:

> "Comparison test calculations were undertaken operating on the same data and using the above simple solution matrix (equation No. 18), and a rigorous least squares iterative solution as contemplated by Bopp and Krauss (1978a) with the added refinement that both measured and object space co-ordinates were considered subject to error. As a result of these tests, the writer would assert that sophisticated least squares solutions, although academically interesting, do not alter end results to any sensible extent for work of this nature. The computer programming problem tends to be complicated and the capacity of the small desk top computer to cope with the rigorous solution is stretched."

The projective transformation parameters (b_{ij} terms) are calculated using equation (18). The expanded forms of the matrices given in equation (18) are shown below.

$$A = \overbrace{\begin{matrix} b_{11} & b_{12} & b_{13} & b_{14} & b_{21} & b_{22} & b_{23} & b_{24} & b_{31} & b_{32} & b_{33} \end{matrix}}^{X^T}$$

$$\begin{bmatrix}
X_1 & Y_1 & Z_1 & 1 & 0 & 0 & 0 & 0 & -x_1X_1 & -x_1Y_1 & -x_1Z_1 \\
X_2 & Y_2 & Z_2 & 1 & 0 & 0 & 0 & 0 & -x_2X_2 & -x_2Y_2 & -x_2Z_2 \\
\cdot & \cdot & \cdot & \cdot & \cdot & \cdot & \cdot & \cdot & \cdot & \cdot & \cdot \\
X_n & Y_n & Z_n & 1 & 0 & 0 & 0 & 0 & -x_nX_n & -x_nY_n & -x_nZ_n \\
0 & 0 & 0 & 0 & X_1 & Y_1 & Z_1 & 1 & -y_1X_1 & -y_1Y_1 & -y_1Z_1 \\
0 & 0 & 0 & 0 & X_2 & Y_2 & Z_2 & 1 & -y_2X_2 & -y_2Y_2 & -y_2Z_2 \\
\cdot & \cdot & \cdot & \cdot & \cdot & \cdot & \cdot & \cdot & \cdot & \cdot & \cdot \\
0 & 0 & 0 & 0 & X_n & Y_n & Z_n & 1 & -y_nX_n & -y_nY_n & -y_nZ_n
\end{bmatrix}
\quad L = \begin{bmatrix} x_1 \\ x_2 \\ \cdot \\ x_n \\ y_1 \\ y_2 \\ \cdot \\ y_n \end{bmatrix} \qquad (19)$$

Thompson (1971a) has shown that once the transformation parameters (b_{ij} terms) have been determined, it is possible to calculate the inner orientation elements for a single photograph.

Summarised, the appropriate equations for the inner orientation elements are:-

Non-zero scalar λ:

$$\lambda^{-2} = b_{31}^2 + b_{32}^2 + b_{33}^2 \tag{20}$$

Principal point co-ordinates (comparator system):

$$x_p = (b_{11}b_{31} + b_{12}b_{32} + b_{13}b_{33})\lambda^2 \tag{21}$$

$$y_p = (b_{21}b_{31} + b_{22}b_{32} + b_{23}b_{33})\lambda^2 \tag{22}$$

Equivalent principal distance f:

$$f_x^2 = (b_{11}^2 + b_{12}^2 + b_{13}^2)\lambda^2 - x_p^2 \tag{23a}$$

$$f_y^2 = (b_{21}^2 + b_{22}^2 + b_{23}^2)\lambda^2 - y_p^2 \tag{23b}$$

Use average of f_x and f_y for f.

If a stereopair has been taken using non-metric cameras, and one intends to plot from the stereopair using a stereoplotter, the above technique can be used to determine the inner orientation elements of the photographs.

The co-ordinates of the perspective centre of the camera used to take the photograph (relative to the space system used to define the control point positions), can be calculated by solving the following equations simultaneously.

$$\begin{aligned} b_{11}\bar{X}_{\bar{0}} + b_{12}\bar{Y}_{\bar{0}} + b_{13}\bar{Z}_{\bar{0}} + b_{14} &= 0 \\ b_{21}\bar{X}_{\bar{0}} + b_{22}\bar{Y}_{\bar{0}} + b_{23}\bar{Z}_{\bar{0}} + b_{24} &= 0 \\ b_{31}\bar{X}_{\bar{0}} + b_{32}\bar{Y}_{\bar{0}} + b_{33}\bar{Z}_{\bar{0}} + 1 &= 0 \end{aligned} \tag{24}$$

4.8.2.2 Calculation of Object Space Co-ordinates from a Stereopair.

Bopp and Krauss (1978a) extended the work of Thompson (1971a) to include the calculation of the position of object points in space using a stereopair of photographs. Once the projective transformation parameters for each photograph of the stereopair have been determined, the object point space co-ordinates can be determined using the following equations.

$$0 = (b_{11} - x_i b_{31})X_i + (b_{12} - x_i b_{32})Y_i + (b_{13} - x_i b_{33})Z_i + b_{14} - x_i \quad (25)$$

$$0 = (b_{21} - y_i b_{31})X_i + (b_{22} - y_i b_{32})Y_i + (b_{23} - y_i b_{33})Z_i + b_{24} - y_i \quad (26)$$

$$0 = (\bar{b}_{11} - \bar{x}_i \bar{b}_{31})X_i + (\bar{b}_{12} - \bar{x}_i \bar{b}_{32})Y_i + (\bar{b}_{13} - \bar{x}_i \bar{b}_{33})Z_i + \bar{b}_{14} - \bar{x}_i \quad (27)$$

$$0 = (\bar{b}_{21} - \bar{y}_i \bar{b}_{31})X_i + (\bar{b}_{22} - \bar{y}_i \bar{b}_{32})Y_i + (\bar{b}_{23} - \bar{y}_i \bar{b}_{33})Z_i + \bar{b}_{24} - \bar{y}_i \quad (28)$$

where the unbarred and barred elements refer to the left and right hand pictures respectively and

$X_i Y_i Z_i$ are the space co-ordinates of point P_i.

$x_i y_i$ are digitised image co-ordinates of point P_i, refered to an arbitrary origin.

b_{ij} are transformation parameters.

We are again faced with the problem of deciding which terms are considered error free. The assumption made here is that if a large enough number of redundant observations are used to determine the transformation parameters, then the results of the adjustment can be adopted as the true (known) parameters. Because we have assumed the b_{ij}'s to be error-free the standard deviations of the XYZ co-ordinates from the adjustment will be optimistic i.e. too small. The measurements $(x, y, \bar{x}, \bar{y})$ are assumed to be of the same precision and are given unit weight.

Any 3 of equations (25) to (28) can be used to provide a solution of the space co-ordinates (XYZ) of an object point. Welham (1982) suggested that all 4 equations be used in a least squares solution. The least squares solution of the object point space co-ordinates is now described.

Expand equation (25) in a Taylor series ignoring second and higher order terms:- (the i subscript is left out for east of notation).

$$\begin{aligned} 0 = {} & (b_{11} - xb_{31})X_0 + (b_{12} - xb_{32})Y_0 + (b_{13} - xb_{33})Z_0 \\ & + b_{14} - x + (b_{11} - xb_{31})dX + (b_{12} - xb_{32})dY \\ & + (b_{13} - xb_{33})dZ - (b_{31}X + b_{32}Y + b_{33}Z + 1)dx \end{aligned} \quad (29)$$

where X_0, Y_0, Z_0 are provisional values.

Substituting co-efficients in equation (29) we get:-

$$0 = AX_0 + BY_0 + CZ_0 + b_{14} - x + AdX + BdY + CdZ - adx \qquad (30)$$

By rearranging and setting $v_x = dx$ we get the condition equation for the x co-ordinate observation:-

$$0 = -av_x + AdX + BdY + CdZ + \{-x + (AX_0 + BY_0 + CZ_0 + b_{14})\} \qquad (31)$$

Similarly we get the condition equations for the other three observations (26), (27) and (28):-

$$0 = -av_y + DdX + EdY + FdZ + \{-y + (DX_0 + EY_0 + FZ_0 + b_{24})\} \qquad (32)$$

$$0 = -\bar{a}v_x + \bar{A}dX + \bar{B}dY + \bar{C}dZ + \{-\bar{x} + (\bar{A}X_0 + \bar{B}Y_0 + \bar{C}Z_0 + \bar{b}_{14})\} \qquad (33)$$

$$0 = -\bar{a}v_y + \bar{D}dX + \bar{E}dY + \bar{F}dZ + \{-\bar{y} + (\bar{D}X_0 + \bar{E}Y_0 + \bar{F}Z_0 + \bar{b}_{24})\} \qquad (34)$$

We again have the combined adjustment case:-

$$BV + AX + W = 0$$

with the general solution equation (14) as before:-

$$X = -(A^T(BB^T)^{-1}A)^{-1}A^T(BB^T)^{-1}W$$

Examining the B matrix we find that it is a diagonal matrix of order (4, 4). The terms of the principal diagonal are;-

(i) for the left hand side

$$a_x = (b_{31}X_0 + b_{32}Y_0 + b_{33}Z_0 + 1)$$

$$a_y = (b_{31}X_0 + b_{32}Y_0 + b_{33}Z_0 + 1)$$

$$a = a_x = a_y$$

(ii) and for the right hand side

$$\bar{a}_x = (\bar{b}_{31}X_0 + \bar{b}_{32}Y_0 + \bar{b}_{33}Z_0 + 1)$$

$$\bar{a}_y = (\bar{b}_{31}X_0 + \bar{b}_{32}Y_0 + \bar{b}_{33}Z_0 + 1)$$

$$\bar{a} = \bar{a}_x = \bar{a}_y$$

The B matrix has the form:-

$$B = \begin{pmatrix} a & o & o & o \\ o & a & o & o \\ o & o & \bar{a} & o \\ o & o & o & \bar{a} \end{pmatrix}$$

Now examine the $(BB^T)^{-1}$ matrix:-

$$(BB^T)^{-1} = \begin{pmatrix} a^{-2} & 0 & 0 & 0 \\ 0 & a^{-2} & 0 & 0 \\ 0 & 0 & \bar{a}^{-2} & 0 \\ 0 & 0 & 0 & \bar{a}^{-2} \end{pmatrix}$$

As before let $\dot{P} = (BB^T)^{-1}$ and L =-W. Substitute into the solution, equation (14)

$$X = (A^T\dot{P}A)^{-1}A^T\dot{P}L, \qquad (35)$$

which is a quasi-parametric adjustment.

In order to determine the co-ordinates XYZ, provisional values $(X_0\ Y_0\ Z_0)$ have to be adopted and substituted into the adjustment formula. The provisional values are updated by the addition of unknowns dX, dY and dZ and the adjustment process re-iterated until $V^T\dot{P}V$ converges.

As a first approximation to the co-ordinates XYZ, the provisional co-ordinates were assumed to be zero. The effect this has on the adjustment is:-

(i) the quasi-weight matrix $\dot{P}$ reduces to the unit matrix

$$\dot{P} = \begin{pmatrix} 1 & 0 & 0 & 0 \\ 0 & 1 & 0 & 0 \\ 0 & 0 & 1 & 0 \\ 0 & 0 & 0 & 1 \end{pmatrix} = I$$

(ii) the L matrix becomes

$$L = \begin{pmatrix} x - b_{14} \\ y - b_{24} \\ \bar{x} - \bar{b}_{14} \\ \bar{y} - \bar{b}_{24} \end{pmatrix}$$

(iii) the X matrix becomes:-

$$X_1 = \begin{pmatrix} X_1 \\ Y_1 \\ Z_1 \end{pmatrix}$$

(iv) $X_1 = (A^TIA)^{-1}A^TIL = (A^TA)^{-1}A^TL$

The first approximation of the co-ordinates is therefore

$$X_1 = (A^T A)^{-1} A^T L \tag{36}$$

The expanded forms of the matrices given in equation (36) are shown below:-

$$A = \overbrace{\begin{matrix} X_1 & Y_1 & Z_1 \end{matrix}}^{X^T} \begin{bmatrix} b_{11} - x_i b_{31} & b_{12} - x_i b_{32} & b_{13} - x_i b_{33} \\ b_{21} - y_i b_{31} & b_{22} - y_i b_{32} & b_{23} - y_i b_{33} \\ \bar{b}_{11} - \bar{x}_i \bar{b}_{31} & \bar{b}_{12} - \bar{x}_i \bar{b}_{32} & \bar{b}_{13} - \bar{x}_i \bar{b}_{33} \\ \bar{b}_{21} - \bar{y}_i \bar{b}_{31} & \bar{b}_{22} - \bar{y}_i \bar{b}_{32} & \bar{b}_{23} - \bar{y}_i \bar{b}_{33} \end{bmatrix} \quad L = \begin{bmatrix} x_i - b_{14} \\ y_i - b_{24} \\ \bar{x}_i - \bar{b}_{14} \\ \bar{y}_i - \bar{b}_{24} \end{bmatrix} \tag{37}$$

Again, iteration is normally assumed necessary but research has shown (Welham, 1982) that the first approximation to the object point co-ordinates, given by equation (36), yields very accurate results. Welham (1982) took stereopairs of the testfield described in Section 4.5 using the Zeiss UMK cameras described in Section 4.4.1. He then analysed the plates using the stereocomparator system described in Section 4.4.3. He calculated the space co-ordinates of the test field targets using equation (36), and also an inerative solution based on equation (35). He concluded that the differences between the two sets of results were negligible.

For the measurement accuracy experiment described in Section 4.8.4 the author used 2 solution techniques to calculate the space co-ordinates of the test field targets namely:-

(1) a solution using equations (25), (26) and (27) only

(2) a solution using equation (36)

The author found that for the configuration described in Section 4.8.4, there was no significant improvement in the results obtained using the least squares solution (equation No 36) compared to the results obtained using only the first 3 equations. However, Welham (1982) found, when using a beam splitter on a non-metric camera for measurement purposes and then subsequently analysing the results using the digitiser tablet/mirror stereoscope/ electronic parallax bar system, that the least square solution's

results were approximately 50% more accurate than results obtained using the 3 equation solution. The author therefore concludes that equation (36) should generally be used to calculate the object point space co-ordinates, but that the three equation solution will often prove to be adequate when using high precision cameras and clearly defined and accurately fixed target points.

4.8.3 Numerical Formulation of the Projective Transformation Theory.

The author wrote two programs, for the Tektronix 4051 micro-computer, based on the projective transformation theory namely;

(1) "TESTFIELD": This program was written to analyse stereo-pairs taken of the test field. Its use is described in Section 4.8.4 and 4.8.6 and the program flow chart is given in Appendix 4A.

(2) "WAVEHEIGHT": This program was written to analyse stereo-pairs taken of the deformed water surface in the wave basin. Its use is described in Sections 4.8.5 and 4.8.6 and the program flow chart is given in Appendix 4B.

The numerical formulation of both programs is very similar, with the basic differences being in their input requirements and output capabilities. The basic formulation of both programs is as follows:

(1) The input data is inserted into arrays. The input data consists of the space (X,Y,Z) co-ordinates of the control points, the control point image co-ordinates for both the left and the right plate, the number of control points observed, and the order in which they were observed.

(2) Using the input data, the terms of the matrices, shown in equations (19) are calculated.

(3) The transformation parameters (b_{ij} terms) for both plates are then solved using equation (18) and utilizing the matrix algebra capabilities of the Tektronix 4051.

(4) Using the control points image co-ordinates for both the left and the right plates, and the calculated projective transformation parameters for both plates, the terms of the matrices shown in equations (37) are calculated.

(5) The space (X,Y,Z) co-ordinates of the control points are

then calculated using equation (36) and utilizing the matrix algebra capabilities of the Tektronix 4051.

(6) The true (assumed error free) ground co-ordinates of the control points are subtracted from their corresponding calculated space co-ordinates, and these differences are printed out. These differences highlight any gross input data errors and also indicate whether the projective transformation parameters are well conditioned or not. These matters are discussed in detail in Section 4.8.5.4. Procedures (1) to (6) are repeated until one is satisfied that a well conditioned set of projective transformation parameters have been calculated.

(7) The projective transformation parameters are then used to determine the inner orientation elements (equations (20) to (23)) and the camera perspective centre (equation (24)) for both the left and the right plates.

(8) The image co-ordinates (from both plates), of the object points which need to be measured are then inputted into arrays.

(9) Using the object point image co-ordinates for both the left and the right plates, and the calculated projective transformation parameters for both plates, the terms shown in equation (37) are calculated.

(10) The space co-ordinates of the object points are then calculated using equation (36) as described previously.

The program "WAVEHEIGHT" has further capabilities which are discussed elsewhere.

4.8.4 Potential Wave Height Measurement Accuracy using Projective Transformations.

Before the wave height measurement configuration was constructed in the Hydraulics Laboratory of the Department of Civil Engineering, it was decided that the measurement potential of stereophotogrammetry linked to the projective transformation analysis should be determined. It was decided that the laboratory configuration envisaged, should be simulated as closely as possible utilising the test field described in Section 4.5.

The two Zeiss cameras were set up on tripods at a distance of approximately 5 m from the 3rd plane (from the wall) of the test field, and with an initial camera base of 1,5 m (the base length was later increased to 1,9 m). The 3rd plane of the test field was assumed to simulate the water surface to be measured. The cameras/ test field configuration is shown in Fig 4-36. The cameras' axes were made parallel to each other and perpendicular to the base, using the cameras' theodolite mountings. A stereopair of photographs was taken of the test field using Kodak plates. The cameras' settings were f stop 32 and a 3 second time exposure using normal lab illumination.

The two plates were then developed and the x and y co-ordinates of the targets determined for both glass plates using the Zeiss stereocomparator system described in Section 4.4.3. 24 targets were then selected as control points from the 80 target test field, namely target no's: 1, 4, 5, 8, 9, 12, 13, 16, 18, 22, 26, 30, 51, 55, 59, 63, 65, 68, 69, 72, 73, 76, 77 and 80 as shown in Fig. 4-14 of Section 4.5. Using 24 control points the A matrix in equation (18) becomes a 48 by 11 matrix, and the Tektronix 4051 must work at the upper limit of its matrix algebra facility to solve the equation. 24 control points is more than adequate to obtain well conditioned projective transformation parameters (see Section 4.8.5.3.A)

The control point image (or plate) co-ordinates for both the left and the right plate were manually entered into the "TESTFIELD" program. The program then calculated the projective transformation parameters, the inner orientation elements for both the left and the right plate, the differences between the calculated control point space co-ordinates and their "true" ground co-ordinates and the perspective centre of each camera. It should be noted that at this stage of the investigation (early 1980) the Tektronix microcomputer system did not include the 4907 filemanager and 4662 plotter, and also that the link between the stereocomparator and micro-computer had not yet been invisaged. Thus, when the space co-ordinates of the other 56 targets observed were calculated, the left and right plate co-ordinates for each point were manually entered into the micro-computer and the space co-ordinates of the the point calculated and printed out before the next set of values were entered. Using this procedure the space co-ordinates of all

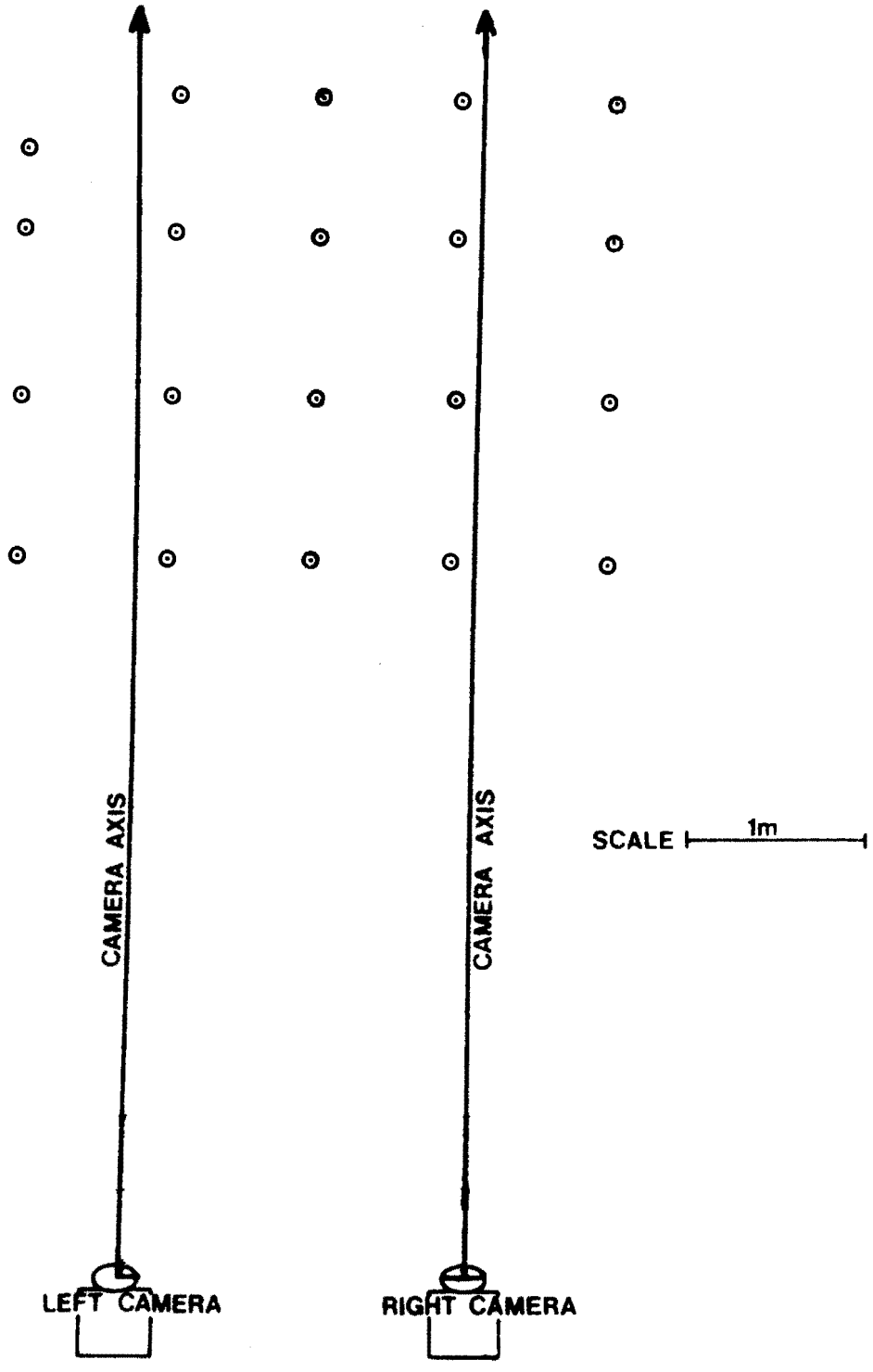

Fig. 4-36 Cameras/test field configuration.

56 remaining targets were calculated.

Since the cameras used were metric cameras, the calibration part of the programme was merely a check of the accuracy of the method. The Zeiss Jena cameras have the facility that when the film is exposed, the principal distance for a focus to infinity is illuminated in the top left hand corner of the film format, and the additional correction, which must be added to this figure to allow a focus at, say, 5 m is located in the top right hand corner. The principal distance f is thus the sum of these two figures. For the 1,5 m spacing situation, the difference between the computed principal distance and the manufacturers' principal distance was 0,07 mm for the left camera (camera no. 74), and 0,05 mm for the right camera (camera no. 49).

To determine the measurement accuracy of the system, the "true" ground co-ordinates for each point were subtracted from the corresponding calculated space co-ordinates for that point. Two measurement accuracy criteria were used namely:

(1) Standard deviation of a single observation (for one co-ordinate value).

$$\sigma = \sqrt{\frac{\sum_{i=1}^{n} \varepsilon_i^2}{n}} \qquad (38)$$

ε_i = ground co-ordinate - calculated co-ordinate - the bias.
n = number of points observed.
σ = stardard deviation of a single observation.

Note: All measurements are assumed to have equal weight.

(2) Average absolute error.

$$AE = \frac{\sum_{i=1}^{n} |\varepsilon_i|}{n} \qquad (39)$$

ε_i = ground co-ordinate - calculated co-ordinate - the bias.
n = number of points observed.
AE = average absolute error.

The results for the 1,5 m base configuration were analysed using the two above mentioned criteria. Since the X and Y co-ordinates were found to differ by only approximately ±0,4 mm on average, and because it is the Z measurement accuracy which we are more interested in, the two accuracy criteria were only applied to the Z co-ordinate differences. The mean of the Z differences was +0,3 and this was taken to be the bias and thus subtracted from all the Z differences before the accuracy criteria were calculated. This bias can be interpreted as an approximate rigid body shift of the entire system in the Z direction and would not affect the wave height measurement accuracy. The standard deviation for a single observation (for the Z co-ordinates only) was 1,87 mm while the average absolute error was 1,5 mm.

It was felt that a more accurate result could be achieved if the camera spacing was increased to 1,9 m. This base length was chosen since it can be seen from Section 4.6.3 that this is the maximum camera spacing which will still give the minimum 6,1 overlap required. The left camera was moved 0,4 m to the position shown in Fig. 4-36 and the entire procedure repeated. The mean of the Z differences was +0,4 mm and this was taken to be the bias and thus subtracted from all the Z differences before the accuracy criteria were calculated. The bias for the X and Y differences was found to be negligible. The X,Y and corrected Z differences obtained for this configuration, with their respective standard deviations and average errors, are shown in Table 4-4. It can be seen that the standard deviation for the Z differences is now 1,35 mm (a 39% improvement over the 1,5 m configuration) while the average absolute error is now 1,0 mm (a 50% increase in accuracy).

It was hypothesised that the calculated Z values were normally distributed about their "true" ground values. To test this hypothesis a χ^2 "Test of Normality" was carried out as described by Crow, et al (1960). The results of this test are shown in Table 4-5. The calculated χ^2 value = 2,638 while for the 5% level of significance χ^2 = 14,07. It can therefore be concluded that at the 5% level of significance the sample distribution is consistent with the hypothesis that the parent distribution is normal.

No	ε_{X_i} (mm)	ε_{Y_i} (mm)	ε_{Z_i} (mm)
Control Pts			
1	-0,4	0,8	-3,7
2	0,8	-0,1	2,4
3	0,0	-0,1	0,2
4	0,1	0,3	-2,0
5	-0,2	0,5	-0,3
6	-0,2	-0,1	1,5
7	0,9	-0,3	-2,1
8	1,1	-0,8	-2,8
9	0,4	-0,3	0,3
10	0,1	-0,4	-2,8
11	-0,1	0,4	-0,2
12	0,5	0,3	-1,1
13	-0,1	-0,6	0,5
14	-0,2	0,2	-0,6
15	0,9	0,7	0,9
16	-0,2	0,1	0,9
17	0,0	0,3	1,7
18	-0,8	0,0	3,0
19	-0,2	0,0	-1,5
20	0,0	-0,4	-1,3
21	0,2	0,3	-1,6
22	-0,8	0,4	1,5
23	0,0	-0,1	-1,1
24	-0,3	0,1	-1,3
Extra Pts			
1	0,0	0,3	1,4
2	0,8	-0,1	0,5
3	0,1	0,1	0,0
4	0,2	-0,1	0,2
5	0,9	0,1	2,9
6	0,5	-0,3	0,6
7	-0,1	-0,1	0,7
8	-0,1	0,6	0,1
9	0,2	-0,5	0,7
10	0,1	0,5	1,1
11	-0,8	0,1	3,0
12	-0,7	0,7	3,2
13	-1,0	0,1	2,1
14	-0,2	-0,2	-0,1
15	0,1	0,5	0,4
16	-0,2	0,8	-0,6

Table 4-4 Results for 1,9 m base configuration.

No	ε_{X_i} (mm)	ε_{Y_i} (mm)	ε_{Z_i} (mm)
Extra Pts Cont.			
17	0,5	0,1	0,4
18	0,2	0,0	-0,1
19	0,2	-0,6	-1,9
20	0,1	-0,3	-1,7
21	0,0	0,2	0,6
22	-0,1	-0,1	1,8
23	0,7	-0,4	0,9
24	-0,1	-0,3	1,2
25	0,3	-0,6	-1,5
26	-0,2	0,2	0,3
27	0,3	-0,4	0,4
28	-0,6	-0,2	2,0
29	0,1	0,1	-0,8
30	0,4	-0,3	-1,5
31	-0,1	0,3	-1,4
32	0,6	0,0	-0,8
33	0,3	-0,6	-1,8
34	0,0	-0,1	-0,9
35	-0,1	-0,1	-0,1
36	0,0	0,3	-0,4
37	0,1	0,9	0,2
38	0,2	-0,2	-0,8
39	-0,2	0,2	0,0
40	-0,6	0,3	1,2
41	-0,2	-0,2	0,4
42	-0,2	0,1	0,3
43	-0,4	-0,1	-0,2
44	-0,4	-0,1	0,2
45	0,0	-0,4	0,2
46	-0,1	0,0	-0,8
47	0,1	0,1	-0,5
48	-0,1	-0,2	-0,1
49	-0,1	-0,3	-0,2
50	-0,5	0,2	-0,4
51	-0,2	0,1	-0,7
52	-0,2	-0,7	0,1
53	-0,1	-0,2	-0,6
54	-0,1	0,4	-0,9
55	-0,7	-0,3	1,1
56	-0,5	0,1	0,9
σ	0,42	0,36	1,35
AE	0,29	0,30	1,04

Table 4-4 cont. Results for the 1,9 m base configuration.

ϵ_i (mm)	$\frac{\epsilon_i}{1,35}$	Cumulative normal probability	Theoretical relative frequency	Theoretical (e_i) frequency	Observed (n_i) frequency	$\frac{(n_i - e_i)^2}{e_i}$
∞	∞	1				
4,0	2,96	0,9985	0,0015	0,12	0	
3,0	2,22	0,9868	0,0117	0,94	2	
2,5	1,85	0,9678	0,0190	1,52	2	0,159
2,0	1,48	0,9306	0,0372	2,98	2,5	
1,5	1,11	0,8665	0,0641	5,13	3,5	0,518
1,0	0,74	0,7704	0,0961	7,69	6	0,371
0,5	0,37	0,6443	0,1261	10,09	10	0,001
0	0,0	0,5000	0,1443	11,54	15	1,037
-0,5	-0,37	0,3557	0,1443	11,54	11,5	0,001
-1,0	-0,74	0,2296	0,1261	10,09	10,5	0,017
-1,5	-1,11	0,1335	0,0961	7,69	6,5	0,184
-2,0	-1,48	0,0694	0,0641	5,13	6,0	0,148
-2,5	-1,85	0,0322	0,0372	2,98	1,5	
-3,0	-2,22	0,0132	0,0190	1,52	2,0	
-4,0	-2,96	0,0015	0,0117	0,94	1,0	0,202
$-\infty$	$-\infty$	0	0,0015	0,12	0	
			1,000	80	80	2,638

Table 4-5 χ^2 "Test of Normality" for Z differences of the 1,9 m base configuration.

As previously mentioned in Section 4.8.2 the author also calculated the test field target space co-ordinates for the 1,9 m base configuration, using a solution based on equations (25), (26) and (27) only. The X and Z values obtained were almost all exactly identical to those calculated using the solution based on equation (36), however, there were very small random differences between the Y values calculated using the two solutions. The author concluded that for the particular configuration tested, either solution could be used successfully, however, as stated previously, the solution based on equation (36) has generally been found to give more accurate results.

A 1,9 m base length was adopted for the wave basin configuration and since most of the points (60 out of 80) in the test field were at distances of 5 m and greater (the maximum was 6,8 m), from the cameras, the potential water surface elevation (Z) measuring accuracy of the system was estimated to be in the range ±1 to 1,4 mm and probably very close to ±1 mm. The potential X and Y co-ordinate measurement accuracy was estimated at ±0,4 mm. The author's prediction that the Z co-ordinates could be determined with a higher accuracy than quoted above for the actual model harbour configuration was shown to be correct. A description of the investigation to determine the model harbour wave height measurement accuracy is given in Section 4.8.5.5. This investigation gave the potential water surface elevation measurement accuracy as ±0,7 to 0,9 mm.

4.8.5 Projective Transformations Wave Height and Pattern Measurement using the Stereocomparator/Micro-computer System.

4.8.5.1 Introduction

To measure the diffraction phenomena in the model harbour configurations, the most accurate wave height and pattern measurement technique was needed. At this stage it is assumed that close range photogrammetric wave height measurement techniques are superior to conventional techniques. A comparison between photogrammetric and conventional wave height measurement techniques is given in Section 4.10.1.1. The photogrammetric technique has the advantage that two stereopairs can be taken of the deformed water surface in a much shorter period of time than is required for a scan using wave probes, and the information contained on the plates is permanent, synoptic and detailed. Furthermore, there is no instrumental interference in wave processes being observed.

The measurement accuracy experiment described in Section 4.8.4 showed that very accurate results could be achieved using the Zeiss cameras to take the stereopairs and the stereocomparator to analyse the plates. Originally the plates were analysed using the stereocomparator system described in Section 4.4.3. This system yielded a hard copy of all the image point co-ordinates which then had to be manually punched into the Tektronix 4051 micro-computer for analysis. This whole procedure was speeded

up by the installation of the stereocomparator/Tektronix 4051 interface described in Section 4.4.5. The stereocomparator/micro-computer analysis system, used for the bulk of the wave diffraction analysis, is shown in Fig. 4-37.

Fig. 4-37 The stereocomparator/micro-computer analysis system.

4.8.5.2 Development of the Measurement Technique using a Polystyrene Wave in the Test Field.

A. Motivation

Before projective transformations were used to measure wave heights in the wave basin, it was decided to simulate the wave basin configuration in the test field. This would enable the author to establish an experimental procedure and to develope the necessary theory and software. It was also hoped that the proposed control

point configuration could be tested at the same time. A simulated typical wave form was to be mounted vertically in the test field and surrounded by control points of a similar configuration to that proposed for the wave basin.

The proposed control configuration in the basin consisted of the original stereoplotter absolute and relative orientation point configuration, shown in Fig. 4-32, without the two relative orientation points below the cameras principle axes. An additional 4 points were to be placed in canisters at levels below the still water level i.e. control points 13 to 16, as shown in Fig. 4-43. The 4 lower control points were to be positioned approximately 70 mm below the still water level and the upper control points approximately 210 mm above the still water level (water depth d = 125 mm). The surface to be measured would therefore lie between two planes of control points and measurement could be defined as interpolations rather than extrapolations as was the case for the stereoplotter situation where the control point plane was situated above the water surface.

B. Experimental Configuration and Procedure.

A sine wave with an amplitude of 35 mm and a wave length of 800 mm was selected as a typical wave. This wave shape was then cut from a polystyrene sheet of plan area 1 400 mm x 900 mm to yield a physical wave form approximately 1,5 wave lengths long. To simulate the relative positions of the waves in the basin between two successive stereopairs, the polysterene wave would have to be moved vertically half a wave length. To achieve this requirement as solidly braced board was constructed, as shown in Fig. 4-38, on which the polystyrene wave could be positioned. The board was 2,4 m high and 1,2 m wide and could be aligned vertically by adjusting the angle iron supports. The structure was steadied by placing 3 concrete beams on the attached base.

Four targets (similar to the test field targets) were set up on the board at the corners of a rectangle and these targets could be used to co-ordinate the board and to detect any movement of the board between stereopairs. Nine further targets were positioned in a grid form on the wave. Three targets were positioned on each crest and three in the trough. The purpose of these were three-fold. Firstly, they could be used to reposition

the wave half a wave length vertically without having the wave wandering off to one side. Secondly they could be used to detect any movement of the wave in the Z direction and thirdly, being well defined points visible on all the photographs, they could be accurately sighted to in the stereocomparator. The board and the polystyrene wave target configurations are shown in Fig. 4-38.

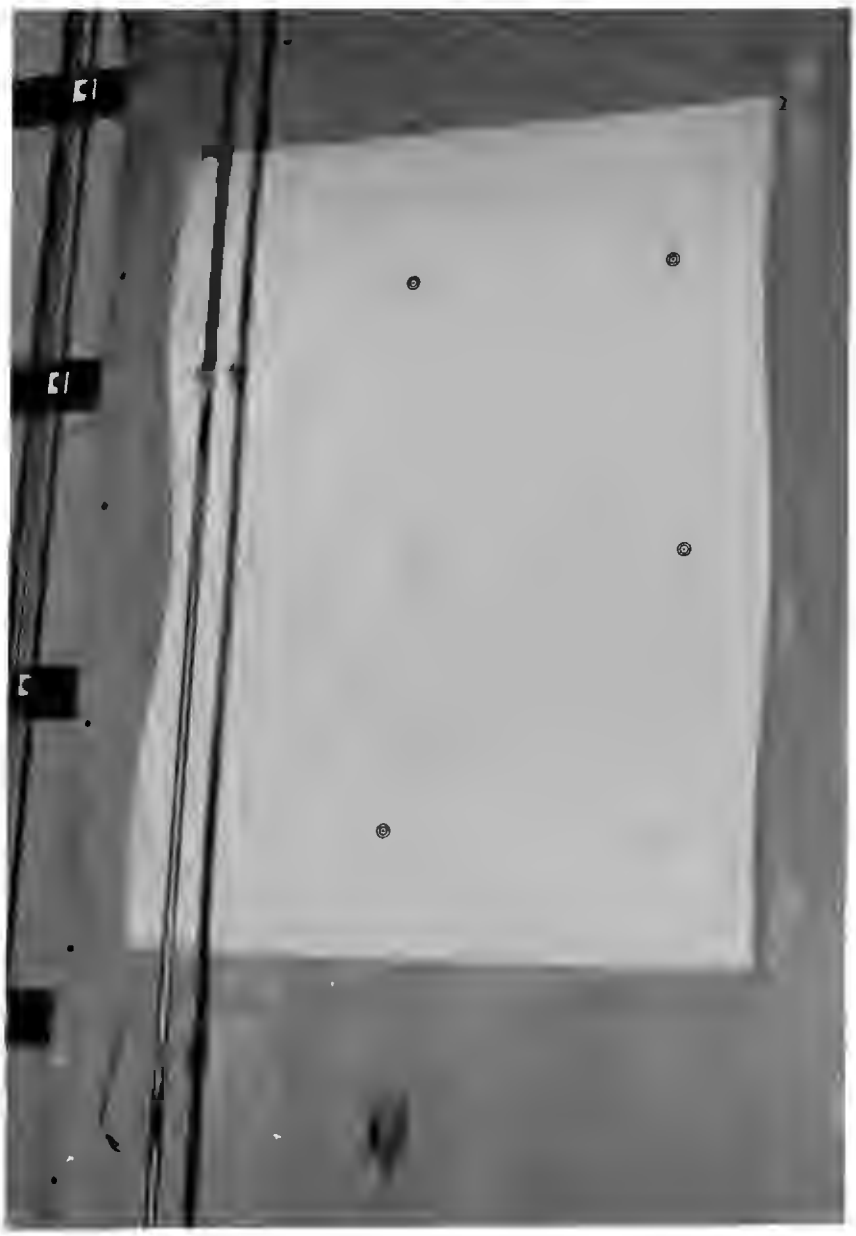

Fig. 4-38 Wave mounted on board with target points shown.

The wave was initially suspended on a string hanger looped over the top of the board and tied to the back. This positioned the wave at the correct height. The string was fixed to two steel needles pushed into the sides of the polystyrene at the top of the wave. Two further steel needles were pushed into the sides

of the polystyrene at the base of the wave and a string hanger tied between them. A weight was hung on this hanger and the wave could be rotated by moving the weight along the string until the top and bottom targets on the left hand side of the wave were vertically aligned. When the wave was correctly positioned, it was firmly fixed to the board by taping masking tape over the four protruding needles. After the wave was moved half a wave length it was retaped to the board in the new position.

To roughly simulate the wave basin control configuration, 4 weighted hangers each having 3 attached lead ball control points were hung inside the calibration field. They were positioned at the edges of the field, with the rearmost two being 70 mm behind the still water position of the solid wave and the foremost two being 210 mm in front of the same position. The hangers were positioned 280 mm apart in the Z direction and 3 000 mm apart in the X direction with each plane of control points parallel to the Y axis. The weights on the hangers were immersed in water to dampen out any movement. A white paper disk was stuck behind each lead ball to highlight each control point.

The two Zeiss cameras were set up 5,2 m from the board with a base of 1,9 m, closely simulating the wave basin configuration. The cameras' axes were aligned parallel to each other and perpendicular to the base by means of their theodolite mountings. A theodolite was set up between the cameras and was used to keep the waves crest and trough targets alligned horizontally and to ensure that when the wave was moved half a wave length in the Y direction, the movement was truely vertical. To provide photographic contrast, an overhead projector was used to project a letraset pattern consisting of black arrows, onto the white surface of the polystyrene wave. A photograph of the entire configuration, taken with the left camera, is shown in Fig. 4-39.

Two stereopairs of the polystyrene wave were taken using the following procedure. The wave was first positioned in the "upper position" on the board, as shown in Fig. 4-39. The room lights and the overhead projector were switched on and a 3 second time exposure taken of the configuration, with each camera. The wave was then moved vertically downwards a distance of half a wave

Fig. 4-39 Polystyrene wave configuration in the test field.

length and taped in position, the alignment of the wave being controlled by means of the theodolite positioned between the two cameras. The cameras were then reloaded and a 3 second time exposure taken of the wave in the "lower position".

Each stereopair of plates was analysed using the following procedure. Both plates were placed in the stereocomparator and then they were correctly aligned so that they could be viewed stereoscopically. The 24 test field target points used in the measurement accuracy experiment described in Section 4.8.4, were selected and their x,y and px, py values determined using the stereocomparator system (see Section 4.4.3). These values were then inputted manually into the Tektronix 4051 and a slightly modified version of "TESTFIELD" (modified to convert the x,y and px, and py data to x,y data for both left and right plates) was used to determine the projective transformation parameters, the inner orientation elements and the camera perspective centre for both the left and

the right plate of the stereopair. The space co-ordinates of the board and ploystyrene wave targets and the 12 lead ball control points were then determined from the comparator observation using the above program.

The calculated space co-ordinates of the lead ball control points were now treated as their "true" ground values and these values, were inputted into another modified version of "TESTFIELD" (modified to accept the 12 lead balls as control points with known "true" space co-ordinates). The projective transformation parameters etc. for both left and right plate were then calculated using the observed x,y, and px,py values for the 12 lead ball control points. Using the 22 projective transformation parameters thus calculated, the space co-ordinates of the polystyrene wave targets were then determined.

C. Results and Conclusions.

The 1st stereopair was taken with the polystyrene wave in the "upper position" and the 2nd stereopair with the wave in the "lower position". Therefore the trough position and the lower crest position of the 1st stereopair respectively co-incided with the upper crest and trough positions of the 2nd stereopair. By subtracting the 6 trough and crest target elevations for the 1st stereopair (calculated using the 24 test field targets), from the respective crest and trough elevations for the 2nd stereopair, the wave heights at these 6 points were determined. The 3 wave heights calculated from the trough target elevations of the 1st stereopair and the upper crest target elevations of the 2nd stereopair, were compared to wave height values physically measured at the trough target positions of the polystyrene wave. These measurements were made by hanging a plumb-bob down each vertical row of targets and measuring the distance from the string to the trough target. The comparison between the calculated and measured wave height is given in Table 4-5 below. It was estimated that these wave heights deviated from the true values by ± 1,5 to 2 mm in the case of the calculated values (see Section 4.8.4) and ±1 to 1,5 mm in the case of the measured values.

Dz (mm) calculated	Dz (mm) measured
66,08	65,5
63,89	63,0
64,34	63,0

Table 4-5 Calculated vz measured wave heights.

The same procedure was followed with the crest and trough elevations calculated using the 12 lead ball control points to determine a similar set of 6 wave heights. The comparison between the wave heights calculated using the 24 test field targets, and the corresponding wave heights calculated using the 12 lead ball control points is shown in Table 4-6 below. As can be seen, the wave height values correspond closely and are well within the expected standard deviation of approximately ±2 mm.

USING 24 TEST FIELD TARGETS (mm)	USING THE 12 LEAD BALL CONTROL POINTS (mm)
66,08	65
63,89	64
64,34	63
63,81	64
59,99	61
62,45	63

Table 4-6 Calculated vz calculated wave heights.

Using the polystyrene wave, the trough position in one stereopair which corresponds to a crest target position in the other stereopair is easily determined since it is marked with a target. When viewing stereopairs taken of water waves in a wave basin however, the crestlines in the 1st stereopair can be fairly easily identified, but it is almost impossible to determine the exact position of the corresponding trough line in the 2nd stereopair. This is because wave basin water waves are generally non-linear and thus have sharply peaked crests with correspondingly very flat troughs (similar to a 2nd or 3rd order Stokes profile). Due to the flatness of the troughs, any secondary effects such as reflection and resonance can easily distort the trough profile, making it very difficult to even estimate the position of the trough line. Some technique is needed to accurately locate the position of the trough point in the 2nd stereopair which corresponds to an observed crest point in the first stereopair and visa versa. The following technique has been proposed by the author:- Equations (7) as restated below for clarity, will yield the left plate comparator image co-ordinates for an object point.

$$x_i = \frac{b_{11} X_i + b_{12} Y_i + b_{13} Z_i + b_{14}}{b_{31} X_i + b_{32} Y_i + b_{33} Z_i + 1} \qquad (40)$$

$$y_i = \frac{b_{21} X_i + b_{22} Y_i + b_{23} Z_i + b_{24}}{b_{31} X_i + b_{32} Y_i + b_{33} Z_i + 1} \qquad (41)$$

The author proposed that the following hypothesis would hold true for two stereopairs taken of monochromatic waves in a laboratory basin, the waves imaged in the 1st stereopair being 180° out of phase relative to the waves imaged in the 2nd stereopair. He proposed that if the calculated $X_i Y_i Z_i$ co-ordinates of a crest point P_i observed using the 1st stereopair and the projective transformation parameters calculated for the left plate of the 2nd stereopair were substituted into equations (40) and (41), these equations would yield the left plate comparator co-ordinates at which the corresponding trough in the 2nd stereopair could be located. These equations would in reality provide the left plate comparator co-ordinates of a point a vertical distance H (H = wave-height at that point) above the required trough point. If the

left camera is almost vertically above the crest/trough point, the calculated trough point and the required trough point will be co-incident. If however, the camera configuration is not ideal, a correction will have to be made to the calculated trough left plate co-ordinates. A detailed description as to how these corrections are calculated is given in Section 4.8.5.4.

To test this hypothesis the following procedure was carried out using each of the lower crest line target points imaged in the 1st stereopair. The calculated XYZ co-ordinates of the lower crest line target point observed using the 1st stereopair and the projective transformation parameters calculated for the left plate of the 2nd stereopair were substituted into equations (40) and (41). The relevant hand wheels of the stereocomparator were then moved until the x,y co-ordinates calculated using equations (40) and (41) were displayed on the digital displays of the Motronic unit (the 2nd stereopair is assumed to be still set up in the comparator). The left plate was then viewed using the left eye piece only and in each case the left measuring mark was found to be positioned in the centre of the corresponding trough line target.

In conclusion the polystyrene wave experiment showed:

(1) that projective transformations could be used for accurate wave height measurements in laboratory wave basins.

(2) that a 12 point control point configuration similar to that used in the test field appeared to be adequate to calculate the plate transformation parameters and thus the wave heights.

(3) that the trough positions which had to be observed could be accurately located using the projective transformation theory.

(4) that the stereocomparator should be interfaced to the micro-computer to speed up the analysis procedure.

4.8.5.3 Wave Basin Control Point Configuration.

A. Determination of the Minimum Number of Control Points Needed and their Most Desireable Configuration.

The proposed 12 point configuration was then established in the

wave basin. The original stereoplotter relative orientation points were braced to give them more rigidity and the original control lights were replaced as described in the next section. The ground co-ordinate of the 12 control points were then determined using the method described in the next section. Two stereo-pairs were then taken of the wave energy front region of a monochromatic wave train entering a basin of still water. The plate projective transformation parameters were calculated using an early version of the program "WAVEHEIGHT" (a version written prior to the installation of the stereocomparator/Tektronix 4051 interface), and using the observed image co-ordinates of the 12 basin control points. The space co-ordinates of the control points were then determined and the differences between the calculated and "true" control point co-ordinates calculated. For the wave diffraction investigation the wave height measurement accuracy is a lot more critical than the X,Y measurement accuracy, and for this reason only the Z differences have been analysed in detail. The standard deviation for a single observation and the average absolute errors were calculated to be 1,45 mm and 1,1 mm respectively. It was thought however, that these accuracies could be improved by:-

(1) increasing the number of control points, and

(2) increasing the Z spread between the control points (it was felt that the 280 mm Z spread for the 12 point control point configuration was inadequate).

The above findings led the author to investigate the relationship between measuring accuracy and:

(1) the number of control points used.

(2) the control point configuration.

Karara and Abdel-Aziz (1974) conducted tests using non-metric cameras to determine the optimum number of object-space control points. To assess the reliability of the solutions obtained using different numbers of control points, they used the statistic, the standard deviation of the standard deviation of object-space co-ordinates. This can be expressed as:-

$$S_s = \frac{S}{\sqrt{\{2(n-u)\}}} \qquad (42)$$

where:-

S_s is the standard deviation of the standard deviation of object space co-ordinates (X, Y or Z).

S is the standard deviation of object space co-ordinates (X, Y or Z).

n is the number of observations (twice the number of object space control points)

u is the number of unknowns; in their case 12 but in ours 11 since we do not have a lens distortion unknown.

Computing S_s for different numbers of object space control points P they obtained the values shown in Table 4-7. Graphically the relationship between S_s and P is plotted in Fig. 4-40.

The Standard Deviation of the Standard Deviation of Object Space Co-ordinates (S_s) Versus the number of object space points (P) used in the solution

P	6	7	10	15	20	30	40	50	100
S_s		0,5S	0,25S	0,17S	0,13S	0,10S	0,08S	0,07S	0,05S

Table 4-7

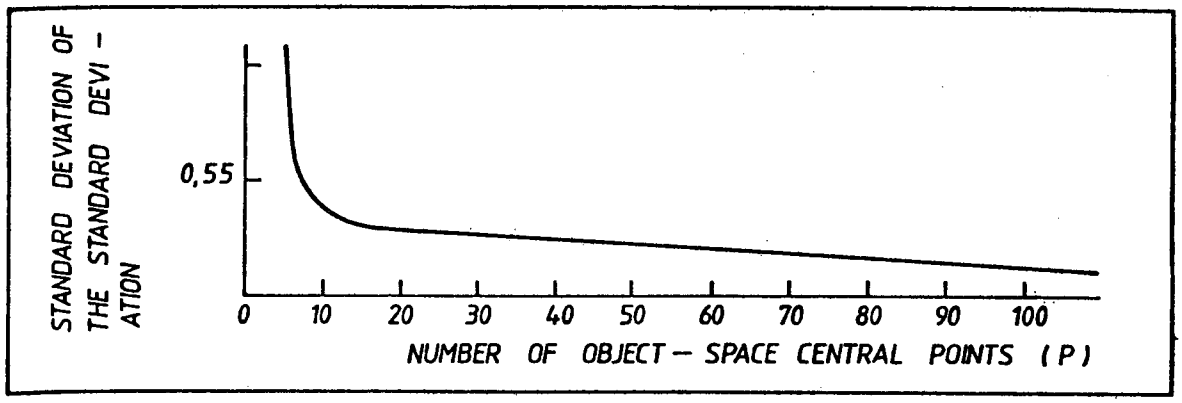

Fig. 4-40 Accuracy as a function of the number of control points.

A study of Fig. 4-40 indicates that beyond some 20 to 25 object-space control points, the improvement of the reliability of the solution is relatively small and in all probability not worth the effort of providing further control points.

To determine the relationship of measurement accuracy versus the number of control points, Welham (1982) in a parallel investigation took two stereopairs of the test field (on 4 and 12 Sept. 1981) using the two Zeiss Cameras. The cameras were positioned approximately 3,6 m from the 4th plane (the plane closest to the cameras) of the test field. The base length was approx 3,3 m and the camera axes were alligned parallel to each other and perpendicular to the base. The projective transformation parameters for each stereopair were calculated using 6, 10, 16, 20 and all 80 of the test field targets as control points. The space co-ordinates of the control points used were then determined and the differences between the calculated and "true" ground co-ordinates calculated.

Welham (1982) used the RMS (root mean square) residual RXYZ as an estimate to the standard deviation S in equation (42). RXYZ is defined as follows:-

$$RXYZ = \sqrt{\frac{1}{n} \Sigma\{X_{ip} - X_{iT})^2 + (Y_{ip} - Y_{iT})^2 + (Z_{ip} - Z_{iT})^2\}} \quad (43)$$

where:

X_{iT}, Y_{iT}, Z_{iT} are the true co-ordinates of the control point P_i.

X_{ip}, Y_{ip}, Z_{ip} are the calculated co-ordinates of the control point.

n = the number of control points used.

He used the standard deviation of RXYZ namely σRXYZ as an estimate to S_s in equation (42). σRXYZ was calculated by dividing the RXYZ value for a particular adjustment by the calculated value of the denominator in equation (42). The values of RXYZ and σRXYZ he obtained, are shown in Table 4-8 and the graphical relationship between σRXYZ and P, the number of control points, is shown in Fig. 4-41.

P / S/S_S		6 0.71	10 0.24	16 0.15	20 0.13	80 0.06
4 SEPT-1	RXYZ	0.20	0.54	0.40	0.47	0.56
12 SEPT-1	RXYZ	0.14	0.75	0.62	0.68	0.67
4 SEPT-1	σRXYZ	0.14	0.13	0.06	0.06	0.03
12 SEPT-1	σRXYZ	0.10	0.18	0.09	0.09	0.04

Table 4-8 (from Welham, 1982).

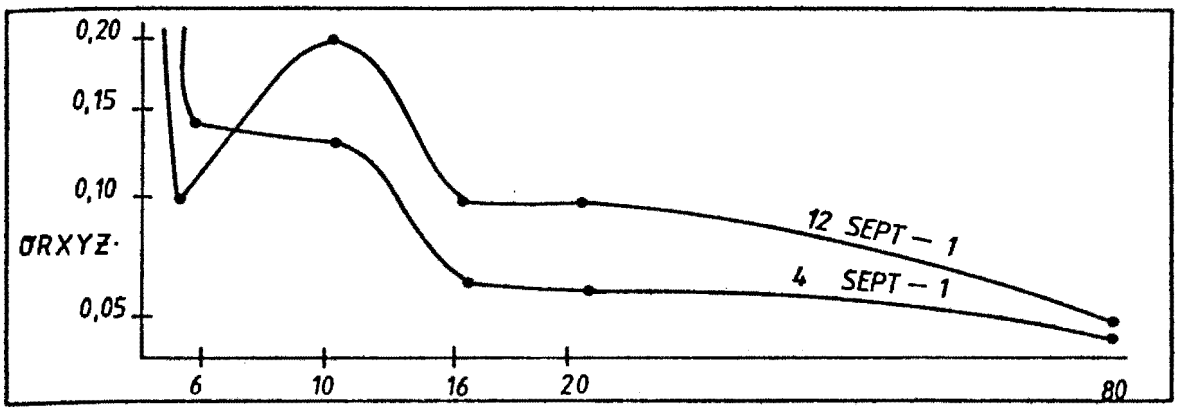

Fig. 4-41 Experimental results, accuracy as a function of the number of control points (from Welham, 1982).

The two graphs shown in Fig. 4-41, confirm the results of Karara and Abdel-Aziz shown in Fig. 4-40. Less than 10 points in the adjustment will not produce a satisfactory result. 10 points will give a result, but it would be more satisfactory to use between 16 and 20 points.

Welham (1982) also investigated the relationship between measurement accuracy and control point configuration. Of interest to the author was Welham's findings that symmetrical, rectangular configurations of 16 and 20 control points, encompassing the area to be measured, gave almost identical measurement accuracies. The author therefore decided to adopt a similar 16 point configuration for the wave basin.

B. The 16 Point Wave Basin Control Point Configuration.

The control point configuration finally adopted for projective transformation wave height and pattern measurements in the wave basin is shown in Fig. 4-43. The configuration consisted of 16 control points in total, arranged in approximately 3 planes. If we assume a water depth of 125 mm, the bottom plane, consisting of 4 points (points 13 to 16 in Fig. 4-43), was situated approximately 70 mm below the mean water level in metal canisters, as shown in Fig. 4-42. The middle plane consisting of 8 control points (points 5 to 12 in Fig. 4-43), was situated approximately 210 mm above the mean water surface. This control point plane was the original stereoplotter control point system which had been subsequently braced to make the control point supports more rigid. The third plane, consisting of 4 control points (points 1 to 4 in Fig. 4-43), was situated approximately 540 mm above the central plane. The total Z spread for the 16 point configuration was 820 mm as opposed to 280 mm for the 12 point configuration.

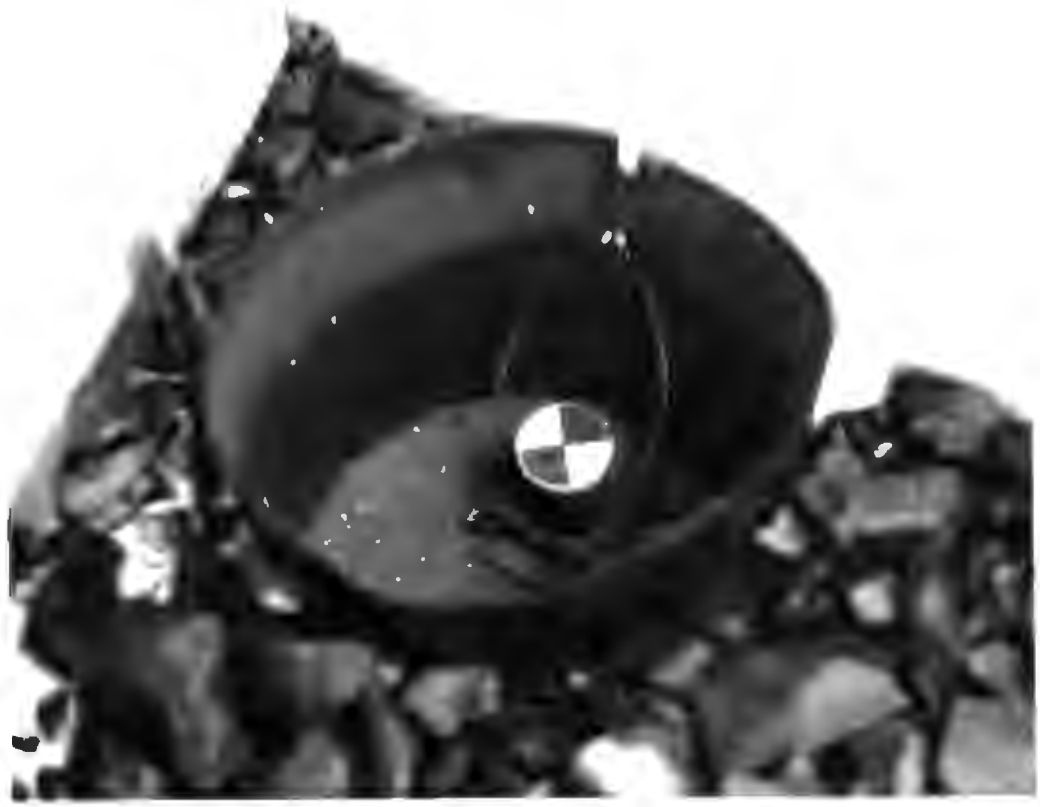

Fig. 4-42 Detail of control point below water surface.

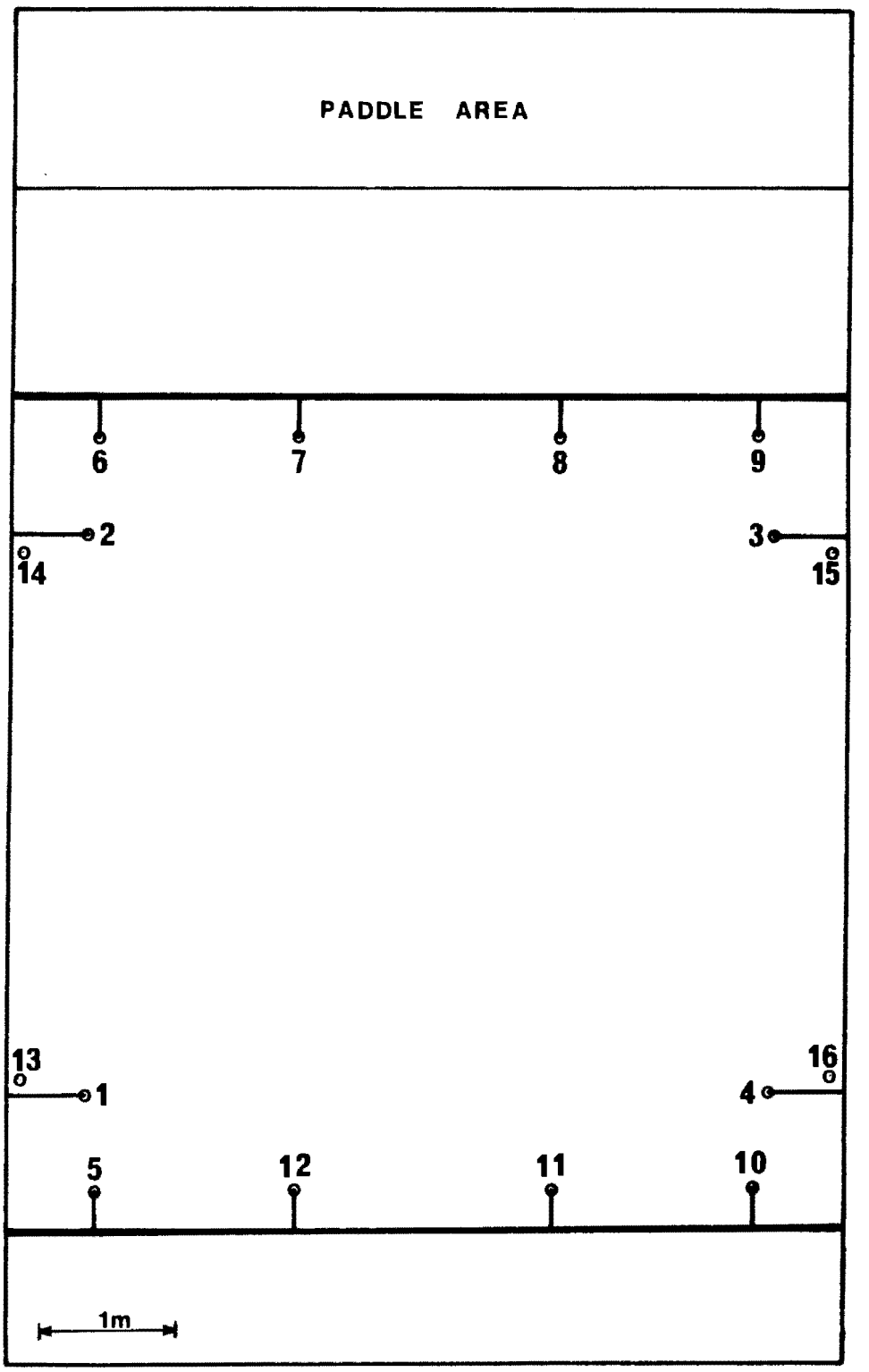

Fig. 4-43. 16 point wave basin control point configuration.

The original control point targets used for the stereoplotter control point system (shown in Fig. 4-33), were replaced with a different type of target which is shown in Fig. 4-42. The target consisted of a plastic cylinder closed at one end with a transparent perspex disc. The cylinder clipped over a 6 volt torchlight bulb fitting so as to be illuminated from the inside. A transparent cross was then stuck to the top of the perspex disc so as to give the effect of a cross of light when viewed from the camera platform. The transparent crosses for all the targets were made by taking 16 photographs of a larger ink cross drawn on a piece of white paper. A high contrast film was used to produce negatives with a completely transparent cross and an opaque black surrounding. Pieces of white paper were cut and fitted into opposite sectors of the crosses to aid in the identification of the target points.

The X,Y,Z ground co-ordinates of the control points were obtained in the following way. The control points were first leveled using a Wild automatic level and a light steel ruler. Each control point was levelled 3 times with the mean reading taken as the true level. It was estimated that a levelling accuracy of close to 0,5 mm was achieved using this system. Then 48 inter-control point measurements were taken with a steel tape and the equivalent plan distances calculated using the control point levels. These 48 corrected distances were then inputted into a least squares adjustment program, written for the Tektronix 4051 microcomputer, by Dr Heinz Rütter of the Department of Surveying. The redundant measurements were used to calculate the most probable X,Y co-ordinates of the control points. The X co-ordinates of the 16 control points were located with a 68% probability of being within ±0,71 mm (on average) of their true values, while the Y co-ordinates were located with a 68% probability of being within ±0,57 mm (on average) from their true values. It was thus estimated that the X,Y,Z co-ordinates had been determined with an accuracy of ±0,7 mm, with the accuracy of the Z co-ordinates being possibly slightly superior to that of the plan co-ordinates. The ground co-ordinates determined for the 16 control points are given in Table 4-9, while their plan positions relative to the X,Y axes (Z is vertically upwards) is given in Fig 4-44.

Point No	X	Y	Z
1	0,520	0,678	0,857
2	0,521	4,696	0,861
3	5,578	4,681	0,857
4	5,575	0,653	0,870
5	0,621	0,024	0,261
6	0,662	5,332	0,264
7	2,079	5,356	0,282
8	4,032	5,352	0,282
9	5,402	5,301	0,272
10	5,445	0,032	0,275
11	4,030	-0,013	0,278
12	2,090	-0,027	0,283
13	0,053	0,784	0,001
14	0,063	4,587	0,0
15	6,037	4,574	0,0
16	6,033	0,760	0,001

Table 4-9 Control point co-ordinates.

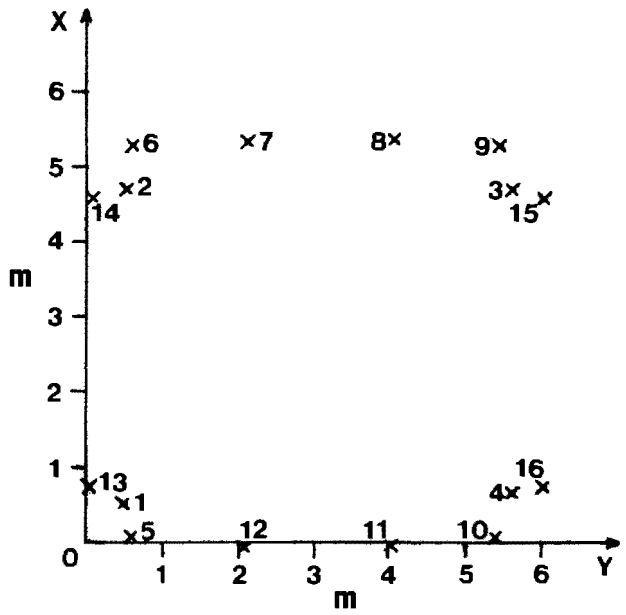

Fig. 4-44 Control point plan positions

The control point target lights were coupled up in series pairs which were powered by the 12 volt lead-acid storage battery used to fire the cameras. A stereopair was taken of the illuminated control points, at night, using the flash system. On observing the control points it became evident that the target points were in some cases obscured by a smudge of light caused by the very bright filament of the torch bulb. To overcome this problem a disc of translucent wax paper was glued to the inside of the perspex disc, this solved the filament problem, but reduced the amount of light reaching the camera. In order to insure that the control point targets were well exposed on the plates a shutter speed of 1/30 seconds had to be adopted for both cameras as opposed to the shutter speed setting of 1/60 second used for the stereoplotter control point configuration.

4.8.5.4 The Procedure for Wave Height and Pattern Measurement Using the Stereocomparator/Micro-computer System.

The technique has been briefly described, in each case with a different emphasis, in the author's publications: Pos (1982a, 1982c) and Pos and Kilner (1982). A detailed description of the technique is given by Pos (1982b). To illustrate the procedure, the analysis of a typical model harbour configuration will be briefly described.

The stereopairs in Fig. 4-46 show waves entering the model harbour basin shown in Fig. 4-45. The basin is 4,5 m long and 4,9 m wide (these dimensions do not include the crushed stone beaches along the side and back walls of the basin). The incident wave train has the following characteristics: wave period 0,67 seconds, mean wave height 55,5 mm, and wave length (calculated using Airy wave theory) 604 mm. The gap to wave length ratio (i.e. B/L ratio) is 1,64. The water depth is 125 mm ±1 mm. The stereopairs shown were taken approximately 14,5 seconds after starting the wave paddle at which stage the wave energy front was at the toe of the back wall beach. The second stereopair was taken with the waves in the basin 180° out of phase relative to the waves imaged in the first stereopair. This means that the troughs imaged in the second stereopair occupy the positions of the crests imaged in the first stereopair. If one subtracts the crest and trough elevations of the first stereopair from their corresponding

elevations in the second stereopair, one will achieve a plot of wave height distribution within the basin. Since the harbour configuration is symmetrical about the centre line, only the left hand side of the basin is shown in Fig. 4-46.

The process of achieving a plot of wave height distributions within the model basin is briefly summarised in Fig. 4-47. The stereopairs are analysed using the Zeiss (Jena) stereocomparator which is interfaced via an analog to digital converter and a data communications interface with a Tektronix 4051 micro-computer. The micro-computer, under program control, stores the x, y and px, py data obtained from the stereocomparator for each point observed. Once a set of points has been observed, the raw data is edited, prepared for transfer to flexible disc, and then stored on tape. The tape is then transferred to another Tektronix 4051 (the CPU for the micro-computer system described in Section 4.4.4) which has a flexible disc file manager, and the data transferred from tape to disc, under program control. All subsequent analysis is carried out using the Tektronix micro-computer system described in Section 4.4.4.

The analysis procedure which is outlined by the procedural flow-chart in Fig. 4-48 is as follows: the control points and crests imaged in the first stereopair and the control points imaged in the second stereopair are observed using the stereocomparator. The observed data is then analysed using the program "WAVEHEIGHT", written by the author, to yield:- the inner orientation elements and projective transformation parameters for the 1st and 2nd stereopairs, the crest elevation data (crest XYZ data) for the 1st stereopair, and the positions at which the troughs must be observed on the 2nd stereopair. The troughs imaged in the 2nd stereopair are then observed at the predetermined points, while the crests are observed at arbitrary points selected by the observer. The 1st stereopair is again placed in the stereocomparator and the imaged control points are observed. This observed data is analysed using the programme "WAVEHEIGHT" to yield:- trough and crest XYZ data for the 2nd stereopair, inner orientation elements and projective transformation parameters for the 1st stereopair (2nd viewing), and the trough positions to be observed in the 1st stereopair (2nd viewing). The troughs imaged

in the 1st stereopair are then observed at the predetermined points. The observed data is then analysed using the program "WAVEHEIGHT" which yields:- the trough XYZ data for the 1st stereopair and the XYH values along the crest lines imaged in the 1st and 2nd stereopairs, H is the wave height at a point within the basin.

The XYH data is then transferred to a file on the UNIVAC 1100 at U.C.T. The Saclant Graphics Package installed on the UNIVAC is then used to interpolate the raw data onto a rectangular equidistant grid. The interpolated data can then be used to plot a contour plot or a 3 dimensional perspective picture of the wave height distributions within the model harbour basin. The stereopairs, shown in Fig. 4-46, were analysed using the procedure described above to yield the contour plot of wave heights within the basin, shown in Fig. 4-49, and the corresponding 3 dimensional perspective view shown in Fig 4-50. Since the harbour configuration is symmetrical about the centre line, only the left hand side of the basin is shown. The dashed lines (in Fig. 4-49) indicate the crest lines plotted from both stereopairs. The black dots indicate the crest line sampling points plotted from both stereopairs.

It should be noted that the calculated x, y co-ordinates of the trough positions to be read, need to be corrected in some cases, due to the phenomenon described in Fig. 4-51.

To calculate a trough position which must be observed on the 2nd stereopair, we use the XYZ values of the corresponding crest position from the 1st stereopair and the projective transformation parameters for the 2nd stereopair. However, from Fig. 4-51, we see that the trough differs in the Z position by H, which is the wave height at that point. Since the computer is in reality calculating a corresponding crest position on the 2nd stereopair, when in fact there is a trough at this position, we are directed to look at the incorrect trough position on the plate, as shown in Fig. 4-51 below. In order to look at the correct trough position a correction Δx must be subtracted from the calculated x value (or added to the calculated x value if this value has a negative sign).

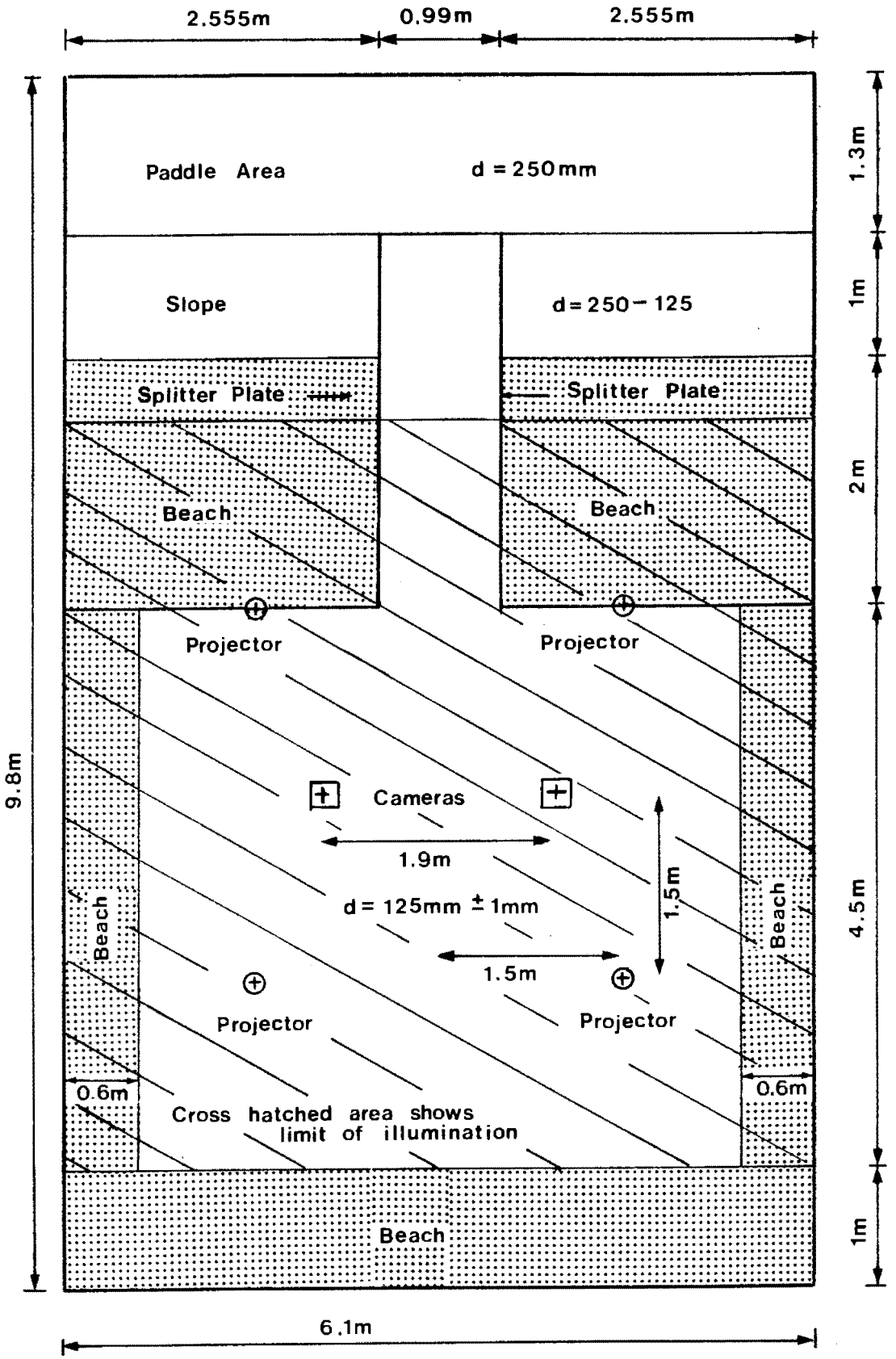

Fig. 4-45 Typical harbour configuration.

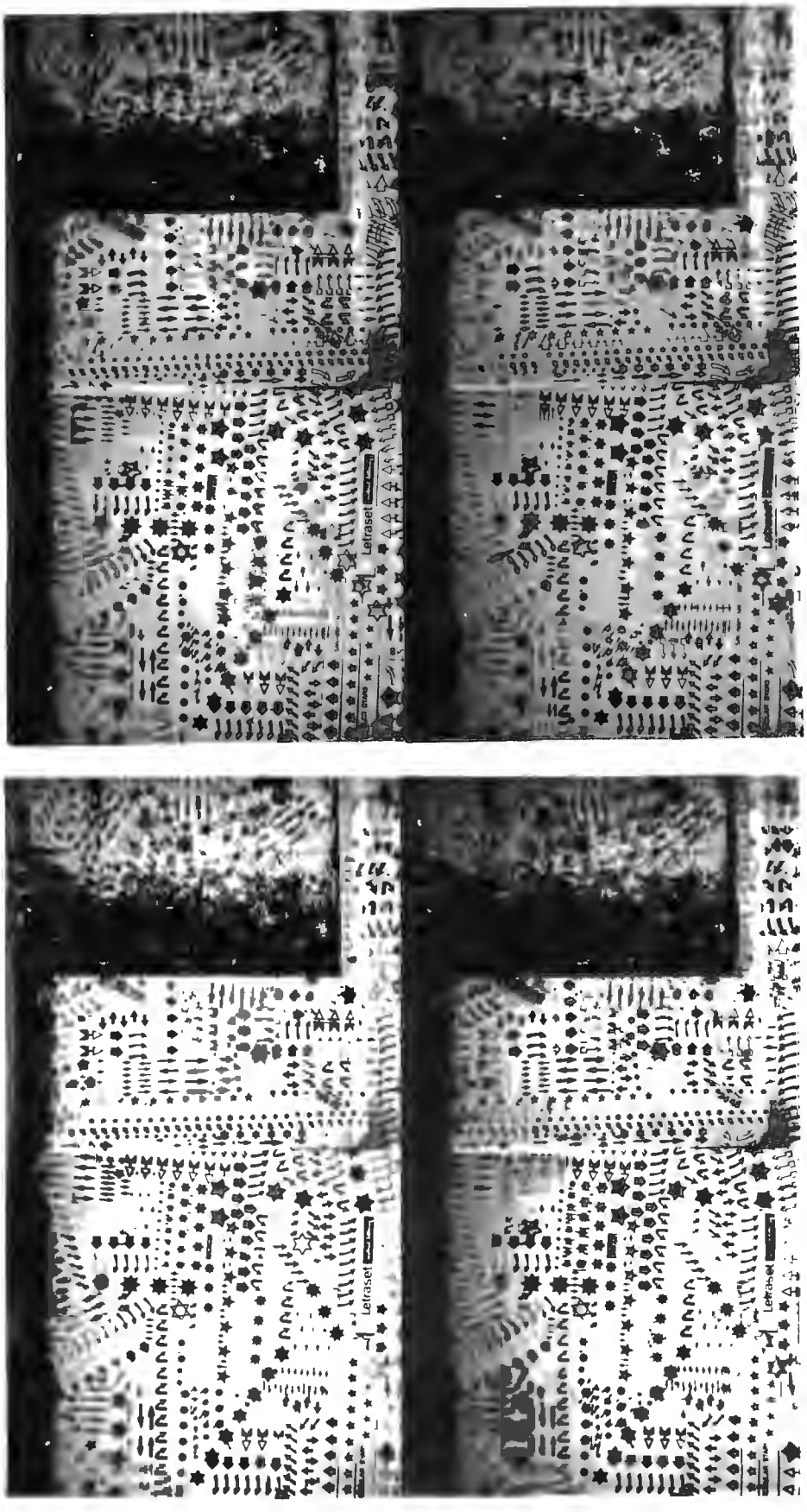

Fig. 4-46 Stereopairs taken of model harbour configuration.

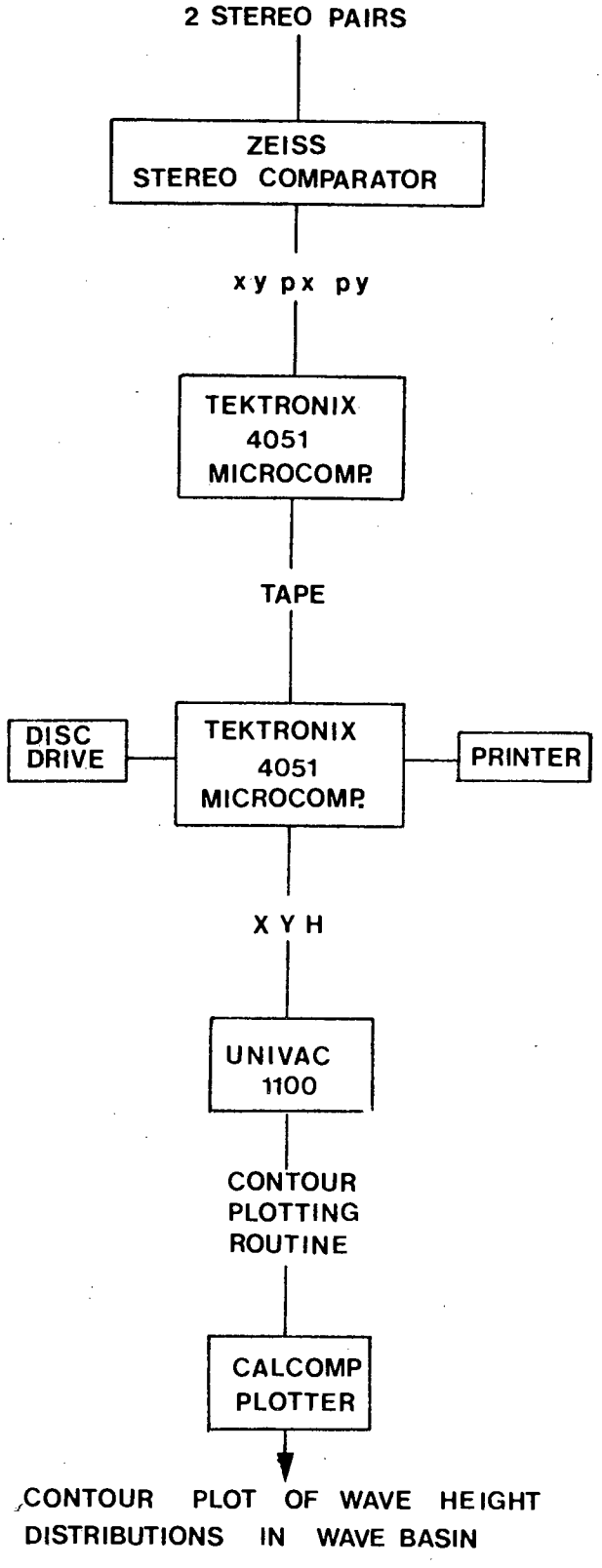

Fig. 4-47 Sequence of analysis.

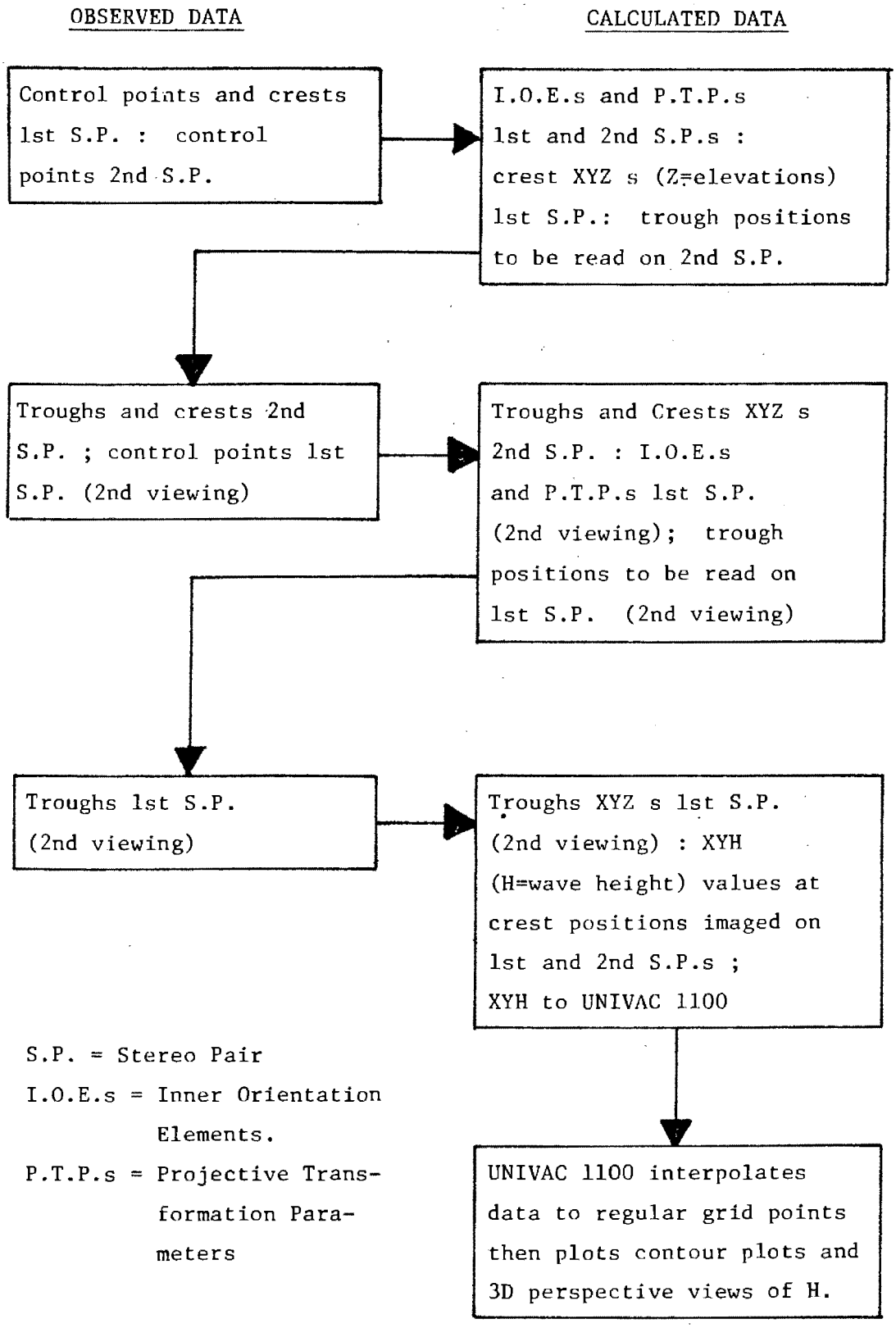

Fig. 4-48 Procedural flowchart.

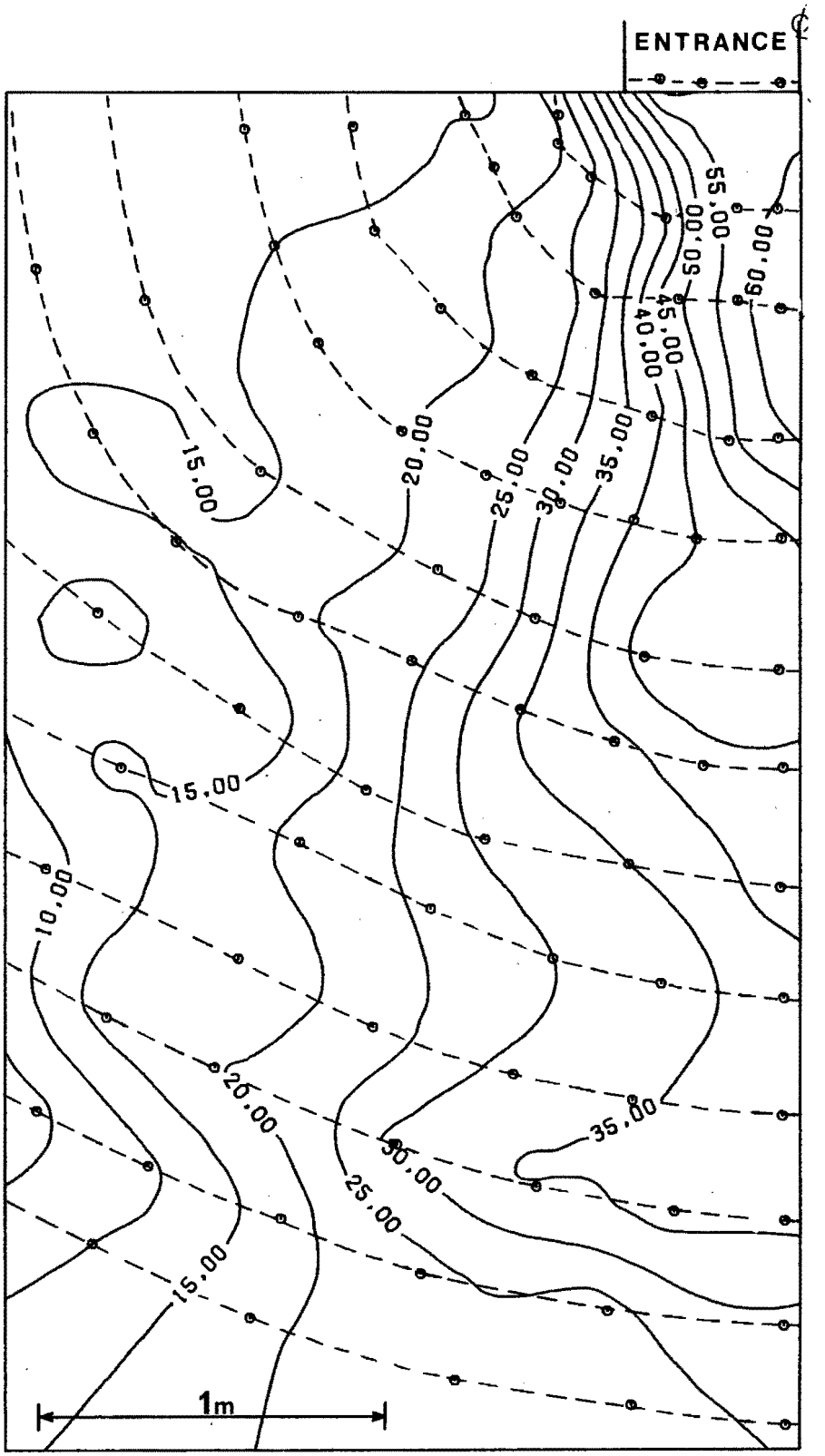

Fig. 4-49 Computer contour plot of wave heights in a model harbour (heights in mm).

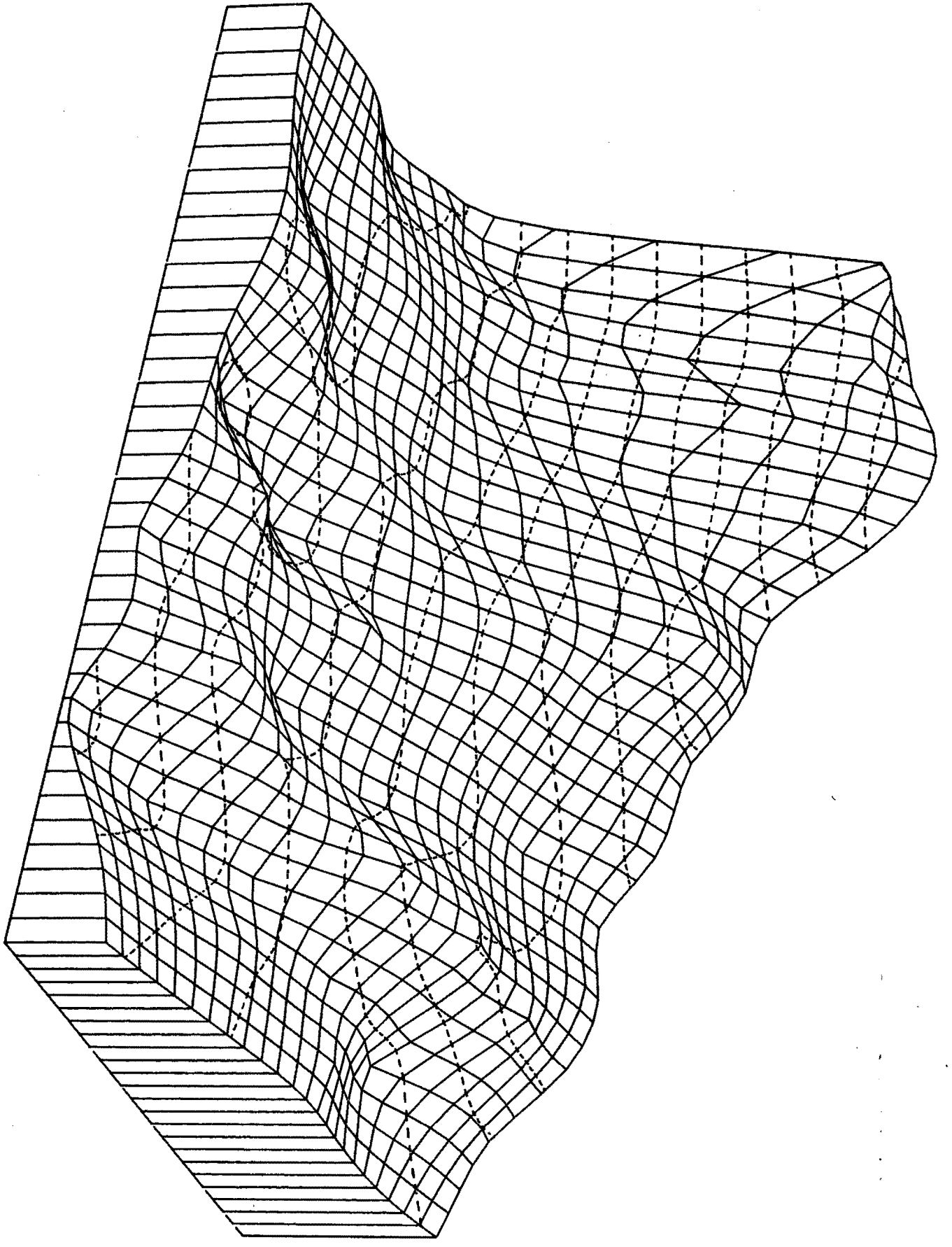

Fig. 4-50 Three dimensional perspective view of wave heights in a model harbour.

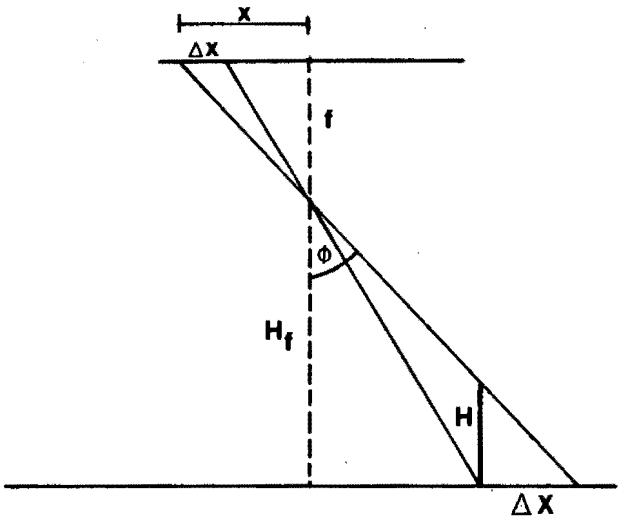

f = 100 mm

H_f = 5200 mm

Scale = 1/52

x = plate co-ordinate

X = ground co-ordinate

Fig. 4-51

The correction $\Delta x = \frac{1}{52} H \tan \phi$ ($\Delta X = H \tan \phi$)

or $$\Delta x = \frac{1}{52} H \frac{x}{f} \qquad (44a)$$

and similarly $$\Delta y = \frac{1}{52} H \frac{y}{f} \qquad (44b)$$

This correction was only applied at points where H > 20 mm and ΔX > 1 mm.

The analysis procedure described above would be the one followed by an experienced stereocomparator operator. The author found however, that a certain training period is required for anyone operating a stereocomparator. The principle which takes the most time to master is the ability to unequivocally perceive the surface of the water in the stereo model and then to subsequently place the "floating dot" onto this perceived surface (the principle of the "floating dot" (or mark) is described in Section 4.9.2.3). Because of the initial difficulties encountered in accurately perceiving the water surface in the stereo model and also accurately observing the control points in the basin, the slower and more complicated stereopair analysis procedure described in the author's publication (Pos, 1982b) is recommended for the inexperienced stereocomparator observer.

The coastal engineer should not however be tempted to let an experienced stereocomparator operator, who has no knowledge of wave phenomena, analyse the stereopairs for the reasons previously mentioned in the stereoplotter analysis in Section 4.7.6. Namely, such an operator would fail to recognise and thus measure areas

of particular interest to the coastal engineer, while he would on the other hand waste time in recording the wave characteristics of areas of no interest to the engineer. Thus, the author advocates that the plates are analysed by the scientist or engineer who is actually investigating the model harbour configuration.

4.8.5.5 Wave Height Measurement Accuracy.

For the wave diffraction experiments carried out by the author, the most important measurement requirement was accurate wave height determinations, while the accurate plan location of the sampling points was not nearly as critical. This is because a few millimetres error in the plan location of a crest point would make a very small difference when plotting the crest lines or alternatively when this value is used to locate the corresponding trough sampling point (due to the flatness of the troughs). However, a few millimetres error in the determination of a wave height, particularly when the wave height is small, say less than 10 mm, would markedly distort the wave height distribution plotted for that area.

In order to obtain an estimate of the water surface measurement accuracy and thus the wave height measurement accuracy, the results obtained during the analysis of the B/L = 1, B/L = 0,75 and B/L = 0,5, diffraction configurations, described in Section 5.5, were analysed in detail. For each configuration the control point co-ordinates were calculated 3 times using the program "WAVEHEIGHT". Twice using the 1st stereopair and once using the 2nd stereopair. Since the author was primarily interested in the Z determination accuracy, only the Z differences were analysed. All 144 Z differences were incorporated in the analysis and the mean was calculated to be exactly 0,0 mm as expected since a least squares solution is used. Therefore, there was no bias and no need to "correct" the calculated Z differences. The standard deviation of a single observation for the Z differences was calculated to be 0,89 mm and the corresponding absolute average error was 0,71 mm. It was therefore estimated that the water surface elevations could be measured with a potential accuracy of ±0,7 to 0,9 mm.

We now need an estimate of the potential wave height measurement accuracy. We know that the wave height is calculated by sub-

tracting the trough elevation from the crest elevation.

i.e. $H = Z_C - Z_T$

From standard error propagation theory (Mikhail and Ackerman, 1976), we would expect the square of the standard deviation of H to be equal to the sum of the squares of the standard deviations of Z_C and Z_T.

i.e. $\sigma_H^2 = \sigma_{Z_C}^2 + \sigma_{Z_T}^2$

and since $\sigma_{Z_C} = \sigma_{Z_T}$ we find that

$$\sigma_H = \sqrt{2}\ \sigma_Z$$

For the purposes of this accuracy estimate, we will assume that this process can also be applied when dealing with average absolute errors (AE's). From above we see that the potential AE and σ for the water surface elevation measurements were 0,7 and 0,9 mm respectively while the corresponding values calculated in Section 4.8.4 were 1 and 1,35 mm respectively. It is suggested that the potential wave height measurement accuracy should be based on the means of these values, which are 0,85 and 1,13 mm respectively. The potential wave height measurement accuracy of the system is therefore ±1,2 to 1,6 mm.

The light penetration of the water surface was estimated as < 1 mm (see Section 4.6.1). It was very difficult to estimate its effect on the stereoplotter operator's ability to place the floating mark on the water surface. When viewed through the stereocomparator, the water surface appeared solid, but it is possible that the very slight light penetration of the water surface could cause a small consistent heighting error to occur. However, this error would be cancelled out when the trough elevation was subtracted from the corresponding crest elevation to calculate the wave height at a point.

It was found that the projective transformation theory could accomodate much larger plate tilts than was allowed for the stereoplotter analysis. However, the glass plates were levelled with the same care, for each stereopair, as for the stereoplotter analysis, since it was found that these large (> 3°) tilts dis-

torted the stereo model of the water surface. This did not in any way affect the measuring accuracy of the technique, but the operator would sometimes perceive seemingly contradictory wave phenomena, such as wave heights getting larger where in fact they were actually decreasing in size. The operator's distorted perception of the water surface could lead him to place a bias on his measurements, leading to erroneous results.

4.8.5.6 Conclusions.

It was concluded that the projective transformation wave height and pattern measurement technique using the stereocomparator/micro-computer system was extreemly accurate. In fact the estimated potential water surface elevation measurement accuracy of ± 0,7 to 0,9 mm calculated in Section 4.8.5.5 is better than the potential measurement accuracy of ±1 to 1,35 mm calculated in Section 4.8.4. This is probably due to the fact that 75% of the targets in the test field were at distances of 5 to 6,8 m from the cameras. The potential wave height measurement accuracy of the system was estimated to be ±1,2 to 1,6 mm. The high accuracy of the technique is due primarily to the use of the high precision Zeiss metric cameras for the photography, and the use of the high precision Zeiss Stereocomparator to analyse the glass plates. The measurement accuracy could have been marginally improved if the control points' ground co-ordinates had been more accurately determined. However, the author is of the opinion that the projective transformation/Zeiss cameras/stereocomparator system used was probably the most accurate system available.

The Zeiss cameras and stereocomparator are however very expensive items. Each camera costs approximately R30 000 and the stereocomparator costs approximately R50 000. These costs would not be excessive for a large hydraulics research laboratory which makes extensive use of the technique, it would however be beyond the reach of smaller research or consulting organisations. Such a system would also be impracticable for "one off" investigations. It was for this reason that the author decided to investigate two cheaper alternative techniques. The first based on projective transformations (Section 4.8.6) and the second based on classical parallax theories (Section 4.9). Integral to a cheaper wave height measurement technique is the use of non-metric

cameras, which are far cheaper than metric cameras. Projective transformations are particularly powerful when non-metric cameras are used and the potential use of non-metric cameras for wave height measurements is dealt with in Section 4.8.7. A general summary of the advantages of projective transformation wave height measurement is given in Section 4.8.8.

4.8.6 The Micro-computer/Digitiser Tablet/Modified Mirror Stereoscope/ Electronic Parallax Bar and the Projective Transformation Theory System as a Potential Wave Height and Pattern Measurement System.

4.8.6.1 Introduction.

The measurement system consisting of the Tektronix micro-computer system described in Section 4.4.4 and the digitiser tablet/modified mirror stereoscope/electronic parallax bar system described in Section 4.4.7 was developed by Professor Adams of the Department of Surveying with the help of Mr Wehuisen of the Department of Electrical Engineering. The author suggests that this system has the following advantages over the stereocomparator/micro-computer system described in Sections 4.4.3, 4.4.5 and 4.8.5.1, namely:-

(1) This system avoids the necessity of purchasing the very expensive stereocomparator, the expensive analogue to to digital conversion unit, and the expensive hardware necessary to link the micro-computer to the analogue to digital conversion unit.

(2) This system lends itself to the analysis of stereopairs taken with cheap (relative to metric cameras), small format, non-metric cameras. Welham (1982) has shown that this system, used to analyse stereopairs taken with a 35 mm Nikonos underwater camera, can achieve measurement accuracies close to that which can be achieved by direct measurement from the 24 x 36 mm format negatives using a stereocomparator. To achieve these accuracies he found that paper print enlargements had to be made from the negatives, with an enlargement factor of 10 times or greater. These paper print enlargements were then viewed stereoscopically using the modified mirror stereoscope, and measurements were taken using the electronix parallax bar/digitiser tablet and micro-computer configuration.

4.8.6.2 Measurement Technique.

To analyse a stereopair taken with a metric or non-metric camera the following steps should be followed, namely:-

(1) Paper enlargements are made of the stereopair.

Once the exposed film has been developed, the relevant stereopairs are selected and enlarged. The degree to which the image can be enlarged is governed by the photographic materials used and the quality of the image. It is best to take a series of photographs using different settings, in order that a good quality image is obtained.

It is important that the resultant enlargement is of good quality and high resolution. If poor enlargements are utilized the resultant three dimensional model will be poor. One of the biggest problems of using poor photography is a "soft" model. The observer cannot height the measuring mark with confidence, and the measuring accuracy is negatively affected.

The bigger the enlargement the more accurate the results, since the effective measuring accuracy of the digitiser is improved proportionately. The user must therefore choose his photographic materials accordingly, if he wishes to maximize accuracy. Big photographic enlargements are expensive, the user must also consider whether the added expense is worth the increase in accuracy.

(2) The images are measured on a digitiser with the aid of a modified mirror stereoscope and an electronix parallax bar.

The two paper print enlargements of the stereopair are placed next to each other on the digitiser tablet, and are positioned such that they can be viewed stereoscopically using the modified mirror stereoscope. Fig. 4-10 of Section 4.4.7 shows such a stereopair mounted on the digitiser tablet below the mirror stereoscope.

The electronic parallax bar, shown in Fig. 4-11 of Section 4.4.7, is placed over the stereopair and then, viewing stereoscopically, the two small red dots on the two cursors are made to fuse and float onto the object point,

seen in the stereo model, which has to be measured. This "floating dot" effect, explained in Section 4.9.2.3, is achieved by the movement of the right cursor which is driven by a small electric motor. Once the "floating dot" has been correctly placed on the point to be measured, the recording switch is pressed and then the left hand and, after a small delay, the right hand digitiser x, y co-ordinates are fed into the computer under program control.

The program "TESTFIELD" could be used directly in its single cursor mode for the above data imput procedure, provided the electronic parallax bar works perfectly. It was found however, that sometimes it did not record the co-ordinates of one of the image points. To overcome this problem a "check" subroutine was included in "TESTFIELD" which checks that both image points have been read before the computer accepts the input data.

(3) The object point space co-ordinates are calculated using projective transformations.

In order that the object point space co-ordinates can be calculated (using projective transformations) from the stereopair observations, it is necessary that the object space or surface (for example a dynamic water surface) is encapsulated within a suitable control point system. It is suggested that 16 or more carefully co-ordinated control points be arranged in two or more planes with the object surface situated within this control point network. Since the author was primarily interested in assessing the measurement accuracy potential of the system, he analysed a stereopair of the test field, taken with the Zeiss cameras, thus largely eliminating lens distortion effects which would influence the results. This measurement accuracy experiment is described in the next section.

The first step in the projective transformation technique of analysing a stereopair using the mirror stereoscope/ electronic parallax bar/digitiser system, is to input the left and right photograph digitiser co-ordinates of each

control point to the computer. This can be done monoscopically using a single cursor or stereoscopically using the electronic parallax bar. The program "TESTFIELD" allows either facility to be used. Using the monoscopic mode and a single cursor, one digitises first the left hand photo image of a control point, and then the right hand image. Using the mirror stereoscope and electronic parallax bar, the control points can be viewed stereoscopically following the procedure explained previously.

The control point left and right image co-ordinates are then used to determine the projective transformation parameters and inner orientation elements for both left and right photographs. The control point's space co-ordinates are then determined and the differences between the calculated and corresponding ground co-ordinate values computed. These differences will highlight any gross observation errors, plus any inadequacies in the control point or camera configuration.

The object points which need to be measured can now be viewed stereoscopically and their left and right image digitiser co-ordinates inputted to the micro-computer, under program control. These observations, plus the projective transformation parameters for both photographs can now be used to calculate the X, Y, Z space co-ordinates of the observed object points.

4.8.6.3 Potential Measurement Accuracy Experiment.

The author decided to test the measurement accuracy potential of the mirror stereoscope/electronic parallax bar/digitiser system to assess its usefulness as an analysis tool for the diffraction configurations. To obtain a direct comparison between the above system and the stereocomparator/micro-computer system, an analysis of the plates used in the measurement accuracy potential experiment, described in Section 4.8.4, was undertaken using the measurement technique described in Section 4.8.6.2.

Enlarged paper prints (2,5 times enlargement) were made of the plates taken of the test field (see Section 4.8.4). The enlargements were then taped to the digitiser board, the left plate

print on the left hand side, and the right plate print on the right hand side. The 24 test field targets used previously as control points were again selected and digitised using the monoscopic mode i.e. with one cursor. The digitiser left and right image co-ordinates were fed into the micro-computer under the control of the program "TESTFIELD". The program then calculated the projective transformation parameters and inner orientation elements for each print, plus the differences between calculated and ground co-ordinate values of the 24 control points. The principal distances, calculated for the left and right prints, were 251,6 mm and 251,05 mm respectively, compared to the corresponding camera principal distances of 100,94 and 101,23 mm. It is thus evident that the prints were approximately 2,5 times larger than the plates.

The differences between the calculated and ground co-ordinate values of the 24 control points is shown in Table 4-10. The corresponding test field target number of each control point is also included in the table, so that one can refer to Fig. 4-14 to identify the targets used as control points. Since the author was primarily interested in the heighting accuracy potential of the system, only the Z differences were analysed. The Z differences were assumed to have no bias due to the nature of the least squares solution of the projective transformation parameters. The standard deviation of a single observation and the average absolute error were calculated to be 3,25 mm and 2,75 mm respectively.

An additional 24 test field targets were then selected as object points, digitised, and their space co-ordinates calculated. The differences between the calculated XYZ co-ordinates and the ground co-ordinates, rounded of to whole numbers, are given in Table 4-11. The corresponding test field target numbers are also included in the table. As before, only the Z differences were analysed. The mean of the Z values was calculated to be +2,9 and this was rounded off to +3 and taken to be the bias. This bias was then subtracted from all the Z differences and all subsequent analysis was carried out using the "corrected" values (see Section 4.8.4). The standard deviation of a single observation and the average absolute error were calculated to be 5,4 mm and 4,5 mm respectively.

The author suggests that the reason for the control point co-ordinates being more accurately determined than the object point co-ordinates, is that the projective transformation parameters were solved by incorporating the control point co-ordinates in a least squares type solution. As a result, the subsequent calculated co-ordinates of these 24 points were a "best fit" adjustment. This was not the case when the object point co-ordinates were calculated. The author believes however, that this discrepancy between the control and object point determination accuracies, is due to errors in the measurement of the left and right print image co-ordinates. When the image points are measured using a stereocomparator, this difference between the control and object point determination accuracies is not evident; in fact, a "reversal" often occurs. Such a situation occured for the corresponding comparator results given in Table 4-4 of Section 4.8.4. The average absolute error for the 24 control points is 1,4 mm compared to 1,0 mm for all 80 points.

We can now compare the accuracies obtained when the plates were analysed using the stereocomparator system, compared to those obtained when the plates were analysed using the digitiser system. For the first case, the standard deviation of a single observation and the average absolute error were 1,35 mm and 1,0 mm respectively, while for the second case the corresponding values were 5,4 mm and 4,5 mm respectively. It therefore appears that if a stereocomparator is used to analyse the plates, the object co-ordinates will be determined 4 to 4,5 times more accurately than if 2,5 times enlargements are analysed using the mirror stereoscope/electronic parallax bar/digitiser system. It is necessary, however, to look at the relative resolution of the two instruments. The stereocomparator reading directly from the glass plates had a resolution of 0,005 mm, while the digitiser board reading from 2,5 times enlargements of the plates had a resolution of 0,1/2,5 = 0,04 mm. Thus, for this example, the stereocomparator had 8 times the resolution of the digitiser board.

From the above results, it can be seen that the accuracy with which the object space co-ordinates can be calculated is directly dependant upon the accuracy with which the corresponding image point co-ordinates are determined. For the digitiser to emulate

No	Target No	DX	DY	DZ
1	1	1,7	-1,1	1,8
2	4	1,3	-1,4	2,4
3	65	0,2	-0,3	0,9
4	68	2,0	0,2	-6,1
5	5	-0,6	1,6	-5,2
6	8	0,2	0,3	5,1
7	69	2,1	1,3	-4,7
8	72	-1,0	0,5	2,3
9	9	0,1	0,6	0,8
10	12	-0,1	1,6	-2,3
11	73	-2,3	-2,5	6,7
12	76	-1,3	1,0	1,8
13	13	-0,9	2,1	-2,1
14	16	0,0	-1,8	-2,4
15	77	0,4	-0,4	-1,8
16	80	2,2	-0,9	-1,2
17	18	-0,8	-0,6	-1,7
18	51	1,1	0,1	-3,7
19	22	-0,6	1,9	3,6
20	55	-1,7	-0,8	-0,2
21	26	-1,4	-1,6	1,1
22	59	-0,1	1,0	4,3
23	30	0,1	-0,9	2,3
24	63	-0,4	0,4	-1,6

Table 4-10 Control point results.

No	Target No	DX	DY	DZ
1	2	0	1	4
2	6	0	-1	9
3	10	-3	1	-8
4	14	-2	0	-5
5	19	-4	-2	-4
6	23	-1	-2	6
7	27	-1	-3	5
8	31	-1	0	-1
9	34	0	3	5
10	38	-1	-1	14
11	42	-1	-1	-2
12	46	0	-1	0
13	35	-1	0	3
14	39	-3	0	6
15	43	-1	1	-1
16	47	-3	0	5
17	50	3	0	5
18	54	1	0	7
19	58	0	-2	-1
20	62	-1	1	-2
21	67	-2	1	11
22	71	-4	-2	10
23	75	0	-3	-1
24	79	-4	-1	4

Table 4-11 Object point results.

the measurement potential of the stereocomparator, enlargements of 0,1/0,005 or 20 times would have to be made. However, from work done by Adams (1981) and Welham (1982), it appears that an enlargement factor of 10 times will give results close to those obtainable with a stereocomparator.

4.8.6.4 Conclusions.

From the results of the measurement accuracy experiment, the author concluded that the mirror stereoscope/electronic parallax bar/digitiser system was not sufficiently accurate to analyse the diffraction configurations to be tested. This was because the wave heights to be measured varied from 70 to 10 mm relative to the cameras "flying height" of 5 m, and the accuracy obtainable using the above system was only of the order of ±5 mm. The mirror stereoscope/electronic parallax bar/digitiser system could therefore not compete with the speed and accuracy which was obtainable using the stereocomparator/micro-computer system. However, to test the feasibility of using the mirror stereoscope/electronic parallax bar/digitiser system for wave height and pattern measurement, the author made 2,5 times enlargements of one of the diffraction stereopairs and experimented with this system. It was found that the stereo model of the deformed water surface was well defined and that the water surface elevations could be determined with an accuracy of approximately ±5 mm.

4.8.7 The Wave Height Measurement Potential of Non-Metric Cameras and the Projective Transformation Theory.

4.8.7.1 Introduction.

It is becoming increasingly clear to researchers, that if photogrammetry is to be applied on an ever increasing scale, one should look for ways and means of releasing the photogrammetric systems from the traditional restrictions of conventional hardware. Through concentrated world wide research efforts, the door has finally been opened for the use of readily available and relatively inexpensive cameras in close range photogrammetry. It has been shown that highly accurate results can be achieved using non-metric cameras in combination with an appropriate analytical data reduction system.

Adams (1981) states:

> "A metric camera is a general term applicable to a camera which has been designed as a survey camera and possesses a well defined inner orientation. That is, a camera possessing a good lens with a wide field of view and small distortion, a calibrated principal distance and in which the position of the principal point can be located in the image plane by reference to fiducial marks. The picture format is normally fairly large and the film is flattened in the focal plane at the instant of photography. Cameras not possessing these characteristics can be defined as simple or non-metric cameras."

The measurement accuracy potential of metric and non-metric cameras has been investigated by researchers such as Karara and Abdel-Aziz (1974) and Kölbl (1976).

4.8.7.2 Non-Metric Vis-A-Vis Metric Cameras.

Compared to metric cameras, non-metric cameras have the following advantages and disadvantages.

The advantages are:-

(1) General availability.
(2) Flexibility in focusing range.
(3) Some are motor driven, allowing for a quick succession of photographs.
(4) They are usually smaller in size and lighter in weight.
(5) They can be easily hand-held and thereby oriented in any direction.
(6) They use readily available film.
(7) The price is considerably less than for metric cameras.

The disadvantages are:-

(1) Lenses are designed for high resolution at the expense of geometric quality, as evidenced by generally large and often irregular distortion.
(2) Instability of interior orientation.
(3) Lack of fiducial marks.
(4) The absence of orientation aids such as level vials and orientation provisions precludes the precise orientation of the camera along desired directions.
(5) The absence of a proper film flattening device.

4.8.7.3 Advantages of Using Projective Transformations to Analyse Photographs taken with Non-Metric Cameras.

If two non-metric cameras are to be used to measure a dynamic process, such as an undulating water surface, one of two approaches can be followed in order to reduce the relevant data from the stereopairs. The first approach is to "metricise" the cameras and to analyse the photographs using conventional analogue techniques; while the second approach is to use a data reduction technique that does not require a knowledge of the cameras' inner orientation elements.

The first approach was adopted by Adams (1978b) for a very close range photogrammetric study of dental palatal casts. He converted a Linhof Technika View camera from its original design for professional photography, to a metric camera suitable for stereophotogrammetry by:-

(1) constructing an attachment to the camera to ensure stability in operation.
(2) providing a facility to introduce an accurate camera base setting for stereophotography.
(3) determining the principal distance at infinity focus and introducing a vernier scale to read principal distances for varying focus settings.
(4) determining the position of the principal point and establishing a fiducial mark system.
(5) checking the positioning of the fiducial marks and the principal distance vernier scale by re-calibrating the camera at very close range.

Adams analysed the stereopairs using the stereoplotter described in Section 4.4.2, and found that if he did not take convergence (see Section 4.7.2.2) into account, the discrepancies between instrument and true height were of the order of 20%. He solved this problem by applying equal and unlike tilts by means of the two instrumental ϕ dials, and checking the height values at the base and top of height control poles positioned within the model overlap.

The second approach, which is to use the theory of projective transformations to analyse the stereopairs, does not require a know-

ledge of the cameras' inner orientation elements. In addition, this technique circumvents the convergency error problem which becomes very pronounced when adopting the traditional approach to short range photogrammetry. Three different formulations of the projective transformation theory have been developed, to analyse photographs taken with non-metric cameras. These can be attributed to:-

(1) Abdel-Aziz and Karara.

Their approach, known as the Direct Linear Transformation approach, was developed at the University of Illinois. The theory has been described by Karara and Abdel-Aziz (1974) and by Atkinson (1980). The innovation in the DLT approach is the concept of direct linear transformation from comparator co-ordinates into object space co-ordinates, thus by-passing the intermediate step of transforming image co-ordinates from the comparator system to a photographic co-ordinate system. As such the DLT approach makes no use of fiducial marks. Karara and Abdel-Aziz concluded that one term (K_1) would be sufficient to model lens distortion and film deformations. They adopted a direct solution for the 12 unknown parameters which consisted of the 11 projective transformation parameters and the lens distortion/film deformation parameter.

(2) Bopp and Krauss.

In the DLT solution described above, the 11 transformation parameters are considered independent. Bopp and Krauss (1978a) developed an exact solution to the DLT basic equations (equations (7) in Section 4.8.2.1), which they named "The 11 Parameter Solution". The solution took into account the dependence between these 11 parameters and the 9 independent parameters, which are necessary to represent "the perfect camera" by introducing two constraints among the 11 parameters. The theory is described by Bopp and Krauss (1978a) and Atkinson (1980). In 1978 the 11 parameter solution was extended for on-the-job calibration of non-metric cameras (Bopp and Krauss (1978b)), by extending equations (7) to include corrections for lens distortion.

(3) Adams.

Adams (1979) adopts a direct solution to the basic DLT equations (i.e. equations (7)), which is given by equation (18). He showed that this solution gave very good results and that there was a negligible improvement in accuracy when using the rigorous least squares solution proposed by Bopp and Krause (1978a). Welham (1982) has shown that once the projective transformation parameters have been determined, the object point space co-ordinates can be calculated using equation (36).

The author adopted the 3rd approach for his wave diffraction investigation. It is suggested that this approach should be adopted by a coastal engineer wanting to measure wave phenomena, using non-metric cameras, due to the approach's comparative simplicity and proven accuracy. Before a particular pair of non-metric cameras are used for measurement purposes, it is recommended that the lens distortion of their respective lenses be determined, using the techniques described in the next section. Non-metric cameras which show very marked and irregular lens distortions should not be used for measurement purposes. Welham (1982) has shown that if the lens distortion of a non-metric camera is fairly symmetrical and not too large, a significant proportion of the linear, and possibly the parabolic, components of this distortion can be accomodated by the projective transformation solution (equation (18)). Therefore, the use of projective transformations to analyse non-metric stereophotography does away with the need to know the cameras' inner orientation elements, as well as accomodating some of the symmetrical lens distortions.

4.8.7.4 Lens Distortion in Non-Metric Cameras.

The author suggests that before a non-metric camera is used for measurement purposes, an investigation of its lens distortion should be carried out. It is suggested that the method of Thompson (1957, 1977), based on the perspective projection model, should be used.

To determine the lens distortion of a non-metric camera, the following procedure is suggested:- An accurately drawn grid of black lines on a white background is constructed. A normal case

photograph is then taken of this grid using the non-metric camera (i.e. with the optical axis perpendicular to the grid). The x, y co-ordinates of the grid intersections are then measured on the resulting negative using a stereocomparator. Deviations from the straight line in the X and Y directions are then calculated, and the vector displacements from the true grid intersections plotted to yield a distortion contour plan.

Welham (1982) has shown that when projective transformations are used, the linear component of the lens distortion is accomodated in the calculation of the projective transformation parameters. By analysing a synthetic normal case photograph of a regular grid, which shows a symmetrical barrel distortion (Fig. 4-52(a)), he calculated the deviation of the calculated grid intersections from their actual positions (Fig. 4-52(b)). The procedure used was as follows:- The known grid X, Y positions and the observed grid intersection x, y image positions measured from the synthetic photographs were used to determine the projective transformation parameters. These calculated projective transformation parameters, plus the observed image positions were then used to calculate the grid X, Y positions. Fig 4-52(b) shows a plot of the calculated grid X, Y positions relative to their true positions.

From Fig. 4-52(a) and (b), it can be seen that linear components of the distortion are taken into account by the transformation parameters. The large distortion introduced to the co-ordinates of the synthetic photograph (Fig. 4-52(a)) has, after the adjustment, been reduced to a much smaller distortion (Fig. 4-52(b)). Welham (1982) suggests that the distortion which remains after the adjustment is the non-linear component plus the observation error. He suggests that if projective transformations are to be used, the researcher need only be concerned with the effect of the non-linear component of distortion plus observer error on the measuring accuracy of the camera.

4.8.7.5 Potential Measurement Accuracy Using Non-Metric Cameras and Projective Transformation Theory.

Schwidefsky (1970), in his paper "Precision photogrammetry at close ranges with simple cameras", defined the term "precision photogrammetry" as being when the relative mean square error of

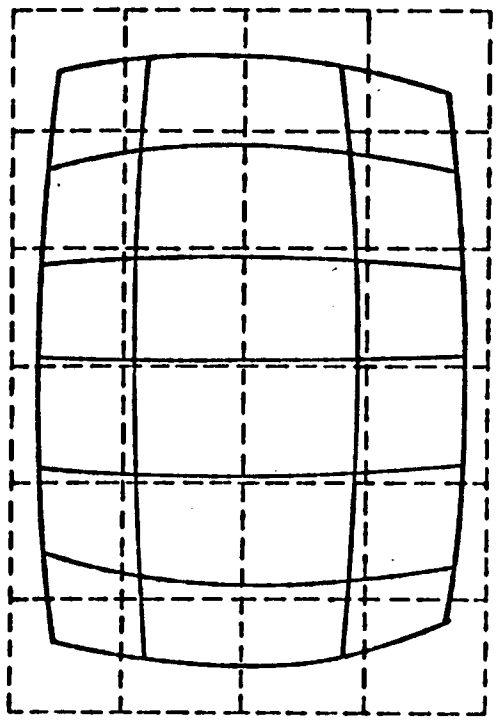

(a) Actual distortion.

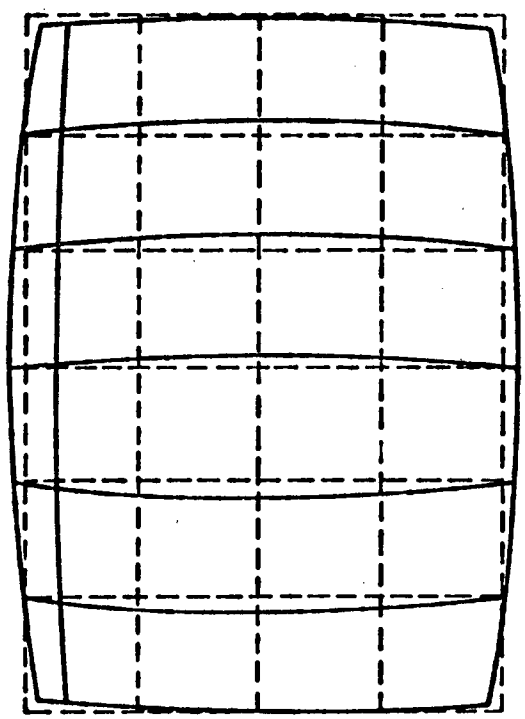

(b) Residual distortion.

Fig. 4-52 Distortion - synthetic photographs (Welham, 1982).

The shape of the distortion is not altered by the adjustment. The magnitude of the distortion is reduced - proving that the adjustment applies a scale factor to reduce the magnitude.

the distances from the camera lies between 1/1000th and 1/10000th of the distances. A "precision" non-metric camera is one capable of achieving measurement accuracies within this range. Cameras not capable of achieving accuracies in this range should not generally be used for measurement purposes.

There are a number of factors which influence the potential measurement accuracy of a metric or non-metric camera when using projective transformations, namely:-

(1) The camera characteristics.
Factors to be considered are:-

A. Lens quality: The degree of the camera's lens distortion, and whether this distortion is symmetrical or not. If the distortion is not too large (< 30 to 35 μm), and is symmetrical, the linear component of this distortion can be accommodated in the calculation of the projective transformation parameters.

B. Film flatness: The film should be perfectly flat and completely in contact with the focal plane. Ideally, glass plates or a réseau to flatten the film during exposure, should be used.

C. Mechanical stability: Certain cameras which have a high mobility of both lens and negative planes, display a relatively weak mechanical stability. Such a camera is the Linhof Technika which was used by Adams (1978b). Adams found that he had to construct an attachment to the camera to ensure stability in operation.

(2) The camera/object configuration.
The geometry of the two cameras, in relation to the object space defined by the control point system, is important when considering accuracy. The two principle elements of the geometry are:-

A. The camera base to range ratio: Generally the larger the ratio, the greater the accuracy.

B. The orientation of the camera axes: This is defined by the convergence of the camera axes in relation to the base line.

For the stereoscopic analysis of a dynamic water surface, the camera axes will have to be nominally parallel. The cameras should be symmetrically situated on either side of the centre of the object space. It is recommended that the base to range ratio should not be less than 0,35.

(3) Control point configuration.

In Section 4.8.5.3 it was shown that the number of control points used and their configuration, effects the potential measurement accuracy considerably. When using projective transformations, it is recommended that 16 to 20 control points be set up in two or more planes encompasing the object surface to be measured. Their XYZ co-ordinates should be determined as accurately as possible, as they are assumed to be error free for the calculation of the projective transformation parameters.

(4) Measurement of image co-ordinates.

The accuracy with which the image co-ordinates can be measured will affect the potential measurement accuracy of the camera system. The image co-ordinates must be measured as accurately as possible, either by measuring directly from the negatives using a precision stereocomparator, or by taking measurements from paper print enlargements using a digitiser tablet.

Welham (1982) undertook a study to determine the measurement potential of a non-metric NIKONOS III underwater camera. He used a 35 mm lens, since he found that it gave the least distortion for photographs taken in air. The experiment was carried out using the test field described in Section 4.5. The base between the camera stations was approximately 4,2 m, and the perpendicular distance between the base and the middle of the test field was 5,7 m. The cameras' axes were aligned approximately parallel to each other and perpendicular to the base. A total of 8 stereopairs were taken with aperture settings of f22 and f8, and focus settings of infinity and 5 m. The projective transformation parameters were determined using all 80 test field targets as control points for maximum accuracy. The average RXYZ residual (from equation (43)) was calculated to be

2,28 mm. This can be expressed in terms of Schwidefsky's (1970) measure of accuracy, by relating the error to the mean point distance from the base. The measuring precision thus calculated is 1:(5700/2,28) or 1:2500.

As a comparison, it is interesting to note the accuracy potential of the Zeiss Jena UMK 10/1318 camera described in Section 4.4.1. Welham (1982) took two stereopairs of the test field using one of the Zeiss metric cameras. The base between the camera stations was approximately 3,3 m, and the perpendicular distance between the base and the centre of the test field was approximately 5 m. Normal case photography was used (camera axes parallel). Again, all 80 test field targets were used as control points to determine the projective transformation parameters. The average RXYZ residual was calculated to be 0,62 mm, and therefore the corresponding measuring precision is 1:8064. The metric camera configuration was thus able to measure the control point co-ordinates with an accuracy 3,2 times superior to that which could be obtained using the non-metric camera configuration. In both cases, the image point co-ordinates were measured directly from the negatives using the stereocomparator in the mono-comparator mode i.e. the left and the right plates/negatives were individually observed while mounted in the left plate holder of the stereocomparator.

4.8.8 Summary of the Advantages of Using the Projective Transformation Method of Wave Height Measurement.

The advantages of using the projective transformation method of wave height measurement are:-

(1) For monochromatic waves only two stereopairs are needed, with the waves imaged in the 1st stereopair 180° out of phase relative to the waves in the 2nd stereopair, in order to determine the wave height distribution in the basin. The technique enables the trough positions in the 2nd stereopair, which correspond to the crest positions observed in the 1st stereopair, to be accurately located (and visa versa)

(2) The method is accurate. The author has estimated that, using his configuration, he is able to measure the wave heights in the wave basin with an accuracy of better than 2 mm.

(3) The method avoids the need to have expensive anologue analysis equipment such as a stereoplotter.

(4) The method enables the coastal engineer to analyse his own photographs using either the stereocomparator/micro-computer system, or the mirror stereoscope/parallax bar/ digitiser tablet/micro-computer system. This cuts down on analysis time since only the wave features of interest are measured. Furthermore, the engineer can merely re-examine the stereopairs whenever further information is needed.

(5) The method short cuts the steps of inner, relative and absolute orientation, and avoids the problem of convergence.

(6) The method is particularly suited to the analysis of photographs taken with non-metric cameras. The method requires no knowledge of the cameras' inner orientation elements, and furthermore, the linear component of the lens distortion is accommodated in the solution of the projective transformation parameters.

(7) The method imposes less restrictions regarding the cameras' positions, principal distances and relative orientation, than conventional anologue procedures. In fact, two cameras with different inner orientation elements could be used to take a stereopair.

(8) The digital wave height data generated using either of the two projective transformation analysis systems described, can be easily processed using standard computer packages, to yield a contour plot or a 3 dimensional perspective picture of the wave height distribution within the wave basin.

4.9 A Feasibility Investigation of a Non-Expensive Wave Height Measurement Method Using the Theory of the Deformed Reference Plane.

4.9.1 Introduction.

For many years aerial photograph stereopairs have been analysed by means of a mirror stereoscope and a parallax bar and using the simple parallax theory introduced in Section 4.1.3. The author was intrigued by the simplicity of this measurement system, and set about testing its potential as a wave height measurement tool. He suggested that such a system would be ideal for the small organization wanting to do a small amount of wave height and pattern analysis.

The system investigated was considered to be the cheapest system capable of analysing a model harbour configuration. Such a system would consist of:-

(1) Two high quality non-metric cameras to take stereopairs.

(2) A parallax bar and mirror stereoscope to take the parallax measurements from the stereopairs.

(3) A micro-computor with a digitiser board to determine the wave heights using the parallax measurements and the theory of the deformed reference plane, and also to calibrate the cameras using the projective transformation theory. The digitiser board would be used as a mono comparator.

This economical analysis method was tested using a simulated model harbour configuration set up in the testfield (see Section 4.9.3.3). However, the Zeiss Jena UMK metric cameras were used instead of non-metric cameras, since the researcher was primarily interested in the maximum possible accuracy of measurement that could be achieved using a parallax bar and mirror stereoscope. The use of non-metric cameras would create additional errors difficult to separate from those caused by the parallax measuring system.

To determine the maximum possible measurement potential of the technique a number of the stereopairs taken with the Zeiss metric cameras were analysed using the stereocomparator. This was an attempt to eliminate all the errors due to lens distortion and measurement, and to highlight the accuracy with which the ground elevations could be determined using the theory of the deformed reference plane.
The parallax measurement procedures for the parallax bar and mirror

stereoscope,and also the stereocomparator are given in most photogrammetry text books, e.g. Wolf (1974),and therefore will not be described here.

4.9.2 Parallax Theory.

4.9.2.1 Theory of the Deformed Reference Plane.

The parallax equations described in Section 4.1.3 are based on the assumptions that the cameras' axes are truly vertical, (no camera tilts) and that the camera stations are at the same height, i.e. the two photos are in horizontal coplane. This is in fact the exception rather than the rule, since both pictures may have been taken with the cameras tilted by unknown amounts in unknown directions, and furthermore, the two cameras may have been at different heights above the datum. The result of such a situation may be seen by studying Figs 4-53 (a) and (b). Fig 4-53(a) shows a section looking along the air base S of two photos which are in horizontal coplane. The ground is a plane with a gradient of 2° laterally across the photographic base. Observation of these photos in horizontal coplane (i.e. flat under the stereoscope), and the application of the before mentioned formulae would result in correct heighting of the ground.

Fig. 4-53(b) shows a section looking along the air base S' of two photos, both of which are equally tilted by 2° around the base line, i.e. the photos are not horizontal coplane. The ground in this case is perfectly flat. Observation of these photos in horizontal co-plane would result in the formulae giving heights exactly as for the first case, and the ground would appear tilted laterally around the air base by 2°.

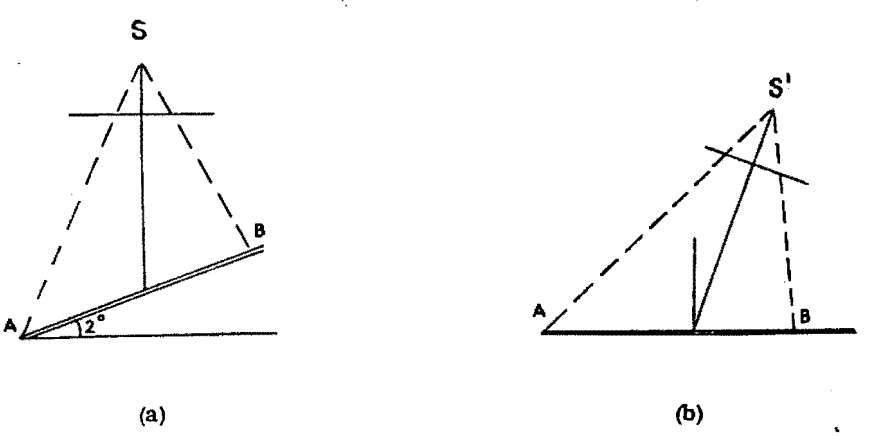

Fig. 4-53 Tilt errors.

In order to obviate such errors, it is necessary to analyse the deformations of the ground which apparently take place because the photographs are measured in horizontal co-plane, as opposed to the various possible attitudes in the air, and to introduce ground control points so as to be able to adjust the results. The two basic types of error are:-

(1) error due to the inclination of the air base,

(2) rotation errors due to tilts of each camera around specific axes in space. These axes and their related rotations are shown in Fig. 4-31.

These accumulated errors can be visulised as being a deformation of the reference plane in such a way that it represents a surface comprised of linear, hyperbolic and parabolic form. Mathematically this surface can be represented by the well known equation:-

$$dh = a_0 + a_1 x + a_2 y + a_3 xy + a_4 x^2 \qquad (45)$$

A detailed discussion on the use of equation (45) is given by Thompson (1954). In the derivation of the above equation it is assumed that the 'flying height' H_f is large compared to the variation in the terrain elevations, and that the tilts are small enough to allow 2nd and higher order terms to be neglected. Also, the origin is taken at the midpoint of the left plate as this minimises the maximum value of the quadratic term $a_4 x^2$.

In the general case, then, when determining the elevation of points on a photographed terrain, the parallax measurements taken from photographs observed in horizontal co-plane can be used to determine the "crude heights" for these points using the basic parallax equations. In order to determine the true heights of these points it is necessary to know the true heights of a minimum of 5 control points in the overlap area, 4 of these points must be at the corners of the overlap, and one in the centre. Normally 6 or more control points are used introducing one or more redundancies.

This information can be used to determine the values of parameters a_0 ---- a_4 in the deformed reference plane, and subsequently the true height of any point in the overlap area can be determined.

4.9.2.2 Photographic "Flight Line" Axes for Parallax Measurement.

Since the x parallax occurs parallel to the direction of flight, the photographic x and $\bar{x}$ axes for parallax measurement must be parallel with the flight line for each of the photographs of a stereopair. (Barred values denote the right hand photograph of a stereopair). For a stereopair the flight line is the line connecting principal points and conjugate principal points. Principal points are located in the usual manner by intersecting the x and y fiducial lines, while the principal of the floating mark can be used to transfer principal points to their conjugate positions.

4.9.2.3 Principle of the Floating Mark.

Parallaxes of points can be measured most quickly and accurately while viewing stereoscopically, using the principle of the "floating mark". While viewing a stereo model through a stereoscope, two small identical marks etched on glass called "half marks" may be placed over the photographs - one on the left photograph and one on the right photograph. The left mark is seen with the left eye and the right mark with the right eye. The half marks may be shifted in position until they fuse together into a single mark which appears to exist in the stereo model and to lie at a particular elevation. If the half marks are moved closer together, the parallax of the half marks is increased, and the fused mark will therefore appear to rise. Conversely, if the half marks are moved apart, parallax is decreased and the fused mark appears to fall. This apparent variation in elevation of the mark as the spacing of the half marks is varied, is the basis of the term "floating mark".

The spacing of the half marks (parallax of the half marks) may be varied so that the floating mark appears to rest exactly on the terrain. This produces the same effect as though an object of the shape of the half marks had existed on the terrain when the photogtaphs were originally taken. The floating mark may be moved about the stereomodel from point to point, and as the terrain varies in elevation the spacing of the half marks may be varied to make the floating mark rest exactly on the terrain. Fig. 4-54 demonstrates the principle of the floating mark and illustrates how the mark may be set exactly on particular points such as A, B and C by placing the half marks at a and $\bar{a}$, b and $\bar{b}$, and c and $\bar{c}$ respectively. The flight line is marked by the principal points and their conjugate positions as shown.

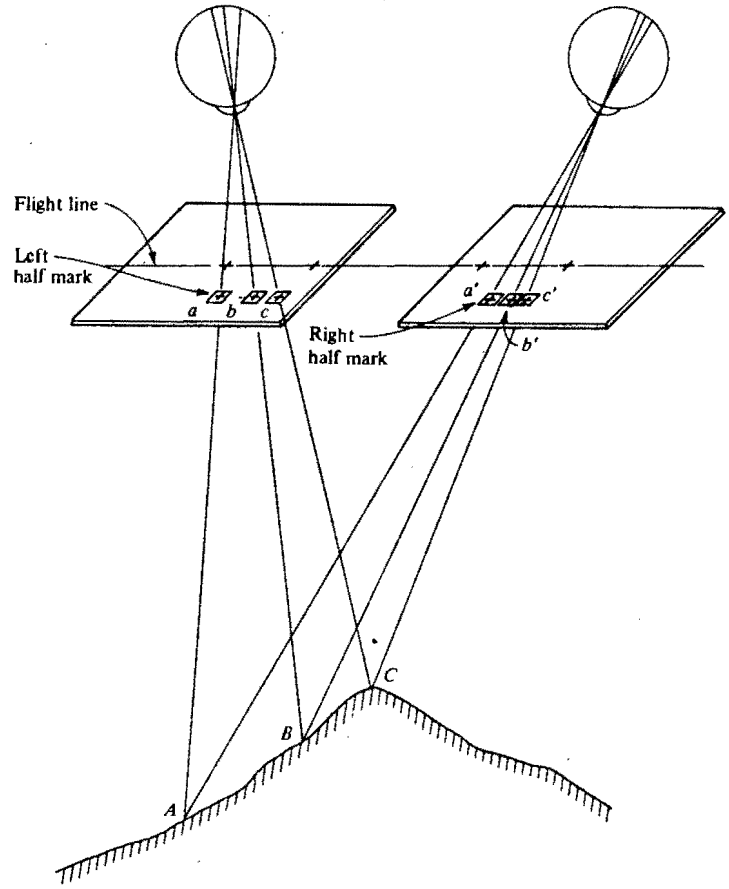

Fig. 4-54 The principle of the floating mark.

4.9.3 Experimental/Analytical Investigation.

4.9.3.1 Introduction.

A series of investigations were carried out to determine the effectiveness of using a parallax bar and mirror stereoscope to measure water surface elevations in a model harbour. The potential accuracy obtainable using the theory of the deformed reference plane was also investigated by analysing stereopairs taken with the Zeiss cameras, on the stereo comparator.

4.9.3.2 Standard Parallax Bar Heighting Program and Initial Results.

A Standard Parallax Bar Heighting program.

The program initally used was developed by the Department of Surving at U.C.T. to determine terrain elevations from inputed parallax bar data. The flow chart for this program (called 'PARA') is given in appendix 4C.

The input data required is as follows;-

(1) For each control point:- the control point number, the x, y co-ordinates of the point from the left photograph, the parallax bar reading, and the point's true height.

(2) The average principal distance of the cameras.

(3) The base length of the two camera stations.

(4) The average height of the camera perspective centres above the median surface (i.e. the "flying height" H_f).

The program calculates the crude heights for each point using the procedure described in Section 4.1.3 and then calculates the coefficients of equation (45) using the matrices shown below.

$$\underset{\text{A matrix}}{\begin{pmatrix} 1 & x_1 & y_1 & x_1y_1 & x_1^2 \\ 1 & x_2 & y_2 & x_2y_2 & x_2^2 \\ . & . & . & . & . \\ . & . & . & . & . \\ 1 & x_n & y_n & x_ny_n & x_1^2 \end{pmatrix}} \quad \underset{\text{G matrix}}{\begin{pmatrix} a_0 \\ a_1 \\ a_2 \\ a_3 \\ a_4 \end{pmatrix}} = \underset{\text{L matrix}}{\begin{pmatrix} dh_1 \\ dh_2 \\ . \\ . \\ dh_n \end{pmatrix}} \qquad (46)$$

where $x_1 y_1$ are the co-ordinates of point 1 taken from the left plate

a_0-a_4 are the transformation parameters for the deformed reference plane.

dh_1 = true height of point 1 minus the calculated crude height of point 1

n = the number of control points used in the adjustment.

The a_0-a_4 transformation parameters are then calculated from equation (47) below

$$G = (A^TA)^{-1}A^TL \qquad (47)$$

Equation (47) has the same form as equations (18) and (36) used to calculate respectively the projective transformation parameters and the object space co-ordinates when using the projective transformation theory. It is assumed that both the image and the control point co-ordinates are error free. The transformation parameters a_0-a_4 are calculated using the first approximation to a quasi-parametric least squares solution which incorporates all redundancies to calculate the 'best fit' parameter values.

The program then calculates the heights of all the control points from

$$h_i = h_{CRi} + dh_i \qquad (48)$$

where h_i = calculated height of point no i

h_{CRi} = calculated crude height of point no i

dh_i = the height correction to accommodate the deformed reference plane calculated using equation (45)

The program output is as follows:-

(1) The transformation parameters of the equation of the deformed datum surface, i.e. a_0 .... a_4 of the equation (45)

(2) For each control point:- the point number, the true height, the calculated height, and the difference between the two in mm.

The program 'PARA' can now be used to determine the heights of any other point in the terrain. The input required is as follows:- the point number, its x co-ordinate, its y co-ordinate, and the parallax bar reading at that point. The output takes the form of the point number and its calculated height.

B Initial Results.

The first stereopair to be analysed was the stereopair (1,9 m spacing) of the test field, used in the measurement accuracy investigation described in Section 4.8.4. The parallaxes of the target points of planes 2 and 3, of the test field, (plane 1 is the plane furthest from the cameras) were measured using the Wild parallax bar and mirror stereoscope (Section 4.4.8). The x, y co-ordinates of the points were determined from a contact print of the left plate. This data was then analysed using the program 'PARA'.

For the first run, all 20 targets of plane 2 were used as control points. The base was 1,9 m, the 'flying height' 5,9 m and the average principal distance 100 mm.

The calculated differences between the true and calculated control point 'heights' or Z values were then analysed. The standard deviation of a single observation and the average absolute error were 2,62 mm and 2,21 mm respectively. The mean of the differences

was zero, as was expected since the control point heights had been incorporated in the least squares solution of the transformation parameters.

For the second run, all 20 targets of plane 3 were used as control points. The base was 1,9 m, the 'flying height' 5 m, and the average principal distance 100 mm. The differences between the true and calculated control point 'heights' were then analysed. The standard deviation of a single observation and the average absolute errors were 1,83 mm and 1,57 mm respectively.

The measuring precision for both planes was calculated by dividing the 'flying heights' by the corresponding standard deviations (of a single observation). The measuring precisions for planes 2 and 3 were 1:2252 and 1:2732 respectively. The principal distances were known since metric cameras were used to take the stereopairs. If however, non-metric cameras were used, the principal distances of both the left and the right photographs would have to be determined using a digitiser tablet and the theory of projective transformations as described in Section 4.8.6.2.

For the 3rd run all 40 targets of both planes 2 and 3 were used as control points. The results calculated for this control point configuration were ludicrous. This anomaly was thought to be due to the fact that the two planes were 900 mm apart, a distance which was large when compared to 'flying height' of 5 m. This situation was not compatible with the assumptions made in the formulation of the equation of the deformed reference plane which required that the height of the cameras above the median surface was approximately constant.

It was thought that a fairer test of the program would be to set up a simulated wave basin configuration in the test field, similar to that used for the stereoplotter analysis. This simululated configuration is described in the next section.

4.9.3.3 Simulated Wave Basin Configuration.

To simulate the water surface 3 plumb bobs were suspended in the test field between planes 2 and 3 as shown in Fig. 4-55 below. The plumb bob on the left hand side was placed approximately 220 mm from plane 3, while the central and right hand plumb bobs were suspended approximately 200 mm from this plane. The plumb bobs were immersed in buckets of water to dampen out small vibrations.

Plane 3 was meant to simulate the absolute and relative orientation point configuration in the wave basin. The simulated water surface and control points were placed further apart than the distance between the control points and the mean water level in the wave basin, (which was approximately 190 mm) in order to simulate measurements taken to the bottom of wave troughs. To identify the plumb bob lines three split lead balls were pinched onto each line. These 9 lead balls then represented the simulated water surface.

Fig. 4-55 The simulated wave basin configuration.

The space co-ordinates of these lead balls had then to be determined, and this was done using the theory of projective transformations. The two Zeiss Jena UMK cameras were set up 1,9 m apart and approximately 5,3 m from the suspended lead balls closely simulating the actual experimental wave basin configuration. A set of photographs was then taken with the cameras set up as follows:- apperture setting f - 32, exposure time 3 secs, and focus setting 5 m. The x, y co-ordinates of the 24 targets selected as control points and the 9 lead balls were then determined from both the left and right plates using the stereo comparator in its monocular mode. The program 'TESTFIELD' was then used to calculate the space co-ordinates of the 9 lead balls. It was

estimated that the Z values or heights of the lead balls had been determined with an accuracy very close to 1 mm. These space co-ordinates were then assumed to be the true co-ordinates for the lead ball positions for all subsequent parallax experiments.

4.9.3.4 Simulated Configuration Analysis Using Standard Program.

A Wild parallax bar and mirror stereoscope was used to measure the parallax differences between the control points of plane 3 and the lead balls. These readings were determined stereoscopically. This data was then analysed using the program 'PARA'.

For the firsr run all 20 targets of plane 3 were used as control points. The base was 1,9 m, the 'flying height' 5 m, and the average principal distance 100 mm. The calculated differences between the true and calculated control point 'heights' were then analysed. The standard deviation of a single observation and the average absolute error were 2,62 mm and 2,13 mm respectively.

The point numbers, co-ordinates and the parallax bar readings for the 9 lead balls were then inputted and their heights computed. The calculated heights of the lead balls were all greater than the true heights, the average error in heighting being + 10,7 mm. It was thought that the lead ball heighting inaccuracies were due to the fact that the lead balls were in a different plane from that of the control points. It was decided to run the program with both the plane 3 and the lead balls as the control points.

For the second run all 20 targets of plane 3 plus the 9 lead balls were used as control points. The camera station data was the same as that used for the previous run. The calculated differences between the true and calculated control point 'heights' were then analysed. The standard deviation of a single observation and the average absolute error were 5,45 mm and 4,79 mm respectively. Furthermore, the average heighting errors of the plane 3 control points and lead balls were +3,27 mm and -7,27 mm respectively.

It was now obvious that the standard program could only be used to calculate the heights of points which closely bracketed a single control point plane. Equation (45) imposed the restriction that the variation in terrain elevations must be small relative to the 'flying height'. It was apparent that the maximum variation of 220 mm between plane 3 and the lead ball plane was too large relative to the 'flying height' of 5 m. It was obvious that the

standard program would have to be modified to accommodate the simulated wave basin configuration.

4.9.3.5. The Modified Parallax Bar Heighting Program and Results.

A Modified Parallax Bar Heighting Program.

The standard parallax bar heighting program was modified by adding a "z" term to the standard equation of the deformed reference plane. the modified equation was now:-

$$dh = a_0 + a_1 x + a_2 y + a_3 xy + a_4 x^2 + a_5 z \qquad (49)$$

The flow chart for the modified parallax bar heighting program (called 'PARAMOD') is given in Appendix 4D. This "z" term was added to allow for appreciable changes in Z the distance from the perspective centre to the surface. The "z" term was calculated for each point using equation (50) below:-

$$\dot{z}_i = (h_1 - h_i + H_f)s \qquad (50)$$

where $\dot{z}_i$ = the 'z' term for point i

h_1 = the true height of point 1

h_i = the true height of point i

H_f = the flying height, taken as the height of the perspective centre above point 1

s = scale = average principal distance/flying height (equation (1)).

The six co-efficients of equation (49) are calculated using the matrices shown below:-

$$\underset{\text{A matrix}}{\begin{bmatrix} 1 & x_1 & y_1 & x_1y_1 & x_1^2 & z_1 \\ 1 & x_2 & y_2 & x_2y_2 & x_2^2 & z_2 \\ . & . & . & . & . & . \\ . & . & . & . & . & . \\ . & . & . & . & . & . \\ 1 & x_n & y_n & x_ny_n & x_n^2 & z_n \end{bmatrix}} \quad \underset{\text{G matrix}}{\begin{bmatrix} a_0 \\ a_1 \\ a_2 \\ a_3 \\ a_4 \\ a_5 \end{bmatrix}} = \underset{\text{L matrix}}{\begin{bmatrix} dh_1 \\ dh_2 \\ . \\ . \\ \\ dh_n \end{bmatrix}} \qquad (51)$$

where x_1, y_1 are the co-ordinates of point 1 taken from the left plate

z_1 = the 'z' term calculated for point 1 using equation (50). This term accommodates the terrain elevation variations.

$a_0 - a_5$ are the transformation parameters for the deformed reference plane.

dh_1 = (true height of point 1 minus the calculated crude height of point 1).

n = the number of control points used in the adjustment.

The transformation parameters, $a_0 - a_5$, are calculated using equation (47). The modified program has the same output as that of the standard program described in section 4.9.3.2.A.

B Simulated Configuration Analysis Using Modified Program.

To test the modified program the procedure followed for the second run of section 4.9.3.4 was repeated. All 20 targets of plane 3 plus the 9 lead balls were used as control points, and the same camera station and control point data used again. The calculated differences between the true and calculated control 'heights' were then analysed. The standard deviation of a single observation and the average absolute error were now 2,23 mm and 1,77 mm respectively. This is similar to the accuracy which was achieved using the standard program when heighting points in a single plane. The modified program is evidently able to accommodate the height differences between the plane 3 targets and the lead balls.

The next experiment was designed to test whether the then existing stereoplotter control point configuration in the basin (described in section 4.7.2.3) was adequate for wave height analysis using the modified program. For this investigation the procedure followed for the first run of section 4.9.3.4 was repeated using the modified program. All 20 targets of plane 3 were used to calculate the transformation parameters and then the heights of the lead balls were calculated. The average absolute heighting error for the balls was 54,5 mm.

The anomalous result described above was thought to be due to the fact that the control points were all approximately in the

same plane. This means that the program was not able to find an appreciable variation in Z and thus could not formulate the correct transformation parameters. It was obvious then that when using this program, control points in more than one plane would have to be used. For a wave height measurement configuration it is suggested that two control point planes be used, situated at levels above and below the water surface.

The next experiment carried out was designed to investigate the heighting accuracies obtainable when the parallaxes are measured using a conventional parallax bar and mirror stereoscope compared to the heighting accuracies obtainable when the parallaxes are measured using a stereocomparator. As the stereoplotter control point configuration had been found inadequate for analysis carried out using the modified program, it was decided that the test field should be used to simulate a control point configuration in which the water surface lay between two control point planes. Four targets from plane 3 (namely 12, 42, 73, and 76) and four targets from plane 2 (namely 5,8,69, and 72) were selected as control points.

The parallax measurements of the test field targets selected as control points, and of the 9 lead balls were taken from the glass plates using the Wild parallax bar and mirror stereoscope, while the x,y co-ordinates for these points were taken from a contact print of the left plate. The parallax measurements of the selected test field targets and lead balls, plus the left plate x,y co-ordinates for these points were also measured stereoscopically using the stereocomparator. These two sets of data were then analysed using the program 'PARAMOD'. The base, 'flying height' and principal distances were 1,9 m, 5 m and 100 mm respectively. Using the parallax bar and mirror stereoscope data, the heights of the lead balls were determined with an average absolute error of 3,40 mm, the corresponding value obtained using the stereocomparator data was 2,89 mm. The corresponding standard deviations of a single observation were 3,83 mm and 3,10 mm respectively.

4.9.3.6 Conclusions.

A The Standard and Modified Parallax Bar Heighting Programs.

The standard program, which is based on equation (45), can only be used when the points to be heighted closely bracket the control

point plane. It is suggested that this technique could be successfully used to measure water surface elevations if the wave heights were small relative to the 'flying height' of the cameras and the control plane level coincided with the still water level.

For configurations where the standard program would give poor results, due to excessive elevation variations relative to the flying height, the author is of the opinion that the 'PARAMOD' program can be used. For this program the control point configuration should consist of two or more planes. Two planes are recommended, at levels above and below the still water level.

B Stereocomparator versus Parallax Bar.

The investigation described in Section 4.9.3.5 B showed that the heights calculated using parallax readings taken with a stereocomparator were 18-24% more accurate that those which were calculated using the parallax bar and mirror stereoscope. This is probably due to the fact that the stereocomparator can measure the parallaxes with an accuracy of 0,002 mm, while the parallax bar has a corresponding accuracy of 0,02 mm. Also, the x and y co-ordinates from the left plate can be measured with an accuracy of 0,005 mm with the stereocomparator, while they can only be measured with an accuracy of 0,2 mm from the positive print of the left plate. The accuracy advantage using the stereocomparator is thus not very great, but its real advantage over the parallax bar and mirror stereoscope is the far greater speed with which it can measure the parallax differences between various points.

4.9.4 General Conclusions and Recommendations.

It was shown (in section 4.9.3.5 B) that a parallax bar and mirror stereoscope could be used to measure water surface elevations with a potential measuring precision of 1:1300. For this experiment the parallax measurements were taken directly from the glass plates, and the point x,y co-ordinates were measured from a contact print of the left hand plate. The data was analysed using the program 'PARAMOD'. Note that for this investigation all the photographs were taken with the Zeiss Jena UMK Metric cameras described in section 4.4.1. In section 4.8.7.5 it was shown that these Zeiss cameras have a potential measuring precision 3,2 times superior to that obtainable using high quality 35 mm non-metric cameras. In the above accuracy comparison the image points were measured directly from both the Zeiss

glass plates and the 35 x 24 mm negatives, using a stereocomparator. It is estimated that if non-metric cameras are used a measuring precision comparable to that achieved with the metric cameras is possible if the parallax measurements are taken from paper print enlargements (10 x enlargements). The principal distances of both the left and right prints of the stereopair would have to be determined using the digitiser tablet and the theory of projective transformations.

The recommended procedure which should be followed in order to measure water surface elevations in a model harbour basin using non-metric cameras and the mirror stereoscope/parallax bar/deformed reference plane theory system is:-

(1) Set up a control point system of 16 or more targets in the wave basin. Make sure that all 16 targets will appear in the stereoscopic overlap area of the two cameras. It is suggested that each target be individually illuminated. Determine the space co-ordinates of the control points using conventional surveying techniques.

(2) Set up two non-metric cameras above the basin. The camera axes should be approximately parallel to each other, perpendicular to the camera base, and normal to the basin floor. The camera base should be as large as possible commensurate with the required stereoscopic overlap area. The camera firing and flash systems should be similar to those described in sections 4.6.4 and 4.6.6 respectively, and the water surface should be rendered opaque by using cutting oil as described in section 4.6.1.

(3) At the predetermined time, take a stereopair of the deformed water surface. Make paper print enlargements (10 x enlargements) from the negatives and determine the principal distance for both the left and the right print. The principal distances are determined by setting up the prints on a digitiser tablet, digitising the left and right print images of each of the 16 control points, and analysing this data using the program 'TESTFIELD'. In addition to determining the principal distances of each print, the program also calculates the space co-ordinates of the perspective centres of the two cameras. The cameras' 'flying height' can thus easily be calculated.

(4) The prints are then set up for stereoscopic viewing and the parallaxes of the 16 control points determined using a parallax bar and mirror stereoscope. The x, y image co-ordinates of these control points are then measured from the left print. This data is then analysed using the program 'PARAMOD' which calculates transformation parameters (i.e. the coefficients of equation (49), the heights of the control points, and the differences between the true and calculated control point heights. These differences will highlight any gross measurement errors made when observing the control points.

(5) The parallaxes and left print image co-ordinates of points on the water surface are then measured using the procedure described above. This data is then analysed using the program 'PARAMOD', which calculates the water surface elevations at the selected points.

The above system would be suitable for the measurement of model harbour water surface elevations using only two non-metric cameras, a mirror stereoscope, parallax bar, digitiser tablet and microcomputer

4.10 Laboratory Wave Height and Pattern Measurement using Close Range Photogrammetry - An Overview and Forwardview.

4.10.1 Laboratory Photogrammetric Wave Height and Pattern Measurement Techniques.

4.10.1.1 Close Range Photogrammetry versus Conventional Wave Height Measurement Techniques.

The general advantages of using close range photogrammetry as a measurement technique have been listed in section 4.1.1. This section will cover the particular advantages of using close range photogrammetric techniques for the measurement of wave heights and patterns in model harbours.

Two main limitations in conventional experimental procedures are encountered when attempting to measure accurately the wave height distributions within model harbours; these are:-

(1) Wave heights in model harbours are commonly measured using parallel wire resistance or capacitance wave probes. A number of these probes are usually mounted on a moveable

instrument carriage which can traverse the wave basin to measure the wave heights. Such a configuration was used by Harms (1976, 1979). The disadvantage of this system is that the wave height at only a limited number of discrete locations can be measured at any one time. The system is also time consuming, since the instrument carriage has to be moved within the wave basin until the entire water surface has been measured. Furthermore, excessive spacing of these wave probes may result in points of maximum wave heights being overlooked.

(2) Wave measurements using the above system necessitate (in most cases) that the wave paddle must run continuously. This enables secondary effects, (such as wave reflections, basin oscillations, cross waves, etc.) to develop and distort the generated wave, thus causing marked anomalous wave height variations along the generated incident wave crests. These problems were encountered by researchers such as Harms (1976, 1979) and Goda et al (1971, 1973) and are discussed in Section 5.3.

The two major problems which prevent the accurate measurement of wave heights in model harbours using conventional techniques have been successfully solved using the photogrammetric technique. Problem (1) is solved since the two stereopairs of photographs can be taken in a much shorter period than is required for a scan using wave probes, and the information contained on the plates is permanent, synoptic and detailed. Furthermore, there is no instrumental interference in wave processes being observed. Problem (2) can be overcome by using the infinite basin technique described in section 5.4, that is by photographing before the wave energy is reflected from internal walls, thus eliminating the distorting effects of wave reflections within a model basin. The infinite basin technique effectively enables the researcher to model accurately the situation of a continuous wave train entering a basin of infinite extent.

Three areas of utilisation for the photogrammetric wave height and pattern recording technique appear possible,

the first is the routine use in applied investigations where refraction or diffraction effects are important, for example, the analysis of model harbour configurations. The second is to make use of the procedures as a check on the validity of various existing wave theories, where the information obtained (instantaneous and high accuracy) should be decisive. The third area of utilisation is to apply the technique in close conjunction with mathematical modelling (such as finite element modelling) in order possibly to calibrate the models and thus improve their predictions.

4.10.1.2 Water Surface Elevation, Wave Height and Pattern Measurement Techniques.

The four techniques developed by the author will be discussed in ascending order of the cost of the required analysis equipment. The techniques are:-

(1) The parallax bar/mirror stereoscope/theory of the deformed reference plane technique.

This technique is the cheapest to use as regards equipment costs. To use this method the following equipment is required, namely: 2 non-metric cameras, a parallax bar, a mirror stereoscope, a digitiser tablet and a micro-computer. The analysis procedure for the technique is described in Section 4.9.4. This system might be the cheapest but though accurate, it is the most time-consuming of the techniques. It is only recommended if a small amount of water surface elevation data is required. The author only investigated the potential of the technique for water surface elevation measurements from a single stereopair. He did not investigate its wave height measurement potential, and this aspect of the technique has yet to be developed.

(2) The mirror stereoscope/electronic parallax bar/digitiser tablet/projective transformation theory technique.
This technique is marginly more expensive than technique (1) since it requires the construction of a modified mirror stereoscope and electronic parallax bar, such as described in Section 4.4.7. However, the greater

expense is compensated by the fact that the method though less accurate, is quicker and easier to use than technique (1) The suggested analysis procedure for technique (2) is described in Section 4.8.6.2. Again, the author only investigated the potential of the method for water surface elevation measurements from a single stereopair. The wave height measurement accuracy potential should be $\pm \sqrt{2}$ times the potential water surface elevation measurement accuracy.

(3) The stereocomparator/micro-computer/projective transformation theory technique.

This technique is the most accurate of the four. The author estimated that the potential wave height measurement precision of this system was 1:3250 or $\pm$1,6 mm at a 'flying height' of 5,2 m. These figures are derived from the potential wave height measurement accuracy investigations described in Sections 4.8.4 and 4.8.5.5. A brief description of the analysis procedure which should be followed when using this system is given in Section 4.8.5.4 .

It is suggested that this technique should be adopted by any research organisation intending to carry out an extensive laboratory wave height and pattern investigation. Due to the measuring precision of a stereocomparator, it is recommended that only precision, large format non-metric or metric cameras be used for the photography.

(4) The stereoplotter technique.

This is the most expensive technique in terms of the specialist analysis equipment needed. The stereoplotter analysis procedure requires that the photographs to be analysed are taken with a metric camera. So to use this method one not only needs a stereoplotter (approximately R100000) but also two large format metric cameras (approximately R16000 - R30000 each). In spite of the fact that this method is the most expensive, it is not as accurate as technique (3), in fact if metric photography is used, the stereocomparator technique is twice as accurate as the stereoplotter technique. Furthermore,

when using a stereoplotter for close range photogrammetric applications, one runs into convergency error problems which do not arise when using the stereocomparator/projective transformations technique. The author would recommend that the stereoplotter technique be used only by an organisation which already possesses a stereoplotter and a pair of metric cameras, and already employs an experienced stereoplotter operator.

A direct comparison of the water surface elevation measurement accuracies obtainable using techniques (1), (3) and (4) was also undertaken. A description of this investigation is given by Adams and Pos (1984). Technique (2) was not included in this comparison since it had been previously ascertained (Section 4.8.6.3) that this method did not meet the accuracy requirements of the author.

The investigation was carried out using the plates for the top most stereopair shown in Fig. 4-46. Details of this model harbour configuration are given in Section 4.8.5.4. Sixteen well defined trough and crest points were selected along the breakwater gap centre line, from between the splitter plates to the back wall beach. The water surface elevations of these points were then determined using the three above mentioned techniques. The results obtained are given in Table 4-12 and again illustrate the superior accuracy of technique (3). On the premise that the average of tabulated results 2-6 were the best elevation values, the standard deviations of single elevation determinations were calculated as indicated. All 16 control points were utilised in the analysis procedures.

For the technique (1) investigation parallax bar measurements were taken using both contact scale and 2x enlargement prints. Furthermore the results were analysed using both the 5 parameter equation (45) solution (program "PARA") and the 6 parameter equation (49) solution (program "PARAMOD"). The high precision obtained by the lowly parallax bar was an interesting feature of this exercise despite the tedium of the observing procedures.

WAVE POINT	PARALLAX		BAR		TOPOCART plotter	STEKO comparator	AVERAGE
	CONTACT SCALE		2X ENLARGEMENT				
	PARAMETERS		PARAMETERS				
	5	6	5	6			
	1	2	3	4	5	6	2 - 6
1	80,6	82,3	84,8	85,0	84	83,6	83,9
2	23,3	26,0	34,8	35,1	33	32,1	32,2
3	76,4	78,2	78,5	78,8	78	76,6	78,0
4	29,9	32,5	32,2	32,6	31	28,9	31,4
5	82,5	84,3	85,0	85,2	88	84,4	85,4
6	33,0	35,7	33,2	33,6	33	35,7	34,2
7	71,4	73,5	70,7	71,0	74	71,1	72,1
8	34,5	37,2	33,0	33,4	36	34,0	34,7
9	65,2	67,5	68,1	68,4	71	69,3	68,9
10	34,1	36,9	33,7	34,1	37	34,9	35,3
11	60,5	62,9	61,7	62,0	64	62,8	62,7
12	39,4	42,2	40,7	41,1	37	37,9	39,8
13	63,4	65,8	68,6	68,8	68	67,2	67,7
14	41,2	44,0	41,0	41,4	39	39,3	40,9
15	60,5	63,0	63,1	63,4	61	61,3	62,4
16	45,5	48,3	46,4	46,7	42	43,8	45,4
STD.DEV-IATION	± 3,14	± 2,40	± 1,21	± 1,24	± 1,80	± 1,16	

4.10.2 Future Developments.

4.10.2.1 Projective Transformations.

A technique which the author suggests has an application in the measurement of wave heights and patterns in a large wave basin is being developed by Professor L.P. Adams and Dr.H. Rüther of the Department of Surveying at U.C.T. Two non-metric cameras are mounted on a steel bar so that the cameras ' base and relative orientations remain constant. Then the projective transformation parameters for both the left and the right camera are determined by taking a stereopair of a test field configuration in the laboratory using the procedure described in Section 4.8.4. Imaged on each photograph are 4 reference marks (similar to fiducial marks) and the measured comparator co-ordinates are transformed so that the new co-ordinate origin coincides with the centre of gravity of the four measuring marks. The camera system can now be used to take stereopairs of any object in or outside the laboratory and the object's space co-ordinates can be calculated using projective transformations. This is achieved by transforming the object stereopair into the exact comparator positions occupied by the test field stereopair, using a Helmert transformation.

Using the above technique the projective transformation parameters of the two rigidly mounted cameras would be determined by taking a stereopair of a test field configuration. The cameras could then be mounted above the wave basin and used to take stereopairs of the deformed water surface. The water surface elevations could then be determined using the projective transformation parameters calculated from the test field stereopair, and the image co-ordinates measured from the wave stereopair, the second stereopair having been transformed into the co-ordinate system of the first. Only two limitations are imposed by the system, namely:-

(1) The cameras' 'flying height' above the water surface must be roughly equivalent to the distance at which the cameras are set up from the centre of the test field control point configuration.

(2) Some sort of ground scale should be included in the stereopairs of the water surface.

4.10.2.2 High Speed Photography.

Some good examples of a photogrammetrist's extraction of valid data from ciné-camera records are given by van Wijk and Zieman (1976). An outline of the generalisation of the photogrammetric central projection is given, followed by a number of examples of applications. In one example a system is described which could be applied to the measurement of dynamic wave phenomena in a glass walled wave flume.

4.10.2.3 Video Recording.

In ciné-photography the sorting of data from the worthwhile frames in the very great number taken in a free-running high speed camera is laborious, and must, of course, await processing of the film and availability of monitoring or projection facilities. For the monitoring of dynamic wave phenomena, videorecording has many advantages over ciné-photography, however the resolution is rather modest. With conventional systems the resolution may be only of the order of 1/500 of the field dimension, but the field is redetermined every 1/25 second, giving possibilities of interactive operation with time integration.

The author used video recording and parallel ray oblique lighting techniques at night to record the radiating second order phenomena in gravity waves described by Biesel(1963, 1966) in the wave basin at U.C.T. Section 5.6 describes this investigation in which the secondary waves radiating from the tips of the breakwaters were recording using video recording and conventional photographic techniques.

5. EXPERIMENTAL WORK

5.1 Previous Wave Diffraction Experimental Work

5.1.1 Introduction

The author was primarily interested in the diffraction of water waves passing through a breakwater gap, and a detailed description of previous experimental work for this configuration is given in the following section. However, the breakwater gap situation can also be thought of as a gap between two semi-infinite breakwaters, and so a brief review of previous semi-infinite breakwater diffraction experimental work is thought to be appropriate. The two major experimental investigations of the semi-infinite breakwater diffraction phenomenon are attributed to:-

(1) Putnam and Arthur (1948)

A semi-infinite breakwater, with a splitter plate located at the tip, and a wave absorbing beach on the seaward face of the breakwater, was tested at several angles of wave incidence. The general model basin layout is shown in Fig. 5-1. The incident wave was measured at a single point (station "A"); typical wave conditions were a water depth of 457 mm, T = 0,70 seconds, L = 762 mm, $H_i/L = 0{,}035$ and $d/L = 0{,}60$ (H_i and L are respectively the incident wave height and wave length). The investigation thus simulated a deep water condition. In addition to the 90° corner, several rounded tips were tested; it was concluded that the geometrical shape of the breakwater tip has no significant influence on the wave diffraction pattern.

It was found that the agreement between theory (Penney and Price solution) and experiment was good within the shadow region of the breakwater, but that in the unprotected region the experimental values were considerably less than the predicted values. Putnam and Arthur present a simplified solution (not valid within a 2 L radius from the tip) and demonstrate that this is in good agreement with experimental results. The effect of wave period upon the diffraction profiles was concluded to be negligible. One wave recorder was always operated at station A, while 5 recorders were operated at selected stations in the lee of

the breakwater. The wave paddle ran continuously while the 5 recorders were moved about the basin until the entire area beyond the breakwater had been covered.

(2) Harms (1976, 1979b)

Laboratory tests were performed for two structural configurations of the breakwater, as shown in Fig. 5-2, and with the waves normally incident upon the breakwater. In one case the tip Section (Tip B in Fig. 5-2) consisted of a vertical steel plate of length 1,6 L that was unobstructed at the extremity for a distance of approximately 0,1 L. The rest of the steel plate was lined with a wave absorbing material. In the second series of experiments, a wave splitter plate of length 1,3 L was additionally mounted to the steel plate tip section, and energy absorbing material added to the tip (Tip A in Fig. 5-2). The first 7,9 m of the structure was provided with a beach of low reflectivity (this section was never altered). The water depth was 270 mm and the incident wave had a period of 0,67 seconds and a mean height of 27 mm. Harms found that the two dimensional motion of the wide wave generator produced highly three dimensional long crested waves. The ratio of maximum to minimum wave height along the crest line was typically $\geq 1,5$. This irregular wave field reduced the validity of the resultant diffraction diagrams.

Harms concluded that in general, satisfactory agreement was obtained between measurement and theory, but that diffraction theory was not found to be conservative (as stated by Putnam and Arthur). In fact, at large distances into the shadow zone, measured wave heights were found to consistently exceed theoretical values. Close to the breakwater outside the shadow zone, the measured maximum wave height was again larger than predicted by theory. He also concluded that the wave splitter plate had only a minor effect within a radius of four wave lengths from the tip, and that the diffraction behavior appeared to be insensitive to the intensity of wave reflections from the seaward side of the breakwater. Furthermore, he stated that no consistent, significant difference could be detected

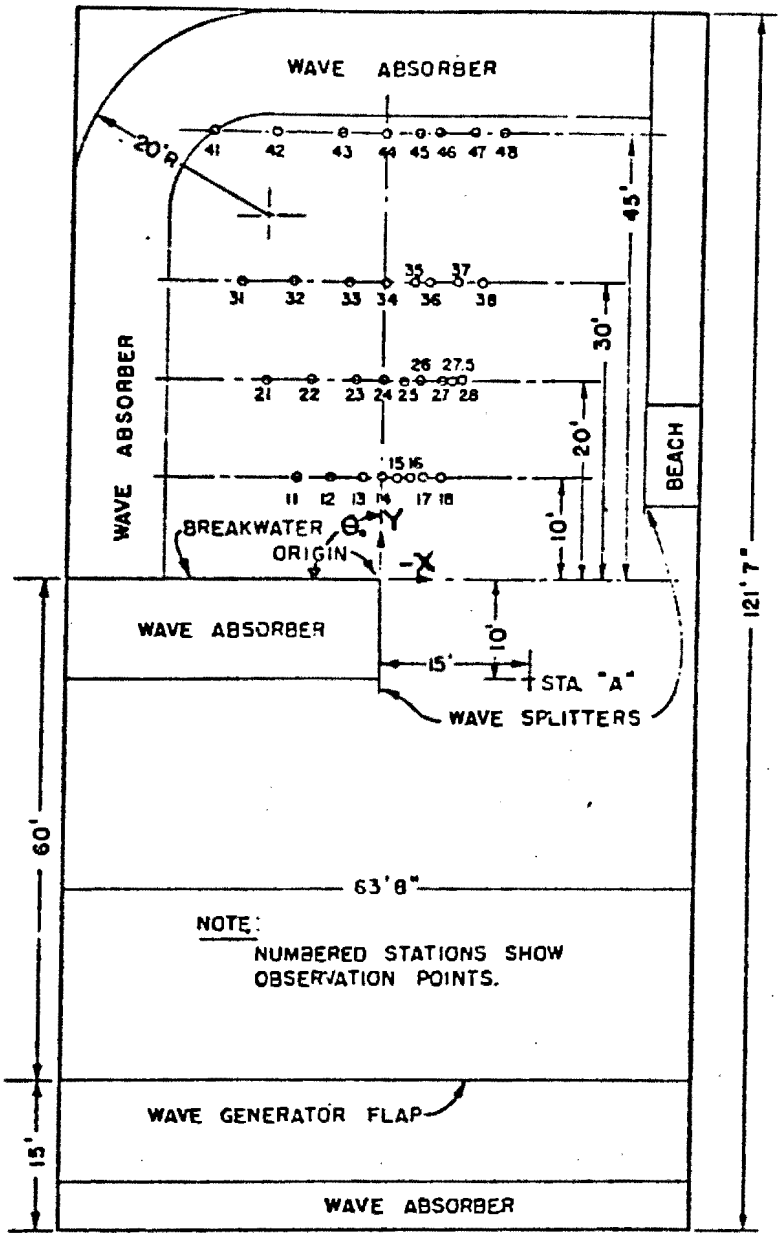

Fig. 5-1 Layout of wave basin for experiments by Putnam and Arthur (from Putnam and Arthur, 1948).

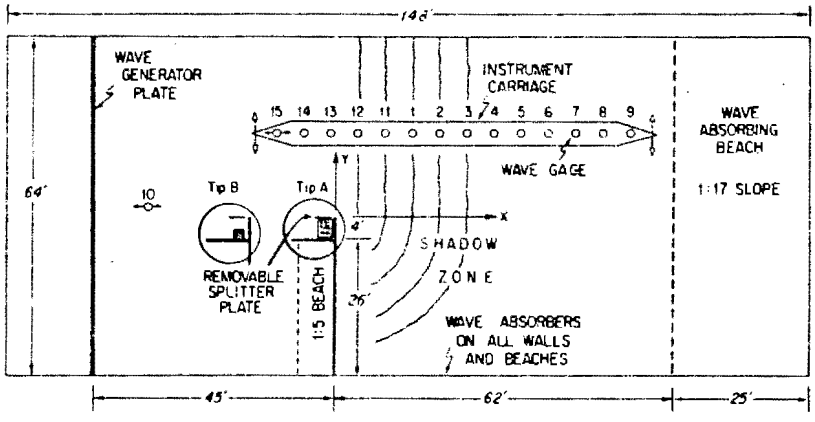

Fig. 5-2 Layout of wave basin for experiments by Harms (Harms, 1979b).

between data obtained by the "intermittent" mode, in which data must be collected before reflections are set up in the basin, and the "continuous" mode in which the generator runs continuously.

A limited diffraction investigation was also carried out by Silvester and Lim (1968) while Mobarek (1962), Pantazaras (1979), Hales (1980) and Houston (1981) looked at the refraction-diffraction problem of a breakwater with a linear bottom slope. It is however apparent that more experimental work is needed to establish whether the diffraction theory for the semi-infinite breakwater is in fact conservative or not.

5.1.2 The Diffraction of Water Waves Passing Through a Breakwater Gap.

Three previous experimental investigations into the diffraction of water waves passing through a breakwater gap are to be examined in detail, namely the investigations of Blue and Johnson (1949) and Carr and Stelzriede (1952) and Memos (1976; 1980c). These investigations are exceptional since they include both experimental results in addition to a detailed theoretical treatment.

5.1.2.1 Blue and Johnson (1949)

It should be noted that the above publication is a condensation of a PhD thesis completed by the senior author at the University of California, Berkeley, 1948 (Blue, 1948).

Blue and Johnson set out to check experimentally the diffraction theory for a gap in a breakwater normal to the incident wave travel direction, using both deep water and shallow water waves. The experiments were carried out in the Fluid Mechanics Laboratory at the University of California. Studies were first made in a small 1,83 m by 3,66 m basin, 305 mm deep, and then later in a larger basin, 19,51 m by 19,81 m in plan by 610 mm deep. The basin floors were horizontal in all tests. The direction of travel of the incident wave was normal to the gap in both the small and large basins.

Fig. 5-3(a) shows, for the small basin, the arrangement of the wave generator, breakwater gap, wave absorbers and the positions at which wave height measurements were made. The basin was used as a half model, one side representing the centre line at the gap. A wave splitter plate extended from the breakwater tip to the wave paddle. The incident wave, therefore, travelled through

a 914 mm long channel before passing into the leeward side of the breakwater. This arrangement was varied by changing the width of the approach channel (or half-gap) to represent full gaps of 305 mm, 457 mm and 610 mm. The arrangement of Fig. 5-3(a) was changed for another set of runs by adding a wall to extend from the edge of the gap into the protected area at angles of 60° and 45° to the wave direction, thus representing a symmetrical breakwater with inclined wings. Tests were carried out for wave periods ranging from 0,26 second upwards and water depths ranging from 41 mm to 183 mm. A wedged-shaped plunger was used for water depths 122 mm to 183 mm, while a curved plunger was used for depths 41 mm to 91 mm.

In the large basin (see Fig. 5-3(b)) all runs were made with a centrally located gap, 1625 mm wide, without wave splitters. The edges of the gap consisted of 6,4 mm sheet metal plates which extended 165 mm beyond the wooden walls forming the breakwater. Waves were generated by a hinged flap wave paddle. Tests were carried out for wave periods ranging from 0,64 to 0,94 seconds and water depths ranging from 146 mm to 457 mm.

Wave heights were measured in both basins using parallel wire resistance wave probes. In the small wave basin, one probe was mounted in the approach channel (see Fig. 5-3(a)) to obtain the incident wave height, while three to five others were mounted on an aluminium beam which could be moved into the various positions in the lee of the breakwater, indicated in Fig. 5-3(a). In the large wave basin, 13 wave probes were mounted at the positions indicated on Fig. 5-3(b). Diffraction co-efficients K′ were found by dividing the station wave heights by the incident wave height recorded at the same time. The experimental wave patterns were traced from photographs taken from a position vertically above the basin. The tests were carried out with the paddle running continuously.

Blue and Johnson's experimental results are now summarised. The author has included his comments where they are thought appropriate. The convention used by Blue and Johnson when describing their results is given in Fig. 5-4. Their findings were as follows:-

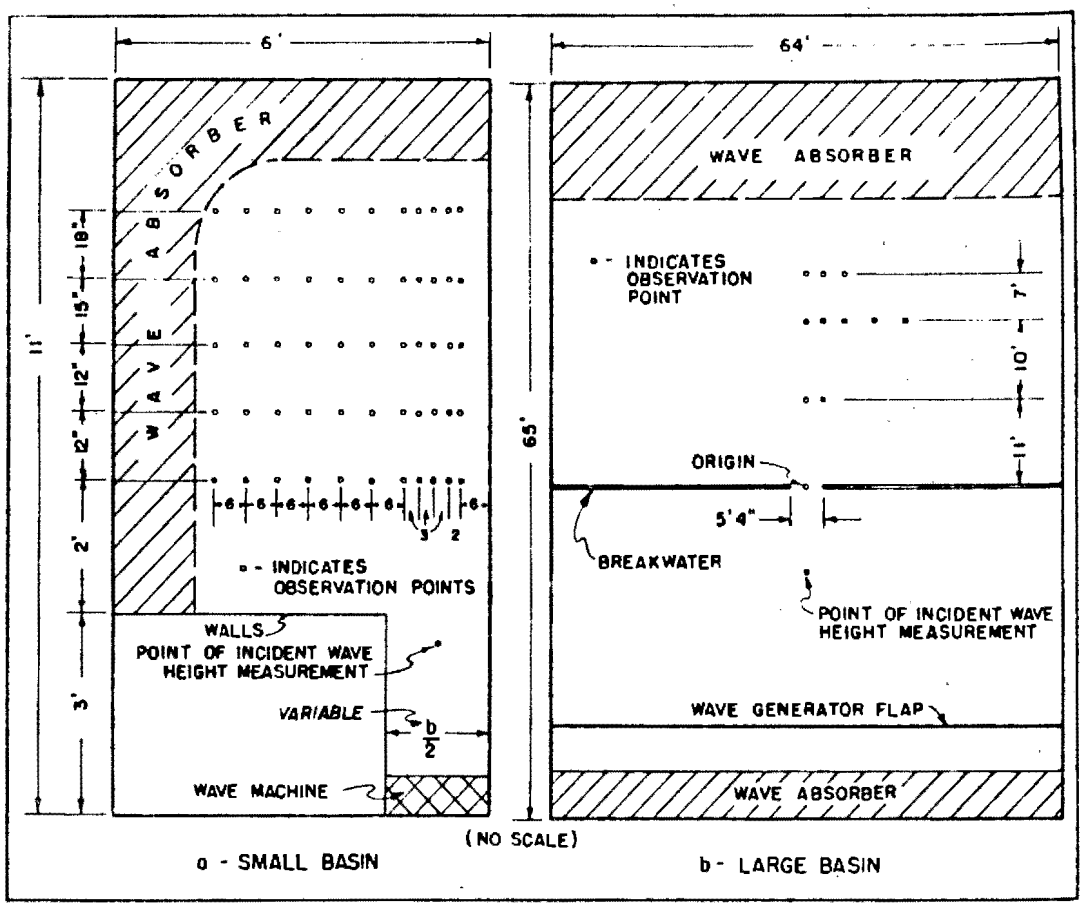

Fig. 5-3 Layout of wave basins used by Blue and Johnson (from Blue and Johnson, 1949).

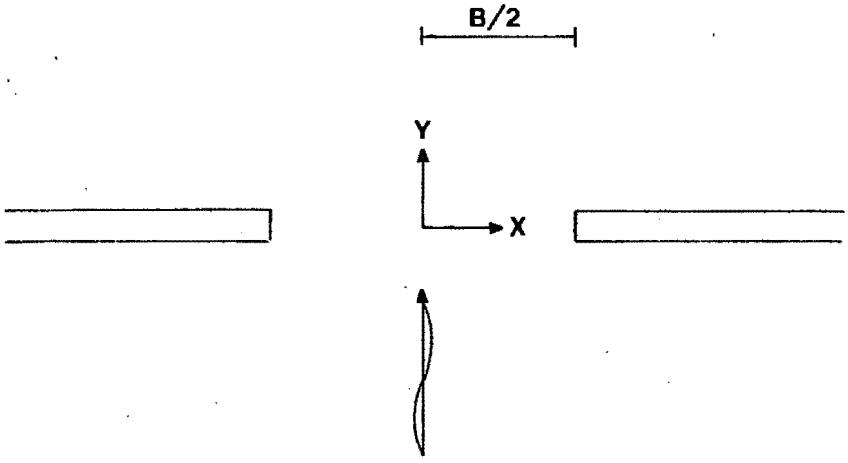

Fig. 5-4 Experimental convention.

(1) For X = 0 (gap centre line) observed K′ (diffraction co-efficient) was found to fall below theoretical K′ with increasing Y/L (L is the incident wave length). This drop off was found to be most rapid for the short waves (minimum L = 140 mm) and less rapid for the longer waves (maximum L = 914 mm). For plots along X = 0 and X = B/2 it appeared that as the waves became longer, experimental K′ approached theoretical K′ as an approximate limit.

NOTE:- The experimental results were compared with the full Penney and Price (1952) solution, as well as a simplified solution, developed by Blue and Johnson, to allow for the effects of the splitter plates. These two solutions are described in Chapter 2.

(2) In areas more distant from the centre line, this dropping off of K′ was less evident. In fact, there was a distinct tendency for experimental K′ to exceed theoretical K′. This was regarded as due to the increased curvature of the wave crests in regions of steepest waves.

(3) Considering the whole width of the observed area, both the region near the centre line and regions distant therefrom, the trend was for the average experimental diffraction co-efficient to drop below the average theoretical co-efficient as Y/L increases, the drop being rapid for short waves and less rapid for long waves.

(4) Although the diffraction co-efficients for shorter waves and small Y/L exhibited considerable scatter, Blue and Johnson proposed that they tended to agree with theoretical values.

NOTE:- The scatter which was apparent for the shorter wave lengths can easily be understood if one takes a closer look at some of the short wave length situations investigated. Four short wave situations are given in Table 5-1.

It is doubtful whether any meaningful diffraction measurements could be made using incident waves of such small wave height, particularly when one considers the test configurations used.

Situation	Wave Length L	H_i/L	Incident Wave Height H_i
A	143 mm	0,05	7,2 mm
B	287 mm	0,07	20,1 mm
C	277 mm	0,06	16,6 mm
D	155 mm	0,09	14,0 mm

Table 5-1 Four short wave situations from Blue and Johnson (1949).

(5) To investigate the effect of friction at the wall located along the gap centre line, runs of the same wave length etc. were carried out both in the half and full model. No consistent difference between the two sets of results was observed.

(6) Runs were made with and without splitter plates, but otherwise they were identical. It was concluded that the splitter plates had no significant effect on the results.

(7) From the photographs, it was observed that successive crest positions tended to be more widely spaced than theoretically predicted along the gap centre line (X = 0), the difference decreasing rapidly as X increases and less rapidly as Y increases. This phenomenon was thought to be wave steepness related, since it was most pronounced in regions were the waves were the steepest.

NOTE:- This is understandable since wave celerity is also a function of wave height for higher order waves.

(8) Zones of wave crest discontinuity were apparent in the wave patterns. It was postulated that these zones were due to the effect of wave steepness combined with the existence of small theoretical diffraction co-efficients at these locations.

NOTE:- A possibly more plausible explanation for these discontinuities is the superposition of wave reflections, cross waves and basin resonance effects upon the diffracted wave pattern.

The conclusions of Blue and Johnson are summarised below. They concluded that:-

(1) The experimental results verified the general form of the wave diffraction theory for breakwater gaps with B/L ratios as small as 1,41 and d/L_0 (d = water depth, and L_0 = deep water wave length) ratios as small as 0,14.

(2) The theoretical wave patterns and diffraction co-efficients are modified by the relative steepness of waves in different areas. The waves in areas of greater steepness are longer than results from application of the theory without regard for steepness. This causes the crests to be sharply curved and the diffraction co-efficients to be smaller than given by the basic theory for such areas, while the diffraction co-efficients are increased in the adjacent areas.

(3) The wave crests tend to develop discontinuities along the zones of small theoretical diffraction co-efficients. This tendency is increased by the use of wave splitters.

(4) The diffraction co-efficients are not greatly affected by incident wave steepness, wave splitters or the use of a half model.

(5) Symmetrical breakwaters with wings inclined at 45° to 90° to the incident wave direction,are not greatly affected by the angle of inclination.

It is the author's opinion that the above conclusions are based on data which exhibits such a high degree of scatter, that only the most general of trends could be discerned. Silvester and Lim (1968) analysed the results of Blue (1948) and concluded that the results contain too much scatter to verify the theory. Figs. 5-5(a) and (b) show experimental results from Blue (1948) as given by Silvester and Lim (1968).

A study of Figures 5-5(a) and (b) (shown overleaf), substantiates the author's claim that no previous, conclusive experimental results have been achieved for the breakwater gap situation.

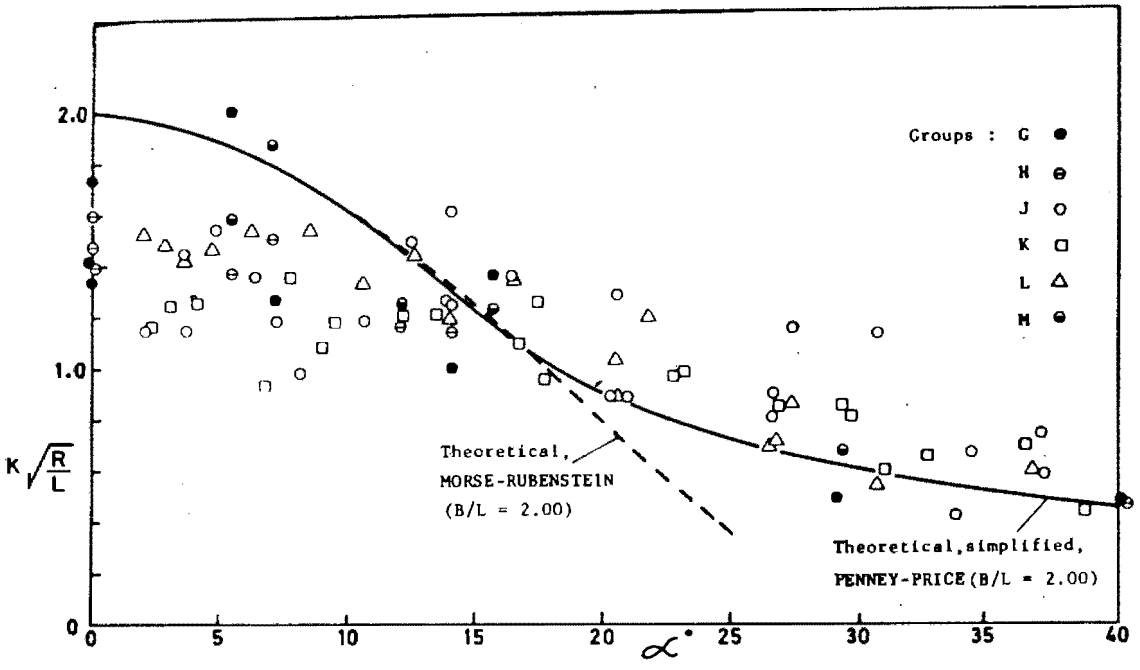

(a) Results for B/L = 1,95 and R/L = 4 to 10

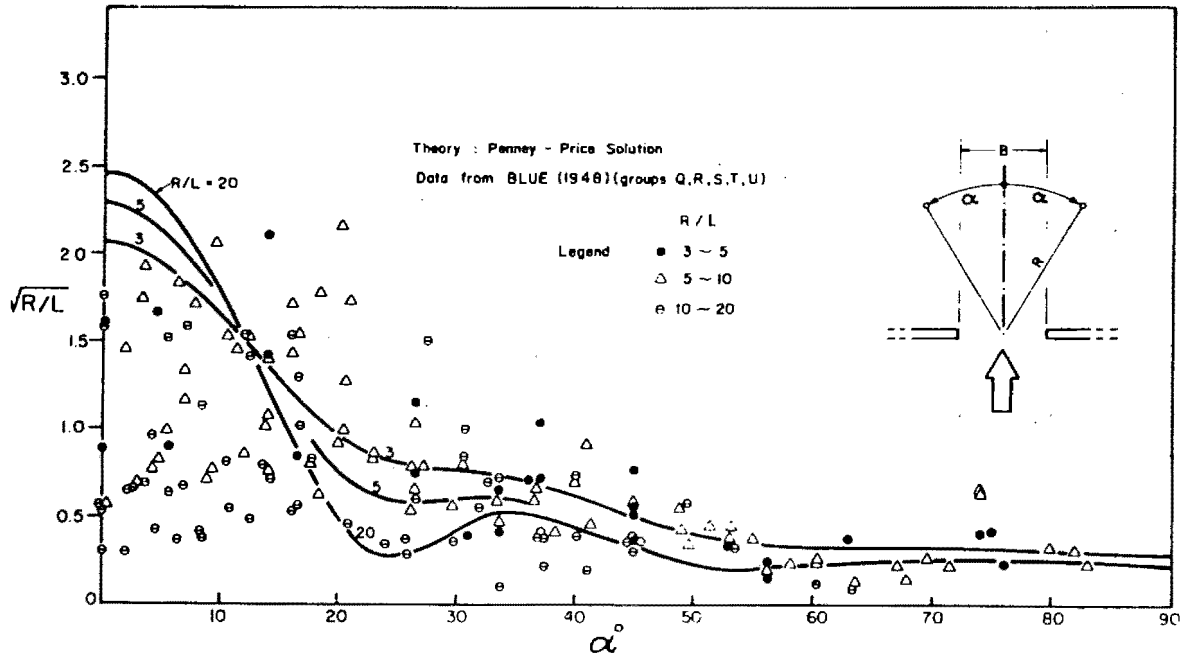

(b) Results for B/L = 2,5 and range of R/L

Fig. 5-5 Experimental results from Blue (1948).

5.1.2.2 Carr and Stelzriede (1952)

The primary purpose of Carr and Stelzriede's experimental program was to check their theoretical results (based on the Morse and Rubenstein (1938) solution) for vertical face, straight breakwaters. Carr and Stelzriede's application of Morse and Rubenstein's diffraction theory to the diffraction of water waves is described in Chapter 2.

The experimental investigation was carried out in the Hydrodynamics laboratory of the California Institute of Technology. The experiments were conducted in an L shaped basin (Fig. 5-6), 6,10 m wide by 18,29 m long, with an off-set portion 3,66 m by 7,32 m at the shallow end. The water depth at one end of the basin was 305 mm to accommodate one of the standard laboratory pneumatic wave generators, with the basin floor rising from this depth at a slope of 1 in 40 to a line where the depth was 76 mm The remainder of the basin had a uniform depth of 76 mm and this was the region in which the breakwaters and "harbour" were located. Pea gravel beaches were placed around the periphery of the harbour as wave energy absorbers. Different angles of wave approach were obtained by rotating the breakwater, the wave machine remaining fixed. The off-set portion of the basin provided space for a damping beach. It was postulated that this beach would prevent the re-entry of waves reflected from the breakwater into the region near the breakwater opening, thus simulating a basin of infinite extent. For cases where the breakwater was aligned at 60° to 90° to the wave direction, waves reflected from the breakwater were not intercepted by the side beach, but travelled the length of the basin, reflected from the wave paddle and so could interfere with the incident wave train. Difficulties of this kind were prevented by providing a sufficient distance from the wave generator to the breakwater, so that measurements could be obtained before waves reflected from the breakwater reached the wave generator.

NOTE:- The approach described above is essentially similar to the infinite basin technique described in Section 5.4, however, the major difference is the method by which the wave heights were measured. For each run Carr and Stelzriede only measured the wave heights at 16 points in a 45° sector with a radius of

5,76 wave lengths centred at the opening. On the other hand, using the infinite basin technique, one could determine the wave height distribution for the whole "harbour" area from only two runs.

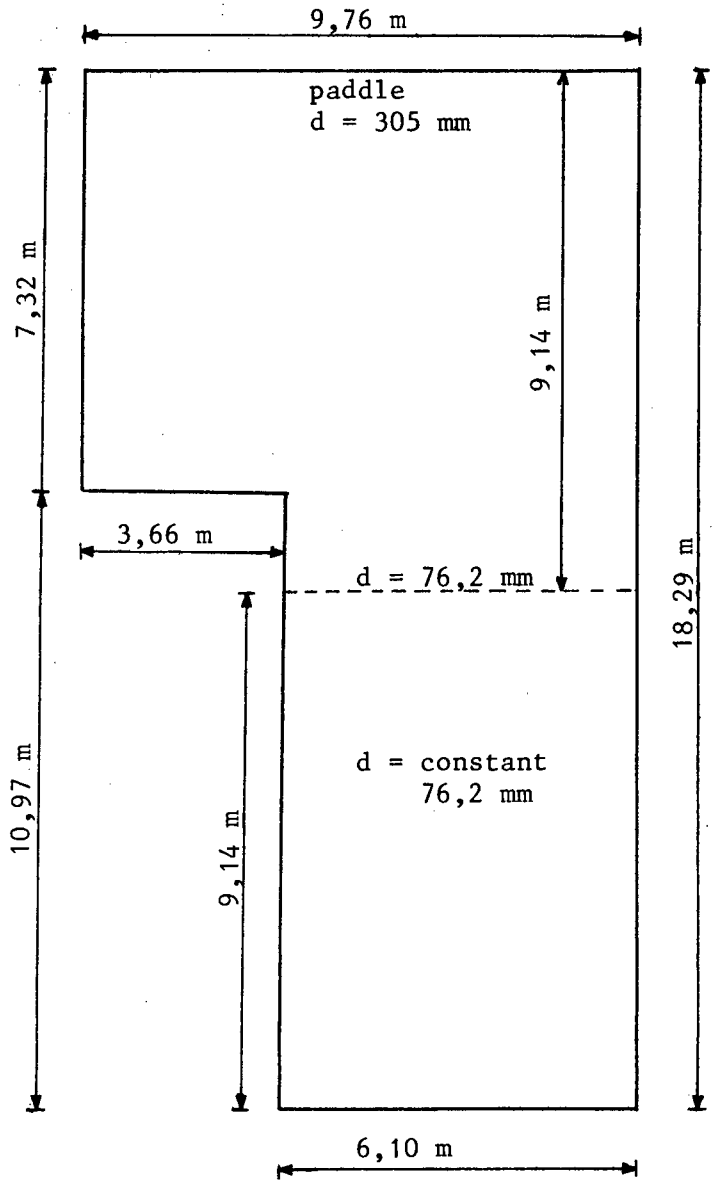

Fig. 5-6 Layout of wave basin used by Carr and Stelzriede.

Carr and Stelzried looked at two aspects of diffraction in their experiments, namely:-

(1) The Total Transmission Factor and the Intensity Factor.

The total transmission Factor $\bar{T}$ is defined as:-

$$\bar{T} = \frac{\int_0^{\pi} (H_{R,\phi})^2 R \, d\phi}{H_i^2 B} \qquad (1a)$$

and the Intensity Factor $I_{R,\phi}$ is defined as:-

$$\frac{(H_{R,\phi})^2 \, R}{(H_i)^2 \, L} \qquad (1b)$$

$H_{R,\phi}$ = wave height measured at ϕ, R inside the breakwater, with the origin at the gap centre.

H_i = wave height incident at the breakwater.

R = radius of the measuring circle.

B = gap width with same units as R.

L = the incident wave length.

The theoretical solutions indicated that for projected widths of openings, in the direction of the wave approach, greater than one half wave length, the effect of diffraction on the energy transmission is minor, but for smaller openings the energy transfer is larger than would be expected from geometrical considerations.

NOTE:- All the configurations investigated in the present investigation had gap widths of one half wave length or larger with the incident waves normal to the breakwater walls, and would therefore have theoretical T values very close to 1.

(2) Diffracted Wave Height Distributions in the Lee of the Breakwater Gap.

Three different types of breakwater configurations were investigated, namely:- (a) straight arms in line with each other, (b) straight arms inclined symmetrically with the axis consisting of the perpendicular bisector of the line of the opening, and (c) straight arms at right angles to each other, the leeward arm parallel, and the seaward arm perpendicular to the incident wave direction. The results of the first two types are summarised below.

(a) The agreement between experiment and theory, while not exact, was thought to be reasonably close, and to support the general conclusions of the theory. In particular, the experimental results verified

that the maximum value of the intensity factor is proportional to the square of the gap width, and that the effect of reducing the gap width is to distribute the energy more uniformly in the region behind the breakwater.

(b) Symmetrical breakwater arms converging seawards are sometimes called "wave traps". The experimental data showed that as the included angle between the breakwater arms was reduced from 180° (straight breakwater configuration) to 90°, there was virtually no change in the energy distribution. For still smaller included angles, marked changes appear due to the partial frustration of the diffraction process, or prevention of the free expansion of the wave crests. Thus the 60° to 30° alignments are marked by a decrease in intensity along the axis of symmetry and a build up in intensity along the breakwater arms.

The theoretical and experimental results presented in the above paper are not labelled or dimensioned and as such (in the author's opinion) can only serve as a qualitative guide to the diffraction phenomenon.

5.1.2.3 Memos (1976, 1980c)

Memos (1976, 1980c) carried out experiments to investigate the diffraction of waves passing through a gap between two breakwater arms forming an angle θ_1 in order to validate his theoretical solution (see Section 2.4.2.5). His experiments were carried out at the Imperial College Hydraulics Laboratory, London. The basin used for the diffraction experiments had inner dimensions 7,4 by 10,35 m. Energy absorbers, consisting of impermeable beaches, were placed along three sides of the basin while the fourth side was occupied by the wave generator which was of the plunger type. The wave heights in the basin were measured using a single parallel wire capacitance wave probe. An example of a typical experimental configuration is given in Fig. 2-20 of Section 2.4.2.5.

The incident wave used for the configuration shown in Fig. 2-20 had the following characteristics; wave period 0,66 seconds,

wave height 28 mm, wave length 680 mm, all for a water depth of 380 mm. The incident waves generated were thus deep water waves. The B/L ratio was 1,845 and the angle of incidence, measured from the leeward side of the left hand breakwater, was 240°. The angle subtended by the two breakwater arms (which were constructed from steel plate) was 120°. The model breakwaters were positioned in such a way that the incident waves were reflected towards the side wall beaches. The wave heights were measured at the positions, in the lee of the breakwaters, marked by small crosses in Fig. 2-20. The wave paddle ran continuously during the measurement period. In Fig. 2-20 both the theoretical diffraction diagram (calculated using the Memos solution) and the experimental diffraction coefficients are given.

From Fig. 2-20 it can be seen that there is a fairly good correlation between the experimental and theoretical results, but it is the author's opinion that the experimental measurements are far too sparse to serve as a really meaningful comparison. Furthermore the diffracted wave heights in the shadow zones would be very difficult to measure accurately due to the small incident wave height of 28 mm and the fact that the paddle ran continuously during the measurement period allowing cross waves, resonance, reflections and other basin effects to be fully developed.

5.1.3 Factors Affecting the Accuracy of Previous Experimental Work.

The advantages of using close range photogrammetric techniques for the measurement of wave heights and patterns in model harbours, have been discussed in Section 4.10.1.1. This Section will summarise the factors which were though to affect the accuracy of the diffraction experimental work reviewed in Sections 5.1.1 and 5.1.2. The factors which were thought to have affected the accuracy of the previous experimental work are:-

(1) Wave heights were measured at relatively few discrete points in the lee of the breakwaters, with the result that there was inadequate data available to compute accurate diffraction diagrams.

(2) In most cases the incident wave height was measured using only one wave probe. Bearing in mind the highly three dimensional long crested waves which can be generated in

a wave basin (Harms 1976, 1979), one wave probe would not generally give an accurate incident wave measurement, thereby further reducing the accuracy of the subsequent diffraction diagrams.

(3) For the bulk of the experiments, the measurements were taken with the wave paddle running continuously, thus enabling basin reflections, cross waves, resonance and other effects to achieve full development.

(4) In a large percentage of the previous experimental investigations, the incident wave heights were less than 30 mm. It is doubtful whether any meaningful diffraction measurements (particularly in the shadow zones) could be made using incident waves of such small wave height, particularly when one considers the additional effects of the previous 3 factors.

(5) In investigations where shallow water depths were used (Blue and Johnson 1949, and Carr and Stelzriede, 1952) any basin floor level anomalies would cause the diffraction results to be distorted by wave refraction effects. Furthermore, these shallow water depths would severely limit the wave heights of generated incident wave trains. The resultant diffracted wave heights would be very small and therefore difficult to measure accurately, particularly when one considers that secondary basin effects could possibly be of the same magnitude as the diffracted wave heights in the lee of the structures.

5.2 Initial Diffraction Experiments.

5.2.1 Introduction.

The initial diffraction experiments and results will be summarised briefly since they led directly to the development of the infinite basin technique (Section 5.4) and the stereoplotter/micro-computer/projective transformation theory technique (Section 4.8.5). A series of refraction configurations, such as waves shoaling on a submerged slope and refracting round a point island, were also investigated, but these results fall outside the scope of this thesis. The stereopairs taken of the point island configuration are shown in Adams and Pos (1981).

The initial diffraction configurations were analysed using the stereoplotter technique described in Section 4.7. The experiments were carried out using the "steady state" mode i.e. the wave paddle ran continuously and a steady state time independent wave field was assumed to exist in the basin. Two configurations were analysed, namely:- the breakwater gap, and a simulated off-shore breakwater. However, the author was primarily interested in the diffraction of waves passing through a breakwater gap, and most of the initial work was carried out on this configuration.

5.2.2 Experimental Configuration.

5.2.2.1 Wave Basin and Control Point Configuration.

The wave basin configuration with the breakwater gap model in position is shown in Fig. 5-7. The breakwater walls, consisting of steel box section tubing (200 by 75 mm), were placed parallel to the wave generator. Wave splitter plates constructed from 6 mm steel plating, were attached perpendicular to the breakwaters, extending from the breakwater tips to the wave paddle. 10 to 30 mm crushed stone beaches were laid out along the seaward side of the breakwaters and along the basin walls, as shown in Fig. 5-7, with a maximum slope of 1:5. The model configuration was therefore effectively modelling the situation of a gap between two totally absorbing breakwaters.

An attempt was made to model the totally reflecting breakwater situation by removing the splitter plates and the gravel beaches on the seaward side of the model breakwaters. For this configuration it was found that, on the seaward side of the breakwaters,

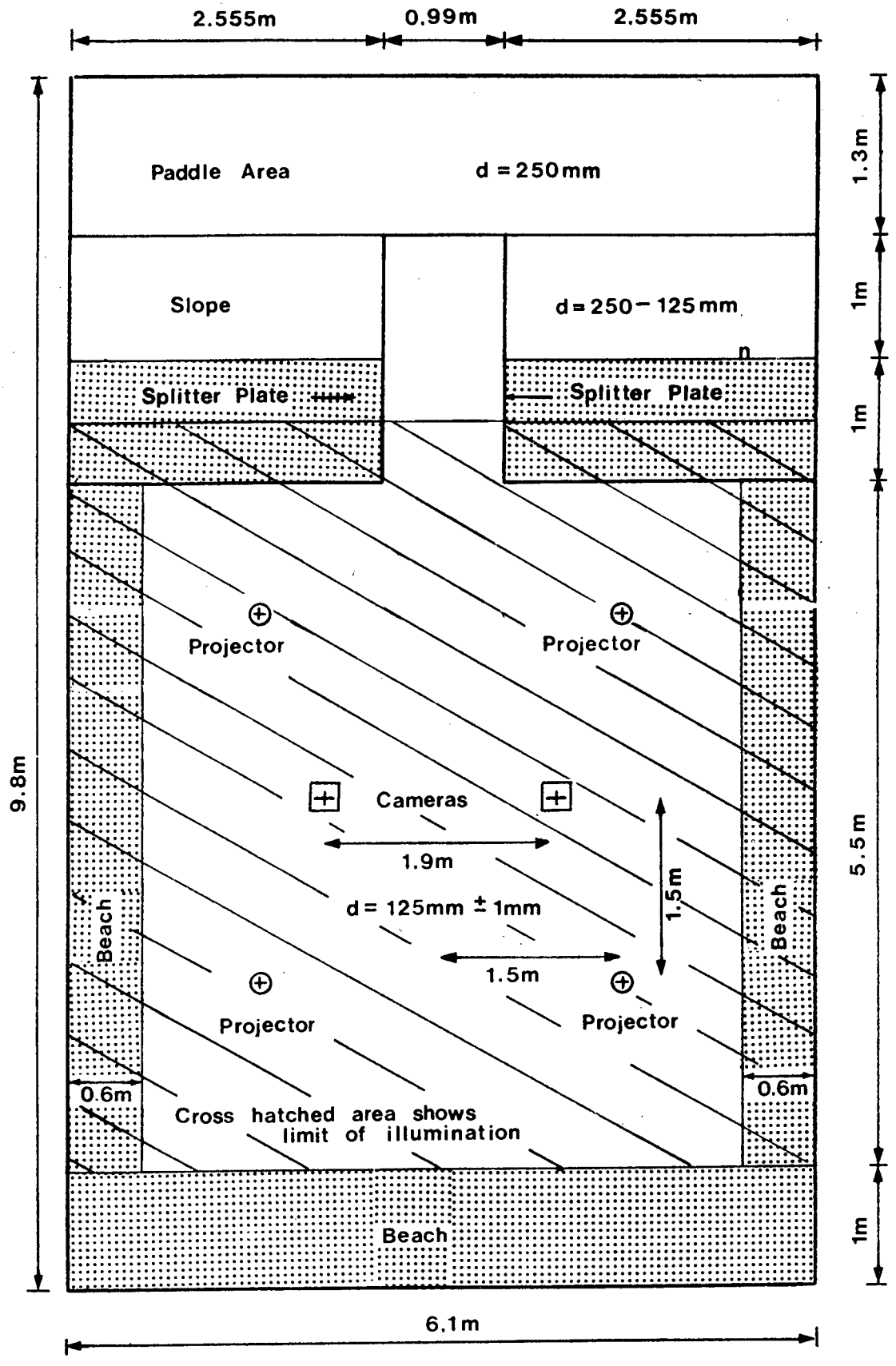

Fig. 5-7 Initial harbour configuration.

the waves reflected backwards and forwards between the breakwaters and the wave paddle and in turn excited resonant cross waves between the basin walls resulting in a very distorted situation in front of the gap. This problem was largely eliminated by placing splitter plates from the breakwater tips extending to the wave paddle and placing absorbing beaches on the seaward side of the breakwaters as described above.

The incident wave height was measured between the splitter plates using a parallel wire capacitance wave probe , as shown in Fig. 5-8. The wave height was sampled at 5 points across the width of the entrance channel and the incident wave height was taken to be the mean of these values. A constant depth of 125 mm was adopted for the level portion of the basin.

Fig. 5-8 Wave probe used to measure incident wave height.

The wave heights in the basin were measured using the stereoplotter wave height measurement technique described in Section 4.7. The control point configuration required for the stereoplotter technique was then set up in the basin. A detailed description of the control point configuration used is given in Section 4.7.2.3.

5.2.2.2 Wave Generator.

A full width wave generator is situated at one end of the wave basin. The wave paddle is driven by an electric motor which has a variable speed control, allowing a range of wave periods to be chosen. The wave heights can also be varied using a number of sizes of off-set cams and an adjustable lever arm.

A diagram of the wave generator mechanism is shown in Fig. 5-9(a). A general view of the wave generator mechanism is shown in Fig. 5-9(b). The back face of the wave paddle is a circular segment (with its centroid at A), to prevent any waves being generated behind the paddle. The size of the off-set cam is chosen to allow the connecting arm between lever arms 1 and 2 to be horizontal (or near horizontal), when generating waves of the required wave height. This ensures that the paddle face closely approximates a simple harmonic motion.

5.2.3 Configurations Tested.

5.2.3.1 Breakwater Gap.

The initial breakwater gap configuration set up in the wave basin is shown in Fig. 5-7. It consisted of a 1 m gap between two effectively, perfectly absorbing (due to the splitter plates) breakwaters, with the breakwater arms parallel to the incident wave crests. A water depth of 125 mm was adopted for all tests.

The experimental procedure was as follows. A specific gap to incident wave length ration (B/L ratio) was selected and the wave period needed to generate waves with the required wave length (in 125 mm deep water) was calculated using Airy wave theory. The paddle stroke was then adjusted to produce a maximum incident wave height, without localised breaking. The paddle was run for a few minutes to allow the basin to achieve a quasi steady state situation, and then the incident wave height was measured between the splitter plates, using the wave probe, as described in Section 5.2.2.1. The 1st stereopair of the water surface was then taken with the cameras triggered by the top micro-switch (see Section 4.6.4). The 2nd stereopair was taken with the cameras triggered by the bottom micro-switch (the waves in the 2nd stereopair were 180° out of phase relative to the waves in the 1st stereopair). The plates were subsequently set up in a stereoplotter and analysed using the procedure described in Section 4.7.4.

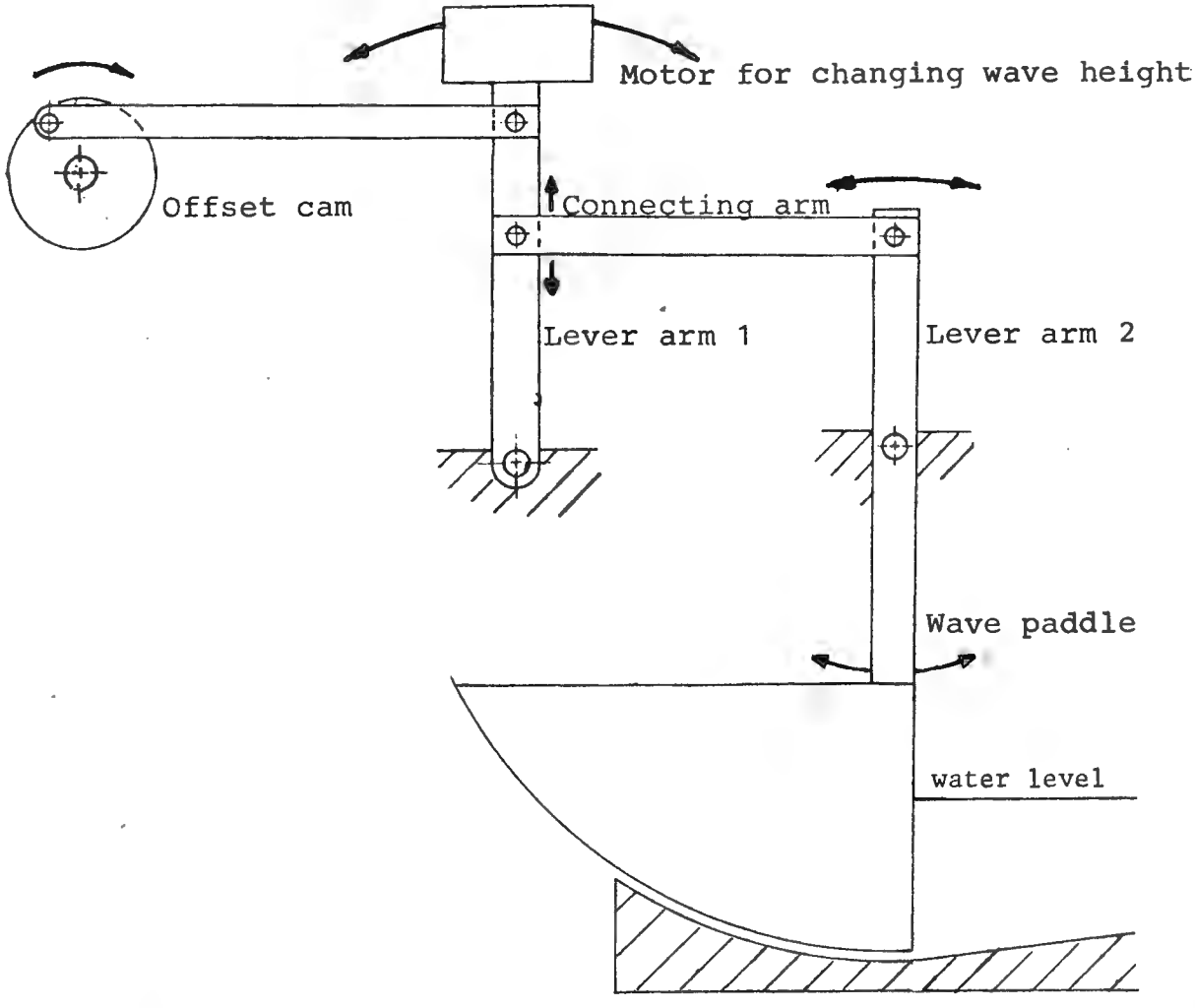

Fig. 5-9(a) Wave Generator Mechanics.

motor speed setting micro-switches wave height adjustment

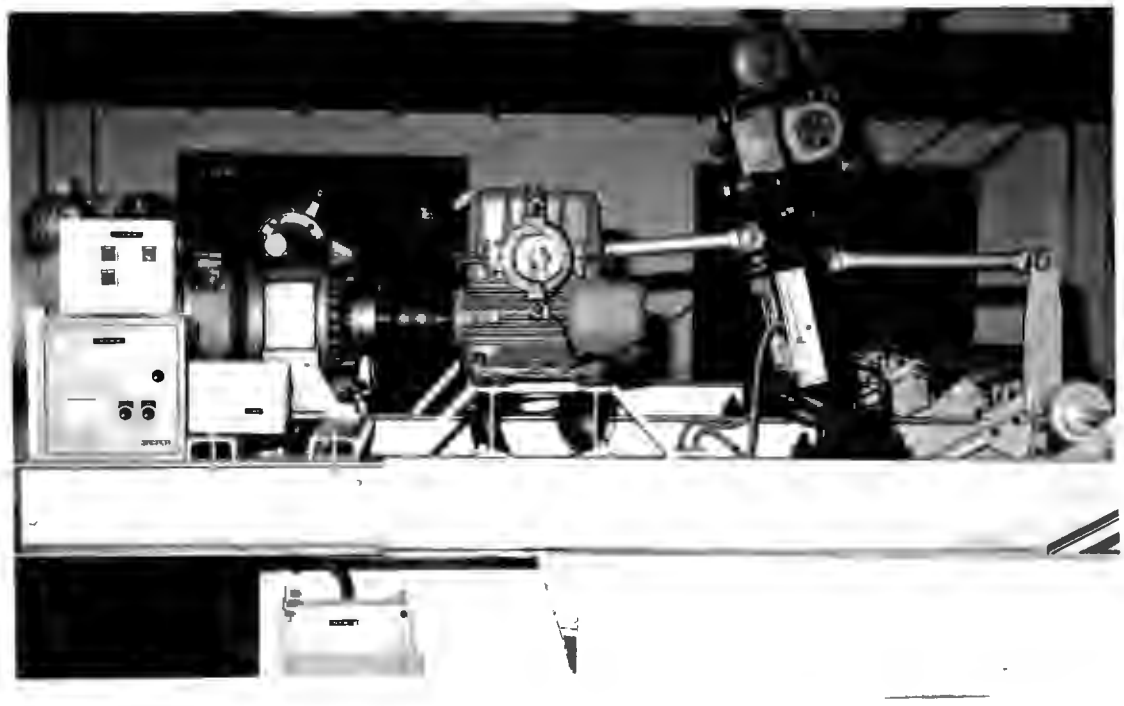

Fig. 5-9(b) General View of Wave Generator.

A series of different B/L ratio configurations were analysed using this technique. Only two configurations are discussed, since they correspond to the configurations tested using the infinite basin technique described in Section 5.5.

The first configuration had a B/L ratio equal to 1. The incident wave train had the following characteristics: wave period 0,99 seconds, mean wave height 65 mm and wave length (calculated) approximately 1 m. The experimental diffraction diagram for this configuration, plotted using the stereoplotter analysis technique, is shown in Fig. 5-10. The corresponding theoretical diffraction diagram from Johnson (1952), plotted for the equivalent, but fully reflecting breakwater situation, is shown in Fig. 5-11. This diagram is based on the diffraction theory of Morse and Rubenstein (1938) and was constructed using the method described by Carr and Stelzriede (1952). The theoretical diagram is shown in a non-dimensional form with a ½ wave length grid interval in the X and the Y (incident wave direction) directions.

The second configuration had a B/L ratio equal to 1,41. The incident wave train had the following characteristics: wave period 0,75 seconds, mean wave height 62 mm and wave length (calculated) 709 mm. The experimental diffraction diagram for this configuration, plotted using the stereoplotter analysis technique, is shown in Fig. 5-12. The corresponding theoretical diffraction diagram from CERC (1977), plotted for the equivalent, but fully reflecting breakwater situation, is shown in Fig. 5-13. This diagram is based on the diffraction theory of Penney and Price (1952) and was constructed using the method described by Johnson (1953). Figure 5-13 is shown in a non-dimensional form with a 1 wave length grid interval in both the X and the Y directions.

The diffraction diagrams shown in Figs. 5-10 to 5-13 are contour plots of equal diffraction co-efficients K'. The diffraction co-efficient (K') is defined as the ratio of the wave height H at a point in the basin, to the incident wave height H_i i.e. $K' = H/H_i$. The experimental diffraction diagrams (Figs. 5-10 and 5-12) were plotted by hand from the crest line spot height values. The crest lines and the crest line spot heights are also shown in these diagrams. As can be seen, the experimental contours of equal K' have now been smoothed.

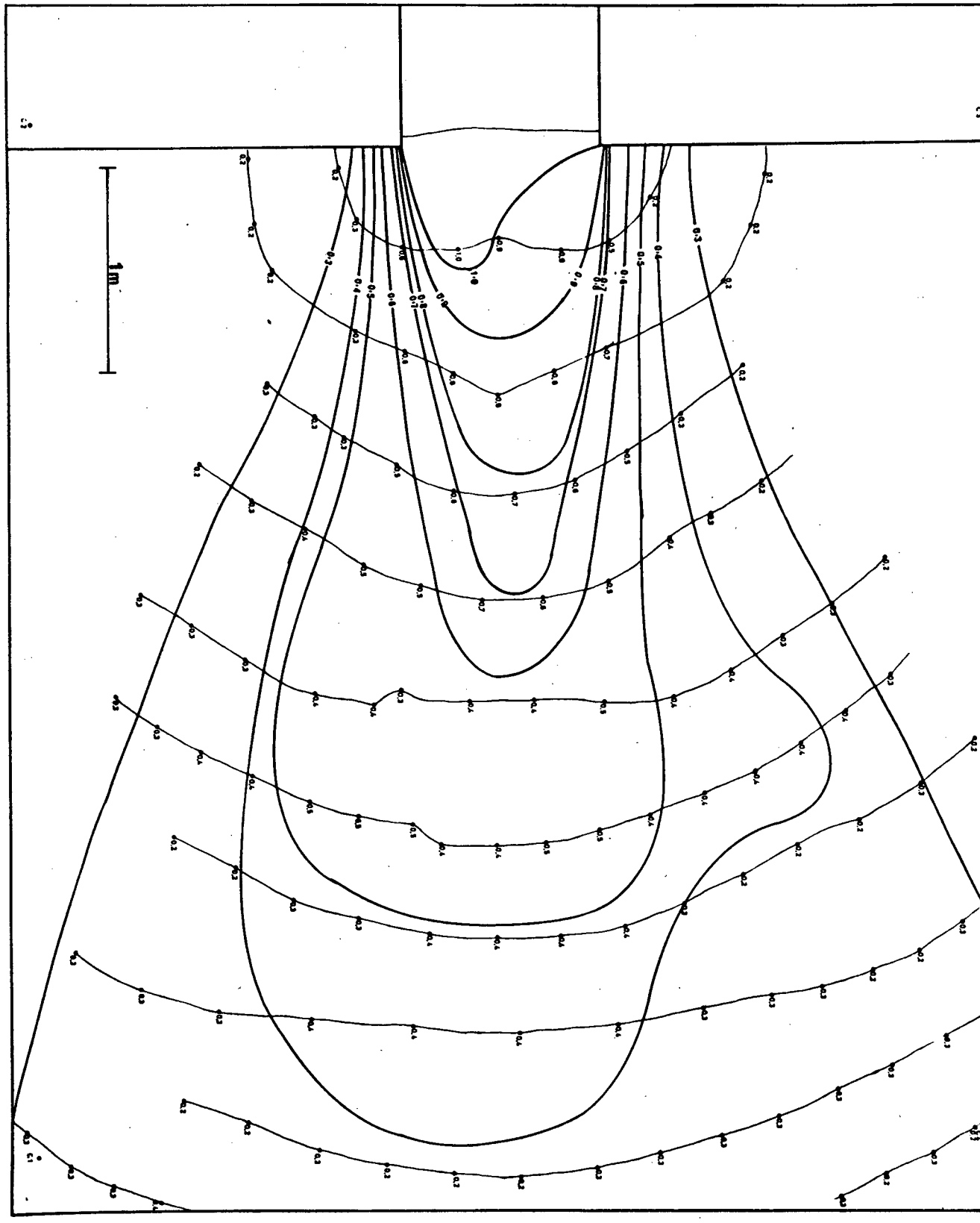

Fig. 5-10 Experimental diffraction diagram for the B/L = 1 breakwater gap configuration.

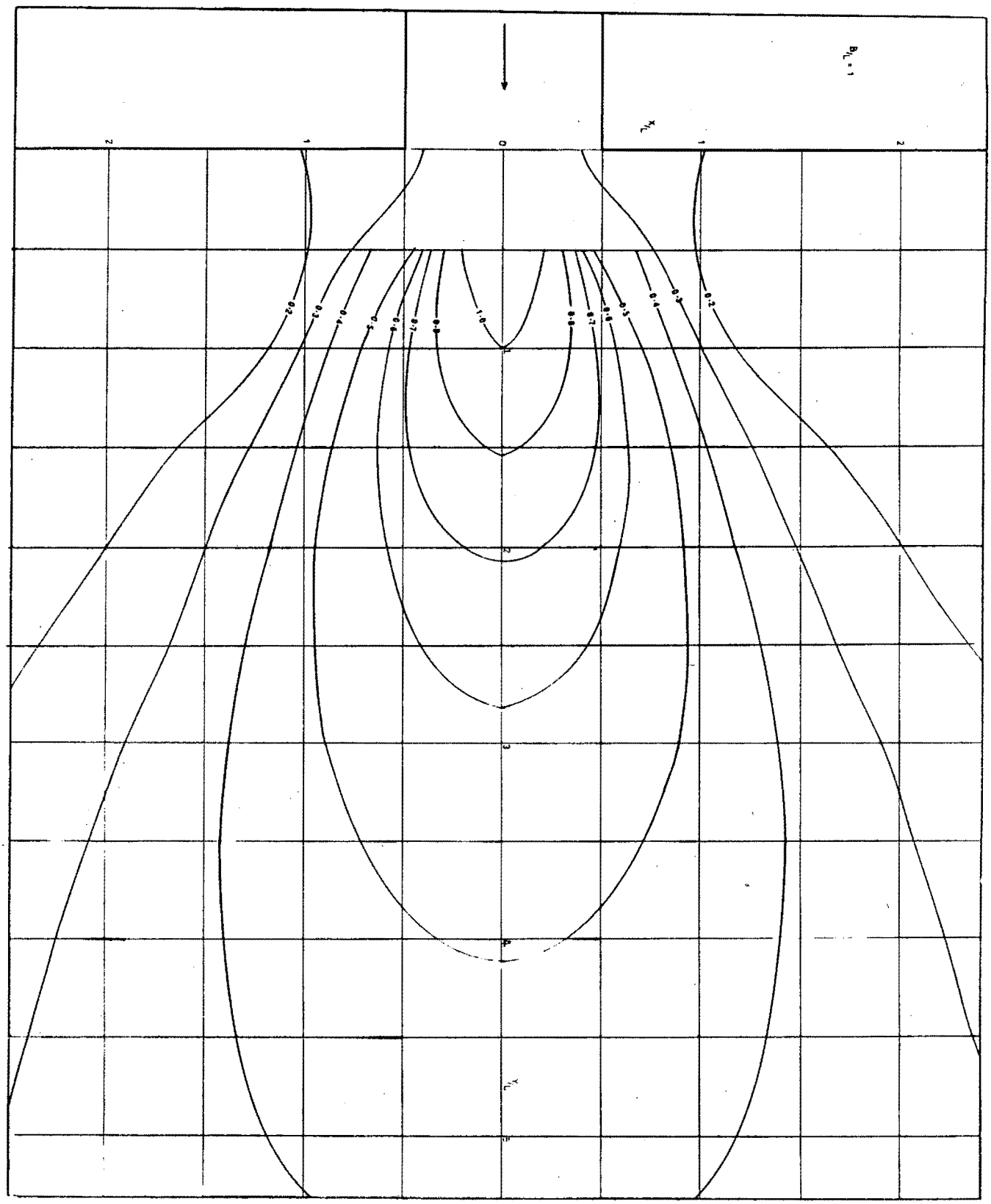

Fig. 5-11 Theoretical diffraction diagram for the B/L = 1 breakwater gap configuration (from Johnson 1952).

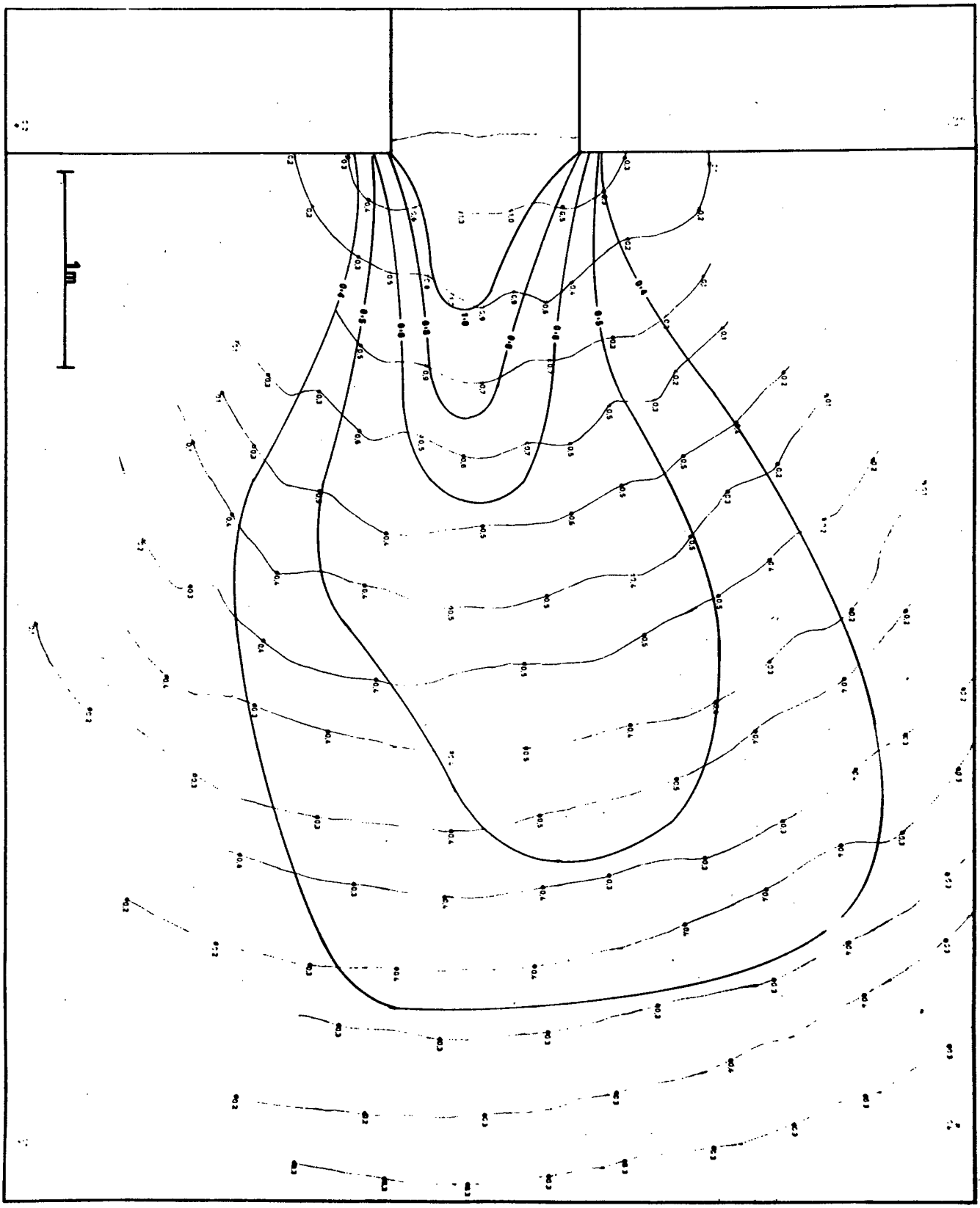

Fig. 5-12 Experimental diffraction diagram for the B/L = 1,41 breakwater gap configuration.

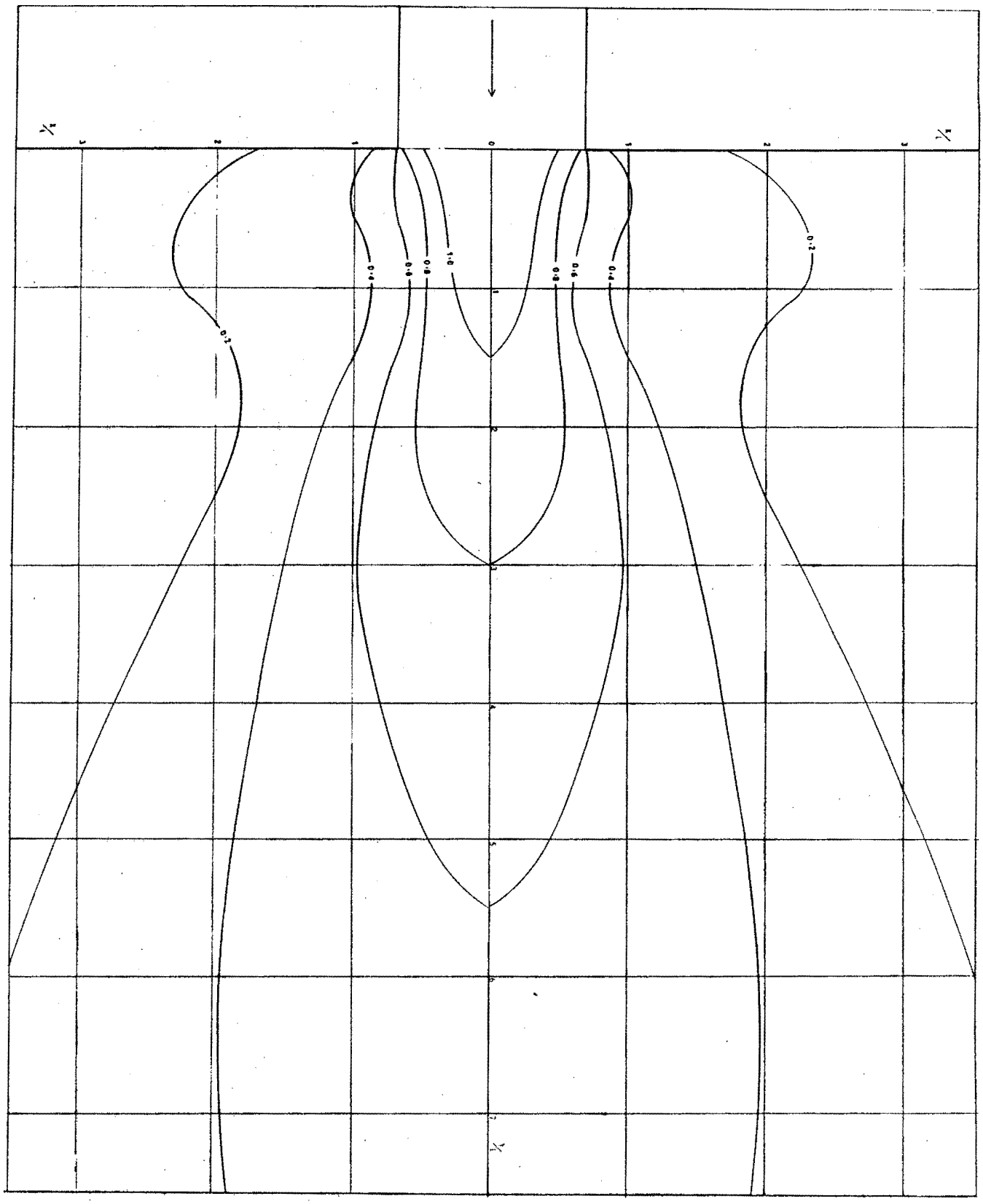

Fig. 5-13 Theoretical diffraction diagram for the B/L = 1,41 breakwater gap configuration (from CERC, 1977).

5.2.3.2 Simulated Off-Shore Breakwater.

The simulated off-shore breakwater configuration is shown in Fig. 5-14. The off-shore breakwater was set up on the same line as the breakwaters for the breakwater gap configuration. It was constructed from one of the breakwater arms shown in Fig. 5-7 by the addition of another splitter plate to the free end of this arm. Two short breakwater arms, with attached splitter plates, were constructed and placed on either side of the off-shore breakwater as shown in Fig. 5-14. Due to the size limitations of the basin, the simulated off-shore breakwater configuration was effectively equivalent to two adjoining gaps in a perfectly absorbing breakwater. It was thought however, that the wave height distribution behind this detached breakwater would be very similar to that which could be achieved using a more ideal model harbour configuration.

The experimental procedure was as described in Section 5.2.3.1. The B/L ratios for the gaps on either side of the detached breakwater were both 1,41. The ratio of the length of the detached breakwater relative to the incident wave length was 3,58. The incident wave train had very similar characteristics to the wave train used for the 2nd configuration described in Section 5.2.3.1 namely: wave period 0,75 seconds, mean wave height 59 mm and wave length (calculated) 709 mm. Fig. 5-15 shows part of the 1st stereopair taken of the configuration. Only the basin area between the two breakwater gap centre lines is shown. The experimental diffraction diagram for this configuration, again plotted using the stereoplotter analysis technique, is shown in Fig. 5-16. The corresponding theoretical diffraction diagram, plotted for the equivalent, but fully reflecting breakwater situation, is shown in Fig. 5-17.

The theoretical diffraction diagram for the simulated off-shore breakwater configuration, shown in Fig. 5-17, was constructed by the superposition of two breakwater gap diffraction diagrams. This diagram was constructed by superimposing the breakwater gap diagram shown in Fig. 5-13, upon an identical diagram with the centre lines of the two diagrams off set by 3,58 wave lengths from each other. Phase effects were not taken into account when constructing this diagram.

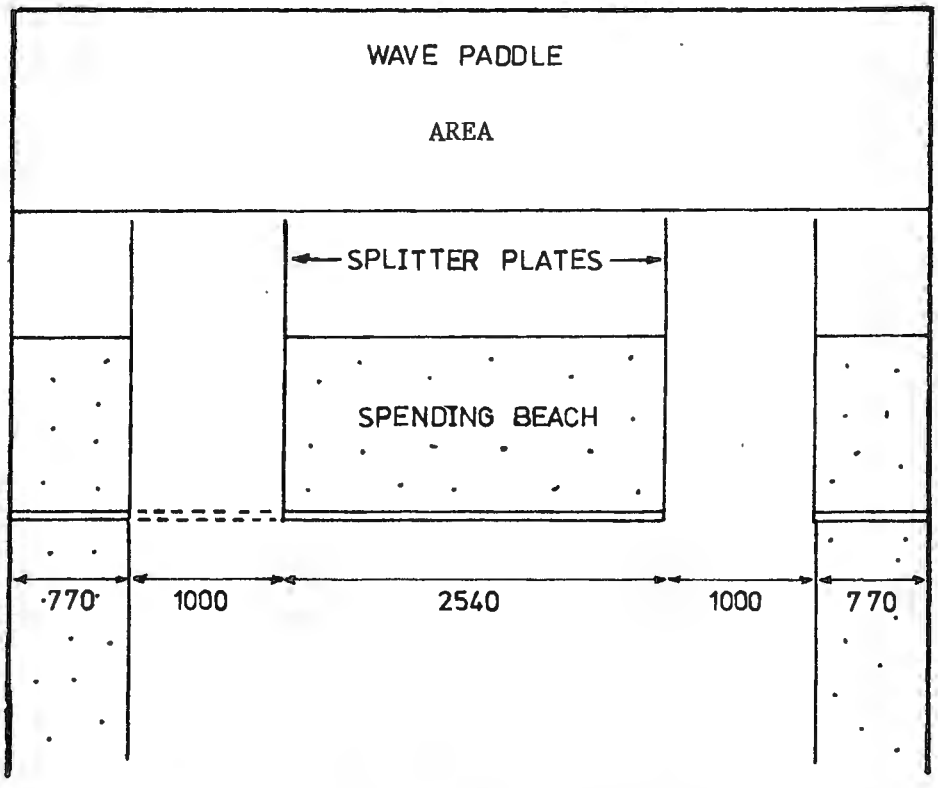

Fig. 5-14 Simulated off-shore breakwater configuration.

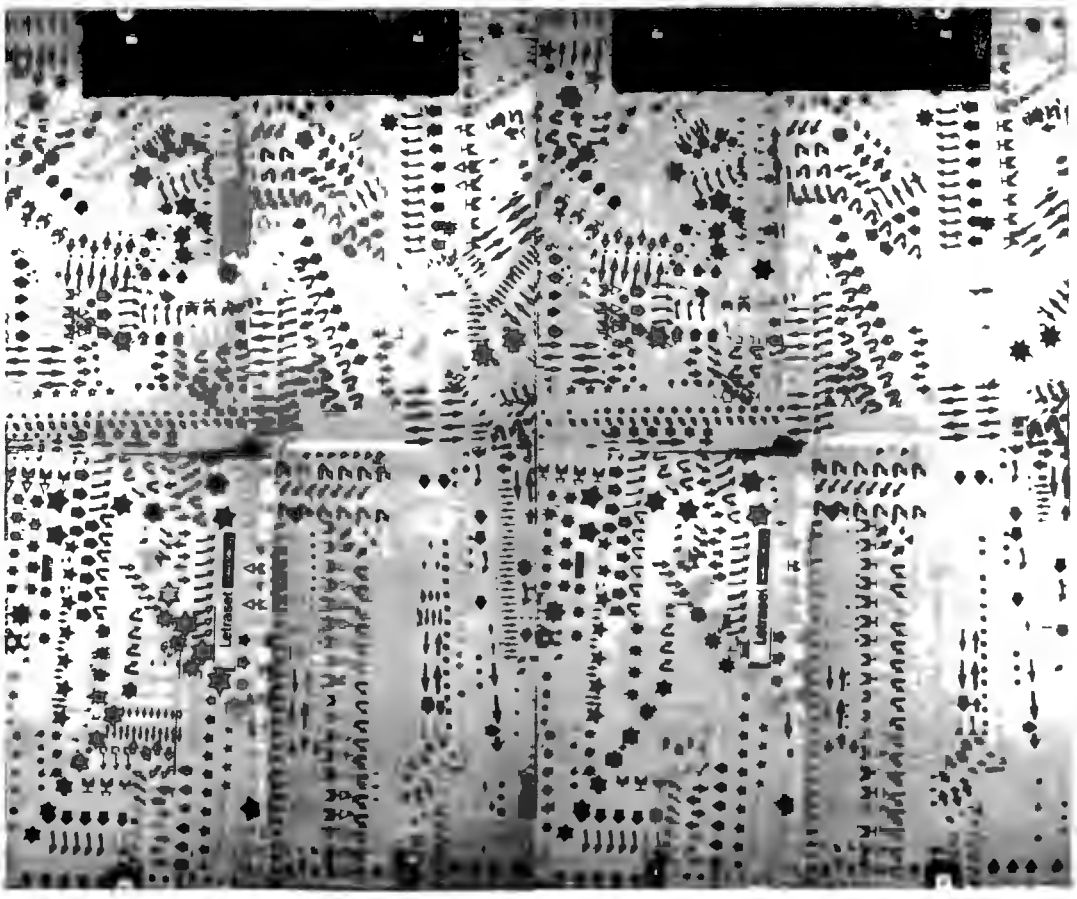

Fig. 5-15 Stereopair of the off-shore breakwater configuration showing basin area between gap centre lines.

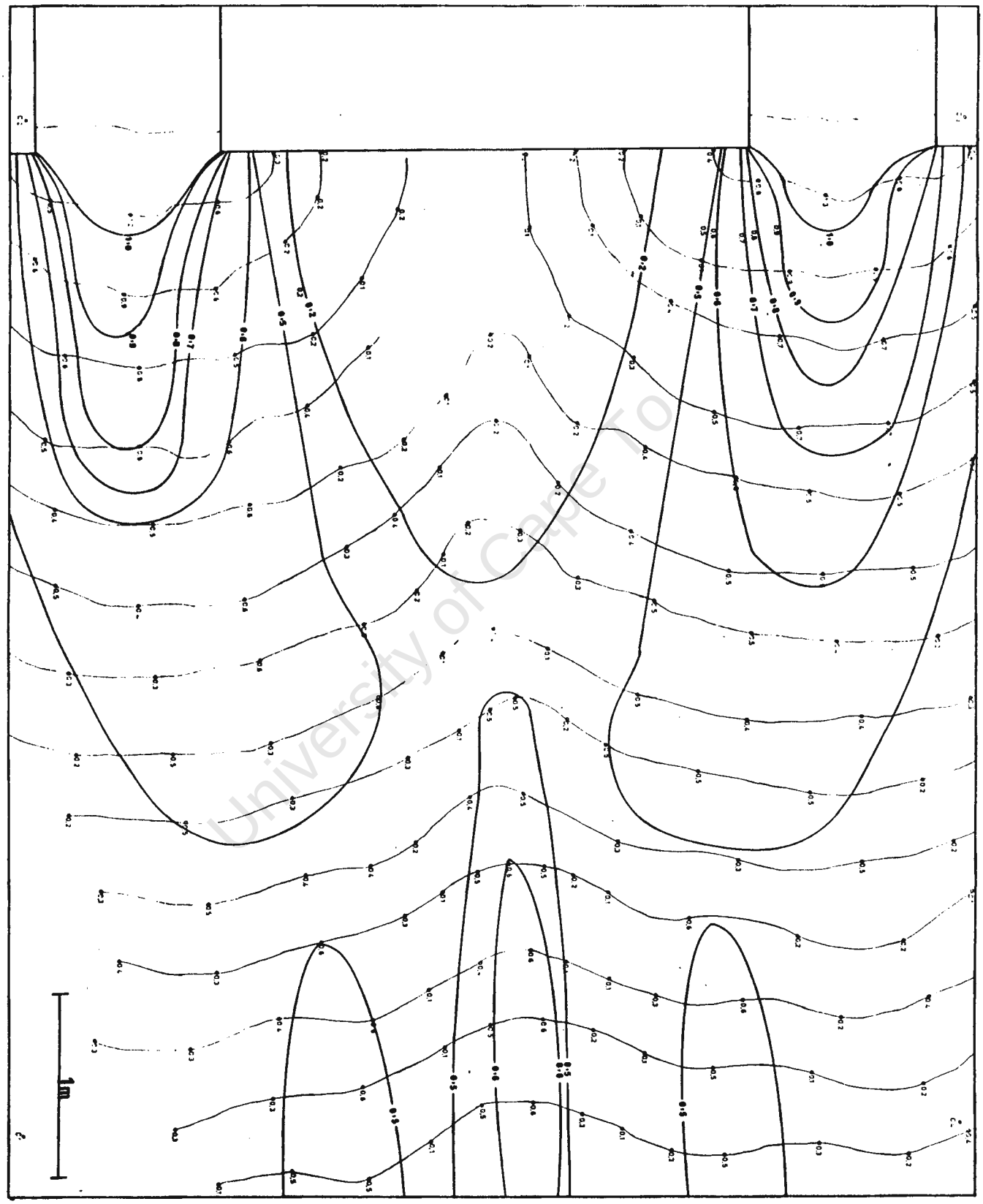

Fig. 5-16 Experimental diffraction diagram for the simulated off-shore breakwater configuration.

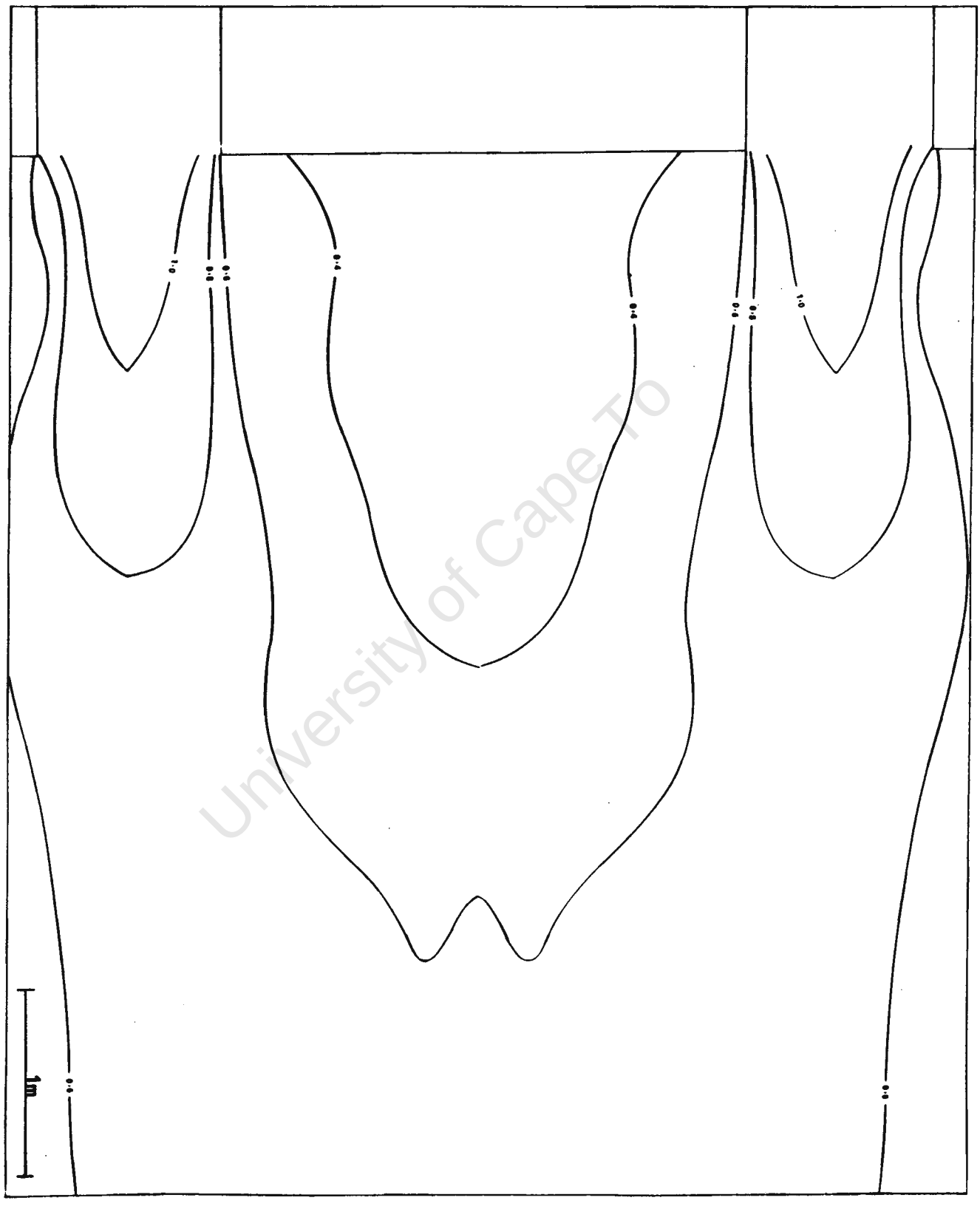

Fig. 5-17 Theoretical diffraction diagram for the simulated off-shore breakwater configuration (phase effects are ignored).

5.2.4 Analysis of Results and Conclusions.

For the B/L = 1 breakwater gap configuration, there is a good correlation between the experimental (Fig. 5-10) and theoretical (Fig. 5-11) diffraction diagrams. This is particularly so for the right hand side of the experimental diagram (when viewed in the incident wave direction). The experimental results indicated however, that the wave height attenuation, in the incident wave direction, occurs more rapidly than predicted by the theory.

For the B/L = 1,41 breakwater gap configuration, when comparing the experimental (Fig. 5-12) and theoretical (Fig. 5-13) diffraction diagrams, it is evident that the theory is very conservative (i.e. the predicted wave heights are larger than found experimentally). Again it was evident that experimentally, the wave height attenuation in the incident wave direction, occurs more rapidly than predicted by the theory.

For the off-shore breakwater configuration, when comparing the experimental (Fig. 5-16) and theoretical (Fig. 5-17) diffraction diagrams, it is again evident that the theory is very conservative. It is also evident that the individual diffraction diagrams for the breakwater gaps on either side of the detached breakwater are very similar to the diffraction diagram for the B/L = 1,41 breakwater gap configuration shown in Fig. 5-12. It is postulated that for the off-shore breakwater and the B/L = 1,41 breakwater gap configurations, the incident wave height was over-estimated. This over-estimation of the incident wave height was thought to be due to the development of resonant cross-waves between the splitter plates which could distort the wave height measurements in this region.

It is evident, when inspecting Figs. 5-10, 5-12 and 5-16, that these diffraction diagrams are all asymmetrical. In fact, these diagrams would show a much larger degree of asymmetry if the contours of equal diffraction co-efficients had not been smoothed to aid in the interpretation of these diagrams. The problem of asymmetrical experimental diffraction patterns is very common when one looks at previous experimental results. This problem is discussed further in Section 5.3.1.

When the wave paddle was switched off and the primary wave field had traversed the basin, a very pronounced secondary wave field

was evident in the basin which took up to three minutes to dissipate entirely. It was evident that this secondary wave field was superimposed upon the primary wave field, and would thus distort the observed diffraction patterns. This secondary wave field is clearly shown in Fig. 5-40, and was investigated as described in Sections 5.3 and 5.6.

When the stereopairs of the experimental diffraction configurations were analysed using the stereoplotter, a small secondary wave crest was observed in the troughs of the primary wave train. These secondary waves were investigated, as described in Section 5.3.3.2, and were found to be due to a discontinuity in the wave paddle motion. Fig. 4-34 clearly shows these secondary crests in the troughs of the primary wave train.

The wave height measurement accuracy of approximately 3 mm using the stereoplotter was thought to be inadequate when measuring the wave heights in the lee of the breakwaters. The stereoplotter operator had great difficulty in discerning the waves in these regions due to their small heights. It was evident that a more accurate alternative photogrammetric wave height measurement technique would have to be developed.

The theoretical diffraction diagrams, Figs. 5-11, 5-13 and 5-17, were all calculated for fully reflecting breakwater situations, whereas the experimental results, due to the use of splitter plates and absorbing beaches (on the seaward sides of the breakwaters), were effectively for fully absorbing breakwater situations. It was therefore desirable that the experimental results be compared to theoretical solutions in which the breakwaters were assumed to be effectively fully absorbing.

Since transitional waves were used for all the experimental diffraction configurations, it was evident that any basin floor level anomalies would cause the observed wave diffraction patterns to be distorted by wave refraction effects. It was obvious that if a pure diffraction pattern was to be achieved when using transitional waves, the basin floor would have to be perfectly level.

It was evident that, if the validity of the experimental diffraction patterns was to be improved, the following factors would have to be investigated and improved:-

(1) The secondary wave field consisting of wave reflections, resonant cross-waves and other parisitic wave forms would have to be minimised.

(2) The basin floor level would have to be checked for any anomalies i.e. the basin floor would have to be rendered perfectly level.

(3) The wave paddle motion would have to be investigated to determine whether or not it was the cause of the secondary waves observed in the troughs of the primary wave train i.e. the paddle motion would have to be made as close to simple harmonic as possible.

(4) Improved methods of determining the incident wave height would have to be investigated and implemented. It was proposed that the incident wave height be measured photogrammetrically and that the resonant cross-wave situation observed between the splitter plates be minimised.

(5) The wave height measurement accuracy of approximately 3 mm using the stereoplotter analysis technique was thought to be inadequate, particularly for the measurement of the waves in the lee of the breakwaters. A more accurate alternative photogrammetric wave height measurement technique would have to be developed.

(6) The theoretical diffraction patterns used were for the fully reflecting breakwater situation, while the experimental results were for the fully absorbing breakwater situation. Although it was recognised that the theoretical solutions for the fully reflecting and fully absorbing breakwater situations would be very similar, it was thought that it would be preferable to have a theoretical solution for the fully absorbing situation. Ideally this theoretical solution should be flexible enough to encompass wave diffraction, refraction and reflection phenomena, plus asymmetrical structures since up to this stage, the experimental configurations which were analysed were severely limited by the available theoretical solutions.

Factors (1) and (4) led to the investigation described in Section 5.3, and to the development of the infinite basin technique des-

cribed in Section 5.4. Factors (2) and (3) led to the investigations and improvements described in Sections 5.3.3.1 and 5.3.3.2. Factor (5) led to the development of the stereocomparator/microcomputer/projective transformation theory measurement system described in Section 4.8.5. Factor (6) led to the modification of the finite element program "WAVE" to run on the UNIVAC 1100 at U.C.T. and its subsequent use to model the experimental configurations, as described in Chapter 3.

5.3 Experimental Difficulties Pertaining to the Generation of Long-Crested Waves in a Laboratory Wave Basin.

5.3.1 Introduction.

During the testing of the experimental diffraction configurations, it became evident that a secondary wave field was superimposed upon the primary wave field. This secondary wave field could be clearly seen in the basin when the wave paddle was switched off and the primary wave train had traversed the basin. It was postulated that this secondary wave field was seriously distorting the diffraction phenomenon which was being measured. An investigation was carried out to determine the generating mechanisms of this secondary wave field, and to find a means of minimising its effect on the diffraction results.

The problem of a secondary wave field distorting the primary wave train is a common problem encountered when one attempts to generate a purely monochromatic wave train in a laboratory wave basin. Experimenters such as Harms (1976, 1979), Goda et al (1971, 1973) and Fairchild (1970) were all faced with the problem of marked wave height variations along the generated incident wave crests. These researchers conducted their experiments with the wave paddle running continuously (refered to as the "steady state mode" for the experiments at U.C.T) and in all cases the wave paddles were long (particularly for the experiments of Goda et al and Harms) relative to the incident wave length.

Harms (1976, 1979) carried out a series of experiments in the wave basin shown in Fig. 5-2, without a model in the basin. He found that the ratio of maximum to minimum wave height along individual generated incident wave crests (for the open basin) ranged from 1,5 to 2,5. The experiments of Goda et al (1971, 1973) were performed in an open basin 16 m by 27,5 m with a 16 m long wave generator at one end, a rubble beach at the other end, and wave absorbing material along the side walls. Incident waves with a wave length of 1,2 m were used, and the wave height varied along the crest from less than 30 mm to more than 50 mm, indicating a lateral maximum to minimum wave height ratio of approximately 2. In the experiments of Fairchild (1970), the wave generator was 12,19 m long and a typical incident wave had a wave length of 5,49 m. The lateral (along the crest) maximum to minimum wave height ratio was again approximately 2.

Memos (1980a) in his discussion on the work of Harms (1979b) suggested that the main cause of the incident wave height irregularities across the basin was the finite length of the wave maker. Quoting the work of Biesel and Suquet (1954) and Wang (1974) he states that: "The wave field produced by the motion of any wave maker can be regarded as a result of superposition of source and multipole potentials along the wave maker. The points of the water surface in the basin face in general at a different angle the length of the wave maker and, therefore, the superposition of the sources and multipoles effects does not give identical results as regards wave amplitudes along a crest."

If a diffraction study is carried out using incident waves with lateral wave height variations of the magnitude quoted above, it is evident that measurements of diffracted wave heights will be of questionable significance. A non-uniform wave field would produce asymmetrical diffraction diagrams and non-repeatable results. The sensitivity of diffraction profiles to variations of wave height in the incident wave train is shown in Fig. 5-18. This figure shows diffraction results obtained by Harms (1976) for diffraction round an off-shore breakwater. The breakwater consists of a steel plate with splitter plates and an absorbing beach on the seaward side. The breakwater length to incident wave ratio is 3,6. This configuration is very similar to the off-shore breakwater configuration tested at U.C.T. (See Section 5.2.3.2) The diffraction profile was measured at a distance 9,5 wave lengths behind the structure on two different occasions with all other conditions being the same. The diffraction profile and the corresponding incident wave height profile for both runs is shown in Fig. 5-18. This figure illustrates the marked asymmetry and non-repeatability of the diffraction profiles obtained in tests where the wave paddle ran continuously.

The bulk of the diffraction experiments conducted by Harms (1976) were performed with the wave paddle running continuously for periods of time of up to 2 hours or more. Harms (1976) stated:

> "It was desirable to perform the diffraction tests in the "continuous" mode because this method reduced the overall testing effort greatly, in comparison to the "intermittent" mode

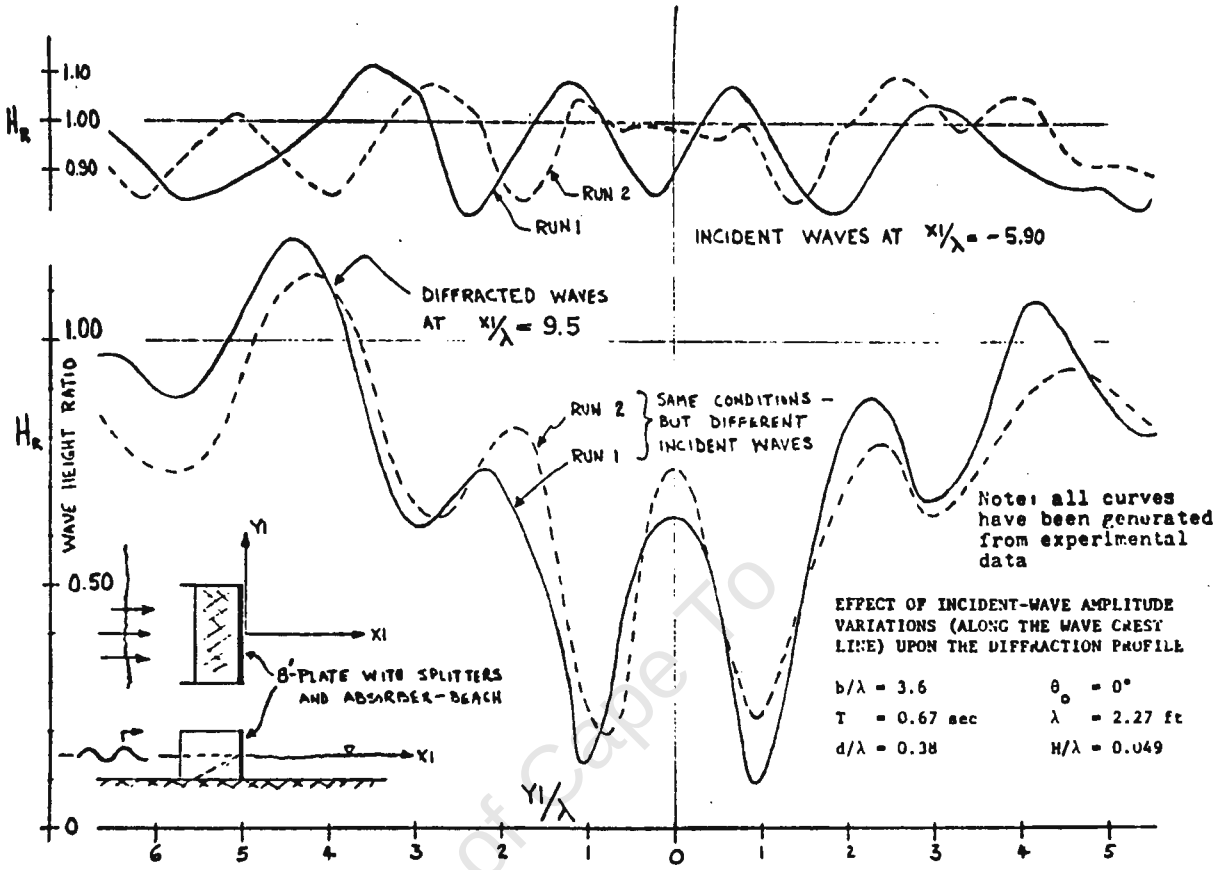

Fig. 5-18 Sensitivity of diffraction profiles to variations of wave height in the incident wave train (from Harms, 1976).

or "burst-method" in which waves are generated only for that short period of time during which reflected waves have not yet reached the testing area, followed by a waiting period during which waves are allowed to die down. It was ascertained that the "intermittent" mode did not, in fact, decrease the lateral wave height variations significantly (as measured without a structure in the basin) and hence the use of the far more efficient "continuous" mode can be justified. As a further verification of the soundness of this approach, several tests were performed in which the wave height distribution about a structure was measured by both methods."

Figs. 5-19(a) & (b) show diffraction profiles, from Harms (1976), for diffraction round an off-shore breakwater obtained using both the "continuous" and "intermittent" data aquisition modes. It is the author's opinion that these profiles do not prove conclusively that the results obtained using both modes are effectively the

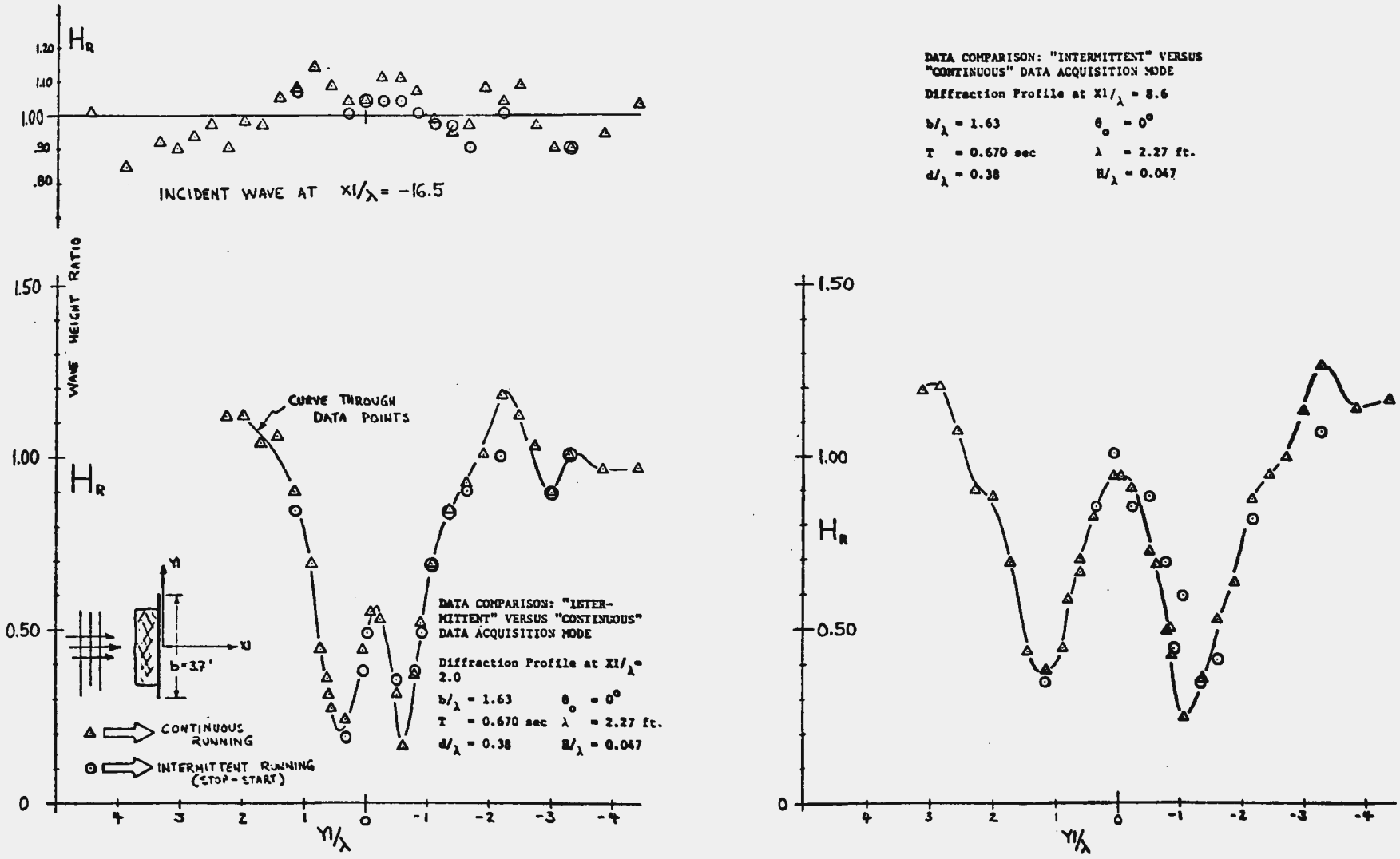

Fig. 5-19 Diffraction profiles obtained using both the "continuous" and "intermittent" data aquisition modes (from Harms, 1976).

same and that the "intermittent" mode does not yield better results than the "continuous" mode. In fact, if one considers the non-repeatability of the diffraction profiles obtained using the continuous mode, as illustrated by Fig. 5-18, it is doubtful whether any definite conclusions can be drawn from the diffraction profiles shown in Fig. 5-19.

5.3.2 The Behaviour of Laboratory Generated Waves.

A brief review of pertinent papers is given to gain some insight into the behaviour of laboratory generated waves.

Galvin (1972a & b) points out that periodic waves produced by the sinusoidal motion of a wave generator can be classified according to shape into three categories as shown in Fig. 5-20. Only the wave labelled "regular" remains periodic and does not change shape as it progresses down the tank. At any location in the basin this regular wave displays an approximately sinusoidal form that does not change with time. The two remaining waves are of non-permanent form; as they progress down the wave basin their shape (surface time history) will be different from point to point. Of these unstable waves, the Benjamin-Feir waves appear only in deep water, and the solitons occur only in shallow water.

Benjamin - Feir Waves (Deep water)

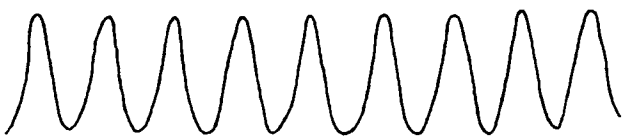

Regular Waves (Intermediate depth)

Solitons (Shallow water)

Fig. 5-20 Shapes of waves produced by sinusoidal motion of piston-type generator (from Galvin 1972b).

Solitons have been found to be limited to relatively shallow water and waves that are fairly steep ($d/L < 0,10$ and $H/d > 0,05$). The The term soliton actually refers to those waves which are a product of disintegration of a regular wave train in shallow water. Most commonly up to 3 solitons are produced, but under extreme conditions Galvin found up to 7. Galvin (1972a) proposed that solitons are caused by a mismatch between generator motion and the water particle motion within the natural wave. Galvin points out that:

> "Camfield and Street (1969) have produced solitary waves with a generator whose time history was programmed to be a hyperbolic tangent, the required particle motion for a solitary wave. When moving this way, the generator produced clean solitary waves that did not split into solitons, thus supporting the hypothesis that solitons are caused by generator motion that is not natural to the stable waves for the given experimental conditions."

The break down of shallow water waves into forms exhibiting several secondary crests was investigated both analytically and experimentally by Madsen et al (1970). They found that for steep waves either generated at the wave generator, or due to forced amplification by decreasing depth, the wave train transforms into three regions. The leading region will be a train of essentially solitary waves followed by a region of cnoidal waves. The third region, that nearest to the wave generator, was found to be a region of weakly interacting cnoidal wave trains. Solitons were observed by Chakrabarti (1980) who performed tests in a 76,2 m by 10 m basin and with a water depth of 1,5 m. He found that at wave periods of 4 seconds and higher, the waves broke and reformed in the tank. This effect, commonly called solitons, was found to be a function of wave height, length and period with the number of solitons increasing with increase in wave period (a maximum of 5 solitons were observed in the tank).

Steep waves entering deep water have been observed to disintegrate into irregular waves of several frequencies. These are the Benjamin-Feir waves. Benjamin and Feir (1967) demonstrated theoretically that a periodic wave train in deep water will become highly irregular if it travels far enough. They found that energy is transferred from the primary wave motion to side band frequencies

as a consequence of coupling through the non linear boundary condition at the free surface. Galvin's (1972a) experimental results indicate that Benjamin-Feir waves are limited to d/L > 0,3 and then only for steep waves.

The results of Galvin's (1972a & b) work is graphically summarised in Fig. 5-21. This diagram was found to be useful since for the experimental work carried out at U.C.T. the wave parameters d/L and H/d could be chosen so as to avoid the formation of solitons or Benjamin-Feir waves.

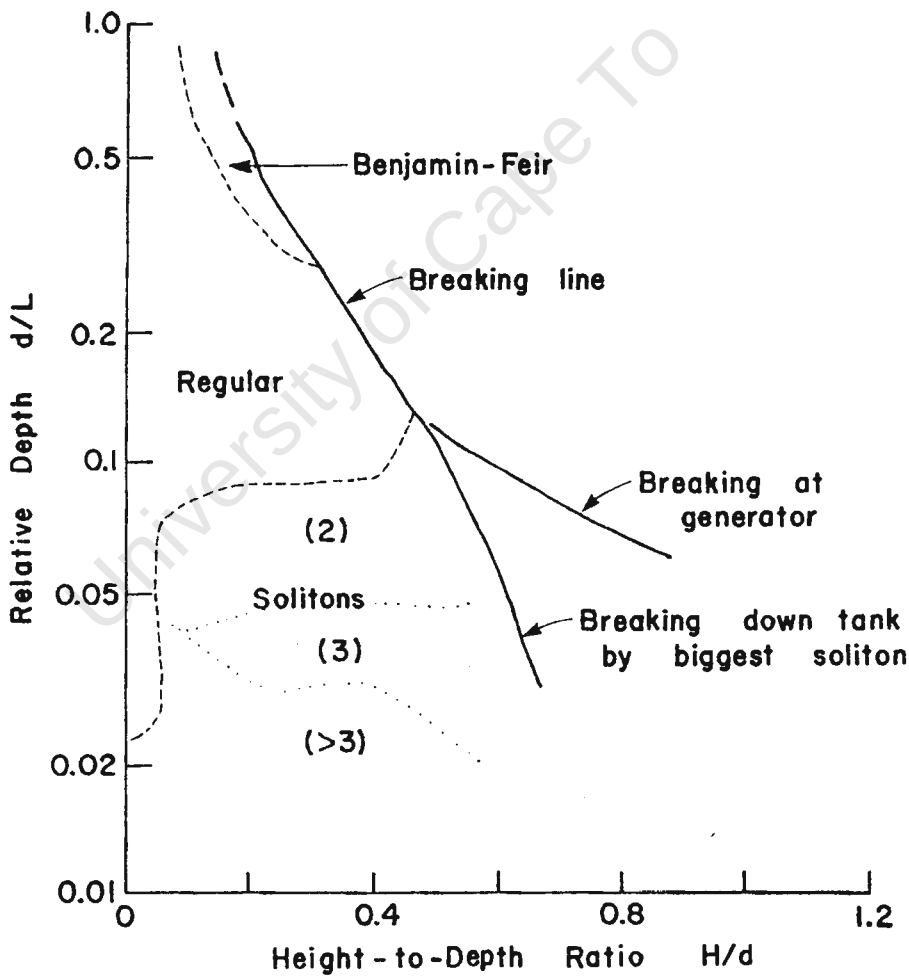

Fig. 5-21 Dependence of wave shape and breaking on relative depth and height-to-depth ratio (from Galvin 1972b).

Fontanet (1961) derived a general second-order solution for waves generated by a plane wave maker in simple harmonic motion. These results are cumbersome to apply with solutions presented only for

piston type wave makers. Madsen (1971) presented a possibly more useful approximation using a Stokes like expansion. However, only piston wave makers were considered and the results are valid only for long waves. Buhr Hansen and Svendsen (1974) carried out experiments in a wave flume and compared their results to the theories of Fontanet (1961), Madsen (1971) and Daugaard (1972). Buhr Hansen and Svendsen found that for $0{,}10 < d/L < 0{,}65$ the waves produced by a sinusoidal piston motion can be described as a second-order Stokes wave superimposed on a free second harmonic wave. These findings were substantiated by the work of Flick and Guza (1980).

Chakrabarti (1980) compared wave lengths measured in a flume with predicted wave lengths calculated using the Airy wave theory, the Stokes third and fifth, the cnoidal first and second order and Keulegan-Patterson theories. His results are summarised in Table 5-2. In this table he refers to the Ursell number (or parameter) U_R which is defined as

$$U_R = \frac{H}{L} \left(\frac{L}{d}\right)^3 \qquad (2)$$

The limits of validity of various wave theories are given by Le Méhauté as shown in Fig. 5-22. The Ursell parameter U_R may be used to establish the boundaries of regions where a particular wave theory should be used. For the linear theory to predict accurately both wave steepness H/L, approximated by H/T^2, and the Ursell parameter U_R must be small as shown in Fig. 5-22.

The Ursell parameters for the incident waves used in experiments at U.C.T. ranged in magnitude from 8 to 45. The corresponding wave steepnesses expressed as H/T^2 ranged from 122 mm/sec^2 (0,4 ft/sec^2) to 45 mm/secs (0,15 ft/sec^2). From Fig. 5-22 it can be seen that the shorter wave length waves used at U.C.T. fall into 3rd Order Stokes region, while the longer waves fall into the cnoidal wave theory region. However, the entire range of incident waves used at U.C.T. would fall into the region of validity of Dean's fifth order Stream Function (Dean, 1965).

The decision as to which wave theory is the best for a particular wave situation is complex. Le Méhauté (1976) states "A compre-

Run number (1)	Wave period, in seconds (2)	Wave height, in feet (3)	Ursell number, U_R (4)	Wave Lengths, in feet						
				Measured (5)	Airy (6)	Third Stokes (7)	Fifth Stokes (8)	First Cnoidal (9)	Second Cnoidal (10)	Keulegan-Patterson Cnoidal (11)
TC504	1.40	0.743	0.65	10.50	10.01	10.48	10.50	—	—	—
TC509	1.60	0.984	1.41	13.39	12.92	13.54	13.57	—	—	—
TC515	2.00	1.220	3.90	19.98	19.04	19.71	19.75	—	—	—
TC521	2.50	1.560	9.13	27.05	26.54	27.49	27.50	—	—	—
TC523	2.75	0.860	6.17	29.95	30.17	30.47	30.51	—	—	—
TC524	2.75	1.526	11.79	31.08	30.17	31.11	31.25	—	—	—
TC552	3.25	0.820	9.45	37.96	37.23	37.67	37.62	37.58	—	35.78
TC553	3.25	1.444	17.42	38.83	37.23	38.36	38.47	39.08	37.37	36.52
TC556	3.50	1.501	21.42	42.24	40.69	41.97	42.27	42.97	40.90	—
TC561	4.00	0.797	13.14	45.39	47.50	48.14	48.08	48.30	47.76	47.31
TC562	4.00	1.589	25.75	45.01	47.50	49.26	50.05	50.67	48.00	—
TC567	4.50	0.623	13.17	51.41	54.21	54.75	54.69	54.83	54.48	54.19
TC568	4.50	1.390	30.40	52.29	54.21	56.26	56.93	57.24	55.05	55.82
TC595	5.00	0.235	6.98	60.92	60.84	61.13	60.93	60.86	—	60.61
TC608	6.00	0.610	21.10	65.75	73.97	75.05	75.06	75.15	74.65	74.71
TC616	7.00	0.503	30.48	87.03	86.96	87.56	88.16	88.13	87.74	87.82
TC617	7.00	1.004	54.40	82.30	86.96	89.60	93.28	90.84	89.32	90.11
TC628	8.00	1.076	68.73	89.03	99.89	103.60	114.80	105.40	103.50	104.60
TC634	9.00	0.596	40.06	91.66	112.80	114.50	117.20	115.40	114.80	115.10
TC636	9.50	0.500	50.51	12.37	119.20	121.40	122.70	121.40	120.90	121.20

Note: 1 ft = 0.305 m.

Table 5-2 Comparison of measured and theoretical wave lengths (from Chakrabarti, 1980).

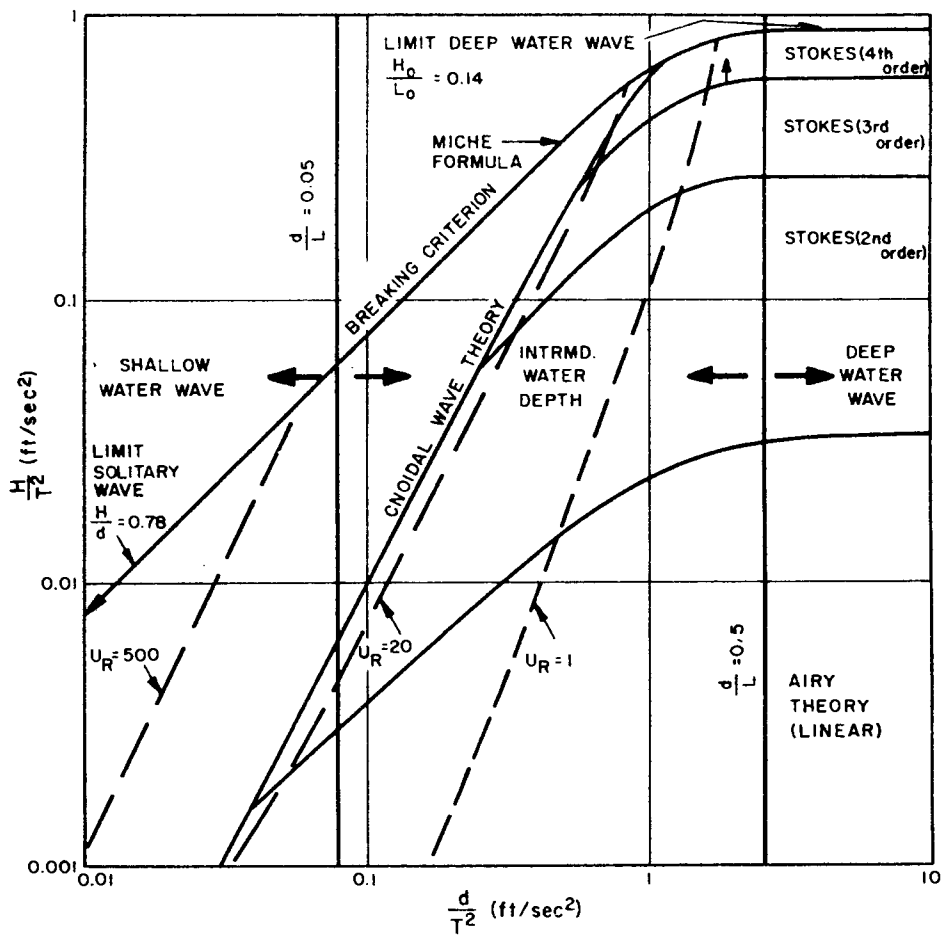

Fig. 5-22 Limits of validity for various wave theories (from LeMéhauté, 1976).

hensive quantitative investigation of the error which is made by using various theories in various domains has not been done so far; hence, such a graph (Fig. 5-22) is somewhat arbitrary and merely qualitative." Dean (1970) states "At present, there are at least twelve available wave theories which can be selected for design wave representation. The engineer confronted with this choice, however, has only general guidelines pertaining to the relative depth conditions for which a particular theory was developed, and also an intuitive belief that the additional effort required to use higher order wave theories should be rewarded by more accurate results."

For the experimental configuration the incident wave period, wave length, celerity and group velocity needed to be calculated. The author decided to use the Airy wave theory since this is the theory upon which the diffraction theory is based and secondly, apart from being much easier to apply, the Airy wave theory has been found to give very good results for wave conditions strictly outside its region of validity, as given in Fig. 5-22. This is born out by the experimental results of Chakrabarti (1980), shown in Table 5-2.

It is the author's opinion that one of the most important causes of wave height variations along incident wave crests generated in a wave basin is the phenomenon known as cross-waves. Cross-waves are standing waves with crests at right angles to the wave generator and a frequency half that of the wave maker. Their effect is particularly pronounced when the generated cross-waves correspond to the natural modes of oscillation of the wave tank. Schuler (1933) discovered empirically that these standing waves with crests at right angles to the wave maker are not produced because of boundary effects. In fact a small paddle oscillating within an effectively infinite basin will generate cross-waves, as will the same generator in a finite basin for any orientation of the paddle with respect to the basin walls. A spherical plunger oscillating up and down was also shown to produce cross-waves at half the frequency of the progressive wave train. The crests of the standing waves extend out radially from the sphere and are superimposed upon the primary, progressive ring waves the plunger emits.

Garrett (1970) noted that cross-waves appear to be a common phenomenon in wave tanks in which the width of the wave maker is rather larger than the wave length of the primary waves being generated. Garrett formulated a second-order theory for the modes of oscillation of a wave channel with vertical boundaries and a generator at each end. By retaining the quadratic terms in the free-surface boundary condition, he was able to develop an equation for the amplitude of the cross-waves which are stated to be a result of non-linear resonance. Garrett (1970) formulated an instability mechanism leading to the generation of cross-waves in a closed channel in which the primary wave field was also a standing wave. His theory is not applicable to long channels where the wave maker produces a primary field which is a progressive wave train. In such cases, the heaving of the mean surface, of considerable significance in the instability mechanism, is confined to the non-propagating field near the wave generator. Mahony (1972) extended Garrett's theory of resonant interactions to describe the energy transfer from this forced localised field to the cross-wave field for progressive waves in a long channel.

Barnard and Pritchard (1972) experimentally investigated the formation of cross-waves in front of a wave maker at one end of a long channel in which the primary field produced was a progressive wave train. Their results are in good agreement with Mahony's theory. Barnard and Pritchard noted that after the early stages in the development of the cross-waves, there was an increase in their growth rate. This new rate was found to be about twice the initial growth rate. They also found the growth rate for the cross-waves was directly proportional to the paddle amplitude i.e. the wave height of the waves in the progressive wave train. Barnard and Pritchard found that a finite time elapsed (sometimes as long as 5 minutes) between the initial and fully developed stages of the cross-waves' development. Spens (1954), by means of a series of photographs (as reported by Harms, 1976) clearly shows the gradual build up of cross-waves to their fully developed stage.

This gradual build up of the cross-waves, as described above, underlines one of the major advantages of using the infinite basin technique (described in Section 5.4) for model harbour studies.

Using this technique, the wave paddle is only operated for short periods of time, and thus it is proposed that even if cross-waves do develop they would not have enough time to progress beyond their initial development stage.

5.3.3 Experimental Investigation.

5.3.3.1 Basin Floor Level Anomalies.

Transitional incident waves were to be used for all the diffraction configurations, and therefore it was recognised that the basin floor would have to be perfectly level to prevent wave refraction effects from distorting the experimental diffraction patterns. A detailed level survey was carried out to determine the levels in the area of the basin used in the diffraction experiments described in Section 5.2.3. The levels were taken on a grid system with a 500 mm interval using a precision level and a steel metre rule. The measurement accuracy was approximately 0,5 mm. A contour plot of the measured basin floor level anomalies, with a contour interval of 1 mm, is given in Fig. 5-23.

On studying Fig. 5-23, it is evident that the right hand side of the basin is on average a few millimetres above the mean level of the left hand side of the basin. As the wave crests passed over the high spots shown in Fig. 5-23, they would shoal slightly and a localised increase in wave height in these areas would probably be evident. It is suggested that the assymmetry evident in the diffraction diagrams described in Section 5.2.3 and particularly, the diffraction diagram for the B/L = 1,41 configuration shown in Fig. 5-12 can be partly explained by wave refraction effects as described above.

A lot of time was subsequently spent in an attempt to render the basin floor perfectly level. The high spots were ground down to a predetermined mean level using a petrol-engine driven concrete floor grinder. The following procedure was used: The high spots were located by carrying our a detailed level survey and their locations marked on the floor with chalk. These areas were ground down, washed clean, relevelled, ground down etc until they were within a millimetre or two of the required level. At this stage the basin floor was covered with a very thin sheet of water to highlight the remaining high spots which were then ground down.

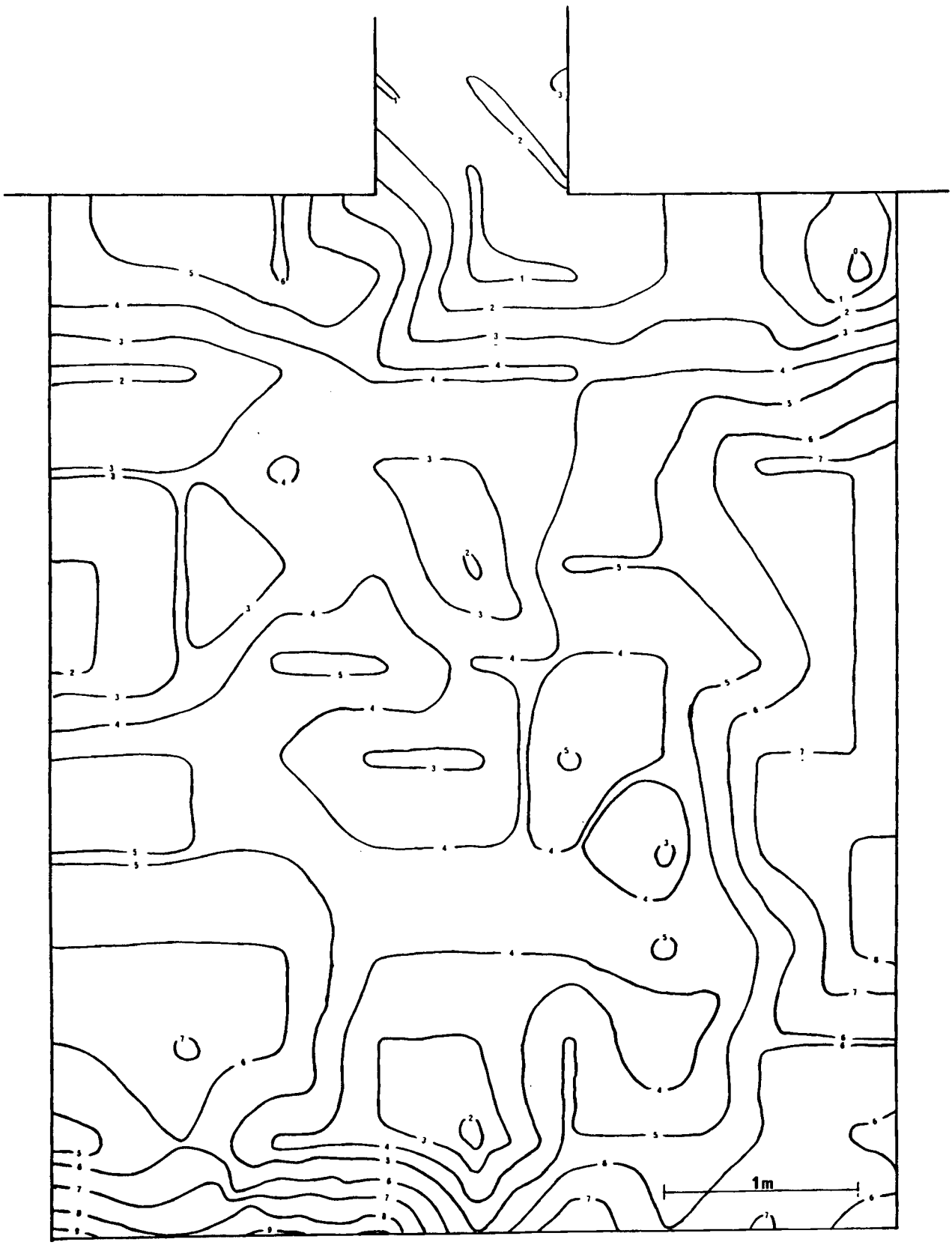

Fig. 5-23 Contour plot of the basin floor level anomalies.

The basin low spots were dealt with in a different manner. Once all the high spots had been ground down, all the low areas (below the predetermined mean level) were identified by again using the thin sheet of water technique and marking the edges of the resultant puddles with chalk. A detailed level survey of these low areas was then undertaken in order that a series of steel spacers of the correct thickness could be made up. The basin floor was then left to dry completely. The steel spacers were then placed in their corresponding positions in the low areas and then these areas were filled up, to the predetermined level, with a self levelling epoxy resin (Epidermix 335).

The slope between the wave paddle and the level basin area was also surveyed. The high spots were removed using the concrete grinder and low spots built up with an epoxy/sand mixture until the slope was uniform along its whole length.

Once the epoxy had cured and all the small anomalies had been dealt with, the level area was again surveyed and was found to deviate from the required level by a maximum of ± 1 mm. This represented a variation of less than 1 % of the 125 mm water depth used for all the diffraction configurations, and therefore for the diffraction experiments described in Section 5.5 it was assumed that experimental wave refraction effects could be disregarded.

5.3.3.2 Wave Generator.

In the initial diffraction experiments described in Section 5.2.3, a small secondary crest was observed in the troughs of the primary wave train. These secondary crests can be clearly seen in the primary wave troughs in the contour plot shown in Fig. 4-34. It was initially thought that these secondary crests were due to reflections from the main beach opposite the wave paddle. To test this hypothesis, a stereopair was taken using a simplified infinite basin technique (see Section 5.4).

The diffraction experiment for the B/L = 1 configuration, desdribed in Section 5.2.3.1, was repeated using an incident wave train with the same characteristics as used in the previous experiment. However, this time the wave paddle did not run continuously. The paddle was started and a stereopair taken

of the water surface just as the waves were seen to reach the (back wall) beach opposite the wave paddle. Using this technique it was assumed that the stereopair had been taken before any wave reflection from the back wall beach could contaminate the primary diffracted wave train. The stereopair was analysed using a stereoplotter, and the secondary crests were again evident in the primary troughs. It was therefore suggested that the secondary crest was being generated by the wave paddle.

Careful observations of the paddle motion showed that the wave paddle was in fact generating the secondary crests. A small hesitation of the paddle at the end of the back stroke was seen to be generating the secondary crests in the troughs of the primary wave train. Two possible causes for this hesitation were suggested namely:-

(1) An excessive flexibility in the paddle itself, and the linkages to the driving-motor which caused a small wip-lash on the back stroke.

(2) For the experiment described above, the connecting arm between lever arms 1 & 2 (shown in Fig. 5-8) was at a distinct angle from the horizontal, and therefore the paddle motion would be non-simple harmonic.

Problem (1) above was dealt with by bracing the wave paddle by means of steel angle irons welded to the top surface of the wave paddle, replacing all worn bearings and ensuring that the entire structure was firmly bolted to the basin wall. Problem (2) was overcome by machining a range of inter-changeable cams so that the connecting arm would remain almost horizontal for all the test settings required.

Once all the modifications to the wave generator were completed, a series of tests were carried out in the basin using the open basin configuration shown in Fig. 5-24. The full range of incident waves needed for the diffraction experiments described in Section 5.5 were tested, and in each case the generator produced a pure wave train of constant form (3rd order Stokes) exhibiting no secondary crests.

5.3.3.3 Experimental Configuration and Procedure.

An investigation was undertaken to investigate the entire range of incident waves needed for the diffraction configurations described in Section 5.5, with the aim of achieving incident wave trains which were highly 2-dimensional (with uniform cross-sectional profiles across the width of the basin). It was recognised from the work of Harms (1976, 1979) and Goda et al (1971, 1973) that a highly 3-dimensional incident wave field (exhibiting marked wave height variations along the crests) would produce poor diffraction results identified by asymmetrical diffraction profiles and the non-repeatability of experimental results. It was the author's intention to experimentally investigate the generation of long crested waves in a model basin with the aim of minimising the secondary distorting effects, such as wave profile degeneration and cross-waves, described in Section 5.3.2. For experimental purposes, the incident waves investigated were assumed to be generated by a wave paddle with a perfect simple harmonic motion (see Section 5.3.3.2) and to propagate across a basin of perfectly uniform water depth (see Section 5.3.3.1).

The open basin configuration, shown in Fig. 5-24, was set up in the basin and was subsequently used for all the incident wave train experiments. Long splitter plates were placed parallel to and 0,3 m from both side walls, and the intervening spaces filled with gravel to protect the 4 control points situated below the mean water level (in canisters). The back wall beach consisted of 10-30 mm crushed stone, with a slope of 1 in 6,7. This back wall beach was used in all the diffraction configurations tested. The incident wave trains tested had the following characteristics:- wave period 0,64 to 1,16 seconds, wave height 50 mm to 60 mm, wave length (calculated using Airy wave theory) 570 mm to 1 200 mm and water depth 125 mm to 140 mm.

The experimental procedure adopted was as follows:-

(1) The incident wave characteristics for a particular run were determined (usually the incident wave characteristics required for a particular diffraction configuration), and the appropriate cam fitted to the wave generator to ensure that the connecting arm was horizontal at the required amplitude setting.

(2) The basin was filled to the predetermined depth and the paddle started.

(3) Visual observations of the incident wave field were made, noting the following:- The initial form of the incident wave field, the time at which secondary effects first became apparent and the nature of these effects; the time at which the secondary effects became fully developed and the subsequent nature of the quasi steady state wave field situation in the basin. For each test the wave paddle ran continuously for 30 minutes before being switched off.

(4) On switching off the wave paddle, the wave field in the basin was carefully observed until no residual waves could be detected.

To aid the interpretation of the experimental observations described in the next section, the range of reflection co-efficients expected for the back wall beach were calculated. The reflection co-efficient χ is defined by:-

$$\chi = \frac{H_r}{H_i} \tag{3}$$

where H_r = reflected wave height
H_i = incident wave height.

The amount of wave energy reflected from a beach depends upon the roughness, permeability and slope of the beach in addition to the steepness and angle of approach of the incident waves. Miche (1951) assumed that the reflection co-efficient for a beach χ could be described by:

$$\chi = \chi_1 \chi_2 \tag{4}$$

where χ_1 depends on the wave steepness, as well as the roughness and permeability of the beach, and is independent of the slope, while χ_2 depends on the slope of the beach and the wave steepness.

The value of χ_1 was estimated from the experimental results of Straub et al (1958) who found that χ_1 for a crushed stone beach varied from about 0,11 with a wave steepness of 0,01 to

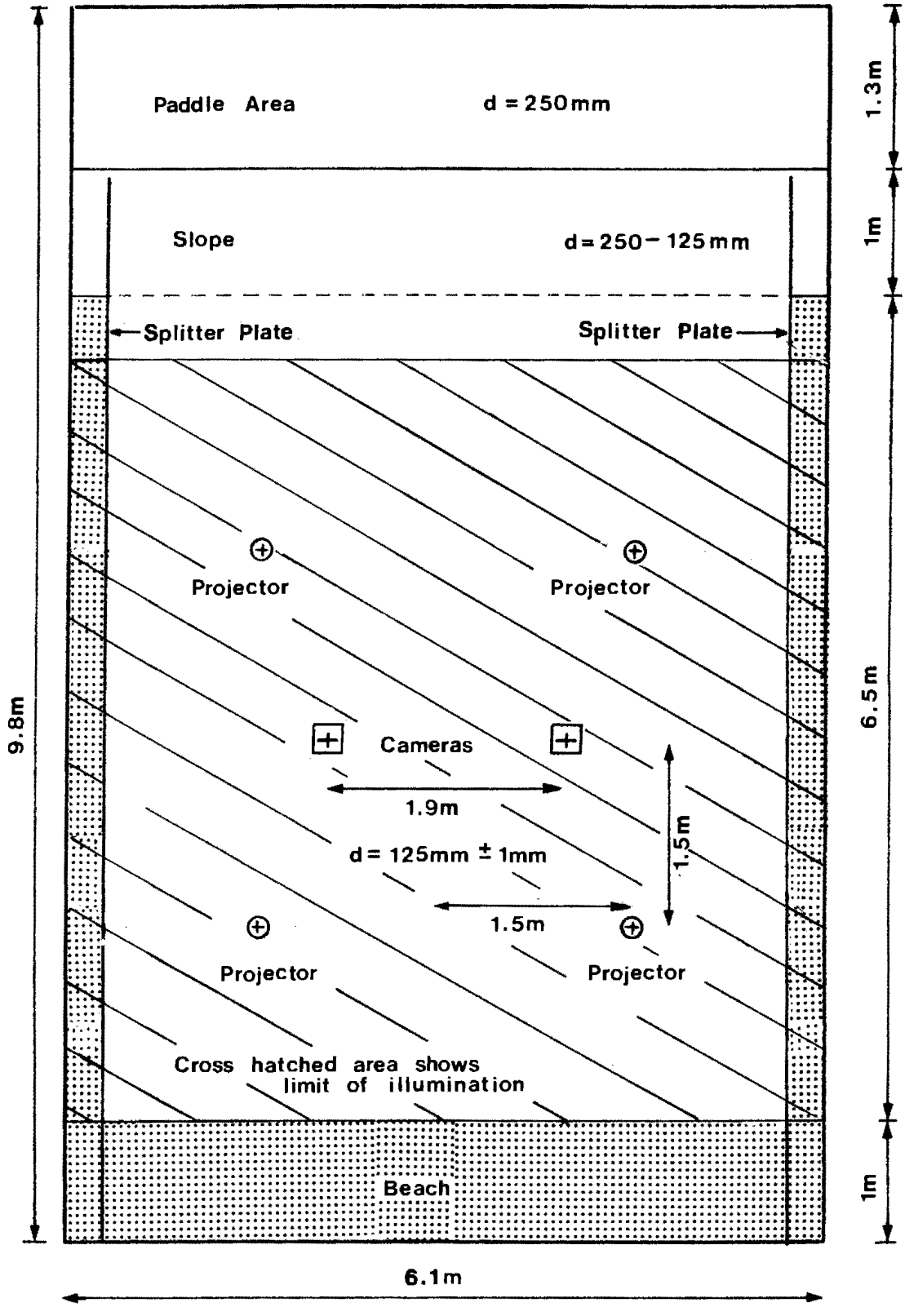

Fig. 5-24 Open basin configuration.

about 0,19 with a wave steepness of 0,07. The value of χ_2 was calculated using the procedure developed by Miche (1951) as described in CERC (1977) (assuming normal incidence).

The values for the reflection co-efficient χ calculated for the back wall beach varied from 0,006 to 0,009 for the range of incident waves used. Theoretically therefore, the back wall beach was virtually perfectly absorbing with the calculated reflected wave H_r approximately 1 % of the incident wave height H_i. The low theoretical reflectivity calculated for the peripheral beaches used in the diffraction configurations led the author to initially believe that the experiments described in Section 5.2 (in which the paddle ran continuously) closely approximated the situation of a continuous wave train entering an infinite basin via a breakwater gap.

The incident wave lengths used were found to not coincide with any corresponding lateral (between the splitter plates) basin resonance modes.

5.3.3.4 Discussion on Experimental Observation.

To discuss the observation made for each run would be far too lengthy; instead a summary of the general trends observed will be made.

It was evident for all the runs that the incident wave train was highly regular until the leading waves reached the back wall beach. At this stage, indications of wave height variations along the incident crests became evident until small localised breaking began to occur. These small localised breaks occurred throughout the basin, but were found to predominate both close to the wave paddle and close to the back wall beach.

The time elapsed from starting the wave paddle to the first signs of the deterioration of the incident wave field was 14 to 16 seconds. A near quasi-steady state situation was achieved after 30 to 35 seconds and the full quasi-steady state situation after 1 minute. In the quasi-steady state situation breaking occurred at approximately fixed positions across the basin possibly indicating a cross-wave basin resonance mode. This mode appeared to be particularly well developed just in front of the wave

generator and this coincided with the theoretical predictions of Mahony (1972) and the experimental findings of Barnard and Pritchard (1972). The localised breaking observed near the back wall beach was though to be due to a combination of beach effects and resonant cross-waves. From these observations it was obvious that the wave field generated in the first 16 seconds was much superior to the wave field evident in the basin after the paddle had been running for 30 or more seconds.

For each run the paddle ran for 30 minutes and during this period the wave field in the basin was carefully examined. A quasi-steady state situation was apparent after the 1st minute and remained in the basin until the end of the run. During this period localised small breaks were seen to occur in specific areas with these breaks slowly migrating within these areas.

When the wave paddle was switched off and the main wave train had traversed the basin, a secondary wave field was evident in the basin which was thought to be superimposed upon the primary wave train under steady state conditions. The secondary wave field consisted of two basin resonance modes and a random radiating field which covered the entire basin. The dominant basin resonance mode was the lateral mode between the side wall splitter plates (maximum antinode wave height of 6 mm), and this disturbance took 2 minutes to dissipate. The random radiating field took approximately 40 seconds to disperse.

It was evident that the incident wave field was regular, with almost uniform wave height along the crests, during the period before the first fully developed wave reached the far beach. It was proposed that the diffraction experiments should be undertaken using this pure incident wave field i.e. the stereopairs should be taken before the wave field has a chance to deteriorate.

The phenomenon of group velocity (velocity of the wave energy front) was apparent in the basin. This is to be expected since the incident wave trains were comprised of transitional waves which have a group velocity c_g of less than the individual wave celerity c ($0{,}5c < c_g < c$). As the incident wave train propagated into the basin of still water, the leading waves were seen to deminish in height. The time which elapsed between the

starting of the paddle and the instant at which the first fully developed wave (with a wave height close to the basin mean) was seen to reach the back wall beach corresponded closely with the time calculated to be needed by the wave energy front to traverse the basin.

It was therefore proposed that the best diffraction results would be obtained if the stereopairs were taken at the instant at which the wave energy front had been calculated to reach the back wall beach. It was postulated that this would have the following advantages:

(1) The incident wave field generated would be pure and undistorted since secondary effects such as resonant cross waves would not have had time to develop.

(2) The diffracted wave field would be pure and undistorted since wave reflections would not have a chance to contaminate this field and secondary effects such as cross waves would not have time to develop.

It was these general ideas which lead to the development of the infinite basin technique described in Section 5.4.

5.4 The Infinite Basin Technique.

5.4.1 Experimental Work to Test the Validity of the Infinite Basin Technique.

The author hypothesized that it would be possible to simulate the steady state situation of a continuous wave train entering an infinite basin by sending a wave train into a model basin of still water and taking a stereopair of the water surface just as the wave energy front reached the peripheral beaches. The author also hypothesized that the wave field immediately behind the wave energy front would be fully developed. To test these hypotheses, two stereopairs were taken of the wave energy front region of a typical wave train entering an open basin (Fig. 5-24) of initially still water. The experimental procedure used (a detailed description of the infinite basin procedure is also given in Section 5.5.2) was briefly as follows.

(1) The time, after starting the paddle, at which the cameras would have to be triggered to photograph the wave energy front region of the wave train as it passed the approximate mid-point of the basin was calculated as described in Section 5.5.2.

(2) The top micro-switch was selected to fire the cameras, the wave paddle started and a stereopair taken of the wave energy front region at the predetermined time.

(3) The wave paddle was switched off and the basin left for a minimum of 5 minutes before the next test.

(4) Step no 2 was repeated, but this time the cameras were triggered by the bottom micro-switch ensuring that the waves in the 2nd stereopair would be 180° out of phase relative to the waves in the 1st stereopair.

(5) The plates were analysed using the stereocomparator/microcomputer/projective transformation analysis system and the procedure described in Section 4.8.5.4. The plates were also analysed using the stereoplotter and the procedure described in Section 4.7.4. The two sets of results agreed very closely. The results obtained are shown in Fig. 5-25.

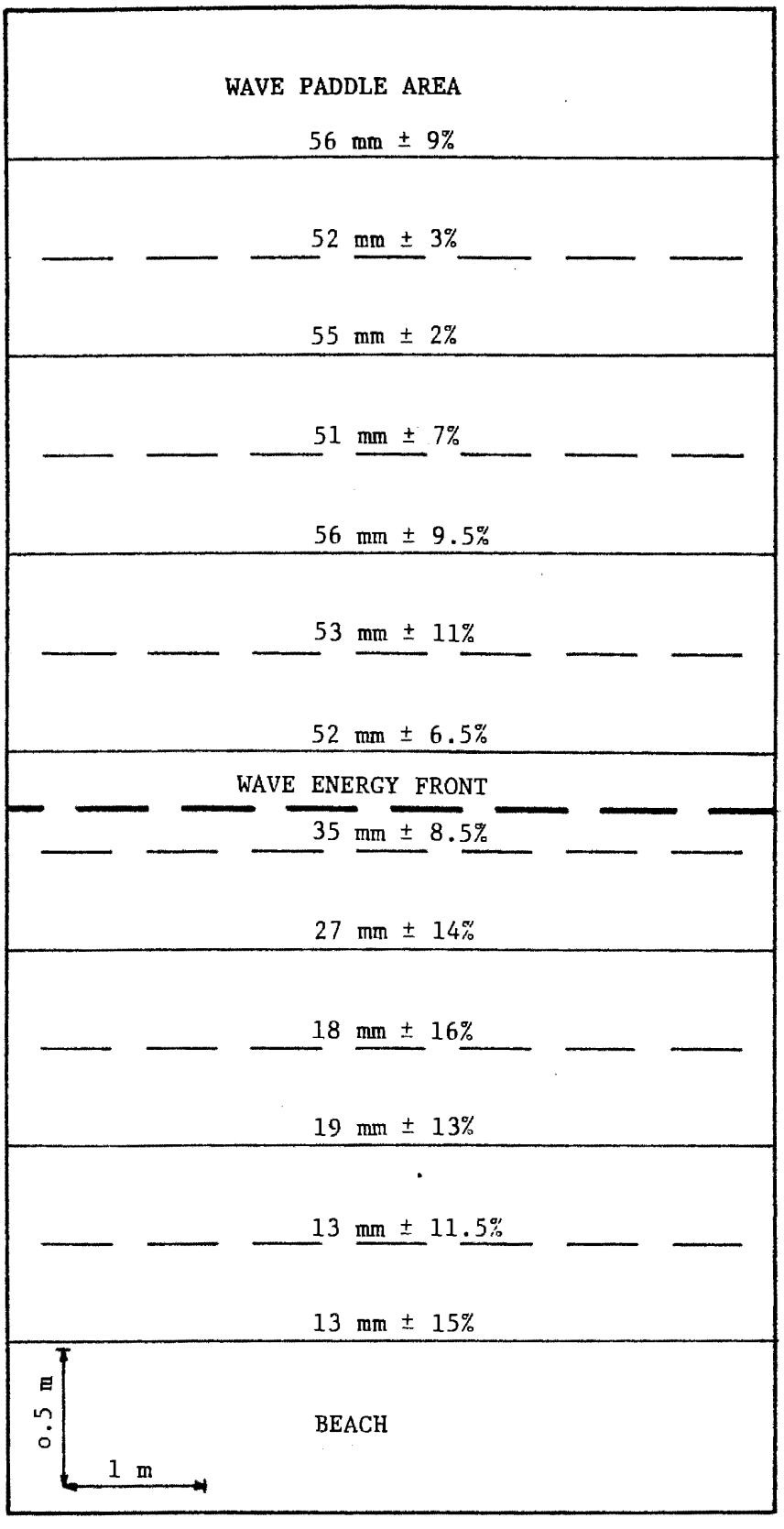

Fig. 5-25 Wave energy front region of a wave train.

The results shown in Fig. 5-25 were obtained using an incident wave train of period T = 0,74 seconds propagating in water depth d = 138 mm. The crestlines observed in the 1st stereopair are shown as solid lines, while the trough lines observed in the 1st stereopair are shown as dashed lines. The calculated position of the wave energy front is shown as a thick dashed lines. The mean wave height plus the observed percentage variation from the mean is shown for each crest and trough line. Note the trough lines observed in the 1st stereopair are coincident with the crest lines observed in the 2nd stereopair and vice versa.

5.4.2 Conclusions and Recommendations.

From Fig. 5-25 it can be seen that the wave heights of the crests immediately behind the wave energy front were closely equal to the mean wave height between the front and the generator. This would indicate that the hypothesis that the wave field immediately behind the wave energy front is fully developed, is correct.

The wave train behind the energy front, as shown in Fig. 5-25, can be seen to be highly regular. The ratio of maximum to minimum wave height along the individual generated crests in this region ranges from 1,04 to 1,25 with an average of 1,15. These ratios are substantially lower than the ratios reported by researchers such as Harms (1976, 1979) and Goda et al (1971, 1973) for tests in which the paddle ran continuously (see Section 5.3.1. for further details). It is therefore evident that the generated incident wave field obtained using the infinite basin technique is markedly superior to a quasi-steady state incident wave field obtained by allowing the paddle to run continuously throughout the entire test.

The procedure recommended for the use of the infinite basin technique in the general study of model harbours is as described above in Section 5.4.1, but with the two stereopairs of the water surface taken just as the wave energy front is calculated to have reached the peripheral beaches (as opposed to the basin mid-point as described above). The infinite basin technique adopted for the analysis of the breakwater gap diffraction configurations is described in Section 5.5.2.

5.5 Breakwater Gap Diffraction Configurations Analysed Using the Infinite Basin Technique.

5.5.1 Introduction.

It was the author's intention to investigate experimentally the situation of a continuous wave train entering a simulated infinite harbour basin via a gap between two effectively perfectly absorbing breakwaters (with long wave splitter plates at their tips). Furthermore, the author was interested in specifically investigating the particular configurations (for which the theoretical solutions are given) which are dealt with in what is probably the most widely used coastal engineering design manual, namely the U.S. Army Corps of Engineers Coastal Engineering Research Centre, Shore Protection Manual (CERC, 1977). The breakwater gap configurations given in the above manual, which were experimentally investigated by the author, are those with the following gap to wave length ratios, or B/L ratios, namely: 1,64 ; 1,41 ; 1 and 0,5. The author also experimentally investigated the B/L = 1,2 and 0,75 breakwater gap configurations.

The author was interested in comparing experimental diffraction results obtained using the infinite basin technique, with those obtained using the more conventional technique in which the wave paddle runs continuously throughout the test. For the purposes of this comparison the B/L = 1,64 breakwater gap configuration was analysed using both the infinite basin and conventional techniques.

All the above breakwater gap configurations are symmetrical about the gap centre line, i.e. the two breakwater arms are aligned along the same straight line. To investigate the effect of asymmetry, the author analysed a B/L = 1,64 breakwater gap configuration in which the one breakwater arm was offset a distance of one wave length in the incident wave direction.

It is the author's contention that the previous experimental results for the breakwater gap configuration described in Section 5.1.2 are inconclusive due to the limitations of the experimental configurations and wave height measurement techniques used. A comparison between conventional and photogrammetric laboratory wave height measurement techniques is given in Section 4.10.1.1. In this investigation every attempt was made to make the experimental results as valid as possible, namely:-

(1) The infinite basin technique was used to prevent cross-waves, basin resonance and wave reflection effects from distorting the incident and diffracted wave trains.

(2) Both the diffracted wave field within the basin and the incident wave train between the splitter plates were measured using the stereocomparator/micro-computer/projective transformation technique (see Section 4.8.5.4) in conjunction with metric photography.

In order that the incident wave height could be determined photogrammetrically, the splitter plates of the initial breakwater gap configuration (Fig. 5-7) were lengthened by 1 metre. In the new configuration (Fig. 5-26) the length of channel (between the splitter plates) which was imaged on the photographic plates was now 1,5 m, making it possible for the incident waves in this area to be measured photogrammetrically.

(3) The wave basin floor was levelled with a tolerance of ±1 mm to prevent wave refraction effects distoring the diffraction results (see Section 5.3.3.1).

(4) The wave paddle motion was constrained to be as close to simple harmonic motion as possible, in order that a highly regular monochromatic incident wave train was generated.

5.5.2 Experimental Procedure.

The wave equations needed for the experimental procedure adopted for the infinite basin technique are given below, and are based on the Airy wave theory.

The wave celerity c is given by

$$c = \frac{g}{k} \tanh (kd) \qquad (5)$$

and also

$$c = \frac{L}{T} \qquad (6)$$

where

g = acceleration due to gravity

k = $2\pi/L$ = the wave number

d = the water depth

L = the wave length

T = the wave period

The group velocity c_g is given by

$$c_g = \bar{n}c \qquad (7)$$

where c = the wave celerity

and $\bar{n} = 0,5 + \frac{kd}{\text{Sinh}(2kd)}$

The infinite basin technique experimental procedure for the breakwater gap configurations tested can be split up into a daytime and night time procedure.

A Daytime Procedure.

The daytime procedure adopted was as follows, namely:

(1) The breakwater gap configuration to be tested was set up in the wave basin (see Fig. 5-26). The gap width was checked and the splitter plates aligned parallel to each other and perpendicular to the wave generator. The basin was then filled with water to a depth of 125 mm and soluble oil dded to the water until an oil/water concentration of 7 ml/litre was achieved.

(2) The wave period to which the wave paddle needed to be set in order to generate waves of the required wave length was calculated using equations (5) and (6) above. The required wave length was determined from the B/L ratio of the breakwater gap configuration to be tested.

(3) The camera firing unit, flash system and control lights were tested for any faults. The cameras were then levelled using the procedure described in Section 4.6.3.

(4) The time T_E required for the wave energy front to traverse the basin from the wave paddle to the back wall beach was then calculated. T_E is given by

$$T_E = c_g D + T_p \qquad (8)$$

where

c_g = the group velocity

D = the distance from the wave paddle to the back wall beach. In this case D = 7,5 m from Fig 5 - 26.

T_p = the paddle start up time. In this case T_p was found to be 2,5 seconds on average.

T_E was found to correspond very closely to the time observed to elapse between starting the wave paddle and the instant the first fully developed wave (with a wave height close to the basic mean) was seen to reach the back wall beach. This served as a means of checking the calculated value of T_E.

(5) The incident wave train passing between the splitter plates was closely observed for the effects of a resonance mode between the parallel plates. If such a resonance mode was apparent its maximum antinode wave height was measured both during the T_E period and when fully developed. To measure the antinode wave height of the resonant mode at any time the wave paddle was stopped, and immediately after the incident wave train had left the region between the splitter plates, the resonance wave height in this region was measured.

(6) With the wave paddle set at the predetermined wave period setting, the paddle amplitude was adjusted to achieve an incident wave train with the largest wave height possible without localised breaking. However, a very small localised break was allowed to develop at the wave/splitter plate interface. The incident wave height needed to be as large as practically possible to ensure that the diffracted wave heights could be measured with sufficient accuracy.

(7) The oscillatory vortices which formed at both breakwater tips and the secondary waves seen to radiate outwards from both tips were closely observed. The significance of the secondary waves and the initial and steady state sizes of the vortices for each run were noted. The author noted that the above phenomena seemed to have a significant effect on the primary diffraction phenomenon. These observations led to the detailed experimental investigation described in Section 5.6.

B Night-time Procedure.

The night-time procedure adopted was as follows, namely:-

(1) The wave paddle period and amplitude settings were checked and then the wave paddle was set in the predetermined

position by setting the micro-switch trigger arm so that it was just touching the top micro-switch.

(2) The control point lights, the camera firing box and the flash circuitry were switched on and the top micro-switch selected using the appropriate switch on the camera firing box (see Fig. 4-22). The cameras were then loaded and the correct plate number selected. These numbers are imaged on the plates and serve to identify the stereopairs taken.

(3) The stop watch and wave paddle were then started simultaneously. The wave paddle was started using a remote stop/start station mounted on the platform above the wave basin. At the predetermined time (after T_E seconds), the reset button on the camera firing box was pressed to fire the camera/flash system.

(4) The wave paddle was then switched off and the secondary wave field in the basin allowed to dissipate entirely. A minimum period of 10 minutes was allowed between each run to allow the secondary waves to dissipate.

(5) The cameras were reloaded, the correct plate numbers selected, the bottom micro-switch selected, and the paddle set at its predetermined position (as described in step no. 1).

(6) Steps nos. 3 and 4 were then repeated.

The stereopairs were then analysed using the stereocomparator/microcomputer/projective transformation theory system, and the procedure described in Pos (1982b), a brief summary of which is given in Section 4.8.5.4. Using this system it is estimated that the wave heights within the basin and between the splitter plates were measured with an accuracy of better than 2 mm.

Initially the wave heights across the entire basin were measured and the resultant diffraction diagrams were found to be highly symmetrical. Therefore, for all the breakwater gap configurations analysed subsequently, only the wave heights in either the left (used most commonly) or the right hand side of the basin were measured.

It should be noted that while the experimental analysis was carried out using the program "WAVEHEIGHT", the flow chart for which is given in Appendix 4B, the author also wrote a suite of support

programs for the Tektronix 4051, namely:-

"EDIT".

This program was used to transfer data from the stereo-comparator to a file on the magnetic tape of the 2nd Tektronix 4051, (not part of the system described in Section 4.4.4). Once all the data had been transfered the file on the tape was closed. This raw data was then edited using the program. The erroneous data was deleted, the remaining data correctly formatted, and this edited data then dumped onto a tape file.

"INPUT"

This program was used to transfer the edited data from an ASCII tape file to memory arrays in the Tektronix micro-computer system (see Section 4.4.4). This data was then conferted to BINARY form and transfered to a file on a flexible disc. This flexible disc file was then accessed by the program "WAVEHEIGHT".

"TRANSFER".

This program was used to transfer data from a BINARY data file on one flexible disc to and equivalent file on a second flexible disc, which was used as a back-up disc if the first one "crashed".

"UNIVAC".

This was a "hand shaking" program to link the 2nd Tektronix 4051 with the UNIVAC 1100 via the data communications interface and remote terminal cable (see Section 4.4.5). Once the link was established the program was used to transfer data, such as XYH or XYH/H_i data, from a Tektronix tape file to a UNIVAC disc file.

Once the wave heights throughout the basin had been calculated, the diffraction diagram was constructed by dividing all the calculated wave heights by the incident wave height H_i. H_i is calculated to be the mean wave height of the imaged incident wave (between the splitter plates) in each stereopair which is the furthest from the model harbour entrance. The calculated XYH/H_i data was then transfered to a file on the UNIVAC 1100 as described above. The Saclant Graphics Package installed on the UNIVAC was then used to interpolate the raw data to a rectangular equidistant grid. The interpolated data was then used to plot a contour plot of equal diffraction coefficients K', where $K' = H/H_i$, thus yielding the experimental diffraction diagram for the configuration tested.

5.5.3 Breakwater Gap Configurations Analysed.

5.5.3.1 The B/L = 1,64 Breakwater Gap Configuration.

The first configuration tested had a B/L ratio equal to 1,64. This experimental configuration is shown in Fig. 4-45 of Section 4.8.5.4. If one refers to the more general breakwater gap diffraction configuration diagram shown in Fig. 5-26, the value B as shown in the diagram would in this case equal 990 mm.

The incident wave train had the following characteristics:- Wave period 0,67 seconds, mean wave height (H_i) 55,5 mm, and wave length (calculated using Airy wave theory) 604 mm. The water depth was 125 mm ±1 mm. The incident wave crests (one in each stereopair) used to determine H_i were respectively 1,25 m and 1,54 m from the model harbour entrance (breakwater gap). Both stereopairs were taken approximately 14,5 seconds after starting the wave paddle, at which stage the wave energy front was at the toe of the back wall beach. The stereopairs which were taken are shown in Fig. 4-46 of Section 4.8.5.4. Since the harbour configuration is symmetrical about the centre line, only the left hand side of the basin is shown.

The experimental diffraction diagram calculated from the above stereopairs is shown in Section 6.1.2, where it is compared to a theoretical finite element diffraction diagram for an equivalent configuration. The experimental diffraction diagram is also compared to a theoretical diffraction diagram for the corresponding fully reflecting breakwater case, namely the relevant diffraction diagram, from CERC (1977), based on the Penney and Price (1952) solution and constructed using the method described by Johnson (1953).

No pronounced resonance mode was seen to develop between the splitter plates in the T_E = 14,5 seconds period prior to taking the stereopairs. After approximately 40 seconds, when a quasi steady state situation had been achieved, a small resonance mode was evident between the splitter plates. A detailed description of the B/L = 1,64 steady state situation is given in Section 5.5.4.

The oscillatory vortices which formed at the breakwater tips, and the secondary waves which radiated from these tips, seemed to have a significant effect on the resultant diffracted wave height distribution, particularly in the region between and just in front of, the breakwater tips. A detailed description of the "radiating

second order phenomena"(Biesel 1963, 1966) observed for the B/L = 1,64 diffraction configuration is given in Section 5.6.3.1.

5.5.3.2 The B/L = 1,41 Breakwater Gap Configuration.

The second diffraction configuration tested had a B/L ratio equal to 1,41. If one refers to the general breakwater gap configuration shown in Fig. 5-26, the value of B shown in the diagram would in this case equal 800 mm. A plan view of the 800 mm wide breakwater gap configuration, taken using one of the Zeiss cameras mounted above the basin, is shown in Fig. 5-27. This photograph is a contact print of the corresponding glass plate negative, and shows the stereoscopic overlap portion of the film format. The 16 control points can be clearly seen in this photograph

The incident wave train for the B/L = 1,41 configuration had the following characteristics: wave period 0,64 seconds, mean wave height (H_i) 52,8 mm, and wave length (calculated) 567 mm. The water depth was 125 mm. The incident wave crests (one in each stereopair) used to determine H_i, were respectively 0,85 m and 1,12 m from the model harbour entrance. Both stereopairs were taken approximately 14 seconds after starting the wave paddle, at which stage the wave energy front was approximately 0,6 m from the toe of the back wall beach. The stereopair of the configuration taken using the top microswitch is shown in Fig. 5-28. Since the harbour configuration is symmetrical about the centre line, only the left hand side of the basin is shown. Both stereopairs and the corresponding diffraction diagram for the B/L = 1,41 configuration are shown in Pos (1982c).

The experimental diffraction diagram for the B/L = 1,41 configuration is shown in Section 6.1.3, where it is compared to a theoretical finite element diffraction diagram for an equivalent configuration. The experimental diffraction diagram is also compared to a theoretical diffraction diagram for the corresponding fully reflecting breakwater case, namely, the relevant diffraction diagram, from CERC (1977), based on the Penney and Price (1952) solution, and constructed using the method described by Johnson(1953).

No pronounced resonance mode was evident between the splitter plates during the 14 seconds period prior to taking the stereopairs, or when the quasi steady state wave field situation in the basin was achieved. However, it was noted that after the

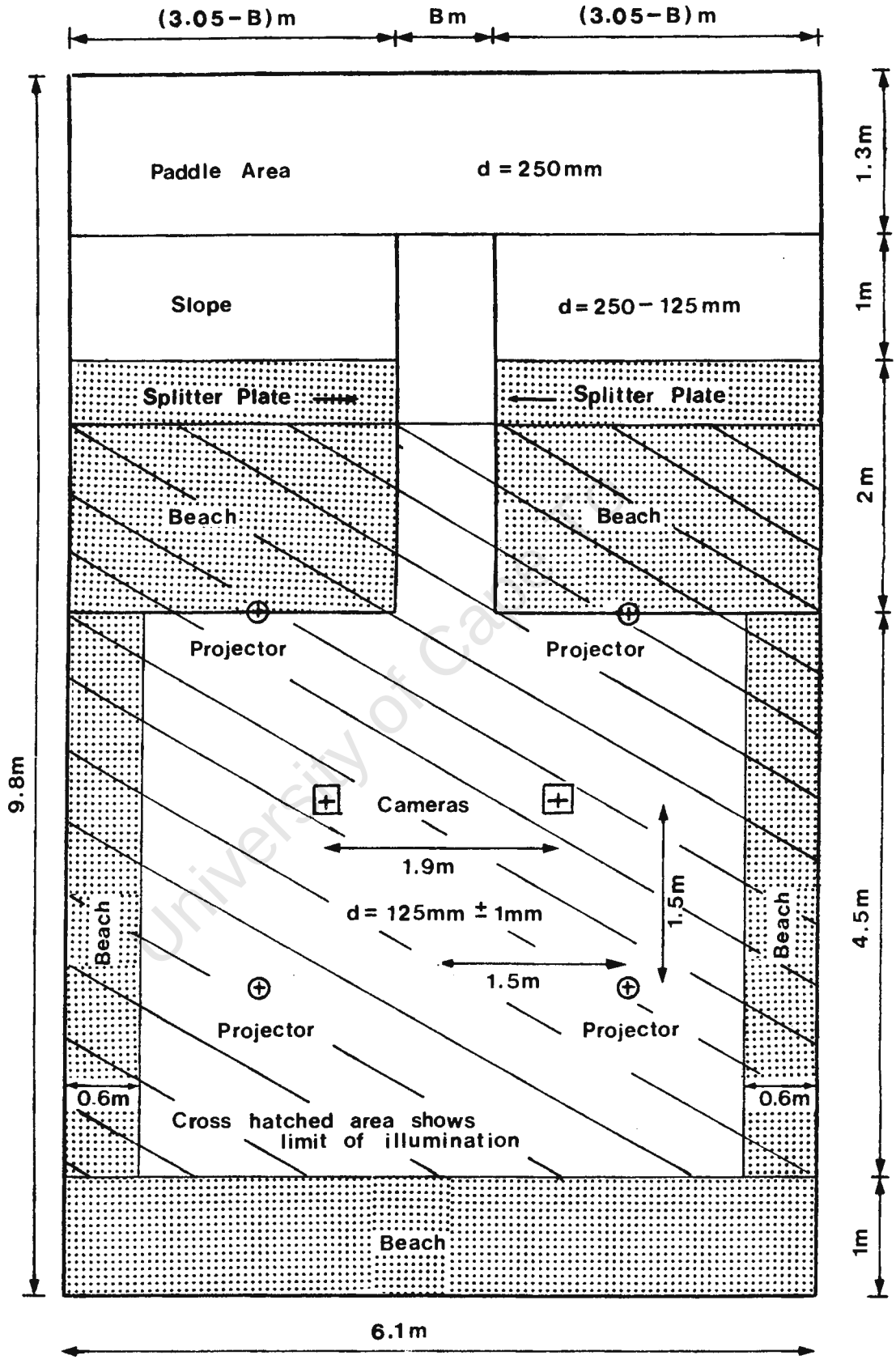

Fig 5-26 Generalised breakwater gap configuration.

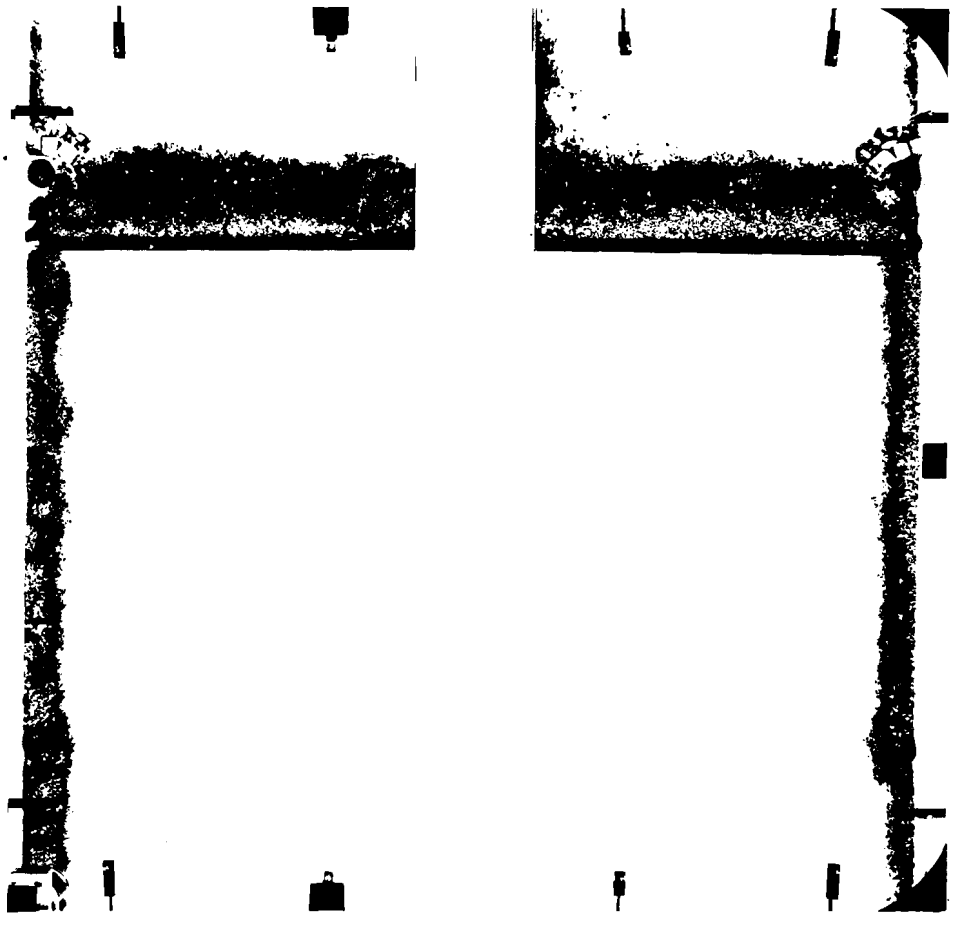

Fig 5-27 Plan view of the 800 mm wide breakwater gap configuration.

paddle had been running for 15 to 16 seconds the incident wave train between the splitter plates started showing signs of deterioration. This deterioration increased marginally until a quasi steady state situation was achieved, after about one minute. The deterioration of the incident wave train was thought to be caused by the development of resonant cross-waves with crests parallel to the splitter plates. The time period needed for these cross-wave effects to develop corresponds with the experimental findings of Barnard and Pritchard (1972) and Spens (1954).

The oscillatory vortices and the radiating second-order waves generated at the breakwater tips were again thought to have a significant effect on the experimental diffraction results. Their effect was most pronounced in regions within 1 wave length of either breakwater tip. The above phenomena are thought to be the cause of the marked wave height peak, which had a maximum measured wave height of 65 mm, situated approximately 600 mm in front of the

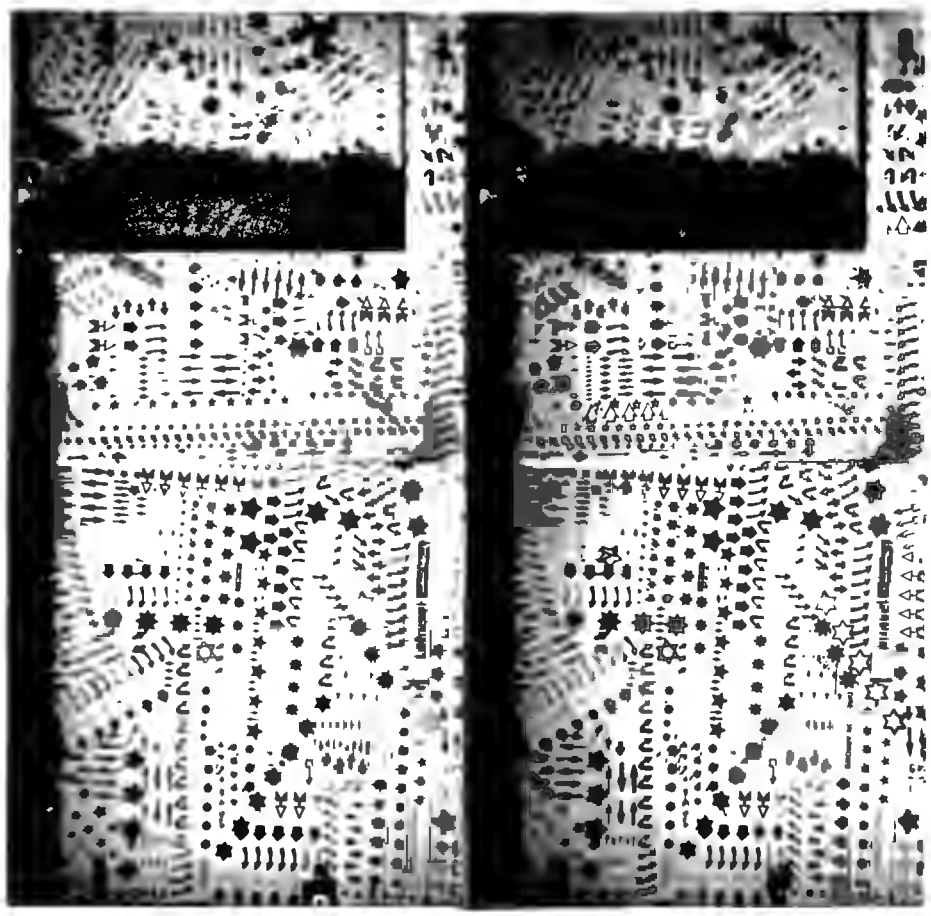

Fig. 5-28 Stereopair of the B/L = 1,41 breakwater gap configuration.

breakwater gap on the centre line. This wave height peak is clearly shown on the experimental diffraction diagram which is given in Section 6.1.3, and can be clearly seen in the stereo-pair of the B/L = 1,41 configuration (Fig. 5-28). Although the secondary waves were clearly seen to radiate into the shadow zones, the primary diffracted waves were still the main mechanism of energy transfer into these regions.

The oscillatory vortices at the breakwater tips reached their max. size as the first 2 to 3 waves passed into the basin, after which their size stabilised to a radius of about 100 mm. The vortex moved forward with the wave crest and backward with the subsequent trough. However, the vortices seemed slightly out of phase with the incident wave, probably due to inertial and drag forces, and seemed consequently to have an opposing current effect on the edges of the wave crests as the crests passed through their areas of influence.

5.5.3.3 The B/L = 1,20 Breakwater Gap Configuration.

The third diffraction configuration tested had a B/L ratio equal to 1,20. The 800 mm wide breakwater gap configuration shown in Fig. 5-27 was again used to test this configuration.

The incident wave train for the B/L = 1,20 configuration had the following characteristics: wave period 0,72 seconds, mean wave height (H_i) 52,8 mm (as for the 1,41 configuration), and wave length (calculated) 666,7 mm. The water depth was 125 mm. The incident wave crests (one in each stereopair) used to determine H_i were respectively 1,07 m and 1,39 m from the model harbour entrance. Both stereopairs were taken approximately 14 seconds after starting the wave paddle, at which stage the wave energy front was at the toe of the back wall beach. The stereopair of the configuration taken using the bottom micro-switch is shown in Fig. 5-29. Only the part of the basin to the left of a line through the right hand splitter plate is shown. Wave height measurements were taken in the basin on and to the left of the line of symmetry through the gap centre point. A more detailed stereoscopic view of the wave height distribution in the vicinity of the breakwater gap is shown in Fig. 5-30.

The experimental diffraction diagram for the B/L = 1,20 configuration is shown in Section 6.1.4 where it is compared to a theoretical finite element diffraction diagram for an equavilent configuration.

A fairly pronounced resonance mode was apparent between the splitter plates, which developed to a steady state condition after 20 seconds. The maximum steady state antinode wave height measured was 8 mm. However, during the T_E = 14 seconds period, the antinode wave height did not exceed 4 mm. The resonance wave length was half the gap width, i.e. 400 mm. The resonance antinodes were situated at the spliter plates, at the gap centre line (line of symmetry) and at the quarter points. This resonance mode was thought to be the major cause of the observed deterioration of the incident wave field.

The oscillatory vortices and radiating second-order waves, generated at the breakwater tips, were again thought to have a pronounced effect on the diffracted wave height distribution in the regions within one wavelength of either breakwater tip. The above

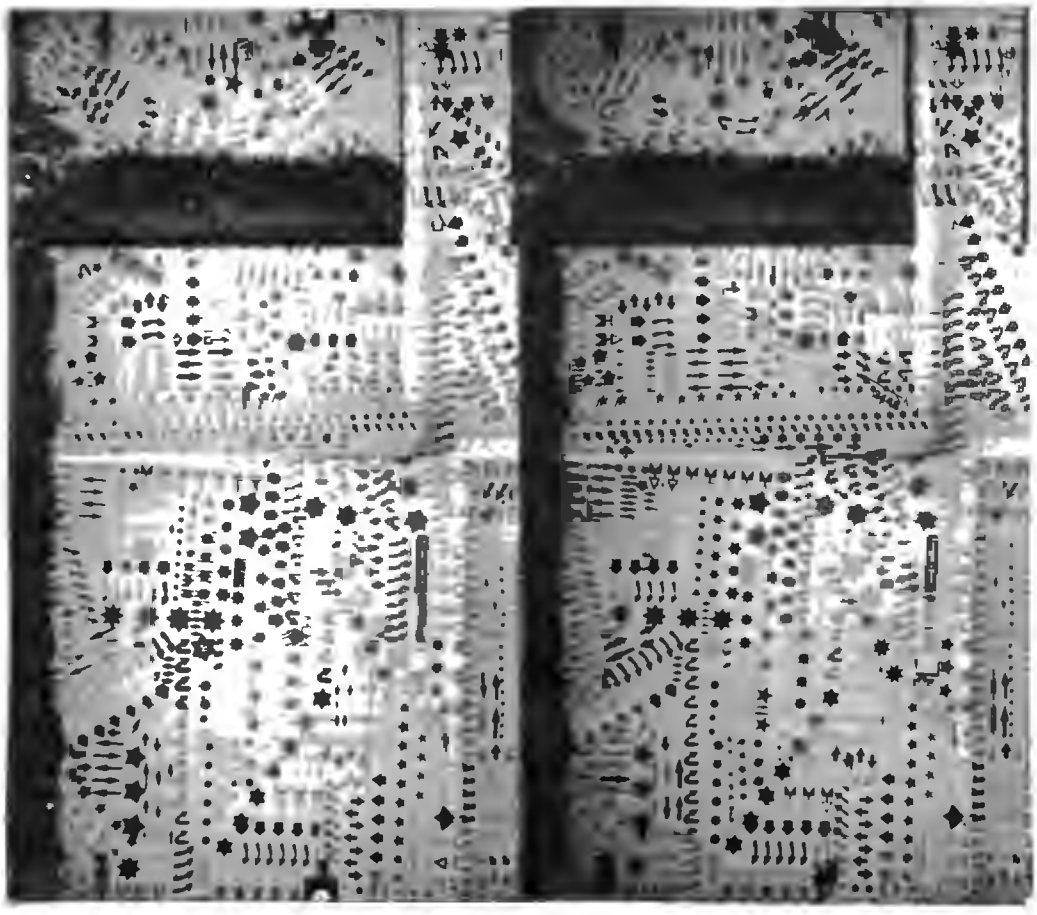

Fig. 5-29 Stereopair of the B/L = 1,20 breakwater gap configuration.

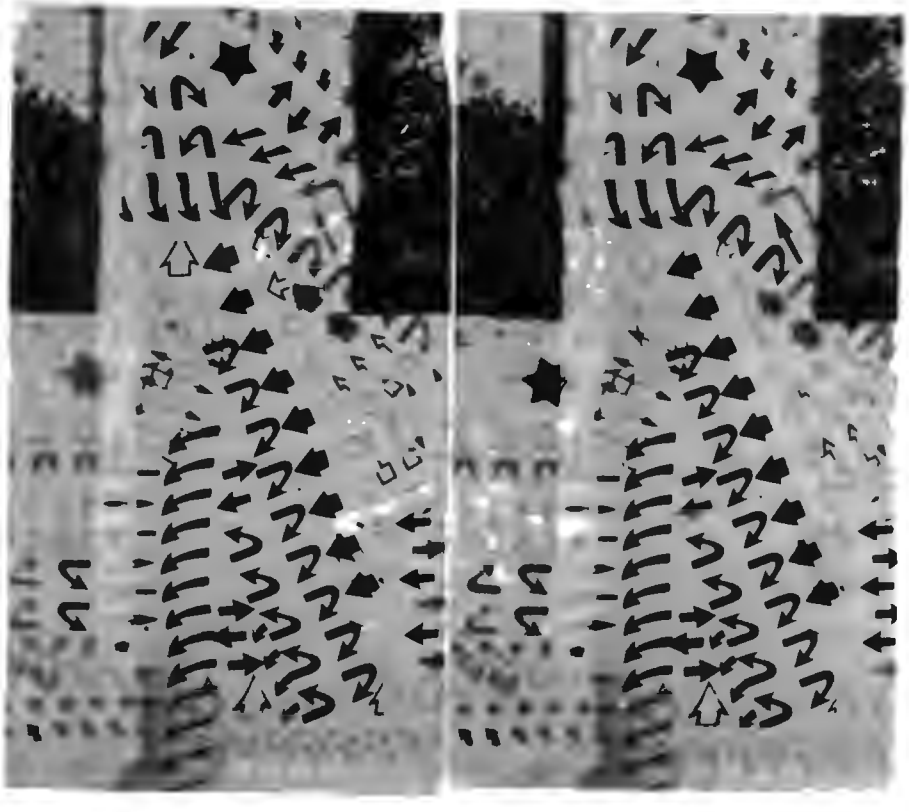

Fig. 5-30 Detailed view of the breakwater gap region of Fig. 5-29 above.

phenomena were thought to be the cause of the marked wave height peak, which had a maximum measured wave height of 73 mm (H/H_i = 1,38), situated 330 mm from the breakwater gap on the line of symmetry (the gap centre line). This wave height peak can be clearly seen in both Figs 5-29 and 5-30. Fig. 5-30 gives a more detailed view of the wave height peak and the vortices at the breakwater tips. Although the second-order waves radiating from the tips were most noticeable in the lee of the breakwaters in the regions of small primary diffracted wave height, it was found that the measured primary diffracted wave heights in these regions were still 2 or more times greater than the measured wave heights of the second-order waves. As regards the vortices, they were again found to have a counter current effect on those portions of the crests passing through their areas of influence.

5.5.3.4 The B/L = 1 Breakwater Gap Configuration.

The fourth diffraction configuration tested had a B/L ratio equal to 1. The 800 mm wide breakwater gap configuration shown in Fig. 5-27 was again used for this configuration.

The incident wave train for the B/L = 1 configuration had the following characteristics: Wave period 0,83 seconds, mean wave height (H_i) 53,2 mm, and wave length (calculated) 800 mm. The water depth was 125 mm. The incident wave crests used to determine H_i were respectively 1,09 m and 1,50 m from the model harbour entrance. Both stereopairs were taken approximately 12,5 seconds after starting the paddle, at which stage the wave energy front was at the toe of the back wall beach. As before, a stereopair of the configuration taken using the bottom micro-switch is shown in Fig. 5-31. Again, only the portion of the basin to the left of a line through the right hand splitter plate is shown. Wave height measurements were again taken on and to the left of the line of symmetry. A more detailed view of the wave height distribution in the vicinity of the breakwater gap is shown in Fig. 5-32.

The experimental diffraction diagram for the B/L = 1 configuration is shown in Section 6.1.5 where it is compared to a theoretical finite element diffraction diagram for an equivalent configuration. This experimental diffraction diagram is also compared to a theoretical diffraction diagram for the fully reflecting breakwater

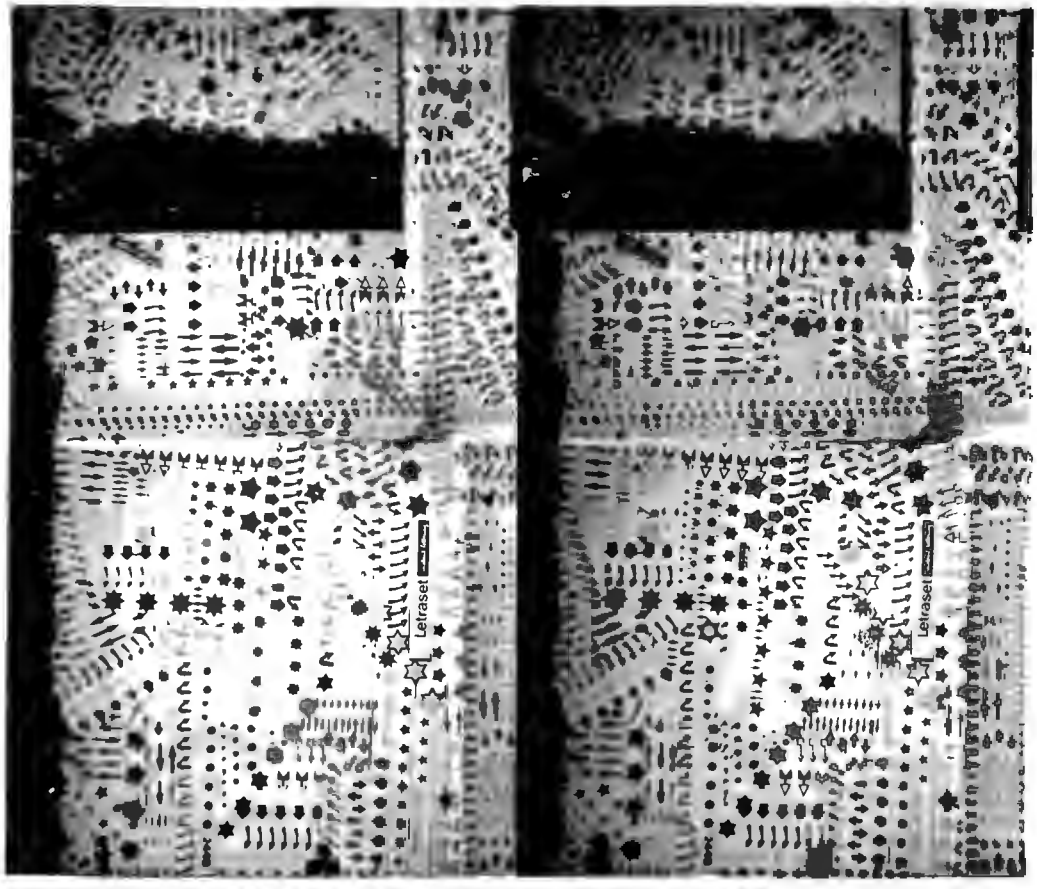

Fig. 5-31 Stereopair of the B/L = 1 breakwater gap configuration.

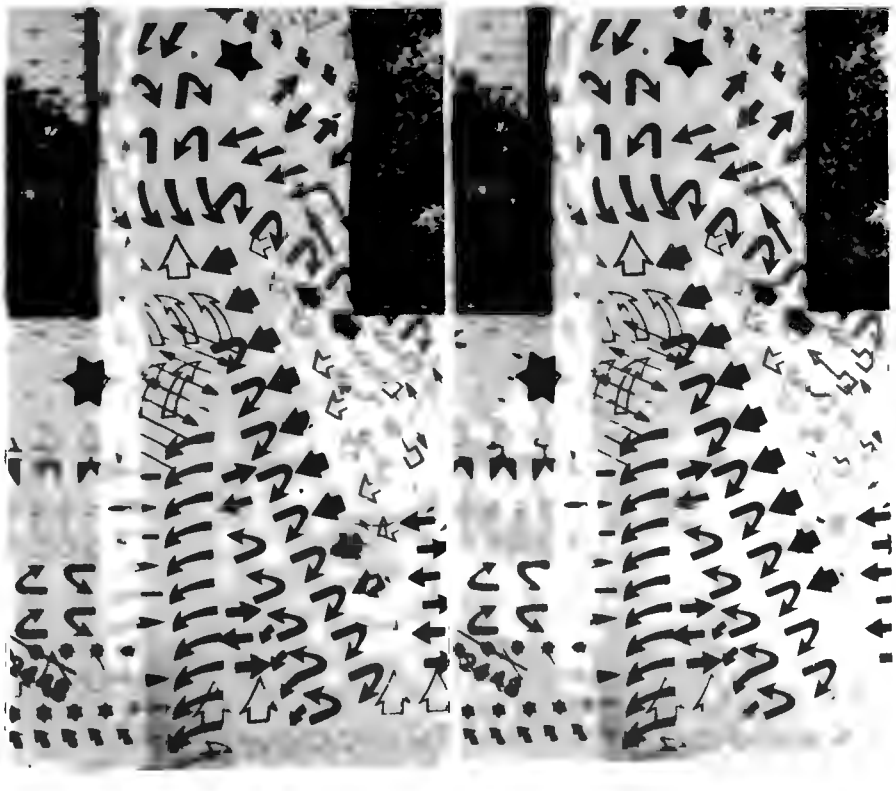

Fig. 5-32 Detailed view of the breakwater gap region of Fig 5-31 above.

case, namely, the relevant theoretical diffraction diagram from Johnson (1952), based on the diffraction theory of Morse and Rubenstein (1938), and constructed using the method described by Carr and Stelzriede (1952).

As could be expected, a fairly pronounced resonance mode developed between the splitter plates, reaching a steady state condition after approximately 30 seconds. The steady state antinode wave height was measured and found to be approximately 7 to 8 mm. However, during the T_E = 12,5 seconds period the antinode wave height did not exceed 4 mm. The resonance wave length was equal to the gap width, i.e. 800 mm. The resonance antinodes were situated at the splitter plates and at the gap centre line. This resonance mode was again thought to be the major cause of the observed deterioration of the incident wave field.

The oscillatory vortices and radiating second-order waves generated at the breakwater tips were again thought to be the cause of the marked wave height peak, with a maximum measured wave height of 78 mm (H/H_i = 1,46), situated 219 mm from the breakwater gap on the line of symmetry. This wave height peak can be clearly seen in both Figs 5-31 and 5-32. A detailed description of the second-order radiating phenomena observed for the B/L = 1 diffraction configuration is given in Section 5.6.3.2.

5.5.3.5 The B/L = 0,75 Breakwater Gap Configuration.

The fifth diffraction configuration tested had a B/L ratio equal to 0,75. The 800 mm wide breakwater gap configuration shown in Fig. 5-27 was used for this configuration.

The incident wave train had the following characteristics: wave period 1,05 seconds, mean wave height (H_i) 57,7 mm, and wave length (calculated) 1066,7 mm. The water depth was 125 mm. The incident wave crests used to determine H_i were respectively 0,94 m and 1,50 m from the model harbour entrance. Both stereopairs were taken approximately 11,5 seconds after starting the wave paddle (i.e. as the wave energy front reached the back wall beach). As before, a stereopair of the configuration taken using the bottom micro-switch is shown in Fig. 5-33. Only the portion of the basin to the left of a line through the right hand splitter plate is shown. Wave height measurements were taken on and to the left

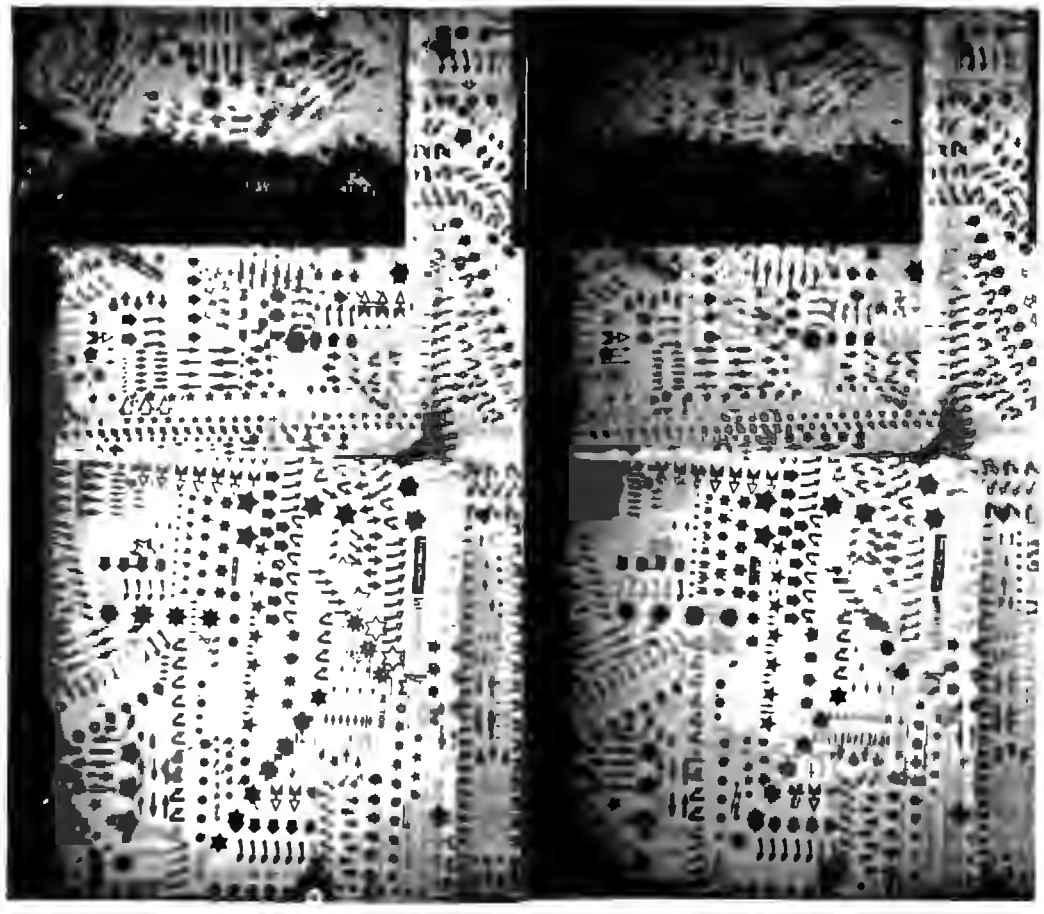

Fig. 5-33 Stereopair of the B/L = 0,75 breakwater gap Configuration.

Fig. 5-34 Detailed view of the breakwater gap region of Fig. 5-33 above.

of the line of symmetry. A more detailed view of the wave height distribution in the vicinity of the breakwater gap is shown in Fig. 5-34

The experimental diffraction diagram for the B/L = 0,75 configuration is shown in Section 6.1.6, where it is compared to a theoretical finite element diffraction diagram for an equivalent configuration.

No pronounced resonance mode was seen to develop between the splitter plates. However, the incident wave field did deteriorate and reached a steady state condition after approximately 40 seconds. It is postulated that the deterioration of this wave field was caused by the formation of resonant cross-waves, and also possibly by a feed back of energy towards the wave generator by the secondary waves radiating from the breakwater tips.

The secondary waves radiating from the breakwater tips were very pronounced for the B/L = 0,75 configuration. Significant secondary waves were seen to be generated at the breakwater tips every time either a crest or a trough passed the tips. Furthermore, the two secondary waves generated by a trough were seen to flatten the centre of the succeeding crest (at the gap centre line) as the crest passed between the breakwater tips. In Figs 5-33 and 5-34 one can clearly see that the centre of the crest just entering the model basin has been flattened by the two secondary waves generated by the preceding trough. This effect can also be seen in the experimental diffraction diagram given in Section 6.1.6. When the plates were viewed using the stereocomparator these secondary crests were clearly seen to be superimposed upon the primary diffracted wave crests.

5.5.3.6 The B/L = 0,5 Breakwater Gap Configuration.

The sixth diffraction configuration tested had a B/L ratio equal to 0,5. If one refers to the general breakwater gap diffraction configuration diagram shown in Fig. 5-26, the value B as shown in the diagram would in this case equal 600 mm.

The incident wave train for the B/L = 0,5 configuration had the following characteristics: Wave period 1,16 seconds, mean wave height (H_i) 61,0 mm, and wave length (calculated), 1200 mm. The water depth was 125 mm. The incident wave crests used to

determine H_i were respectively 0,74 m and 1,36 m from the model harbour entrance. Both stereopairs were taken (T_E) 11 seconds after starting the wave paddle. The stereopairs for this configuration are not shown, since the small wave heights in the basin make stereoscopic viewing with a pocket viewer difficult.

The experimental diffraction diagram for the B/L = 0,5 configuration is shown in Section 6.1.7, where it is compared to a theoretical finite element diffraction diagram for an equivalent configuration. This experimental diffraction diagram is also compared to a theoretical diffraction diagram for the fully reflecting breakwater case, namely, the relevant theoretical diffraction diagram from Johnson (1952), based on the diffraction theory of Morse and Rubenstein (1938), and constructed using the method described by Carr and Stelzriede (1952).

No pronounced resonance mode was seen to develop between the splitter plates in the T_E= 11 seconds period prior to taking the stereopairs. A quasi steady state condition was achieved after approximately 45 seconds, during which time a small resonance mode was seen to develop between the splitter plates. The resonance wave length was the same as the incident wave length , i.e. 1200 mm. The resonance antinodes were situated at the splitter plates.

The oscillatory vortices and radiating secondary waves generated at the breakwater tips were again very pronounced. Due to the relatively small gap width, the oscillatory vortices (with radii of ±150 mm) had a very pronounced effect on the incident wave crests as they passed between the breakwater tips. A detailed account of the vortices and the radiating second-order phenomena observed for the B/L = 0,5 diffraction configuration is given in Section 5.6.3.3.

5.5.3.7 The B/L = 1,64 Asymmetrical Breakwater Gap Configuration.

The seventh diffraction configuration tested was an asymmetrical breakwater gap configuration with a B/L ratio equal to 1,64. To construct this configuration, the left hand breakwater of the B/L = 1,64 breakwater gap configuration shown in Fig. 4-45 was shifted a distance of 604 mm (the incident wave length), in the incident wave direction, with the two breakwater arms kept parallel to each other. To accommodate this shift, the attached splitter plate was extended by 604 mm.

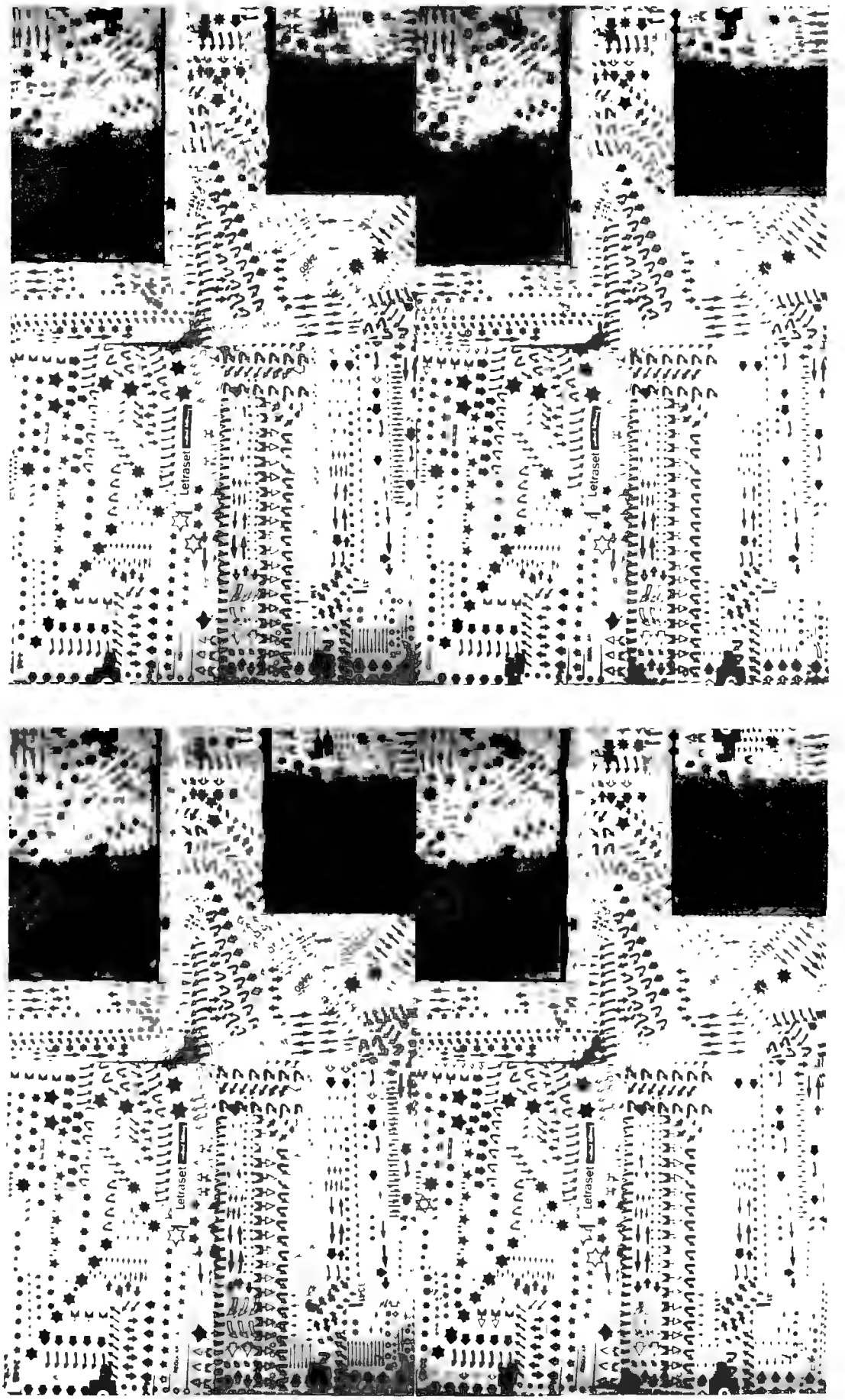

Fig. 5-35 Stereopairs taken of the asymmetrical B/L = 1,64 breakwater gap configuration.

The incident wave train had almost identical characteristics with the incident wave train used in the symmetrical B/L = 1,64 breakwater gap configuration described in Section 5.5.3.1, namely: Wave period 0,67 seconds, mean wave height (H_i) 52,8 mm, and wave length (calculated), 604 mm. The water depth was 125 mm. The incident wave crests, (one in each stereopair) used to determine H_i were respectively 1,28 m and 1,60 m from the model harbour entrance. Both stereopairs were taken at T_E = 14,5 seconds after starting the wave paddle. The stereopairs which were taken are shown in Fig. 5-35. Due to space limitations, only the central portion of the basin is shown in the stereopairs. Since the configuration was asymmetrical, wave height measurements were taken across the full width of the basin. The experimental and finite element diffraction diagrams for this configuration are given in Section 6.1.8.

As before, no pronounced resonance mode was seen to develop between the splitter plates in the T_E = 14,5 seconds prior to taking the stereopairs. A small resonance mode was subsequently seen to develop of similar wave length and wave height to the resonance mode described in Section 5.5.4.

Oscillatory vortices and radiating secondary waves were again generated at the breakwater tips, and seemed to have a pronounced effect on a wave crest as it passed each tip. Secondary waves were seen to radiate across the primary wave crest as it passed a breakwater tip. A detailed description of the breakwater tip effects observed for this configuration is given in Section 5.6.3.4.

5.5.4 Infinite Basin vs Conventional Technique.

Previous researchers such as Putnam and Arthur (1948), Harms (1976, 1979), Blue and Johnson (1949), Silvester and Lim (1968) and Goda et al (1971, 1973) carried out wave diffraction experiments in which the wave paddle ran continuously throughout the entire test period for a particular configuration. Carr and Stelzriede (1952) were the first researchers to try an "infinite basin" type technique (See Section 5.1.2.2). However, their published results are at best inconclusive. Harms (1976, 1979) also experimented with an "infinite basin" type technique which he termed "the intermittent data aquisition mode" (see Section 5.3.1). However, he abandoned this approach and adopted the conventional technique in which the paddle ran continuously throughout the test.

The author was interested in comparing the experimental diffraction results obtained using the infinite basin technique with those obtained using the more conventional technique described above. As a comparison, the B/L = 1,64 breakwater gap configuration, previously analysed using the infinite basin technique (see Section 5.5.3.1), was analysed using the conventional technique. When using the conventional technique, it is generally assumed that the waves are effectively perfectly absorbed by the peripheral beaches. Since the wave basin beaches were calculated to have very low reflection coefficients (see Section 5.3.3.3) it was thought that the above configuration would offer a very fair test of the conventional technique.

The experimental configuration is described in Section 5.5.3.1. The incident wave train had the following characteristics: wave period 0,67 seconds, mean wave height (H_i) 52,0 mm and wave length 604 mm. The water depth was 125 mm ± 1 mm as before. The incident wave crests used to determine H_i were respectively 1,22 m and 1,53 m from the model harbour entrance. The first stereopair was taken (using the top micro-switch) after the wave paddle had been running for a minute i.e. as soon as a quasi-steady state condition was seen to exist in the basin. The cameras were reloaded and the second stereopair was taken (using the bottom micro-switch) after the wave paddle had been running for three minutes. The paddle ran continuously throughout the test. The stereopairs which were taken are not shown, since through a pocket viewer they appear almost exactly identical to the stereopairs shown in Fig. 4-46 of Section 4.8.5.4, i.e. to the stereopairs taken using the infinite basin technique. However, when the stereopairs taken using the conventional technique were viewed using a stereocomparator, it could be seen that a random secondary wave field was superimposed upon the primary diffracted wave field. This secondary wave field was observed to cause small random wave height variations along the primary diffracted wave crests.

The experimental diffraction diagram calculated from the above stereopairs is shown in Fig. 5-36. This diagram can now be compared to the equivalent experimental diffraction diagram (constructed from stereopairs taken using the infinite basin technique) shown in Section 6.1.2. As one would expect the two

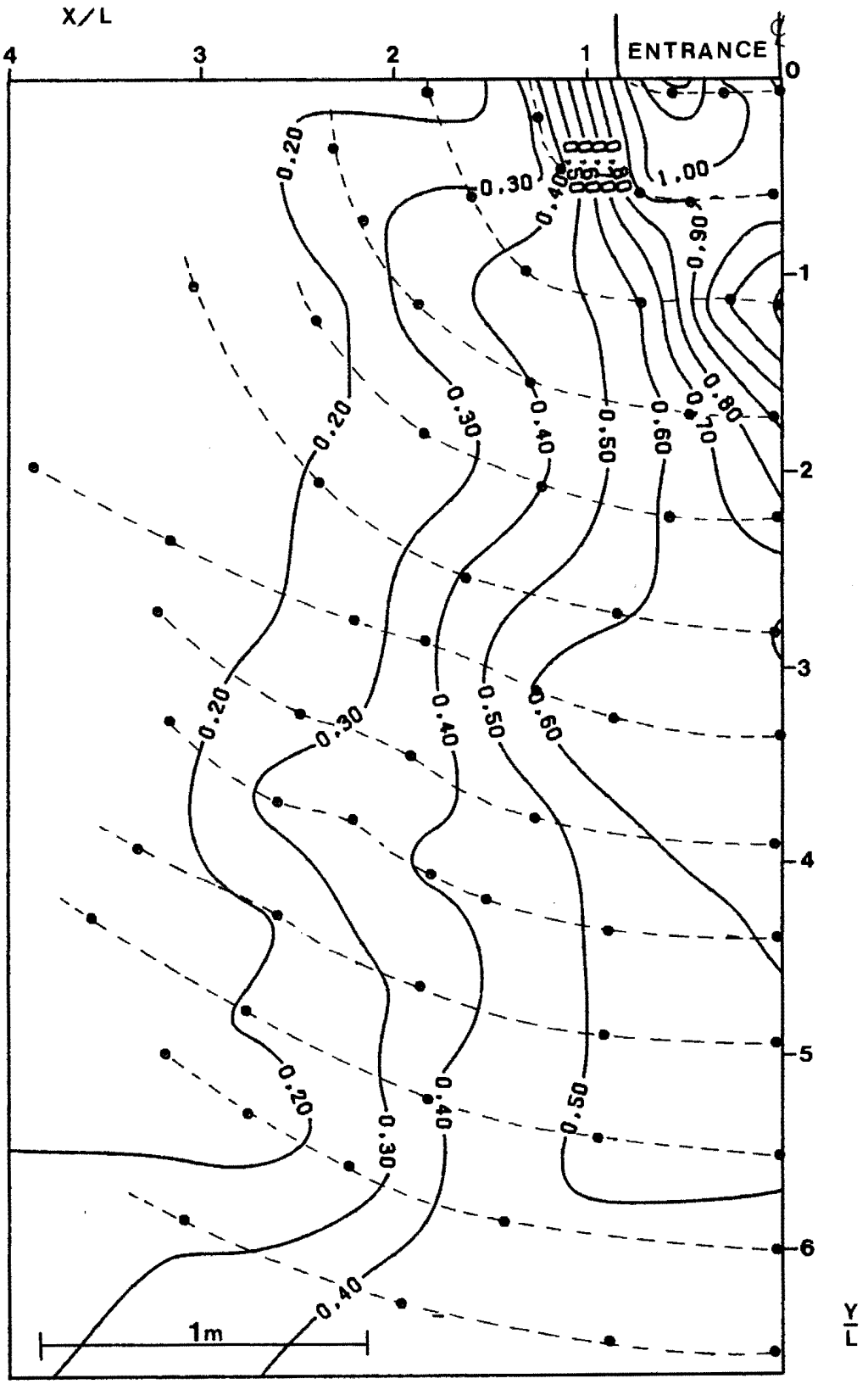

Fig. 5-36 Experimental diffraction diagram for the B/L = 1,64 breakwater gap configuration tested using the conventional technique.

diffraction patterns are similar in form. This is particularly the case in regions where the diffracted wave height is relatively large. However, the greatest differences between the two patterns can be seen where the diffracted wave heights are relatively small (compared to H_i). When analysing the plates taken using the conventional technique, the author found that, in regions of low wave height, the random secondary wave field in the basin made it very difficult for one to clearly discern the diffracted primary wave crests and to therefore take accurate measurements. The author suggests that this is the reason for the wave heights being lower in the lee of the breakwaters in the conventional technique diagram, than shown in the infinite basin diagram. Furthermore, as noted in Section 5.5.3.1, a small resonance mode developed between the splitter plates after approximately 40 seconds. The maximum steady state antinode wave height was 6 mm. The resonance wave length was 2/3 B i.e. 660 mm with antinodes at the splitter plates and 1/3 points. This resonant mode caused a wave height variation along the incident crests reducing the accuracy with which H_i could be calculated.

This experiment has thus shown that even if diffraction experiments are carried out with configurations having peripheral beaches of very low reflectivity (as in this case) a random secondary wave field will develop in the basin when using the conventional technique. This random secondary wave field will distort the diffracted primary wave field and reduce the accuracy, particularly in regions of small wave height, with which the diffracted wave heights (of the primary wave field) can be measured. It is therefore recommended that the infinite basin technique be used for diffraction configurations in which a infinite basin situation needs to be simulated.

5.6 Experimental Investigation of the Radiating Second-Order Phenomenon.

5.6.1 Introduction.

The theoretical principles of the radiating second-order phenomenon, as described by Biesel (1963, 1966), have been summarised in Chapter Two. This phenomenon was observed in all the wave diffraction experiments undertaken by the author. Furthermore, it would appear that the secondary waves, which are generated at and radiate from the breakwater tips, have a pronounced effect on the wave height distribution both close to the tips and in the lee of the breakwaters.

The author decided to investigate this phenomenon in more detail. The author experienced difficulty in identifying the radiating secondary waves in the stereopairs due to their very small wave height. A method was needed to highlight these secondary waves so that their effect on the primary wave train could be more easily determined.

Two natural highlighting techniques have been investigated by researchers who have used aerial photographs to determine the wave characteristics of particular coastal locations, namely:

(1) A low sun angle causes the wave crests to be highlighted by the reflective and shadow effects (Fig. 5-37a). It can be seen that the most effective highlighting occurs when the wave crests are aligned nearly perpendicular to the sun's rays.

(2) A high sun angle causes a sun spot to be imaged on the photograph. The wave crests are highlighted where they are tangent to the sun spot circle (see Fig. 5-37b).

When analysing a random sea in which a number of different wave trains are superimposed upon each other, it can be seen that a high sun angle will provide information on waves moving in all directions, whereas a low sun angle will provide good enhancement only for those waves whose crests are nearly perpendicular to the sun's rays. The author found however, that the first technique, which involves the use of low angle or oblique lighting, was more effective and easier to use than the second technique, when studying monochromatic waves generated in a laboratory basin.

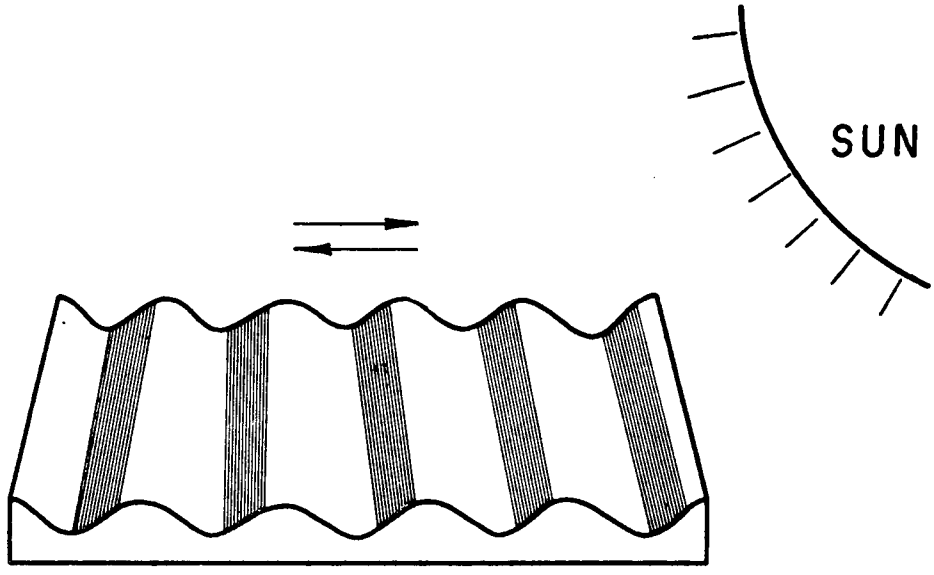

(a) Low sun angle highlighting.

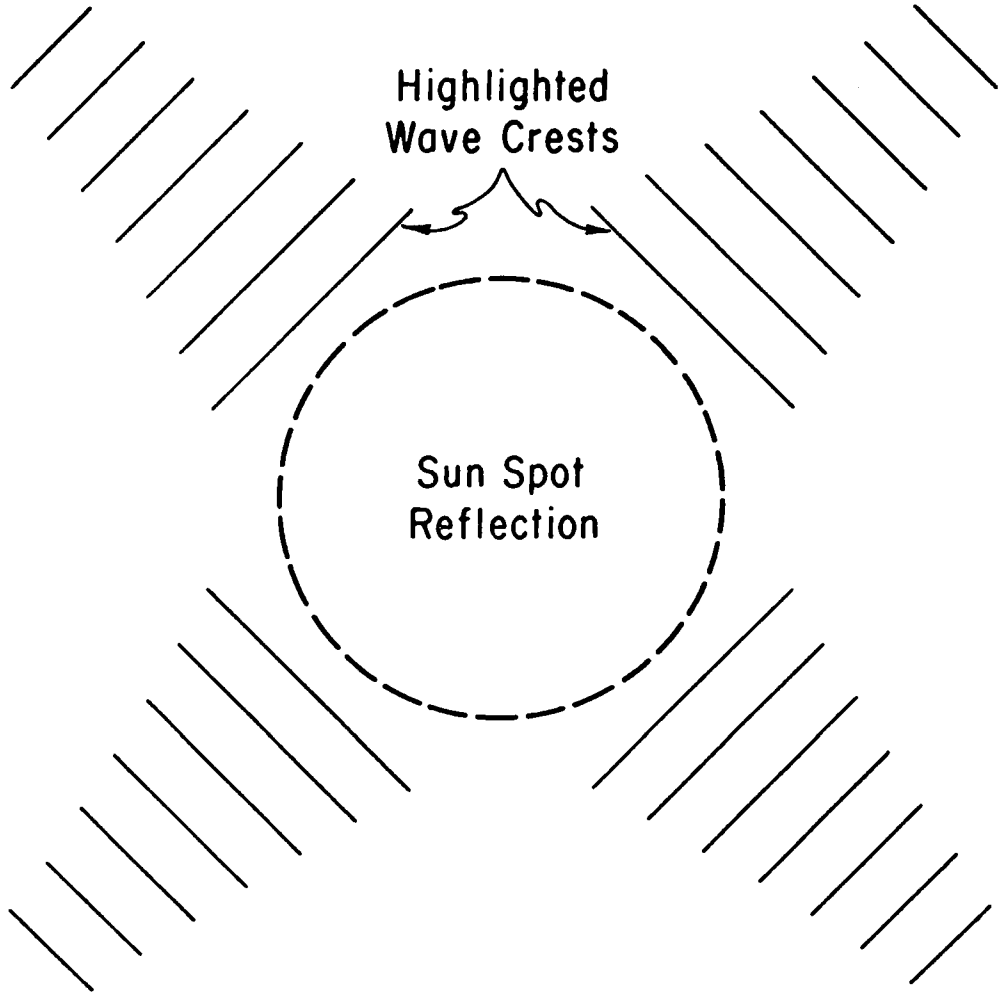

(b) High sun angle highlighting.

Fig. 5-37 Natural wave crest highlighting.

Four breakwater gap diffraction configurations were analysed using the first technique, namely: the symmetrical B/L = 1,64; 1; and 0,5 configurations and the asymmetrical B/L = 1,64 configuration.

5.6.2 Experimental Apparatus and Technique.

The author needed to simulate a low sun angle situation (in which the light rays strike the water at an oblique angle and are parallel to each other) in the wave basin.

The basin was spanned with a steel channel section, which was fixed 6 m from and parallel to the wave paddle (see Fig. 5-26). Five 500 W halogen lamps were then suspended from the steel beam, with one lamp on the gap centre line and the others spaced symmetrically about this line. The lamps were positioned 200 mm above the water surface and were carefully aligned so that all the rays of light were parallel to each other and perpendicular to the wave paddle.

The vortices and radiating secondary waves generated at the breakwater tips were recorded using a Phillips Studio model video camera linked to a Phillips video recorder and television set. Photographs were also taken of the breakwater tip phenomena using a 35 mm reflex camera and 400 ASA Agfa black and white film.

Each breakwater gap configuration was analysed using the following procedure, namely:

(1) The breakwater gap configuration to be analysed was set up in the wave basin. The same wave paddle period and amplitude settings as used in the corresponding configuration analysed using the infinite basin technique (see Section 5.5.3), were used. The water depth was 125 mm ± 1 mm as before. Cutting oil was again used to render the water surface virtually opaque.

(2) The breakwater tip phenomena were recorded with the video camera mounted in three different positions relative to the breakwater gap. In the first position the camera was mounted on the left hand side of the basin and 6 m from the wave paddle (see Fig. 5-26). In the second position the camera was mounted next to the left hand breakwater tip as shown in Fig. 5-38. In the third position the camera was mounted directly above the breakwater gap on

the platform above the wave basin. Photographs were also taken from the above positions (plus a number of other positions) using the 35 mm camera.

(3) For each of the 3 camera positions described above, the recording procedure was as follows: The video camera was focused on the breakwater gap (i.e. the model harbour entrance) and the recorder started. The wave paddle was then started. A 15 minute recording was made of the breakwater tip phenomena from the time that the first wave entered the basin of still water to the time that a well established quasi-steady state situation existed in the basin. Phenomena, such as resonance modes between the splitter plates, were also recorded. When the video camera was in the second position, small quantities of crushed charcoal where thrown into the centre of the right hand vortex in order to highlight its motion.

Fig. 5-38 Video camera positioned next to left hand breakwater.

(4) The video and photographic records of the vortices and radiating second-order phenomena for each configuration

were then analysed. The video recordings and photographs which were taken of the above phenomena greatly aided the author in his interpretation of the experimental breakwater gap diffraction results given in Section 6.1.

5.6.3 Configurations Analysed and Results.

5.6.3.1 The B/L = 1,64 Breakwater Gap Configuration.

The experimental configuration and incident wave train characteristics are as described in Section 5.5.3.1. The incident wave train characteristics were assumed to be the same as before, since the wave paddle settings used in the previous investigation were duplicated.

The vortices and radiating secondary waves were first generated at the breakwater tips by the first significant wave to pass into the model harbour basin at approximately the time at which the wave energy front was calculated to have entered the basin. The oscillatory vortices were seen to move forward with the crests, and backwards (towards the wave paddle) with the troughs, and had a radius of approximately 100 mm. When the crushed charcoal was thrown into the right hand vortex, it was immediately expelled by the next crest to arrive at the breakwater tip. As the crest passed the breakwater tip, it "collapsed" into the lee of the breakwater expelling any charcoal trapped in the vortex. Silvester and Lim (1968) compared this phenomenon to the instantaneous bursting of a dam wall. Once the charcoal had been expelled from the right hand vortex, the charcoal in the lee of the breakwater was seen to migrate very slowly to the side wall beach (due to the low wave heights in this region), while outside the shadow zone, the charcoal was rapidly transported to the back wall beach.

The secondary waves radiating from the breakwater tips are clearly shown in Fig. 5-39. These waves were seen to radiate through an angle of 270° from each breakwater tip. A secondary wave was seen to be generated whenever either a crest or a trough of the primary wave train passed a breakwater tip. In Fig. 5-39 it can be clearly seen that at each breakwater tip there are two secondary wave crests (one generated by the primary crest and the other by the succeeding primary trough) in each trough

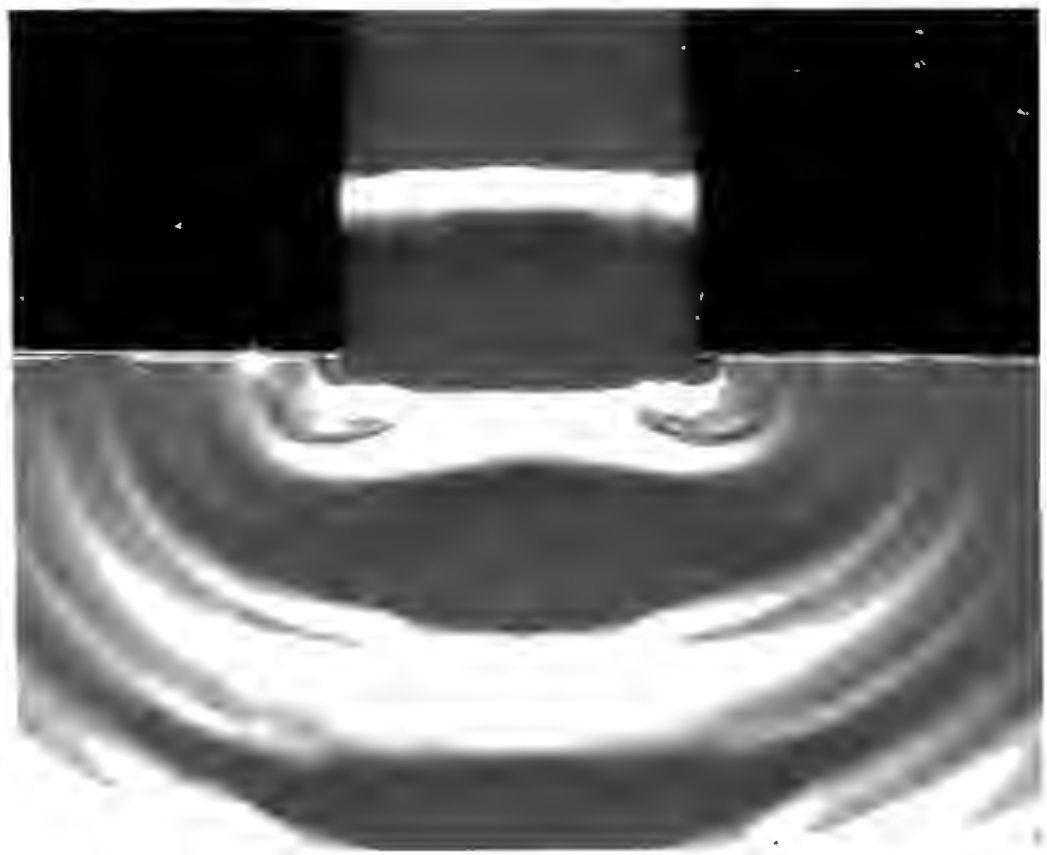

Fig. 5-39 Radiating second-order waves, at the breakwater tips, for the B/L = 1,64 configuration.

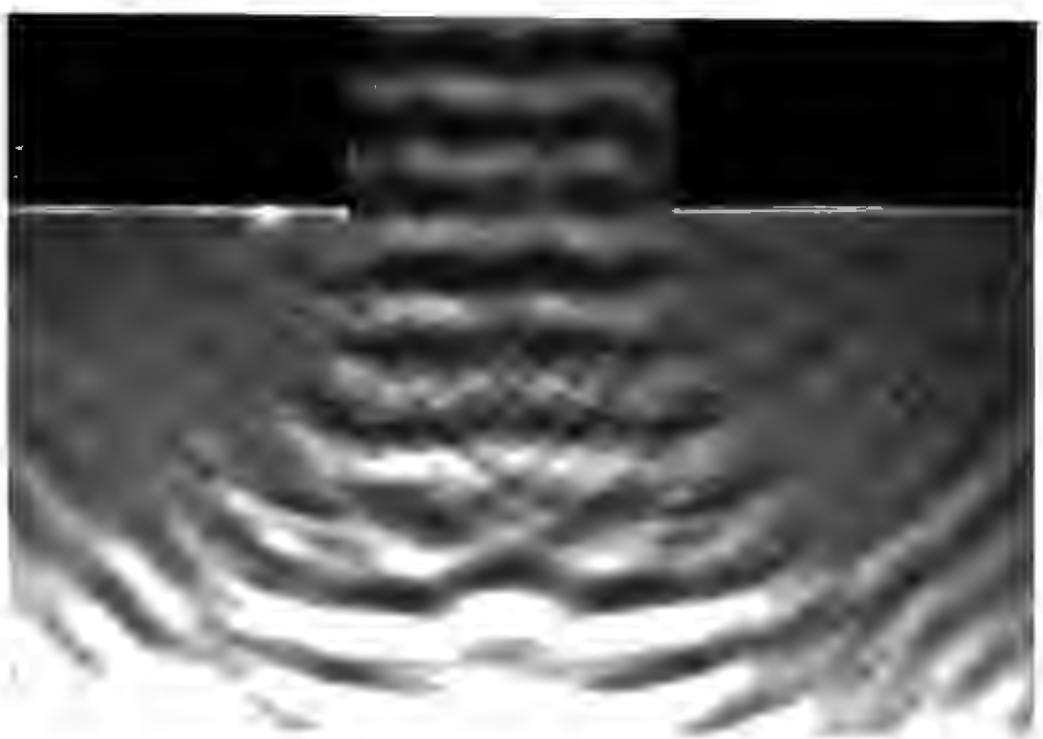

Fig. 5-40 Secondary wave field in the basin after the paddle has been stopped (B/L = 1,64 configuration).

of the primary diffracted wave train. From the above, it follows that the period of the secondary or second-order waves (Biesel 1963, 1966) would be half that of the primary wave train i.e. 0,335 seconds. Their wave length (calculated using Airy wave theory) would therefore be approximately 175 mm.

To be consistent with Biesel's terminology and to prevent confusion with other observed secondary phenomena, the secondary waves radiating from the breakwater tips will now be referred to as second-order waves. In the shadow zones close to the breakwaters, the primary waves are still the primary disturbance in these areas. The measured primary wave heights in these areas were found to be approximately twice as large as the second-order wave heights. This is contrary to the findings of Biesel (1963, 1966) who predicted that the second-order waves would be the main wave action in these areas.

The second-order waves radiating from the breakwater tips were seen to have a pronounced effect on the incident wave crests as these crests entered the model harbour basin. These second-order waves were seen to radiate across the incident wave crests. The radiating wave train generated by the left hand breakwater tip was thus superimposed upon the radiating wave train generated by the right hand tip, and caused the primary wave crests to peak up at the gap centre line as these crests entered the model harbour basin. This peaking of the wave crests, at the gap centre line, as they enter the model harbour can be clearly seen in Fig. 5-39. Also, the small resonance mode described in Section 5.5.4 was again evident.

When the wave paddle was stopped (after running for 15 minutes) and the primary wave train had traversed the basin, a secondary wave field was evident in the basin as shown in Fig. 5-40. This consisted of a regular wave train with a wave length approximately half that of the incident wave train superimposed upon a completely random wave field. The regular wave component of the secondary wave field died down within approximately 10 seconds, while the random wave field persisted for up to 1 minute after the wave paddle had been stopped. It is suggested that this secondary wave field had been superimposed upon the primary quasi-steady state wave field in the basin.

5.6.3.2 The B/L = 1 Breakwater Gap Configuration.

The experimental configuration and incident wave train characteristics are as described in Section 5.5.3.4. The incident wave train characteristics were assumed to be the same as before, since the wave paddle settings used in the previous investigation were duplicated.

As in the previous configuration, the vortices and radiating second-order waves were again seen to be generated at the breakwater tips as soon as the first significant wave crest passed into the model harbour basin. Charcoal thrown into the right hand vortex was again immediately expelled by the succeeding crest; migrating slowly to the side wall beach in the shadow zone, or more rapidly to the back wall beach outside the shadow zone. The second-order waves generated at the breakwater tips can be clearly seen in Figs. 5-41. As before, a second-order wave was generated each time a crest or a trough of the primary wave train passed a breakwater tip. Their wave length in this case was calculated to be approximately 267 mm. These two second-order wave crests (one generated by the primary trough and the other by the primary crest) can be seen in the primary wave trough, adjacent to each breakwater tip, shown in Figs. 5-41.

In the shadow zones close to the breakwaters, the primary diffracted waves were again found to have a greater wave height than the second-order waves in these regions. Outside the shadow zones, the second-order waves radiating from the breakwater tips were again seen to have a pronounced effect on the incident wave crests as these crests entered the model harbour basin. As before, the second-order waves caused the primary wave crests to peak up at the gap centre line as these crests entered the basin. This phenomenon is clearly evident in Figs. 5-41 and was found to be very pronounced for the B/L = 1 configuration. This coincides with the findings of the experimental investigation described in Section 5.5.3.4 in which a diffraction coefficient (H/H_i) of 1,46 was calculated for this region.

As one would expect, a pronounced resonance mode developed between the splitter plates. This resonance mode has been described in detail in Section 5.5.3.4. When the wave paddle was stopped

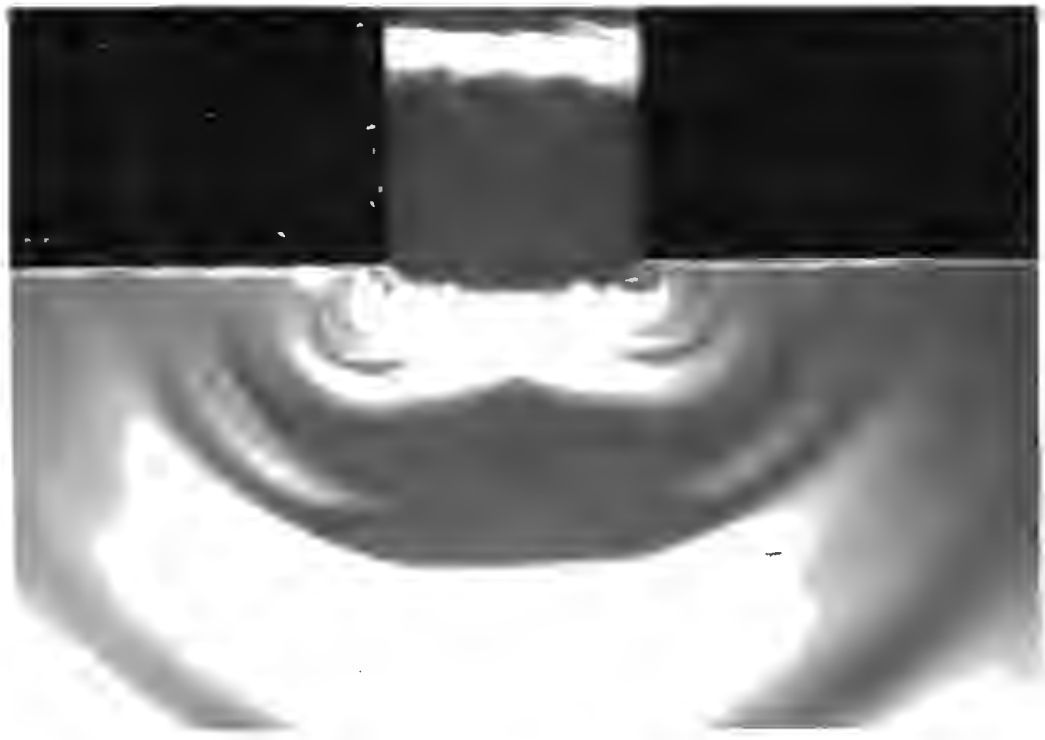

(a) Breakwater gap viewed from above.

(b) Breakwater gap viewed from the right hand side of the basin.

Fig. 5-41 Radiating second-order waves at the breakwater tips for the B/L = 1 configuration.

(after running for 15 minutes), this resonance mode took approximately 1 minute to dissipate. Also, when the paddle was stopped and the primary wave train had traversed the basin, a secondary wave field similar to that described in the previous section was again evident in the basin. The regular component died down after 9 seconds while the random component persisted for approximately 50 seconds.

5.6.3.3 The B/L = 0,5 Breakwater Gap Configuration.

The experimental configuration and incident wave train characteristics are as described in Section 5.5.3.6. The incident wave characteristics were again assumed to be the same as those described in the above section, since the wave paddle settings used in the previous investigation were duplicated.

For the B/L = 0,5 configuration the vortices and second-order waves generated at the breakwater tips were very pronounced, as can be seen in Figs. 5-42. These second-order waves (wave length approximately 485 mm) were seen to flatten the incident wave crests at the gap centre line, as the incident wave train entered the model harbour basin. In the shadow zones close to the breakwaters, the primary diffracted waves were found to have wave heights approximately 2 to 3 times larger than those of the second-order waves in these regions. This was in part due to the fact that in the shadow regions close to the breakwater tips, the vortices (of approximately 150 mm radius) caused a localised breaking of the primary wave as it diffracted round the breakwater tip, accentuating the wave height in this region. Charcoal thrown into the right hand vortex was again expelled as described in the previous two sections.

A small resonance mode was evident between the splitter plates after the paddle had been running for approximately 40 seconds. This resonance mode had a wave length of 1 200 mm (i.e. the incident wave length) and the antinodes, which were situated at the splitter plates, had a maximum wave height of 5 mm. When the paddle was stopped (after running for 15 minutes) this resonance mode took approximately 40 seconds to dissipate. As before, when the wave paddle was stopped and the primary wave train had traversed the basin, a secondary wave field similar

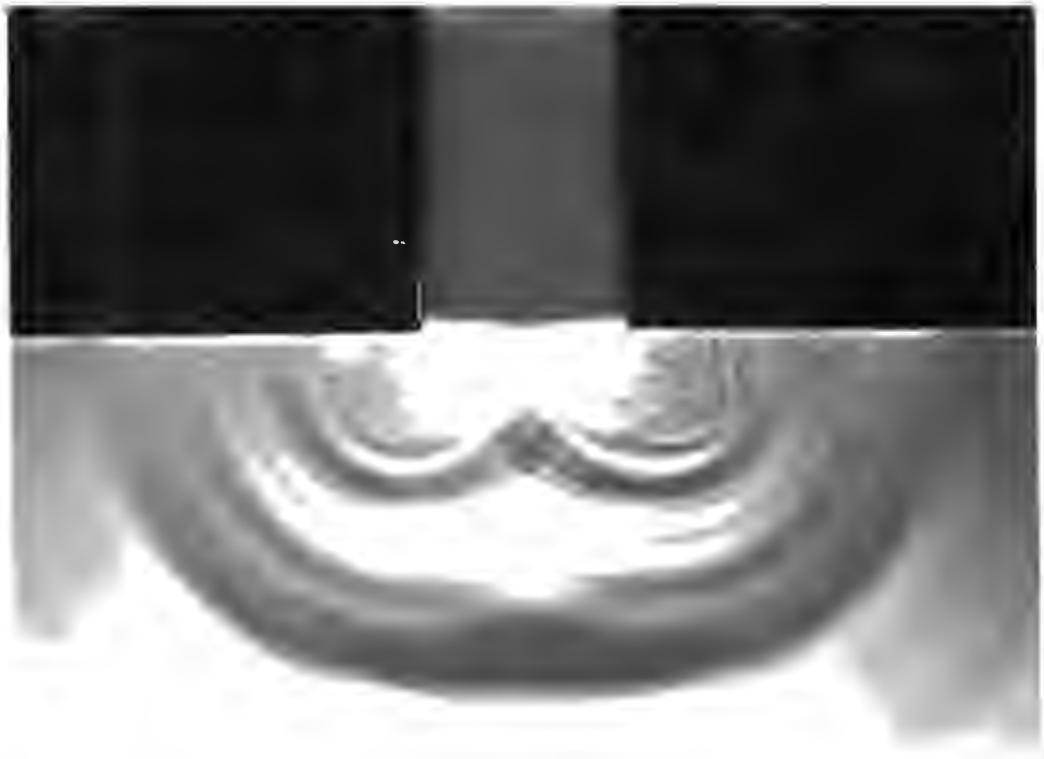

(a) Breakwater gap viewed from above.

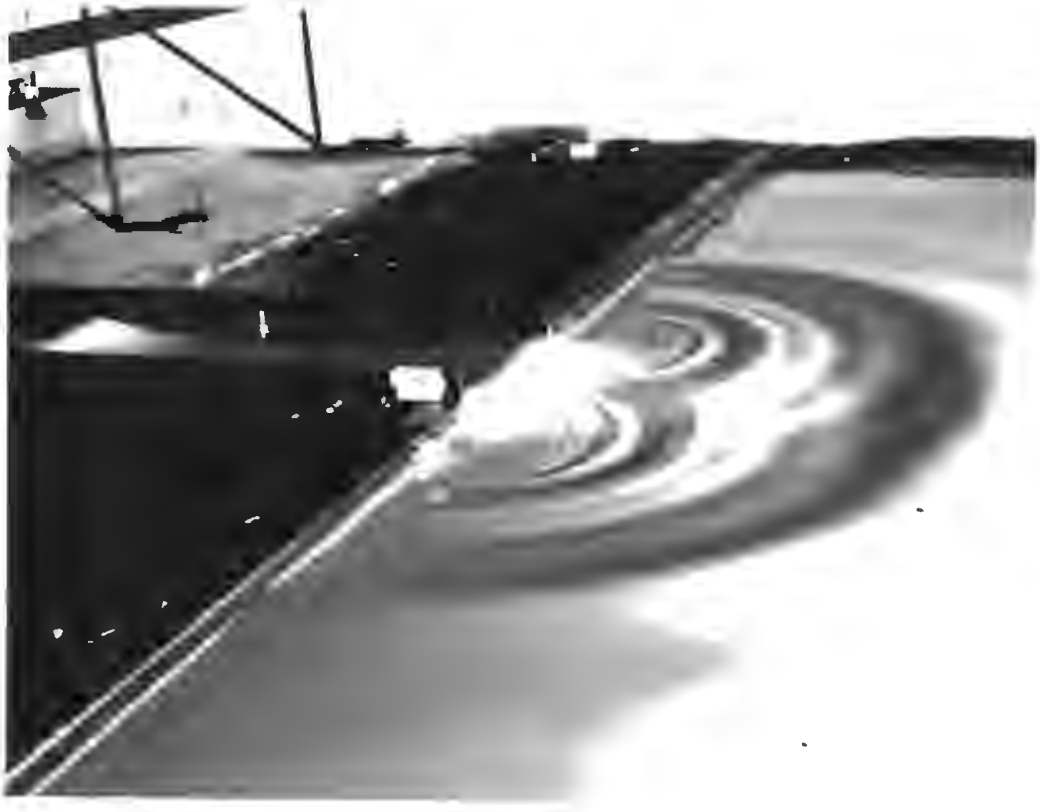

(b) Breakwater gap viewed from the left hand side of the basin.

Fig. 5-42 Radiating second-order waves at the breakwater tips, for the B/L = 0,5 configuration.

to that described in the previous two sections was again evident in the basin.

5.6.3.4 The B/L = 1,64 Asymmetrical Breakwater Gap Configuration.

The experimental configuration and incident wave train characteristics are as described in Section 5.5.3.7. As before, the wave paddle settings used in the previous investigation were duplicated.

As the incident wave train characteristics for this configuration were almost identical to those adopted for the corresponding symmetrical breakwater gap configuration, the author was not surprised to find the observations made regarding the breakwater tip phenomena were in general very similar to those made in Section 5.6.3.1. However, in the asymmetrical configuration, the breakwater tips were more isolated from each other than in the symmetrical configuration. This meant that second-order waves generated at one breakwater tip were not as strongly influenced by the corresponding second-order waves generated at the adjacent tip, as was observed in the symmetrical configuration. Furthermore, since the offset between the breakwater arms was exactly one incident wave length, a primary wave crest (or trough) would be positioned at both breakwater tips at the same time, with the result that the second-order waves generated at these tips would be in phase.

The author decided to exploit the relative isolation of the breakwater tips in the asymmetrical configuration, and investigate the second-order waves generated at the left hand breakwater tip. To highlight the waves generated at this tip, two 500 W halogen lamps were positioned on the side wall beach, approximately 600 mm from the left hand breakwater. The lamps were adjusted so that their respective light rays were parallel to each other and directed towards the left hand breakwater tip. This configuration highlighted the way in which the second-order waves spread out through a 270° arc. This phenomenon is clearly shown in Fig. 5-43 in which the second-order waves can be seen propagating across the incident wave crest next to the left hand breakwater tip.

As was expected, a small resonance mode developed between the

splitter plates of similar wave length and wave height to that described in Section 5.5.4. Furthermore, when the paddle was stopped and the primary wave train had traversed the basin, a secondary wave field, with characteristics almost identical to those of the corresponding wave field described in Section 5.6.3.1, was evident in the basin.

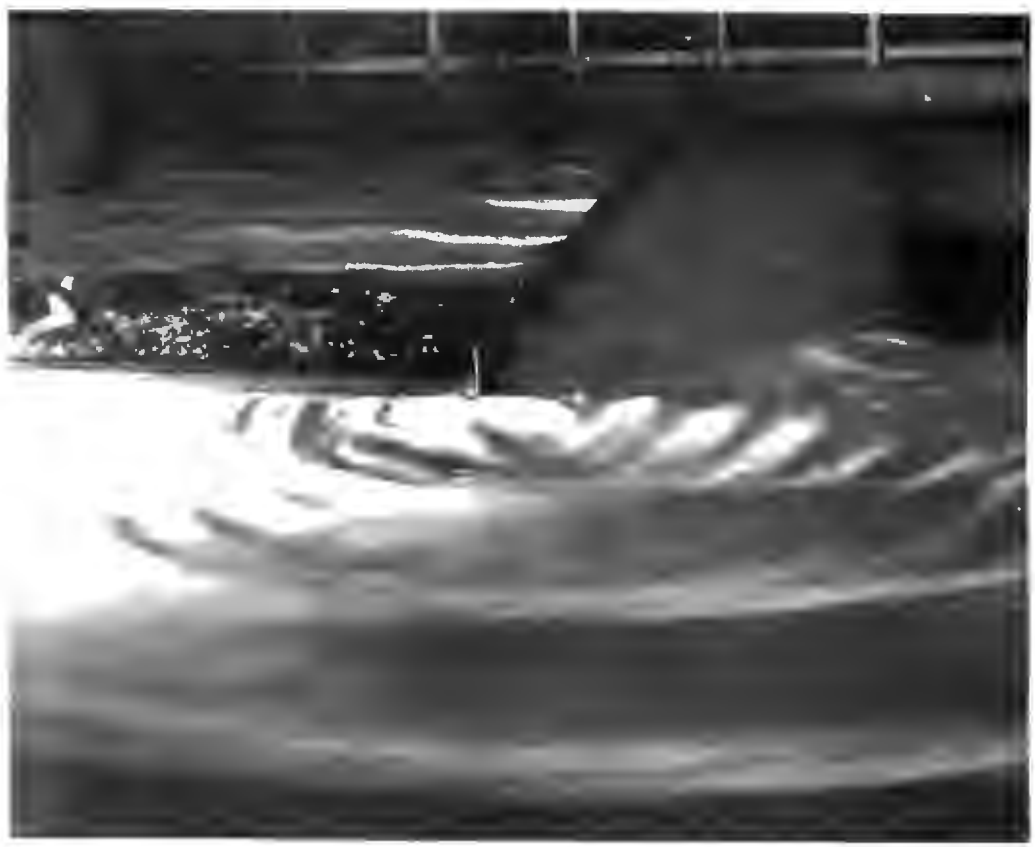

Fig. 5-43 Second-order waves radiating from the left hand breakwater tip of the asymmetrical B/L = 1,64 configuration.

5.6.4 Conclusions.

This investigation clearly showed that the oscillatory vortices and radiating second-order waves generated at the breakwater tips had a very significant influence on the diffracted wave height distributions measured in the model harbour configurations. The author suggests that the marked differences between the experimental and theoretical diffraction diagrams in the breakwater gap regions, discussed in Section 6.1, were caused by these non-linear breakwater tip effects.

The second-order waves were seen to be generated at a breakwater tip every time either a crest or a trough of the primary wave train passed this tip. Therefore the period of the second-order waves would be half that of the primary wave train. This coincides with the predictions of Biesel (1963, 1966) who stated that:-

> "... the frequency of the pressure fluctuations is twice that of the first-order wave." And "... any local surface pressure fluctuations of a given frequency will give rise to a circular wave of the same frequency and radiating energy in all directions." (from Biesel, 1963)

Biesel's prediction that second-order waves would be generated by the first-order phenomena and then radiate independently, as free waves, was proved to be correct.

Contrary to the predictions of Biesel (1963, 1966) the second-order waves were not found to be the predominant distrubance in the shadow zones close to the breakwaters. In all the configurations tested, the primary diffracted waves had larger wave heights than the second-order waves in these zones. However in these zones, the second-order waves had wave heights of 40 to 60 % H, where H is the primary diffracted wave height. The contribution of the second-order waves to the measured diffracted wave heights was most significant in regions where these secondary waves were seen to be superimposed upon the primary wave crests.

In conclusion, the effect of the second-order radiating phenomenon on the diffracted wave height distribution in the basin was most pronounced in a semi-circular domain, centred at the gap center line, with a radius of 2 to 3 L (L is the primary wave length). It was thought that the higher energy (then predicted theoretically) in the lee of the breakwaters and also the wave height peaks on the gap centre line just in front of the entrance, observed experimentally, could be attributed to the above phenomenon.

6. ANALYSIS OF EXPERIMENTAL AND NUMERICAL WAVE DIFFRACTION RESULTS AND DISCUSSION ON GENERAL THESIS TOPICS

6.1 Diffraction Configurations Analysed : Experimental and Numerical Results.

6.1.1 Introduction.

In this chapter the experimental, numerical and available analytical diffraction diagrams for the breakwater gap configurations investigated are compared. These diffraction diagrams have been drawn to the same scale and only the model basin areas have been considered, so that they can be easily compared with each other. Note, for the symmetrical configurations only the left-hand side of the basin is considered. In the experimental diffraction diagrams the dashed lines indicate the crest lines plotted from both stereopairs and the black dots indicate the crest line sampling points, again plotted from both stereopairs. For the symmetrical diagrams dimensionless X/L and Y/L axes are shown, with the Y axis in the incident wave direction. L is the theoretical wave length for each configuration, calculated using linear wave theory. A meter scale is also included in each diagram. In each diagram the edge of the geometric shadow zone is marked by a thick dashed line. In the experimental diagrams it will be noted that, in the region outside the shadow zone and close to the entrance, the experimental wave lengths are generally greater than the theoretical prediction. It is recognised that in this region the waves are quite steep and that a higher order wave theory would probably supply slightly more accurate wave length predictions.

Great care has been taken to ensure that the experimental diffraction diagrams shown are accurate. Some of the stereopairs were observed up to three times to check measurements which appeared anomalous. The same care has been taken with the finite element diffraction diagrams and for some configurations up to 8 different element meshes were tested before the author was satisfied with the results. The experimental and numerical diffraction diagrams are for the channel entrance case, which is thought to closely approximate the case where the seaward faces of the breakwater are totally absorbing. The analytical diffraction diagrams, where

supplied, are for the fully reflecting breakwater case. It was decided not to include finite element diffraction diagrams for the fully reflecting breakwater case, for the reasons given in Section 3.6.

It should be noted that four of the configurations analysed, i.e. the B/L = 1,64; 1,41; 1 and 0,5 configurations are included in the CERC (1977) Manual and the corresponding analytical diffraction diagrams included in this chapter are actually taken from the above manual. It is hoped that the experimental and numerical results given in this chapter will aid coastal engineers using the CERC (1977) or similar manuals.

6.1.2 The B/L = 1,64 Breakwater Gap Configuration

The experimental B/L = 1,64 breakwater gap configuration tested (see Fig. 4-46) is described in Section 5.5.3.1. The incident wave characteristics were : T = 0,67 seconds, H_i = 55,5 mm and L(theoretical) = 604 mm, with d = 125 mm. The experimental diffraction diagram is shown in Fig. 6-1 and the corresponding finite element diffraction diagram is shown in Fig. 6-2. The analytical diffraction diagram (fully reflecting case), shown in Fig. 6-3, was taken from the CERC (1977) manual. This diagram is based on the Penney and Price (1952) solution and was constructed using the method proposed by Johnson (1953). (See Section 2.4.2.2)

If one compares Fig. 6-1 with Fig. 6-2, it is evident that there is a fairly good correlation between the experimental and finite element results. For example, the position and magnitude of the wave height peak in front of the entrance is well predicted by the finite element model. There are two basic differences, however, namely : 1) experimentally there is found to be more energy in the lee (or shadow zones) of the breakwaters than predicted by the finite element model; 2) the wave height attenuation, in the incident wave direction, occurs more rapidly than predicted by the finite element model.

It is thought that the higher energy in the lee (shadow zone) of the breakwaters (and also possibly the wave height peak on the centre line just in front of the entrance), observed experimentally, could be partly attributed to the radiating second-order

phenomena described by Biesel (1963, 1966). Radiating second-order waves(generated at each breakwater tip) were clearly evident in the experimental configuration as shown in Fig.5-39. It was thought that the super position of certain of these radiating secondary waves upon the primary diffracted wave crests could explain the higher wave heights measured in the shadow zones, particularly in the immediate lee of the breakwaters. The low spot shown near the bottom left hand corner of Fig. 6-1, although predicted by the finite element model, is thought to be due to a localised loss of energy from the wave crest as its edge runs along the toe of the crushed stone side wall beach.

The phenomenon of more rapid wave attenuation in the incident wave direction and also the greater energy in the shadow zones, observed experimentally, was also perceived by Blue and Johnson (1949) who stated in their conclusions that "the waves in areas of great steepness are longer than results from the application of the theory without regard for steepness. This causes the crests to be more sharply curved and the diffraction coefficients to be smaller than given by the basic theory for such areas, while the diffraction coefficients are increased in the adjacent areas." These conclusions are borne out, to a large extent, by the experimental results shown in Fig. 6-1.

If one compares Fig. 6-2, the finite element solution for the diffraction of waves passing though a gap in an approximate totally absorbing breakwater, with Fig. 6-3, the analytical solution for the equivalent fully reflecting breakwater case, it is evident that the correlation is very good. For example, the position and magnitude of the wave height peak in front of the entrance and also the position and shape of the 0,2 contour line in the lee of the breakwater, are both well predicted. The analytical solution predicts a slightly greater penetration of wave energy into the basin than predicted by the finite element solution. This is understandable, since for the fully reflecting breakwater case a small amount of the energy reflected from the seaward faces of the breakwater arms will be diffracted into the basin. The differences between these two theoretical solutions is consistent with the findings of Daemrich and Kohlhase(1978) shown in Fig.2-9.

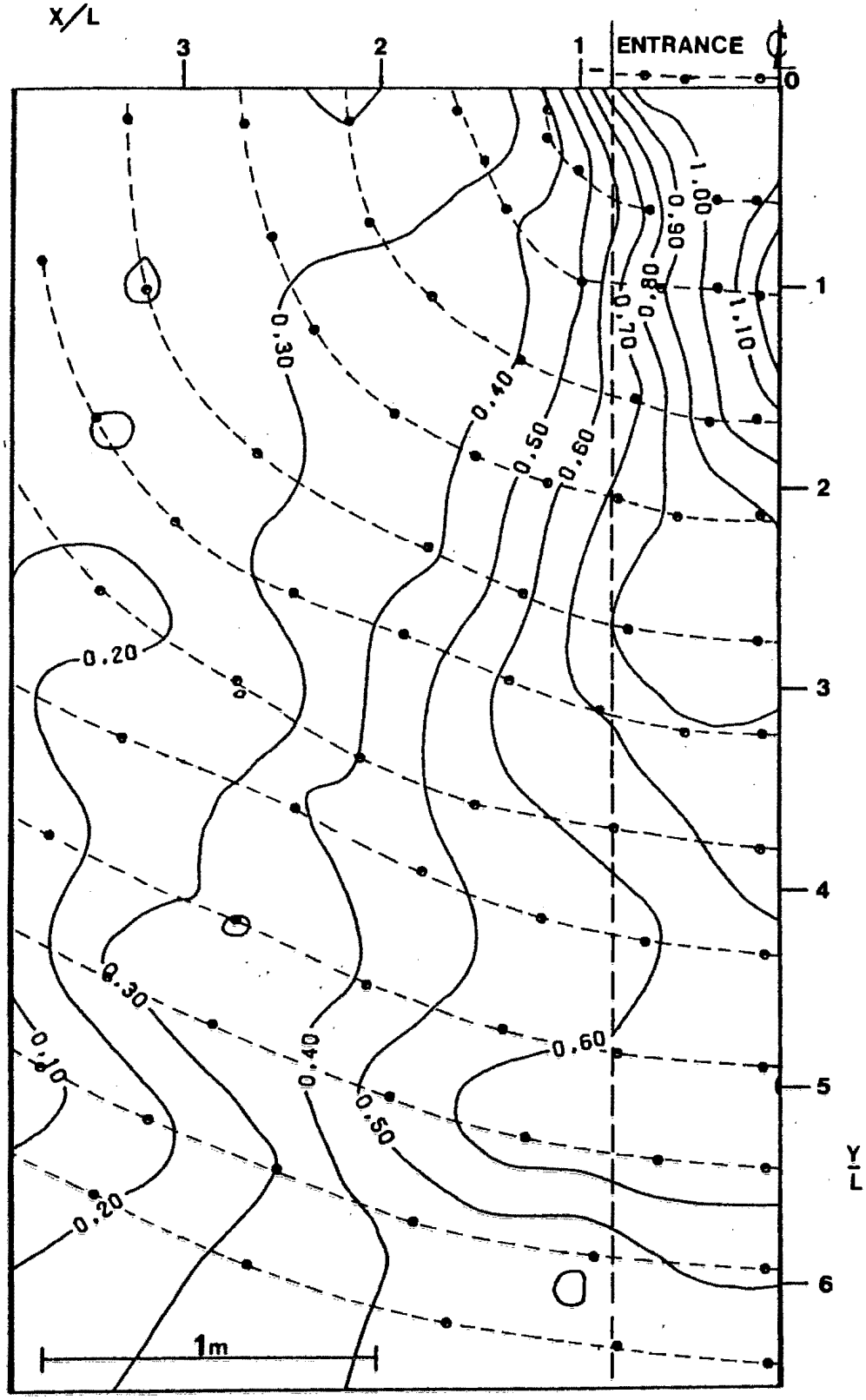

Fig. 6-1 Experimental diffraction diagram for the B/L = 1,64 breakwater gap configuration.

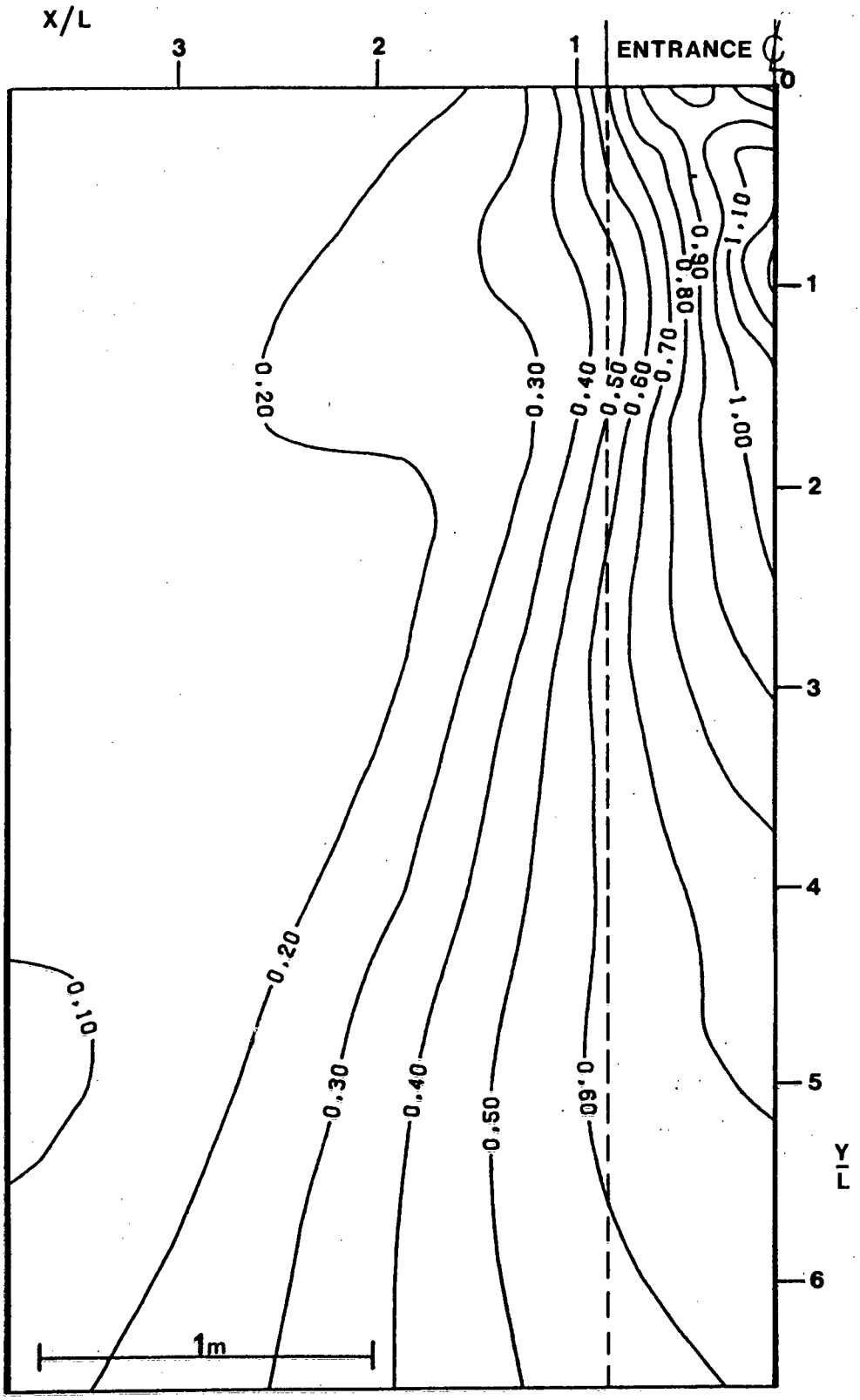

Fig. 6-2 Finite element diffraction diagram for the B/L = 1,64 breakwater gap configuration.

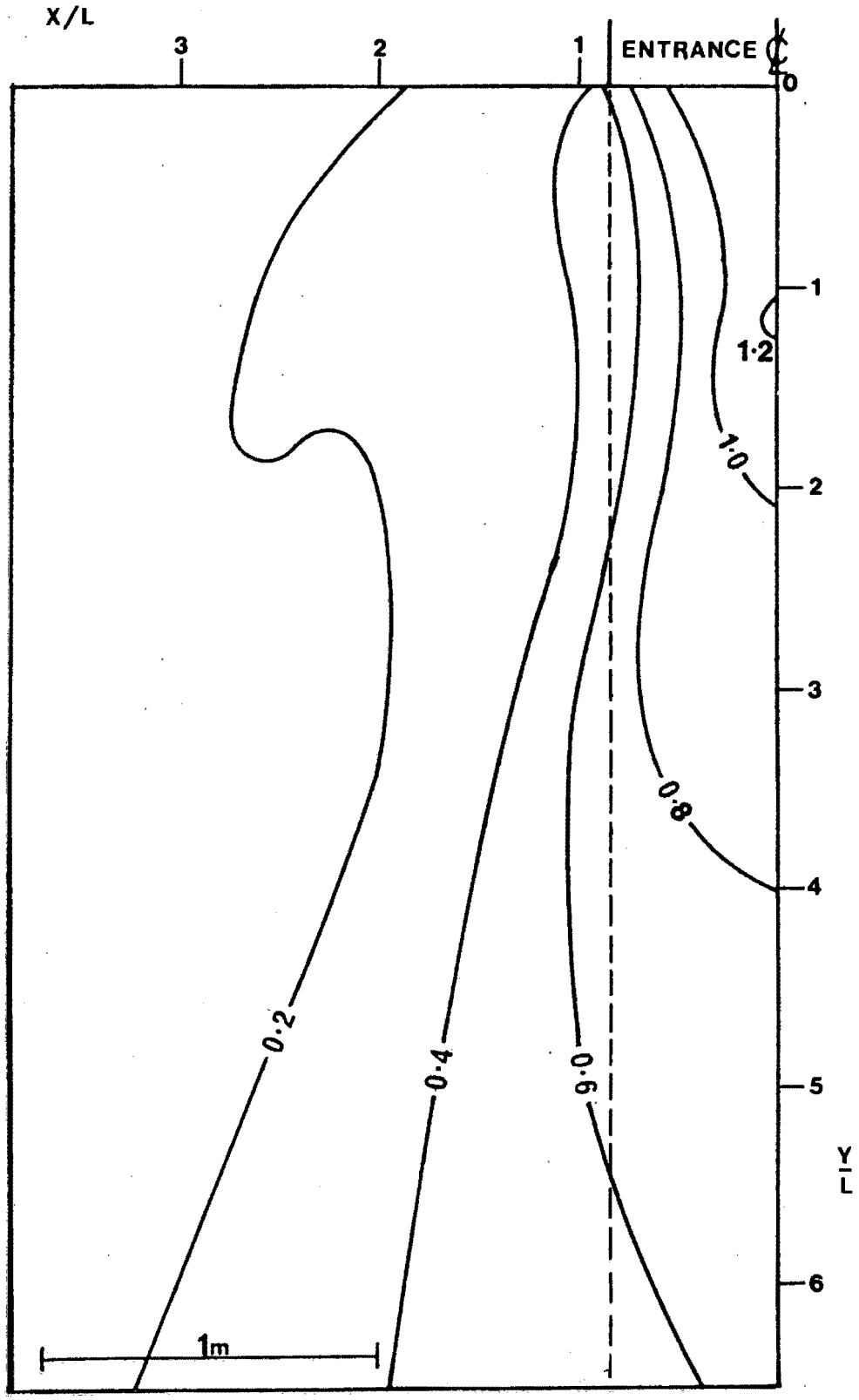

Fig. 6-3 Analytical diffraction diagram for the B/L = 1,64 breakwater gap configuration, from CERC (1977).

6.1.3 The B/L = 1,41 Breakwater Gap Configuration

The experimental B/L = 1,41 breakwater gap configuration tested is described in Section 5.5.3.2. The incident wave characteristics were : T = 0,64 seconds, H_i = 52,8 mm, and L (theoretical) = 567 mm, with d = 125 mm. The experimental diffraction diagram is shown in Fig. 6-4 and the corresponding finite element diffraction diagram in Fig. 6-5. The analytical diffraction diagram (fully reflecting breakwater case), shown in Fig. 6-6, was again taken from the CERC (1977) manual. As before, this diagram is based on the Penney and Price (1952) solution and was constructed using the method proposed by Johnson (1953).

If one compares Fig. 6-4 with Fig. 6-5, it is evident that the correlation between the experimental and finite element results is fairly good (although not quite as good as in the previous configuration). For example the magnitude and position of the high spot in front of the gap is well predicted by the finite element model. As before, there are two basic differences, namely : 1) experimentally there is found to be more energy in shadow zones behind the breakwaters than predicted by the finite element model; 2) the wave height attenuation, in the incident wave direction, occurs more rapidly than predicted by the finite element model.

Again, it is thought that the higher energy in the lee (shadow zones) of the breakwaters (and also possibly the wave height peak on the centre line just in front of the entrance), observed experimentally, could be partly attributed to the radiating second-order phenomena described by Biesel (1963, 1966). Radiating second-order waves (generated at the breakwater tips) were again evident in the basin and it is proposed that the higher wave heights measured in the immediate lee of the breakwater are due to the superposition of these secondary waves upon the diffracted primary wave crests. The low spot near the bottom left-hand corner of Fig. 6-4 is again thought to be due to a localised loss of energy from the edge of the crest.

The phenomenon of more rapid (compared to the finite element and analytical results) wave height attenuation in the incident wave direction, and also the higher energy in the shadow zones, is thought

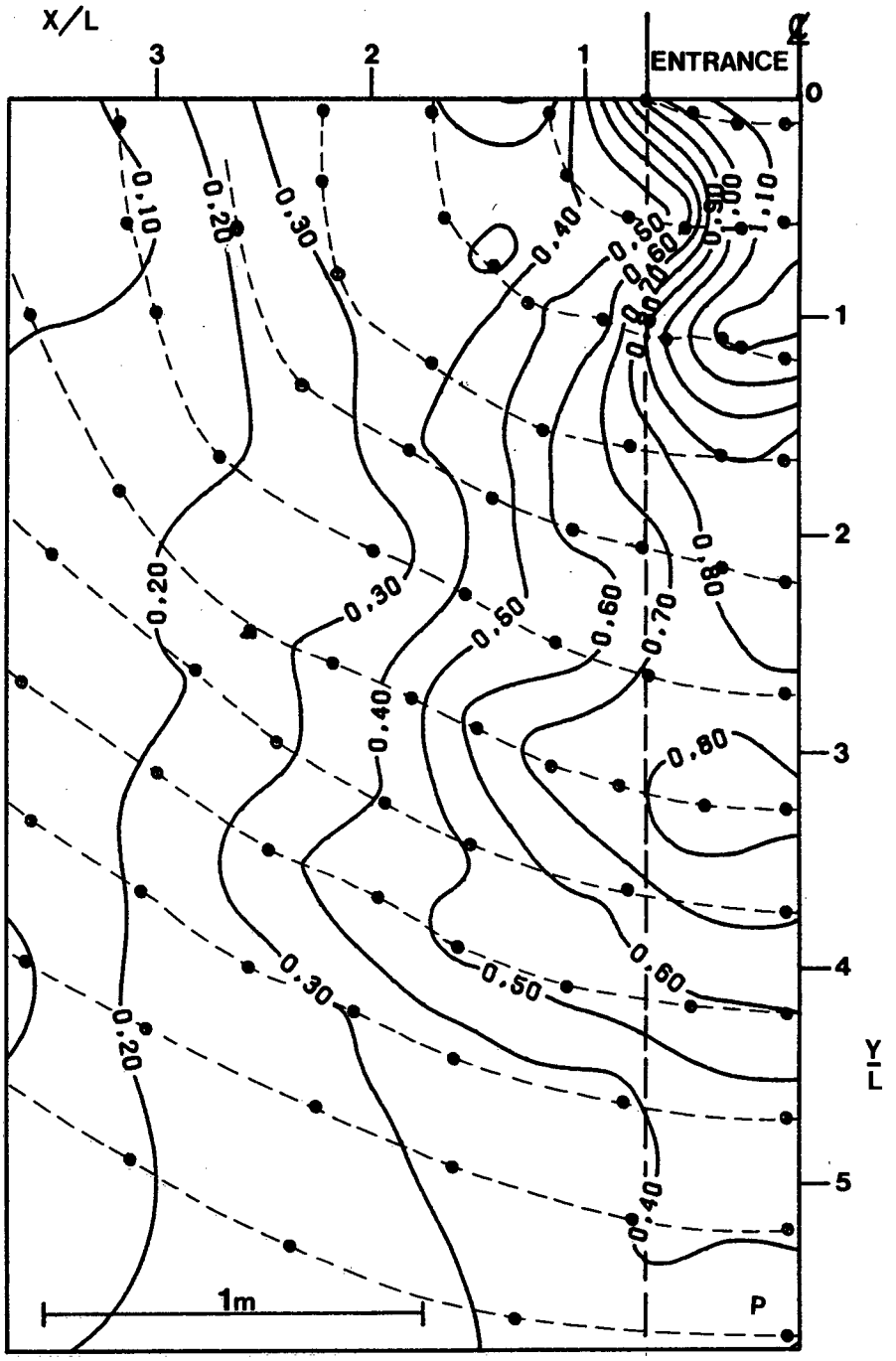

Fig. 6-4 Experimental diffraction diagram for the B/L = 1,41 breakwater gap configuration.

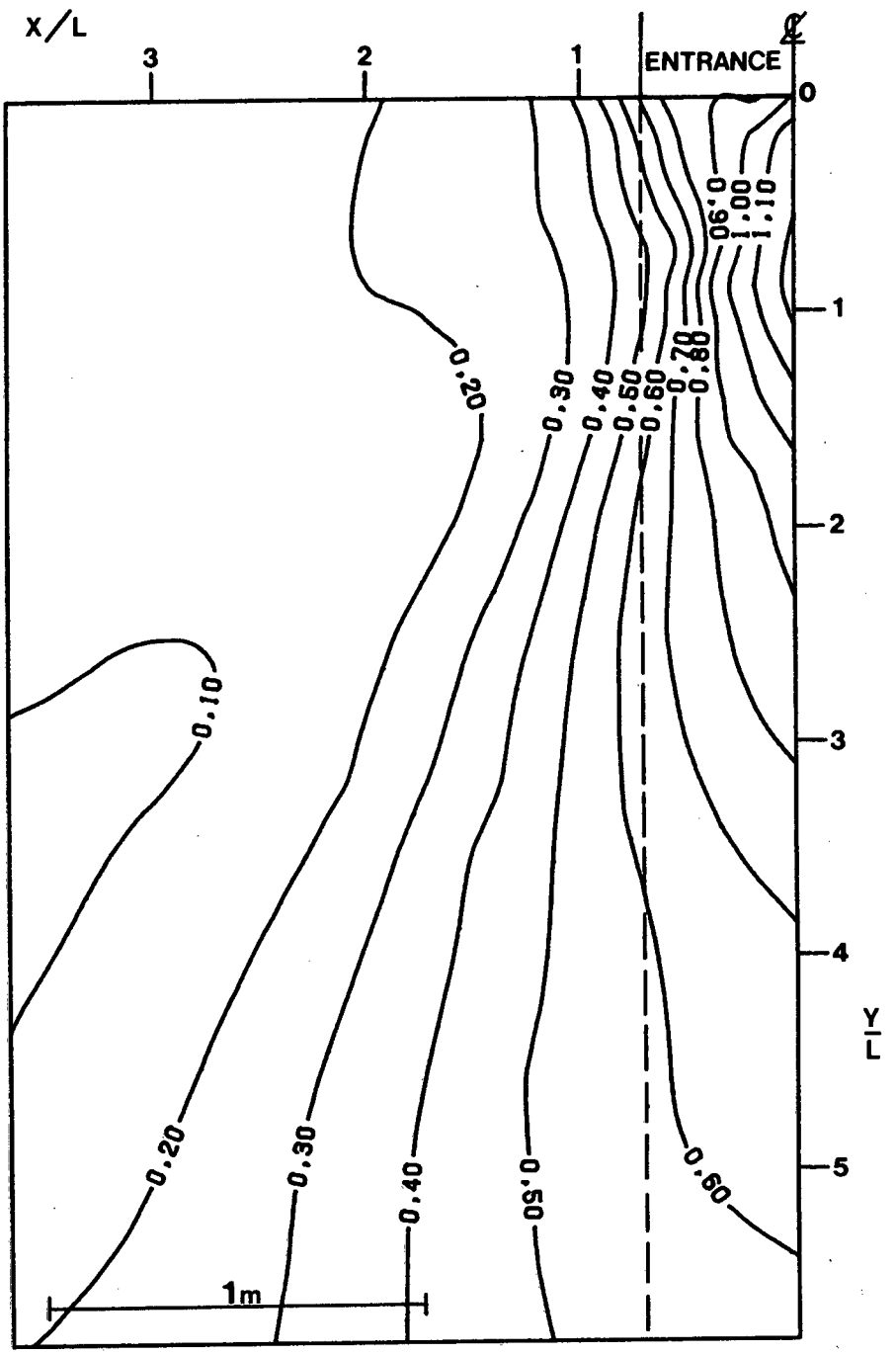

Fig. 6-5 Finite element diffraction diagram for the B/L = 1,41 breakwater gap configuration.

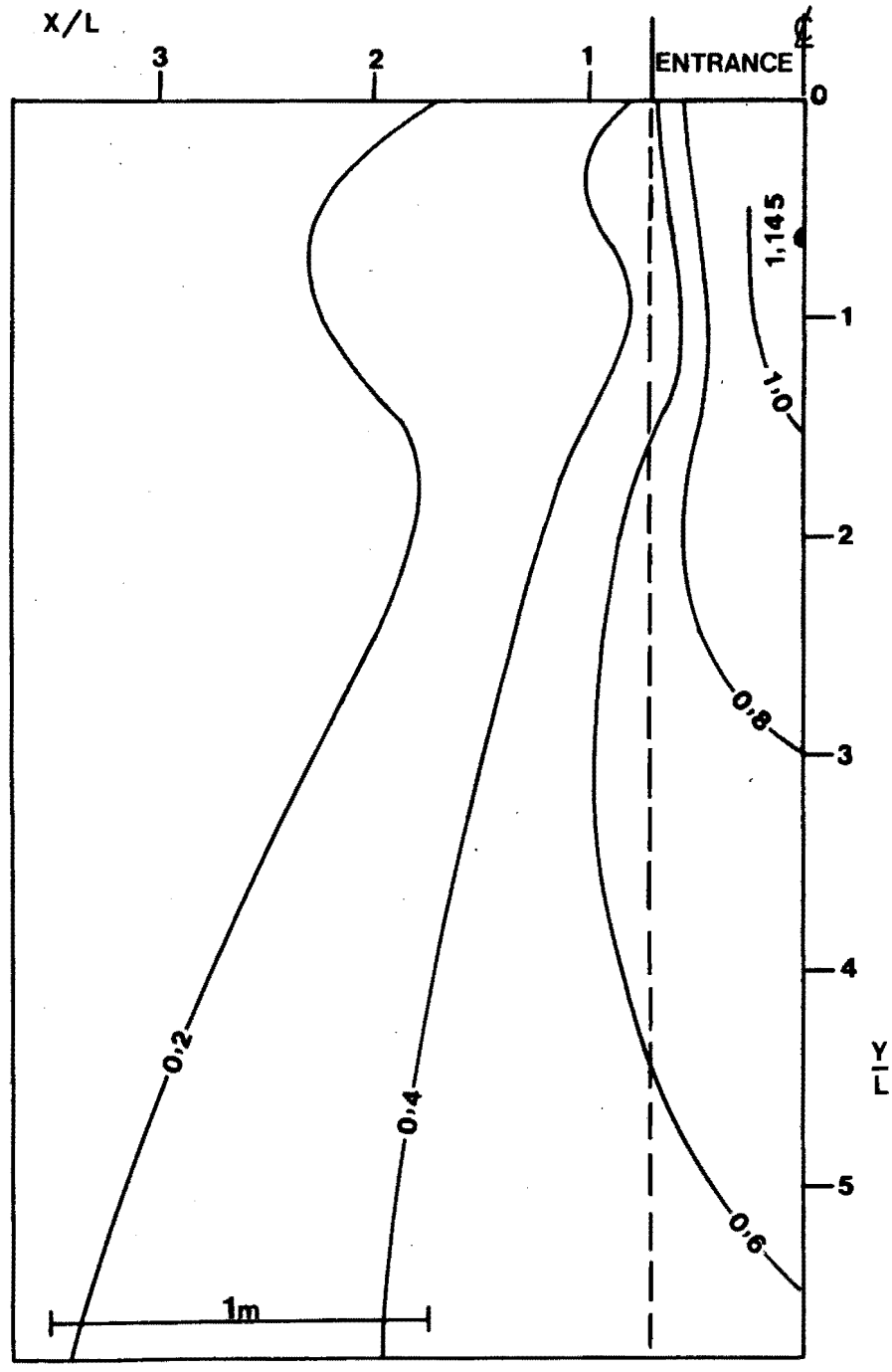

Fig. 6-6 Analytical diffraction diagram for the B/L = 1,41 breakwater gap configuration, from CERC (1977).

to be related to the steepness of the waves, in the region outside the shadow zones (i.e. near the gap centre line). The greater height of the waves in this region causes the segment of a crest in this region to move forward with a slightly greater velocity than the adjacent portions of the crest within the shadow zones. The crests in the region of greater wave steepness thus become more sharply curved. The increased curvature caused by differences in wave steepnesses increases the divergence of the orthogonals near the gap centre line, that is, the tendency of the wave energy to flow outward from the centre line is greater than indicated by the theory. This results in decreased wave energy per metre of crest and consequently decreased wave heights and K´ values near the gap centre line, and an increase in these quantities in the adjacent shadow zones.

If one compares Fig. 6-5, the finite element solution for the diffraction of waves passing through a gap in an approximate totally absorbing breakwater, with Fig. 6-6, the analytical solution for the equivalent fully reflecting breakwater case, it is evident that the correlation is extremely good. As before, the position and magnitude of the wave height peak in front of the entrance and also (to a slightly lesser extent) the position and shape of the 0,2 contour line in the lee of the breakwater, are both well predicted. The analytical solution does, however, predict a slightly greater penetration of energy into the shadow zones and this is consistent with the findings of Daemrich and Kohlhase (1978) shown in Fig. 2-9.

6.1.4 The B/L = 1,2 Breakwater Gap Configuration.

The experimental B/L = 1,2 breakwater gap configuration tested is described in Section 5.5.3.3. The incident wave characteristics were : T = 0,72 seconds, H_i = 52,8 mm (as for the 1,41 configuration), and L (theoretical) = 666,7 mm, with d = 125 mm. The experimental diffraction diagram is shown in Fig. 6-7 and the corresponding finite element diffraction diagram is shown in Fig. 6-8. No analytical solution was available for this configuration.

If one compares Fig. 6-7 with Fig. 6-8 it is evident that there is a fairly good correlation between the experimental and finite element results. There are three basic differences, however,

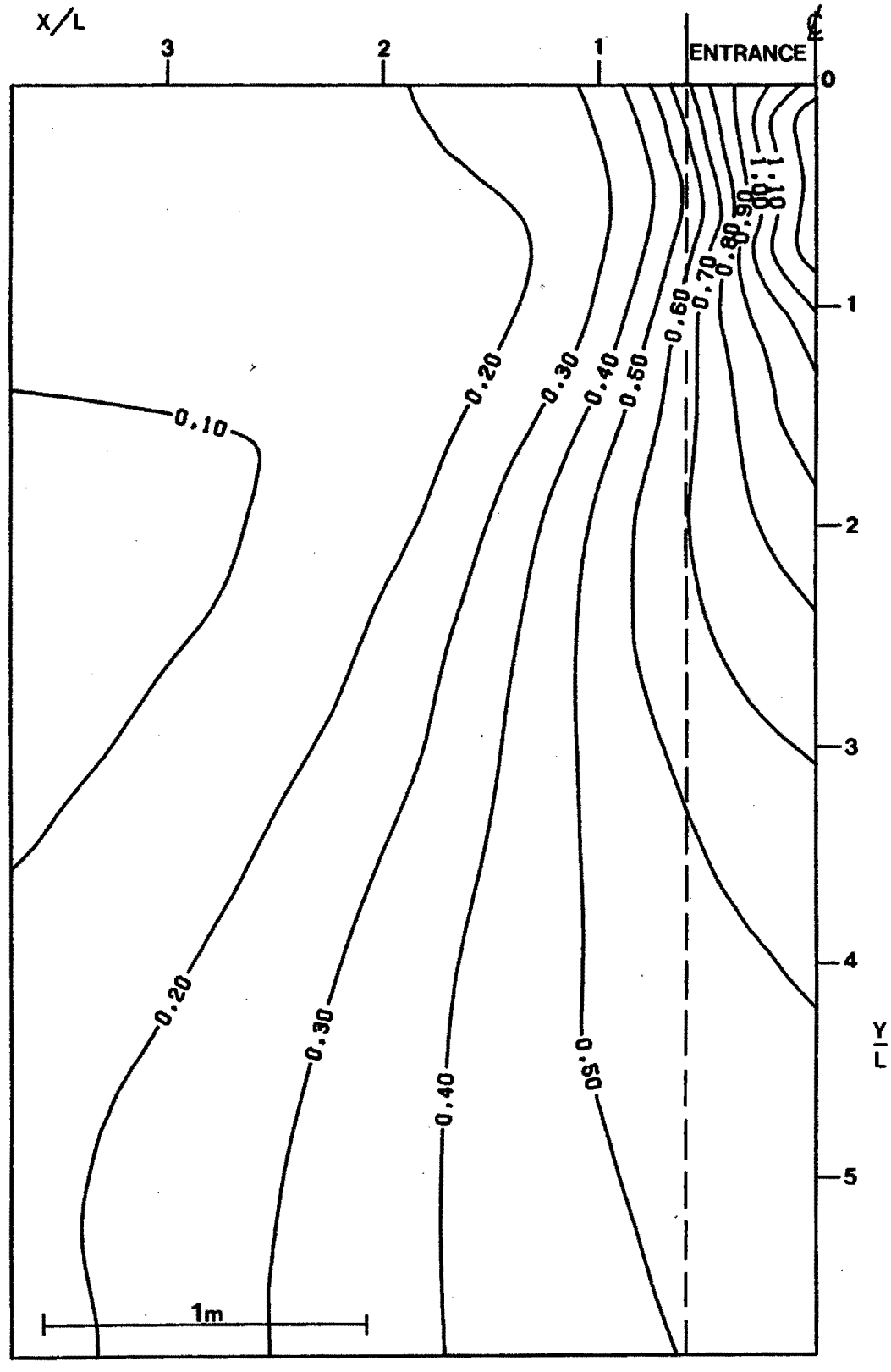

Fig. 6-8 Finite element diffraction diagram for the B/L = 1,2 breakwater gap configuration.

namely : 1) the experimental wave height peak, in front of the entrance, was higher ($K' = 1,3$ as opposed to 1,2) than predicted by the finite element model; 2) experimentally, there is found to be more energy in the lee (shadow zones) of the breakwaters than predicted by the finite element model; 3) the wave height attenuation, in the incident wave direction, occurs more rapidly than predicted by the finite element model.

It is thought that the higher energy in the lee of the breakwaters and also the higher wave height peak on the centre line just in front of the entrance, observed experimentally, could be partly attributed to the radiating second-order phenomena described by Biesel (1963, 1966). Radiating second-order waves were clearly evident in the experimental configuration and it is proposed that this phenomenon is partly responsible for the high wave height peak observed in the basin. This wave height peak can be clearly seen in the stereopairs Figs. 5-29 and 5-30. It is also proposed that, apart from the wave height peak, the higher wave heights measured in the immediate lee of the breakwater are due to the superposition of these second-order waves upon the diffracted primary wave crests.

Once again, the phenomenon of more rapid (compared to the finite element results) wave height attenuation in the incident wave direction, and also the higher energy in the shadow zones, is thought to be related to the steepness of the waves in the region outside the shadow zones. Due to their steepness the wave crests in this zone are more sharply curved, and their wave heights smaller than predicted numerically, while their wave heights are correspondingly increased in the shadow zones.

6.1.5 The B/L = 1 Breakwater Gap Configuration.

The experimental B/L = 1 breakwater gap configuration tested is described in Section 5.5.3.4. The incident wave characteristics were : T = 0,83 seconds, H_i = 53,2 mm, and L (theoretical) = 800 mm, with d = 125 mm. The experimental diffraction diagram is shown in Fig. 6-9 and the corresponding finite element diffraction diagram is shown in Fig. 6-10. The analytical diffraction diagram (fully reflecting breakwater case), shown in Fig. 6-11, was again taken

from CERC (1977) and was originally published by Johnson (1952). This diagram is based on the Morse and Rubenstein (1938)/Carr and Stelzriede (1952) solution described in Section 2.4.2.3.

If one compares Fig. 6-9 with Fig. 6-10, it is evident that the correlation between the experimental and finite element results is quite good. For example, the correlation between the experimental and finite element contours in the region outside the shadow zone (close to the gap centre line) is quite good. There are four basic differences, however, namely : 1) the experimental wave height peak, in front of the entrance, is higher (K′ = 1,4 as opposed to 1,3) than predicted by the finite element model; 2) experimentally there is found to be more energy in the lee (shadow zones) of the breakwaters than predicted by the finite element model; 3) the wave height attenuation, in the incident wave direction, occurs less rapidly in the region 0 - 4,5 L from the gap than predicted by the finite element model; 4) the wave height attenuation, in the incident wave direction, occurs more rapidly in the region further than 4,5 L from the gap than predicted by the finite element model.

It is thought that the higher wave height peak on the centre line just in front of the entrance, and also the higher energy in the lee of the breakwaters, could be attributed to radiating second-order waves (Biesel, 1963, 1966) generated at the tip of each breakwater. These radiating secondary waves were clearly present in the experimental configuration, as shown in Figs. 5-41. It is proposed that the superposition of these second-order waves upon the primary diffracted wave crests is at least partly responsible for both the higher wave height peak in front of the entrance and also the greater energy in the immediate lee of the breakwaters. The wave height peak in front of the entrance can be clearly seen in the stereopairs Figs. 5-31 and 5-32.

The phenomenon of more rapid (compared to the finite element and analytical results) wave height attenuation in the incident wave direction, in the region greater than 4,5 L from the gap, observed experimentally, and also the greater energy in the shadow zones is again thought to be due to the steepness of the waves near the gap centre line. It is proposed that the greater curvature caused

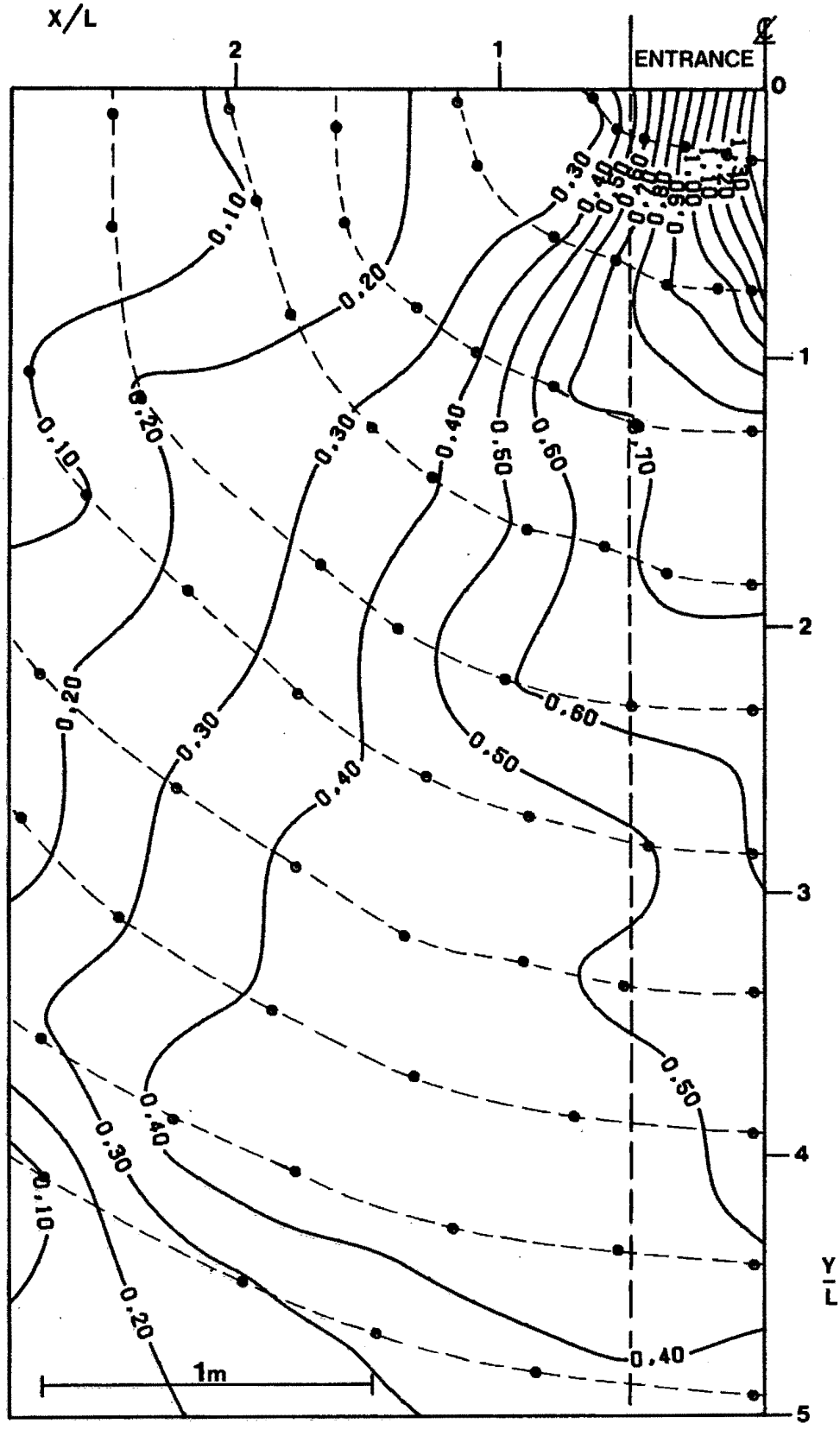

Fig. 6-9 Experimental diffraction diagram for the B/L = 1 breakwater gap configuration.

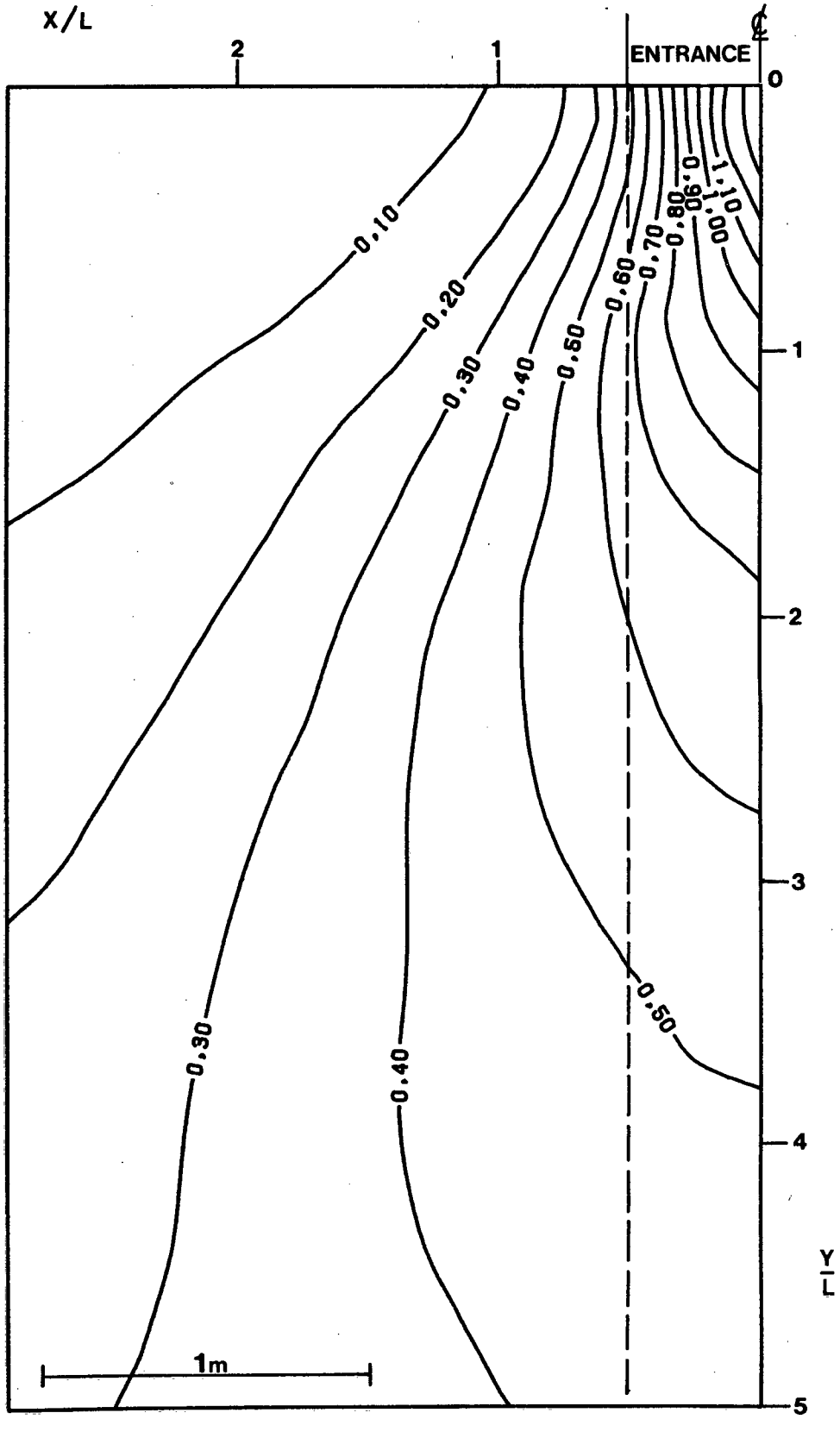

Fig. 6-10 Finite element diffraction diagram for the B/L = 1 breakwater gap configuration.

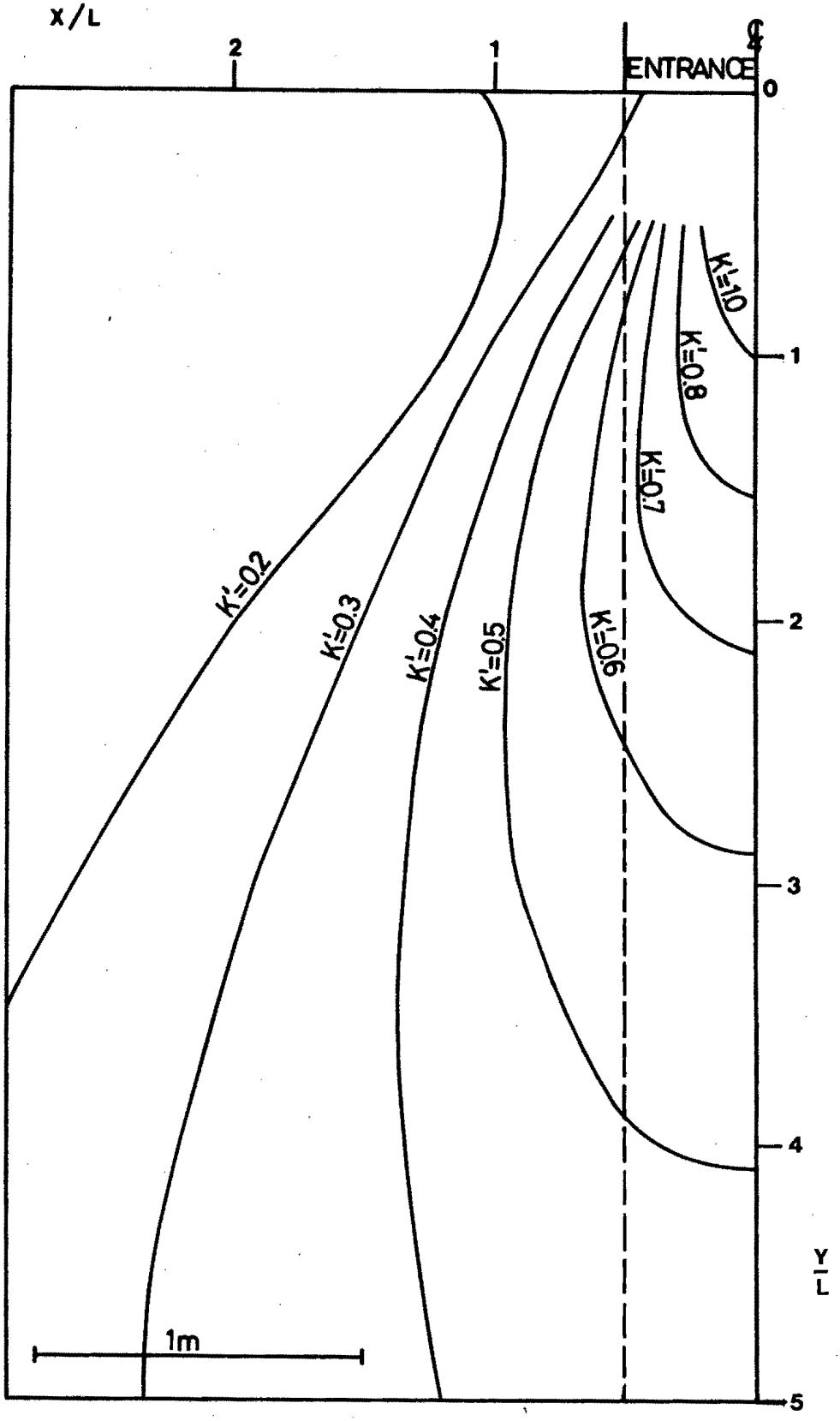

Fig. 6-11 Analytical diffraction diagram for the B/L = 1 breakwater gap configuration, from CERC (1977).

by differences in wave steepness increases the divergence of the orthogonals near the gap centre line with the result that the lateral outflow of energy from the centre line is greater than indicated by the theory.

In the region 0 - 4,5 L from the gap, however, the experimental wave height attenuation in the incident wave direction is less than predicted by the finite element model and very similar to that predicted analytically (Fig. 6-11). This is due to the fact that in the experimental configuration it appears that the wave energy (K´ contours 0,5 and 0,6) in the region 2,5 - 4,5 L from the gap has been more closely focused on the gap centre line than predicted either numerically or analytically. However, adjacent to this region of focused wave energy, the lateral dispersion of wave energy (K´ = 0,4) is also greater than predicted theoretically. It is proposed that the superposition of the breakwater tip phenomena (oscillatory vortices and radiating second-order waves) upon the primary waves as they enter the basin is in part responsible for the observed wave energy focusing.

If one compares Fig. 6-10, the finite element solution for the diffraction of waves passing through a gap in an approximate totally absorbing breakwater, with Fig. 6-11, the analytical solution for the equivalent fully reflecting breakwater case, it is evident that the correlation is very good. Again, the analytical solution predicts a greater penetration (predominantly in the incident wave direction) of wave energy into the basin than predicted by the finite element solution. This is understandable since for the fully reflecting breakwater case a small amount of the energy reflected from the seaward faces of the breakwater arms will be diffracted into the basin. The differences between these two theoretical solutions is consistent with the findings of Daemrich and Kohlhase (1978) shown in Fig. 2-9.

6.1.6 The B/L = 0,75 Breakwater Gap Configuration.

The experimental B/L = 0,75 breakwater gap configuration tested is described in Section 5.5.3.5. The incident wave characteristics were : T = 1,05 seconds, H_i = 57,7 mm, and L (theoretical) = 1066,7 mm, with d = 125 mm. The experimental diffraction diagram

is shown in Fig. 6-12 and the corresponding finite element diffraction diagram is shown in Fig. 6-13. No analytical solution was available for this configuration.

If one compares Fig. 6-12 with Fig. 6-13 it is evident that there is a good correlation between the experimental and finite element results. There are three basic differences, however, namely : 1) In the experimental configuration two wave height peaks are seen which straddled the centre line just in front of the entrance; 2) the wave height attenuation, in the incident wave direction, occurs less rapidly in the region 0 - 3 L from the gap than predicted by the finite element model; 3) the wave heights in the region close to the side wall beach are smaller than predicted by the finite element model.

In the experimental configuration the radiating secondary waves (called second-order waves) generated by each primary trough were seen to flatten the centre of the succeeding crest (at the gap centre line) as the crest passed between the breakwater tips. This phenomenon is clearly shown in Figs. 5-33 and 5-34 and explains the offset wave height peak shown in Fig. 6-12. These radiating second-order waves could also explain the higher energy in the lee of the breakwaters close to the breakwater tips, observed experimentally.

In the region 0 - 3 L from the gap and close to the gap centre line the measured wave heights are significantly larger than predicted by the finite element model. This greater (experimental) penetration of wave energy into the basin in the regions 3 to 4 L from the gap was also observed (but was less marked) in the B/L = 1 configuration. It is thought that the wave energy is somehow focused along the gap centre line in this region and it is again proposed that this focusing is in part due to the effect of the breakwater tip phenomena on the primary diffracted wave field.

In the wave basin lower wave heights were measured adjacent to the side wall beach than predicted by the finite element model. This phenomenon is thought to be partly due to a localised loss of energy from each wave crest as its edge is absorbed by the side wall beach.

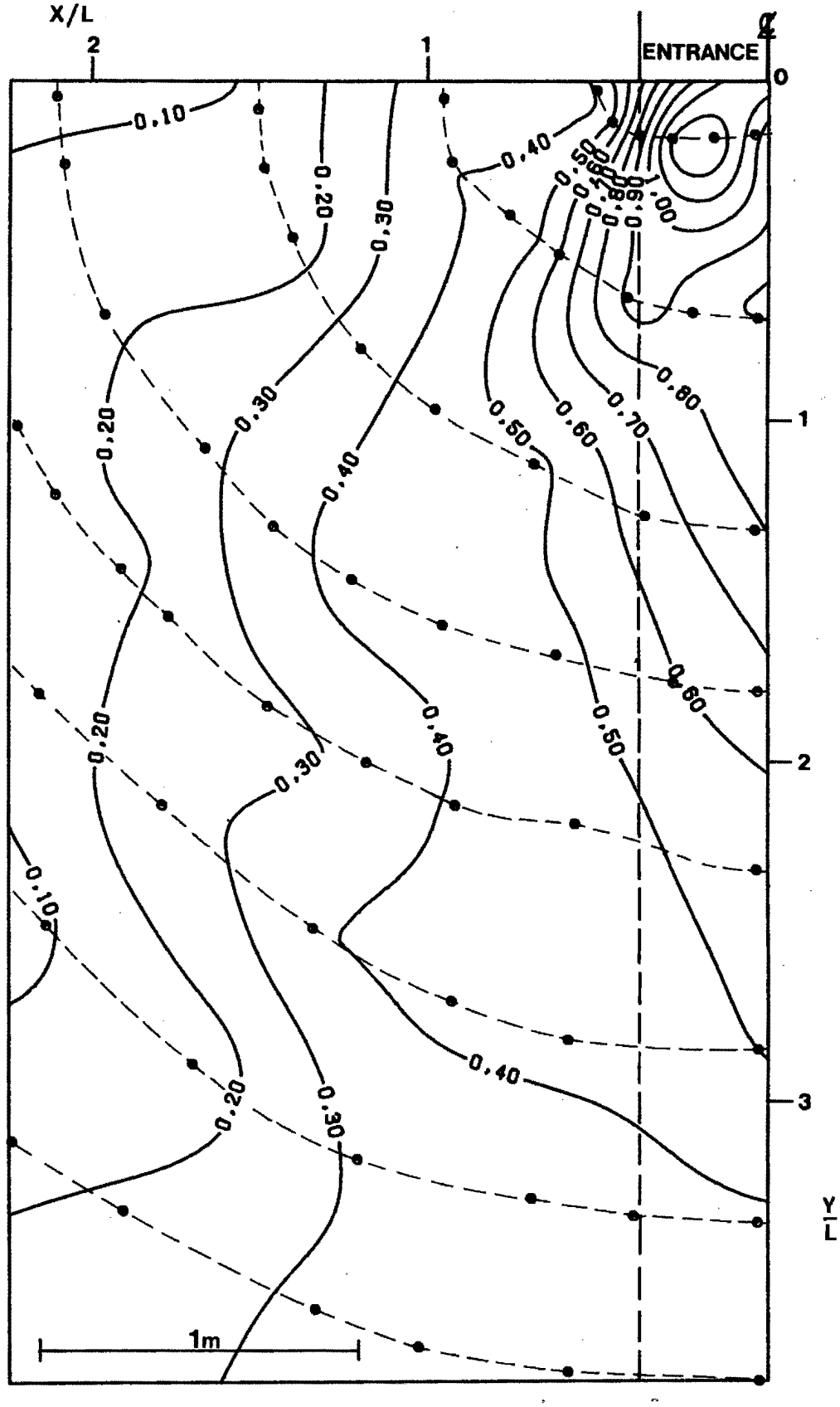

Fig. 6-12 Experimental diffraction diagram for the B/L = 0,75 breakwater gap configuration.

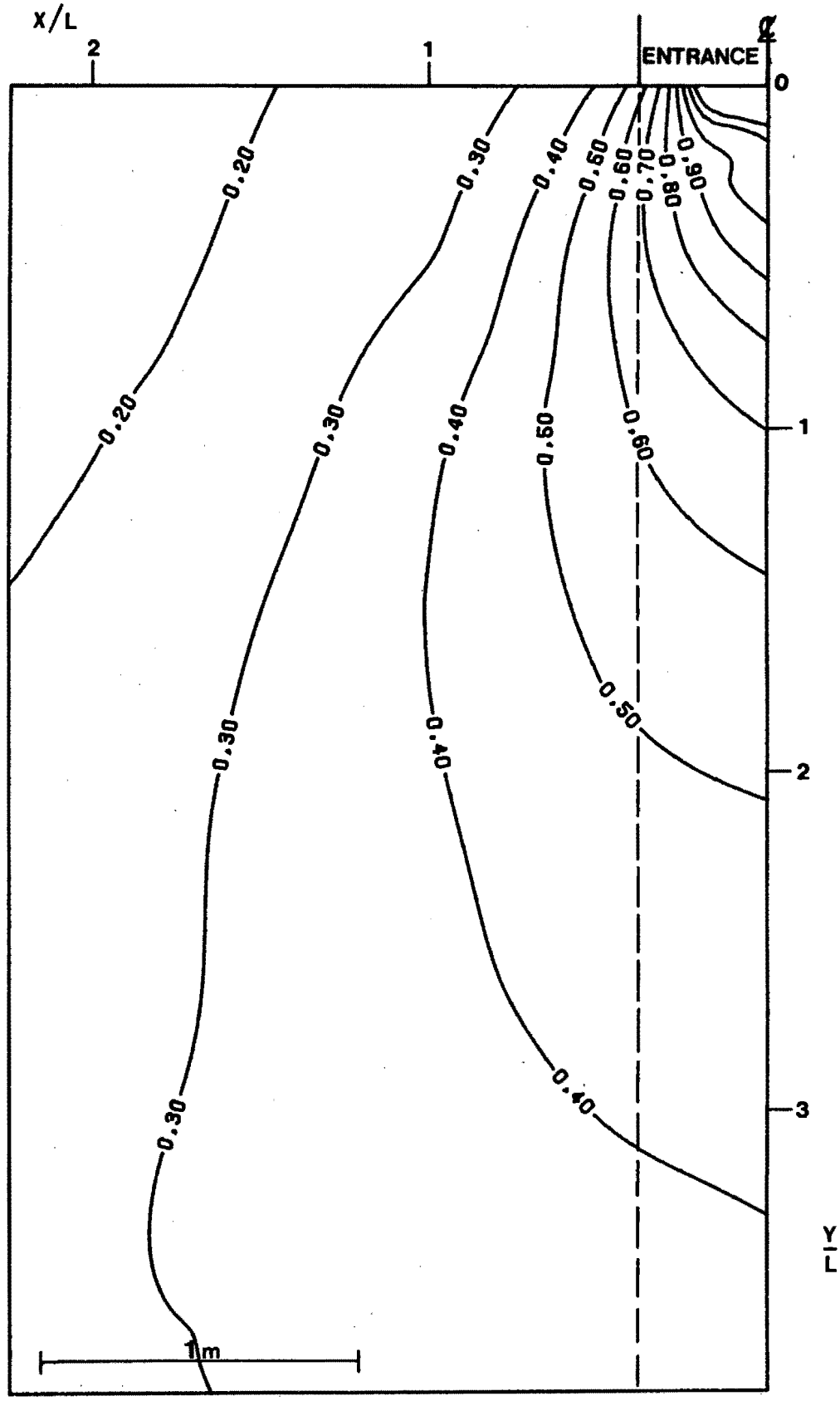

Fig. 6-13 Finite element diffraction diagram for the B/L = 0,75 breakwater gap configuration.

6.1.7 The B/L = 0,5 Breakwater Gap Configuration

The experimental B/L = 0,5 breakwater gap configuration tested is described in Section 5.5.3.6. The incident wave characteristics were : T = 1,16 seconds, H_i = 61,0 mm, L (theoretical) = 1200 mm, with d = 125 mm. The experimental diffraction diagram is shown in Fig. 6-14 and the corresponding finite element diffraction diagram is shown in Fig. 6-15. The analytical diffraction diagram (fully reflecting breakwater case), shown in Fig. 6-16, was again taken from CERC (1977) and was originally published by Johnson (1952). This diagram is based on the Morse and Rubenstein (1938)/ Carr and Stelzriede (1952) solution described in Section 2.4.2.3.

If one compares Fig. 6-14 with Fig. 6-15 it is evident that the correlation between the finite element results is quite good. There are three basic differences, however, namely : 1) the wave height attenuation in the incident wave direction occurs less rapidly in the region 0 - 2,5 L from the gap than predicted by the finite element model; 2) the wave height attenuation, in the incident wave direction, occurs more rapidly in the region farther than 2,5 L from the gap than predicted by the finite element model; 3) experimentally there is found to be, on average, less energy in the shadow zones behind the breakwaters than predicted by the finite element model.

The experimental (Fig. 6-14) wave energy penetration into the region outside the shadow zones and 0 - 2,5 L from the gap is clearly greater than that predicted by the finite element model (Fig. 6-15). In this region it appears that the available wave energy has somehow been more closely focused along the centre line (than predicted theoretically) since the lateral wave energy penetration adjacent to this region is less marked than predicted theoretically. It is proposed that the focusing of wave energy in this region could be due to the combined effect of both the pronounced oscillatory vortices and the radiating second-order waves generated at the two breakwater tips(as shown in Figs.5-42) on the primary waves as they enter the basin. Beyond this region the experimental wave height attenuation, in the incident wave direction, is again greater than predicted either numerically or analytically. However, there is not really sufficient data to tell whether this is a definite trend.

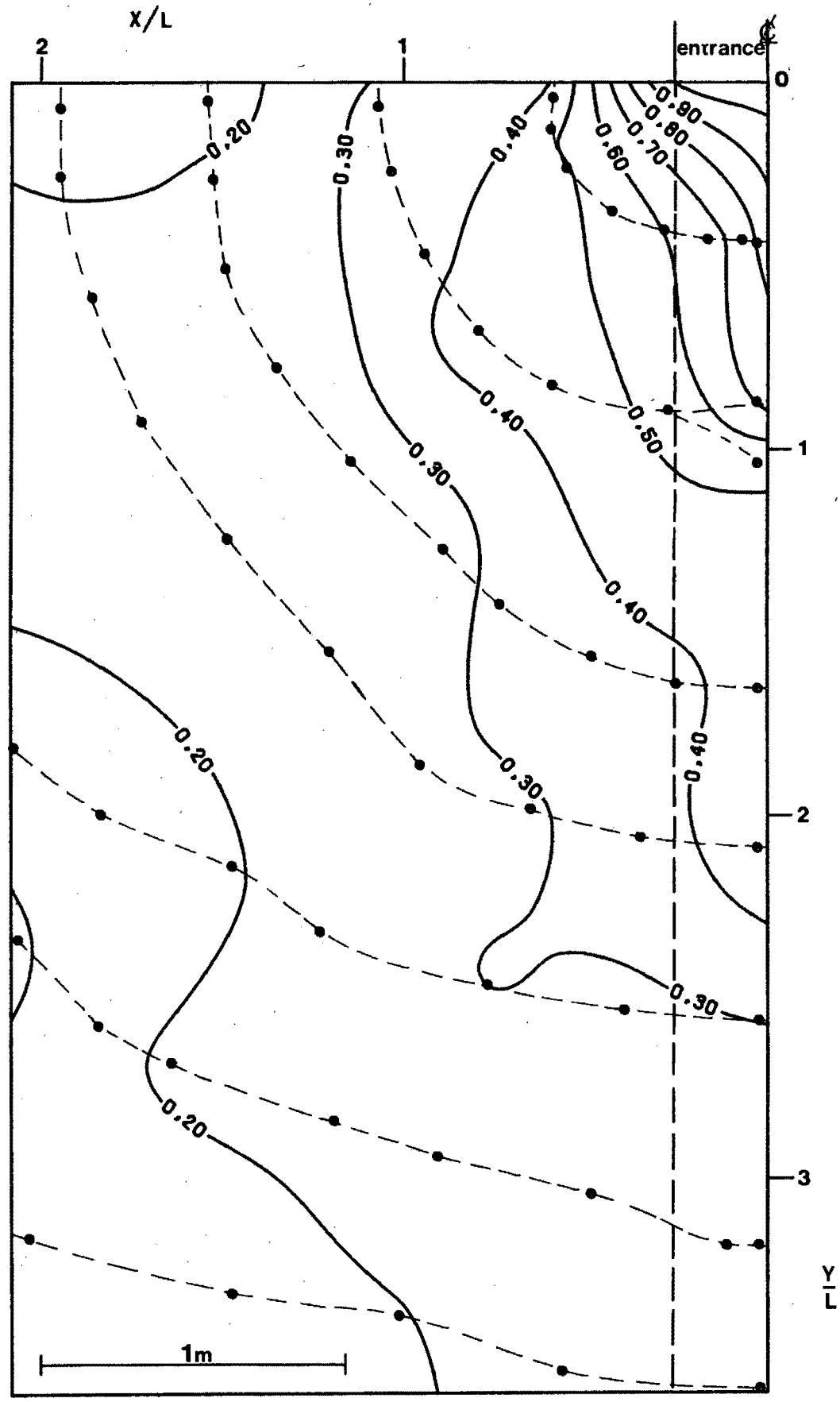

Fig. 6-14 Experimental diffraction diagram for the B/L = 0,5 breakwater gap configuration.

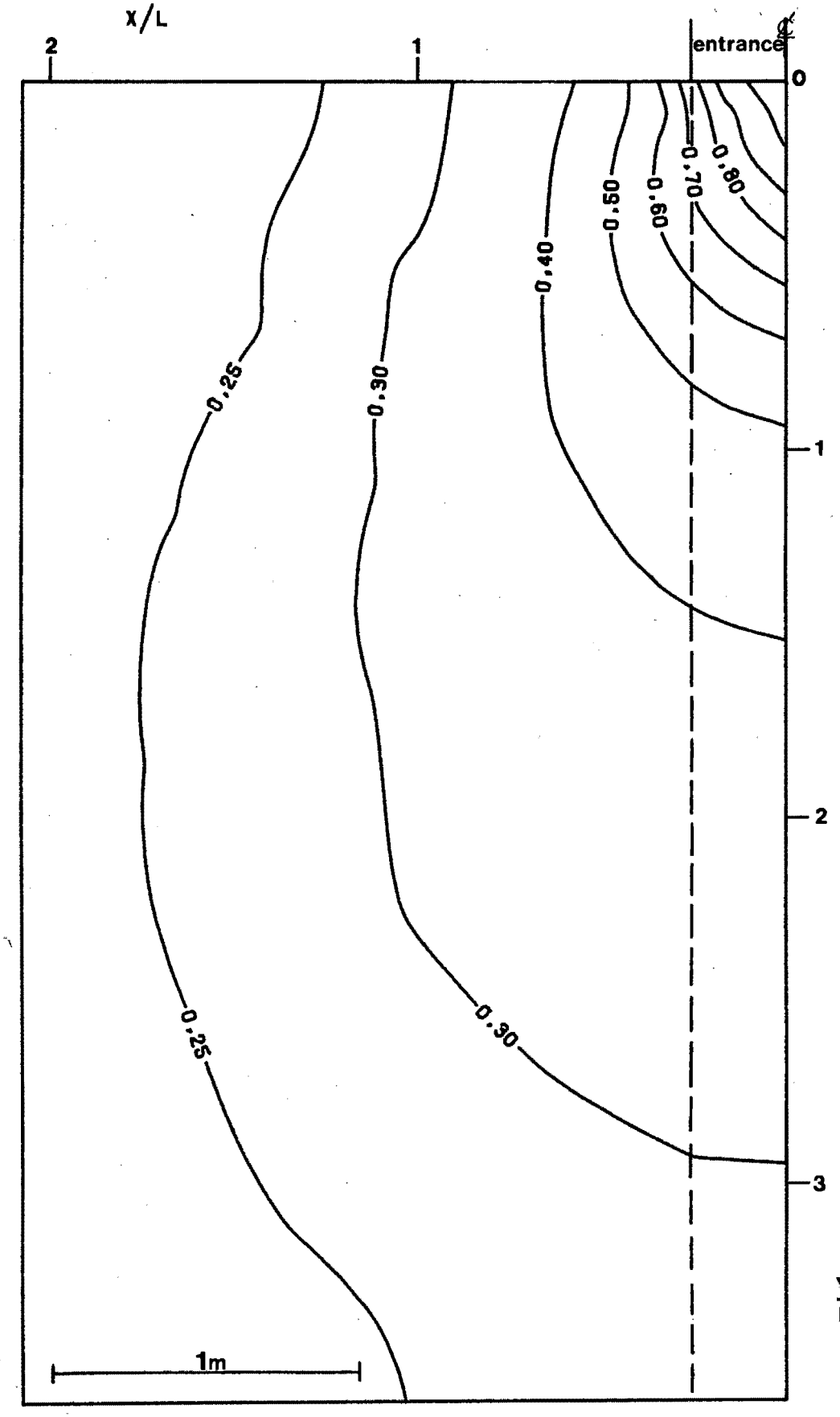

Fig. 6-15 Finite element diffraction diagram for the B/L = 0,5 breakwater gap configuration.

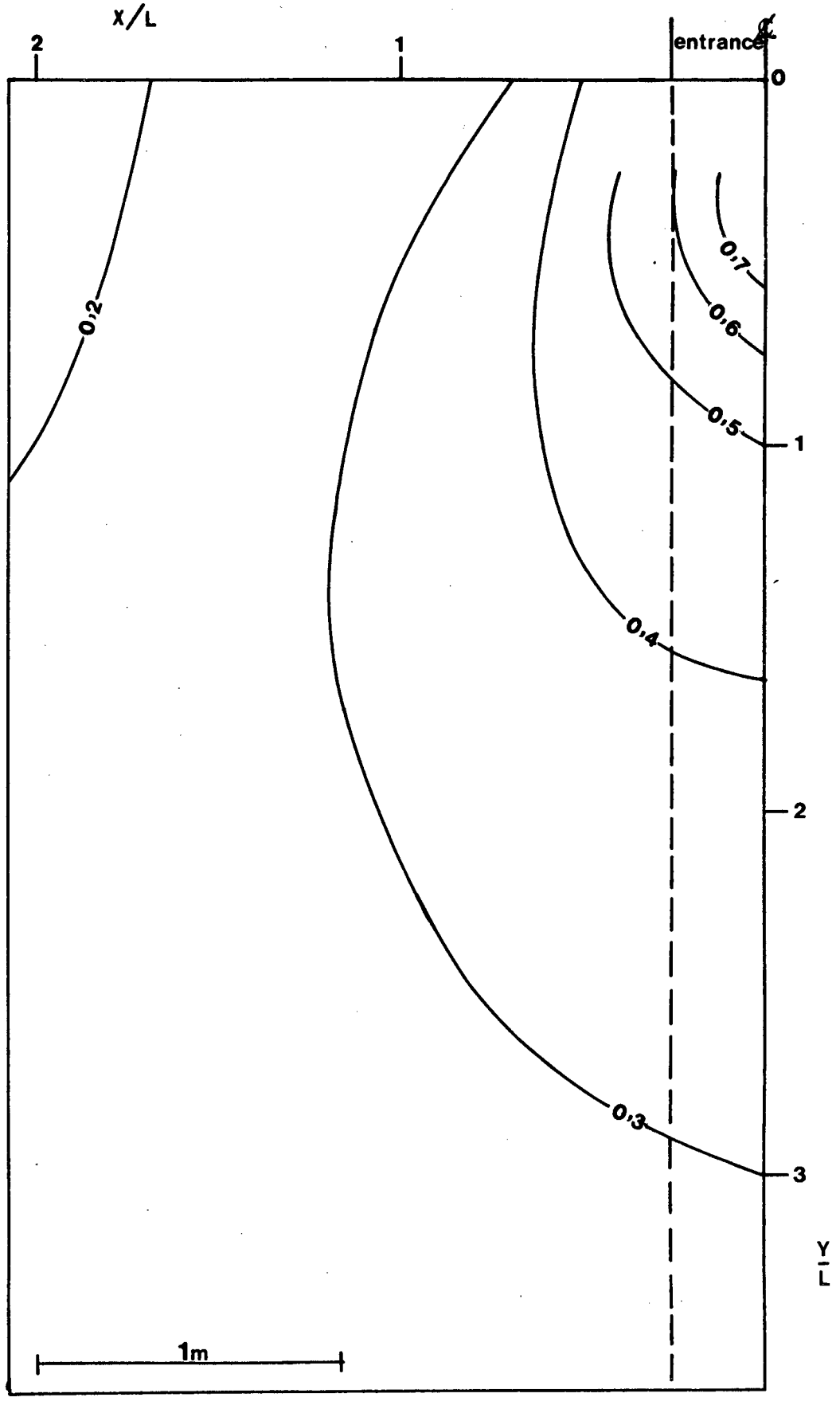

Fig. 6-16 Analytical diffraction diagram for the B/L = 0,5 breakwater gap configuration, from CERC (1977).

Experimentally it can be seen that there is less energy in the shadow zones than predicted by the finite element model. This is thought to be due to possibly two reasons : 1) the available wave energy has been focused more closely along the centre line, 0 - 2,5 L from the gap, and thus there is less energy in the adjacent areas (i.e. in the shadow zones); 2) a localised loss of energy from each wave crest occurs as its edge is absorbed by the side wall beach, with the result that the wave energy in the region adjacent to the beach is less than predicted theoretically.

If one compares Fig. 6-15, the finite element solution for the diffraction of waves passing through a gap in an approximate totally absorbing breakwater, with Fig. 6-16, the analytical solution for the equivalent fully reflecting breakwater case, it is evident that the correlation is extremely good. The analytical solution predicts a slightly greater penetration (in the incident wave direction) of wave energy into the basin which is again probably due to the small contribution from the waves reflected off the seaward faces of the breakwaters in the analytical configuration. The differences between the two theoretical solutions is again consistent with the findings of Daemrich and Kohlhase (1978) shown in Fig. 2 - 9.

6.1.8 The B/L = 1,64 Asymmetrical Breakwater Gap Configuration

The experimental B/L = 1,64 asymmetrical breakwater gap configuration is described in Section 5.5.3.7. The incident wave characteristics were : T = 0,67 seconds, H_i = 52,8 mm, L (theoretical) = 604 mm, with d = 125 mm (i.e. almost exactly the same as for the B/L = 1,64 symmetrical configuration). The experimental diffraction diagram is shown in Fig. 6-17 and the corresponding finite element diffraction diagram is shown in Fig. 6-18. Note, in Fig. 6-18, the unmarked contours in the channel all have a value of 1. No analytical diffraction diagram was available for this configuration.

If one compares Fig. 6-17 with Fig. 6-18, it is evident that there is good correlation between the experimental and finite element results. For example, the magnitude and position of the wave height peak to the right of the left-hand breakwater tip and the

diffraction pattern in the lee of the right-hand breakwater, measured experimentally, are fairly accurately predicted by the finite element model. The two basic differences are : 1) experimentally there is found to be more energy in the lee (shadow zones) of the breakwaters than predicted by the finite element model; 2) the wave height attenuation, in the incident wave direction, occurs more rapidly than predicted by the finite element model.

Again it is thought that the higher energy in the immediate lee of the breakwaters and also the wave height peak to the right of the left-hand breakwater tip, observed experimentally, could be attributed to the superposition of the radiating second-order waves generated at the breakwater tips upon the diffracted primary wave crests. For example, the radiating second-order waves generated at the left-hand breakwater tip can be clearly seen in Fig. 5-43. The wave height peak to the right of the left-hand breakwater tip can be clearly seen in the top stereopair of Fig. 5-35.

Once again, the phenomenon of more rapid (compared to the finite element results) wave height attenuation in the incident wave direction, and also the greater wave energy in the shadow zones, is thought to be related to the steepness of the waves in the region outside the shadow zones. The increased curvature caused by the differences in wave steepness increases the divergence of the orthogonals near the gap centre line. This results in a decrease in the H and K′ values near the centre line while in the adjacent areas these quantities are increased.

If one compares the experimental and finite element results for both the symmetrical and asymmetrical B/L = 1,64 configurations, certain features of the asymmetrical diffraction patterns become apparent, namely : 1) there is a pronounced wave height peak ($K' > 1,3$) to the right of the left-hand breakwater tip; 2) the $K' = 0,2$ contour protrudes deeply into the lee of the right-hand breakwater and is bracketed by regions of low wave height; 3) the greater (compared to the finite element results) experimental wave height attenuation, in the incident wave direction, is more

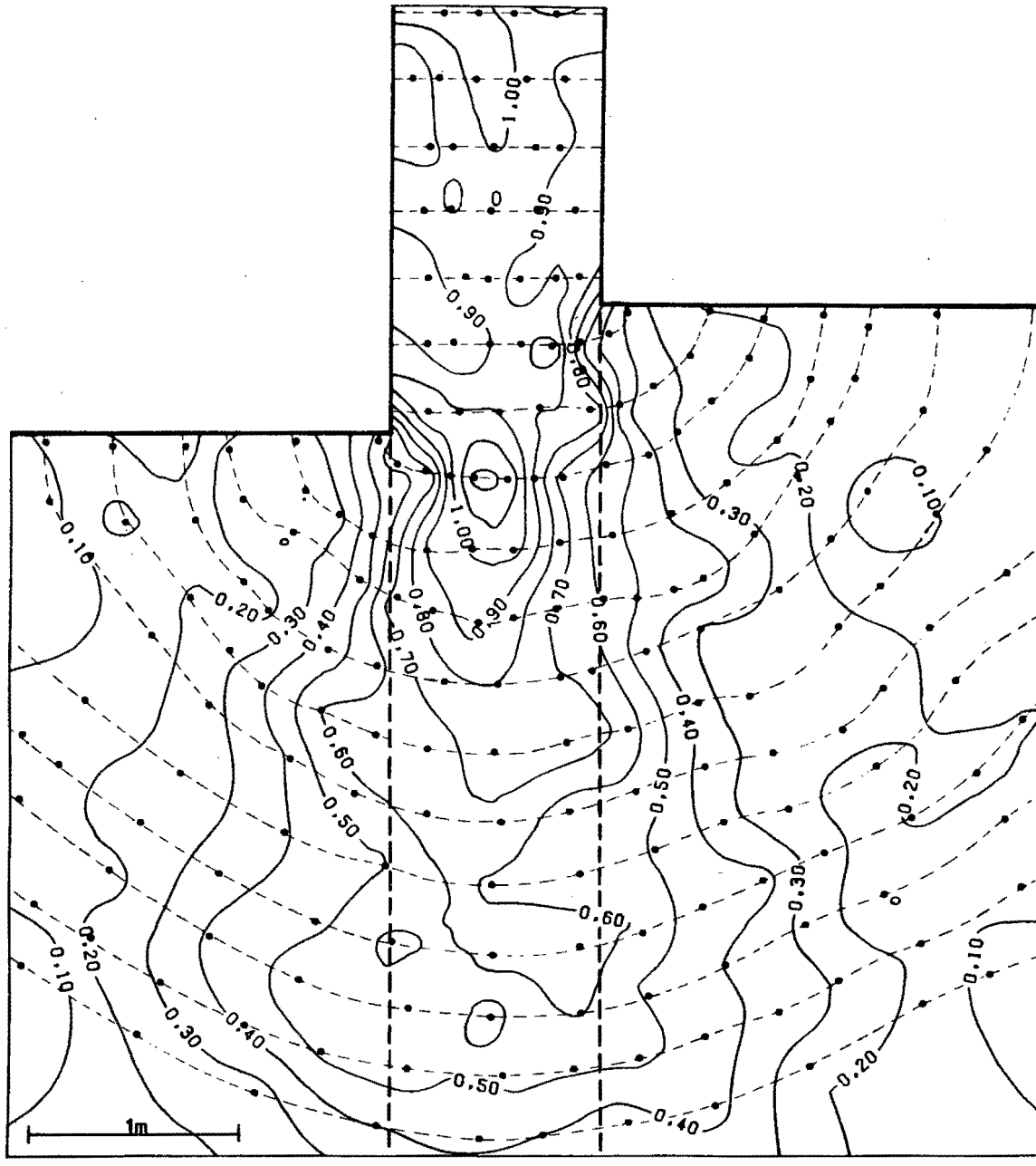

Fig. 6-17 Experimental diffraction diagram for the B/L = 1,64 asymmetrical breakwater gap configuration.

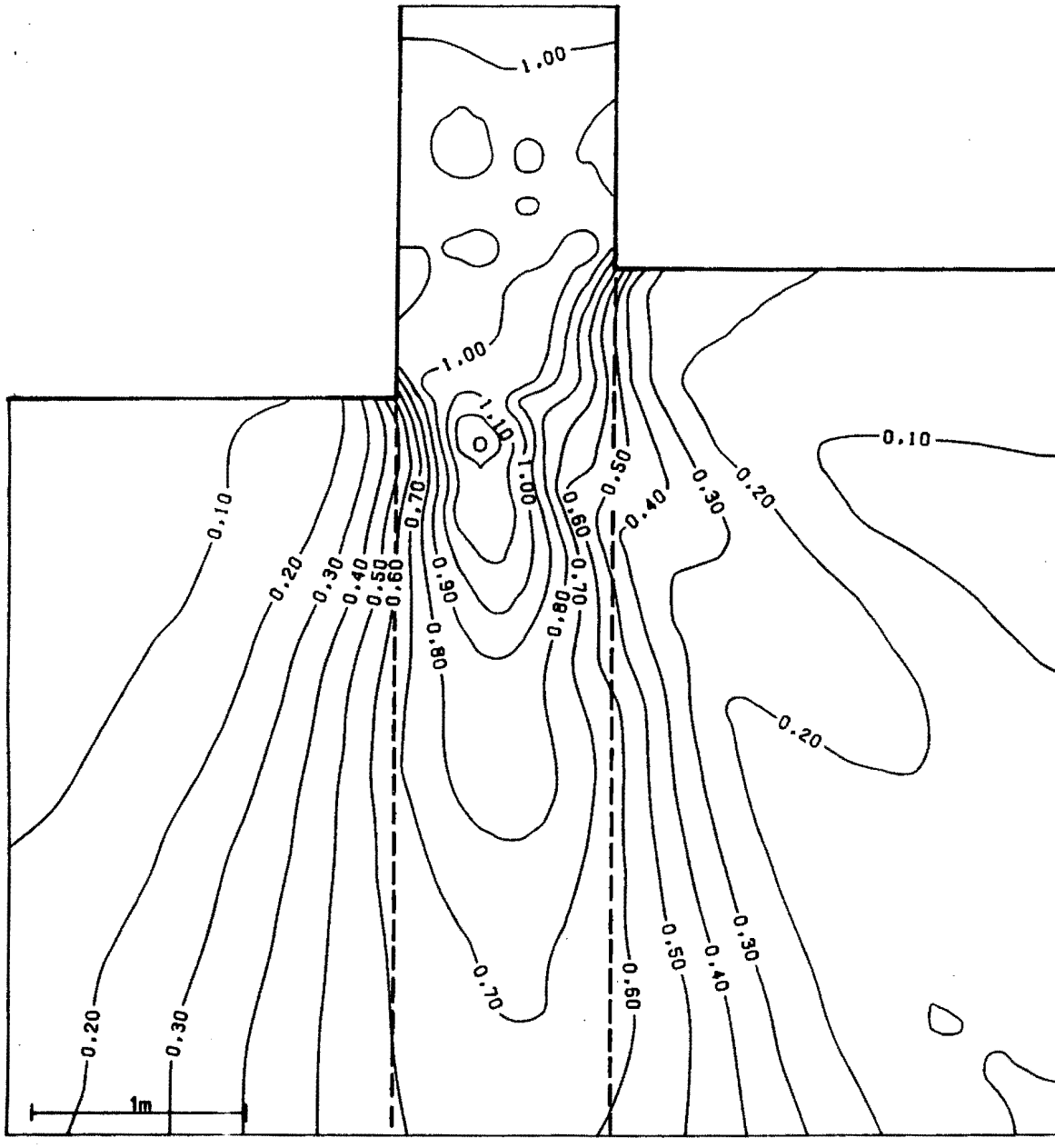

Fig. 6-18 Finite element diffraction diagram for the B/L = 1,64 asymmetrical breakwater gap configuration.

pronounced than for the symmetrical configuration.

The wave height peak to the right of the left-hand breakwater tip, seen in the asymmetrical diffraction diagrams, occupies a position which corresponds to the position of the wave height peak seen in the symmetrical diagrams. Experimentally this peak is thought to be in part due to the radiating second-order phenomenon at the breakwater tips.

For the symmetrical configuration the protrusion of the K′ = 0 2 contour into the shadow zones behind the two breakwater arms is predicted experimentally (Fig. 6-1), using finite and infinite elements (Fig. 6-2) and analytically (Fig. 6-3). For the asymmetrical configuration no such protrusion occurs, either experimentally or numerically, in the shadow zone behind the left-hand breakwater, whilst in the shadow zone behind the right-hand breakwater the protrusion of the K′ = 0,2 contour is very pronounced. This pronounced protrusion of the K′= 0,2 contour into the lee of the righthand breakwater is possibly caused by the reflection of wave energy from the lefthand wall of the entrance channel in the region close to the tip of the lefthand breakwater.

Compared to the corresponding finite element results, the experimental wave height attenuation, in the incident wave direction, for the asymmetrical configuration, is greater than for the symmetrical configuration. It is proposed that this is due to a greater lateral loss of energy experimentally, as the incident waves traverse the area between the two breakwater tips, than predicted by the finite element model. This greater lateral loss of energy could in part be explained by the differences in wave steepness along the crests which would cause a sharper divergence of the orthogonals near the gap centre line (see Section 6.1.3 for a full description of this phenomenon). A detailed comparison of the experimental and finite element results for the B/L = 1,64 (symmetrical and asymmetrical) configurations, described above, is also given by Pos (1984).

6.2 Discussion on General Thesis Topics.

6.2.1 Breakwater Gap Wave Diffraction : Summary of Results and Trends Observed.

6.2.1.1 A Comparison of the Experimental and Finite Element Results.

A summary of the basic differences and areas of agreement between the experimental and finite element results for each breakwater gap configuration analysed is given. The general trends observed are then discussed.

A. B/L = 1,64 Breakwater Gap.

Agreement : 1) the experimental wave height peak ($K' = 1,2$), in front of entrance, is fairly accurately predicted by the finite element model.

Differences : 1) experimentally there is found to be more energy in the shadow zones than predicted numerically; 2) the wave height attenuation, in the incident wave direction, occurs more rapidly than predicted numerically.

B. B/L = 1,41 Breakwater Gap.

Agreement : As for the B/L = 1,64 configuration above.

Differences : As for the B/L = 1,64 configuration above.

C. B/L = 1,2 Breakwater Gap.

Differences : 1) the experimental wave height peak, in front of the entrance, is slightly higher ($K' = 1,3$ as opposed to 1,2) than predicted numerically; 2) experimentally there is found to be more energy in the shadow zones than predicted numerically; 3) the wave height attenuation, in the incident wave direction, occurs more rapidly than predicted numerically.

D. B/L = 1 Breakwater Gap.

Differences : 1) the experimental wave height peak, in front of the entrance, is slightly higher ($K' = 1,4$ as opposed to 1,3) than predicted numerically; 2) experimentally there is found to be more energy in the shadow zones than predicted numerically; 3) the wave height attenuation, in the incident wave direction, occurs less rapidly in the region 0 - 4,5 L from the gap than predicted numerically; 4) the wave height attenuation, in the incident wave direction, occurs more rapidly in the region farther than 4,5 L from the gap than predicted numerically.

E. B/L = 0,75 Breakwater Gap.

Differences : 1) in the experimental configuration two wave height peaks are seen which straddled the centre line just in front of the entrance; 2) the wave height attenuation, in the incident wave direction, occurs less rapidly in the region 0 - 3 L from the gap than predicted numerically; 3) the wave heights in the region close to the side wall beach are smaller than predicted numerically.

F. B/L = 0,5 Breakwater Gap.

Differences : 1) experimentally there is found to be, on average, less energy in the shadow zones than predicted numerically; 2) the wave height attenuation, in the incident wave direction, occurs less rapidly in the region 0 - 2,5 L from the gap than predicted numerically; 3) the wave height attenuation, in the incident wave direction, occurs more rapidly in the region farther than 2,5 L from the gap than predicted numerically.

G. B/L = 1,64 Asymmetrical Breakwater Gap.

Agreement : 1) the experimental wave height peak to the right of the left-hand breakwater tip, and 2) the diffraction pattern in the lee of the right-hand breakwater, are fairly accurately predicted numerically.

Differences : 1) experimentally there is found to be more energy in the shadow zones than predicted numerically; 2) the wave height attenuation, in the incident wave direction, occurs more rapidly than predicted numerically.

From the above summary certain trends are apparent. Firstly wave height peaks are shown, both experimentally and numerically, to occur just in front of the entrance for the B/L = 1,64; 1,41; 1,2; 1 and 1,64 asymmetrical configurations. For the B/L = 1,2 and 1 configurations the experimental wave height peaks were higher than predicted. The more pronounced peaks observed experimentally are thought to be caused by the superposition of the radiating second-order waves generated at the breakwater tips upon the primary wave crests entering the basin.

The second trend observed is that experimentally there is found to be more energy in the shadow zones than predicted numerically for

the B/L = 1,64; 1,41; 1,2; 1 and 1,64 asymmetrical configurations. The increased energy in the immediate lee of the breakwaters, observed experimentally, is thought to be due to the superposition of the radiating second-order waves generated at the breakwater tips upon the primary diffracted wave crests in these regions. The increased energy in the shadow zones, observed experimentally, in regions more distant (> 2 L) from the gap is thought to be due to differences in wave steepness along the crests, particularly in the regions outside the shadow zones. The increased crest curvature caused by differences in wave steepness increases the divergence of the orthogonals near the gap centre line resulting in decreased wave heights and K′ values near the gap centre line and an increase in these quantities in the adjacent shadow zones.

The third trend observed is that experimentally, the wave height attenuation, in the incident wave direction, occurs more rapidly than predicted numerically for the B/L = 1,64; 1,41; 1,2 and 1,64 asymmetrical configurations. This phenomenon was also observed for the B/L = 1 and 0,5 configurations, but only for those regions farther than 4,5 L and 2,5 L from the gap respectively. This phenomenon is again thought to be due to differences in steepness along the wave crests in regions near the gap centre line. As explained previously, this results in a decrease in H and K′ near the gap centre line and a corresponding increase in these quantities in the adjacent shadow zones.

The fourth trend observed is that experimentally, the wave height attenuation, in the incident wave direction, occurs less rapidly than predicted numerically for the B/L = 1; 0,75 and 0,5 configurations in the regions 0 - 4,5 L; 0 - 3 L and 0 - 2,5 L from the gap respectively. In these regions it appears that the wave energy has been more closely focused along the centre line than predicted numerically. It is proposed that the focusing of wave energy in this region is due to the combined effect of both the oscillatory vortices and the radiating second-order waves generated at the breakwater tips on the primary wave crests entering the basin. This hypothesis is supported by the fact that for the smaller B/L ratios these breakwater tip phenomena have a very significant effect (across the full width of the entrance) on the primary wave train entering the basin.

6.2.1.2 A Comparison of the Finite Element and Analytical Results.

A summary of the basic differences and areas of agreement between the finite element and analytical results is given. The general trends observed are then discussed. The finite element results are for the case of waves passing through a gap in an approximate (channel entrance) totally absorbing breakwater while the analytical results (from CERC, 1977), are for the equivalent fully reflecting breakwater case.

A. B/L = 1,64 Breakwater Gap.

Agreement : 1) the position and magnitude of the analytical wave height peak in front of the entrance, and 2) the position and shape of the 0,2 contour in the lee of the breakwater, are fairly accurately predicted numerically.

Differences : 1) the numerical wave height attenuation, in the incident wave direction, occurs slightly more rapidly than predicted analytically.

B. B/L = 1,41 Breakwater Gap.

Agreement : 1) in general the numerical and analytical diffraction diagrams agree closely.

Differences : 1) analytically there is found to be slightly more energy in the shadow zones than predicted numerically.

C. B/L = 1 Breakwater Gap.

Differences : 1) analytically there is found to be more wave energy in the shadow zones than predicted numerically; 2) the numerical wave height attenuation, in the incident wave direction, occurs more rapidly than predicted analytically.

D. B/L = 0,5 Breakwater Gap.

Agreement : 1) in general the numerical and analytical diffraction diagrams agree closely.

Differences : 1) the numerical wave height attenuation, in the incident wave direction, occurs slightly more rapidly than predicted analytically.

The general trend observed is that the analytical results predict a slightly greater penetration of wave energy into the basin than calculated numerically. This greater penetration of wave energy into the basin manifests itself in two ways; namely :

1) analytically there is found to be more wave energy in the shadow zones than predicted numerically (B/L = 1,41 and 1); 2) the numerical wave height attenuation, in the incident wave direction, occurs more rapidly than predicted analytically (B/L = 1,64; 1 and 0,5). It is proposed that the reason the analytical solutions predict a slightly greater penetration of wave energy into the basin (than calculated numerically) is that for the fully reflecting breakwater case a small amount of the energy reflected from the seaward faces of the breakwater arms will be diffracted into the basin. For the fully absorbing breakwater (or channel entrance) case no such contribution from the seaward faces of the breakwaters would occur. The differences between the numerical and analytical results, described above, are consistent with the findings of Daemrich and Kohlhase (1978) shown in Fig. 2-9.

6.2.2 Linear Wave Diffraction Theory and Non-Linear Experimental Phenomena.

Both the numerical (refraction - diffraction) and analytical (diffraction) formulations are based on the linear wave theory. This theory has the following limitations, namely : 1) an ideal (non-viscous), incompressible, homogeneous fluid subjected to a gravity force field; 2) an irrotational motion, which leads to a potential formulation; 3) infinitesimally small amplitude waves; and 4) a motion which is only simple harmonic in time. The linear theory cannot, therefore, predict certain non-linear phenomena observed experimentally, namely :

1) Oscillatory Vortices at the Breakwater Tips

As waves enter a model harbour basin, the high velocity gradients, at the two breakwater tips forming the entrance, produce viscous forces which retard the flow leading to separation and the formation of a vortex at each tip. The motion of these vortices is tied to the wave kinematics i.e. they rotate into the basin with the crests and in the opposite direction with the troughs. Due to the inertia of the system each vortex exhibits a small phase lag relative to the incident wave train and as a result it has a "shoaling" effect on that portion of each crest passing through its sphere of influence. In the experimental configurations it was noted

that the importance of the breakwater tip vortex effects increased as the the gap width decreased.

2) Radiating Second-Order Waves

In the experimental configurations, a radiating second-order wave was generated at each breakwater tip whenever either a crest or a trough passed the tips, i.e. a circular wave train was generated at each tip with a period half that of the primary wave train. A detailed investigation of this breakwater tip phenomenon is described in Section 5.6. For the experimental $B/L \geqslant 1$ breakwater gap configurations it is proposed that this phenomenon is partly responsible for the greater wave energy penetration (than predicted numerically) measured in the immediate lee of the breakwaters. For the experimental $B/L \leqslant 1$ configurations it is proposed that this phenomenon is responsible for the observed greater focusing (than predicted numerically) of wave energy along the centre line close to the entrance.

3) Cross-Waves

Cross-waves are standing waves with crests at right angles to the wave generator and a frequency half that of the wave maker. Their effect is particularly pronounced when the generated cross-waves correspond to a natural lateral mode of oscillation of the basin. Spens (1954) and Barnard and Pritchard (1972) have shown experimentally that cross-waves require a certain finite time (from starting the paddle) to become fully developed. This growth rate is proportional to the height of the waves in the generated primary wave train and also to the instantaneous amplitude of the growing cross-wave field (i.e. the growth rate increases as the cross-waves increase in size). Cross-waves are thus thought to be a major cause of wave height variations along incident wave crests (see Section 5.3.2). In the investigation described in Section 5.3.3.4 the author found that a fully developed cross-wave field developed in the basin, close to the paddle, after the paddle had been running for approximately 30 seconds.

This gradual build-up of the cross-waves, as described above, underlines one of the major advantages of using the infinite basin technique (described in Section 5.4) for model harbour studies.

Using this technique the wave paddle is only operated for short periods of time, and thus it is proposed that even if cross-waves do develop, they would not have enough time to progress beyond their initial development stage.

4) Wave Steepness Effects

Wave steepness effects were thought to be a major reason for the observed differences between experimental and theoretical results for the $B/L \geq 1$ configurations. In the experimental diffraction configurations investigated the steepest waves occurred along the gap centre line, with the result that the wave lengths (and celerities) of these waves were larger than predicted using linear wave theory. It is proposed that the increased crest curvature caused by these differences in wave steepness (along the crests) increases the divergence of the orthogonals near the gap centre line, resulting in decreased wave heights and K' values near the centre line and an increase in these values in the adjacent shadow zones.

5) Wave Reflection Effects

Whenever one attempts to model an essentially infinite domain problem, such as semi-infinite breakwater and breakwater gap wave diffraction problems, one runs into the problem of dealing with wave reflections. The general approach adopted by researchers such as Harms (1976, 1979b), Memos (1976, 1980c), Blue and Johnson (1949) and Putnam and Arthur (1948) was to place absorbing beaches (or other materials) along the basin walls and then subsequently to assume that these beaches are effectively totally absorbing. Based on this assumption, the above researchers adopted the convenient procedure of allowing the wave paddle to run continuously during a test.

The author adopted the above approach for the initial wave diffraction investigation described in Section 5.2. It was found that when the paddle ran continuously, a secondary wave field developed in the basin consisting of wave reflections, resonant cross-waves and other parasitic wave forms. This secondary wave field was superimposed upon the primary diffracted wave field and reduced the accuracy with which the primary diffracted wave heights could be measured. The effect of this secondary wave field on the wave height measurement

accuracy was most pronounced in those regions, such as in the immediate lee of the breakwaters, where the primary diffracted wave heights were small. It was found that the use of the infinite basin technique, described in Sections 5.4 and 5.5.2, largely prevented the development of the secondary wave field, since the stereopairs were taken before much energy could be reflected from the peripheral beaches. The superiority of the infinite basin technique, when compared to the more conventional technique described above, was clearly demonstrated by the investigation described in Section 5.5.4.

6.2.3 Laboratory Photogrammetric Wave Height Measurement and the Infinite Basin Technique.

This thesis describes the development of a laboratory photogrammetric wave height measurement technique which the author considers to be superior to conventional techniques for the experimental analysis of essentially infinite domain problems such as breakwater gap wave diffraction. Conventional techniques based on the parallel wire resistance or capacity wave probe usually employ a number of these probes, which are mounted on a movable instrument carriage which can traverse the wave basin to measure the wave heights. Using this technique only a limited number of discrete locations can be measured at any one time. Furthermore, excessive spacing of these wave probes may result in points of maximum wave heights being overlooked. The technique is also time consuming, since the instrument carriage has to be moved within the basin until the entire water surface has been measured. Generally, when using the conventional technique, the wave paddle is allowed to run continuously. This enables secondary effects (wave reflections, basin oscillations, cross-waves, etc.) to develop and distort the primary wave field.

The author has shown that using his photogrammetric technique (for monochromatic wave problems) the wave height distribution across the entire basin (at 1/2 wave length intervals) can be determined by taking only two stereopairs of the water surface. The stereopairs are taken such that the waves imaged in the 1st stereopair are 180° out of phase relative to those imaged in the second stereopair using a triggering device attached to the wave generator. The wave height measurement accuracy depends on factors such as analysis procedures and the quality of the cameras, and the author has shown that an accuracy of better than 2 mm (for a camera "flying height" of 5 m) can be consistently achieved. The information contained on the plates is permanent, synoptic and detailed and furthermore, there is no instrumental interference in the wave processes being observed. The photogrammetric technique led to the development of the infinite basin technique, in which the stereopairs are taken just before the wave energy front reaches the peripheral beaches, thus eliminating the distorting effects of wave

reflections, and other secondary effects, within the basin. The infinite basin technique enables the researcher to model accurately the situation of a continuous wave train entering a basin of infinite extent.

The development of the photogrammetric wave height measurement technique will now be briefly summarised. As illustrated by Fig. 4-16 a major problem in the photogrammetric measurement of a dynamic water surface is to clearly define this surface. The author solved this problem by adding cutting oil (7 ml/ℓ) to the basin water (see Section 4.6.1). However, the addition of the cutting oil introduces serious photographic contrast problems, since the water surface takes on the appearance of a large white projection screen. This problem was solved by projecting concentric circle patterns onto the water surface using four overhead projectors mounted above the wave basin (Section 4.6.2). The equipment needed to allow two stereopairs to be taken, with the imaged waves 180° out of phase, etc., was then developed (Section 4.6.4). When, however, the first plates were examined using a stereoplotter, certain problems were encountered (Section 4.6.5). It was evident that the overhead projectors provided insufficient illumination and that the cameras were not synchronised and exhibited shutter speed anomalies. These problems were overcome by converting the overhead projectors into flash units (Section 4.6.6). Also, the concentric circle patterns were replaced by random assemblies of stars and arrows (Section 4.6.7).

The basic photographic system was now complete and various methods were available to analyse the stereopairs. Since a stereoplotter and an operator were available this was the initial method used to analyse the plates. The control point configuration, needed for the stereoplotter analysis, was set up in the basin (Section 4.7.2.3) and the stereopairs analysed using the procedure described in Section 4.7.4. The initial wave diffraction configurations, described in Section 5.2 were analysed using this procedure. Certain problems were encountered in the use of a stereoplotter for wave height and pattern measurement, as described in Section 4.7.6. For example; 1) the stereoplotter operator would neglect to measure points of interest to the author; 2) the measurement accuracy of 3-4mm

(Section 4.7.3) was inadequate when measuring the waves in the immediate lee of the breakwaters; 3) the stereoplotter analysis system was very expensive since a stereoplotter, an operator and two metric cameras were required. Another problem encountered during the initial investigation described in Section 5.2 was that of secondary basin effects which were linked to the conventional procedure adopted initially of allowing the wave paddle to run continuously throughout a test. These problems led to the development of the infinite basin technique described in Sections 5.4 and 5.5.2.

Due to the problems encountered with the stereoplotter analysis technique the author developed an alternative, more accurate technique based on the theory of projective transformations (Section 4.8.2) in which the coastal engineer could analyse the plates himself using a stereocomparator linked to a microcomputer. To develop the necessary procedures and software the author simulated the wave basin configuration using a polystyrene wave set up in the photogrammetric testfield (Section 4.8.5.2). An investigation was carried out to determine the number of control points needed and their most desirable configuration (Section 4.8.5.3). This investigation was aided by a parallel investigation carried out by Welham (1982). A 16-point configuration was adopted and this was set up in the basin. The stereocomparator/microcomputer/projective transformation procedure finally developed is very briefly outlined in Section 4.8.5.4 and the full procedure is outlined by Pos (1982b). The above procedure was used to analyse the breakwater gap diffraction configurations described in Section 5.5.3. It was established in Sections 4.8.4 and 4.8.5.5 that the potential wave height measurement accuracy of the system was ± 1,2 - 1,6 mm (at a "flying height" of 5m). Flowcharts of the programs used are given in Appendices 4A and 4B.

The author also investigated two cheaper photogrammetric water surface elevation measurement techniques. The first technique is based on the theory of projective transformations. In this technique enlargements made from the plates are analysed using a modified mirror stereoscope, an electronic parallax bar, a digitiser tablet linked to a microcomputer and the procedure outlined in Section 4.8.6.2. However, it was found (Section 4.8.6.3) that this system was not accurate enough to analyse the experimental configurations

to be tested. Techniques based on the theory of projective transformations are ideally suited to the analysis of stereopairs taken with simple non-metric cameras. The wave height measurement potential of non-metric photogrammetry is discussed in Section 4.8.7.

The second, and least expensive technique investigated, is based on the theory of the deformed reference plane (Section 4.9.2.1). Based on tests carried out using a simulated basin configuration in the testfield (Section 4.9.3.4) it became apparent that the basic theory had to be modified for close range applications. With this technique enlargements made from the plates are analysed using a conventional mirror stereoscope and parallax bar and analysed on a microcomputer using a computer program based on the modified theory (Section 4.9.3.5). The procedure to be adopted when using this technique is described in Section 4.9.4 and flow charts of the programs used are given in Appendices 4C and 4D. This technique was found to be surprisingly accurate (see Table 4-12) but is, however, the most laborious of all the techniques investigated.

This research has shown that the stereocomparator/microcomputer/ projective transformations technique is a powerful and accurate method for measuring wave heights and patterns in a laboratory basin. The technique is particularly suited to the experimental investigation of infinite domain problems such as breakwater gap wave diffraction. A current interest of the author is to use the technique to measure the two-dimensional energy spectrum of random waves generated in a laboratory basin using procedures similar to those described by Holthuijsen (1983a, 1983b). The author does not believe that the photogrammetric technique will replace sophisticated conventional (wave probe) techniques, such as the ADACS system used at the U.S. Army Engineer Waterways Experimental Station (Hales, 1980), since conventional techniques are still quite adequate for general laboratory investigations. However, for the experimental analysis of infinite domain type problems the photogrammetric technique is clearly superior.

6.2.4 The Modelling of Breakwater Gap Wave Diffraction Configurations Using the "WAVE" Program.

From the numerical results given in Section 6.1, it can be clearly seen that the finite and infinite element program "WAVE" was ideally suited to the modelling of the experimental breakwater gap configurations described in Section 5.5.3. It has been shown that the program can accurately model the diffraction of waves entering an infinite basin via a rectangular channel. This configuration, the author believes, closely approximates the diffraction of waves passing through a gap in a totally absorbing breakwater.

As described in Section 3.5, it has been shown that these approximate totally absorbing breakwater gap diffraction problems can be accurately modelled using relatively coarse meshes. With the proviso, however, that the number of elements per wave length for any portion of the mesh should be a function of the wave height gradients for the corresponding region in the basin. A radial mesh, centred at the breakwater gap mid-point, would thus be the best suited to model such configurations. The author now found that, on average, the minimum number of elements required per wave length in the radial direction was 6 in the breakwater gap region, and 2,5 outside this region. The element meshes used to model the experimental breakwater gap configurations are shown in Appendix 3B.

As described in Section 3.6 the author also used the "WAVE" program to model the diffraction of waves passing through a gap in a perfectly reflecting breakwater. A B/L = 1 breakwater gap configuration was analysed, however, when the finite element results (Fig.3-8) are compared to the equivalent analytical results (Fig. 6-11), it can be seen that, in the incident wave direction, the correlation is quite poor. Based on these findings and also correspondence with Dr. Bettess (Bettess, 1983) the author concluded that there are certain deficiencies in the present program which explain the relatively poor results obtained for the fully reflecting breakwater case. This is a problem which the author intends to investigate.

In the investigation described in this thesis, the full potential of the "WAVE" program was not used since only pure diffraction problems

were considered. However, the accuracy with which the program modelled these relatively simple problems has increased the author's confidence in the program's ability to model more complex refraction - diffraction problems. The author has just completed supervising an experimental photogrammetric investigation of the combined refraction - diffraction of waves by a circular island on a parabolic shoal and hopes to model this configuration using the "WAVE" program.

7. GENERAL CONCLUSIONS

7.1 Breakwater Gap Wave Diffraction.

In this investigation every effort was made to achieve the most accurate experimental results possible. A novel photogrammetric wave height measurement technique coupled with the infinite basin technique was used to obtain accurate experimental wave height measurements. The author believes that the experimental results obtained are superior to those which could be obtained using conventional techniques.

The finite and infinite element program "WAVE" was installed on the UNIVAC and successfully used to model the experimental breakwater gap diffraction configurations. The correlation between the numerical (channel entrance case) and the analytical (fully reflecting breakwater case) results are very good, with the analytical solution predicting a slightly greater penetration of wave energy into the basin. These differences between the numerical and analytical results are consistent with the findings of Daemrich and Kohlhase (1978) shown in Fig. 2-9.

The differences between the experimental and the numerical results show certain trends namely :

1) experimentally there is found to be more energy in the shadow zones (in the lee of the breakwaters) than predicted numerically for the $B/L \geq 1$ breakwater gap configurations. The increased energy in the immediate lee of the breakwaters is thought to be due to the radiating second-order waves generated at the breakwater tips. The increased energy in the shadow zones > 2 L from the gap is thought to be due to wave orthogonal spreading near the gap centre line caused by wave steepness differences along the crests, resulting in subsequent wave orthogonal bunching and higher waves in the shadow zones;

2) experimentally it is found that the wave height attenuation, in the incident wave direction, occurs more rapidly than predicted numerically for the $B/L \geq 1,2$ breakwater gap configurations. This phenomenon is again thought to be due to wave orthogonal spreading near the gap centre line caused by wave steepness differences along the crests;

3) experimentally it is found that the wave height attenuation, in the incident wave direction, occurs less rapidly than predicted

numerically in the region 3-4 L from the entrance for the B/L $\leq$ 1 breakwater gap configurations. This was though to be due to the wave energy focusing effect that the breakwater tip phenomena (oscillatory vortices and radiating second-order waves) have on the primary waves entering the basin. Beyond this region trend 2) is again apparent.

The general conclusion is that the linear wave diffraction theory is on the whole conservative when compared with the experimental results, particularly in the regions outside the shadow zones. This tendency for the linear wave diffraction theory to be conservative in the region outside the shadow zones was particularly evident in the B/L $\geq$ 1,2 breakwater gap configurations. For the B/L $\leq$ 1 configurations the linear theory was not conservative outside the shadow zones in the regions 3-4 L from the gap. However, beyond this region it was again found to be on the whole conservative. For the B/L $\geq$ 1 configurations the linear wave theory was found not to be conservative for the regions within the shadow zones.

The author therefore concludes that the linear wave diffraction theory can be used, with confidence, to model general breakwater gap wave diffraction problems. In regions outside the shadow zones the linear theory will be conservative, except close to small gaps (B/L $\leq$ 1). Within the shadow zones the linear theory is not conservative, and one will have to allow for non-linear effects such as radiating second-order waves generated at the breakwater tips and increased wave orthogonal spreading near the gap centre line caused by wave steepness differences along the crests.

7.2 Laboratory Photogrammetric Wave Height Measurement.

This thesis describes the development of a laboratory photogrammetric wave height measurement technique which the author considers to be superior to conventional techniques for many experimental configurations. When the infinite basin technique is used this photogrammetric method is a particularly accurate tool for the experimental analysis of essentially infinite domain problems such as breakwater gap wave diffraction. It has been shown that the photogrammetric method based on the theory of projective transformations, and in which the stereopairs are analysed using a stereocomparator linked to a microcomputer, yields the most accurate results. This method is particularly powerful since the stereopairs can be taken with non-metric cameras. It has

been shown that with cameras positioned 5m above the water surface wave height measurement accuracies of better than 2 mm can be achieved.

An accurate photogrammetric method is now available for the measurement of monochromatic waves in laboratory basins. The author believes that this technique can be used to supplement or replace conventional techniques particularly for the experimental analysis of infinite domain problems. With further development, the photogrammetric technique could also be used to analyse experimental irregular wave configurations.

7.3 Finite and Infinite Elements.

The numerical results obtained have shown that the finite and infinite element program "WAVE" is ideally suited to the modelling of both the symmetrical and asymmetrical experimental breakwater gap configurations tested. It has been shown that the program can very accurately model the diffraction of water waves entering an infinite basin via a rectangular channel. However, it has also been shown that the program will have to be further refined before it can accurately model the diffraction of waves passing through a gap in a perfectly reflecting breakwater.

Channel entrance configurations (which are thought to closely approximate the diffraction of waves passing through a gap in a perfectly absorbing breakwater) can be accurately modelled using relatively coarse meshes, provided the number of elements per wavelength for any portion of the mesh is directly related to the wave height gradients for the corresponding region in the basin. It has been shown that the "WAVE" program can accurately model pure diffraction problems such as the experimental breakwater gap configurations tested.

The author believes that, provided the bed slopes are kept comparatively mild, the program will also accurately model combined refraction - diffraction problems.

REFERENCES

Abbott, M.B., Petersen, H.M. and Skovgaard, O.	1978	On the numerical modelling of short waves in shallow water. J. Hydraul.Res., Vol. 16, pp. 173-203.
Abbott, M.B., McCowan, A.D. and Warren, I.R.	1980	Numerical modelling of free surface flows that are two-dimensional in plan. Proc. Int.Symp. on Predictive Abilities of Surface Water Flow and Transport Models, Berkeley.
Adams, L.P.	1978a	The use of photogrammetry in the study of the sea. Proc. 6th Conf. South African Surveyors, 6 - 10 Feb. 1978.
Adams, L.P.	1978b	The use of non-metric cameras for very short range dental stereophotogrammetry. Photogrammetric Record, Vol. 9, No. 51, pp. 405-414.
Adams, L.P.	1979	An experiment with analytical shadow stereophotogrammetry. Photogram. Rec., Vol. 9, No. 51, pp. 835-847.
Adams, L.P.	1980	The use of short range stereophotogrammetry in the study of the morphology of the shoebill bill. Photogram.Rec., Vol.10, No. 55, pp. 73-84.
Adams, L.P.	1981	The use of non-metric cameras in short-range photogrammetry. Photogrammetria, Vol. 36, pp. 51-60.
Adams, L.P. and Pos, J.D.	1981	Model harbour wave form studies by short range photogrammetry. Photogram.Rec., Vol. 10, No. 58, pp. 457-470.
Adams, L.P. and Hurley, R.F.	1983	Maclear's grand parade baseline and St. George's Cathedral. South African Survey Journal, Vol. 19, Part 1, pp. 4-17.
Adams, L.P. and Pos, J.D.	1984	Wave height measurements in model harbours using close range photogrammetry. To be presented at the 15th Congress. Int.Soc. Photogrammetry and Remote Sensing. Rio de Janeiro, June 1984.
Aranha, J.A., Mei, C.C. and Yue, D.K.P.	1979	Some properties of a hybrid element method for water waves. Int.J.Num.Meth.Eng., Vol. 14, pp. 1627-1641.
Atkinson, K.B.	1969	Some recent developments in non-topographic photogrammetry. Photogram.Rec., Vol. 6, No. 34, pp. 357-378.

Atkinson, K.B.	1976	A review of close-range engineering photogrammetry. Photogrammetric Engineering and Remote Sensing, Vol. 42, No. 1, pp. 57-69.
Atkinson, K.B.(ed.)	1980	Developments in Close Range Photogrammetry -1. Applied Science Publishers, London.
Bai, K.J.	1972	A Variational Method in Potential Flows with a Free Surface. Ph.D., University of California, Berkeley.
Bai, K.J. and Yeung, R.W.	1974	Numerical solutions to free surface flow problems. Proc. 10th Symp.Naval Hyd., Cambridge, Mass., pp. 609-647.
Banaugh, R.P.	1962	The Scattering of Acoustic and Elastic Waves by Surfaces of Arbitrary Shape. Ph.D., University of California.
Barnard, B.J. and Pritchard, W.G.	1972	Cross-waves. Part 2. Experiments. J. Fluid Mechanics, Vol. 55, No.2, pp. 245-255.
Barsoum, R.S.	1976	On the use of isoparametric finite elements in linear fracture mechanics. Int. J.Num.Meth.Eng., Vol. 10, pp. 25-37.
Barsoum, R.S.	1977	Triangular quarter-point elements as elastic and perfectly-plastic crack tip elements. Int.J.Num.Meth.Eng., Vol. 11, pp. 85-98.
Battjes, J.A.	1968	Refraction of water waves. Proc.Am. Soc. Civ. Eng., Vol. 94, WW4, pp. 437-451.
Becker, E.B., Carey,G.F. and Oden, J.T.	1981	Finite Elements An Introduction. Vol. 1, Prentice-Hall,Inc., New Jersey.
Benjamin, T.B. and Feir, J.E.	1967	The disintegration of wave trains on deepwater. Part 1. Theory. J.Fluid Mechanics, Vol.27, Part 3, pp.417-430.
Berkhoff, J.C.W.	1972	Computation of combined refraction-diffraction. Proc. 13th Int. Conf. Coastal Eng., Vancouver, pp. 471-490.
Berkhoff, J.C.W.	1973	Refraction and Diffraction of Water Waves; Derivation and Method of Solution of the Two-Dimensional Refraction-Diffraction Equation. Report on mathematical investigation Delft Hyd.Lab., W154-1.

Berkhoff, J.C.W.	1974	Linear Wave Propagation Problems and the Finite Element Method. Delft Hyd.Lab., publication No. 124.
Berkhoff, J.C.W.	1975	Linear wave propagation problems and the finite element method. Finite Elements in Fluids, Vol. 1 (Eds. R.H. Gallagher et al), Wiley, London, pp. 251-264.
Berkhoff, J.C.W.	1976	Mathematical Models for Simple Harmonic Linear Water Waves, Wave Diffraction and Refraction. Delft Hyd.Lab., publication No. 163.
Bettess, P. and Bettess, J.A.	1976	Wave, a Finite Element Program for Solving the Wave Equation. Dept. Civ. Eng, Univ. College of Swansea, Wales, Computer Rep. No. 81.
Bettess, J.A.	1977	A data structure for finite element analysis. Int.J.Num.Met.Eng., Vol. 11, pp. 1779-1799.
Bettess, P.	1977	Infinite Elements. Int.J.Num.Meth.Eng., Vol. 11, pp. 53-64.
Bettess, P. and Zienkiewicz, O.C.	1977	Diffraction and refraction of surface waves using finite and infinite elements. Int.J. Num. Met. Eng., Vol. 11, pp. 1271-1290.
Bettess, P.	1983	Private communication.
Bettess, P., Liang, S.C. and Bettess, J.A.	1983	Diffraction of Waves by Semi-Infinite Breakwater using Finite and Infinite Elements. Dept.Civ.Eng., Univ.College of Swansea, Wales, Rep.No.C/R/437/83.
Biesel, F. and Suquet, F.	1954	Laboratory wave generating apparatus. English translation of a series of articles from 'La Houille Blanche', St Anthony Falls Hydraulic Laboratory, Univ. of Minnesota, Report 39.
Biesel, F.	1963	Radiating second-order phenomena in gravity waves. Int.Assoc. for Hydraulic Research, 10th Congress, London. Recent Research in Coastal Hydraulics, Vol.1, pp. 197-203.
Biesel, F.	1966	Les phénoménes du second ordre rayonnants dans les ondes de gravité. La Houille Blanche, No. 4, pp. 403-420.

Biesel, F.	1972	Refraction de la houle avec diffraction modérée. Proc. 13th Int. Conf. Coastal Eng., Vancouver.
Black, J.L.	1975	Wave forces on vertical axi-symmetric bodies. J.Fluid Mech., Vol. 67, pp. 369-376
Blue, F.L.	1948	Diffraction of Water Waves Passing Through a Breakwater Gap. Ph.D., Univ. of California, Berkeley.
Blue, F.L. and Johnson, J.W.	1949	Diffraction of water waves passing through a breakwater gap. Transactions, American Geophysical Union, Vol. 30, No.5, pp. 705-718.
Bopp, H. and Krauss, H.	1978a	An orientation and calibration method for non-topographic applications. Photogram. Eng., Vol. 44, No. 9, pp. 1191-1196.
Bopp, H. and Krauss, H.	1978b	Extension of the 11 parameter solution for on-the-job calibrations of non-metric cameras. International Archives of Photogrammetry, Vol. 22, No.5, pp. 7-12.
Boreel, J.	1974	Wave action on large off-shore structures. Proc.Conf. Off-Shore Structures, I.C.E., London, pp. 7-14.
Boussinesq, J.	1872	Théorie des ondes et des remous qui se propagent le long d'un canal rectangulaire horizontal, en communiquant au liquide contenu dans ce canal des vitesses sensiblement pareilles de la surface au fond. J.Math.Pures et Appl., 2nd series, Vol. 17, pp. 55-108.
Brebbia, C.A.	1978	Recent Advances in Boundary Element Methods. Pentech Press, London. 424 pages.
Buhr Hansen, J. and Svendsen, I.A.	1974	Laboratory generation of waves of constant form. Proc. 14th Int. Conf. Coastal Eng., Copenhagen, Denmark, pp. 321-339.
Camfield, F.E. and Street, R.L.	1969	Shoaling of solitary waves on small slopes. J. Waterways and Harbors Div.,ASCE, Vol. 95, pp. 1-22.
Camfield, F.E.	1983	Chief, Coastal Design Branch, Coastal Eng. Res. Cen., Virginia. Private Communication.
Carr, J.H. and Stelzriede, M.E.	1952	Diffraction of water waves by breakwaters. Ch.14, Gravity Waves, U.S. National Bureau of Standards, Circular No. 521, pp.109-125.
CERC	1977	Shore Protection Manual Vol. 1, U.S. Army Coastal Engineering Research Centre, Third Edition, 1977.

Chakrabarti, S.K.	1980	Laboratory generated waves and wave theories. Jour. of the Waterway, Port, Coastal and Ocean Division, Proc.ASCE, Vol. 106, No. WW3, pp. 349-368.
Chen, H.S. and Mei, C.C.	1974	Oscillations and wave forces in a man made harbour in the open sea. Proc.10th Naval Hyd. Symp.
Christiansen, P.L.	1974	Diffraction of gravity waves by large islands. Proc. 14th Int.Conf. Coastal Eng., Copenhagen, pp. 601-614.
Chung, T.J.	1978	Finite Element Analysis in Fluid Dynamics, McGraw-Hill, New York.
Cote, L.J. et al	1960	The directional spectrum of a wind generated sea as determined from data obtained from the stereo wave observation project. Meteorological Papers, Vol. 2, No. 6, College of Engineering, New York University, 88 pages.
Crow, E.L., Davis, F.A. and Maxfield, M.W.	1960	Statistics Manual. Dover Publications, Inc. New York.
Cruset, J.	1952	Photogrammetric measurement of the sea swell. Photogrammetria, pp. 122-125.
Daemrich, K-F.	1978	Diffraktion Gebeugter Wellen, Ein Beitrag zur Untersuchung der Wellenunruhe in Häfen. Mitteilungen des Franzius-Instituts für Wasserbau und Küsteningenieurwesen der Technischen Universität Hannover, Heft 47.
Daemrich, K-F., and Kohlhase, S.	1978	Influence of breakwater-reflection on diffraction. Proc. 16th Int.Conf. Coastal Eng., Hamburg, pp. 651-663.
Daugaard, E.	1972	Generation of Regular Waves in the Laboratory. Ph.D., Tech.Univ., Denmark.
Dean, R.G.	1965	Stream function representation of nonlinear ocean waves. Journal of Geophysical Research, Vol. 7, No. 18, pp. 4561-4572.
Dean, R.G.	1970	Relative validities of water wave theories. J. Waterways and Harbour Division, Proc. ASCE, Vol. 96, No. WW1, pp. 105-119.
Dickerson, L.A.	1950	Stereogrammetric wave measurement. The Bulletin of the Beach Erosion Board, Vol. 4, No. 4, pp. 40-45.

Döhler, M.	1965	Neues verfahren zur photographischen Aufnahme bewegter Flüssigkeitsoberflächen. Bildmessung und Luftbildwesen, Vol.33, No. 4, pp. 184-185.
Eatock-Taylor, R. and Dolla, J.P.	1980	Hydrodynamic loads on vertical bodies of revolution. Supp. Papers of R.I.N.A., Vol. 122, pp. 285-297.
Eatock-Taylor, R. and Zietsman, J.	1981a	A comparison of localized finite element formulations for two-dimensional wave diffraction and radiation problems. Int. J. Num. Meth.Eng., Vol. 17, pp.1355-1384.
Eatock-Taylor, R. and Zietsman, J.	1981b	Implementation of coupled formulations for hydrodynamic analysis in three dimensions. Numerical Methods for Coupled Problems, (Eds. Hinton, E., Bettess, P. and Lewis, R.W.) Pineridge Press, Swansea, pp. 281-290.
Eckart, C.	1952	The propagation of gravity waves from deep to shallow water. Gravity Waves, U.S. Natl. Bur.Std., Circ. No. 521.
Fairchild, J.C.	1970	Laboratory test of longshore transport. Proc. 12th Int.Conf. Coastal Eng., Washington, pp. 867-891.
Fan, S., Cumming, J.D. and Wiegel, R.L.	1967	Computer Solution of Wave Diffraction by Semi-Infinite Breakwater, Univ.California, Berkeley, Col. Eng., Tech.Rep.No. HEL-1-8.
Fan, S. and Borgman, L.E.	1970	Computer modelling of diffraction of wind waves. Proc. 12th Int.Conf. Coastal Eng., Washington, pp. 473-487.
Fenton, J.D.	1978	Wave forces on vertical bodies of revolution. J.Fluid Mech., Vol. 85, pp. 241-255.
Flick, R.E. and Guza, R.T.	1980	Paddle generated waves in laboratory channels. J.Waterway, Port, Coastal and Ocean Division, Proc. ASCE, Vol. 106, No. WW1, pp. 79-97.
Flokstra, C. and Berkhoff, J.C.W.	1977	Propagation of short waves over a circular shoal. Delft Hyd. Lab., Rep. W 154-V (in Dutch).
Fontanet, P.	1961	Théorie de la génération de la houle par un batteur plàn. La Houille Blanche, No. 1, 1961.
Galvin, C.J.	1972a	Finite-amplitude, shallow-water waves of periodically recurring form. Proc. Symp. on Long Waves, Newark, Delaware, 1972.

Galvin, C.J.	1972b	Waves breaking in shallow water. Waves on Beaches and Resulting Sediment Transport, Academic Press, New York, pp. 413-456.
Garabedian, P.	1964	Partial Differential Equations, Mc Graw-Hill, New York.
Garrett, C.J.R.	1970	On cross-waves. J.Fluid Mech., Vol. 41, part 4, pp. 837-849.
Garrison, C.J. and Seetharama Rao, V.	1971	Interaction of waves with submerged objects. J.Wat. Harb. Coastal Eng.Div., Proc. ASCE, Vol. 97, pp. 259-277.
Garrison, C.J.	1974	Hydrodynamics of large objects in the sea. Part 1 - Hydrodynamic analysis. J. Hydronautics, Vol. 8, pp. 5-12.
Garrison, C.J.	1978	Hydrodynamic loading of large offshore structures : three-dimensional source distribution methods. Ch. 3 of Numerical Methods in Offshore Engineering, (Eds. Zienkiewicz, O.C., Lewis, R. and Stagg, K.G.).
Goda, Y., Yoshimura, T. and Ito, M.	1971	Reflection and diffraction of water waves by an insular breakwater, Report of the Port and Harbour Research Institute, Vol. 10, No. 2, pp. 4-51.
Goda,Y . and Yoshimura, T.	1973	Discussion on wave diffraction by detached breakwater. J. Waterways, Harbours and Coastal Engineering Division, Proc.ASCE, Vol. 99, No.WW2, pp.285-288.
Goda, Y., Takayama, T. and Suzuki, Y.	1978	Diffraction diagrams for directional random waves. Proc. 16th Int.Conf. Coastal Eng., Hamburg, pp. 628-650.
Hales, L.Z.	1980	Erosion Control of Scour During Construction, Report 3, Experimental Measurements of Refraction, Diffraction, and Current Patterns Near Jetties, U.S. Army Eng. Waterways Exp. Stn, Tech.Rep. HL-80-3.
Hales, L.Z.	1981	Floating Breakwaters : State-of-the-Art Literature Review. U.S. Army Eng.Waterways Exp. Stn, Tech.Rep. No. 81-1.
Hara, H., Zienkiewicz, O.C. and Bettess, P.	1979	Application of Finite Elements to Determination of Wave Effects on Offshore Structures. Dept.Civ.Eng., Univ.College of Swansea, Wales, Rep.No. C/R/343/79.

Harms, V.W.	1976	Diffraction of Water Waves by Cylindrical Structures of Arbitrary Shape, University of California, Berkeley, Ph.D.
Harms, V.W.	1979a	Diffraction of water waves by isolated structures. J.Waterway Port Coastal and Ocean Div., Proc.ASCE, Vol. 105, No. WW2, pp. 131-147.
Harms, V.W.	1979b	Diffraction of waves by a shore-connected breakwater. J.Hyd.Div., Proc.ASCE, Vol. 105, No. HY12, pp. 1501-1519.
Hauguel, A.	1978	A combined FE-BIE method for water waves. Proc. 16th Int. Conf. Coastal Eng., Hamburg, pp. 715-721.
Hauguel, A.	1980	A numerical model of storm waves in shallow water. Proc. 17th Int. Conf. Coastal Eng., Sydney, pp. 746-762.
Hauguel, A. and Pechon, P.	1982	Applications of a numerical shallow water wave model. Proc. 18th Int.Conf. Coastal Eng., Cape Town.
Henshell, R.D. and Shaw, K.G.	1975	Crack tip finite elements are unnecessary. Int.J. Num. Meth. Eng., Vol. 9, pp. 495-507.
Hinton, E. and Owen, D.R.J.	1979	An Introduction to Finite Element Computations. Pineridge Press Ltd, Swansea.
Holthuijsen, L.H.	1979	Stereophotography of Ocean Waves. Delft Univ. of Technology, Department of Civil Engineering, Report No. 79-1.
Holthuijsen, L.H.	1983a	Observations of the directional distribution of ocean-wave energy in fetch limited conditions. J.Physical Oceanography, Vol. 13, No. 2, pp. 191-207.
Holthuijsen, L.H.	1983b	Stereophotography of ocean waves. Applied Ocean Research, Vol. 5, No. 4, pp. 204-209.
Homma, S.	1950	On the behavior of seismic sea waves around a circular island. Geophys. Mag., Vol. 21, Part 3, pp. 199-208.
Hotta, S.	1978	Wave height distribution around permeable breakwaters. Proc. 16th Int. Conf. on Coastal Eng., Hamburg, pp. 695-714.
Houston, J.R.	1976	Private communication with C.C. Mei. Details given in Mei (1978).

Houston, J.R.	1981	Combined refraction and diffraction of short waves using the finite element method. Applied Ocean Research, Vol. 3, No. 4, pp. 163-170.
Hwang, L. and Tuck, E.O.	1970	On the oscillations of harbours of arbitrary shape. J.Fluid Mech., Vol. 42, pp. 447-464.
Irons, B.M.	1970	A frontal solution program for finite element analysis. Int.J. Num. Meth. Eng., Vol. 2, pp. 5-32.
Irons, B.M. and Ahmad, S.	1980	Techniques of Finite Elements. Ellis Horwood Limited, Chichester.
Ito, Y. and Tanimoto, K.	1972	A method of numerical analysis of wave propagation - Application to wave diffraction and refraction. Proc. 13th Int. Conf. Coastal Eng., Vancouver, pp. 503-522.
Jaggi, M.	1975	Anwendung der Photogrammetrie bei Hydraulischen Modellversuchen. Mitteilung der Versuchsanstalt für Wasserbau, Hydrologie und Glaziologie, Eidgenössischen Technischen Hochschule, Zürich, Nr. 16 (95 pages).
Jahnke, E. and Emde, F.	1945	Tables of Functions with Formulae and Curves. New York.
John, F.	1950	On the motion of floating bodies - II. Commun. Pure Appl. Math., Vol. 3, pp. 45-101.
Johnson, J.W.	1952	Generalised wave diffraction diagrams. Proc. 2nd Int. Conf. Coastal Eng., Houston, Texas, pp. 6-23.
Johnson, J.W.	1953	Engineering aspects of diffraction and refraction, Trans. ASCE, Vol. 118, No. 2556, pp. 617-648.
Jonsson, I.G., Skovgaard, O. and Brink-Kjaer, O.	1976	Diffraction and refraction calculations for waves incident on an island. J. Marine Res., Vol. 34, No. 3, pp. 469-496.
Karara, H.M. and Abdel-Aziz, Y.I.	1974	Accuracy aspects of non-metric imageries. Photogrammetric Engineering, Vol. 40, No. 9, pp. 1107-1117.
Karara, H.M.	1976	Non-topographic photogrammetry, 1972-1976. Photogram.Eng. and Rem.Sen., Vol. 42, No. 1, pp. 37-45.

Karara, H.M. (ed.)	1979	Handbook of Non-Topographic Photogrammetry. American Society of Photogrammetry, Falls Church.
Keller, J.B.	1958	Surface waves on water of non-uniform depth. J.Fluid Mech., Vol. 4, pp. 607-614.
Keller, J.B.	1962	Geometrical theory of diffraction. J. Optical Soc.Am., Vol. 52, No. 2, pp. 116-130.
Klein, F.	1908	Elementary Mathematics from an Advanced Standpoint - Geometry. Translated from German 1939. Dover Publications Inc. USA.
Kölbl, O.R.	1976	Metric or non-metric cameras. Photogram. Eng. and Rem. Sen., Vol. 42, No. 1, pp. 103-113.
Lacombe, H.	1952	The diffraction of a swell. A practical approximate solution and its justification. Gravity Waves, U.S. Natl. Bur.Std., Circ. No. 521, pp. 129-140.
Larras, J.	1966	Diffraction de la houle par les obstacles rectilignes semi-indéfinis sous incidence oblique. Cahiers Océanographiques, Vol. 18, pp. 661-667.
Lautenbacher, C.C.	1970	Gravity wave refraction by islands. J. Fluid Mech., Vol. 41, part 3, pp.655-672.
Lee, J.J.	1971	Wave induced oscillations in harbours of arbitrary geometry. J.Fluid Mech., Vol. 45. Part 2, pp. 375-394.
LeMéhauté, B.	1976	An Introduction to Hydrodynamics and Water Waves, Springer-Verlag, New York.
Liu, P.L.-F.	1975	Scattering of water waves by a pair of semi-infinite barriers. J. Appl. Mech., Vol. 42, pp. 777-779.
Liu, P.L.-F. and Mei, C.C.	1976	Water motion on a beach in the presence of a breakwater, 1 Waves, 2 Mean currents. J. Geophys. Res., Vol. 81, No. 18, pp. 3079-3094.
Liu, P.L.-F., Lozano, C.J. and Pantazaras, N.	1979	An asymptotic theory of combined refraction and diffraction. Applied Ocean Res., Vol. 1, No. 3, pp. 137-146.
Liu, P.L.-F.	1982	Combined refraction and diffraction : Comparison between theory and experiments. J. Geophys.Res., Vol. 87, No. C8, pp. 5723-5730.

Lozano, C.J. and Meyer, R.	1976	Leakage and responses of water waves trapped by round islands. J.Phys. Fluids, Vol. 19, pp. 1075-1088.
Lozano, C.J. and Liu, P.L.-F.	1980	Refraction-diffraction model for linear surface water waves. J.Fluid Mech., Vol. 101, Part 4, pp. 705-720.
MacCamy, R.C. and Fuchs, R.A.	1952	Wave Forces on Piles : A Diffraction Theory. Inst. Eng. Res., Waves Investigation Lab., Berkeley, California, Series 3, Issue 334.
MacPhee, S.B.	1981	Aerial hydrography laser bathymetry and air photo interpretation techniques for obtaining inshore hydrography. Commission 4, FIG 16th Int. Congress, Montreux, Switzerland.
Madsen, O.S., Mei, C.C. and Savage, R.P.	1970	The evolution of time-periodic long waves of finite amplitude. J.Fluid Mech., Vol. 44, Part 1, pp. 195-208.
Madsen, O.S.	1971	On the generation of long waves. J.Geophys. Res., Vol. 76, No. 36, pp. 8672-8683.
Mahony, J.J.	1972	Cross-waves. Part 1. Theory. J. Fluid Mech., Vol. 55, Part 2, pp. 229-244.
Maresca, J.W. and Seibel, E.	1976	Terrestrial photogrammetric measurements of breaking waves and longshore currents in the nearshore zone. Proc. 15th Int. Conf. Coastal Eng., Honolulu, Hawaii, pp. 681-700.
Marks, W. and Ronne, F.C.	1955	Aerial stereo-photography and ocean waves. Photogram. Eng., Vol. 2, No. 1, pp. 107-110.
Mattioli, F.	1978	Wave-induced oscillations in harbours of variable depth. Computers and Fluids, Vol. 6, pp. 161-172.
Mattioli, F. and Tinti, S.	1980	Response of coastal harbours. Int.J. Num.Meth.Eng., Vol. 15, pp. 296-301.
Mattioli, F.	1981	Wave diffraction of breakwaters in the presence of a coastline. Applied Ocean. Res., Vol.3, No.1, pp. 37-42.
McClenan, C.M. and Harris, D.L.	1975	The Use of Aerial Photography in the Study of Wave Characteristics in the Coastal Zone. U.S. Army Corps of Engineers, Coastal Engineering Research Center, Technical Memorandum No.48, 72 pages.

McCowan, A.D. 1982 Numerical short wave modelling - an evaluation. Proc. 18th Int. Conf. Coastal Eng., Cape Town.

Mei, C.C. and Chen, H.S. 1975 Hybrid-element method for water waves, Proc. 2nd An.Symp. Waterways, Harbours and Coastal Eng. Div. ASCE, Symp. on Modelling Techniques, Vol. 1, pp.63-81.

Mei, C.C. 1978 Numerical methods in water-wave diffraction and radiation. Ann. Rev.Fluid Mech., Vol. 10, pp. 393-416.

Memos, C.D. 1976 Diffraction of Waves Through a Gap Between Two Inclined Breakwaters. Ph.D., Univ. London.

Memos, C.D. 1980a Discussion on paper Harms (1979b) J. Hydraulics Div., Proc. ASCE, Vol. 106, No. HY11, pp. 1949-1951.

Memos, C.D. 1980b An extended approach to wave scattering through a harbor entrance. Bull.PIANC, Vol. 1.

Memos, C.D. 1980c Water waves diffracted by two breakwaters. J. Hyd. Res., Vol. 18, No. 4, pp. 343-357.

Miche, M. 1951 The reflecting power of maritime works exposed to action of the waves. Annals des Ponts et Chaussées, June 1951. Partial translation by the Beach Erosion Board, Vol. 7, Bull. No. 2, April 1953.

Mikhail, E.M. and Ackermann, F.E. 1976 Observations and Least Squares. Harper and Row, New York.

Mitsui, H. and Murakami, H. 1967 Wellenhöhenverteilung an diskontinuierlichen Teilen von Küstenbauwerken. Kaigen Kôgagu Kôenkai, Vol. 14(in Japanese).

Mitsuyasa, H. et al 1975 Observation of the directional spectrum of ocean waves using a cloverleaf buoy. J. Geophys. Res., Vol. 5, No. 4, pp. 750-760.

Mobarek, I. 1962 Effect of Bottom Slope on Wave Diffraction. Univ. California, Berkeley, Tech.Rep. No. HEL-1-1.

Mobarek, I. and Wiegel, R.L. 1966 Diffraction of wind generated waves. Proc. 10th Int.Conf. Coastal Eng., Vol. 1. pp. 185-206.

Moffitt, F.H.	1968	Wave surface configuration. Photogram. Eng., Vol. 34, pp. 179-188.
Monahan, E.C.	1969	Fresh water whitecaps. J. Atmospheric Sciences, Vol. 26, No.5, pp. 1026-1029.
Morse, P.M. and Rubinstein, P.J.	1938	The diffraction of waves by ribbons and by slits. Physical Review, Vol. 54, Dec. 1938, pp. 895-898.
Oshima, T.	1976	Recent development of industrial photogrammetry in Japan. Photogram.Eng. and Rem.Sen., Vol. 42, No. 3, pp. 339-342.
Pantazaras, N.	1979	Combined Diffraction and Refraction of Water Waves. M.S. thesis, Dept of Environ. Eng., Cornell University, Ithaca.
Penney, W.G. and Price, A.T.	1944	Diffraction of sea waves by breakwaters. Directorate, Misc.Weapons Development Technical History 26, Artificial Harbours, Sec. 3D.
Penney, W.G. and Price, A.T.	1952	The diffraction theory of sea waves and the shelter afforded by breakwaters. Phil. Trans.Royal Soc. London, Vol. A224, pp. 236-253.
Pierson, W.J.	1951	The Interpretation of Crossed Orthogonals in Wave Refraction Phenomena, U.S. Army, B.E.B., Tech. Memo No. 21.
Pierson, W.J. and Marks, W.	1952	The power spectrum analysis of ocean wave records. Trans.Am.Geoph.Union, Vol. 33, No. 6.
Polcyn, F.C. and Sattinger, I.J.	1969	Water depth determinations using remote sensing techniques. Proc. 6th Int. Symposium on Remote Sensing of Environment, Vol. 2, pp. 1017-1028.
Polderman, A.H.	1976	Mapping of shipwrecks. Non-topographic photogrammetry at the survey department of Rijkswaterstaat. Presented papers of the 13th Int. Congress of Photogrammetry, Helsinki, Vol. 6, No. 541.
Pos, J.D.	1982a	Photogrammetric wave height measurements in model harbours. Proc. The Seminar on Photogrammetry and the Sea, University of Cape Town, 26 April 1982.
Pos, J.D.	1982b	Photogrammetric Wave Height Measurement in Model Harbours. A Detailed Laboratory Procedure. Notes for thesis students, Department of Civil Engineering, Univ.of Cape Town, South Africa, September 1982.

Pos, J.D.	1982c	Photogrammetric wave height measurements in model harbours using projective transformations. South African Survey Journal, Vol. 18, Part 6, pp. 15-22.
Pos, J.D. and Kilner, F.A.	1982	Laboratory photogrammetric wave height measurement. Proc. 18th Int. Conf. Coastal Eng., Cape Town, pp. 695-709.
Pos, J.D.	1983	Wave diffraction using finite and infinite elements. Proc.Finite Element Methods in South Africa 1983 Symposium, Cape Town, South Africa. Also published in Computer Methods in Applied Mechanics and Engineering, Vol. 41, No. 2, pp. 219-235.
Pos, J.D.	1984	Asymmetrical breakwater gap wave diffraction using finite and infinite elements. Proc. Finite Element Methods in South Africa 1984 Symposium, Pretoria, South Africa.
Putnam, J.A. and Arthur, R.S.	1948	Diffraction of water waves by breakwaters. Trans.Am. Geoph.Union, Vol. 29, No. 4, pp. 481-490.
Radder, A.C.	1979	On the parabolic equation method for water-wave propagation. J.Fluid Mech., Vol. 95, Part 1, pp. 159-176.
Raissi, H. and Wiegel, R.L.	1978	Wind generated wave diffraction by breakwater gap. Proc. 16th Int. Conf. Coastal Eng., Hamburg, pp. 609-627.
Rüther, H.	1982	Relative Orientation with Limited Control in Close Range Photogrammetry. Univ. of Cape Town, Ph.D.
Schönfeld, J.C.	1972	Propagation of Two-dimensional Short Waves, Manuscript (in Dutch), Delft Univ.Tech.
Schuler, M.	1933	Der Umschlag von Oberflächenwellen. Zeitschrift für Angew. Math. u. Mech., Vol. 13, p.443.
Schumacher, A.	1939	Stereophotogrammetrische Wellenaufnahmen. Wiss.Erg.Dtsch. Atlant. Exped. "Meteor" 1925/7,7, Heft 2, Lfg. 1, Berlin.
Schumacher, A.	1952	Results of exact wave measurements (by stereophotogrammetry) with special reference to more recent theoretical investigations. Gravity Waves, U.S.Natl. Bur.Std., Circ.No. 521, pp. 69-78.

Schwidefsky, K.	1970	Precision photogrammetry at close ranges with simple cameras. Photogrammetric Record, Vol. 6, No. 36, pp. 567-589.
Serre, F.	1953	Contribution à l'étude des écoulements permanents et variables dans les canaux. La Houille Blanche, pp. 374-388 and pp. 830-872.
Shaw, R.P.	1979	Boundary integral equation methods applied to wave problems. Ch.6 of Developments in Boundary Element Methods - 1 (Eds. Banerjee, P.K. and Butterfield, R.) Applied Science Publishers, London.
Silvester, R. and Lim, T.	1968	Application of wave diffraction data. Proc. 11th Int. Conf. Coastal Eng., London, Vol. 1, pp. 248-270.
Smith, R. and Sprinks, T.	1975	Scattering of surface waves by a conical island. J. Fluid Mech., Vol. 72, Part 2, pp. 373-384.
Sommerfeld, A.	1896	Mathematische Theorie der Diffraktion. Mathematische Annalen, Vol. 47, pp. 317-374.
Sommerfeld, A.	1949	Partial Differential Equations in Physics. Academic Press, New York.
Spens, P.	1954	Report on wave research. Cross waves. Tech. Memo. Admiralty Experimental Works, Haslar, England.
Stoker, J.J.	1957	Water Waves. Interscience Publishers Inc., New York.
Straub, L.G., Bowers, C.E. and Herbich, J.B.	1958	Laboratory Tests of Permeable Wave Absorbers. St. Anthony Falls Hydraulic Laboratory, Technical Paper No.18, Series A.
Szczechowski, B. and Mucha, A.	1980	The photogrammetric measurements of water ripples on hydrotechnic models. International Archives of Photogrammetry, Vol. 23, No. B5, pp. 724-731.
Takayama, T. and Kamiyama, Y.	1977	Diffraction of sea waves by rigid or cushion type breakwaters. Rep. Port and Harbour Res.Inst., Vol. 16, No. 3, pp. 3-37.
Thompson, E.H.	1954	Heights from parallax measurements. Photogram. Rec., Vol. 1, No. 4, pp. 38-49.

Thompson, E.H.	1957	The geometrical theory of the camera and its application in photogrammetry. Photogram.Rec., Vol. 2, No. 10, pp. 241-263.
Thompson, E.H.	1971a	Space resection without interior orientation. Photogram. Rec., Vol. 7, No.37, pp. 39-45.
Thompson, E.H.	1971b	The development of photogrammetry in the seventies. Photogram.Rec., Vol. 7, No. 38, pp. 195-200.
Thompson, E.H.	1975	Convergence. Photogram. Rec., Vol. 8, No. 45, pp. 330-332.
Thompson, E.H.	1977	A note on distortion. Photogram. Rec., Vol. 9, No. 49, pp. 93-99.
Torlegård, A.K.I.	1976	State-of-the-art of close-range photogrammetry. Photogram. Eng. and Rem. Sen., Vol. 42, No. 1, pp. 71-79.
Tsay, T.-K. and Liu, P.L.-F.	1982	Numerical solution of water-wave refraction and diffraction problems in the parabolic approximation. J.Geoph.Res., Vol. 87, No. C10, pp. 7932-7940.
Tsay, T.-K. and Liu, P.L.-F.	1983	A finite element model for wave refraction and diffraction. Applied Ocean Res., Vol. 5, No. 1, pp. 30-37.
Van Dorn, W.G.	1970	Tsunami response at Wake Island : a model study. J.Marine Res., Vol. 28, No.3, pp. 336-344.
Van Wijk, M.C. and Ziemann, H.	1976	The use of non-metric cameras in monitoring high speed processes. Photogram.Eng. and Rem. Sen., Vol. 42, No. 1, pp. 91-102.
Vastano, A.C. and Reid, R.O.	1967	Tsunami response for islands : Verification of a numerical procedure. J. Marine Res., Vol. 25, No. 2, pp. 129-139.
Vastano, A.C. and Reid, R.O.	1970	Tsunami response at Wake Island : Comparison of the hydraulic and numerical approaches. J. Marine Res., Vol. 28, No. 3. pp. 345-356.
Vastano, A.C. and Bernard, E.N.	1973	Transient long-wave response for a multiple-island system. J.Physical Oceanography, Vol. 3, No. 4, pp. 406-418.
Wang, S.	1974	Plunger-type wavemakers : theory and experiment. J. Hyd. Res., Vol. 12, pp. 357-388.

Wehausen, J.V. and Laitone, E.V.	1960	Surface waves. Encyclopedia of Physics, Vol. 9, pp. 446-778.
Welham, L.G.	1982	Underwater Stereometrology for Scientists and Engineers using Non-Metric Cameras. University of Cape Town, M.Sc.
Whalin, R.W.	1971	The Limit of Applicability of Linear Wave Refraction Theory in a Convergence Zone. U.S. Army Eng. Waterways Exp.Stn, Vicksburg, Res.Rep. H-71-3.
Wiegel, R.L.	1962	Diffraction of waves by a semi-infinite breakwater. J.Hyd.Div., ASCE, Vol. 88, Part HY1, pp. 27-44.
Wolf, P.R.	1974	Elements of Photogrammetry. McGraw-Hill, Inc., New York.
Yue, D.K.P., Chen, H.S. and Mei, C.C.	1978	A hybrid element method for diffraction of water waves by three-dimensional bodies. Int.J. Num. Meth. Eng., Vol. 12, pp. 245-266.
Zienkiewicz, O.C. and Newton, R.E.	1969	Coupled vibrations of a structure submerged in a compressible fluid. Proc. Symp. Finite Element Techniques, Institut für Statik und Dynamik der Luft- und Baum-fahrtkonstruktionen, Univ. Stuttgart.
Zienkiewicz, O.C. and Bettess, P.	1975	Infinite elements in the study of fluid-structure interaction problems. Proc. 2nd Int. Symp. Comp. Meth. Appl. Sci.and Eng., Versailles, pp. 133-172.
Zienkiewicz, O.C.	1977	The Finite Element Method. 3rd edition, McGraw-Hill, London.
Zienkiewicz, O.C., Kelly, D.W. and Bettess, P.	1977a	The Sommerfeld (radiation) condition on infinite domains and its modelling in numerical procedures. Proc. 3rd Int. Symp. Comp. Meth. Appl. Sci. and Eng., Versailles, pp. 169-203.
Zienkiewicz, O.C., Kelly, D.W. and Bettess, P.	1977b	The coupling of the finite element method and boundary solution procedures. Int. J. Num. Meth. Eng., Vol. 11, pp.355-375.
Zienkiewicz, O.C., Bettess, P. and Kelly, D.W.	1978	The finite element method for determining fluid loadings on rigid structures : Two- and three-dimensional formulations. Ch.4 of Numerical Methods in Offshore Engineering (Eds. Zienkiewicz, O.C., Lewis, R., and Stagg, K.G.) Wiley, London.

Zienkiewicz, O.C., Kelly, D.W. and Bettess, P. 1979 Marriage à la mode - The best of both worlds (finite elements and boundary integrals). Ch.5 of Energy Methods in Finite Element Analysis, (Eds. Glowinski, R., Rodin, E.Y. and Zienkiewicz, O.C.), Wiley, Chichester.

Zietsman, J.F.W. 1982 Localized Finite Element Formulations for Ocean Wave Diffraction and Radiation Problems. Ph.D., Univ. London.

APPENDIX 3A

APPENDIX TO CHAPTER THREE

3.A Program "WAVE" Call Chart and Description of Subroutines

3.A.1 Call Chart

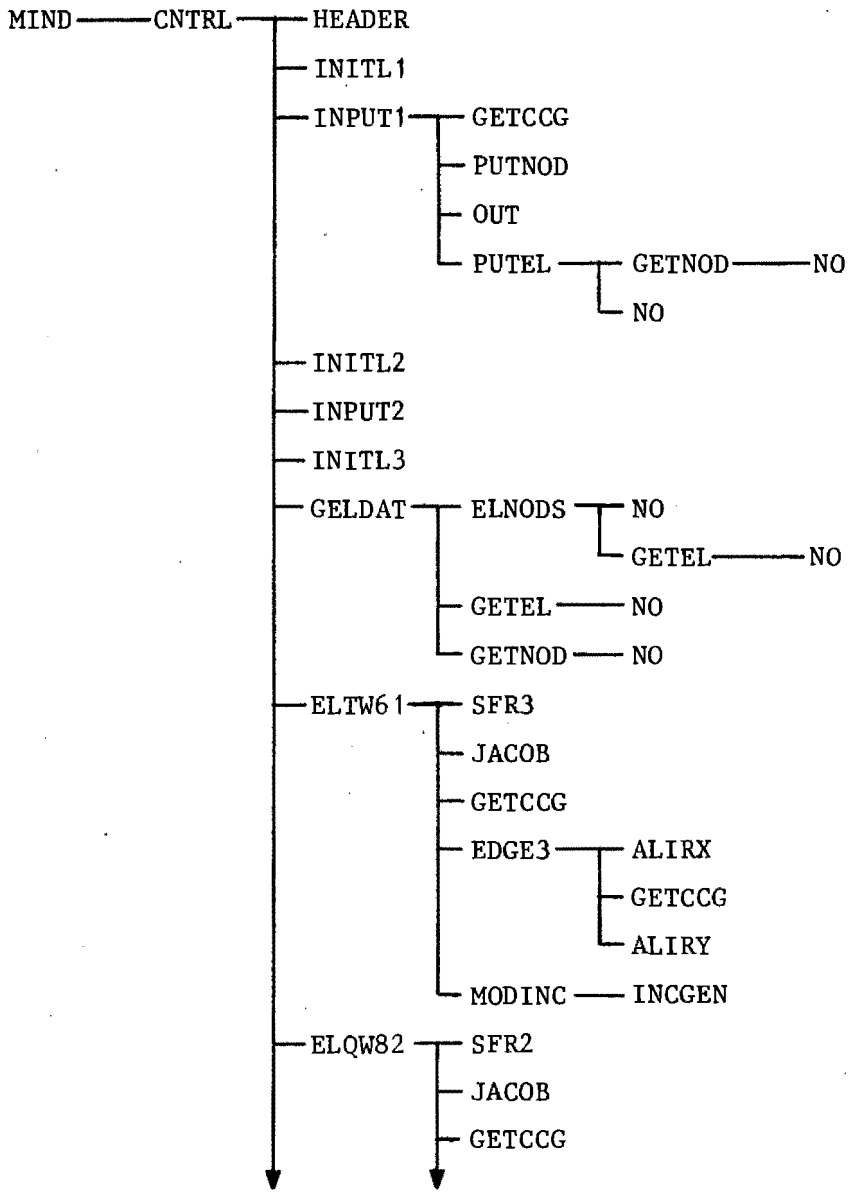

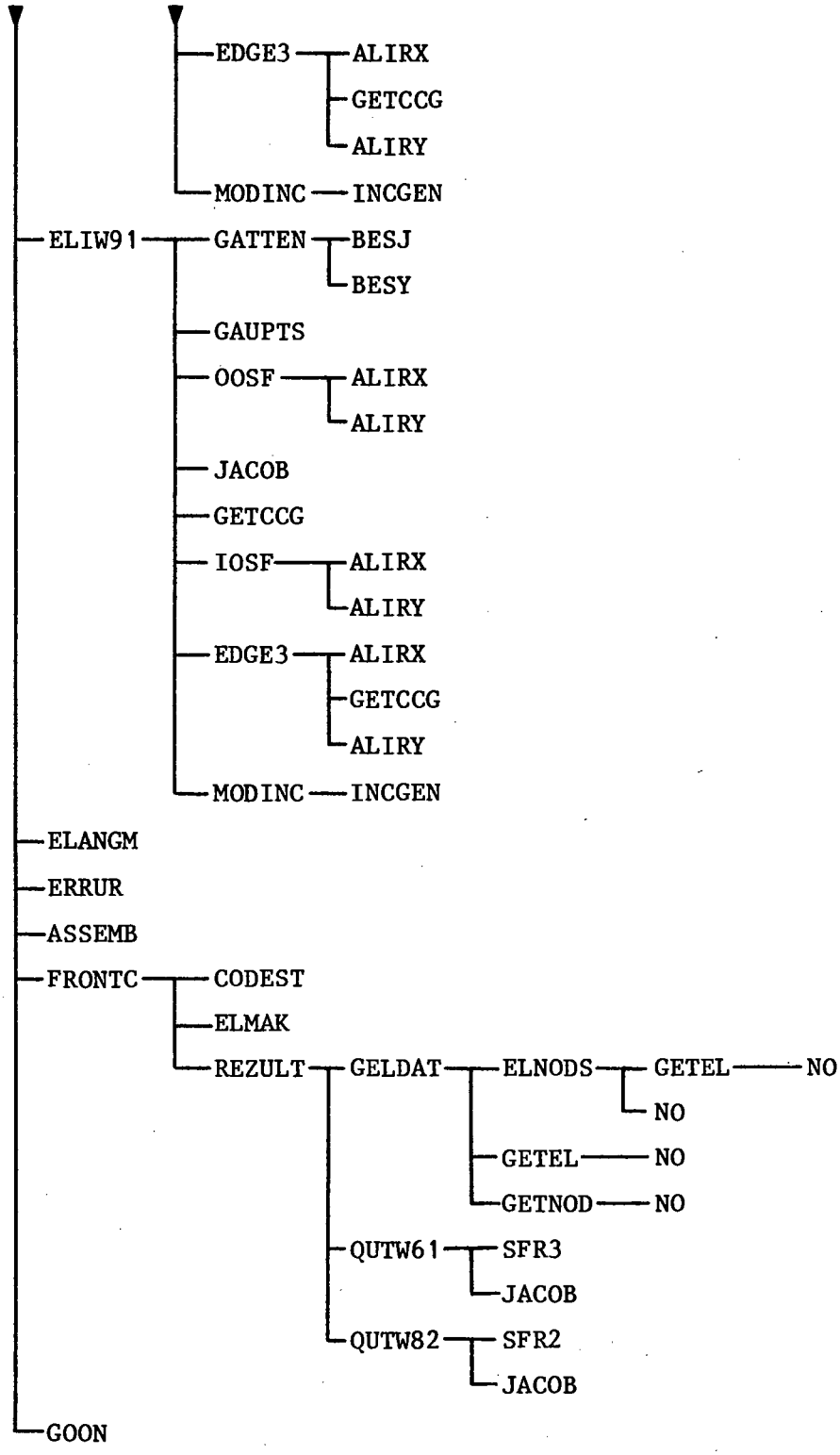
EDGE3
ALIRX
GETCCG
ALIRY
MODINC
INCGEN
ELIW91
GATTEN
BESJ
BESY
GAUPTS
OOSF
ALIRX
ALIRY
JACOB
GETCCG
IOSF
ALIRX
ALIRY
EDGE3
ALIRX
GETCCG
ALIRY
MODINC
INCGEN
ELANGM
ERRUR
ASSEMB
FRONTC
CODEST
ELMAK
REZULT
GELDAT
ELNODS
GETEL
NO
NO
GETEL
NO
GETNOD
NO
QUTW61
SFR3
JACOB
QUTW82
SFR2
JACOB
GOON

3.A.2 The "WAVE" Program Subroutines

ALEIR Calculates the infinite exponential harmonic shape function for the infite element.

ALIRX A Lagrange interpolation routine in the x (or ξ) direction.

ALIRY A Lagrange interpolation routine in the y (or $\bar{\eta}$) direction.

ASSEMB Writes element stiffness matrices and force vectors to disc.

BDATA Contains data such as Gauss-Legendre abscissae and weights, etc. Not called directly; must be included in the "Absolute" version of the Program.

BESJ Calculates Bessel functions of the first kind and order N i.e. $J_N(x)$.

BESY Calculates Bessel functions of the second kind and order N i.e. $Y_N(x)$.

CNTRL This subroutine controls the main flow of the program. It first prints the title and then carries out necessary initialisations and reads input data. For each element, the data is obtained and the element stiffness matrix formed and stored on disc. The Front-Solver solution routine is then called, and the velocity potentials are found for each node and stored. For all elements the nodal velocity potentials and elevations are then printed (see REZULT).

CODEST Used by FRONTC to code element numbers.

EDGE3 The subroutine evaluates the line integral terms on the edges of elements, which arise if the boundary of the element lies on the boundary in the mathematical model between total wave heights and radiated wave heights. The integral is given by the second term of equation (Ch. 3-18).

ELANGM Reads in an element matrix. Can be used to test new elements, worked out by hand, or by other programs, or to apply Lagrange multiplier or penalty functions constraints.

ELIW91 Given element coordinates and properties it forms an element matrix for a 9-noded infinite element. It uses Gauss abscissae and weights in the $\bar{\eta}$ direction and special abscissae and weights in the ξ or $\bar{s}$ direction.

ELMAK Used by FRONTC to read and write files from and to discs.

ELNODS Returns the nodes defining an element. Details in Bettess, J.A. (1977).

ELQW82 Given element coordinates and properties, it forms an element matrix for the 8-noded isoparametric quadrilateral finite element.

ELTW61 Given element coordinates and properties, it forms an element matrix for the 6-noded isoparametric triangle finite element.

ERRUR Prints out error number. Not fully implemented.

FRONTC The frontal solution program of B.M. Irons (Irons, 1970) adapted to the solution of equations with complex coefficients. See also Irons and Ahmad (1980), Chapter 13.

GATTEN Calculates an attenuation length L_d for the infinite element.

GAUPTS Sets up integration abscissae and weights for functions of the form given by equation (Ch. 3-12).

GELDAT Given an element number, GELDAT will retrieve all element information e.g. node numbers, options and the element geometry.

GETCCG Given angular frequency ω, g and depth d, this routine solves the wave number, k, the wave celerity c, and the group velocity, c_g.

GETEL Retrieves an element entry from the data structure. Details are given in Bettess, J.A. (1977).

GETNOD Retrieves a node entry from the data structure. Details are given in Bettess, J.A. (1977).

GOON Sets the variable ICONT to zero and prints it.

HEADER Prints the title.

INCGEN Given the coordinates of a point, and the direction of the incident wave and other information about it, this routine calculates the complex incident wave potential at that point.

INITL1 This routine does some preliminary initialisation; it reads in the no. of nodes and elements and reserves space for appropriate entries in the data structure.

INITL2 Sets up a few parameters needed by FRONTC. Details in Irons (1970).

INITL3 Rewinds disc channel 4.

INPUT1 This routine reads most of the problem data with the exception of that read by INITL1. It reads all the physical properties for the problem such as wave amplitude, frequency etc. It reads the nodal coordinates and element data and stores it all in the data structure.

INPUT2 Does nothing. Not fully implemented.

IOSF Exactly as for OOSF, except that XSF is now a complex, infinite, exponential, harmonic shape function, generated by ALEIR.

JACOB Forms the Jacobian matrix.

MIND The master control routine, it calls CNTRL. It contains all the data preparation instructions for the "WAVE" program.

MODINC As well as the line integral, arising from a change from radiated wave ϕ^R to total wave ϕ(see EDGE3), nodal values must be changed. This occurs along edges, and also at individual nodes, where only 1 node of an element touches this boundary. This routine prepares for the element the number of nodes to be changed, and the internal numbers of these nodes. Then the adjustments are made to the element load vector using values of ϕ^I computed by INCGEN.

NEWT(function) Function NEWT locates an element in the upper triangular half of a symmetrical matrix, stored by columns.

NO(function) A direct access disc file is mapped onto a fixed area of core in such a way that to the user it appears as if the amount of core available is as big as the disc file. The access is implemented by the function NO. Details are given in Bettess, J.A. (1977).

NODELS Returns the elements connected to a node. Details are given in Bettess, J.A. (1977).

OOSF Given the two ordinary Lagrange shape functions XSF and YSF, in the x and y (or ξ and $\bar{\eta}$) directions, this routine multiplies them together to give a 2-dimensional Lagrange interpolation shape function.

OUT This routine prints out the contents of the data structure when this data is needed for diagnostic purposes.

PUTEL Inserts an element entry into the data structure. Details are given in Bettess, J.A. (1977).

PUTNOD Inserts a node entry into the data structure. Details are given in Bettess, J.A. (1977).

QUQW82 Integrates absolute wave elevations and square of absolute wave elevations over an 8-noded quadrilateral element.

QUTW61 Integrates absolute wave elevations and square of absolute wave elevations over a triangular 6-noded element.

REZULT Prints out the complex and absolute values of the velocity potential and the wave elevation for all nodes in an element. It also prints out the same quantities for the original incident wave. It calculates the area of the element, the integral of absolute elevations over the element, and the square of the absolute elevations over the element area (using QUQW82 or QUTW61). It will also maintain up to 5 separate running totals of this quantity. The author added a facility to calculate the average diffraction coefficient K′ over an element. K′ is calculated by dividing the integral of the absolute amplitudes over the element by the product of the incident wave amplitude and the element area.

SFR2 Forms the shape function and derivatives for the 8-noded quadrilateral element.

SFR3 Forms the shape function and derivatives for the 6-noded triangular element.

APPENDIX 3B

APPENDIX TO CHAPTER THREE

Element Meshes used to Model the Experimental Breakwater Gap Diffraction Configurations.

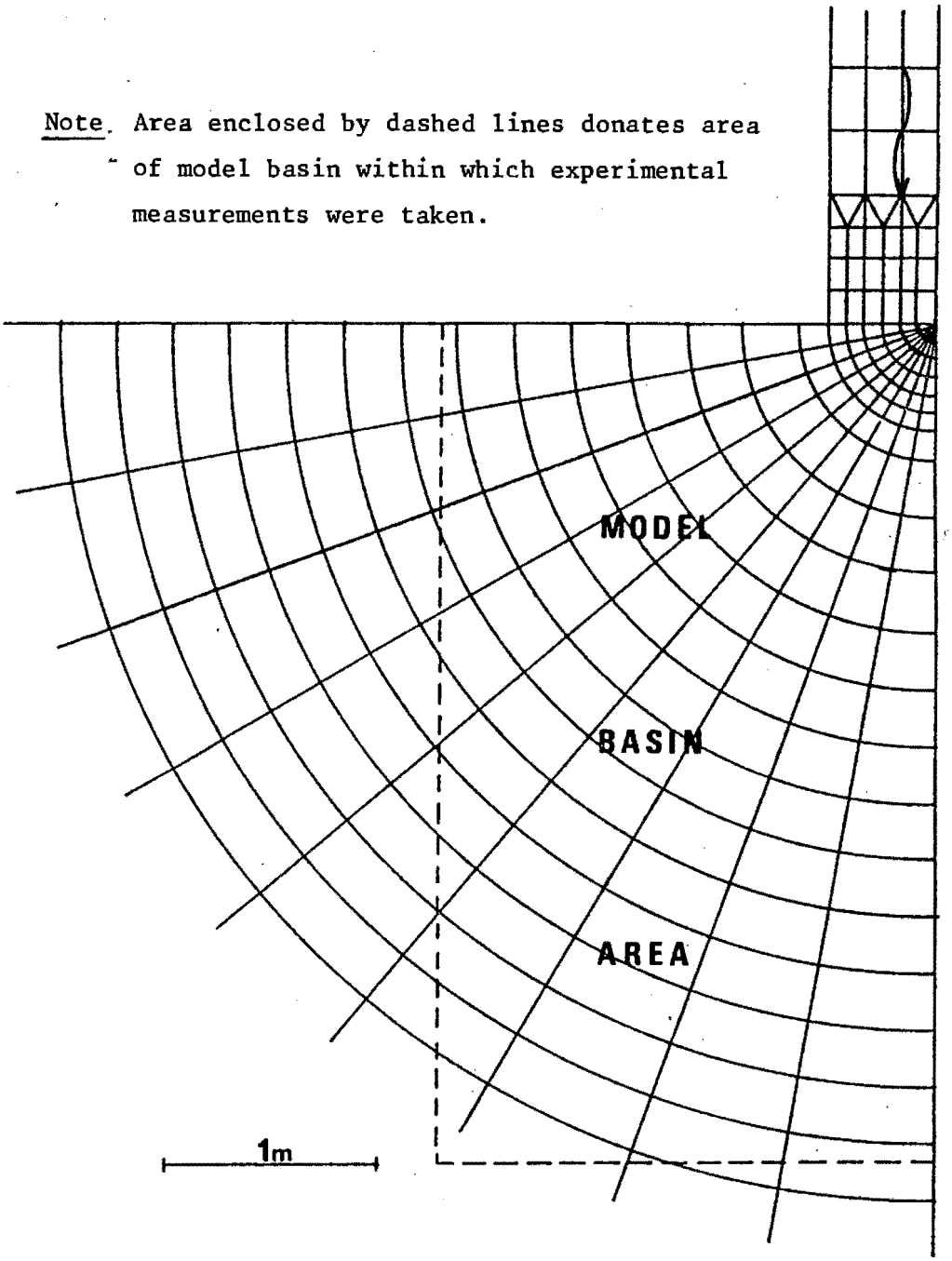

Fig. 3B-1 Element mesh for the B/L = 1,64 breakwater gap configuration.

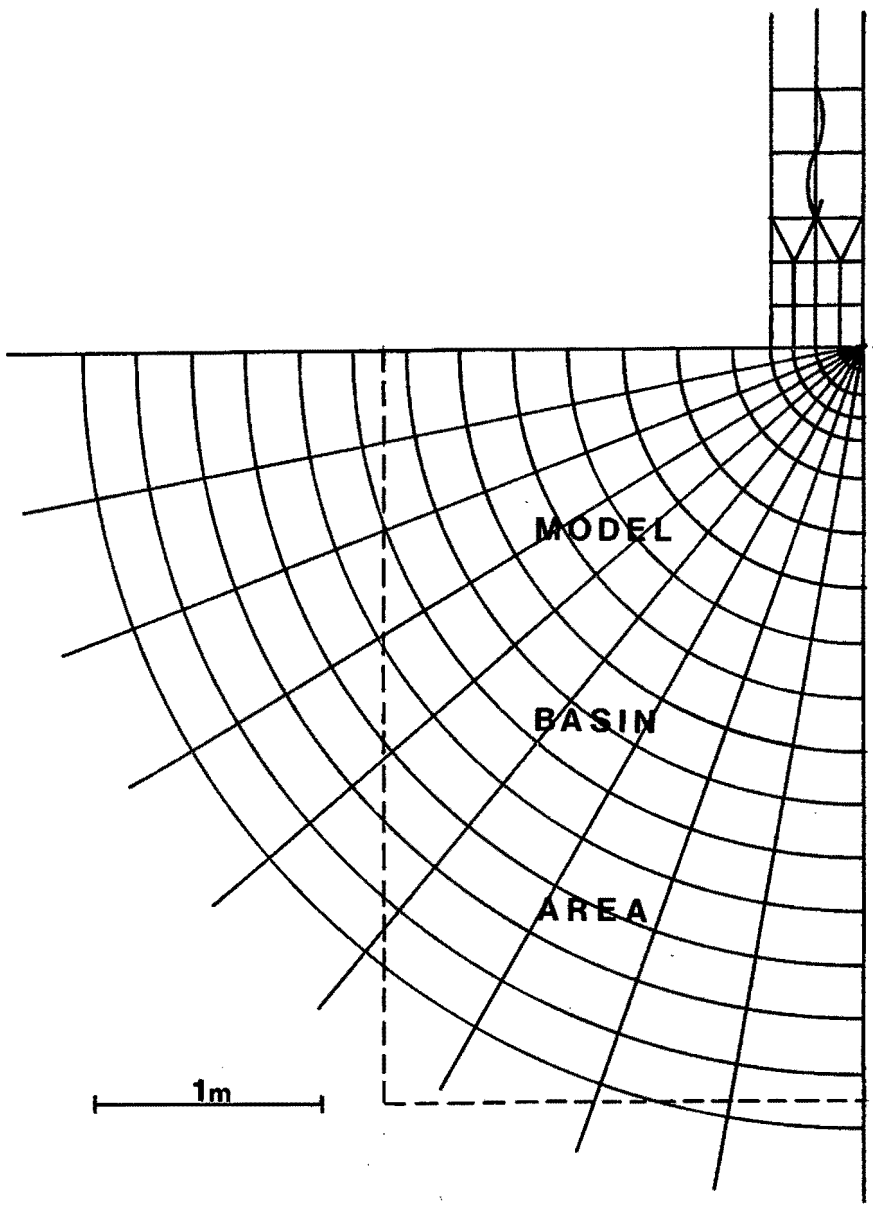

Fig. 3B-2 Element mesh for the B/L = 1,41 breakwater gap configuration.

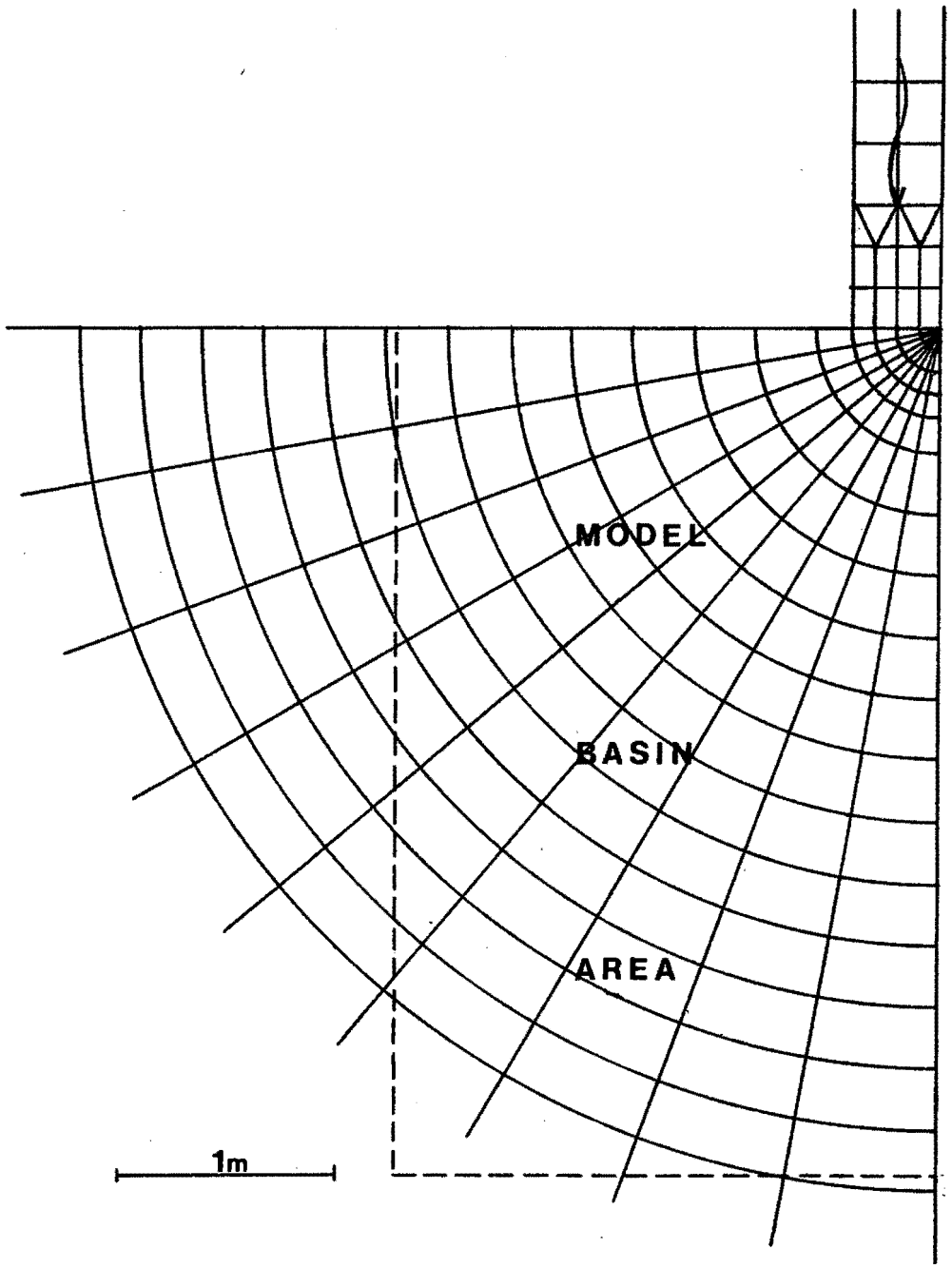

Fig. 3B-3 Element mesh for the B/L = 1,2 breakwater gap configuration.

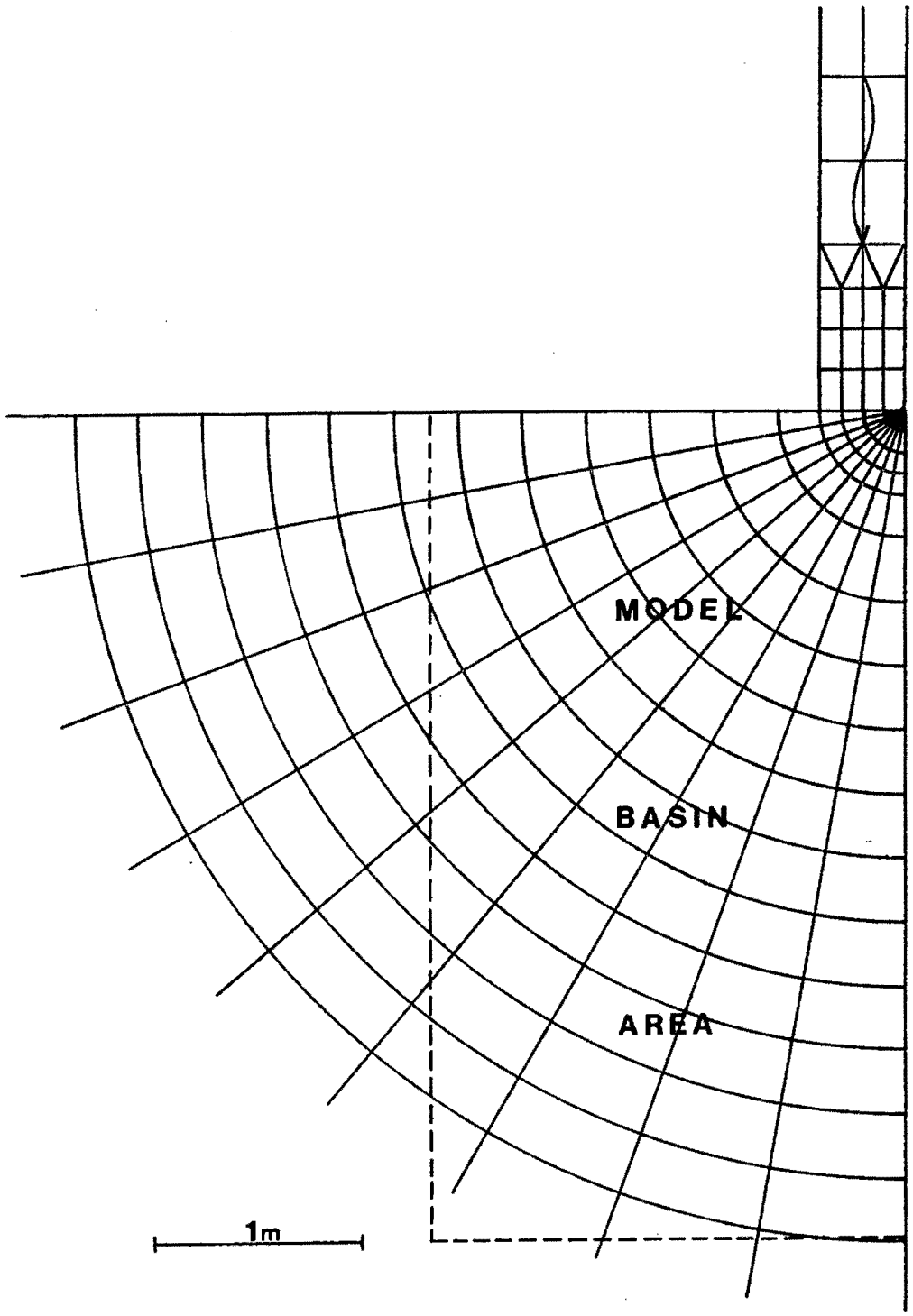

Fig. 3B-4 Element mesh for the B/L = 1 breakwater gap configuration.

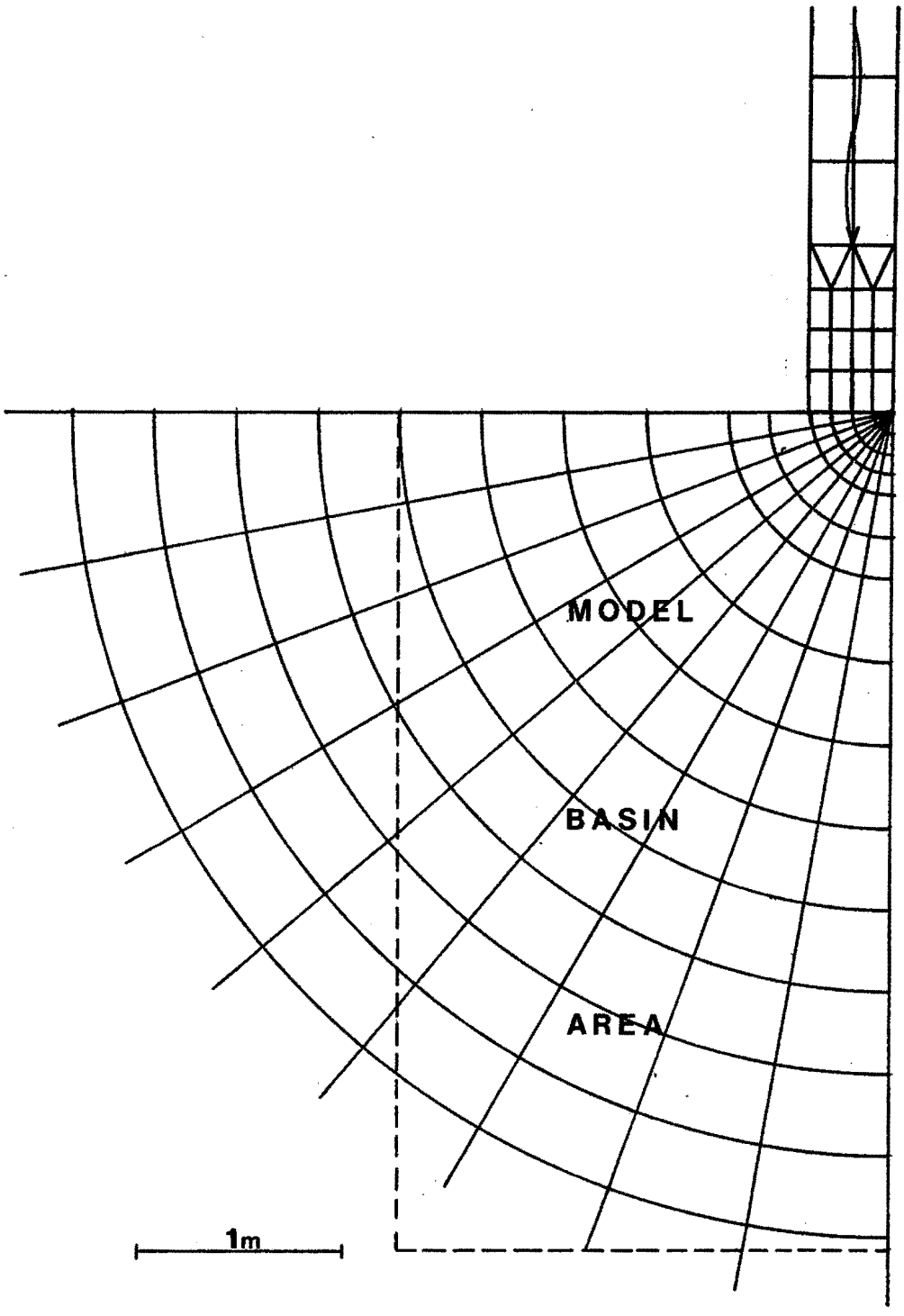

Fig. 3B-5 Element mesh for the B/L = 0,75 breakwater gap configuration.

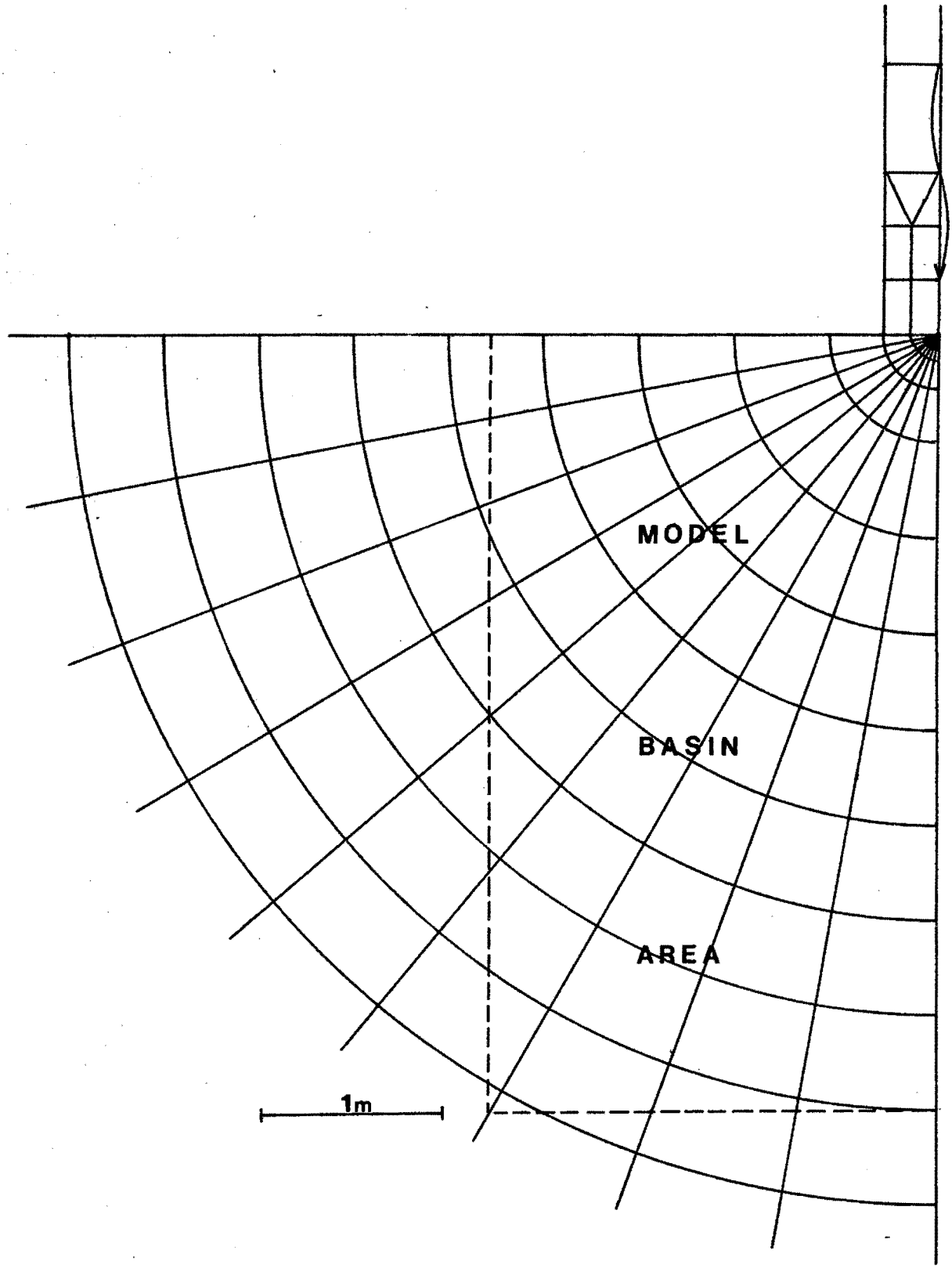

Fig. 3B-6 Element mesh for the B/L = 0,5 breakwater gap configuration.

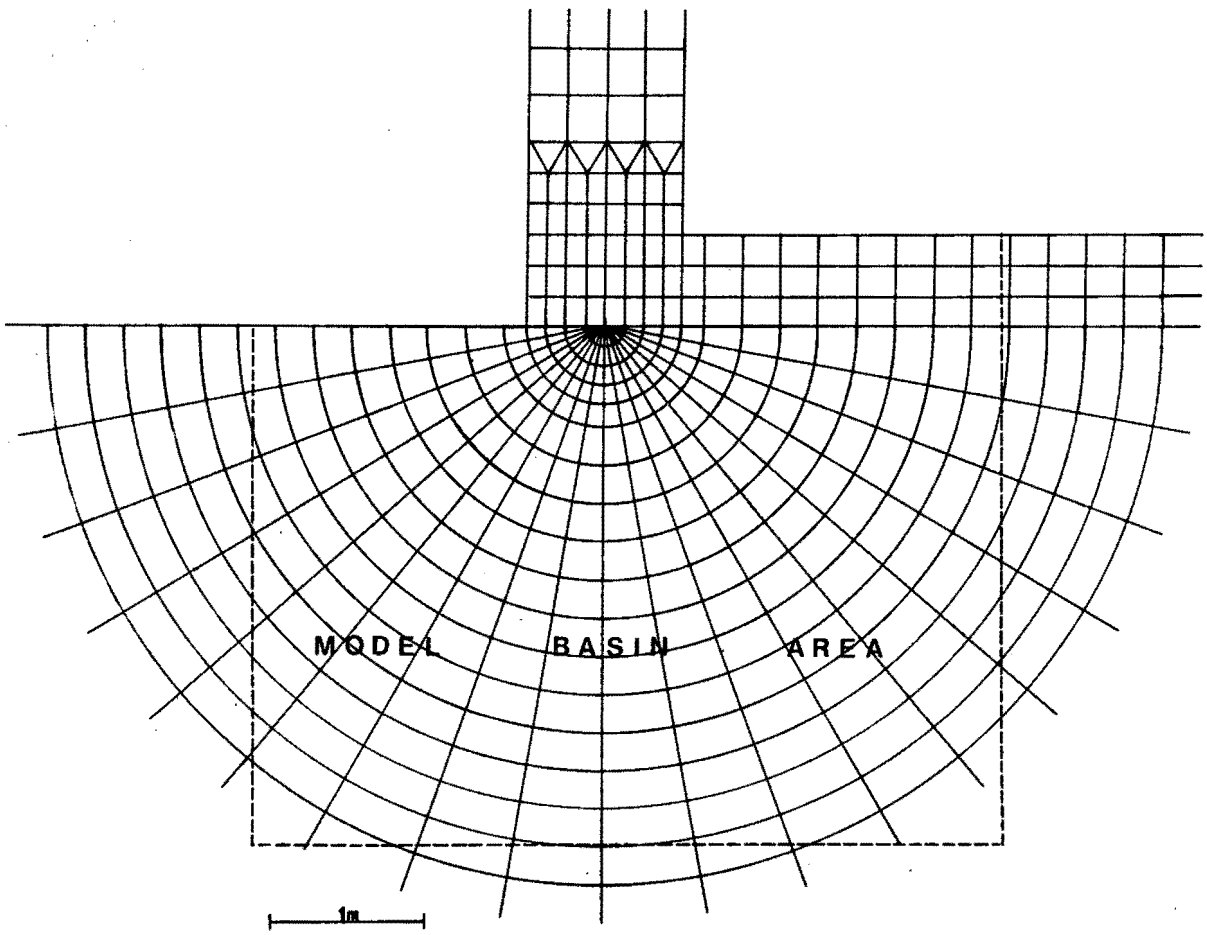

Fig. 3B-7 Element mesh for the B/L = 1,64 asymmetrical breakwater gap configuration.

APPENDIX 4A

APPENDIX TO CHAPTER FOUR

PROGRAM "TESTFIELD" FLOW CHART

Macro Flow Chart

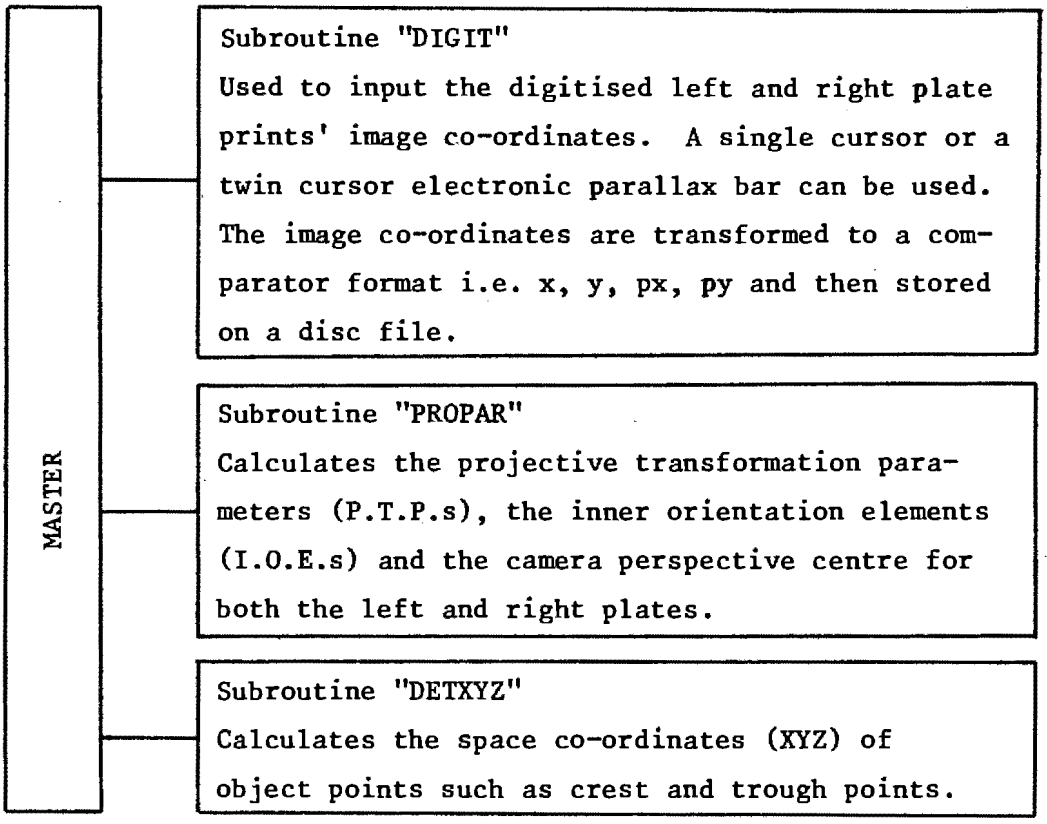

For Subroutines "PROPAR" and "DETXYZ", it is assumed that the image co-ordinates are in a comparator format on a disc file. If a stereopair is analysed using the digitiser tablet, then the image co-ordinates are transfered to a disc file using Subroutine "DIGIT" of Program "TESTFIELD". If the stereopair is to be analysed using the stereocomparator, the image co-ordinates are transfered to a disc file using Programs "EDIT" and "INPUT" (see Section 5.5.2). Flow charts for Subroutines "PROPAR" and "DETXYZ" are now given. The equations referred to are given in Chapter 4.

Subroutine "PROPAR" Flow Chart

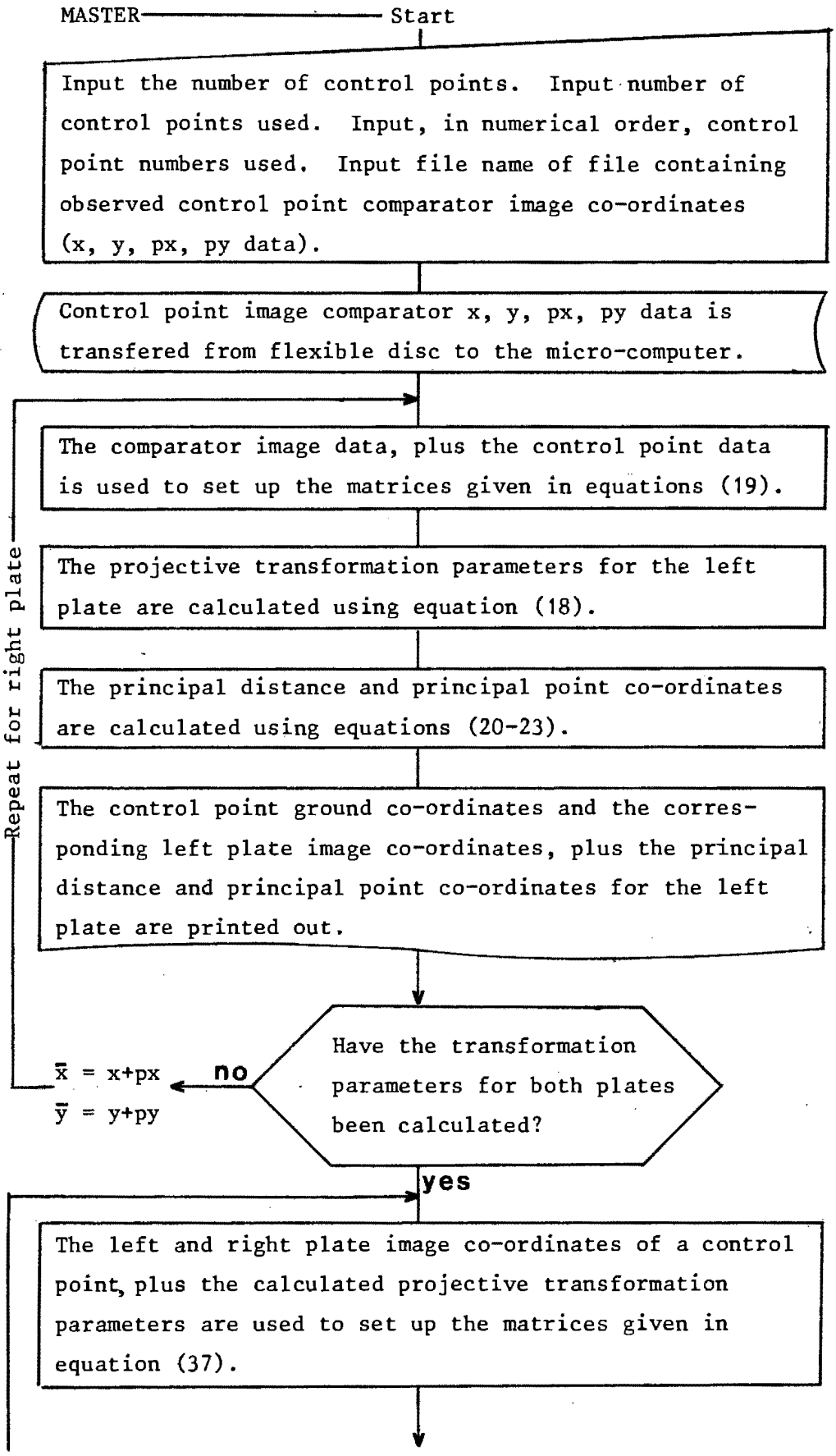

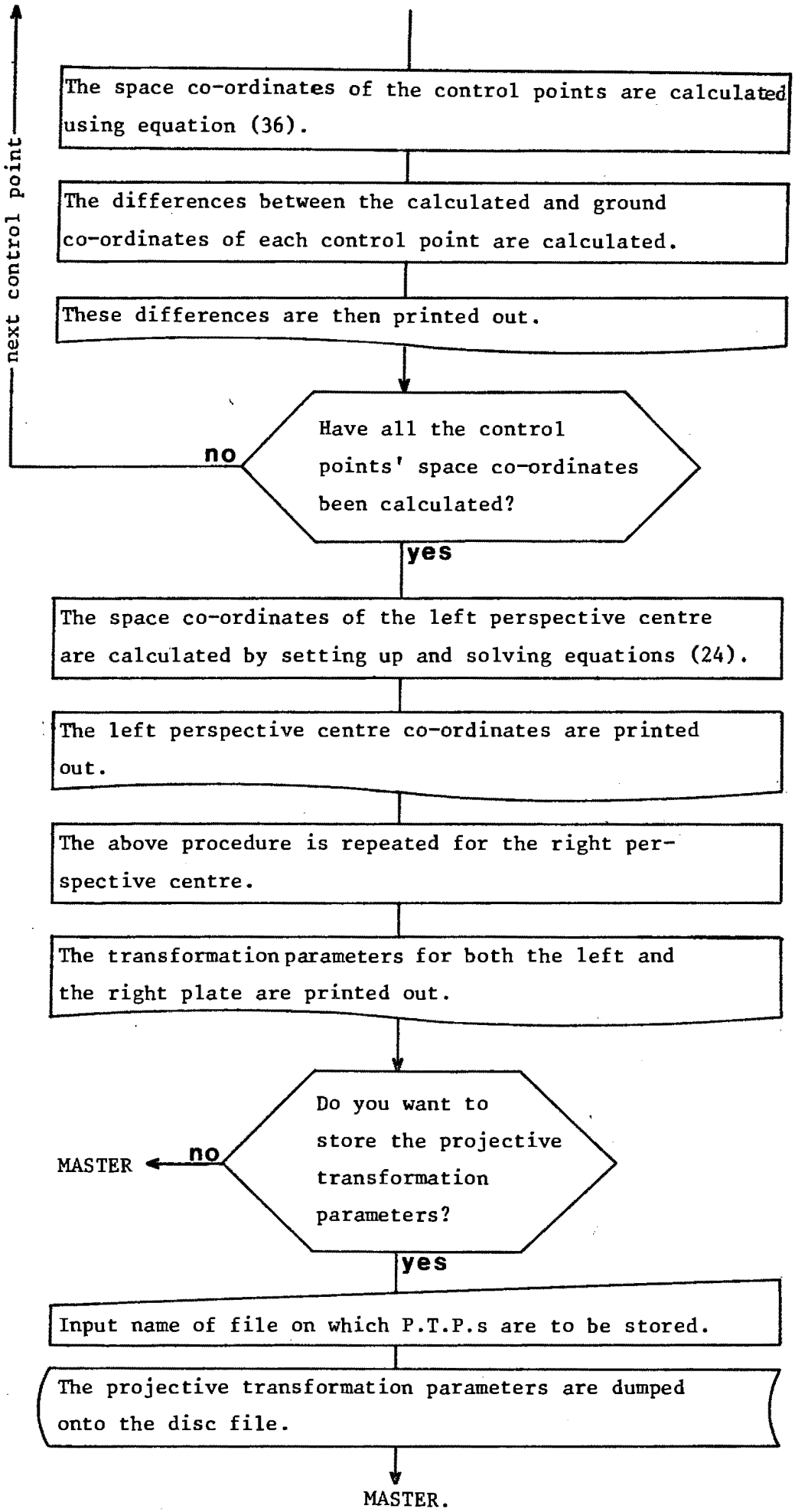
The space co-ordinates of the control points are calculated using equation (36).
The differences between the calculated and ground co-ordinates of each control point are calculated.
These differences are then printed out.
next control point
Have all the control points' space co-ordinates been calculated?
no
yes
The space co-ordinates of the left perspective centre are calculated by setting up and solving equations (24).
The left perspective centre co-ordinates are printed out.
The above procedure is repeated for the right perspective centre.
The transformation parameters for both the left and the right plate are printed out.
Do you want to store the projective transformation parameters?
MASTER
no
yes
Input name of file on which P.T.P.s are to be stored.
The projective transformation parameters are dumped onto the disc file.
MASTER.

Subroutine "DETXYZ" Flow Chart

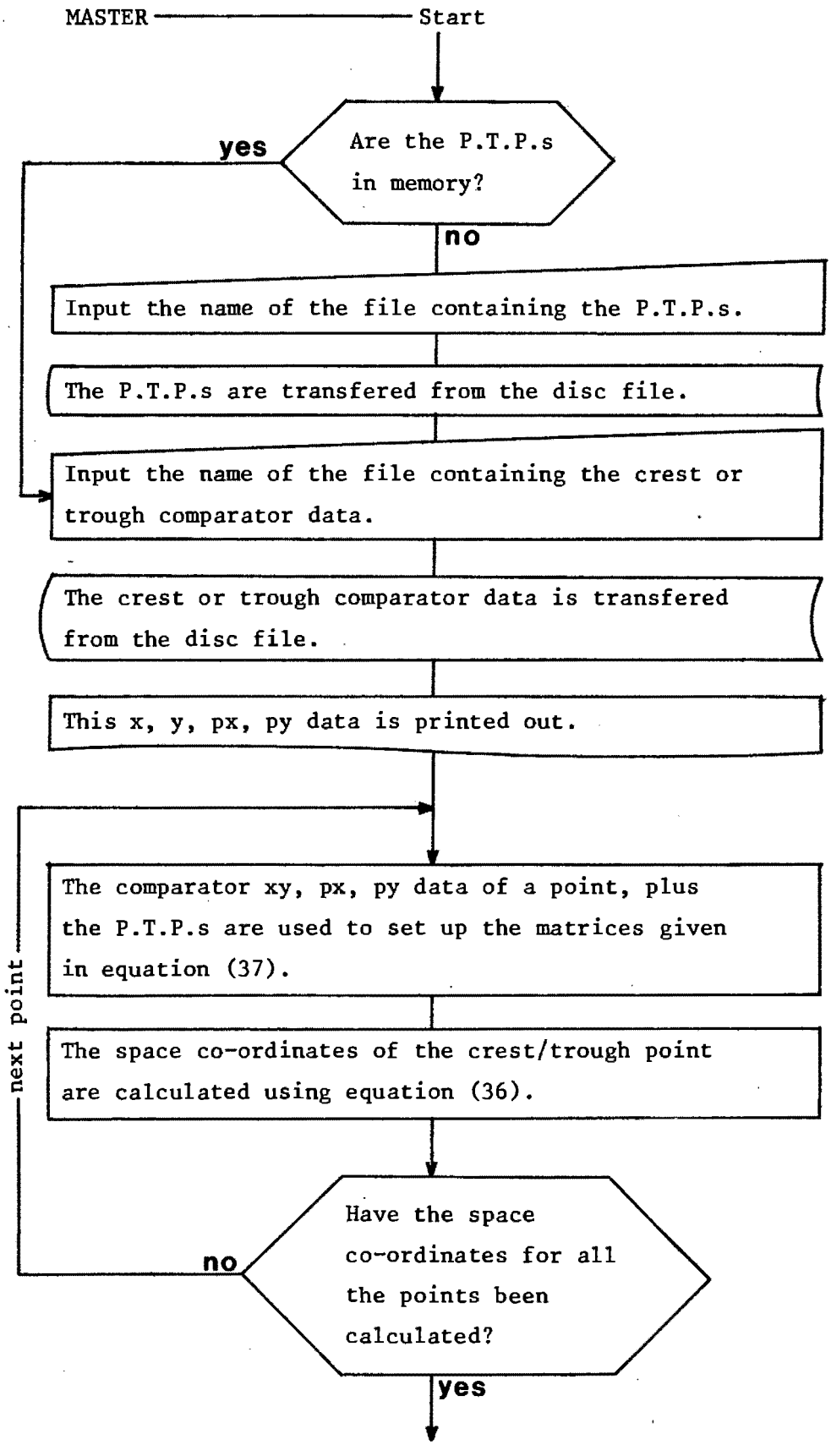

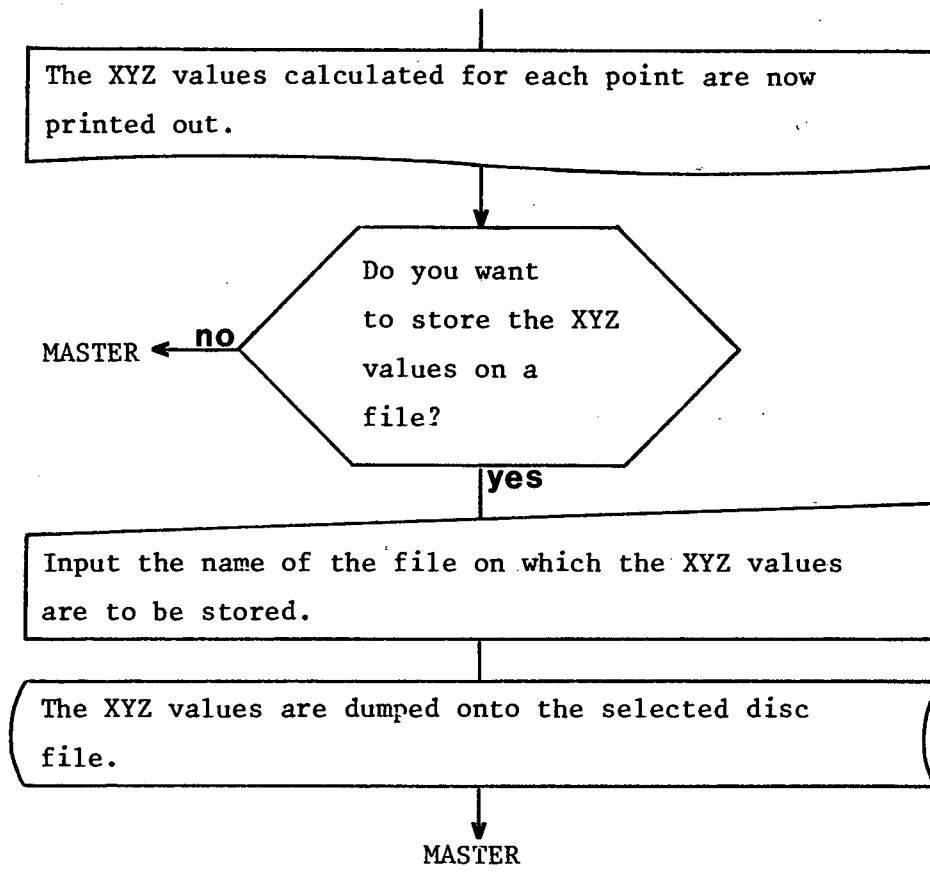
The XYZ values calculated for each point are now printed out.
Do you want to store the XYZ values on a file?
no
MASTER
yes
Input the name of the file on which the XYZ values are to be stored.
The XYZ values are dumped onto the selected disc file.
MASTER

APPENDIX 4B

APPENDIX TO CHAPTER FOUR

PROGRAM TO "WAVEHEIGHT" FLOW CHART

Macro Flow Chart

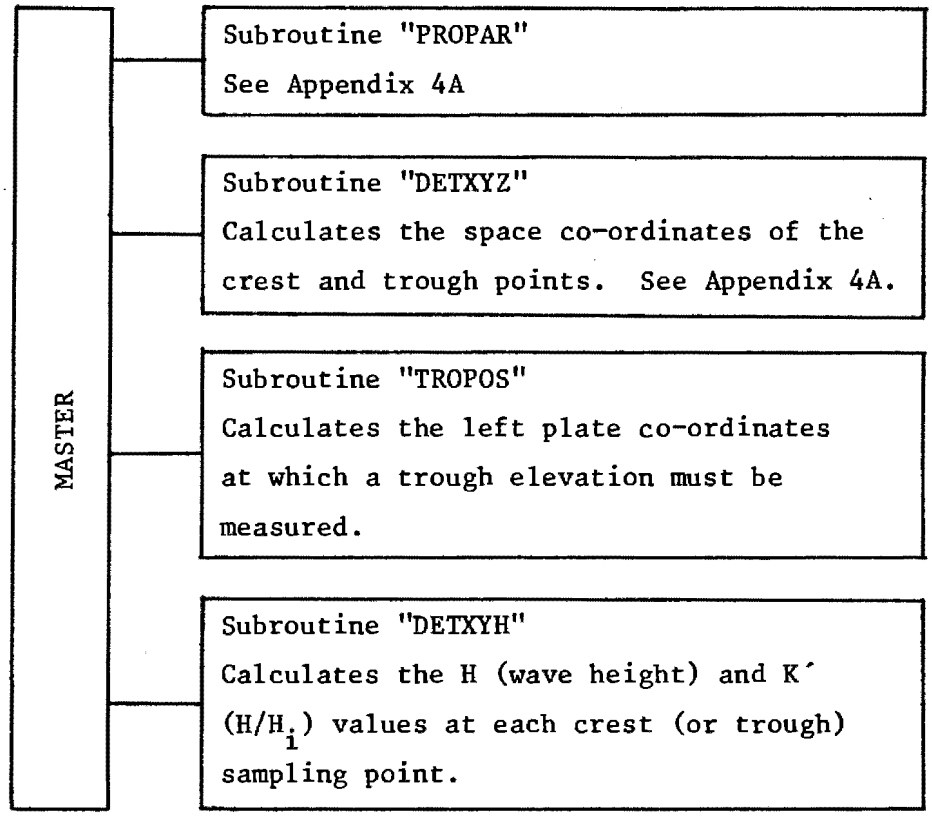

Flow charts for Subroutines "TROPOS" and "DETXYH" are now given. The equations referred to are given in Chapter 4.

Subroutine "TROPOS" Flow Chart

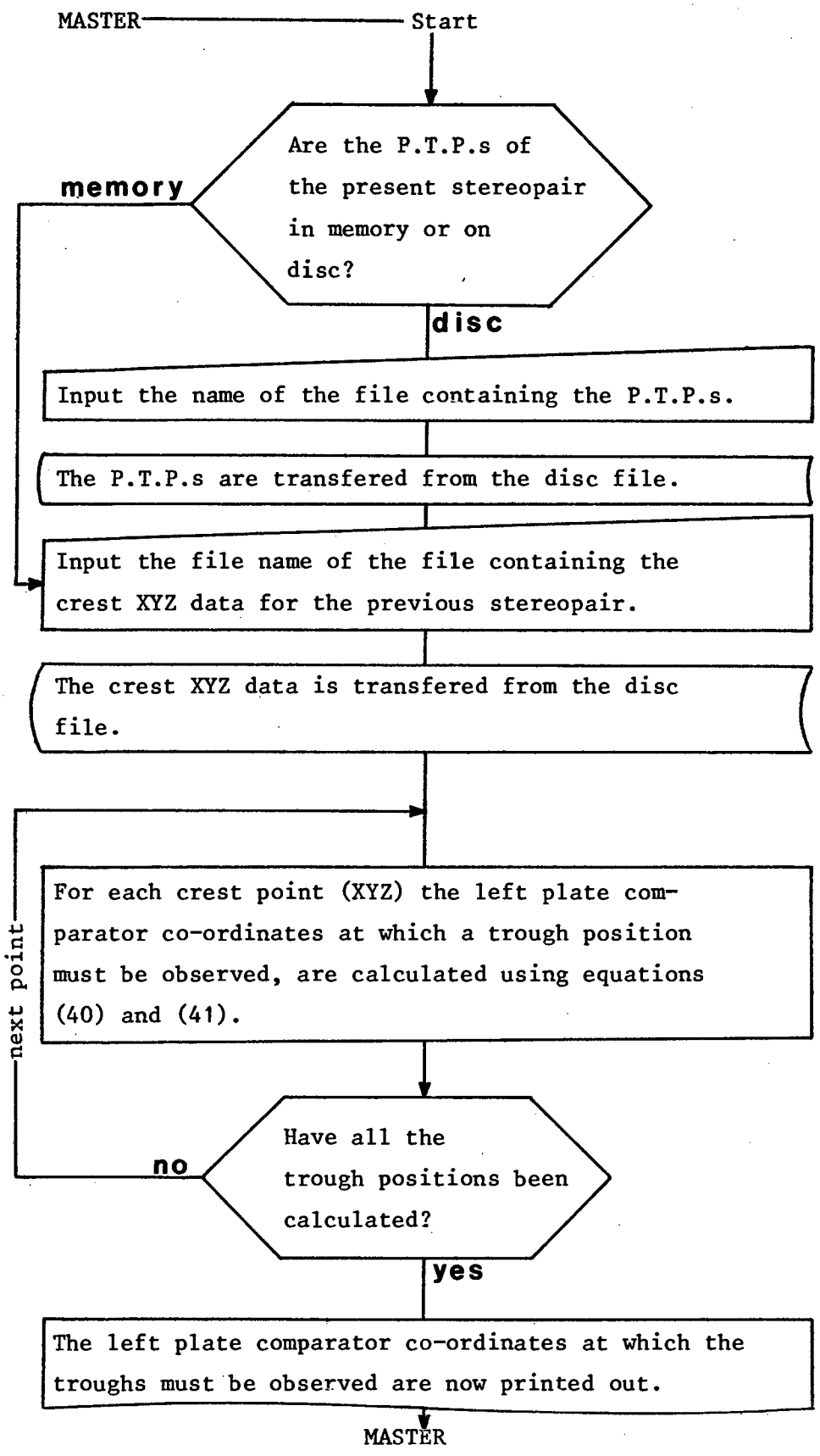

NOTE: These values must be manually corrected where necessary, using equations (44) as described in Section 4.8.5.4.

Subroutine "DETXYH" Flow Chart.

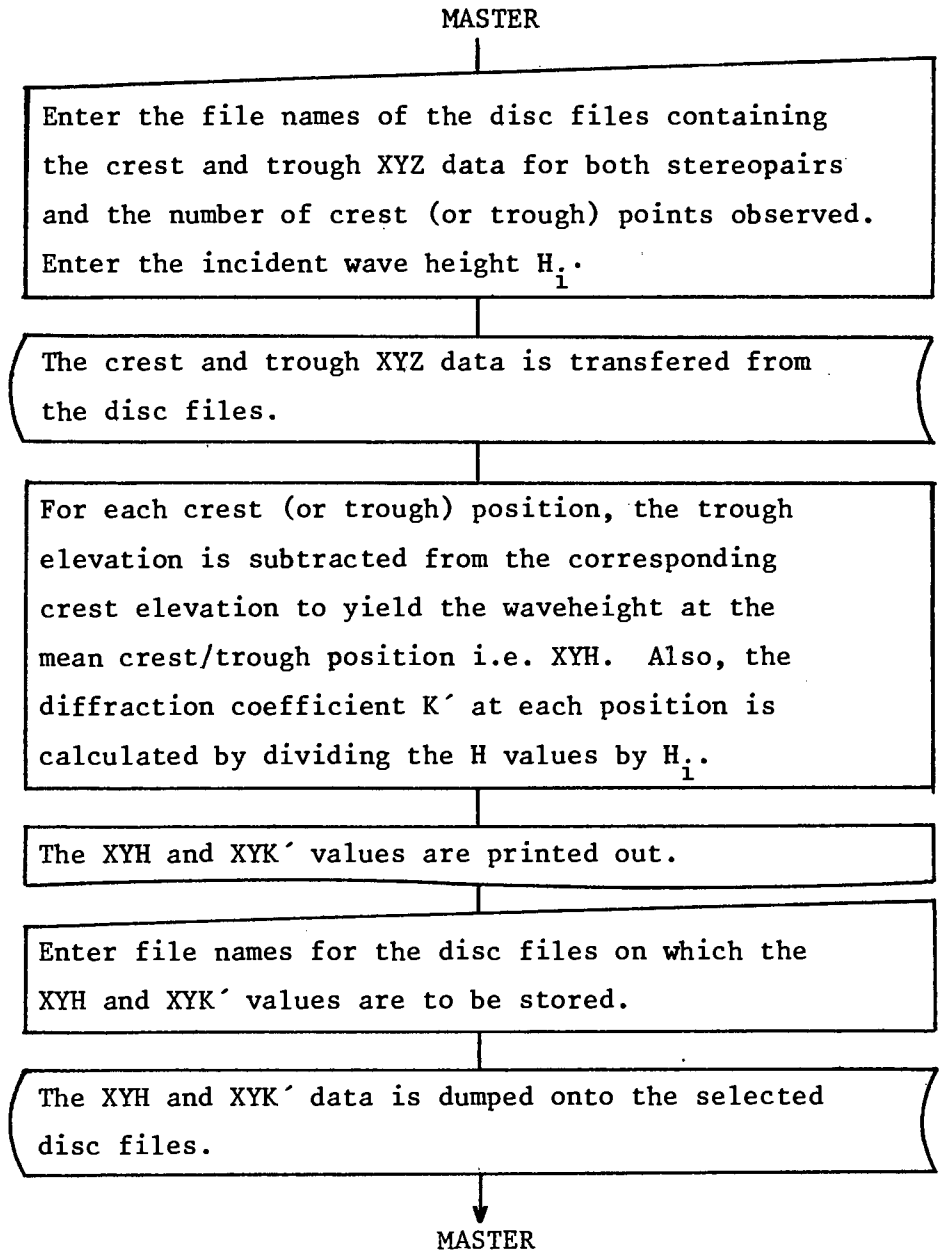

APPENDIX 4C

APPENDIX TO CHAPTER FOUR

PROGRAM "PARA" FLOW CHART

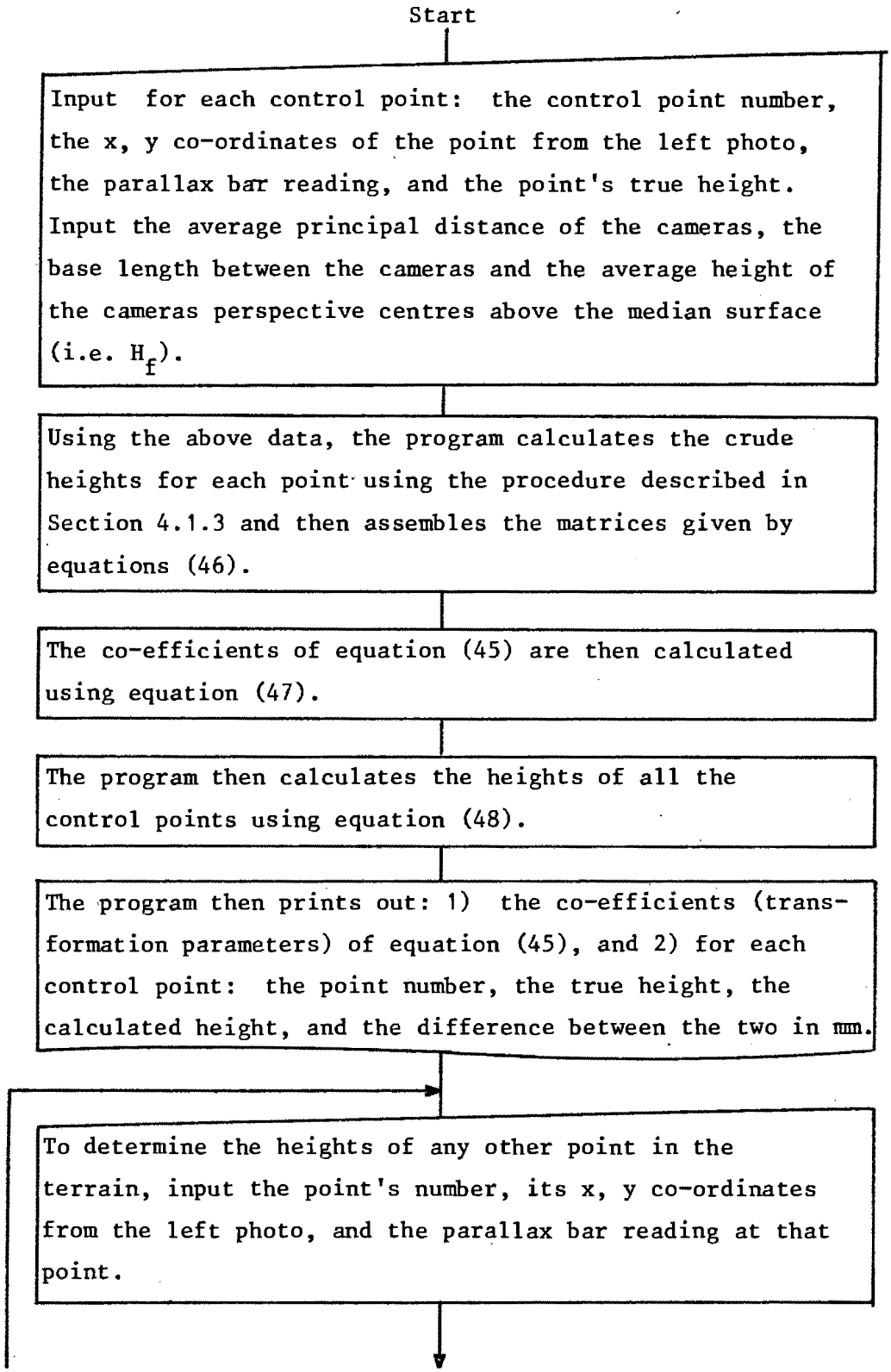

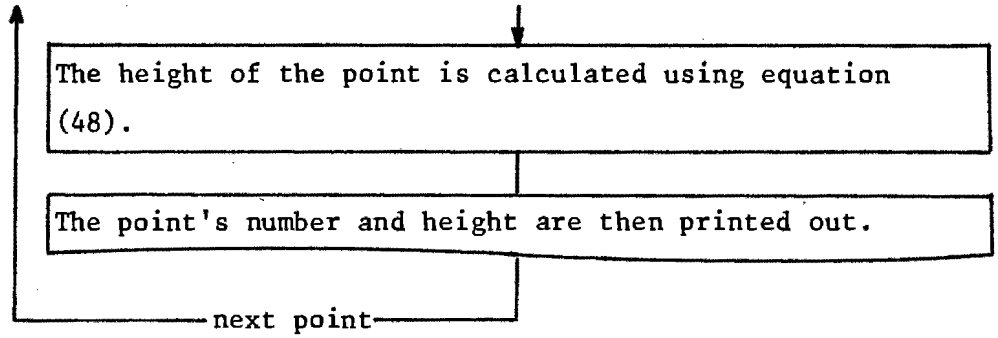

"BREAK" to end.

Note The equations refered to are given in Chapter 4.

APPENDIX 4D

APPENDIX TO CHAPTER FOUR

PROGRAM "PARAMOD" FLOW CHART

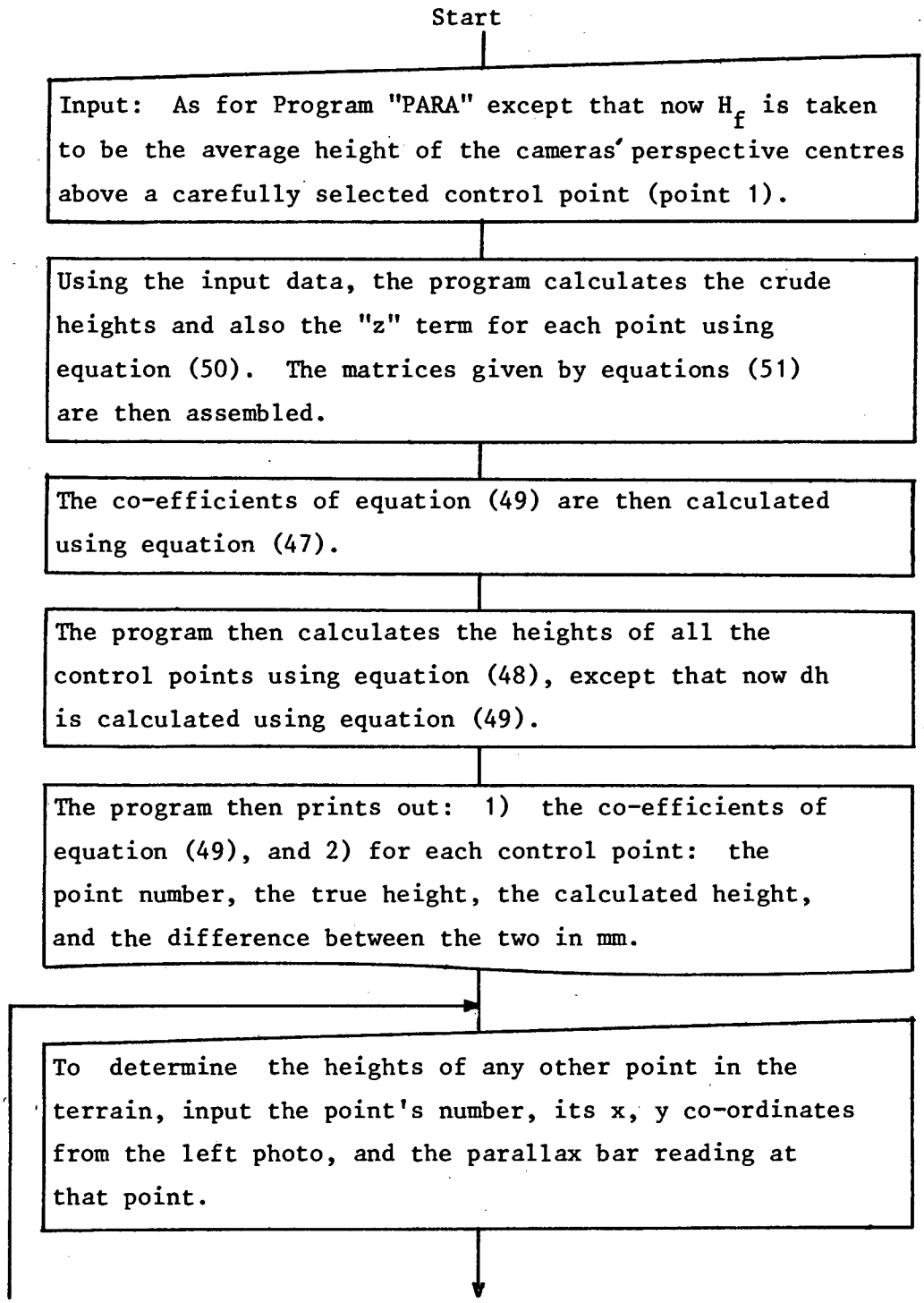

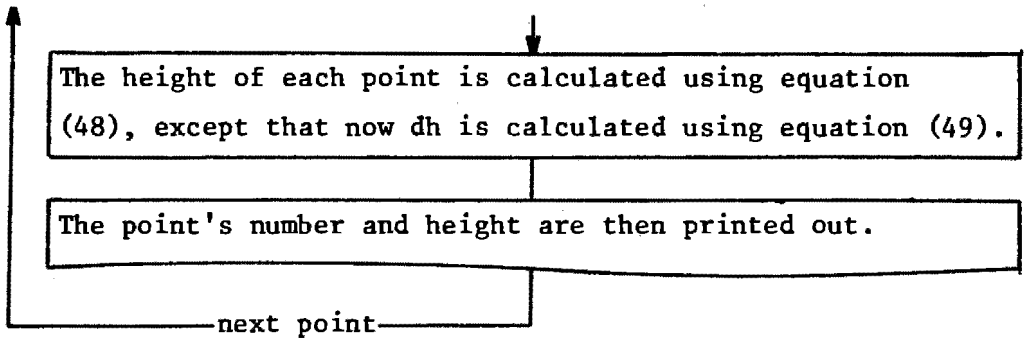

"BREAK" to end.

Note The equations refered to are given in Chapter 4.